

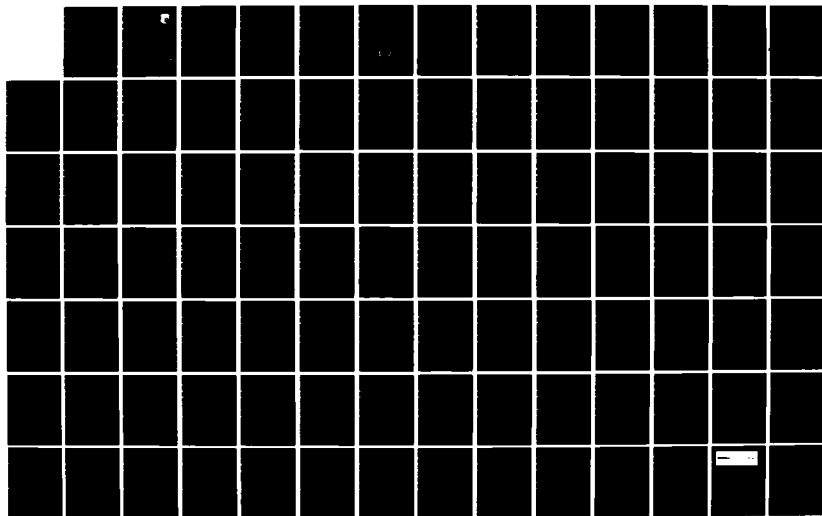
AD-A153 020

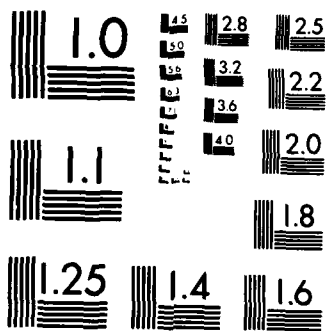
PROCEEDINGS OF THE US AIR FORCE AND THE FEDERAL  
REPUBLIC OF GERMANY DATA. (U) AIR FORCE WRIGHT  
AERONAUTICAL LABS WRIGHT-PATTERSON AFB OH A W FIORE  
AUG 84 F/G 20/4

1/4

UNCLASSIFIED

NL





MICROCOPY RESOLUTION TEST CHART  
NATIONAL BUREAU OF STANDARDS 1963-A

(2)

**AD-A153 020**



VISCOUS AND INTERACTING FLOW FIELD EFFECTS  
PROCEEDINGS OF THE 9TH U.S. AIR FORCE AND  
THE FEDERAL REPUBLIC OF GERMANY DATA  
EXCHANGE AGREEMENT MEETING

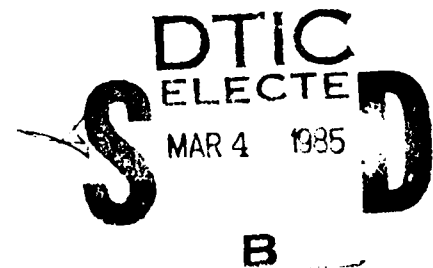
Dr. Anthony W. Fiore  
Aerodynamics Group  
Aeromechanics Division

August 1984

Technical Proceedings Report for Period May 1982 - May 1984

DTIC FILE COPY

Approved for public release; distribution unlimited.



FLIGHT DYNAMICS LABORATORY  
AIR FORCE WRIGHT AERONAUTICAL LABORATORIES  
AIR FORCE SYSTEMS COMMAND  
WRIGHT-PATTERSON AIR FORCE BASE, OHIO 45433

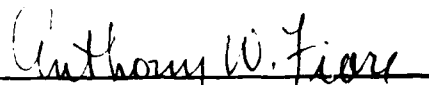
85 02 19 065

NOTICE

When Government drawings, specifications, or other data are used for any purpose other than in connection with a definitely related Government procurement operation, the United States Government thereby incurs no responsibility nor any obligation whatsoever; and the fact that the government may have formulated, furnished, or in any way supplied the said drawings, specifications, or other data, is not to be regarded by implication or otherwise as in any manner licensing the holder or any other person or corporation, or conveying any rights or permission to manufacture use, or sell any patented invention that may in any way be related thereto.

This report has been reviewed by the Office of Public Affairs (ASD/PA) and is releasable to the National Technical Information Service (NTIS). At NTIS, it will be available to the general public, including foreign nations.

This technical report has been reviewed and is approved for publication.

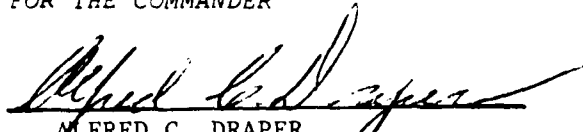


Dr. Anthony W. Fiore  
U.S. Project Officer  
AFWAL/FIMG



Mr. Melvin L. Buck  
Asst. For Exp. Research  
Aeromechanics Division

FOR THE COMMANDER



ALFRED C. DRAPER  
Acting Chief, Aeromechanics Division  
Flight Dynamics Laboratory

"If your address has changed, if you wish to be removed from our mailing list, or if the addressee is no longer employed by your organization please notify AFWAL/FIMG, W-PAFB, OH 45433 to help us maintain a current mailing list".

Copies of this report should not be returned unless return is required by security considerations, contractual obligations, or notice on a specific document.



AD-A153020

REPORT DOCUMENTATION PAGE

1a. REPORT SECURITY CLASSIFICATION UNCLASSIFIED		1b. RESTRICTIVE MARKINGS	
2a. SECURITY CLASSIFICATION AUTHORITY		3. DISTRIBUTION/AVAILABILITY OF REPORT Approved for Public Release, Distribution unlimited.	
2b. DECLASSIFICATION/DOWNGRADING SCHEDULE		5. MONITORING ORGANIZATION REPORT NUMBER(S)	
4. PERFORMING ORGANIZATION REPORT NUMBER(S)		7a. NAME OF MONITORING ORGANIZATION	
6a. NAME OF PERFORMING ORGANIZATION Naval Surface Warfare Center	6b. OFFICE SYMBOL (If applicable) ALWAL/ELM	7b. ADDRESS (City, State and ZIP Code)	
8a. NAME OF FUNDING SPONSORING ORGANIZATION		8b. OFFICE SYMBOL (If applicable)	
8c. ADDRESS (City, State and ZIP Code)		9. PROCUREMENT INSTRUMENT IDENTIFICATION NUMBER	
11. TITLE (Include Security Classification) Cont'd Interaction Flow Field Effects		10. SOURCE OF FUNDING NOS.	
12. PERSONAL AUTHOR(S)		PROGRAM ELEMENT NO. MWDPA	PROJECT NO. AL-71
13a. TYPE OF REPORT		TASK NO.	WORK UNIT NO. 244
13b. TIME COVERED FROM 1 May 84 TO May 84		14. DATE OF REPORT (Yr, Mo., Day) August 1984	
13c. DATE OF REPORT (Yr, Mo., Day)		15. PAGE COUNT 31	
16. SUPPLEMENTARY NOTATION			
17. MOSATI CODES		18. SUBJECT TERMS (Continue on reverse if necessary and identify by block number)	
FIELD	GROUP	SUB GR	
		boundary layer, numerical methods, viscous interaction, fluid mechanics, high Reynolds number.	
19. ABSTRACT (Continue on reverse if necessary and identify by block number)			
<p>The Naval Surface Warfare Center and the Federal Republic of Germany signed a Memorandum of Understanding (MOU) in 1974 titled "Viscous and Interacting Flow Field Effect". The purpose of this MOU was to foster cooperation in the area of boundary layer research. It included both theoretical and experimental boundary layer research at speeds from subsonic to hypersonic flow in the presence of laminar, transitional, and turbulent boundary layers. The primary research area has been on turbulent boundary layers; both attached and separated. The research presented in this report covers the period May 1982 to May 1984. The results were presented at the 1984 Symposium on Naval Surface Weapons Center in Silver Spring, Maryland. The research was conducted in the Department of Aeronautics and Astronautics, Princeton University, and the Naval Surface Warfare Center, Dahlgren Division, F.V.L., and various companies and universities.</p>			
20. DISTRIBUTION/AVAILABILITY OF ABSTRACT UNCLASSIFIED UNLIMITED <input checked="" type="checkbox"/> SAME AS RPT <input type="checkbox"/> DTIC USERS <input type="checkbox"/>		21. ABSTRACT SECURITY CLASSIFICATION UNCLASSIFIED	
22a. NAME OF RESPONSIBLE INDIVIDUAL		22b. TELEPHONE NUMBER (Include Area Code) 134-954-7002	22c. OFFICE SYMBOL ALWAL/ELM

UNCLASSIFIED

SECURITY CLASSIFICATION OF THIS PAGE

11. (Continued)

- Proceedings of the 9th U.S. Air Force and the Federal Republic of Germany Data Exchange Agreement Meeting (UNCLASSIFIED).

UNCLASSIFIED

SECURITY CLASSIFICATION OF THIS PAGE

## FOREWORD

The 9th U.S. Air Force/Federal Republic of Germany Data Exchange Agreement Meeting entitled "Viscous and Interacting Flow Field Effects" numbered MWDDEA AF-75-G-7440 was sponsored by the Air Force Flight Dynamics Laboratory and hosted by the U.S. Navy with Dr. Robert L.P. Voisinnet of the Naval Surface Weapons Center as organizer. It was held on 9/10 May 1984 at the Naval Surface Weapons Center in Silver Springs Maryland. This report contains the detailed proceedings of that meeting. It contains both theoretical and experimental results concerning a great variety of topics in the area of boundary layer research. The speed range extends from subsonic to hypersonic Mach numbers. The types of boundary layers reported include laminar, transitional, and turbulent in the presence of attached and/or separated conditions.

The Air Force wishes to thank Dr. Robert L.P. Voisinnet of the Naval Surface Weapons Center for his fine work in preparing this meeting. Thanks is also extended to the Commander of the Naval Surface Weapons Center for the use of his facilities. In addition, the Air Force wishes to thank all the participants for their scientific contributions.

**DTIC**  
**ELECTE**  
**S** MAR 4 1985 **D**  
**B**

Approved for		<input checked="checked" type="checkbox"/>
Distribution		<input type="checkbox"/>
Availability Codes		<input type="checkbox"/>
Avail and/or		
Special		
A-1		



# TABLE OF CONTENTS

<u>No.</u>	<u>Title</u>	<u>Page</u>
1	A Discrete Element Prediction Approach for Turbulent Flow Over Rough Surfaces: R.T. Taylor, H.W. Coleman, and B.K. Hodge. Mississippi State University. . . . .	1
2	Mixing-Length Formulations For Turbulent Boundary Layers Over Arbitrarily Rough Surfaces: P.S. Granville. David W. Taylor Naval Ship R&D Center. . . . .	13
3	Shock/Boundary Layer Interaction Model For Three-Dimensional Transonic Flow Calculations: J.D. McLean and T.K. Matoi. Boeing Commercial Airplane Company. . . . .	45
4	Boundary Layer Separation Due to "Weak" and "Strong" Viscous - inviscid Interaction On An Inclined Body of Revolution; H.P. Kreplin. D.F.V.L.R. - A.V.A. Germany. . . . .	79
5	Experimental Study of Vortical Features In Three-Dimensional Separated Flow: H. Bippers. D.F.V.L.R. Germany . . . . .	97
6	Axisymmetric Bluff - Body Drag Reduction Through Geometrical Modifications: F.G. Howard and W.L. Goodman. NASA Langley Research Center. . . . .	119
7	Experimental Investigations On Bodies With Noncircular Cross Sections In Compressible Flow (Pressure Distributions): W. Schneider. D.F.V.L.R. - A.V.A. Germany . . . . .	131
8	Mach 3 Three-Dimensional Boundary Layer Turbulence Transport Properties On a Spherically Blunt Cone: D.W. Asherman and W.J. Yanta. Naval Surface Weapons Center. . . . .	155
9	An Experimental Investigation of The Stability of the Laminar Boundary Layer On A Cone at M=8: K.F. Stetson, E.R. Thompson, J.C. Donaldson, and L.G. Siler. Wright-Patterson Air Force Base . . . . .	179
10	Boundary Layer Transition On Blunt Slender Cones at MACH 10: J.A.F. Hill and R.L. Bell. Naval Surface Weapons Center . . . .	187
11	Low Reynolds Number Hypersonic Testing In the NSWC Hypervelocity Wind Tunnel 9: E.R. Hedlund, W.C. Ragsdale, and R.L.P. Voisinet. Naval Surface Weapons Center. . . . .	207
12	Navier-Stokes Computations of Transonic Flow Over A Projectile With a Two-Equation Model of Turbulence: J. Sahu and J.E. Danberg. U.S. Army Ballistic Research Laboratory . . . . .	243

# TABLE OF CONTENTS (CONT'D)

<u>No.</u>	<u>Title</u>	<u>Page</u>
13	P.N.S. Computations For Non-Circular and Finned Body Configurations At Supersonic Velocities: R.U. Jettmar, N.S.W.C. and W. Kardiella, D.F.V.L.R. . . . .	257
14	Effects of Propulsive Jet On The Flow Field In The Tail Region Of A Missile In A Supersonic Stream: G. Kappenwallner, D. Rammenzweig, and W. Stahl. D.F.V.L.R. - A.V.A. . . . .	271
15	Navier-Stokes Calculations of Base Region Flow Fields For Bodies Of Revolution. J. Saher, C.J. Mietubicz, and J.L. Steger. U.S. Army Ballistic Research Laboratory and NASA Ames Research Center . . . . .	293
	LIST OF PARTICIPANTS. . . . .	305

A Discrete Element Prediction Approach for  
Turbulent Flow Over Rough Surfaces

by

Robert P. Taylor, Hugh W. Coleman and B. Keith Hodge  
Mechanical and Nuclear Engineering Department  
Mississippi State University  
Mississippi State, MS 39762

ABSTRACT

A discrete element model for turbulent flow over rough surfaces has been rigorously derived from basic principles. This model includes surface roughness effects as a constituent part of the partial differential equations which describe momentum and energy transport in turbulent flows. The model includes the necessary empirical information on the interaction between the roughness elements and the flow around and between the elements in a general way which does not require experimental data on each specific surface. This empirical information is input via algebraic models for the local element drag coefficient and Nusselt number. These models were calibrated by comparison with base data sets from surfaces with three-dimensional (distributed) roughness elements. Calculations using the present model have been compared with experimental data from 118 separate experimental runs. The results of these comparisons ranged from good to excellent. The calculations compared equally well with both transitionally rough and fully rough turbulent flow results without modification of the roughness model.

## 1. Introduction

In this paper, the authors present a synopsis of the results of a research effort on the prediction of skin friction and heat transfer in turbulent flow over rough surfaces. Details of the development of the discrete element approach, a review of previous work, and more comparisons of predictions with experimental data can be found in References 1-3.

## 2. Modeling of Roughness Effects on Turbulent Flow

In turbulent flow analysis, use of time-averaged equations leads to the necessity of formulating a turbulence model (with empirical input) to achieve closure. A similar situation exists in analysis of flow over rough surfaces. Unless the equations can be solved on a grid which is fine enough to resolve the surface roughness boundary condition, a roughness model (with empirical input) is necessary for closure. Considering the capabilities of present computers, both turbulence and roughness models must be formulated for analysis of practical problems in turbulent flow over rough surfaces. In References 1-3, the authors have described in detail both the classical equivalent sandgrain roughness approach and their discrete element method which incorporates more basic physics of the surface-flow interaction and requires less surface-specific empirical information. A summary is presented below.

Schlichting (4) first proposed the equivalent sandgrain roughness ( $k_s$ ) concept and experimentally determined  $k_s$  for a range of rough surfaces. He defined  $k_s$  as the size of sandgrain in Nikuradse's (5) pipe flow experiments which would give the same skin friction as that observed on a particular rough surface. One problem in using this approach is determining  $k_s$  for a specific surface of interest when no skin friction data are available for that surface. Dvorak (6), Simpson (7) and Dirling (8) all presented correlations which essentially allowed  $k_s$  to be determined based on various geometric characteristics of the roughness elements on the surface. These correlations suffer from two basic problems: (1) they do not correlate the available data well, and (2) they rely primarily on Schlichting's experimental results. The authors (9) have shown that, due to erroneous assumptions in data reduction, Schlichting's results for skin friction are high by amounts

ranging up to 73% and his results for  $k_s$  are high by 26% to 555%. Thus the validity of previous roughness work which has relied heavily on Schlichting's results is open to serious question. In addition, the idea that the effects of all rough surfaces can be modeled using a single length scale ( $k_s$ ) has not been successful in application.

The discrete element roughness model of the authors is totally divorced from any  $k_s$  concepts. In formulating the model, the continuity, momentum and energy equations for a boundary layer were derived from first principles. Included in the derivations were the influences of the surface roughness elements which are shown in Figure 1. These influences are the blockage, the form drag, and the local heat transfer between the fluid and the elements.

The resulting equations, formulated for the special case of three-dimensional uniform roughness elements (such as spheres, hemispheres, cones, etc.), are shown in Figure 2. The shape, size and spacing of the elements are included explicitly through the geometrical descriptors of the roughness-- $D(y)$ ,  $L$  and  $\ell$ . The empirical information is input through algebraic expressions for the element drag coefficient

$$C_D = C_D(\text{Re}(y))$$

and element Nusselt number

$$\text{Nu} = \text{Nu}(\text{Re}(y)) \quad .$$

The  $C_D$  model was calibrated using the corrected (9) skin friction data sets of Schlichting (4) for surfaces with roughness elements of spherical, spherical segment, and conical shapes. The  $\text{Nu}$  model was calibrated using a zero pressure gradient, constant wall temperature data set of Pimenta (10) for a surface of spherical elements in the most dense packing. Once the  $C_D$  and  $\text{Nu}$  models were calibrated, they remained invariant for all subsequent calculations. No empirical information is used for any specific rough surface--only the geometrical description of the roughness is input for "new" surfaces with three-dimensional type roughness. Comparisons of calculations with the calibration data are shown in Figures 3-6.



### 3. Comparisons of Predictions and Data

Comparisons of discrete element model predictions with various additional data sets are presented in References 1-3. Comparisons of predictions with the data of two experimental investigations are presented here as an indication of the merit of the discrete element model.

Chen (11) reported detailed turbulence and skin friction measurements for fully developed air flow through a 0.19 meter diameter pipe roughened with hemispheres. He investigated three roughness densities-- $\ell/k = 18.5$ , 10.7 and 6.4, where  $k$  is the maximum roughness element height. Chen stated that the first two cases ( $\ell/k = 18.5$  and 10.7) were in the transitionally rough regime and the third ( $\ell/k = 6.4$ ) was "nearly" in the fully rough regime. The most interesting part of Chen's work (from the point of view of the present work) is the segregation of the two components of the apparent wall shear stress: (1) that due to the viscous shear ( $\tau_s$ ) on the smooth surface between the roughness elements, and (2) that due to the form drag on the roughness elements. Chen obtained the form drag term by measuring the force on a single element using a force balance. The portion due to the smooth surface was determined by subtracting the roughness element drag component from the total wall shear stress ( $\tau_T$ ) which was determined from pressure drop measurements.

The discrete element model was solved in the appropriate internal circular coordinates and the resulting predictions were compared with Chen's data. Figure 7 shows the comparisons for the skin friction coefficient and the ratio of the smooth wall component to the total shear stress. The comparisons indicate very good agreement. The comparisons of the relative contribution of viscous shear forces between the elements and the drag on the elements are of particular interest. One of the major advantages of the discrete element model is that these two forces and their interactions are accounted for in the model. Inspection of Figure 7 reveals good agreement between the predictions and data for  $\tau_s/\tau_T$ . The maximum disagreement is about 12% and the preponderance of the points agree within 5%. This agreement indicates that the present discrete element model correctly incorporates much of the physics of the interaction between the roughness elements and the flow.

Coleman (12) reported turbulence measurements and skin friction and Stanton number measurements for turbulent boundary layer air flows

over a flat plate with 1.27 mm diameter spherical roughness elements in the most dense packing. Shown in Figure 8 are comparisons of the discrete element model predictions with data for a constant wall temperature, favorable pressure gradient case. The boundary layer was in the fully rough flow regime. The agreement is excellent, with the predictions everywhere within the data uncertainty. Shown in Figure 9 are comparisons of the predictions with data for a variable wall temperature, zero pressure gradient case. Again, the agreement is excellent.

#### 4. Summary

Several points which should be emphasized are: (1) NO information from the Chen or Coleman data sets other than the geometrical description of the rough surfaces was used in the discrete element model calculations. The calculations are therefore truly predictions. (2) The turbulence model used was the standard mixing length model with Van Driest damping, which is widely used for smooth wall flows. No modifications were made because of the roughness. (3) The present discrete element model has been formulated and proven only for three-dimensional type roughness elements which can be approximated as having circular cross-sections in the xz plane. (The development for such elements which are randomly shaped and are of random spacing is given in References 1-3).

This research was sponsored by the Air Force Armament Laboratory, Eglin Air Force Base, FL. under contract F08635-82-K-0062. The authors wish to thank Lt Bruce Haupt, Dr. Lawrence Lijewski and Dr. Donald Daniel for their support and encouragement.

$$u^* = \frac{1}{\kappa \ell^*} \left( \frac{1}{2} - \sqrt{\ell^{*2} + \frac{1}{4}} \right) - \frac{1}{\kappa \ell_w^*} \left( \frac{1}{2} - \sqrt{\ell_w^{*2} + \frac{1}{4}} \right) + \frac{1}{\kappa} \ln \left( \frac{\ell^* + \sqrt{\ell^{*2} + \frac{1}{4}}}{\ell_w^* + \sqrt{\ell_w^{*2} + \frac{1}{4}}} \right) \quad (22)$$

At higher values of  $y^*$ , this relation reduces to the usual log law, Equation (1), so that

$$B_1 = \frac{1}{\kappa} (\ln 4\kappa - 1) - \frac{1}{\kappa \ell_w^*} \left( \frac{1}{2} - \sqrt{\ell_w^{*2} + \frac{1}{4}} \right) - \frac{1}{\kappa} \ln \left( 2\ell_w^* + 2\sqrt{\ell_w^{*2} + \frac{1}{4}} \right) \quad (23)$$

This relates  $B_1$  and  $\ell_w^*$ ; therefore, the velocity profile, Equation (10), is a function of  $y^*$  and  $B_1$ .

## ROTTA II

Rotta<sup>8</sup> seems to have abandoned the laminar sublayer approach in analyzing rough surfaces after the whole concept of a purely laminar flow next to the wall became untenable. Since there are turbulent stresses even in the laminar sublayer, the sublayer has been renamed the viscous sublayer.

Rotta extended the van Driest formulation for smooth surfaces to rough surfaces by adding a length  $\Delta y$  to the  $y$  coordinate such that

$$\ell^* = \kappa(y^* + \Delta y^*) \left\{ 1 - \exp \left[ \frac{-(y^* + \Delta y^*)}{\lambda_{v,s}^*} \right] \right\} \quad (24)$$

Likewise, for the hyperbolic tangent M

$$\frac{v_t}{v} = \frac{2\kappa^2}{\lambda_h^2} y^{*4} + \dots \quad (18)$$

#### EXISTING MIXING-LENGTH METHODS FOR ROUGH SURFACES

Some pertinent existing mixing-length methods for rough surfaces are now critically examined.

##### ROTTA I

An extension of the Prandtl wall mixing length method to rough surfaces, initially proposed by Rotta,<sup>7</sup> assumed a laminar sublayer thickness that would decrease with roughness or

$$\ell^* = \kappa(y^* - y_L^*) \quad (19)$$

where  $y_L$  is the laminar sublayer thickness and  $y_L^* = u_\tau y_L / \nu$ . The introduction of  $\ell^*$  in Equation (10) resulted in an integration in elementary functions and a relation between  $y_L^*$  and  $B_1$

$$y_L^* = B_1 + \frac{1}{\kappa} (1 - \ln 4\kappa) \quad (20)$$

With increasing roughness, the laminar sublayer finally vanishes,  $y_L^* = 0$ , and  $B_1 = -1/\kappa (1 - \ln 4\kappa)$ . This is now considered to be the beginning of the fully rough regime and the end of the intermediate roughness regime.

For the fully rough regime, Rotta assumed an initial mixing length  $\ell_w^*$  at the wall

$$\ell^* = \ell_w^* + \kappa y^* \quad (21)$$

The introduction of this mixing length for the fully rough regime into the velocity profile, Equation (10), results in an analytical solution.

Why  $M$  should equal zero at  $y^* = 0$  requires some further discussion. Theoretical investigations<sup>5</sup> indicate that the eddy viscosity  $\nu_t$  should vary with  $y^{*3}$  or  $y^{*4}$  at  $y^* = 0$ . Now Equation (A.6) in Appendix A relates the eddy viscosity to the mixing length. A Maclaurin expansion gives

$$\frac{\nu_t}{\nu} = 2 \ell^{*2} + \dots \quad (14)$$

or

$$\frac{\nu_t}{\nu} = 2\kappa^2 y^{*2} M^2 + \dots$$

A nonzero value of  $M$  at  $y^* = 0$  such as  $M_1$  would then result in

$$\frac{\nu_t}{\nu} = 2\kappa^2 M_1^2 y^{*2} + \dots \quad (15)$$

which is not acceptable.

A Maclaurin expansion of the van Driest  $M$  gives

$$M = \frac{y^*}{\lambda_v^*} + \dots \quad (16)$$

and

$$\frac{\nu_t}{\nu} = \frac{2\kappa^2}{\lambda_v^{*2}} y^{*4} + \dots \quad (17)$$

which is acceptable.

where  $\ell^*$  is a nondimensional mixing length,  $\ell^* = u_\tau \ell / \nu$ , and  $u^*$  is a nondimensional velocity,  $u^* = u / u_\tau$ .

Solving for  $du^*/dy^*$  as a quadratic expression and integrating from the wall, where  $y^* = 0$  and  $u^* = 0$ , results in a velocity profile

$$u^* = \int_0^{y^*} \frac{2}{1 + \sqrt{1 + (2\ell^*)^2}} dy^* \quad (10)$$

Close to the wall Prandtl proposed a linear variation of mixing length with distance from the wall

$$\ell^* = \kappa y^* \quad (11)$$

where  $\kappa$  is the von Kármán constant. Use of this relation, in Equation (10), leads to a logarithmic velocity law with  $A = 1/\kappa$ . However, an erroneous value of  $B_1$  results. Furthermore, in so far as the logarithmic velocity law does not hold right up to the wall, so the Prandtl wall mixing length does not hold. To remedy this, a modification function  $M(\ell^* = M\kappa y^*)$  is needed as a function of  $y^*$  and  $\lambda^*$  where  $\lambda^*$  is an additional nondimensional length,  $\lambda^* = u_\tau \lambda / \nu$ . Furthermore,  $M$  should equal zero at  $y^* = 0$  and equal unity at  $y^* \rightarrow \infty$ .

For smooth surfaces, van Driest proposed<sup>14</sup> the representation

$$M = 1 - \exp\left(\frac{-y^*}{\lambda_v^*}\right) \quad (12)$$

where  $\lambda_v^*$  is the  $\lambda^*$  associated with van Driest.

Other modification functions may be formulated as, for example, the hyperbolic tangent function alluded to by Patel<sup>15</sup>

$$M = \sqrt{\tanh\left(\frac{y^*}{\lambda_h^*}\right)^2} \quad (13)$$

where  $\lambda_h^*$  is the  $\lambda^*$  used here.

$$\Delta B [k^*, T] = B_1 [k^*, T] - B_{1,s} \quad (6)$$

As defined,  $\Delta B$  is always negative for rough surfaces. Nikuradse<sup>10</sup> used the  $B_r$ -characterization while Hama<sup>11</sup> preferred the  $\Delta B$  (actually  $-\Delta B$ ) characterization.

To experimentally determine a characterization for a specific arbitrarily rough surface, there are various procedures available. The direct procedure requires velocity measurements close to the wall to define a logarithmic law as well as the measurement of the wall shear stress. Simpler, indirect procedures may be used involving measurement of the average velocity of pipe flow,<sup>10</sup> the total drag of a flat plate,<sup>12</sup> or the torque of a rotating disk.<sup>13</sup>

#### MIXING-LENGTH THEORY

According to the Prandtl mixing-length theory, the turbulent shear stress ( $\tau_t$ ) is related to the velocity gradient by

$$\frac{\tau_t}{\rho} = \ell^2 \left( \frac{du}{dy} \right)^2 \quad (7)$$

where  $\ell$  is the mixing length which, in general, is not constant, but is a function of its position in the flow field.

The total shear stress  $\tau$  at a point in the flow field is the sum of laminar  $\tau_l$  and turbulent  $\tau_t$  shear stresses or

$$\frac{\tau}{\rho} = \nu \frac{du}{dy} + \ell^2 \left( \frac{du}{dy} \right)^2 \quad (8)$$

where  $\frac{\tau_l}{\rho} = \nu \frac{du}{dy}$ , the Newtonian Law of Viscosity.

For a shear layer with zero longitudinal pressure gradient,  $\tau \approx \tau_w$  close to the wall. With this approximation, Equation (8) may be written in a nondimensional form

$$\ell^{*2} \left( \frac{du^*}{dy^*} \right)^2 + \frac{du^*}{dy^*} = 1 \quad (9)$$

$$B_r = B_1 + A \ln k^* \quad (3)$$

Here  $u$  = streamwise velocity component

$u_\tau$  = shear velocity,  $u_\tau = \sqrt{\tau_w/\rho}$

$\tau_w$  = wall shear stress

$\rho$  = density of fluid

$y^* = u_\tau y/\nu$

$y$  = normal distance from wall

$\nu$  = kinematic viscosity of fluid

$T$  = texture of roughness configuration,  $T = k/k_1, k_1/k_2 \dots$

$k^*$  = roughness Reynolds number,  $k^* = u_\tau k/\nu$

Either  $B_1$  or  $B_r$  may be considered to be a roughness drag characterization function. Both  $B_1$  and  $B_2$  are functions of roughness Reynolds number  $k^*$  and texture  $T$ .

The usual roughness regimes are

1. Hydraulically smooth

$$B_1 = B_{1,s} = \text{constant} \quad (4)$$

$$B_r = B_{1,s} + A \ln k^*$$

2. Intermediate roughness

Both  $B_1$  and  $B_r$  vary with  $k^*$  for the same  $T$

3. Fully rough

$$B_r = \hat{B}_r [T] = \text{constant} \quad (5)$$

$$B_1 = \hat{B}_r [T] - A \ln k^*$$

Another drag characterization is given by  $\Delta B$  which represents a deviation from smooth conditions or



van Driest modification to the Prandtl wall mixing-length formulation provided a turbulent shear stress which started at the wall. Rotta<sup>8</sup> then adapted the van Driest-Prandtl mixing length for smooth surfaces to rough surfaces by shifting the position of the reference wall an appropriate distance. Rotta presented the numerical results in graphical form for two well-known roughnesses: the Nikuradse sand-grain roughness and the Colebrook-White engineering roughness. Later Cebeci and Smith<sup>2</sup> provided an analytical fit to the wall shift for the sand-grain roughness which was then used by Cebeci and Chang<sup>9</sup> for calculations of turbulent boundary layers over rough surfaces.

For arbitrarily rough surfaces, the van Driest factor is correlated in this paper with the roughness drag characterization function until a limiting value of zero is reached. This is considered to represent the beginning of the fully rough regime. Then, for the fully rough regime, the mixing length is considered to assume an initial value at the wall in accordance with Rotta's original (1950) analysis.

For purposes of comparison, the second Rotta analysis of a wall shift is generalized to produce numerical results for the drag characterization of arbitrary roughness. In Appendix A, an explicit conversion of mixing-lengths to eddy viscosities is derived. In Appendix B, the associated turbulent kinetic energies ( $k$ ) and turbulent dissipation rate ( $\epsilon$ ) are developed.

#### CHARACTERIZATION OF ROUGHNESS DRAG

A brief review is presented of pertinent features of the velocity similarity laws and the associated drag characterizations of rough surfaces.

Close to the wall, the logarithmic velocity law for an arbitrarily rough surface, defined by a sufficient number of length factors  $k, k_1, k_2, \dots$ , is given in what may be called the Reynolds-number mode as

$$\frac{u}{u_\tau} = A \ln y^* + B_1 [k^*, T] \quad (1)$$

and, in what may be called the relative-roughness mode, as

$$\frac{u}{u_\tau} = A \ln \frac{y}{k} + B_r [k^*, T] \quad (2)$$

where

MIXING-LENGTH FORMULATIONS FOR TURBULENT BOUNDARY LAYERS  
OVER ARBITRARILY ROUGH SURFACES

By

Paul S. Granville  
David W. Taylor Naval Ship R&D Center  
Bethesda, Maryland 20084

ABSTRACT

Mixing lengths are formulated for turbulent boundary layers over arbitrarily rough surfaces from both the van Driest and Rotta procedures. The associated eddy viscosities, turbulent kinetic energies and dissipation rates are also formulated.

INTRODUCTION

The development of turbulent boundary layers over arbitrarily rough surfaces may be predicted by mixing-length formulations close to the boundary wall. Existing calculation methods for smooth surfaces using the Prandtl-van Driest wall mixing length may be adapted to arbitrarily rough surfaces. Such methods for smooth surfaces are the method of Patankar and Spalding,<sup>1\*</sup> the method of Cebeci and Smith,<sup>2</sup> or its subsequent modification by Nituch et al.<sup>3</sup> and the method of Huang et al.<sup>4</sup>

Wall mixing lengths, or rather the associated eddy viscosities, are also required for heat or mass transfer methods using turbulent Prandtl numbers or turbulent Schmidt numbers to predict the turbulent diffusivities of heat or mass.<sup>5</sup> Furthermore, mixing lengths or eddy viscosities near the wall may be required as boundary conditions to the  $k$ - $\epsilon$  transport equations for improved predictions of the development of turbulent boundary layers.<sup>6</sup> In general, the mixing length increases with distance away from the wall until a limiting value is reached which is compatible to the mixing length for the outer region.

Initially, in 1950, Rotta<sup>7</sup> considered the Prandtl wall mixing length for turbulent shear stress to apply only outside the laminar sublayer and was able to correlate the laminar sublayer thickness with the roughness drag characterization function. However, subsequent turbulence measurements showed that turbulent shear stresses start at the wall. The concept of a purely laminar sublayer was discarded and the laminar sublayer was renamed the viscous sublayer. For smooth surfaces, the

---

\*A complete listing of references is given on page 43.

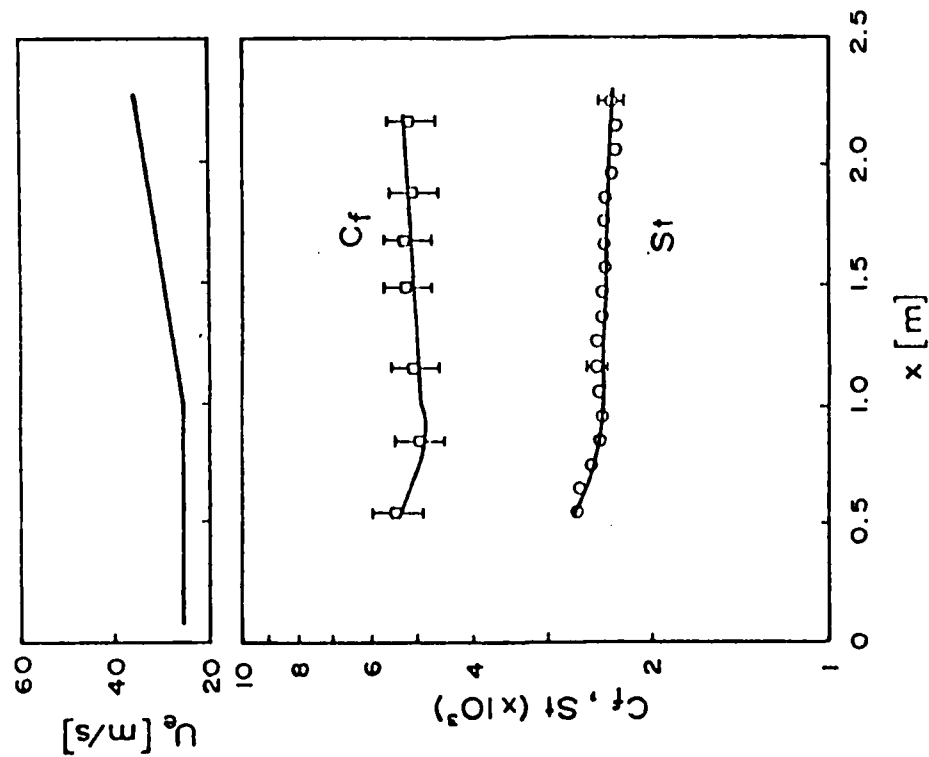


Figure 8. Comparison of Predictions with Data of Coleman for Turbulent Boundary Layer on a Constant Temperature Flat Plate with Favorable Pressure Gradient Imposed

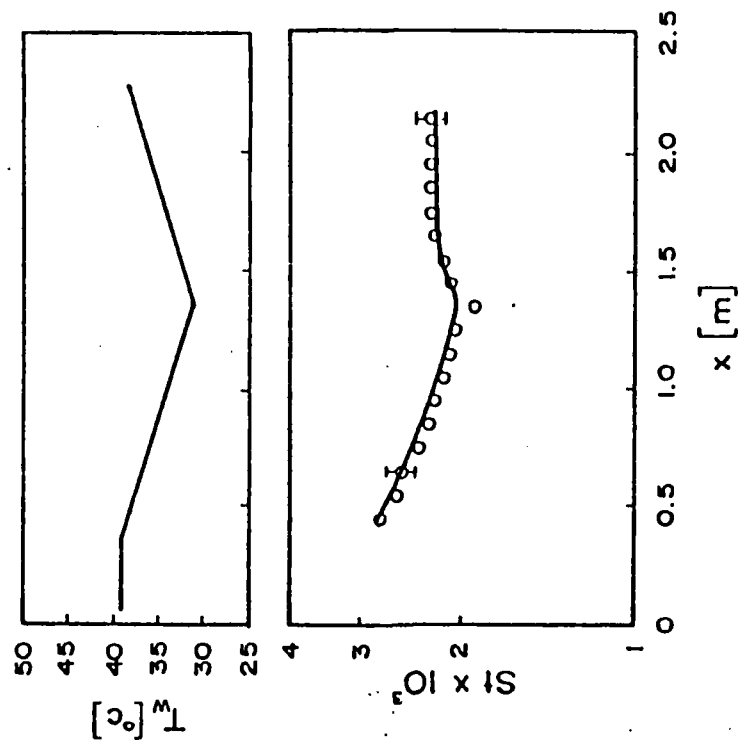


Figure 9. Comparison of Calculations with the Data of Coleman; Bi-linear Wall Temperature Distribution

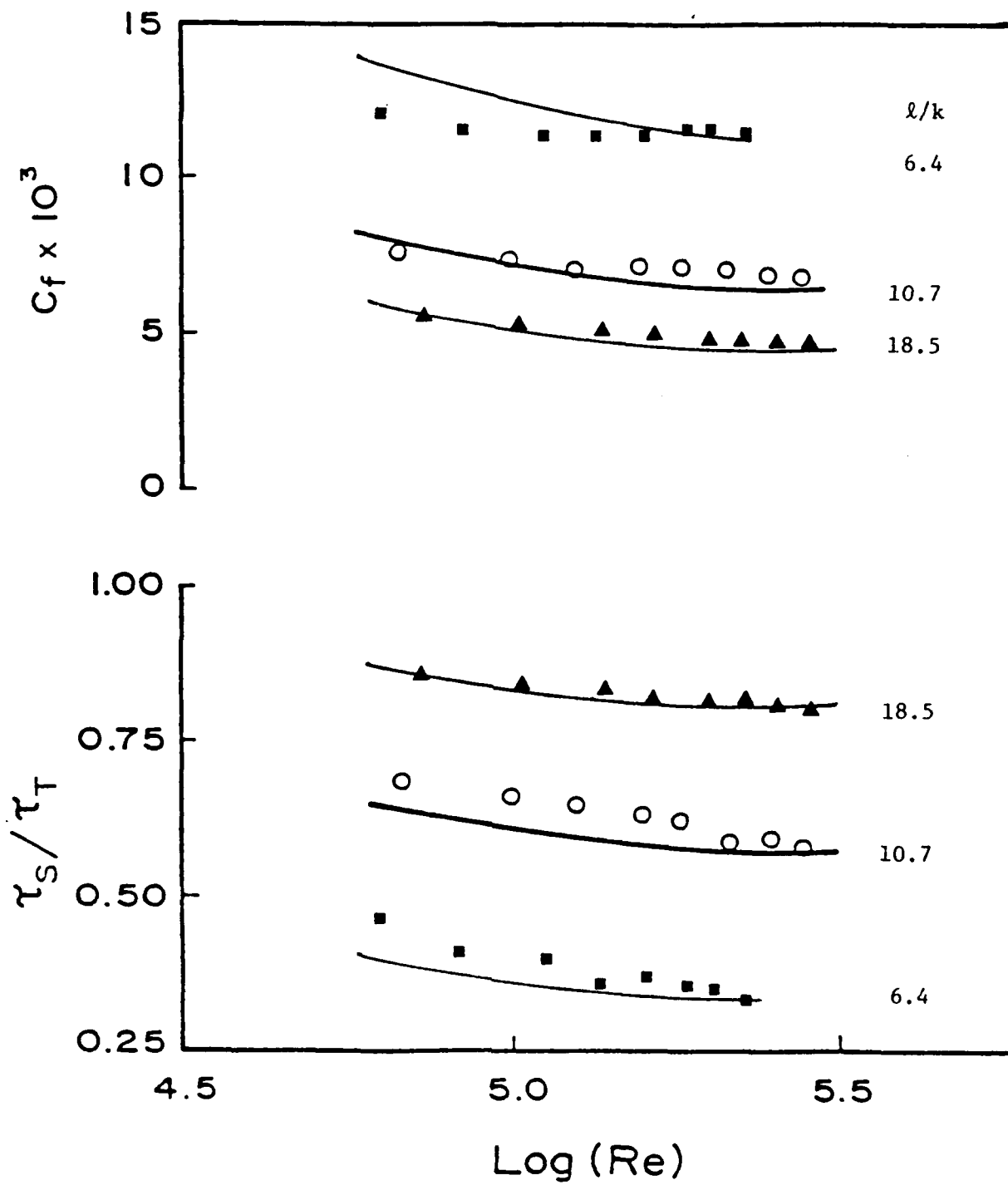


Figure 7. Comparison of Discrete Element Model Predictions with the Data of Chen

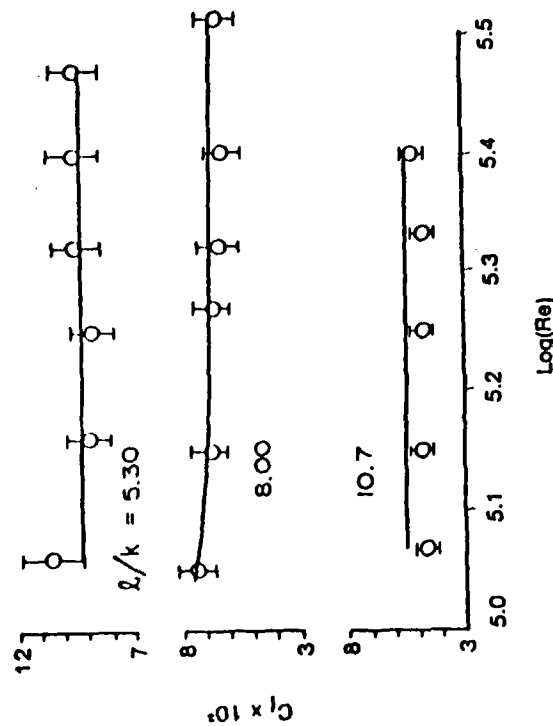


Figure 5. Comparison of Calculations with the Corrected Skin Friction Data of Schlichting for Cones (Calibration Data)

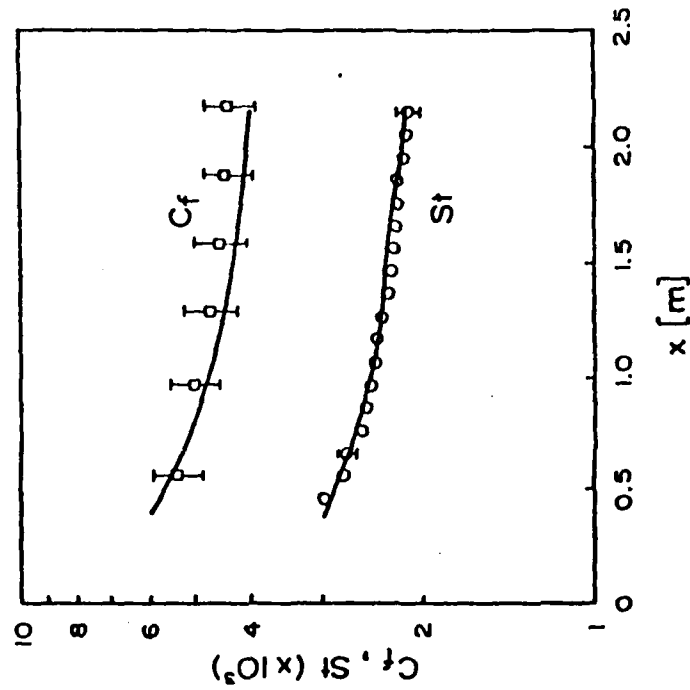


Figure 6. Comparison of Calculations with the Flat Plate Stanton Number (Calibration) Data of Pimenta and Comparison of Predictions with Skin Friction Data.  
 $u_{\infty} = 27 \text{ m/sec.}$

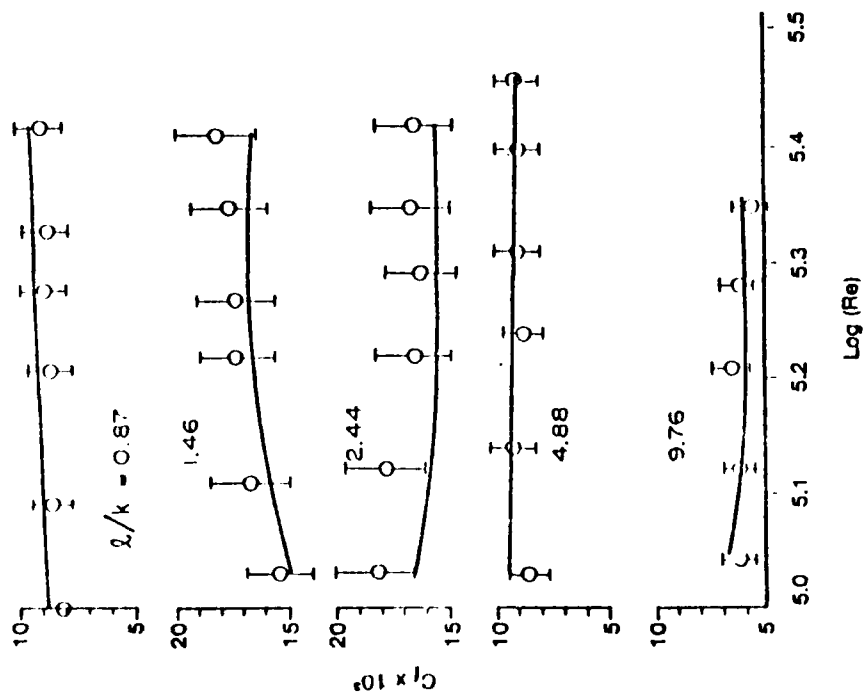


Figure 3. Comparison of Calculations with the Corrected Skin Friction Data of Schlichting for Spheres (Calibration Data)

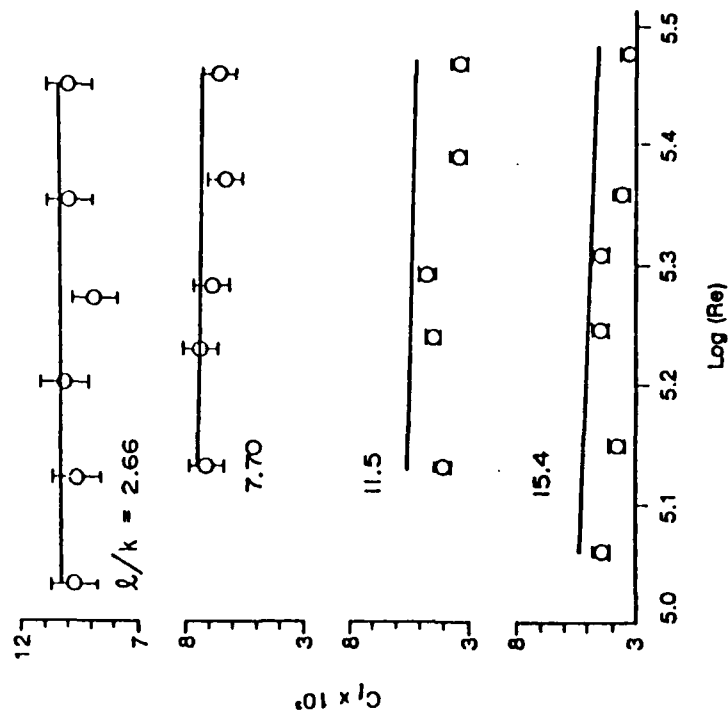


Figure 4. Comparison of Calculations with the Corrected Skin Friction Data of Schlichting for Spherical Segments (Calibration Data)

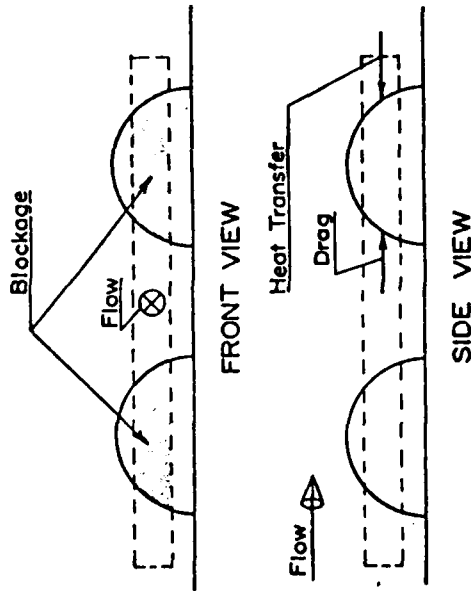


Figure 1. Schematic of Rough Surface Showing Physical Effects Included in Discrete Element Modeling Approach

MASS:

$$\frac{\partial}{\partial x} (\rho \beta_{yz} u) + \frac{\partial}{\partial y} (\rho \beta_{xz} v) = 0$$

MOMENTUM:

$$\rho \beta_{yz} u \frac{\partial u}{\partial x} + \rho \beta_{xz} v \frac{\partial u}{\partial y} = - \frac{\partial}{\partial x} (\beta_{yz} p) + \frac{\partial}{\partial y} (\beta_{xz} \tau) - \rho C_D u^2 b(y) / 2Ll$$

ENERGY:

$$\begin{aligned} \rho \beta_{yz} u \frac{\partial h}{\partial x} + \rho \beta_{xz} v \frac{\partial h}{\partial y} = & - \frac{\partial}{\partial y} (\beta_{xz} q) - (\beta_{xz} \tau) \frac{\partial u}{\partial y} \\ & + u \frac{\partial}{\partial x} (\beta_{yz} p) + \rho C_D u^3 b(y) / 2Ll \\ & + \pi \mu c (Nu) (T_R - T) / Pr Ll \end{aligned}$$

Where:  $\beta_{xz} = \beta_{yz} = (1 - \frac{\pi D^2(y)}{4Ll})$ , the blockage factor  
 $C_D = C_D(Re(y))$ , the roughness element drag coefficient  
 $Nu = Nu(Re(y))$ , the roughness element Nusselt number  
 $Re(y) = u(y)D(y)/\nu$ , the local Reynolds number  
 $D(y) =$  roughness element diameter  
 $L, l =$  roughness element spacing in longitudinal and transverse directions

Figure 2. 2-D Compressible Turbulent Boundary Layer Equations Including Roughness Effects

## REFERENCES

1. Coleman, H. W., Hodge, B. K., and Taylor, R. P., "Generalized Roughness Effects on Turbulent Boundary Layer Heat Transfer," USAF AFATL-TR-83-90, November 1983.
2. Taylor, R. P., Coleman, H. W., and Hodge, B. K., "A Discrete Element Prediction Approach for Turbulent Flow Over Rough Surfaces," Report TFD-84-1, Mech. and Nuc. Eng. Dept., Miss. State Univ., February 1984.
3. Taylor, R. P., "A Discrete Element Prediction Approach for Turbulent Flow Over Rough Surfaces," Ph.D. Dissertation, Mississippi State University, 1983.
4. Schlichting, H., "Experimental Investigation of the Problem of Surface Roughness," Ingenieur-Archiv, Vol. VII, No. 1, 1936; NACA TM 823, 1937.
5. Nikuradse, J., "Laws for Flows in Rough Pipes," VDI-Forschungsheft 361, Series B, Vol. 4, 1933; NACA TM 1292, 1950.
6. Dvorak, F. A., "Calculation of Turbulent Boundary Layers on Rough Surfaces in Pressure Gradients," AIAA Journal, Vol. 7, 1969, pp. 1752-1759.
7. Simpson, R. L., "A Generalized Correlation of Roughness Density Effects on the Turbulent Boundary Layer," AIAA Journal, Vol. 11, 1973, pp. 242-244.
8. Dirling, R. B., Jr., "A Method for Computing Rough Wall Heat Transfer Rates on Reentry Nose Tips," AIAA Paper No. 73-763, 1973.
9. Coleman, H. W., Hodge, B. K., and Taylor, R. P., "A Re-Evaluation of Schlichting's Surface Roughness Experiment," accepted for publication in J. Fluids Engrg., 1984.
10. Pimenta, M. M., "The Turbulent Boundary Layer: An Experimental Study of the Transport of Momentum and Heat with the Effect of Roughness," Ph.D. Dissertation, Dept. Mech. Eng., Stanford Univ., 1975; Report HMT-21.
11. Chen, C. K., "Characteristics of Turbulent Flow Resistance in Pipes Roughened with Hemispheres," Ph.D. Dissertation, Washington State Univ., 1971.
12. Coleman, H. W., "Momentum and Energy Transport in the Accelerated Fully Rough Turbulent Boundary Layer," Ph.D. Dissertation, Dept. Mech. Eng., Stanford Univ., 1976; Report HMT-24.



where  $\lambda_{v,s}^*$  is the value of  $\lambda_v^*$  for smooth surfaces. When this mixing length is incorporated into the velocity profile, Equation (10), and related to the logarithmic law, Equation (1),  $\Delta y^*$  becomes a function of  $B_1[k^*, T]$ . Instead of solving the general case of  $\Delta y^* = f[B_1]$ , Rotta solved  $\Delta y^* = f[k^*]$  for the Nikuradse sand-grain roughness and  $\Delta y^* = f[k^*]$  for the Colebrook-White engineering roughness and presented the results graphically. Cebeci and Smith<sup>2</sup> fitted the results for the Nikuradse sand-grain roughness to an empirical formula. Subsequently, Cebeci and Chang<sup>9</sup> used this formula in boundary-layer calculations.

The Rotta formulation leads to an initial value of  $\ell^*$ , namely,  $\ell_w^*$  at the wall (for  $y^* = 0$ ) or

$$\ell_w^* = \kappa \Delta y^* \left[ 1 - \exp \left( \frac{-\Delta y^*}{\lambda_{v,s}^*} \right) \right] \quad (25)$$

Hence  $\ell_w^* = f[B_1] = f[k^*, T]$  for all roughness regimes.

DAHM

Dahm<sup>16</sup> proposed a differential equation for the mixing lengths of rough surfaces based on empirical considerations, which, for zero mass injection, becomes

$$\frac{d\ell^*}{dy^*} = \frac{0.4 y^* - (\ell^* - \ell_w^*)}{11.83} \quad (26)$$

Examination indicates that this equation is a linear differential equation with a solution given by

$$\ell^* = 0.4 y^* + \ell_w^* + (0.4)(11.83) \left( \frac{1}{e^{y^*/11.83}} - 1 \right) \quad (27)$$

It may be noted that this formula resembles that of Rotta, Equation (21), for the fully rough regime ( $\kappa=0.4$ ; also at  $y^*=0$ , and  $\ell^*=\ell_w^*$ ). In actual use, values of  $\ell_w^*$  would have to be correlated with drag characterization ( $B_1$ ).

#### PROPOSED NEAR-WALL MIXING LENGTHS\* FOR ROUGH SURFACES

##### GENERAL

Equating the velocity profiles obtained from mixing lengths, Equation (10), and the logarithmic law, Equation (1), produces

$$B_1 = \int_0^{\tilde{y}^*} \frac{2}{1 + \sqrt{1 + (2\ell^*)^2}} dy^* - \frac{1}{\kappa} \ln \tilde{y}^* \quad (28)$$

and with

$$\ln \tilde{y}^* = \int_1^{\tilde{y}^*} \frac{dy^*}{y^*} \quad (29)$$

$$B_1 = \int_0^1 \frac{2}{1 + \sqrt{1 + (2\ell^*)^2}} dy^* + \int_1^{\tilde{y}^*} \left[ \frac{2}{1 + \sqrt{1 + (2\ell^*)^2}} - \frac{1}{\kappa y^*} \right] dy^* \quad (30)$$

or

$$B_1 = I_1 + I_2 \quad (31)$$

where  $\tilde{y}^*$  is a sufficiently large value of  $y^*$  so that the second integrand of Equation (30),  $dI_2/dy^*$ , becomes negligible.

##### INTERMEDIATE ROUGHNESS REGIME

With the Prandtl-van Driest mixing length,

$$\ell^* = \kappa y^* \left[ 1 - \exp \left( \frac{-y^*}{\lambda_v^*} \right) \right] \quad (32)$$

in Equation (30), the van Driest factor  $\lambda_v^*$  becomes a function of  $B_1$  and, hence, a function of roughness factors,  $k^*$  and  $T$  or  $\lambda_v^* = f[B_1] = f[k^*, T]$ .

Numerically then,  $\lambda_v^*$  from the preceding equation decreases with decreasing values of  $B_1$  until the limit  $\lambda_v^* = 0$  is reached. Then,  $\ell^* = \kappa y^*$ . This is the same limit as Rotta I where the laminar sublayer disappears.

The range of  $\lambda_v^*$  from its smooth value of  $\lambda_{v,s}^*$  to its zero limit, may be considered to cover the intermediate roughness regime, at  $\lambda_{v,s}^* > \lambda_v^* > 0$ .

#### FULLY ROUGH REGIME

The original Rotta I proposal of an initial mixing length  $\ell_w^*$  at the wall for the fully rough regime will now be considered appropriate. Accordingly, Equations (11), (22), and (23) apply.

#### GENERALIZED ROTTA II

In order to make comparisons, the Rotta II method of an additional length  $\Delta y$  is now generalized. The Rotta II mixing length for rough surfaces, Equation (24), is substituted into either Equation (28) or (30) for  $B_1$  so that  $\Delta y^*$  becomes a function of  $B_1$ , so that  $\Delta y^* = f[B_1] = f[k^*, T]$ .

#### DISCUSSION

Two methods have been described for the prediction of mixing lengths for arbitrarily rough surfaces. There is the Rotta II method which is generalized in terms of the roughness characterization function and applies to both the intermediate and fully rough regimes. The Rotta II method extends the van Driest formula for smooth surfaces to rough surfaces by means of a normal distance parameter.

The other method described consists of an extension of the van Driest formula to the intermediate roughness regime; the van Driest factor is correlated to the roughness characterization function. For the fully rough regime the Rotta I method is to be used in which a wall mixing length is related to the roughness characterization function. The relative merits of each method are now discussed.

For the intermediate roughness regime, the Rotta II method leads to an initial mixing length, Equation (25), at the wall while the van Driest factor method gives

a zero mixing length. A nonzero mixing length at the wall implies the existence of a nonzero turbulent shear stress and a nonzero eddy viscosity at the wall as is demonstrated next.

Now the turbulent shear stress near the wall, Equation (7), nondimensionalized to

$$\frac{\tau_t}{\tau_w} = \ell^{*2} \left( \frac{du^*}{dy^*} \right)^2 \quad (33)$$

becomes, by use of Equation (10) for  $du^*/dy^*$

$$\frac{\tau_t}{\tau_w} = \left[ \frac{2\ell^*}{1 + \sqrt{1 + (2\ell^*)^2}} \right]^2 \quad (34)$$

then, at the wall  $y^* = 0$ ,

$$\left( \frac{\tau_t}{\tau_w} \right)_w = \left[ \frac{2\ell_w^*}{1 + \sqrt{1 + (2\ell_w^*)^2}} \right]^2 \quad (35)$$

Consequently, at the wall, the Rotta II method has a wall value of turbulent shear stress, but the van Driest factor method has none.

Also for the eddy viscosity, Equation (A.6) gives

$$\left( \frac{\nu_t}{\nu} \right)_w = \frac{1}{2} \sqrt{1 + (2\ell_w^*)^2} - \frac{1}{2} \quad (36)$$

Again, the Rotta II method has an initial value of eddy viscosity at the wall while the van Driest factor method has none. In fact, the van Driest factor method applied to the intermediate rough regime retains the variation of eddy viscosity with  $y^{*4}$  at the wall.

For the intermediate roughness regime, an initial value of mixing length, turbulent shear stress, and eddy viscosity at the wall may all be considered objectionable.

## NUMERICAL RESULTS

In determining  $B_1$  from an integration of mixing lengths by means of Equation (30), it is necessary to specify a limiting value of  $y^*$  so that the integrand of  $I_2$  becomes practically zero. As an example, the integrand  $y^* (dI_2/dy^*)$  is plotted in Figure 1 for the smooth case  $\lambda_v^* = 26$  and for the case of the beginning of the fully rough regime  $\lambda_v^* = 0$  with  $\kappa = 0.4$  (the same case as for ROTTA II). To compensate for the logarithmic abscissa, the ordinate is multiplied by  $y^*$  so that the area under the curve represents the integral  $I_2$ . Then,  $dI_2/dy^* = y^* (dI_2/dy^*) (d \ln y^* / dy^*)$ . At values of  $y^*$  above about 200 the integrand is close to zero.

In Figure 2, the van Driest factor  $\lambda_v^*$  is correlated with drag characterization function  $B_1$  for the intermediate roughness regime by means of Equation (35). This accommodates any arbitrary roughness. The limiting value is  $B_1 = -1.325$  for  $\lambda_v^* = 0$ . Smaller values of  $B_1$  are then in the fully rough regime.

The wall mixing length  $\ell_w^*$  for the fully rough regime is plotted against the drag characterization function  $B_1$  in Figure 3 in accordance with the Rotta I relation, Equation (23).

In Figures 4 and 5 the Rotta factor  $\Delta y^*$  is plotted against the drag characterization function  $B_1$ , as a result of solving Equations (24) and (30). This correlation applies to any arbitrary rough surface and, consequently, includes the Nikuradse sand-grain roughness and the Colebrook-White roughness.

A comparison is shown in Figure 6 for the mixing length  $\ell_w^*$  at the wall as a function of the roughness characterization function  $B_1$ . It should be noted that the Rotta II formulation has values of  $\ell_w^*$  in the intermediate roughness regime in accordance with Equation (25). On the other hand, the van Driest formulation has a zero value. For the fully rough regime the Rotta I values are compared to the Rotta II values of  $\ell_w^*$ .

A comparison of the variation of mixing lengths  $\ell^*$  with normal distance  $y^*$  is displayed in Figure 7 for various formulations on the basis of equal values of  $B_1$ . The smooth case is shown for a van Driest factor of 26. As an example of the intermediate roughness regime, a comparison is shown between the van Driest and

Rotta II formulations for  $B_1 = 2$ . It is to be noted that the Rotta II value of the mixing length is larger close to the wall. This is a result of having an initial value  $\ell_w^*$  at the wall. Mixing lengths at the border between the intermediate roughness and fully rough regimes are also compared. Here  $\lambda_v^* = 0$  and  $B_1 = -1.325$ . For the fully rough regime, an example comparison is shown for  $B_1 = -6$ . It is to be further noted that for large values of  $y^*$  all the values of  $\ell^*$  tend to converge to the original Prandtl wall mixing length of  $\ell^* = \kappa y^*$  as expected.

#### SUMMARY

For arbitrarily rough surfaces, two procedures have been developed. First is the extension of the Prandtl-van Driest formulation, Equation (12), to the intermediate roughness regime. Here the van Driest factor  $\lambda_v^*$  is correlated with drag characterization  $B_1$  in Figure 2. For the fully rough regime, the Rotta I procedure may be used as given by Equation (23) which is plotted in Figure 3 as  $\ell_w^*$  against  $B_1$ . Second, there is the Rotta II correlation, Equation (24), developed for arbitrarily rough surfaces. Figure 4 shows the correlation of  $\Delta y^*$  with  $B_1$  for the intermediate roughness regime and Figure 5 shows that for the fully rough regime.

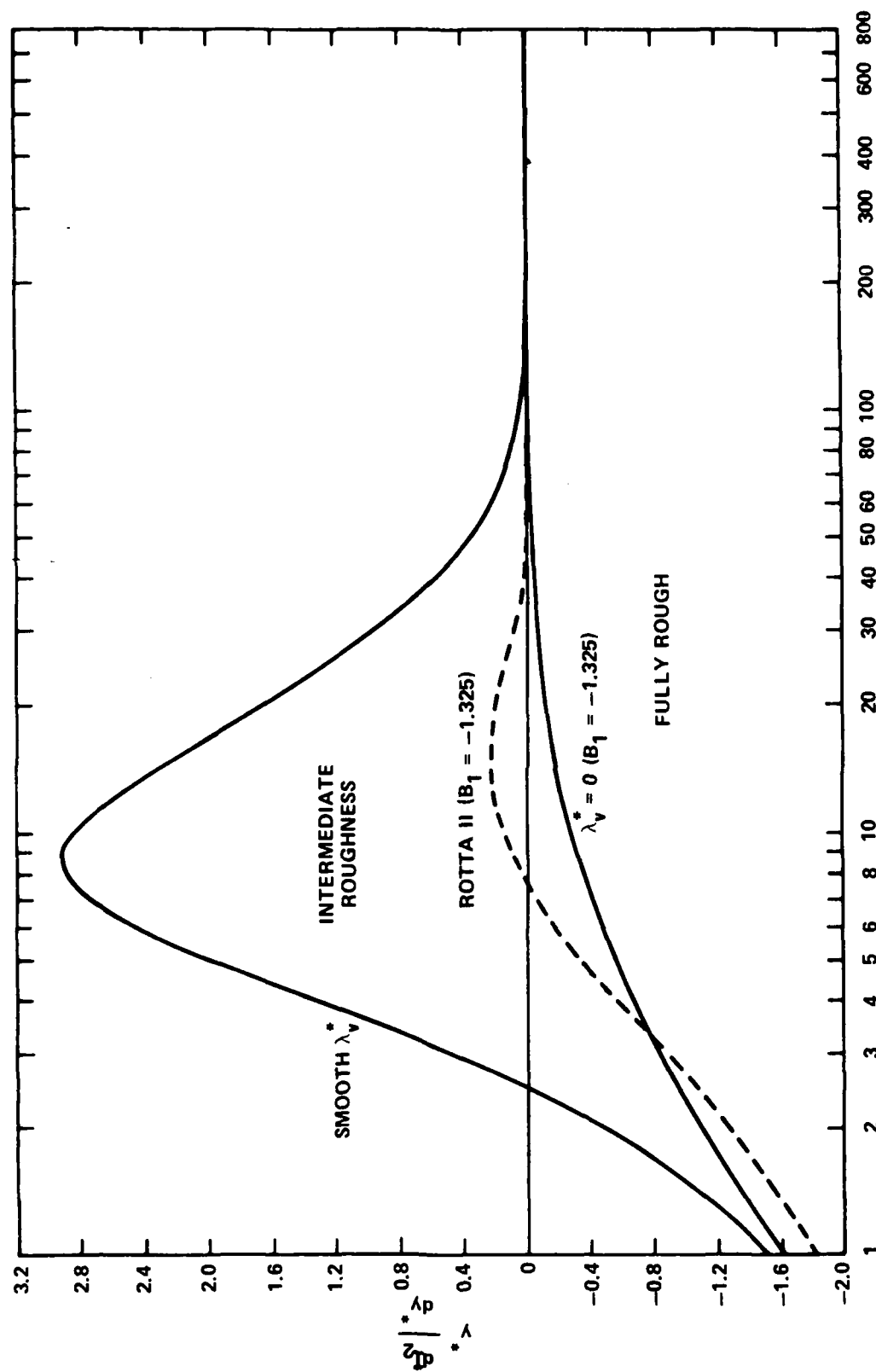


Figure 1 - Variation of Integrand  $y^* \left( \frac{dI_2}{dy} \right)^*$  with  $y$

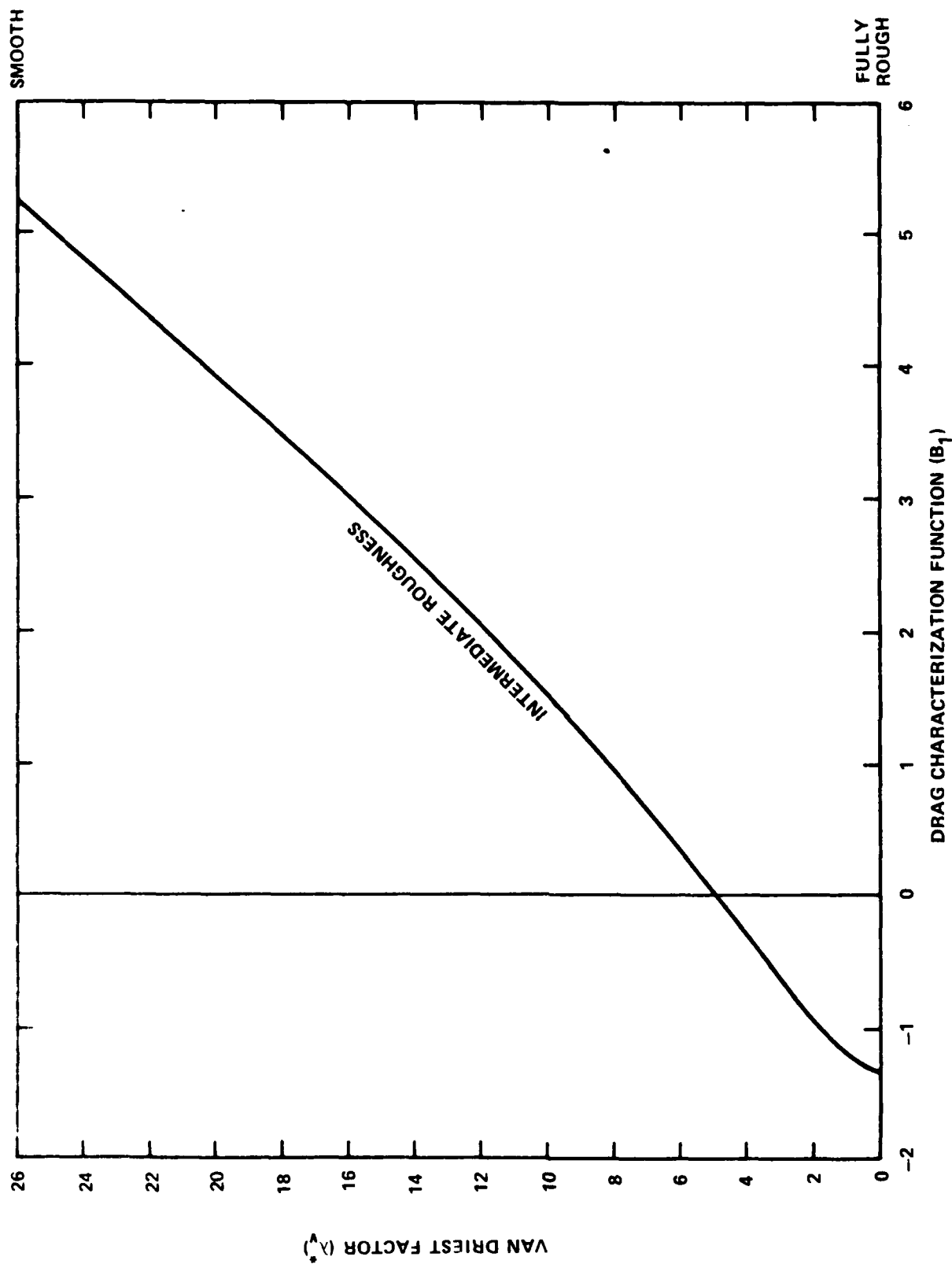


Figure 2 - Plot of  $\lambda_v^*$  versus  $B_1$  for Intermediate Roughness Regime



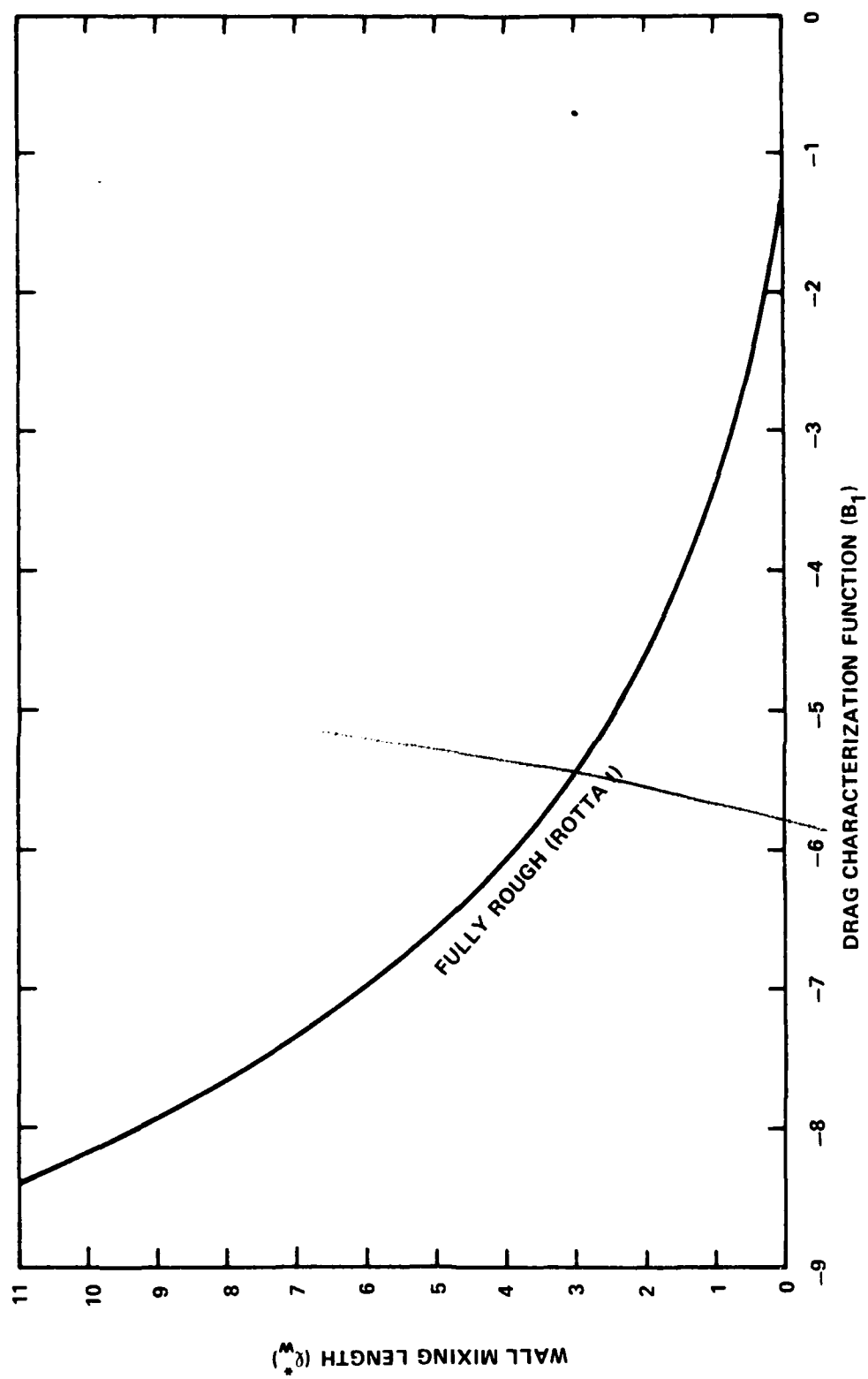


Figure 3 - Plot of Rotta I  $l_w^*$  versus  $B_1$  for Fully Rough Regime

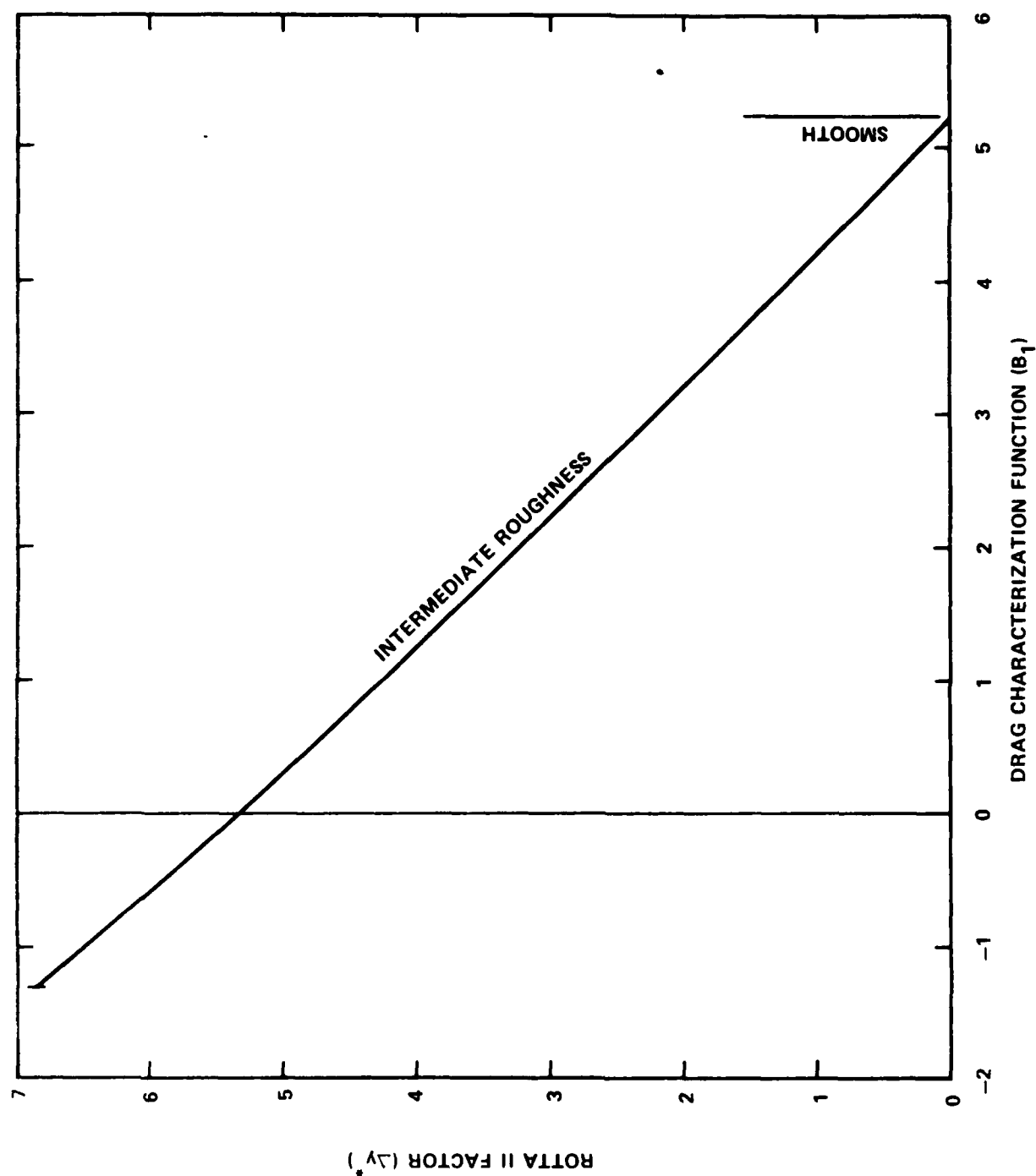


Figure 4 - Correlation of Rotta II Factor  $\Delta y^*$  with  $B_1$  for Intermediate Roughness Regime

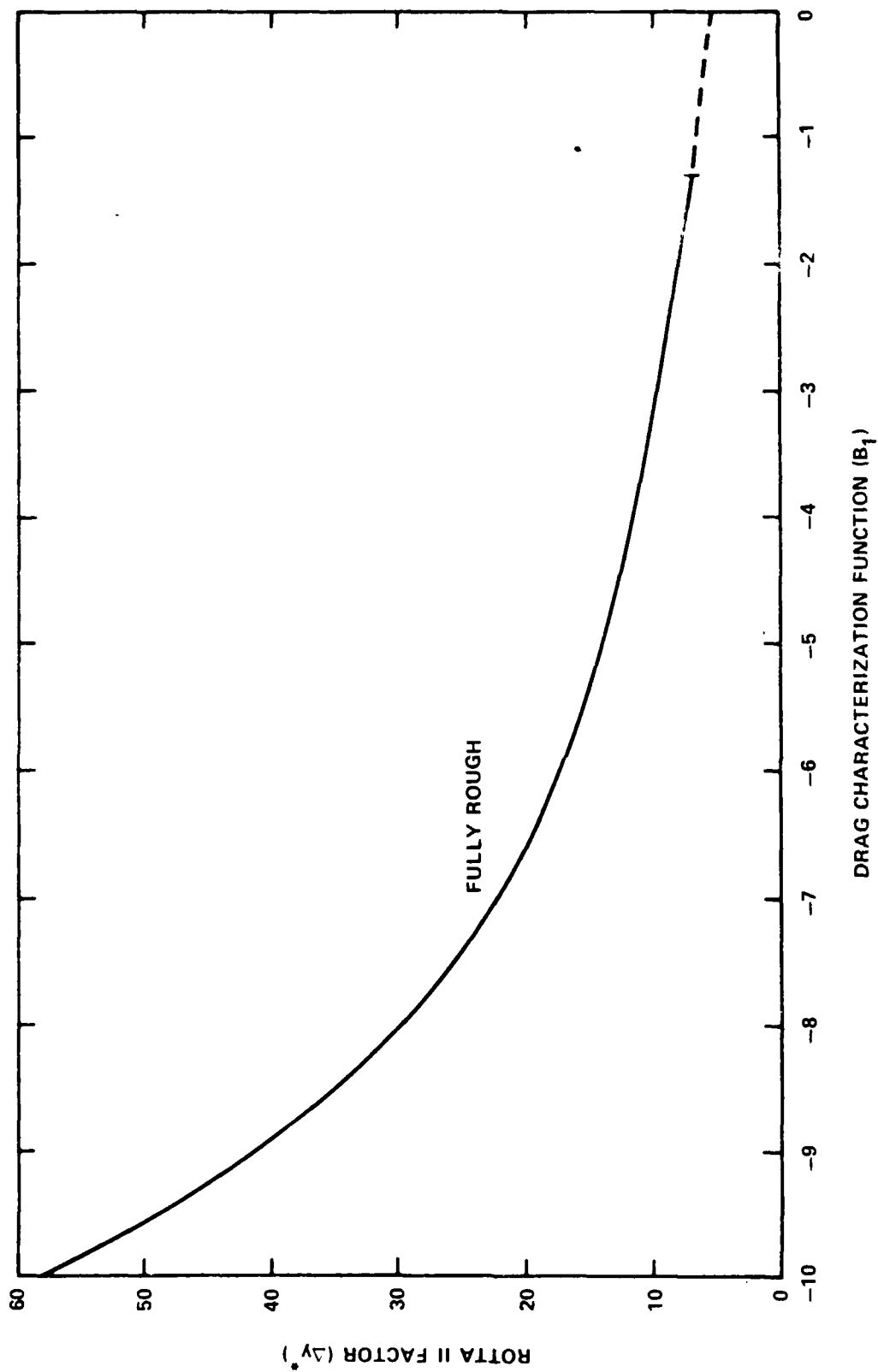


Figure 5 - Correlation of Rotta II Factor  $\Delta y^*$  with  $B_1$  for Fully Rough Regime

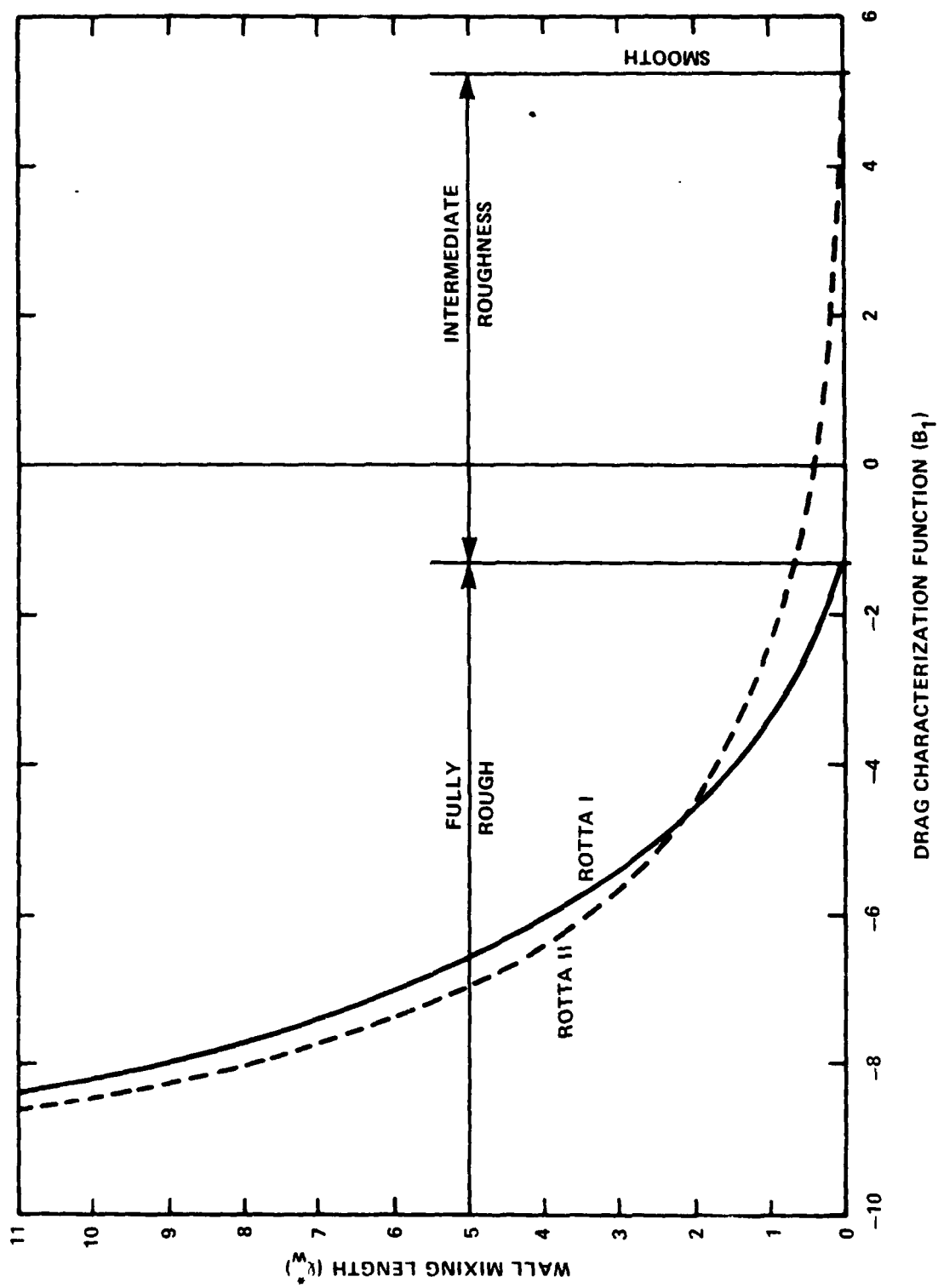


Figure 6 - Comparison of Rotta I and Rotta II Wall Mixing Lengths  $\ell_w^*$

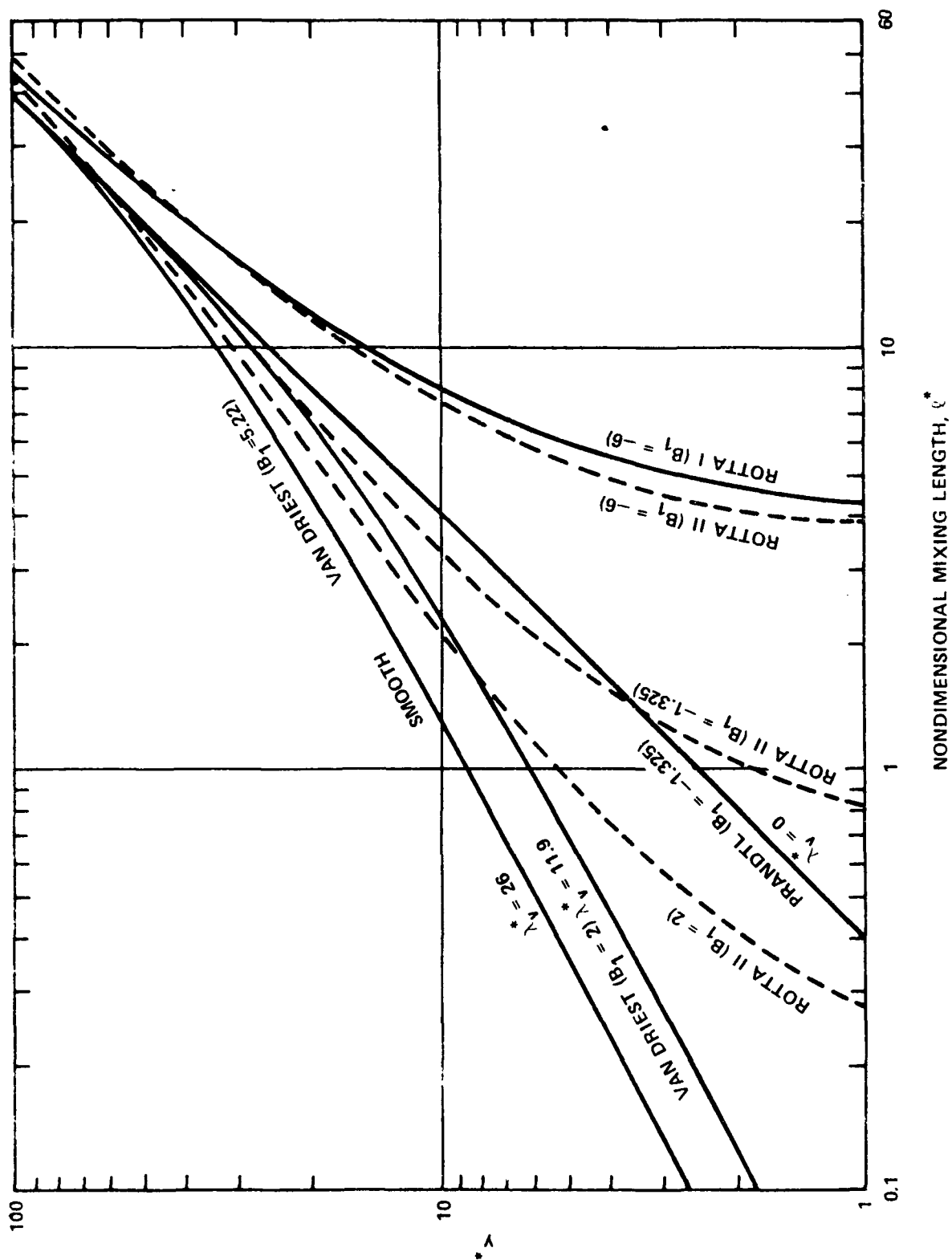


Figure 7 - Comparison of Mixing Lengths

# APPENDIX A CONVERSION OF MIXING LENGTHS TO EDDY VISCOSITIES

The concept of eddy viscosity  $\nu_t$  (more properly eddy kinematic viscosity) was originally proposed during the last century by Boussinesq for turbulent flows as an analogy to the usual viscosity for laminar flows or

$$\frac{\tau_t}{\rho} = \nu_t \frac{du}{dy} \quad (A.1)$$

Equating this to the turbulent shear stress given in terms of mixing lengths, Equation (7), produces the well known expression

$$\nu_t = \ell^2 \frac{du}{dy} \quad (A.2)$$

Note that eddy viscosity unlike laminar viscosity is not a property of the fluid, but depends upon its position in the flow.

For various reasons it may be more desirable to relate eddy viscosity ( $\nu_t$ ) to mixing length without the presence of velocity gradient  $du/dy$ .

In general, shear stress ( $\tau$ ) has laminar and turbulent contributions such that

$$\frac{\tau}{\rho} = (\nu + \nu_t) \frac{du}{dy} \quad (A.3)$$

Close to the wall  $\tau = \tau_w$  and then, nondimensionally,

$$\frac{du^*}{dy^*} = \frac{1}{1 + \frac{\nu_t}{\nu}} \quad (A.4)$$

Now from Equation (10)

$$\frac{du^*}{dy^*} = \frac{2}{1 + \sqrt{1 + (2\ell^*)^2}} \quad (A.5)$$

integral parameters are computed by an algebraic transformation of the velocity profiles at the station immediately upstream on the same chordline. With the velocity profiles thus determined, the three-dimensional displacement thickness  $\delta^*$  is computed by integration of the continuity equation, using a procedure that has been modified so that the resulting  $\delta^*$  provides the desired "viscous-wedge" effect on the outer flow. When all of these operations are completed, all of the same solution variables are defined as would have been defined by solving the boundary-layer equations, had the station not been in the shock zone. For purposes of operations at adjacent stations, the solution variables defined for a station inside the shock zone are treated the same logically as if they had come from the boundary-layer equations. For example, solution variables defined within the shock zone can be referenced by the finite difference formulas used at adjacent stations where the boundary layer equations are being solved. Because of this, the treatment of the shock on one chordline is relatively independent of what happens on adjacent chordlines, and program logic is kept relatively simple.

#### Shock-Jump Conditions and Separation Criterion

Our model for the effects of a shock on a three-dimensional turbulent boundary layer is based on an existing two-dimensional model extended to three dimensions by the following physical arguments. When a transonic shock impinges on a solid surface, it represents a region of very strong pressure gradient concentrated in a relatively narrow band on the surface, which we will refer to as the "shock/solid-surface intersection". The surface isobars are closely spaced in the region of interaction and tend to assume the same orientation as the shock/solid-surface intersection itself. Thus the pressure gradient in the direction parallel to the shock/solid-surface intersection is very weak relative to the pressure gradient in the perpendicular direction. If we assume that the pressure gradient in the parallel direction is negligible, then we can expect that the flow will behave locally like the flow on an infinite span swept wing, in which the spanwise derivatives of all flow quantities are zero. A well-known result in infinite-swept-wing boundary layer theory, known as the independence principle, states that the boundary-layer velocity profiles in the direction perpendicular to the isobars are independent of the spanwise flow and are therefore the same as would occur in the corresponding two-dimensional flow in the perpendicular-to-the-isobars direction. The independence principle is exact only for laminar, incompressible boundary layers. However, it has been found that the effects of turbulence do not cause large deviations from the behavior predicted by the independence principle (Reference 10), and we would not expect the effects of compressibility, at least at transonic speeds, to cause substantial deviations either. It thus seems reasonable to apply empiricism from two-dimensional shock-boundary-layer interactions to the computation of velocity profiles in the direction perpendicular to the shock/solid-surface intersection, to compute the mass flux in the parallel direction.

It is important to note that this model does not base a model the development of the shock-boundary-layer interaction on laminar flow. At this end, we again note that the model does not take into account the effects of the pressure gradient in the direction parallel to the shock/solid-surface intersection, which is reasonable to assume since the pressure gradient is perpendicular to the shock-parallel direction. The pressure gradient in the shock-parallel direction is relatively weak compared to the pressure gradient in the shock-perpendicular direction, and it is not expected that this weak pressure gradient will cause significant deviations from the model.

This determination of shock locations is based on the behavior of the shock-perpendicular Mach number. Resolving the local Mach number into a shock-perpendicular component requires that the shock sweep be known, which in principle requires that the shock location already be known, both locally and at adjacent chordlines. We make the simplifying assumption that the shock sweep is perpendicular to the pressure gradient at a point in the shock zone where the magnitude of the gradient is maximum. The shock sweep can then be calculated a priori for each candidate shock zone without the actual shock location's being known, and the determination of shock location can thus be carried out independently for each chordline in the boundary-layer grid without iteration. The boundaries  $z_1$  and  $z_2$  are determined by applying a sequence of criteria based on the value and gradient of the shock-perpendicular Mach number. These criteria were tuned by trial-and-error to give a reliable definition of the full extent of the zone over which the shock was smeared in the inviscid-flow solution.

The treatment of the shock/boundary-layer interaction model within the boundary-layer grid can be easily understood with reference to a typical wing boundary-layer grid as shown in Figure 2. The grid consists of a curvilinear, orthogonal mesh of grid stations on the wing surface arranged as a series of spanlines and chordlines. Hereafter, the term "station" will refer to a surface grid point as shown in Figure 2. Each station has associated with it a column of grid points extending from the surface in the normal direction through the boundary layer. The boundary-layer solution is determined in a marching sequence in which the program logic "visits" each station only once, determining the solution there once and for all as a function of the solution already determined at other stations upstream. The basic marching direction is from the leading edge attachment line to trailing edge, taking each spanline in turn, while along each spanline, the marching is from root to tip. The shock/boundary-layer interaction model does not alter the basic marching sequence; it merely calls for a different set of operations to be carried out at stations associated with the shock zone, while the boundary-layer equations are solved as usual at all other stations. All grid stations in the range  $z_1 \leq z \leq z_2$  and the first station downstream of  $z_2$  are considered to be associated with the shock zone. The code can handle up to two shock zones on each chordline.

When the program logic "visits" the first station associated with a shock zone, the empirical shock-jump conditions for that shock zone are computed. This consists of computing the integral parameters of the velocity profile perpendicular to the shock/wing-surface intersection upstream of the shock,

$\delta^*_{\perp 1}$ ,  $H_{\perp 1}$ , and  $C_{f\perp 1}$  at  $z = z_1$ , and the corresponding downstream parameters

$\delta^*_{\perp 2}$ ,  $H_{\perp 2}$ , and  $C_{f\perp 2}$  at  $z = z_2$  using the jump conditions described below.

The computation of the velocity profiles at each station associated with the shock zone takes place as follows. First, the local values of the shock-perpendicular integral parameters  $\delta^*_{\perp}$ ,  $H_{\perp}$ , and  $C_{f\perp}$  are interpolated from the upstream and downstream values using interpolation functions that depend on the local value of perpendicular Mach number as sketched in Figure 3. Three-dimensional boundary layer velocity profiles consistent with these



An important consequence of item 2) is that the boundary-layer solution will often predict separation for cases in which the shock is moderately strong, but in which no separation appears in the real flow.

The alternative approach explored in this paper differs from the simple scheme described above in two basic areas: the treatment of the effects of the shock on the boundary layer, and the treatment of the effects of the boundary layer on the shock in the outer inviscid flow. First, the treatment of the effects of the shock on the boundary layer is improved by replacing the boundary-layer equations in the shock zone with a set of semi-empirical jump conditions for the changes in boundary-layer quantities through the shock. The boundary-layer equations are still used upstream and downstream of the shock zone. Several investigators (References 1, 2, 3) have shown that models of this type offer an improvement over the boundary-layer equations, and Inger (Reference 4) has used such a model in coupled transonic flow calculations for 2-D airfoils. Second, the effect of the boundary layer on the outer flow is modelled by defining the displacement thickness in the shock zone so as to produce the same effect as the "viscous-wedge" model proposed by Yoshihara (Reference 5), that is, to encourage the inviscid solution to produce a perpendicular Mach number slightly less than unity downstream of the shock.

In this paper, we describe the extension of this basic approach to three dimensions and its application to coupled viscous-inviscid three-dimensional transonic flow calculations. The approach has been incorporated into two major computer programs that carry out such coupled calculations automatically. One program treats wing-body and wing-body-strut-nacelle flows using a transonic full-potential method (Reference 6) for the inviscid flow, and the other program treats nacelle-center-body flows using an Euler equation method (Reference 7). Both programs use a three-dimensional finite-difference boundary-layer method (References 8 and 9) for the basic boundary-layer calculations, modified to also carry out the calculations associated with the semi-empirical shock-jump conditions.

### The Shock-Boundary Layer Interaction Model

#### Basic Operation

The interaction between the boundary layer and the inviscid flow is calculated by a classical direct-iteration scheme, as diagrammed in Figure 1(a). In each cycle of the iterative procedure, the viscous flow is computed in the direct mode, i.e. the latest inviscid-flow velocity components on the surface are used as boundary conditions, and the distribution of displacement thickness  $s^*$  on the surface is computed as part of the solution. A weighted average of this new  $s^*$  and the  $s^*$  from the previous cycle is then used to modify the surface shape for the next cycle.

The calculation of the viscous flow for each cycle involves several steps, as shown in Figure 1(b). First, the curvilinear, orthogonal surface grid required for an ordinary, three-dimensional boundary-layer calculation is generated and the inviscid flow velocity vectors are appropriately transformed and interpolated into this grid. Based on the inviscid-flow data thus defined in the boundary-layer grid, the intersections of the shocks with the downstream boundary-layer grid lines are located. These shock locations are actually defined by upstream and downstream boundaries  $z_1$  and  $z_2$  of "shock zones" over which the shock is located in the inviscid-flow solution, as shown for a typical wing boundary in the grid in Figure 2.

# SHOCK/BOUNDARY-LAYER INTERACTION MODEL FOR THREE-DIMENSIONAL TRANSONIC FLOW CALCULATIONS

by

J. D. McLean and T. K. Matoi

Boeing Commercial Airplane Company

## Introduction

Several widely used computer programs for calculating viscous transonic flow in both two and three dimensions use a classical direct-iteration scheme to couple an inviscid-flow solution for the outer flow with a solution to boundary-layer equations for the viscous flow near the surface. In transonic flow, shocks usually appear in the flow field. In the portion of the field that is modelled as inviscid, these shocks appear as discontinuities in weak solutions to the inviscid-flow equations, either potential or Euler. Such discontinuities are in principle inappropriate as input to the boundary-layer equations, since they require smooth boundary conditions. In practice, however, the inviscid solution is generated numerically, and the shock discontinuities are smeared over several grid cells. It is a common practice to feed the numerically generated inviscid solution directly into the boundary-layer equations (sometimes with interpolation onto a finer grid for the boundary-layer calculations), allowing the boundary-layer solution to respond to the smeared shock jumps just as it would to any other pressure gradient. For very weak shocks the thickening of the boundary-layer through the shock predicted in this way should be very nearly correct, but for stronger shocks there are two major drawbacks to this approach:

- 1) The prediction of the viscous flow development through the shock is inaccurate because the assumptions inherent in the simple boundary-layer equations are violated in such a strong-interaction region, and
- 2) The coupled solution has an unrealistic (and non-physical) dependence on the grid spacing used in the inviscid solution. In the real flow the smearing of the pressure rise through the shock (as seen at the surface) results from the interaction of the shock with the boundary layer, while in coupled calculations the smearing depends strongly on the grid spacing of the inviscid solution, especially with the relatively crude grids generally used in three-dimensional calculations.

12. Granville, P.S., "The Frictional Resistance and Turbulent Boundary Layer of Rough Surfaces," Journal of Ship Research, Vol. 2, No. 3, pp. 52-74 (Dec 1958).
13. Granville, P.S., "Drag-Characterization Method for Arbitrarily Rough Surfaces by Means of Rotating Disks," Journal of Fluids Engineering, Vol. 104, No. 3, pp. 373-374 (Sep 1982).
14. van Driest, E.R., "On Turbulent Flow Near A Wall," Journal of Aeronautical Sciences, Vol. 23, pp. 1007-1011, 1036 (1956).
15. Patel, V.C., "A Unified View of the Law of the Wall Using Mixing-Length Theory," Aeronautical Quarterly, Vol. 24, Part 1, pp. 55-70 (Feb 1973).
16. Dahm, T., Personal Communication to T.C. Lin and R.J. Bywater, "Turbulence Models for High-Speed Rough-Wall Boundary Layers," AIAA Journal, Vol. 20, No. 3, pp. 325-333 (Mar 1982).

# REFERENCES

1. Patankar, S.V. and D.B. Spalding, "Heat and Mass Transfer in Boundary Layers," C.R.C. Press, Cleveland, Ohio (1968).
2. Cebeci, T. and A.M.O. Smith, "Analysis of Turbulent Boundary Layers," Academic Press, N.Y. (1974).
3. Nituch, M.J., S.S. Sjolander and M.R. Head, "An Improved Version of Cebeci-Smith Eddy-Viscosity Model," Aeronautical Quarterly, Vol. 29, Part 3, pp. 207-225 (Aug 1978).
4. Huang, T.T., N. Santelli and G. Belt, "Stern Boundary-Layer on Axisymmetric Bodies," 12th Symposium on Naval Hydrodynamics, National Academy of Sciences, Washington, D.C. (1979).
5. Sideman, S. and W.V. Pinczewski, "Turbulent Heat and Mass Transfer at Interfaces: Transport Models and Mechanisms," in "Topics in Transport Phenomena," C. Gutfinger, ed., pp. 47-207, Hemisphere Publishing Corporation, Washington, D.C. (1975).
6. Arora, R., K.K. Kuo and M.K. Rezaian, "Near-Wall Treatment for Turbulent Boundary-Layer Computations," AIAA Journal, Vol. 20, No. 11, pp. 1481-1482 (Nov 1982).
7. Rotta, J., "Das in Wandnahe <sup>g</sup>ultige Geschwindigkeitsgesetz turbulenter Strömungen," Ingenieur-Archiv, Vol. 18, pp. 277-280 (1950).
8. Rotta, J., "Turbulent Boundary Layers in Incompressible Flow," in "Progress in Aeronautical Sciences," Vol. 2, A. Ferri, D. Küchemann and L.H.G. Sterne, eds., pp. 1-219, Pergamon Press, N.Y. (1962).
9. Cebeci, T. and K.C. Chang, "Calculation of Incompressible Rough-Wall Boundary-Layer Flows," AIAA Journal, Vol. 16, No. 7, pp. 730-735 (Jul 1978).
10. Nikuradse, J., "Laws of Flow in Rough Pipes," NACA TM 1292 (Nov 1950) (Translation from VDI-Forschungsheft 361, Jul/Aug 1933).
11. Hama, F.R., "Boundary-Layer Characteristics for Smooth and Rough Surfaces," Transactions, Society of Naval Architects and Marine Engineers, Vol. 62, pp. 333-358 (1954).

$y^*$	Nondimensional $y$ , $y^* = u_\tau y / \nu$
$y_L$	Laminar sublayer thickness
$y_L^*$	Nondimensional $y_L$ , $y_L^* = u_\tau y_L / \nu$
$\Delta B$	Drag characterization, $\Delta B = B_1 - B_{1,s}$
$\Delta y^*$	Rotta II shift
$\epsilon$	Turbulent dissipation rate
$\kappa$	von Kármán constant
$\lambda$	Length factor in modification function
$\lambda^*$	Nondimensional $\lambda$ , $\lambda^* = u_\tau \lambda / \nu$
$\lambda_h^*$	$\lambda^*$ for hyperbolic-tangent modification function
$\lambda_v^*$	$\lambda^*$ for van Driest modification function
$\lambda_{v,s}^*$	$\lambda_v^*$ for smooth surfaces
$\nu$	Kinematic viscosity of fluid
$\nu_t$	Turbulent eddy viscosity
$\rho$	Density of fluid
$\tau$	Shearing stress
$\tau_\ell$	Laminar shearing stress
$\tau_t$	Turbulent shear stress
$\tau_w$	Wall shearing stress

# NOTATION

$A$	Slope of logarithmic velocity law, $A = 1/\kappa$
$B_1$	Intercept of logarithmic velocity law in Reynolds-number mode (also drag characterization function)
$B_{1,s}$	Value of $B_1$ for smooth surfaces
$B_r$	Intercept of logarithmic velocity law in relative-roughness mode
$\hat{B}_r$	Value of $B_r$ for fully rough regime
$I_1, I_2$	Integrals defined by Equation (30)
$k$	Roughness height
$k_1, k_2, \dots$	Other roughness lengths
$k^*$	Roughness Reynolds number, $k^* = u_\tau k/\nu$
$k$	Turbulent kinetic energy
$\ell$	Mixing length
$\ell^*$	Nondimensional mixing length, $\ell^* = u_\tau \ell/\nu$
$\ell_w^*$	Value of $\ell^*$ at the wall
$M$	Modification function
$T$	Roughness texture, $T = k/k_1, k_1/k_2, \dots$
$u$	Streamwise velocity component
$u^*$	Nondimensional $u$ , $u^* = u/u_\tau$
$u_\tau$	Shear velocity, $u_\tau = \sqrt{\tau_w/\rho}$
$w$	Subscript denoting conditions at the wall, $y = 0$
$y$	Normal distance from wall

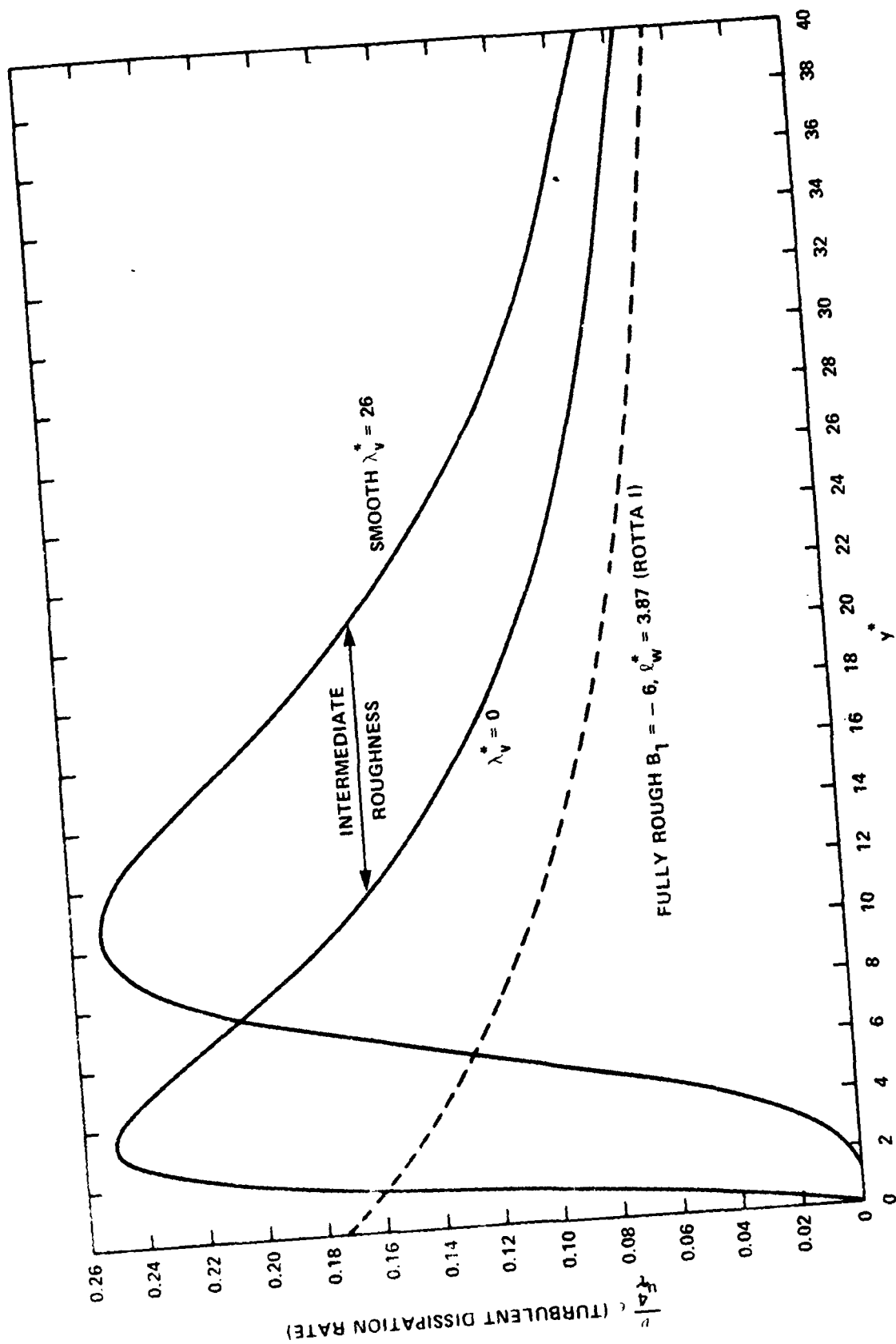


Figure B.2 - Variation of Turbulent Dissipation Rate Near Wall

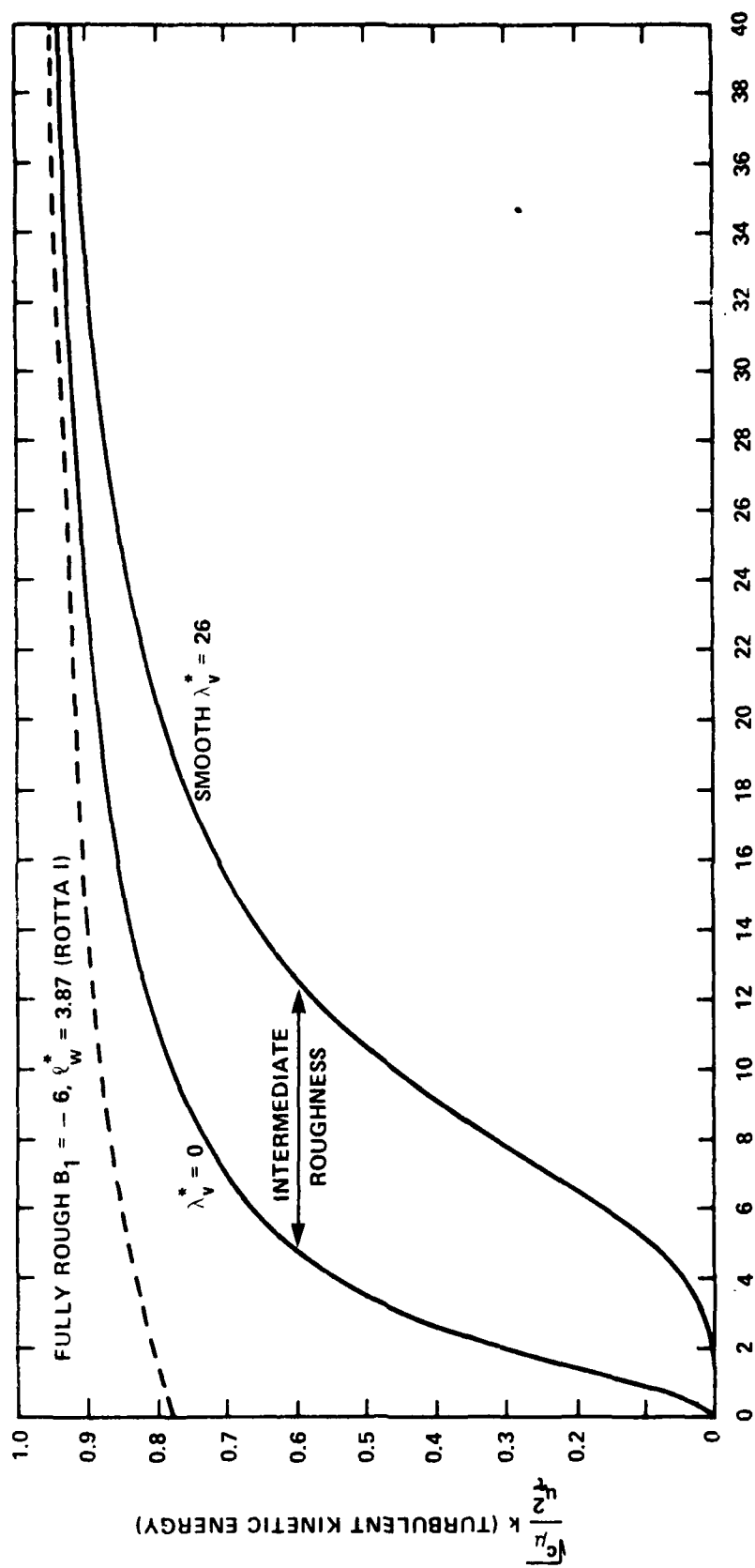


Figure B.1 - Variation of Turbulent Kinetic Energy Near Wall



and

$$\frac{\nu}{u_{\tau}} \epsilon = \ell^{*2} \left( \frac{du^*}{dy^*} \right)^3 \quad (\text{B.5})$$

Substitution of  $du^*/dy^*$  from Equation (10) produces

$$\frac{\sqrt{c_{\mu}}}{u_{\tau}} k = \left[ \frac{2\ell^*}{1 + \sqrt{1 + (2\ell^*)^2}} \right]^2 \quad (\text{B.6})$$

and

$$\frac{\nu}{u_{\tau}} \epsilon = \ell^{*2} \left[ \frac{2}{1 + \sqrt{1 + (2\ell^*)^2}} \right]^3 \quad (\text{B.7})$$

Some general properties of  $k$  and  $\epsilon$  are now deduced. At higher values of  $\ell^*$ ,  $(\sqrt{c_{\mu}}/u_{\tau}^2)k$  approaches 1 and  $(\nu/u_{\tau}^4)\epsilon$  approaches  $1/\ell^*$ .

Also  $(\nu/u_{\tau}^4)\epsilon$  reaches a maximum value of  $1/4$  at  $\ell^* = \sqrt{2}$ .

This maximum value is independent of the mixing-length model.

In Figures B.1 and B.2, the variation of  $k$  and  $\epsilon$  with  $y^*$  are shown for selected roughness conditions.

APPENDIX B  
NEAR-WALL VALUES OF TURBULENT KINETIC ENERGY ( $k$ )  
AND TURBULENT DISSIPATION RATE ( $\epsilon$ )

A modeling method for current turbulence determines the turbulent shear stress from the eddy viscosity which, in turn, is obtained from the turbulent kinetic energy ( $k$ ) and the turbulent dissipation rate ( $\epsilon$ ) from

$$\nu_t = c_\mu \frac{k^2}{\epsilon} \quad (\text{B.1})$$

where  $c_\mu$  is a constant.

Values of  $k$  and  $\epsilon$  are obtained from solutions of convection equations which are partial differential equations. However, close to the wall it has been found that values of  $k$  and  $\epsilon$  obtained from mixing lengths may be used as inputs to the partial differential equations for  $k$  and  $\epsilon$  with an improved accuracy<sup>6</sup> in the solutions of the equations.

By equating the production and dissipation terms of the  $k$ -equation, Arora et al.<sup>6</sup> related  $k$  and  $\epsilon$  to the mixing length close to the wall as follows,

$$k = \frac{\ell^2}{\sqrt{c_\mu}} \left( \frac{du}{dy} \right)^2 \quad (\text{B.2})$$

and

$$\epsilon = \ell^2 \left( \frac{du}{dy} \right)^3 \quad (\text{B.3})$$

Elimination of the velocity gradient  $du/dy$  produces a direct relation between  $k$  and  $\epsilon$  with  $\ell$  as follows. First the relation for  $k$  and  $\epsilon$  are nondimensionalized to

$$\frac{\sqrt{c_\mu}}{u_\tau^2} k = \ell^{*2} \left( \frac{du^*}{dy^*} \right)^2 \quad (\text{B.4})$$

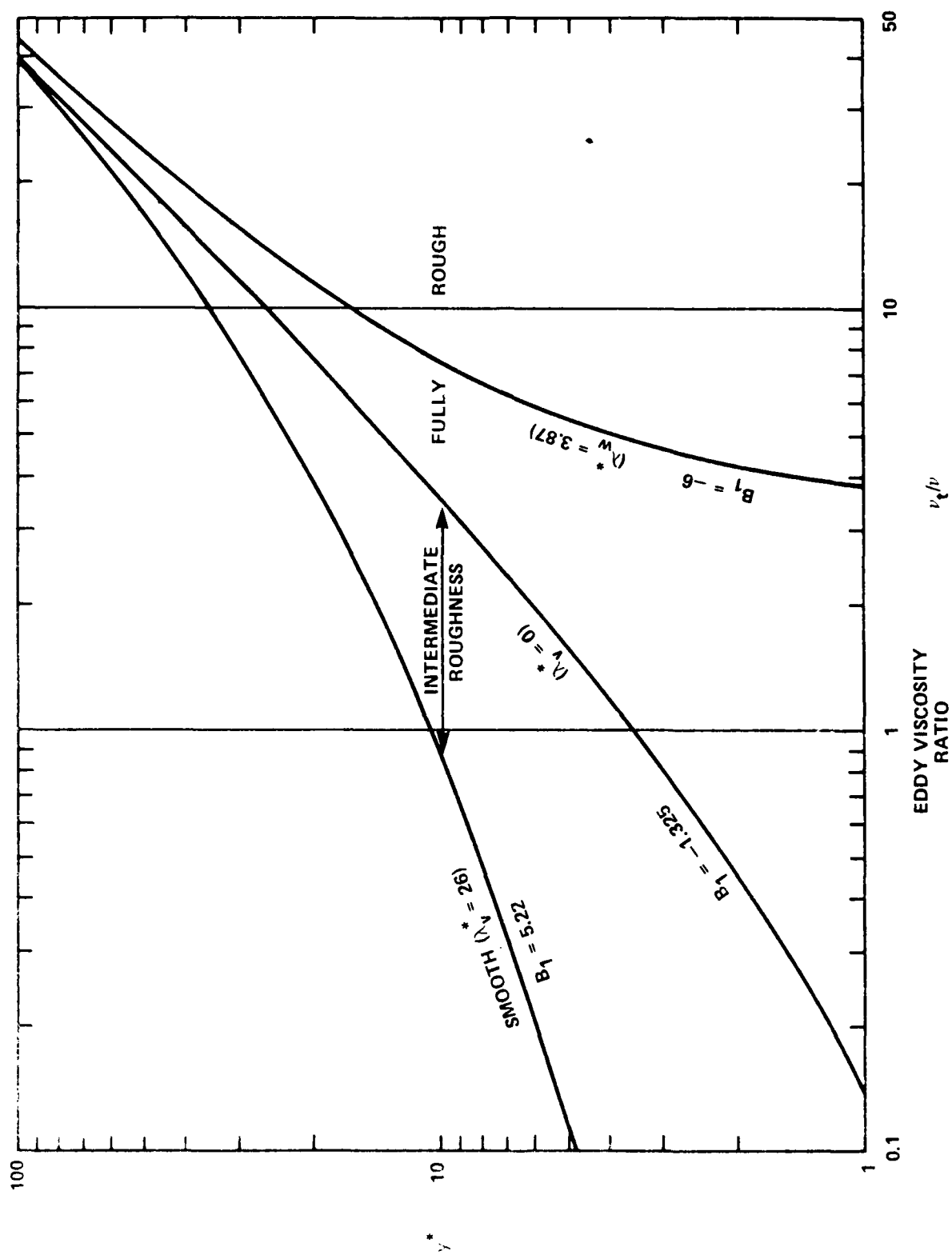


Figure A.1 - Eddy Viscosities Over Rough Surfaces

Equating the two expressions for  $du^*/dy^*$  results in

$$\frac{v_t}{\nu} = \frac{1}{2} \sqrt{1 + (2\ell^*)^2} - \frac{1}{2} \quad (A.6)$$

This is the desired relation for converting mixing lengths to eddy viscosities.

At large values of  $\ell^*$ ,  $(v_t/\nu) \rightarrow \ell^* \rightarrow \kappa y^*$  or  $v_t \rightarrow u_{\tau}^* \rightarrow \kappa u_{\tau}^* y^*$ .

For the van Driest formulation for arbitrarily rough surfaces, Figure A.1 shows the variation of eddy viscosity ratio  $v_t/\nu$  with normal distance  $y^*$ . The smooth case is shown as well as the case for the boundary between the intermediate and fully rough regimes. Also, as an example of the fully rough regime  $v_t/\nu$  is shown for  $B_1 = -6$ . At large values of  $y^*$ ,  $(v_t/\nu) \rightarrow \kappa y^*$  as seen in Figure A.1.

It is to be noted that the increase of  $v_t/\nu$  with  $y^*$  presented here applies only to the boundary-layer region next to the wall. A limiting value is reached which corresponds to outer-region values such as those given by Cebeci and Smith.<sup>2</sup>

change in the shock-parallel velocity component either. We, therefore, construct the parallel-direction velocity profiles on the assumption that the shock-parallel velocity component is unchanged along streamlines of the flow through the shock zone.

The jump conditions for  $\delta_{\perp}^*$  and  $H_{\perp}$  are the same ones used by Bozatli (Reference 3) in his study of two-dimensional airfoil flows using an integral boundary layer method. The  $\delta_{\perp}^*$  jump condition was derived from a numerical, non-asymptotic, triple-deck theory of transonic shock/boundary-layer interaction developed by Inger (Reference 1). The following algebraic curve-fit was developed by Deane (Reference 11), who ran Inger's program for an extensive matrix of flow conditions:

$$\Delta \delta_{\perp}^* = \delta_{\perp 1}^* \left[ 5.17 + 8.65 (H_{\perp 1 i} - 1.3) \right] 1.11 (M_{e \perp 1} - 1) \tanh(\log_{10} R_{\delta \perp 1}^* - 2.35), \quad (1)$$

$$\text{where } H_{\perp 1 i} = \left( H_{\perp 1} - 0.273 M_{e \perp 1}^2 \right) / \left( 1. + 0.1175 M_{e \perp 1}^2 \right), \quad (2)$$

$$\text{and } R_{\delta \perp 1}^* = \frac{\delta_{\perp 1}^* U_{e \perp 1}}{v_{e 1}} \quad (3)$$

To derive the jump condition for  $H_{\perp}$ , we use an integral conservation analysis proposed by investigators at ONERA (Reference 2) and illustrated in Figure 4. A correlation supporting the choice of  $K_m = 0.5$  for the entrainment parameter is presented in Figure 5. The resulting expression for  $H_{\perp 2}$  is:

$$H_{\perp 2} = \frac{\delta_{\perp 2}^*}{e_{\perp 2}}, \quad (4)$$

where

$$e_{\perp 2} = U_2 - \delta_{\perp 2}^* C_2 \delta_2, \quad (5)$$

$$\delta_2 = \left( U_1 - \delta_{\perp 2}^* \right) / C_2 \delta_2, \quad (6)$$

$$C_1 = K_m V_r - 1, \quad (7)$$

$$U_1 = V_r \left[ \delta_{\perp 1}^* - \delta_1 (K_m - 1) \right], \quad (8)$$

$$C_2 = K_m V_r \frac{U_{e1}}{U_{e2}} - 1 - \frac{1}{2} (C_{p2} - C_{p1}) V_r \frac{U_{e1}}{U_{e2}}, \quad (9)$$

$$U_2 = V_r \frac{U_{e1}}{U_{e2}} \left[ \theta_1 + \delta_{11}^* + \delta_1 (K_m - 1) \right], \quad (10)$$

$$V_r = \frac{U_{e1}}{U_{e2}} \left\{ \frac{1 + 0.2 M_{e2}^2}{1 + 0.2 M_{e1}^2} \right\}^{2.5}, \quad (11)$$

and  $K_m = 0.5$

For the shock-perpendicular skin-friction coefficient downstream of the shock, we have derived a simplified curve-fit of Deane's results (Figure 40 of Reference 11):

$$C_{f12} = C_{f11} \left[ -2.125 M_{e1}^2 + 2.6 M_{e1} + 0.525 \right], \quad (12)$$

This completes the calculation of the jump conditions  $\Delta \delta_1^*$ ,  $H_{12}$ , and  $C_{f1}$ . The dependence of these quantities on shock strength ( $M_{e1}$ ) is illustrated for typical conditions in Figure 6.

The criterion for shock-induced separation is based primarily on the upstream perpendicular Mach number  $M_{e1}$  and is applied in two stages. As  $M_{e1}$

increases, the first indication of shock-induced separation is given by the code when  $M_{e1}$  exceeds a threshold value that depends weakly on the

shock-perpendicular, incompressible shape factor of the upstream boundary layer:

$$M_{e1, \text{sep}} = 1.5 - 0.139 H_{11}, \quad (13)$$

This expression is shown in Figure 7 superimposed on experimental data of Reference 2. If  $M_{e1}$  increases above this first threshold, the boundary-layer program continues to generate a solution in the shock zone and downstream of the shock zone until a second threshold is reached when  $M_{e1} = 1.4$ , at which point the value of  $C_{f12}$  given by eqn. (12) (see also Figure 6) becomes

negative. When this happens, the program cannot produce a solution in the shock zone, and the remainder of the chordline becomes a forbidden zone in the boundary-layer solution domain, where no solution exists and where solution variables are not available to be referenced by differencing operations at neighboring stations. These forbidden zones, and similar ones that can arise in solving the boundary-layer equations outside the shock zone, are discussed in Reference 9.

## Generation of Velocity Profiles in the Shock Zone

At each station associated with the shock zone, the integral parameters of the shock-perpendicular velocity profile are determined by the interpolations illustrated in Figure 3. Shock-perpendicular velocity profiles consistent with these parameters are then calculated by an algebraic transformation of the profiles at the station immediately upstream on the same chordline. Thus, for a particular shock on a particular chordline (see Figure 2), the velocity profiles at all the stations associated with the shock zone stem from the profiles at the last station upstream of the shock zone, having been altered by repetitive applications of the algebraic transformation procedure.

The new velocity profiles at the current station are required to match the three integral parameters  $\delta_{\perp}^*$ ,  $H_{\perp}$ , and  $C_{f\perp}$ , using velocity profiles from the station upstream for which these integral parameters had different values. Also, the new velocity profiles must be defined at the regular grid points of the solution-adaptive normal coordinate  $\eta = \frac{y}{\delta_m^*}$ , where  $\delta_m^*$  is an integral measure of the local thickness of the boundary layer:

$$\delta_m^* = \int_0^{\infty} y \left\{ \left( \frac{\partial u}{\partial y} \right)^2 + \left( \frac{\partial w}{\partial y} \right)^2 \right\}^{1/2} dy. \quad (14)$$

Consistency requires that the value of  $\delta_m^*$  be determined so that the velocity profiles defined as functions of  $\eta$  satisfy the relation:

$$\int_0^{\infty} \eta \left\{ \left( \frac{\partial u}{\partial \eta} \right)^2 + \left( \frac{\partial w}{\partial \eta} \right)^2 \right\}^{1/2} d\eta = 1 \quad (15)$$

The transformation therefore involves four input parameters, including  $\delta_m^*$ , and an iterative procedure is used to determine these inputs so as to match the three required outputs and the consistency condition, eqn. 15.

The calculation of the shock-parallel velocity profiles is based on the idea that the parallel velocity component should be constant along streamlines of the flow, or that it should remain constant as a function of a stream function based on the shock-perpendicular velocity profile:

$$\Psi(\eta) = \int_0^{\eta} e^{u_{\perp}} \delta_m^* d\eta \quad (16)$$

To begin the calculation,  $\Psi$  is computed for the upstream station and for the current station, where the  $u_{\perp}$  profile has just been computed by the transformation described above. The new shock-parallel velocity profile is then interpolated from the corresponding profile at the upstream station, using  $\Psi$  as the independent variable in the interpolation.

### Viscous Wedge Model

The viscous flow solution, including the shock/boundary-layer interaction model, affects the inviscid solution only through the distribution of displacement thickness  $\delta^*$ . Outside the shock zone,  $\delta^*$  is determined by the

three-dimensional boundary-layer velocity field through integration of the continuity equation. Inside the shock zone the same integration is carried out, but the resulting,  $\delta^*$  is then modified so as to have the desired "viscous-wedge" effect on the outer flow, i.e., to push  $M_{e12}$  toward a value slightly less than one on each chordline. A new value,  $\delta^*_{\text{new}}$ , is calculated so that the  $\delta^*$  derivative in the chordwise direction,  $\partial\delta^*/\partial z$ , is changed by a factor  $F_D$  that depends on the downstream perpendicular Mach number  $M_{e12}$ , i.e.,

$$\frac{\partial \delta^*_{\text{new}}}{\partial z} = F_D M_{e12} \frac{\partial \delta^*_{\text{old}}}{\partial z} \quad (17)$$

The function  $F_D (M_{e12})$ , plotted in Figure 8, is intended to provide the desired viscous-wedge behavior. The growth of  $\delta^*$  is increased strongly if  $M_{e12}$  is too low ( $M_{e12} < .95$ ) and is decreased if  $M_{e12}$  is too high ( $M_{e12} > .99$ ). When  $M_{e12}$  is in the desired range  $.95 \leq M_{e12} \leq .99$ , the original result of the  $\delta^*$  integration is left unaltered, i.e.,  $\delta^*_{\text{new}} = \delta^*_{\text{old}}$ . This dependence of the  $\delta^*$  slope on  $M_{e12}$  has proven to be fairly effective in driving  $M_{e12}$  toward the desired range of values, though it usually takes several viscous-inviscid iteration cycles for  $M_{e12}$ , and thus the post-shock pressure level, to converge.

#### Comparisons with Two-Dimensional Airfoil Experiments

In the experimental investigation reported by Cook, McDonald, and Firmin (Refence 12), surface pressures and boundary layer development were measured on the upper surface of an RAE 2822 airfoil for several transonic flow conditions. To test the performance of the shock/boundary-layer interaction model we chose three cases with moderate-to-strong shocks and attached flow. We ran these cases in the boundary-layer program in the direct infinite-yawed-wing mode at zero sweep (assuming two-dimensional, planar flow), using the measured pressure distributions as boundary conditions and the measured velocity profiles at  $x/c = .179$  as initial conditions. The boundary conditions were interpolated onto a finer  $x/c$  grid to improve integration accuracy and ensure an essentially grid-independent solution in the boundary-layer program. Two calculations were made for each case: One using the boundary-layer equations everywhere, and one using the shock/boundary-layer interaction model to bridge the shock zone and boundary-layer equations everywhere else.

The flow conditions for the three cases chosen are summarized in the following table:

CASE	$M_\infty$	$R_{e_c} \times 10^{-6}$	$\alpha$ (deg)	$C_n$	max $M_{e11}$
1	.725	6.5	2.55	.658	1.196
9	.730	6.5	3.19	.803	1.291
13A	.740	2.7	3.19	.733	1.288



In Case 7 the shock strength is moderate, while Cases 9 and 13A are on the verge of shock-induced separation at two different Reynolds numbers.

Figs. 9, 10 and 11 show the measured pressure distributions and the measured and calculated boundary-layer integral parameters. The abrupt increases in  $\delta^*$  and  $\theta$  through the shock, starting at  $x/c \approx .50$ , are evident in all three cases. In Case 7 (Figure 9) where the shock strength is moderate, the boundary-layer equations (dashed lines) under-predict the increases in  $\delta^*$  and  $\theta$  through the shock, and the predictions with the shock/boundary-layer interaction model agree better with the experimental data aft of the shock. The shock/boundary-layer interaction model also moves the predicted  $H$  closer to the data, but there is little to choose between the two  $C_f$  predictions. In Case 9 (Figure 10), where the shock is considerably stronger, there is surprisingly little difference between the two predictions, with the shock/boundary-layer interaction model being favored slightly. In Case 13A (Figure 11), also with a strong shock, but at a lower Reynolds number, the jump in  $\delta^*$  through the shock agrees well with the data in both calculations, but the calculation with the shock/boundary-layer interaction model agrees much better with the data from there aft. The shock/boundary-layer interaction model also predicts the change in  $C_f$  through the shock more accurately in this case (the calculation with the boundary-layer equations nearly separated). At this low Reynolds number,  $H$  aft of the shock is poorly predicted by both calculations, an effect also seen in the integral boundary-layer calculations presented by Bozatlí (Reference 3).

#### Three-Dimensional Wing Calculations

To test the new model for three-dimensional swept wings, two wing-body configurations were chosen for which experimental pressure data were available over a range of flow conditions including the onset of shock-induced separation: an experimental wing design tested in the Boeing transonic wind tunnel, and the 747 wing-body half-model tested at high Reynolds number in the NASA Ames 11 foot pressure tunnel. For each configuration, calculations were carried out over a range of flow conditions. Each flow condition was calculated both with and without the new model. The nominal experimental flight conditions (Mach number and Reynolds number) were used for all calculations. For the experimental wing, experimental values of  $\alpha$  were increased by a constant increment of  $0.32^\circ$  for the calculations to give better agreement with upper-surface roof-top pressure levels and thus shock strengths. For the 747 test cases, the experimental values of  $\alpha$  were used without adjustment. The experimental trip locations were used in all calculations with the exception that if the calculation encountered laminar separation ahead of the designated trip location, transition was automatically moved forward to the laminar separation point. All of the calculations were run for 6 complete potential-flow/boundary-layer cycles, using 100 coarse, 100 medium, and 10 fine mesh sweeps in cycle 1 followed by 30 fine mesh sweeps in each succeeding cycle.

The test cases are summarized in the following table:

CONFIGURATION	$M_\infty$	$\alpha$ (deg.)		with new model*	without new model*	$C_p$ comparisons in fig.
		W.T.	Analysis			
Experimental wing	.77	2.20	2.51	✓	✓	12
	.79	1.41	1.73	✓	X	13
	"	2.14	2.46	✓		14
	"	2.60	2.92	X		
747 Wing-body	.84	2.73	2.73	✓	✓	16
	.86	2.70	2.70	✓	✓	17
	.88	2.74	2.74	✓	X	18

\*key to table symbols

✓ Reasonable convergence was achieved

X Separation was predicted at the shock over much of the span

The experimental wing was run once at the cruise Mach number of .77 and then for a series of  $\alpha$ 's at the higher Mach number of .79, for which the calculations without the new model prematurely indicated separation at the shock. The 747 wing-body was run at essentially constant  $\alpha$  for a series of Mach numbers up to a point where the calculations without the new model predicted separation at the shock over most of the span.

The predicted pressure distributions for the experimental wing are compared with experiment in figs. 12-14. Near the cruise point (Figure 12) both calculations give reasonably good agreement, especially near mid-semi-span. The shock location and post-shock pressure distribution are predicted slightly better by the new model. The smearing of the shock in both calculations is greater than in the experiment. Outboard of mid-semi-span both calculations underpredict the roof-top suction and the lift, and inboard of mid-semi-span both calculations predict the shock too far aft.

At the high Mach number of .79, all of the calculations without the new model prematurely predicted separation at the shock, and the pressure predictions are therefore meaningless. The pressure predictions for 6-cycle calculations with the new model are shown in figs. 13 and 14. The agreement at  $\alpha = 1.73^\circ$  ( $\alpha = 1.4^\circ$  experimental) in fig. 13 is not bad considering that this is a case for which the calculations without the new model were unable to obtain a converged solution. With increasing  $\alpha$  (figs. 13 and 14) the calculations show an increasing tendency to predict the shock too far aft and with too low a post-shock Mach number. We have found that running more viscous-inviscid iteration cycles tends to push the post-shock Mach number in the right direction, but the convergence is very slow.

At the highest angle of attack ( $\alpha = 2.92^\circ$ ;  $\alpha = 2.6^\circ$  experimental) the shock/boundary-layer interaction model's first separation criterion (eqn. 13) was exceeded over a large fraction of the span, and the final separation criterion ( $M_{e1} > 1.4$ ) was exceeded over most of the outboard half of the semi-

span, causing a zone of forbidden solution there. The pressure predictions for this case are therefore not presented. The progression of shock-induced separation prediction with angle of attack is illustrated in Figure 15, which shows the location on the platform where the two criteria were exceeded. At

$\alpha = 1.73^\circ$ , neither criterion is exceeded, at  $\alpha = 2.46^\circ$  the first criterion is exceeded over part of the outboard wing, and at  $\alpha = 2.92^\circ$  both criteria are exceeded as already described. An examination of the experimental pressure data showed that trailing-edge pressure divergence has just begun at  $\alpha = 2.6^\circ$ , suggesting that in this case the onset of shock-induced separation in the experiment correlates roughly with the final separation criterion ( $M_{e_{11}} > 1.4$ ) built into our model.

Test-theory comparisons for the 747 wing-body are shown for Mach numbers of .84, .86, and .88 in Figures 16, 17 and 18 respectively. This is a more difficult configuration for the calculations because of the more complex shock pattern. Particularly at  $M_\infty = .86$  and .88, there is a double shock inboard of mid-semi-span and a single shock outboard. The supersonic-to-supersonic forward shock on the inboard wing tends not to be resolved well by the finite-volume method in the inviscid-flow program, as can be seen in the figures for all three Mach numbers. It is interesting, however, that in the calculations with the new model the shock-location algorithm was able to identify the forward shock. A characteristic  $\lambda$ -shock pattern is seen for all three cases when the shock locations found by the algorithm are plotted on the platform, as shown in Figure 19. The circular symbols on these plots indicate the locations where the first shock-induced separation criterion (eqn. 13) was exceeded, and they are seen to span most of the outboard wing at  $M_\infty = .88$ . The final separation criterion ( $M_{e_{11}} > 1.4$ ), however, was never exceeded. The

experimental data show no signs of trailing-edge pressure divergence, indicating that shock-induced separation has not yet begun. Calculations at any higher Mach numbers were not attempted, however, because the calculations with the new model display an increasing tendency toward trailing-edge separation with increasing  $M_\infty$ , as shown by the dashed boundary. In the calculations without the new model, there was no trailing-edge separation indicated at  $M_\infty = .84$  and .86, while at  $M_\infty = .88$  separation was encountered at the aft shock over most of the span (also shown in Figure 19), making the pressure predictions meaningless in this case. (Thus, only the pressure predictions with the new model are shown for this case in Figure 18.) Again, the new model was able to obtain a reasonable result for one case ( $M_\infty = .88$ ) in which the calculations without the model failed due to premature prediction of shock-induced separation.

### Three-Dimensional Nacelle Calculations

The new model is also being used routinely for modeling flows about transport-aircraft fan-cowls. For one particular case, comparison calculations were made both with and without the new model.

Both sets of calculations for this case were run for 4 complete cycles. In the calculations without the new model, the boundary-layer program encountered separation at the shock (at about 20 percent chord near the crown line of the external surface) on cycles 1 and 4. Thus, it is unlikely that the comparison calculations would ever have converged, and the corresponding pressure predictions are therefore meaningless. In the calculations with the new model, the solution is not very well converged at cycle 4, but there is no separation and the solution is converging. In Figure 20 external-surface pressure distributions calculated at cycle 4 with the new model are compared with experiment at three constant- $\theta$  cuts. Already, agreement with the data is quite good, except that the forward suction peak is underpredicted at  $\theta = 90^\circ$ .

## Conclusions

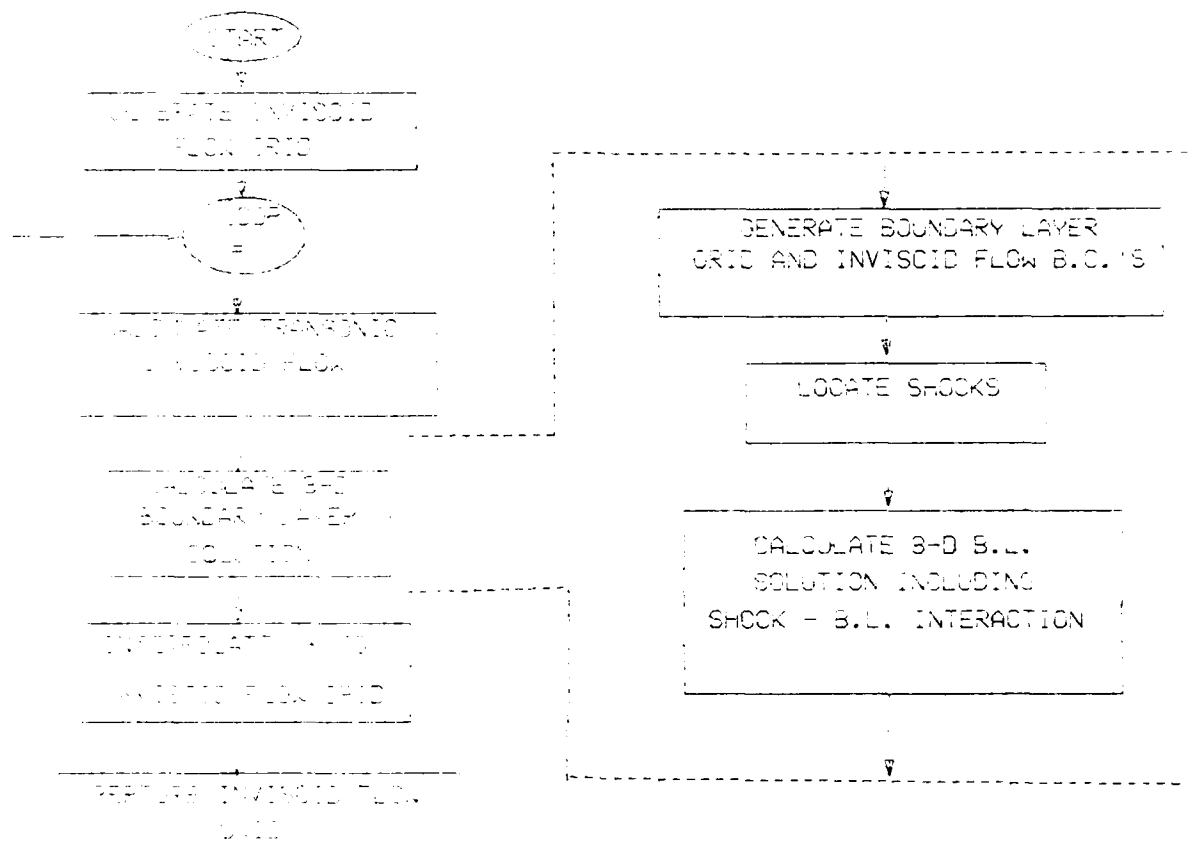
A new computational model for three-dimensional shock-boundary layer interaction has been developed for use in viscous transonic flow calculations. In general, the new model has been found to be an improvement over the old method in which the boundary-layer equations are simply integrated through the shock. The basic empirical content of the method was tested against detailed boundary-layer measurements in two-dimensional transonic airfoil flows, and the new model was found, in general, to give better agreement with experiment. The new model has also been tested in coupled viscous-inviscid interaction calculations for wings and for nacelles. From comparisons with measured pressure distributions the following conclusions can be drawn:

- 1) For cases with weak-to-moderate shocks the new model gives a slight improvement in agreement over the old method.
- 2) For cases with strong shocks that caused the old method to fail by predicting shock-induced separation prematurely, the new model continues to converge (slowly), providing reasonable agreement with experiment.
- 3) The new model appears to be able to predict, at least crudely, the onset of shock-induced separation, provided the onset is not preceded by significant trailing-edge separation.

## References

1. Inger, G. R., "Some Features of a Shock-Turbulent Boundary-Layer Interaction Theory in Transonic Flow-Fields", Computation of Viscous-Inviscid Interactions, AGARD Conference Proceedings No. 291, October, 1980.
2. Sirieix, M., Director, ONERA, private communication.
3. Bozatli, A. N., "Shock-Boundary Layer Interaction", Unpublished Boeing Report, April, 1982.
4. Inger, G. R., "Application of a Shock-Turbulent Boundary Layer Interaction Theory in Transonic Flow Field Analysis", Transonic Perspective - A Critique of Transonic Flow Research, NASA Ames Research Center, February, 1981.
5. Yoshihara, H., and Zonars, D., "An Analysis of Pressure Distributions on Planar Supercritical Profiles with and without Jet Flaps at High Reynolds Numbers", GDCA-ERR-1684, December, 1971.
6. Yu, N. J., "Transonic Flow Simulations for Complex Configurations with Surface-Fitted Grids", AIAA Paper No. 81-1258, 1981.
7. Chen, H. C.; Yu, N. J. and Rubbert, P. E.; "Flow Simulations for General Nacelle Configurations using Euler Equations", AIAA Paper No. 83-0539, 1983.

8. McLean, J. D. and Randall, J. L., "Computer Program to Calculate Three-Dimensional Boundary-Layer Flows over Wings with Wall Mass Transfer", NASA CR-3123, May, 1979.
9. McLean, J. D., and Randall, J. L., "Three-Dimensional Boundary-Layer Calculations for Fuselages", 5th U.S. - German Data Exchange Agreement Meeting on Viscous and Interacting Flow Field Effects, 1980.
10. Nash, J. F., and Tseng, R. R., "The Three-Dimensional Turbulent Boundary Layer on an Infinite Yawed Wing", The Aeronautical Quarterly, November, 1971.
11. Deane, A. E., "Reynolds Number and Shape Factor Effects on Transonic Shock-Turbulent Boundary Layer Interactions, including Incipient Separation", M.S. Thesis, Dept. of Aerospace Engineering, Virginia Polytechnic Institute and State University, Blacksburg, Virginia, December, 1980.
12. Cook, P. H.; McDonald, M. A. and Firmin, M.C.P.; "Aerofoil RAE2822 - Pressure Distributions and Boundary Layer and Wake Measurements", AGARD AR-138, 1979.



1. The flow is calculated by the method of characteristics (MOC) for the inviscid flow field. The boundary layer is calculated by the method of characteristics (MOC) for the boundary layer portion of the flow field. The shock wave is located by the method of characteristics (MOC) for the shock wave portion of the flow field. The flow is then calculated by the method of characteristics (MOC) for the entire flow field.

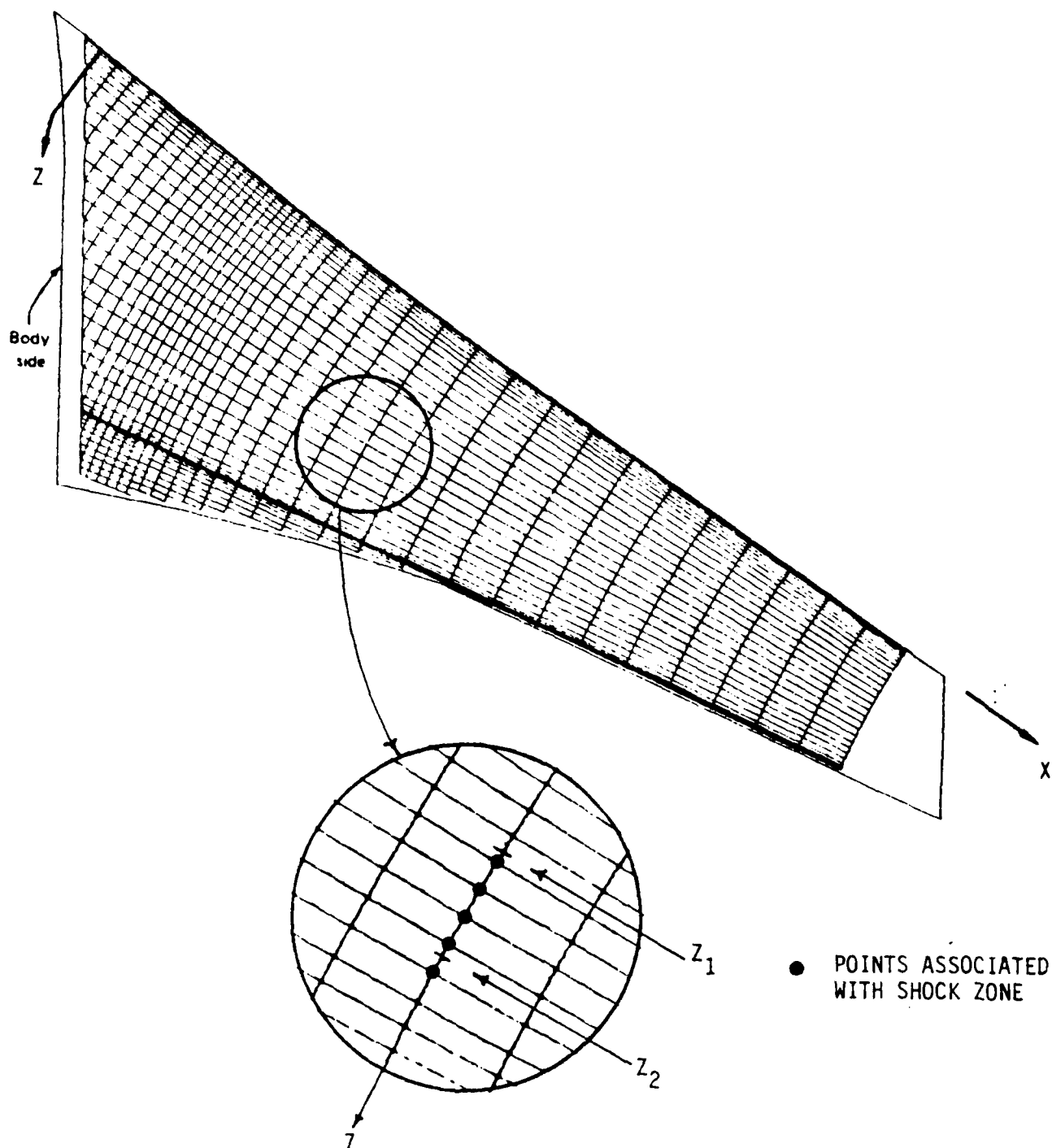


FIGURE 2 TYPICAL WING SURFACE GRID USED BY 3-D  
BOUNDARY LAYER PROGRAM ILLUSTRATING  
THE DEFINITION OF A SHOCK ZONE ON ONE CHORDLINE.

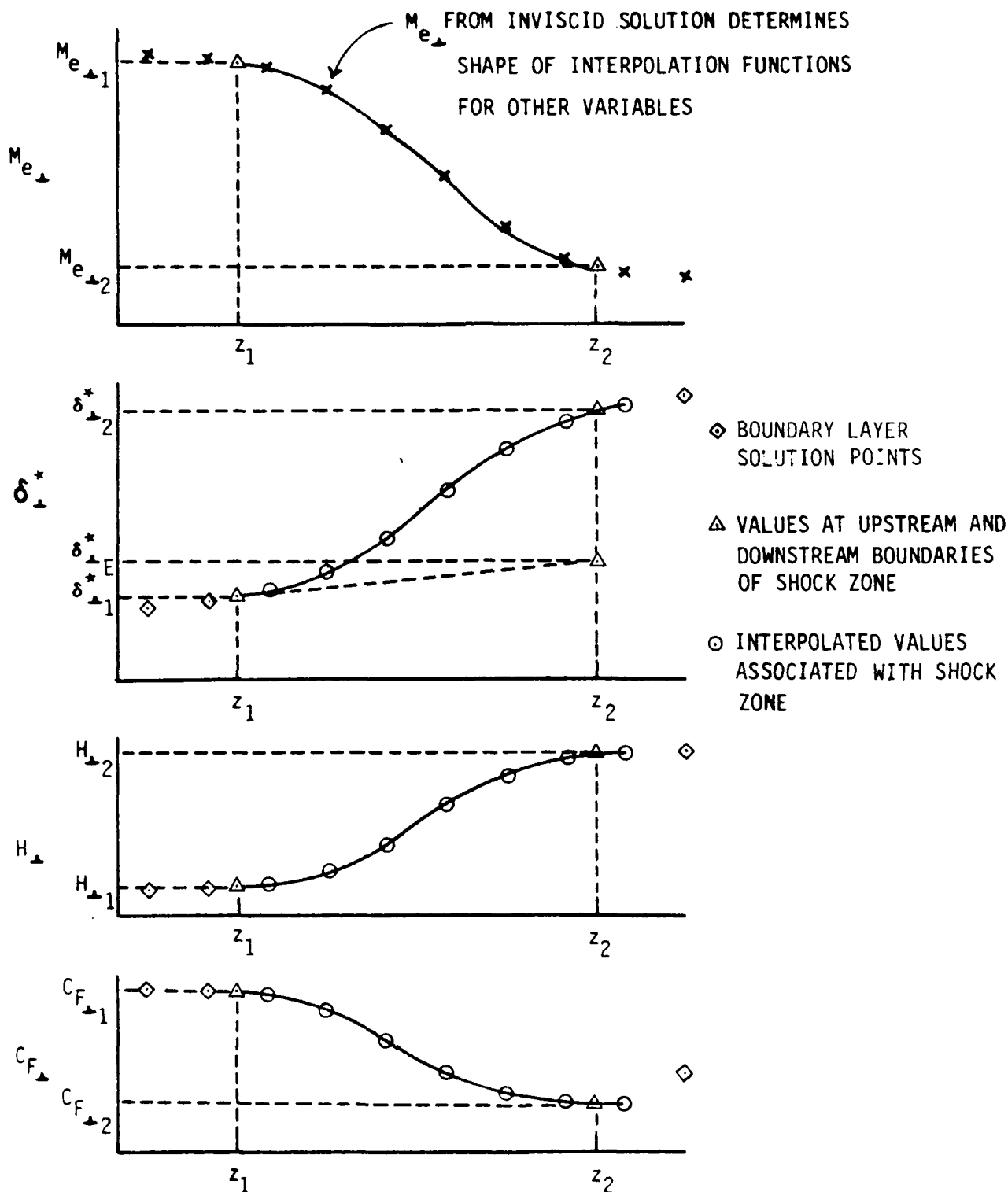
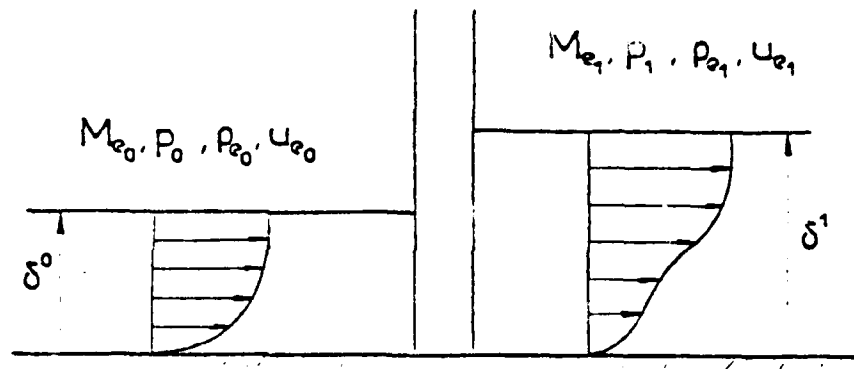


FIGURE 3 ILLUSTRATION OF INTERPOLATION FUNCTIONS USED TO DETERMINE BOUNDARY LAYER INTEGRAL PARAMETERS INSIDE SHOCK ZONE.



# SHOCK / BOUNDARY LAYER INTERACTION DISCONTINUITY ANALYSIS



Mass conservation

$$\int_0^{\delta^1} \rho u \, dy = \int_0^{\delta^0} \rho u \, dy + K_m \rho_{e0} u_{e0} (\delta^1 - \delta^0)$$

Momentum conservation

$$\int_0^{\delta^1} \rho u^2 \, dy = \int_0^{\delta^0} \rho u^2 \, dy + K_m \rho_{e0} u_{e0}^2 (\delta^1 - \delta^0) - \delta^1 (P_1 - P_0)$$

$K_m = 1 \rightarrow$  KLINEBERG's relation for "super-subcritical" jump  
 $K_m = 0 \rightarrow$  GREEN, COUSTEIX-HOUDEVILLE hypothesis

FIGURE 3 ILLUSTRATION OF INTEGRAL CONSERVATION ANALYSIS (EQNS. 3.3.9-10) USED TO DETERMINE  $H_{\perp 2}$ . REPRODUCED FROM REF. 2 WITH ORIGINAL ONERA NOMENCLATURE.

# SHOCK / BOUNDARY LAYER INTERACTION GLOBAL MASS ENTRAINMENT COEFFICIENT

$$H_{i_0} = 1,27$$

$$K_m = \frac{q_{m1} - q_{m0}}{\rho_{e0} u_{e0} (\delta' - \delta^0)}$$

$$q_m = \int_0^{\delta} \rho u dy = \rho_e u_e (\delta - \delta_1)$$

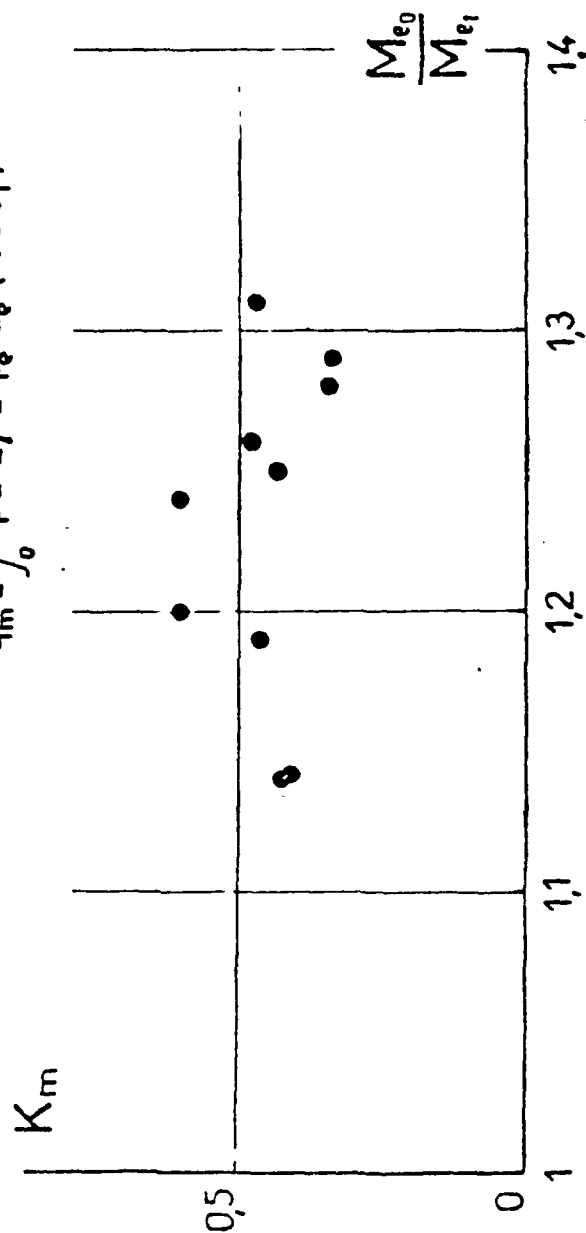
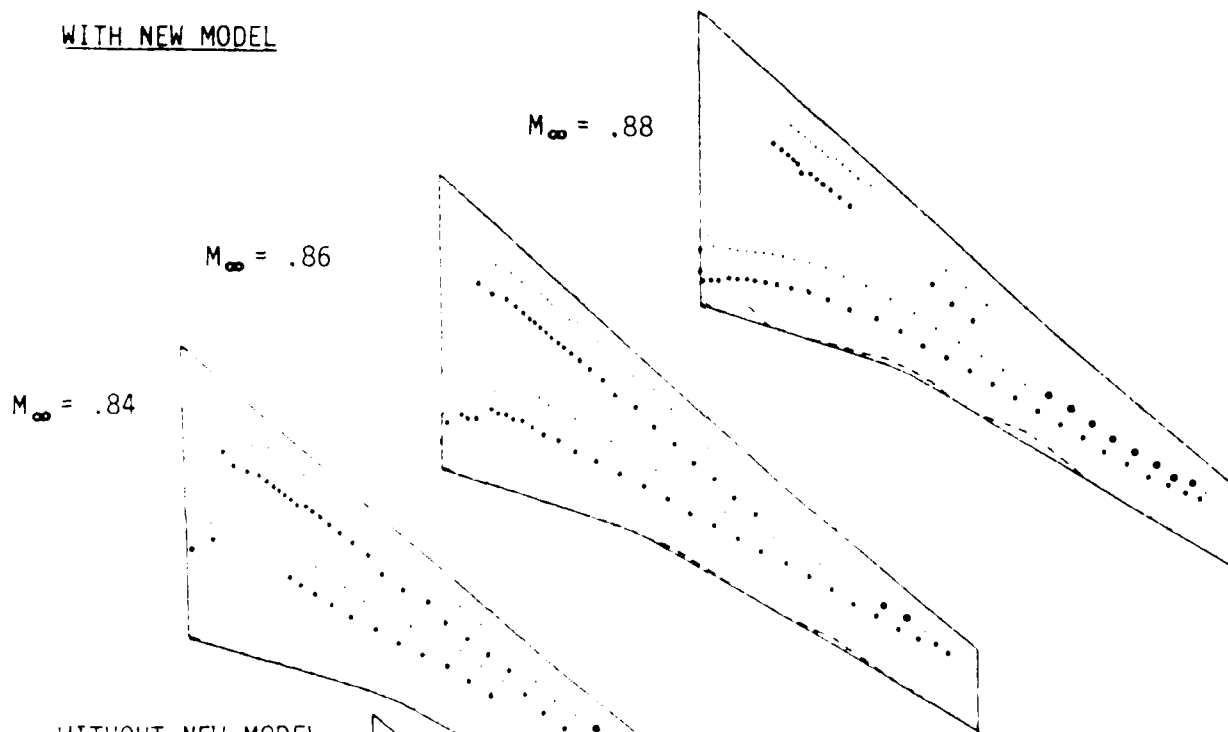


FIGURE 5 CORRELATION DEVELOPED AT ONERA FOR COEFFICIENT  $K_m$ . REPRODUCED FROM REF. 2 WITH ORIGINAL ONERA NOMENCLATURE.

WITH NEW MODEL



WITHOUT NEW MODEL

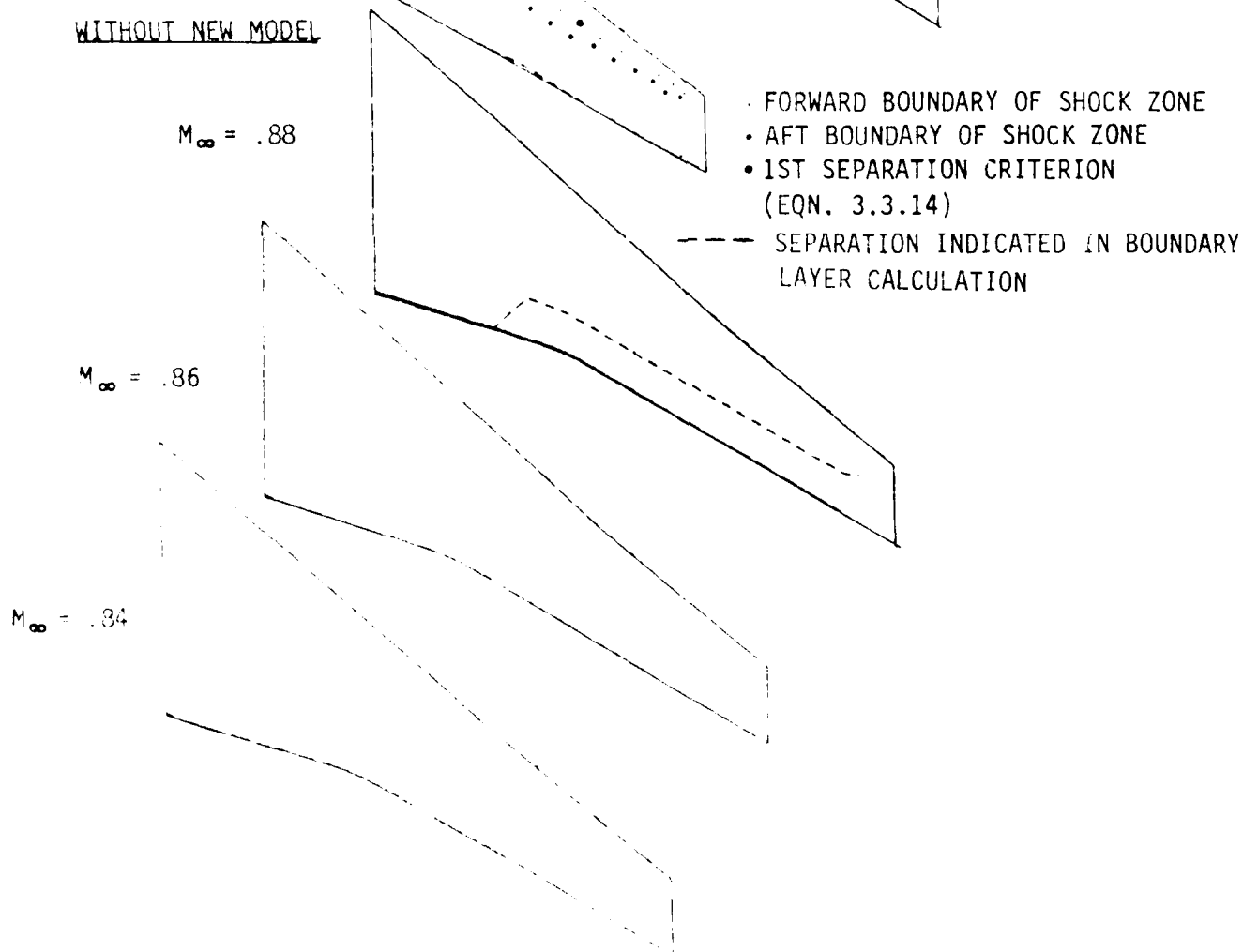


FIGURE 14. PREDICTED SHOCK PATTERNS AND SOLUTION BOUNDARIES FOR 747 WING - BODY AT  $\alpha = 2.7^\circ$

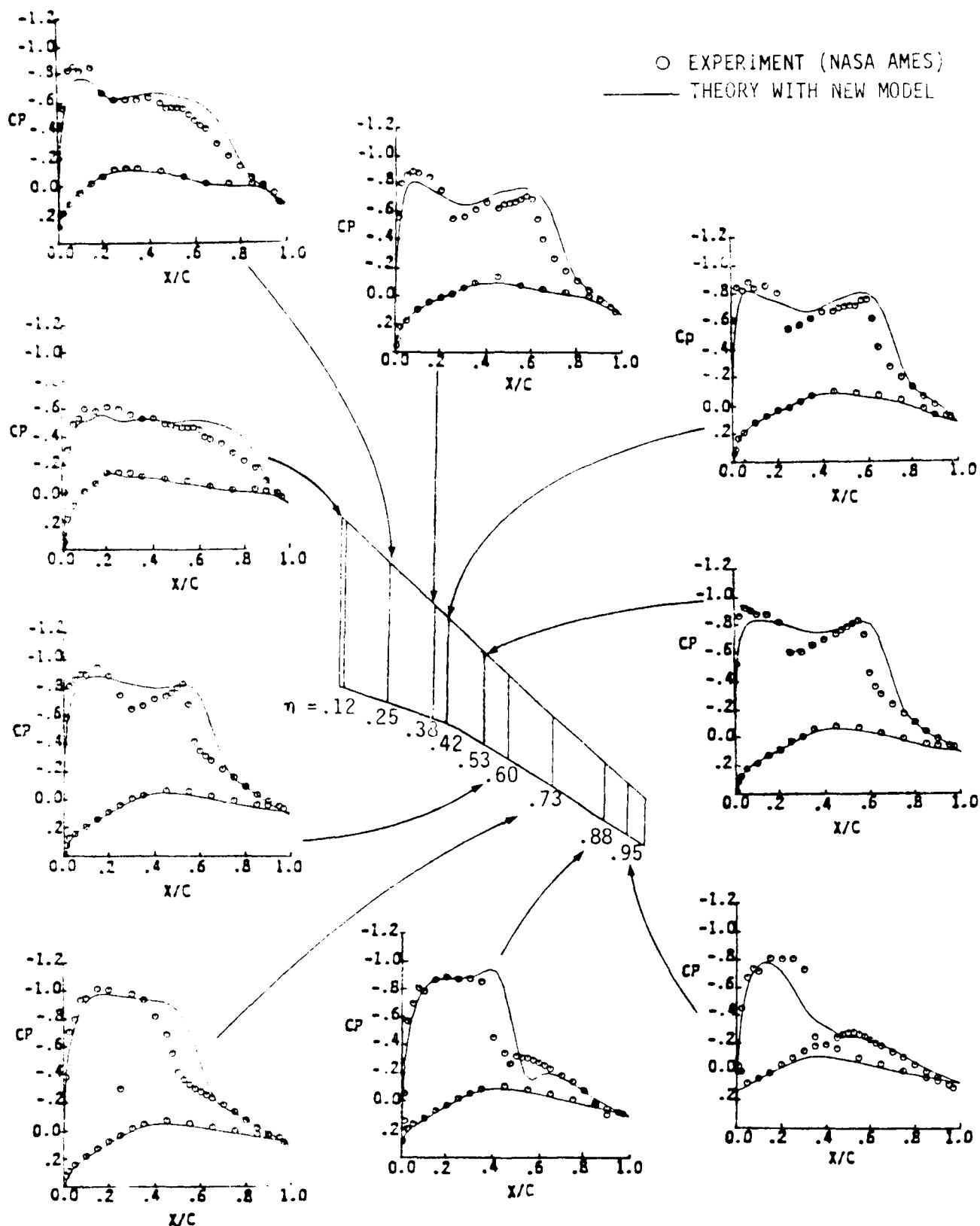


FIGURE 18 TEST - THEORY COMPARISON FOR 747 WING - BODY

$M_\infty = .88$   
 $\alpha = 2.74^\circ$

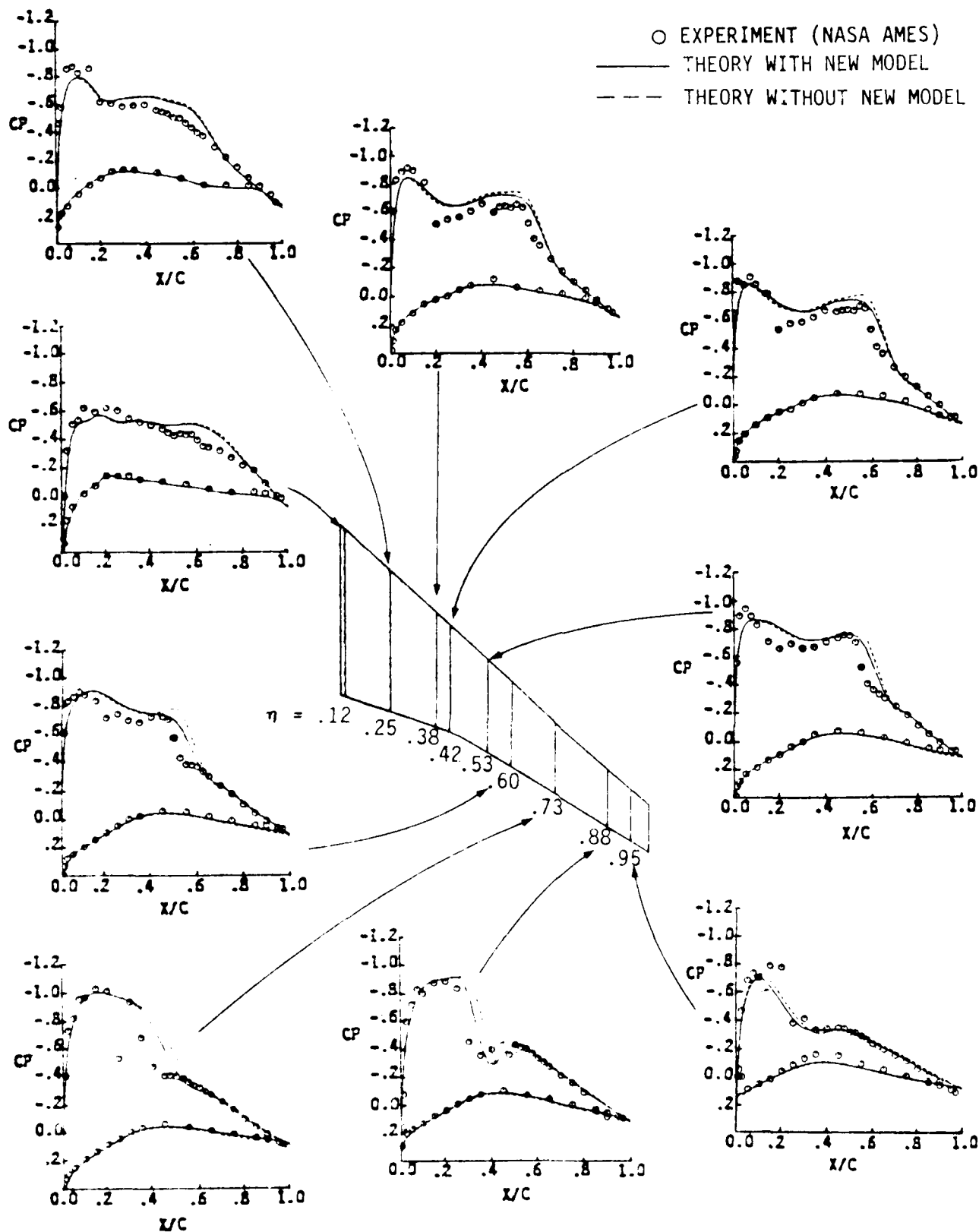


FIGURE 17 TEST - THEORY COMPARISON FOR 747 WING - BODY

$M_\infty = .86$

$\alpha = 2.70^\circ$

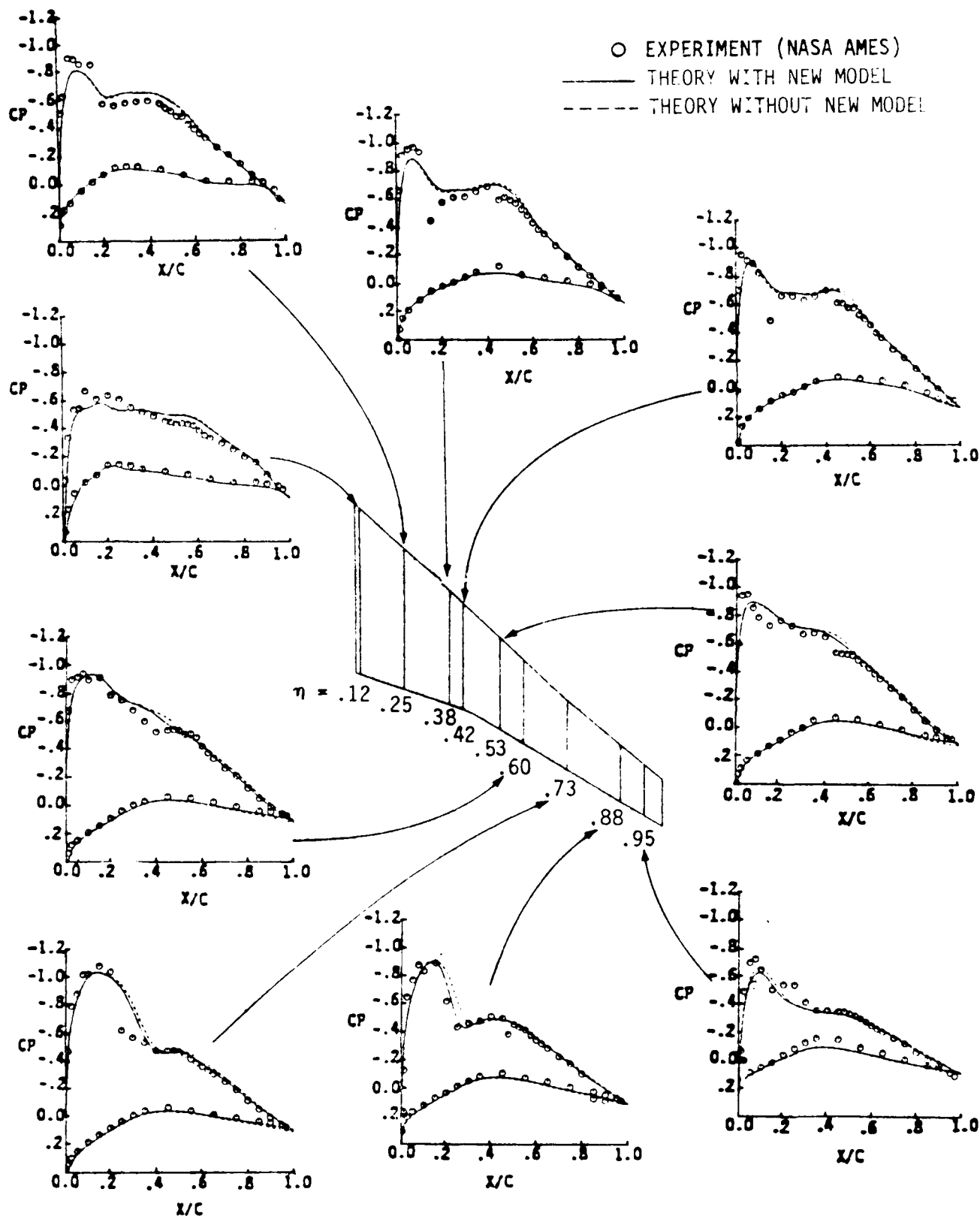


FIGURE 16 TEST - THEORY COMPARISON FOR 747 WING - BODY

$$M_{\infty} = .84$$

$$\alpha = 2.73^{\circ}$$

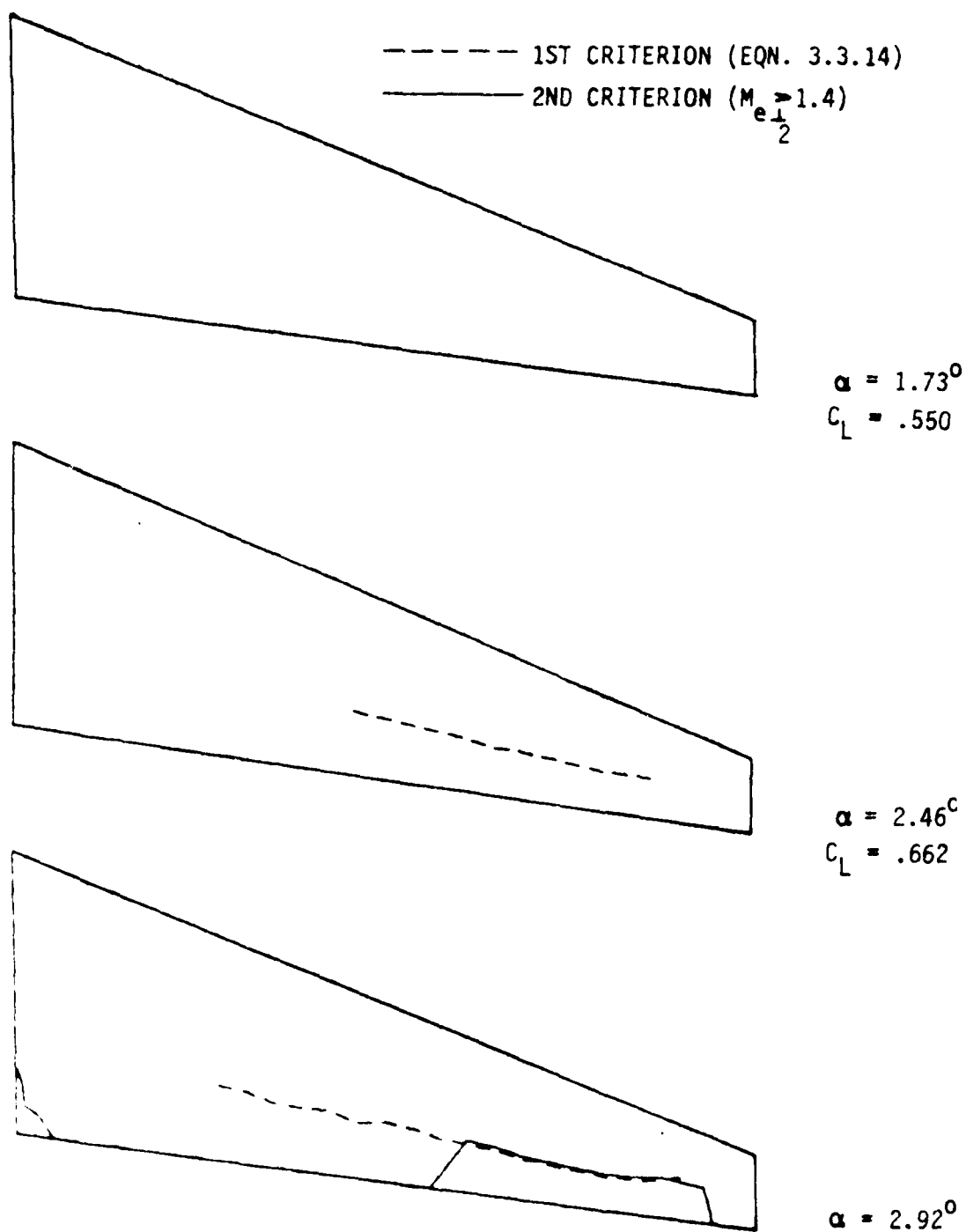


FIGURE 15 PLANFORM PLOTS SHOWING WHERE FIRST AND SECOND SHOCK-INDUCED  
 SEPARATION CRITERIA WERE EXCEEDED FOR EXPERIMENTAL WING AT  
 $M = .79$

○ EXPERIMENT BTWT 1836  $\alpha = 2.137^\circ$  ;  $C_L = .625$   
 — THEORY WITH NEW MODEL  $\alpha = 2.46^\circ$  ;  $C_L = .662$

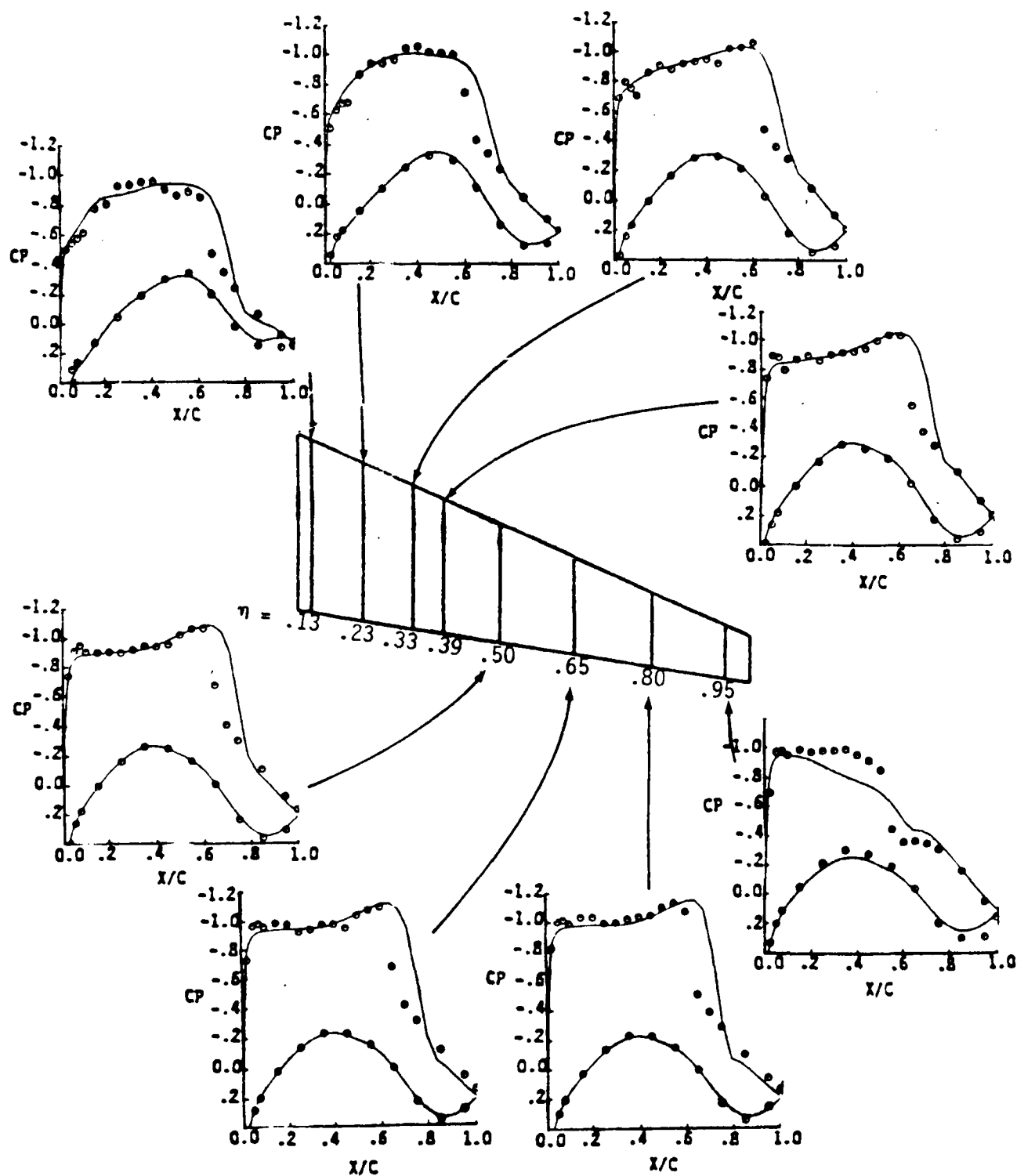


FIGURE 14 TEST - THEORY COMPARISON FOR EXPERIMENTAL WING  
 $M_\infty = .79$



EXPERIMENT BTWT 1836  $\alpha = 1.405^\circ$  ;  $C_L = .526$   
 THEORY WITH NEW MODEL  $\alpha = 1.73^\circ$  ;  $C_L = .55$

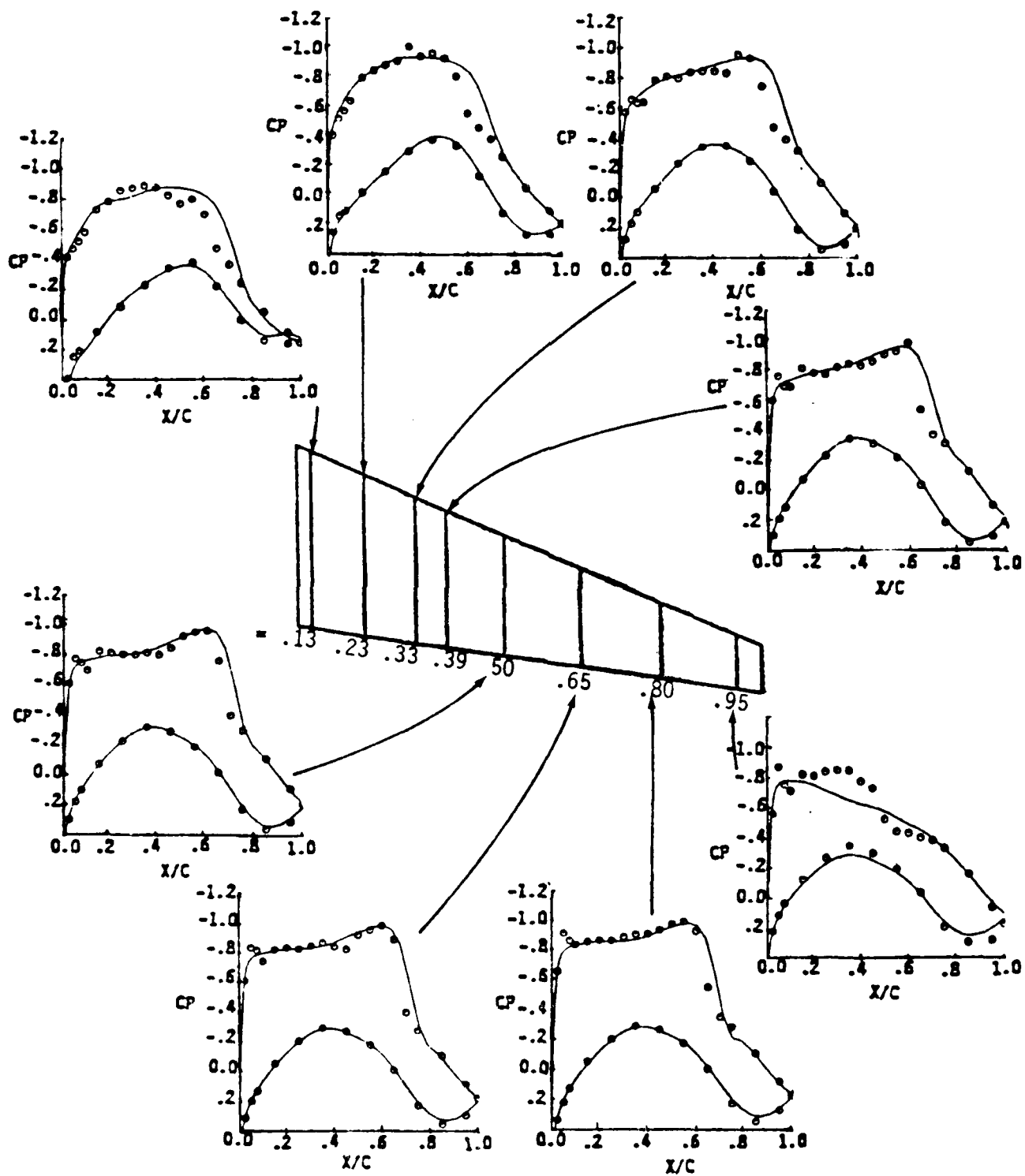


FIGURE 13 TEST - THEORY COMPARISON FOR EXPERIMENTAL WING  
 $M = .79$

○ EXPERIMENT BTWT 1836     $\alpha = 2.22^\circ$  ;  $C_L = .620$   
 — THEORY WITH NEW MODEL     $\alpha = 2.51^\circ$  ;  $C_L = .615$   
 - - - THEORY WITHOUT NEW MODEL     $\alpha = 2.51^\circ$  ;  $C_L = .633$

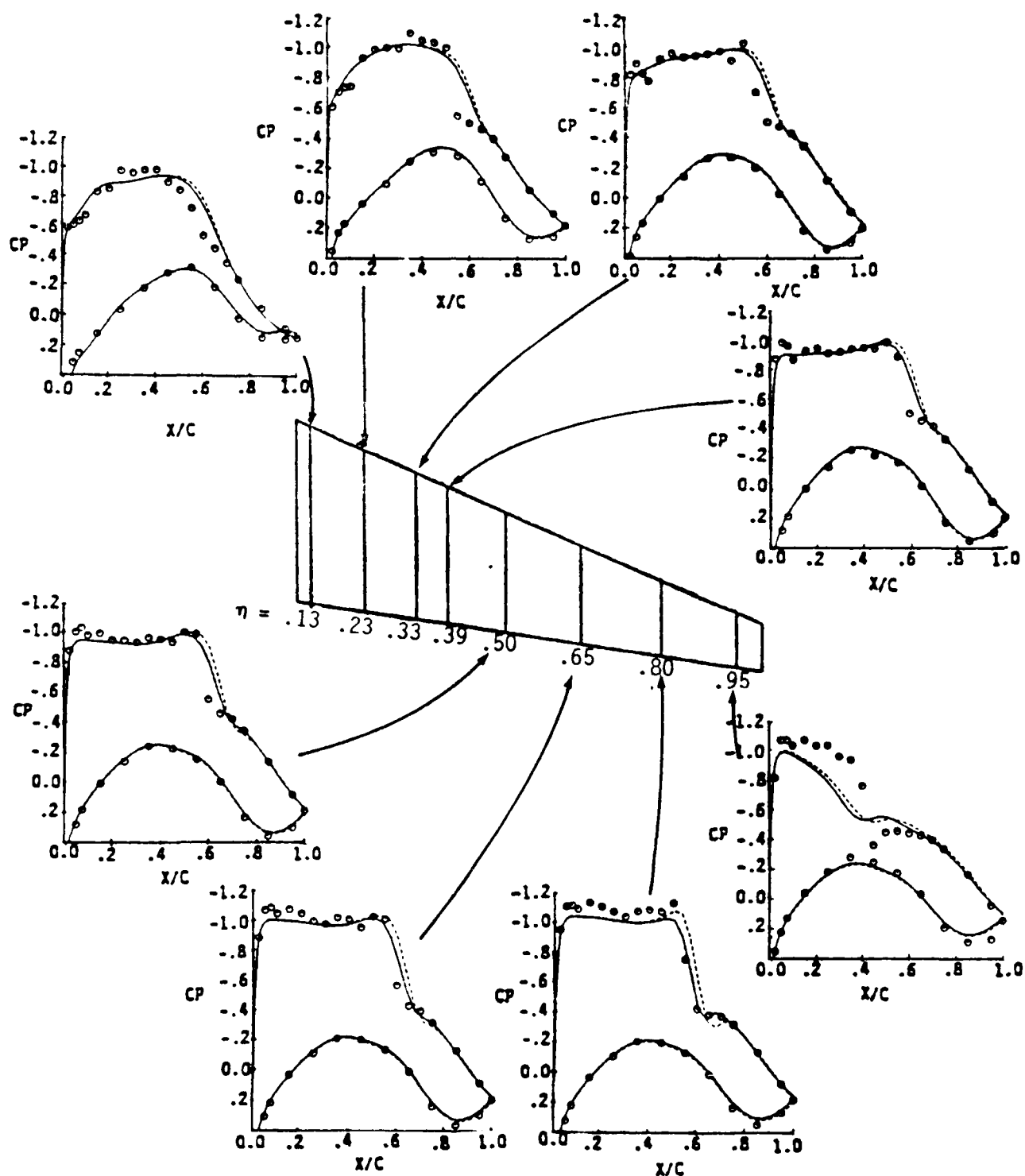


FIGURE 12 TEST - THEORY COMPARISON FOR EXPERIMENTAL WING  
 $M_\infty = .77$

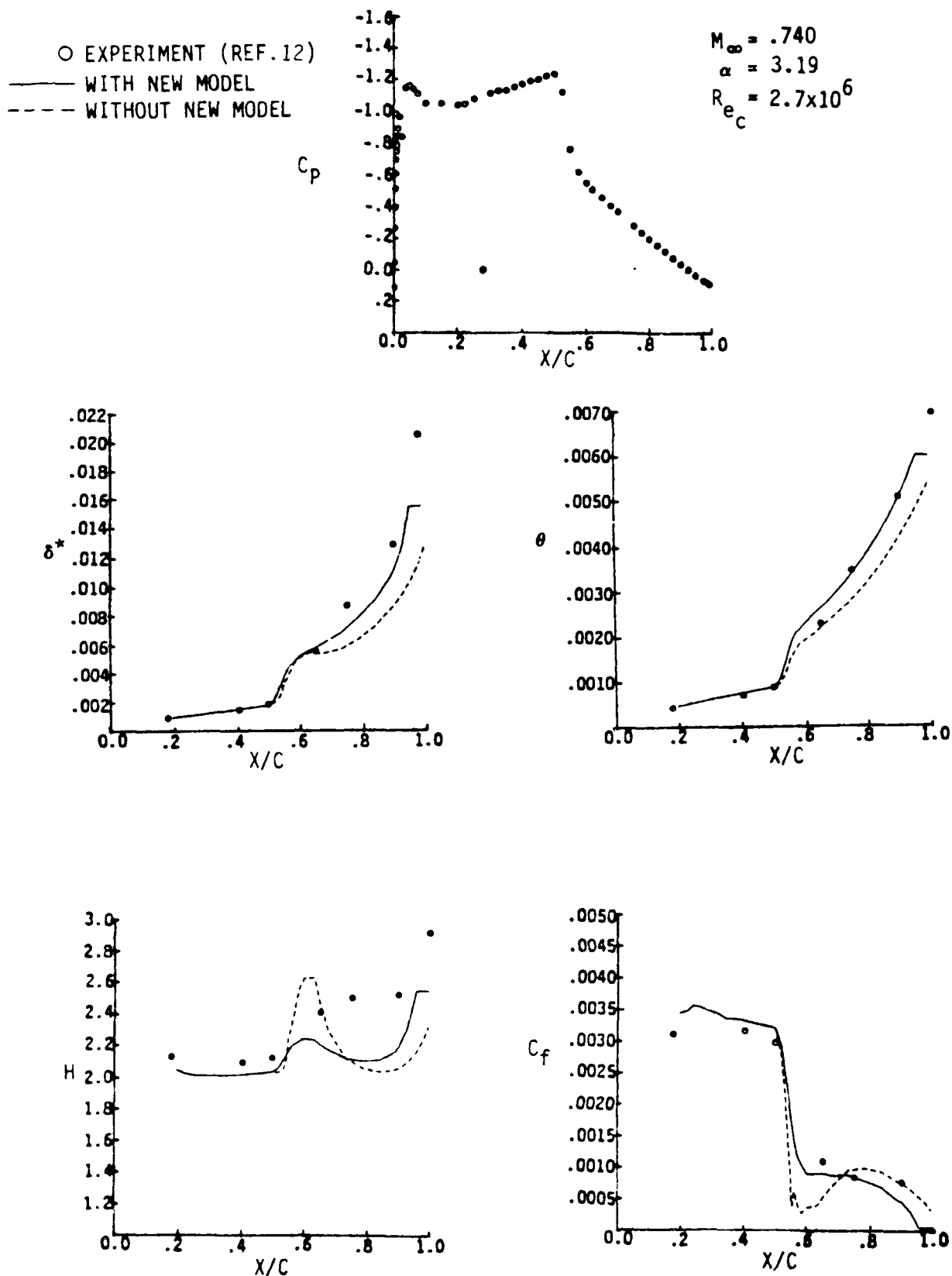


FIGURE 11 PREDICTED INTEGRAL PARAMETERS COMPARED WITH EXPERIMENT  
 FOR TWO-DIMENSIONAL RAE 2822 AIRFOIL CASE 13A.

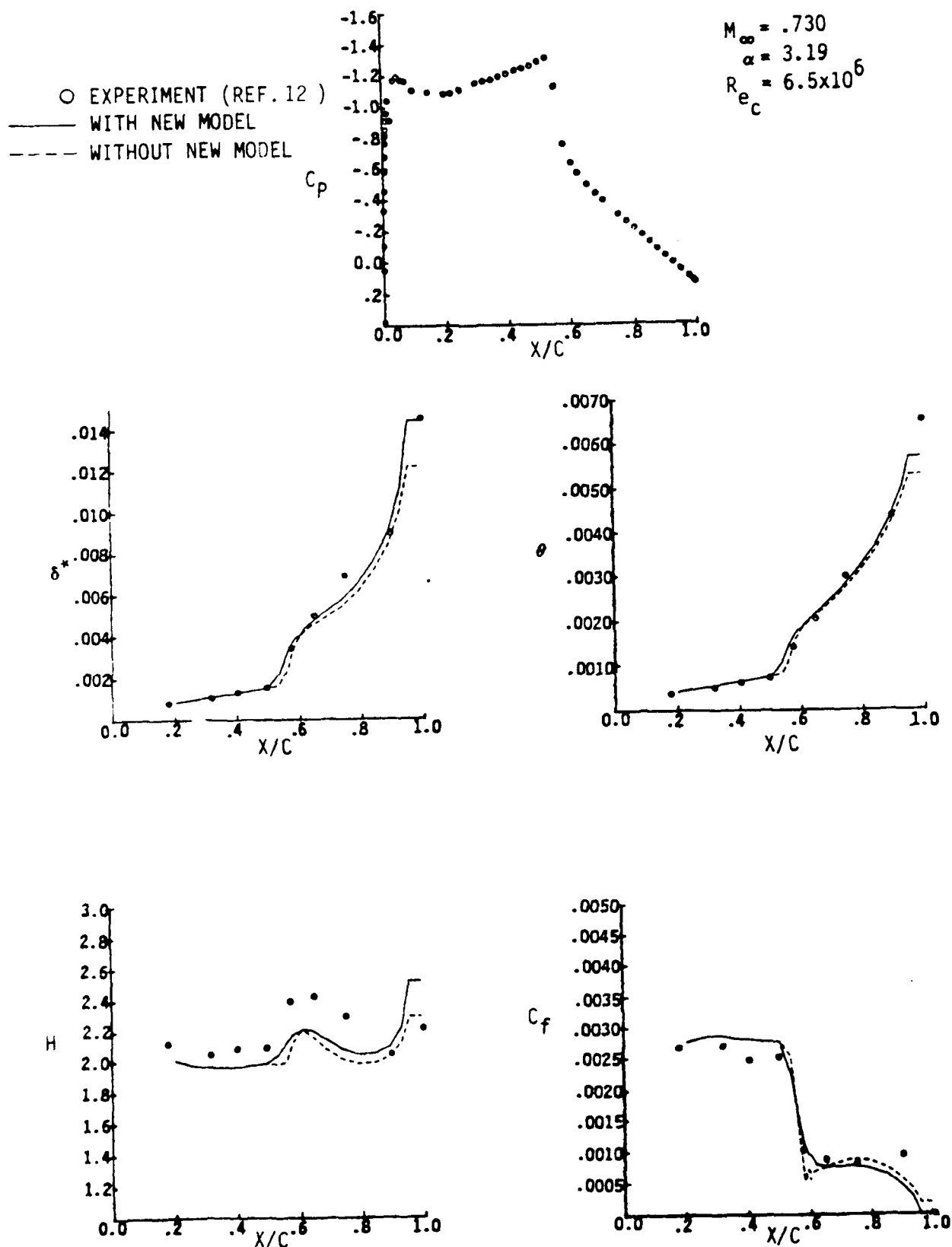


FIGURE 10 PREDICTED INTEGRAL PARAMETERS COMPARED WITH EXPERIMENT FOR TWO-DIMENSIONAL RAE 2822 AIRFOIL CASE 9

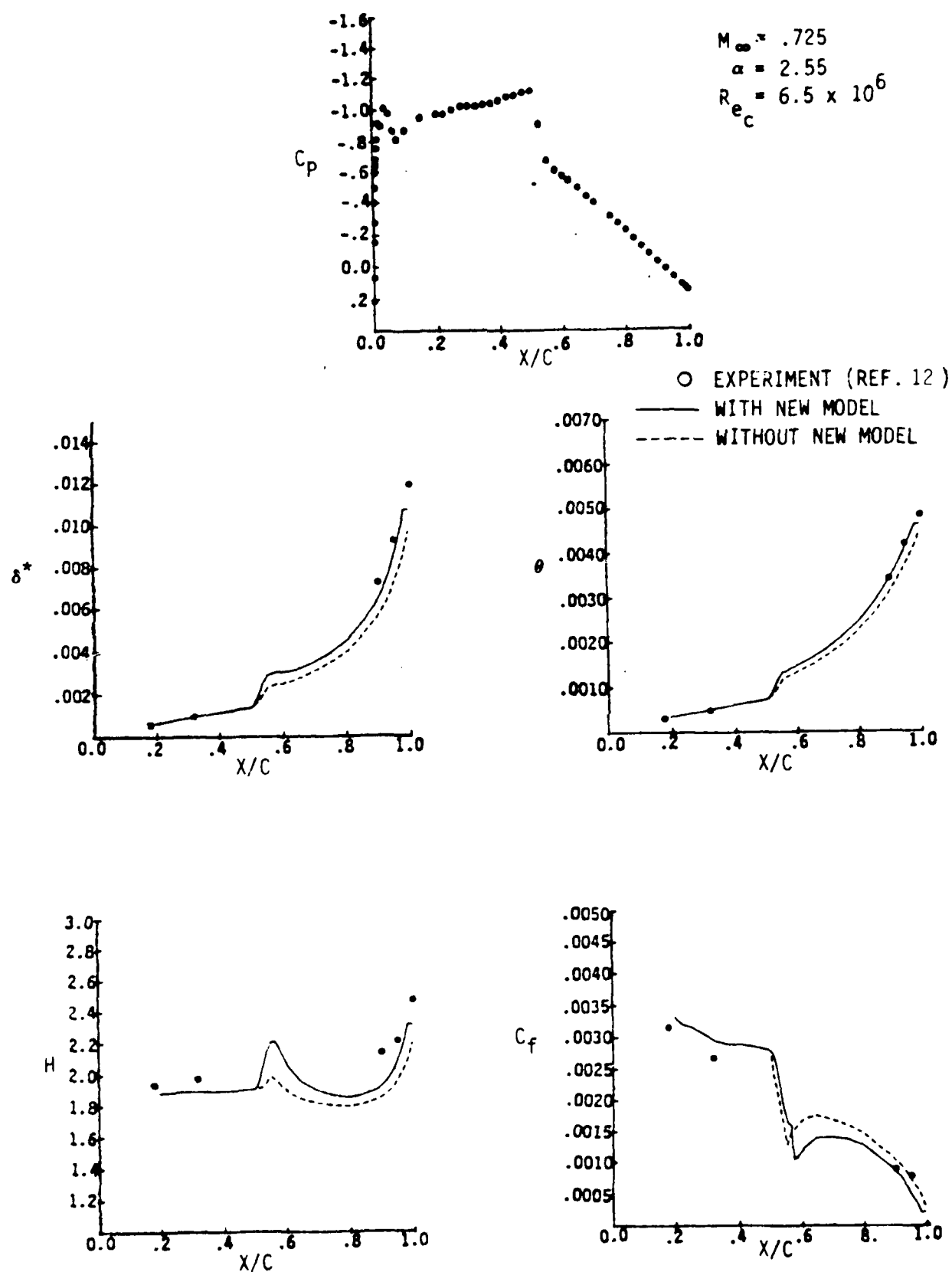


FIGURE 9 PREDICTED INTEGRAL PARAMETERS COMPARED WITH EXPERIMENT FOR TWO-DIMENSIONAL RAE 2822 AIRFOIL CASE 7.

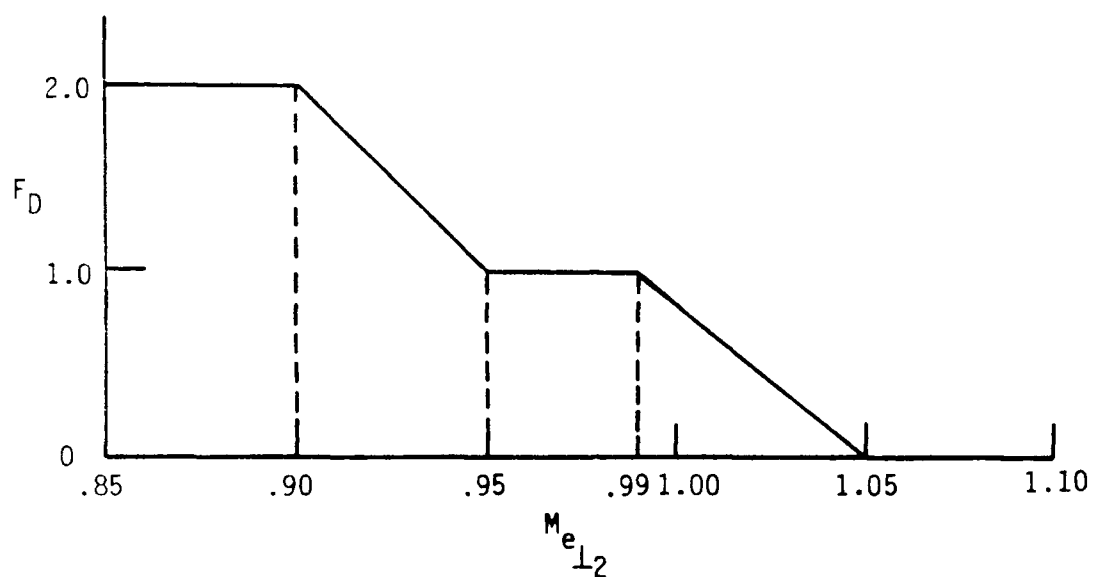


FIGURE 8 FUNCTION  $F_D (M_{e\perp 2})$  USED TO MODIFY  $\delta^*$  FOR VISCOUS-WEDGE EFFECT (EQN. 17)

# SEPARATION LIMIT IN ( $M_{e0}, H_{i0}$ ) PLANE

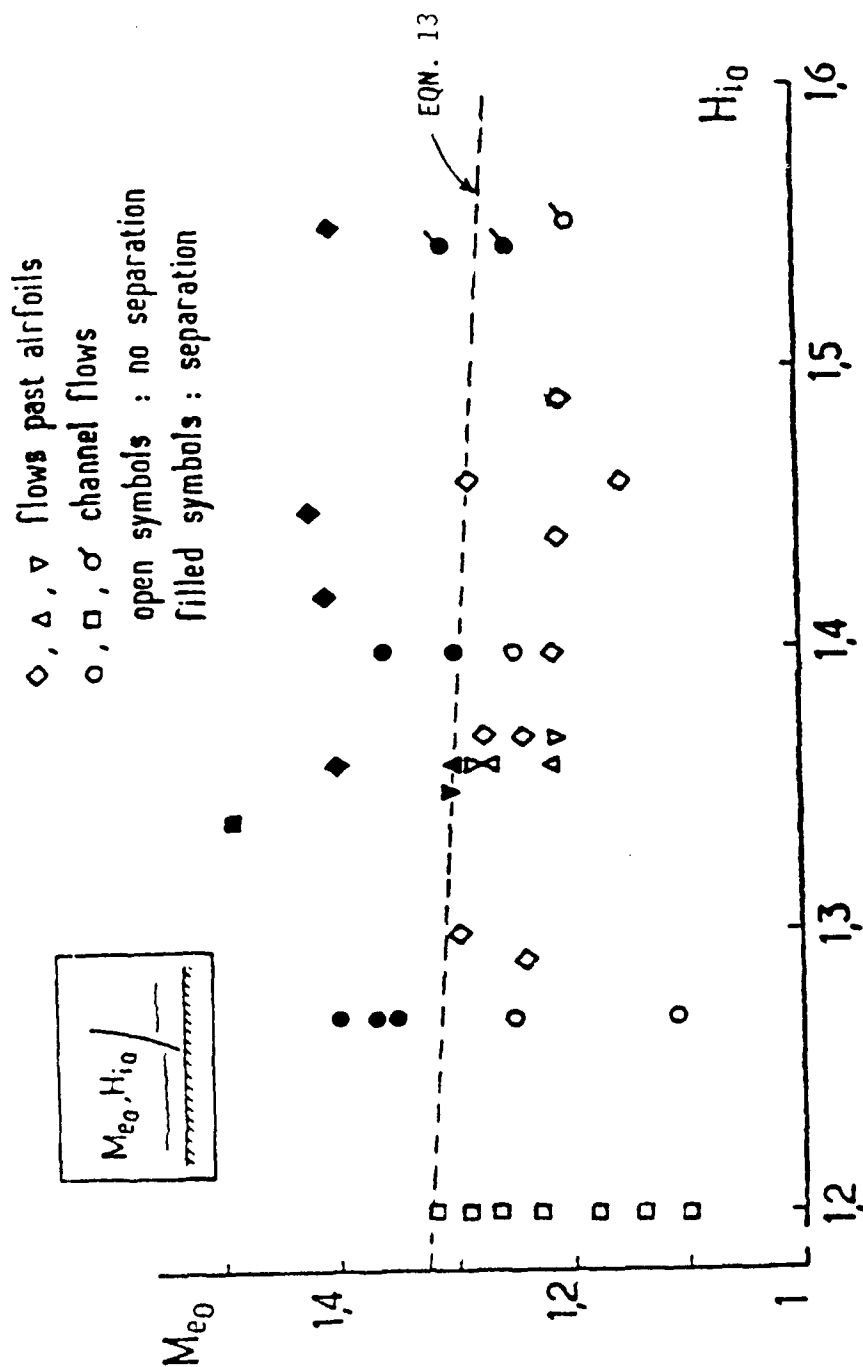


FIGURE 7 EXPERIMENTAL DATA CORRELATION FROM ONERA FOR SHOCK-INDUCED SEPARATION. REPRODUCED FROM REF. 2 WITH ORIGINAL ONERA NOMENCLATURE AND LINE REPRESENTING EQN. 13 ADDED.

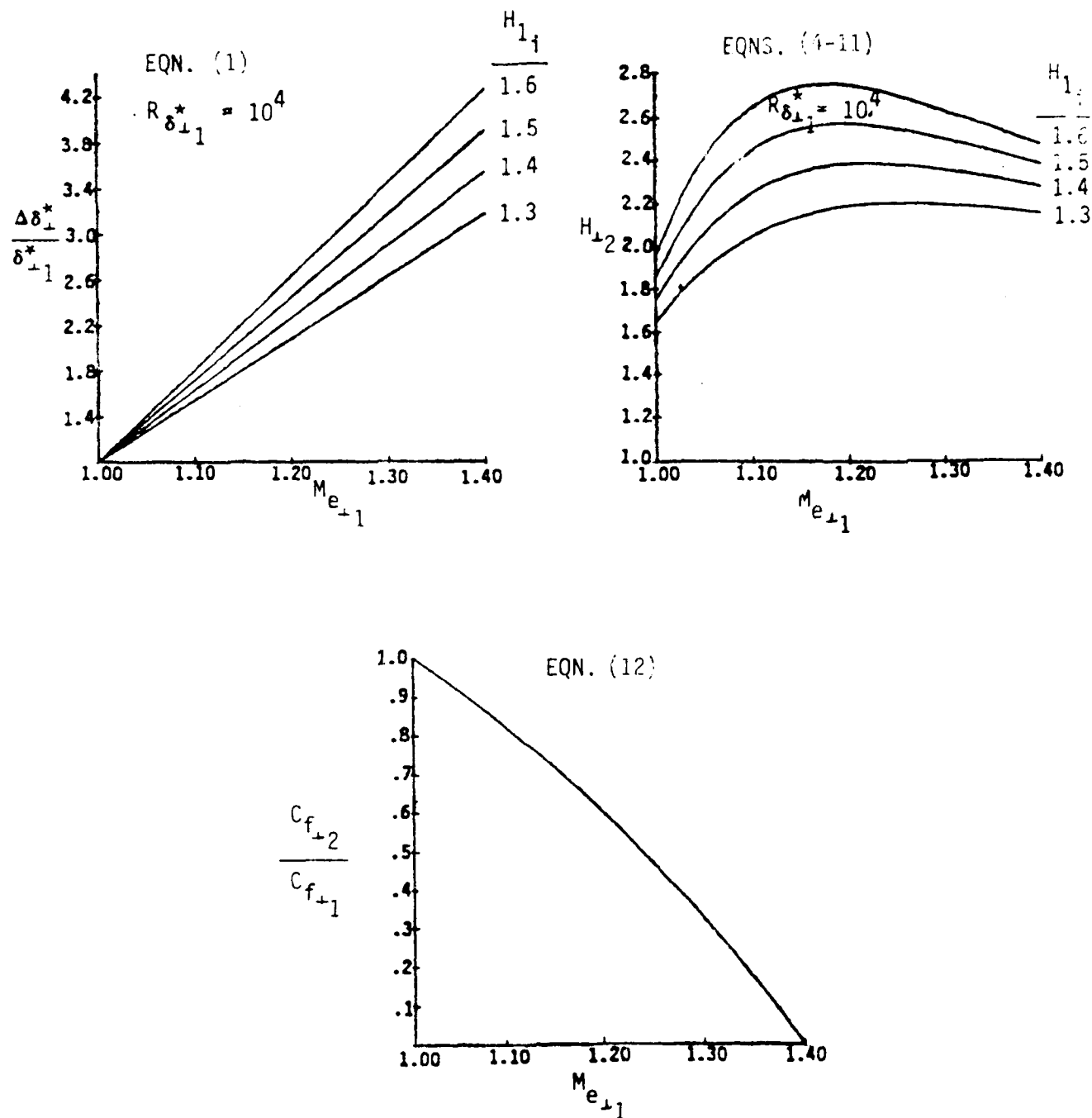


FIGURE 6 JUMP CONDITIONS FOR  $\delta_{\perp}^*$ ,  $H_{\perp}$ , AND  $C_{f_{\perp}}$



$$M_{\infty} = .84$$

$$\alpha = 7.16^{\circ}$$

— THEORY WITH NEW MODEL



EXPERIMENT

$C_p$

$\theta = 30^{\circ}$

$X/C$

$C_p$

$\theta = 90^{\circ}$

$X/C$

$C_p$

$\theta = 180^{\circ}$

$X/C$

FIGURE 20 PREDICTED PRESSURE DISTRIBUTIONS FOR A NACELLE

BOUNDARY LAYER SEPARATION DUE TO "WEAK" AND  
"STRONG" VISCOUS-INVISID INTERACTION ON AN  
INCLINED BODY OF REVOLUTION

H.U. Meier, H.-P. Kreplin  
DFVLR, Institute for Experimental Fluid Mechanics,  
Bunsenstr. 10, D-3400 Göttingen

ABSTRACT

Detailed measurements in three-dimensional boundary layers and separated flow fields, developing on a prolate spheroid and flow visualizations are presented. The discussion is concentrated on the possible topological structure of separation patterns resulting from laminar or turbulent boundary layer flows at different Reynolds numbers.

## CONTENTS

1. Experiments .....	80
2. Results .....	81
3. Summary .....	83
4. References .....	85
5. Figures .....	87

### 1. EXPERIMENTS

The model investigated in the 3m x 3m Low Speed Wind Tunnel of the DFVLR Göttingen is a sting-mounted prolate spheroid of axis ratio 1:6 (Fig. 1). The wind tunnel model was especially designed for the investigation of three-dimensional boundary layers and separated flow fields. The measuring techniques used are described in detail in Refs. [1], [2], [3]

The quantitative measurements were supplemented by different flow visualization techniques like oil flow patterns, Laser light sheets and hydrogen bubble method in a water towing tank. For this purpose wind tunnel models of various sizes were used:

3m Low Speed Wind Tunnel  $L = 2a = 2400$  mm (cf. Fig. 1)

1m Low Speed Wind Tunnel  $L = 480$  mm

Pressurized Low Speed Wind Tunnel ( $p_{\max} = 100$  bar)  $L = 480$  mm

The application of different model sizes and different wind tunnels enabled us to cover a Reynolds number range  $Re = U_{\infty} L / \nu = 1.5 \times 10^6$  to  $90 \times 10^6$ .

## 2. RESULTS

As has been found from surface hot film measurements, Ref. [3], the boundary layer flow over the prolate spheroid is completely laminar at an angle of incidence  $\alpha = 10^\circ$  and a free stream Reynolds number of  $Re = 1.6 \times 10^6$ . As demonstrated in [3] one can calculate wall streamlines from measured wall shear stress vectors. Fig. 2 shows the derived wall streamlines and a typical example of wall shear stress vectors measured in the cross section  $x_0/2a \sim 0.48$  for this flow case.

This result clearly indicates two facts:

1. One obtains converging streamlines which merge to an envelope.
2. In the regime of the enveloping streamline the wall shear stress reaches a minimum and its circumferential component vanishes, if the co-ordinate system of Fig. 1 is applied.

This wall streamline pattern is difficult to understand if the corresponding wall pressure distribution (Fig. 3) is considered. At a first glance the differences between the measured and the potential flow pressure distributions do not lead to the supposition that a vortex flow is created. However, it is clearly indicated that in the regime where negative deviations between the derivatives  $(\partial p / \partial \phi)_{exp.}$  and  $(\partial p / \partial \phi)_{pot.}$  occur (compare Figs. 4a,b), an enveloping limiting streamline was found. But the cross flows induced from the vortex flow are still small compared to the longitudinal velocity and cause a weak viscous-inviscid interaction.

An oil flow pattern (Fig. 5) obtained in the 1m Low Speed Wind Tunnel is in excellent agreement with the wall streamlines derived from measured wall shear stress values. For comparison, the calculated line of the boundary layer separation is shown in Fig. 6. This result published in [4] does not change significantly, if other calculation methods are applied (Refs. [5] to [9]).

In order to obtain some more detailed information about the topological structure of the separated flow field the Laser light sheet technique in the 1m Wind Tunnel and the hydrogen bubble method in the DFVLR Water Towing Tank [10] were applied. Both flow visualization techniques lead to a flow pattern

on the leeward side of the prolate spheroid which is shown in perspective sketch in Fig. 7. In an attempt to describe three-dimensional separated flows unambiguously, Hornung and Perry [11] introduce the concepts of streamsurface bifurcation. In this manner they avoid using the terminology of two-dimensional flow. Streamsurfaces, rather than streamlines constitute the boundaries between distinct regions of space. A detailed description of streamsurface bifurcations in Fig. 7 is given in Ref. [12].

The schematic flow pattern of "Cross Section b" in Fig. 7 is confirmed by experiments shown in Figs. 8a and 8b, where measured velocity vectors in the  $(y_0-z_0)$ -plane at  $x_0/2a = 0.73$  are shown. These measurements were carried out in the 3m x 3m Low Speed Wind Tunnel on the 2.4 m long model.

The measured velocity field (Fig. 8a) clearly indicates a strong vortex with a core at about  $\phi \sim 200^\circ$ . An enlargement of the details between  $\phi = 210^\circ$  and  $\phi = 240^\circ$  (Fig. 8b) elucidates the existence of two additional vortices. The directions of rotation are identical with those shown in Fig. 7. Even a free saddle point is indicated, so that the supposed topological structure of the separation is clearly supported by experimental evidence. The experimental results suggest that the sectional streamline emerging from "S" toward the body is not the same one as that following into the halfsaddle on the body. However, the experimental technique could not resolve this detail.

This topological structure is similar to that obtained for laminar flow at  $\alpha = 10^\circ$  and  $Re = 1.6 \times 10^5$ . It is confirmed by the wall streamline patterns obtained from wall shear stress measurements (cf. Ref. [3]), and corresponding oil flow patterns (compare Figs. 5 and 9). The main difference which can be observed in the oil flow patterns is the shift of the separation line to higher circumferential angles  $\phi$ .

The pressure distribution in the turbulent case differs considerably from corresponding values calculated by potential theory (Fig. 10). This implies that we have, in contrast to the laminar flow separation (Fig. 5 and 6), a strong viscous-inviscid interaction on the leeward side flow field but a comparable topological structure of the separated flow field.

If we increase the free stream velocity  $U_\infty$  to 45 m/s, at an angle of incidence  $\alpha = 10^\circ$  we can expect to have a separation of a three-dimensional turbulent boundary layer in the cross section  $x_0/2a = 0.64$  (compare Ref. [3]). The surface pressure distribution for this flow condition is very similar to

that shown in Fig. 3. However, the topological structure of the flow separation seems to differ considerably from that we found for the laminar case. In Fig. 11 the development of the limiting wall streamlines indicates a convergence only at the rear part of the model which is confirmed again by the corresponding oil flow pattern (Fig. 12) obtained in the Pressurized Low Speed Wind Tunnel. That means we have only one pair of vortices at the rear part of the prolate spheroid. These vortices do not cause a secondary boundary layer separation as it was determined in the laminar case (Figs. 2 and 5). The topological structure of the flow separation can be described by detail (b) in Fig. 7.

The measured boundary layer profiles in three cross sections indicate a considerable increase of the boundary layer thickness on the leeward side of the prolate spheroid (Fig. 13). For the body oriented co-ordinate system (Fig. 1) negative cross flow occurs at smaller angles  $\phi$ , with increasing distance  $x_0$ . The vortical structure within the boundary layer may be interpreted as a longitudinal vortex embedded inside of a thickening boundary layer. This vortex appears to grow in "size" and "strength" and moves away from the surface. The negative crossflow is certainly not an unequivocal identification of a flow separation, because its location depends on the co-ordinate system chosen for the data reduction procedure. Consequently, for the identification of separation other criteria should be applied which have to be independent of co-ordinate systems. These may be obtained by calculating the divergence of the wall shear stress and/or determining the eigen-values of the Jacobian matrix of the velocity field, cf. Ref. [13].

### 3. SUMMARY

The investigations lead to the following results and conclusions:

- The topological structure of the separation patterns on the prolate spheroid indicates considerable differences at an angle of incidence  $\alpha = 10^\circ$  between laminar and turbulent three-dimensional boundary layer flow.
- The viscous-inviscid interaction at  $\alpha = 10^\circ$  is weak, thus only small cross flows compared to the longitudinal velocity occur. For this reason differences between the measured and the calculated potential flow surface pres-

sure  $c_p$ , which would indicate a flow separation, are not recognizable. The corresponding derivatives  $\partial c_p / \partial \phi$  and  $\partial c_p / \partial x_0$  lead to systematical deviations in a region where flow visualizations and wall shear stress measurements indicate negative streamsurface bifurcations.

- The topological structure of the separation pattern at an angle of incidence  $\alpha = 10^\circ$  for laminar boundary layer flow is similar to that observed at  $\alpha = 30^\circ$  with turbulent boundary layer separation. This separation pattern is discussed in detail and compared with experimental results.

#### Acknowledgement

The authors gratefully acknowledge the support of Mr. H.J. Bendig and Mr. H. Mittmann performing the flow visualization in the Pressurized Low Speed Wind Tunnel of the "Hauptabteilung Windkanäle".

#### 4. REFERENCES

- [1] Kreplin, H.-P.; Meier, H.U.; Maier, A.: Wind Tunnel Model and Measuring Techniques for the Investigation of Three-dimensional Turbulent Boundary Layers. Proc. AIAA 10th Aerodynamic Testing Conf., San Diego, Cal., Paper 78-781, 1978.
- [2] Meier, H.U.; Kreplin, H.-P.: Experimental Investigation of the Boundary Layer Transition and Separation on a Body of Revolution. Z. Flugwiss. Weltraumforschung 4, Heft 2, pp. 65-71, 1980.
- [3] Kreplin, H.-P.; Vollmers, H.; Meier, H.U.: Measurements of the Wall Shear Stress on an Inclined Prolate Spheroid. Zeitschrift für Flugwissenschaft und Weltraumforschung 6, Heft 4, pp. 248-252, 1982.
- [4] Schneider, G.: Calculation of Three-dimensional Boundary Layers on Bodies of Revolution at Incidence. Presented at 5th US-FRG DEA-Meeting, Annapolis, Maryland, April 16-18, 1980, AFFDL-TR-80-3088, pp. 287-314, 1980.
- [5] Geißler, W.: Calculation of Three-dimensional Laminar Boundary Layer Around Bodies of Revolution at Incidence and With Separation. AGARD-CP-168, 1975.
- [6] Gebeci, T.; Knattab, A.K.; Stewartson; Keith: Three-dimensional Laminar Boundary Layers and the Ok of Accessibility. J. Fluid Mech. Vol. 107, pp. 57-87, 1981.
- [7] Stock, H.W.: Computation of the Boundary Layer and Separation Lines on Inclined Ellipsoids and of Separated Flows on Infinite Swept Wings. Presented at the 5th US-FRG DEA-Meeting, Annapolis, Maryland, April 16-18, 1980, AFFDL-TR-80-3088, 1980.
- [8] Wang, K.C.: Boundary Layer Over a Blunt Body at Low Incidence With Circumferential Reversed Flow. J. Fluid Mech. 72, pp. 49-65, 1975.



- [9] Patel, V.C.; Baek, J.H.: Calculation of Three-dimensional Boundary Layers on Bodies at Incidence. Presented at the 7th US-FRG DEA-Meeting Aberdeen, Maryland, May 26-27, 1982.
- [10] Bippes, H.; Maier, A.: Research Programme and Measurement Techniques in the Water Towing Tank of DFVLR in Göttingen. Proc. ICIASF Congr., Dayton, Ohio, Sept. 30-Oct. 2, 1981, ICIASF '81 Record, pp. 53-60, 1981.
- [11] Hornung, H.; Perry, A.E.: Stream Surface Bifurcation, Vortex Skeletons and Separation. DFVLR-Report, 1B 222-82 A 25, 1982.
- [12] Meier, H.U.; Kreplin, H.-P.; Vollmers, H.: Development of Boundary Layers and Separation Patterns on a Body of Revolution at Incidence. Proc. 2nd Symp. on "Numerical and Physical Aspects of Aerodynamic Flows", California State University, Long Beach, Cal., Jan. 17-20, 1983.
- [13] Vollmers, H.; Kreplin, H.-P.; Meier, H.U.: Separation and Vortical-type Flow Around a Prolate Spheroid - Evaluation of Relevant Parameters - . AGARD Conf. Proc. No. 342, Aerodynamics of Vortical Type Flows in Three Dimensions, pp. 14-1 - 14-14, 1983.

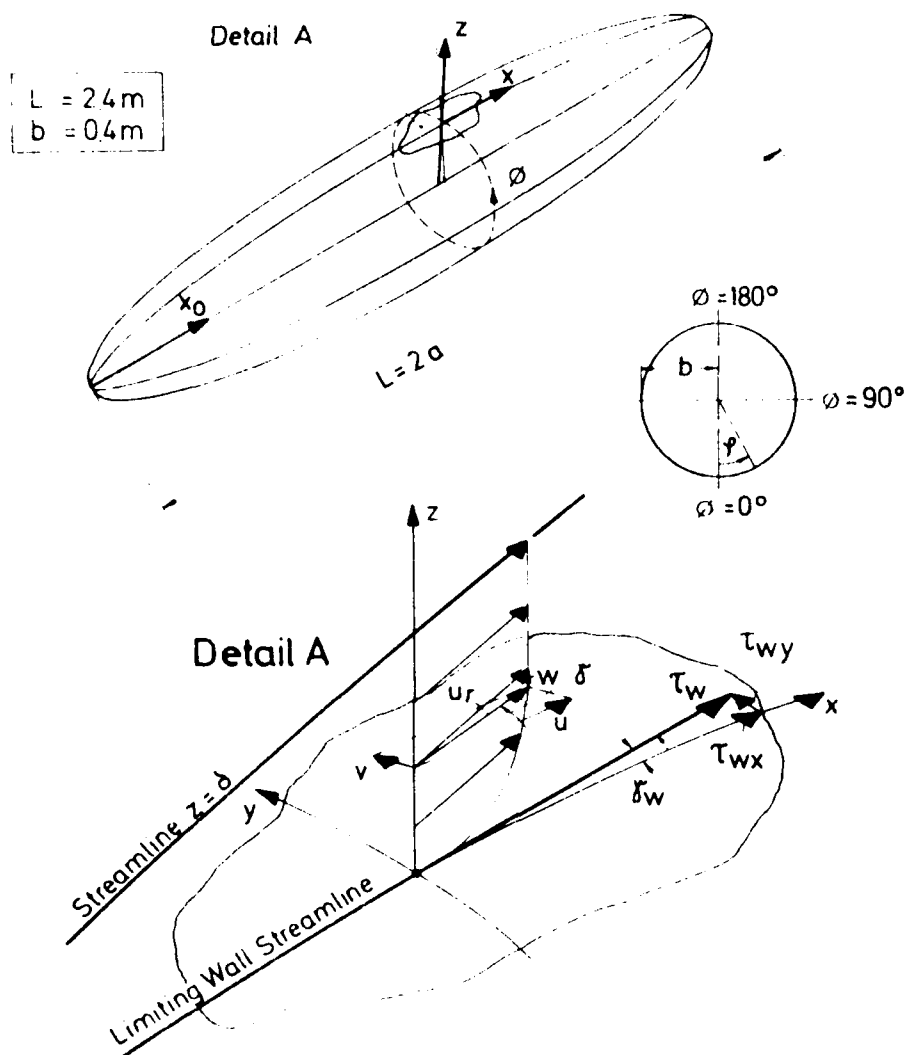


Fig. 1: Model and boundary layer co-ordinate system

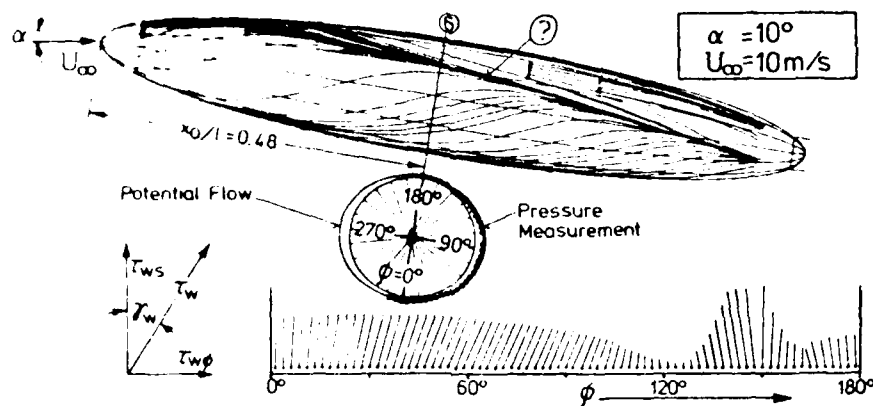


Fig. 2: Wall streamlines calculated from measured wall shear stress values in 12 cross sections. The wall shear stress vectors for laminar boundary layer flow in the cross section  $x_0/2a = 0.48$  are shown as an example ( $Re = U_\infty L/\nu = 1.6 \times 10^6$ ).

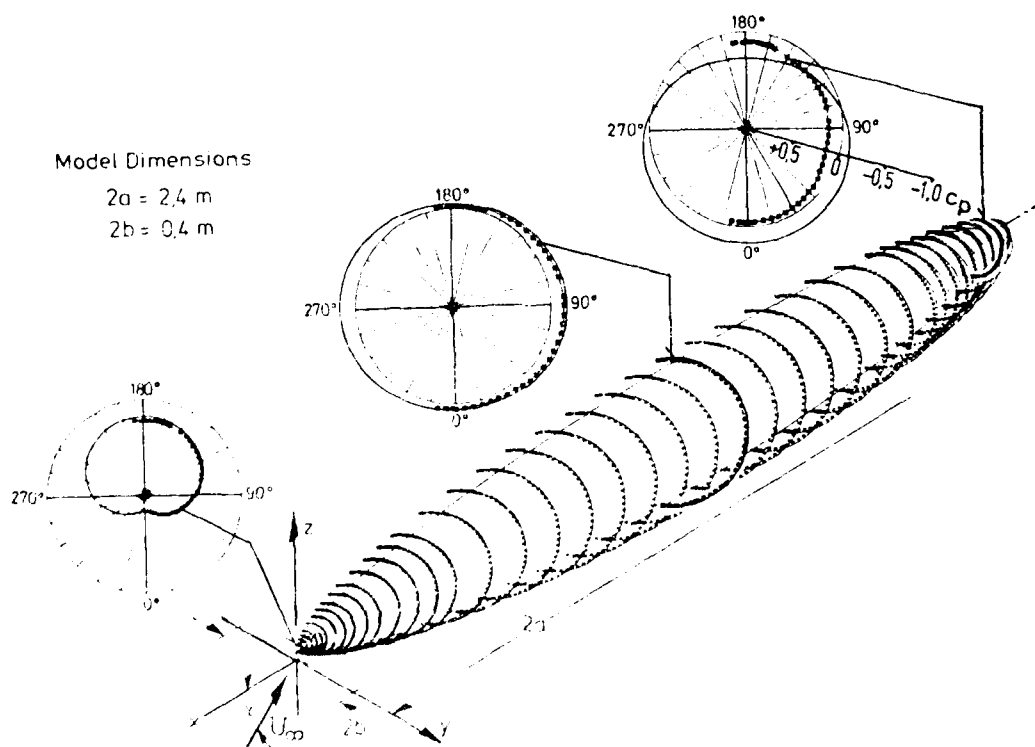


Fig. 3: Measured surface pressure distributions in comparison with calculated values from potential flow theory ( $\alpha = 10^\circ$ ,  $U_\infty = 10 \text{ m/s}$ ,  $Re = 1.6 \times 10^6$ ).

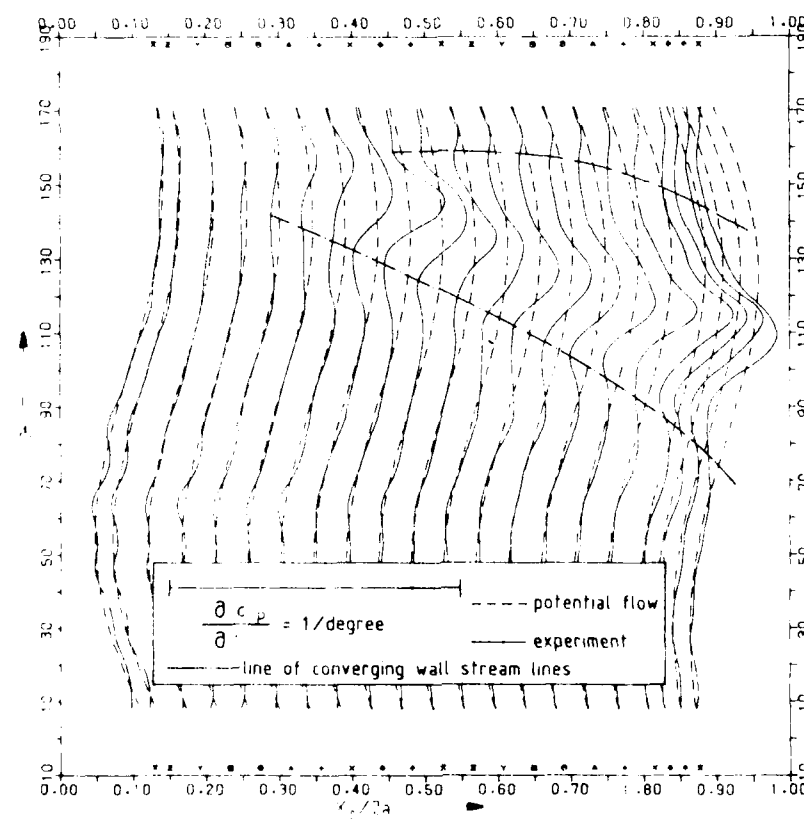
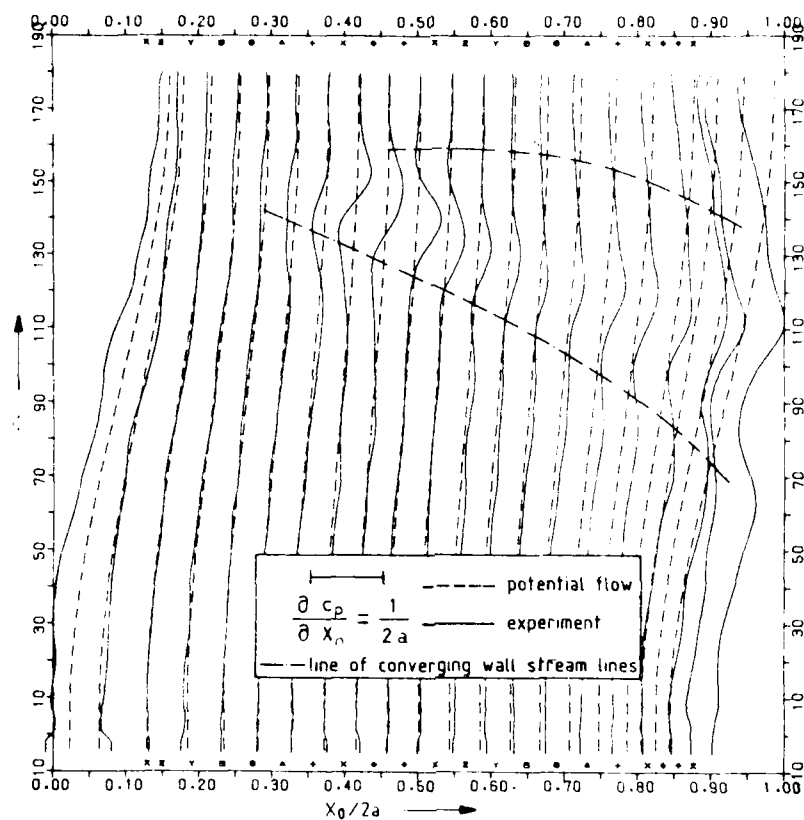


Fig. 4.10. Derivatives  $\frac{\partial c_p}{\partial x_n}$  and  $\frac{\partial c_p}{\partial s}$  for cross sections  $x_0/2a = \text{const.}$  ( $\alpha = 10^\circ$ ,  $Re = 1.6 \times 10^6$ ).



Fig. 5: Oil flow pattern for laminar boundary layer flow ( $\alpha = 10^\circ$ ,  $U_\infty = 50$  m/s,  $p_0 = 1$  bar, model length  $L = 48$  cm,  $Re = 1.6 \times 10^5$ ) DEFLER Im Low Speed Wind Tunnel.

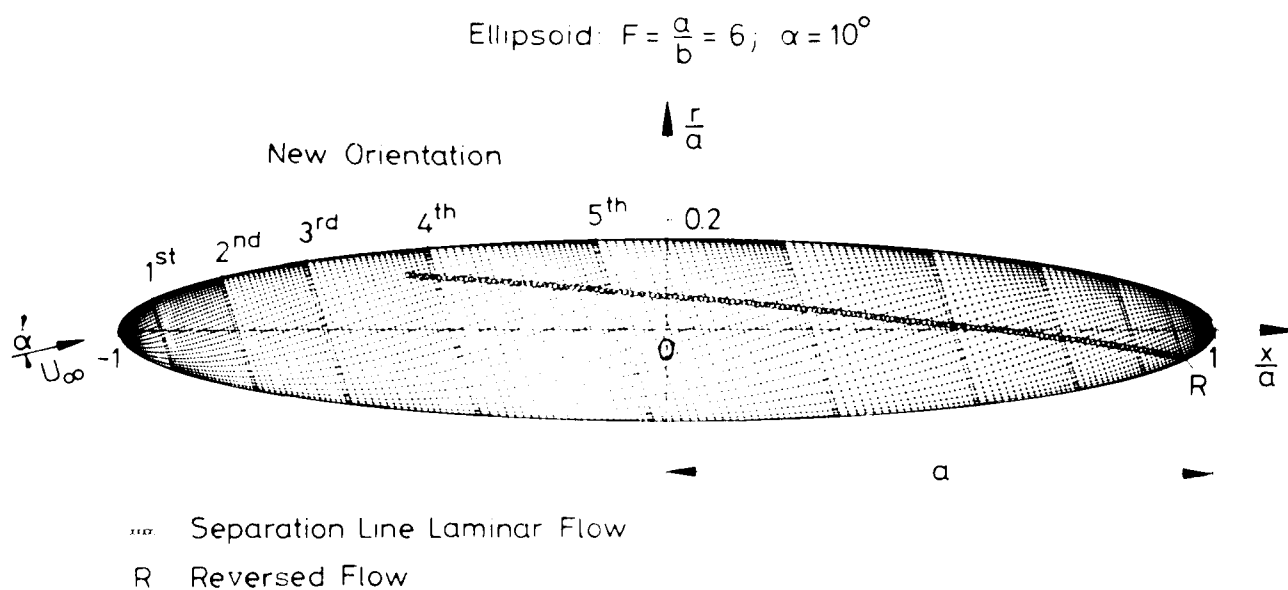
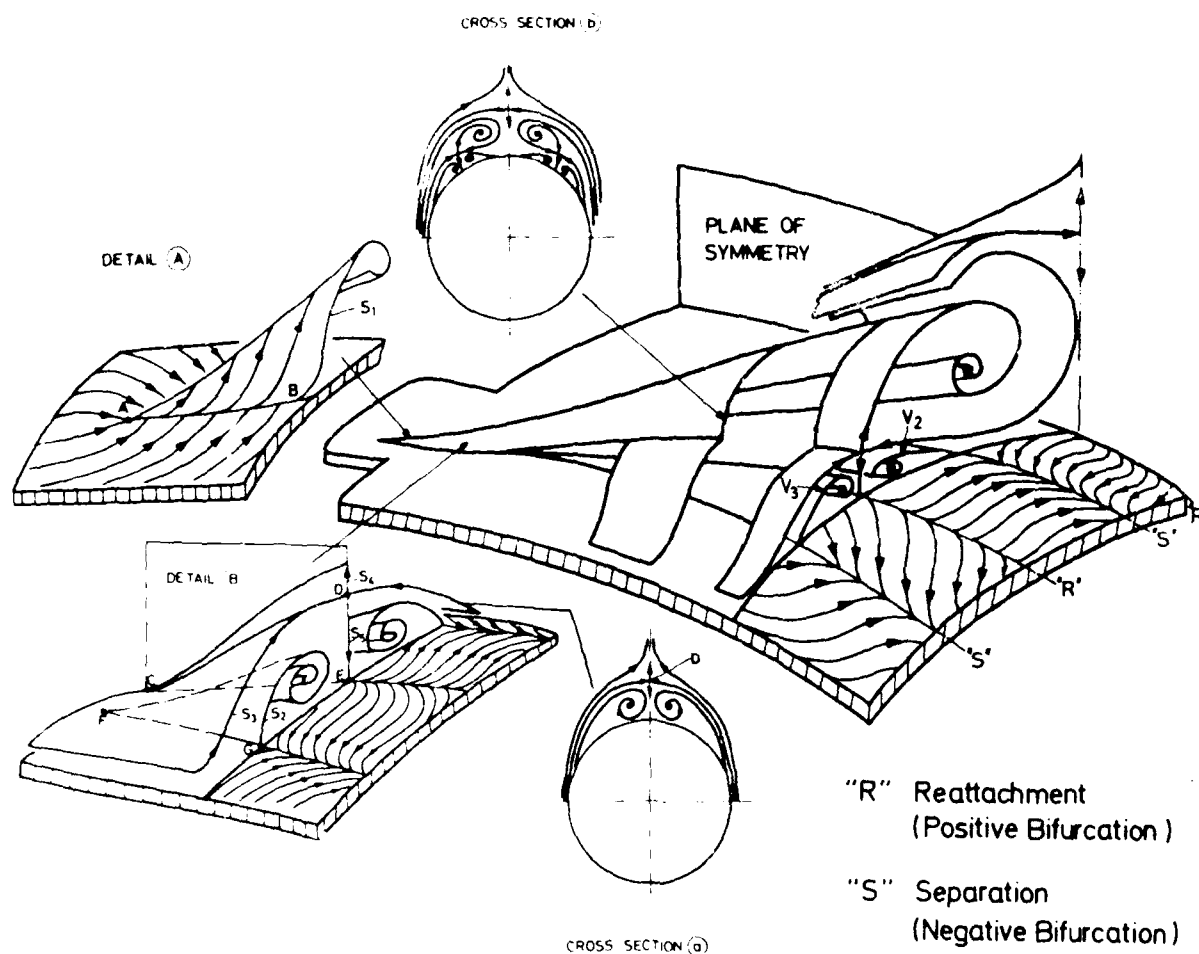


Fig. 6: Calculated "Separation Line" for laminar boundary layer flow (see [7]).



## Topological Considerations of the Separation Pattern on an Inclined Prolate Spheroid

Fig. 1. Topological considerations of the separation pattern on an inclined prolate spheroid.

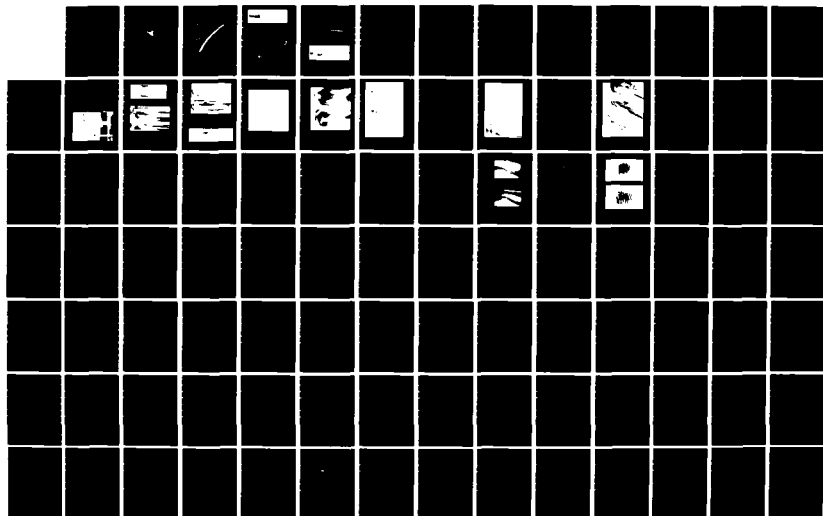
AD-A153 020

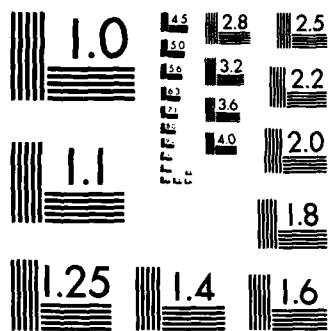
PROCEEDINGS OF THE US AIR FORCE AND THE FEDERAL  
REPUBLIC OF GERMANY DATA. (U) AIR FORCE WRIGHT  
AERONAUTICAL LABS WRIGHT-PATTERSON AFB OH A W FIORE  
AUG 84 F/G 20/4

2/4

UNCLASSIFIED

NL





MICROCOPY RESOLUTION TEST CHART  
NATIONAL BUREAU OF STANDARDS-1963-A



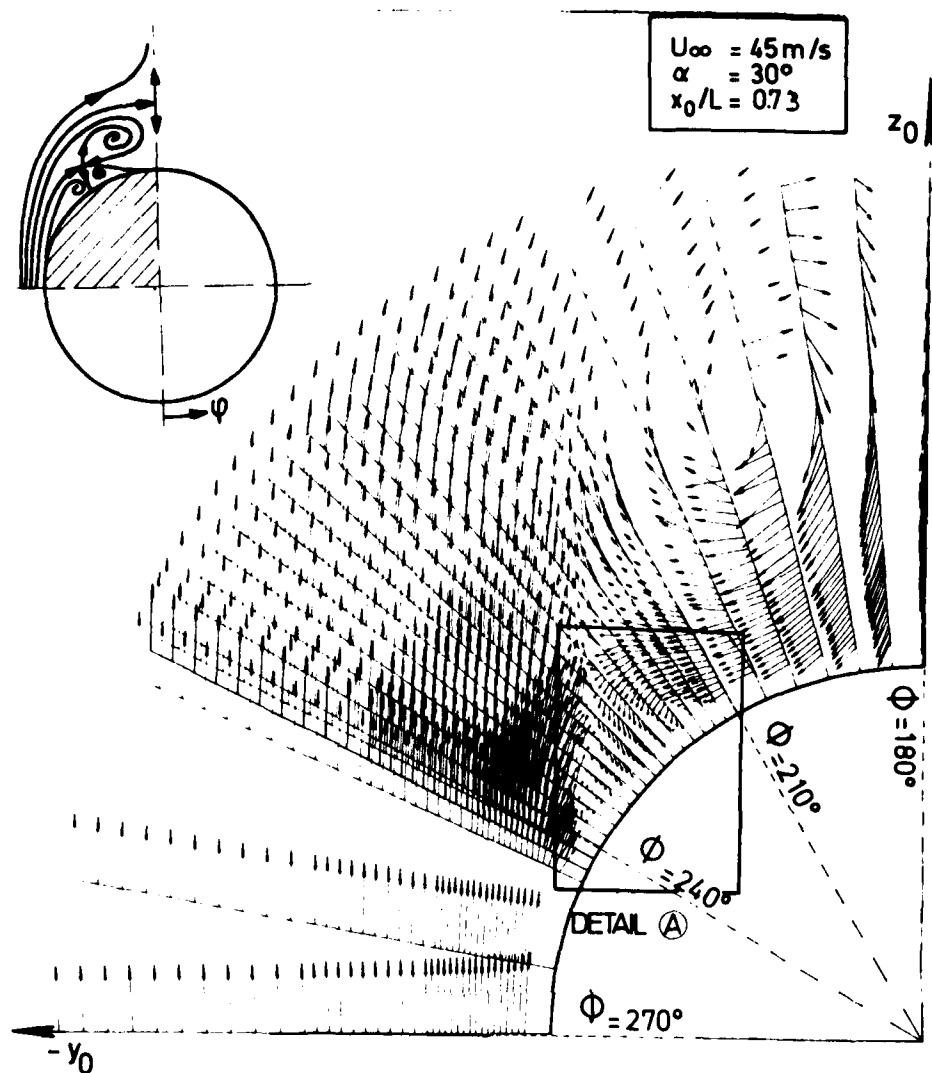


Fig. 8a: Cross flow velocity components in the  $y_0$ - $z_0$ -plane of the leeward flow field on an inclined prolate spheroid. (Turbulent boundary layer separation in the cross section  $x_0/L = 0.73$  at  $\alpha = 30^\circ$ ,  $U_{\infty} = 45 \text{ m/s}$ ,  $Re = 7 \times 10^6$ ).

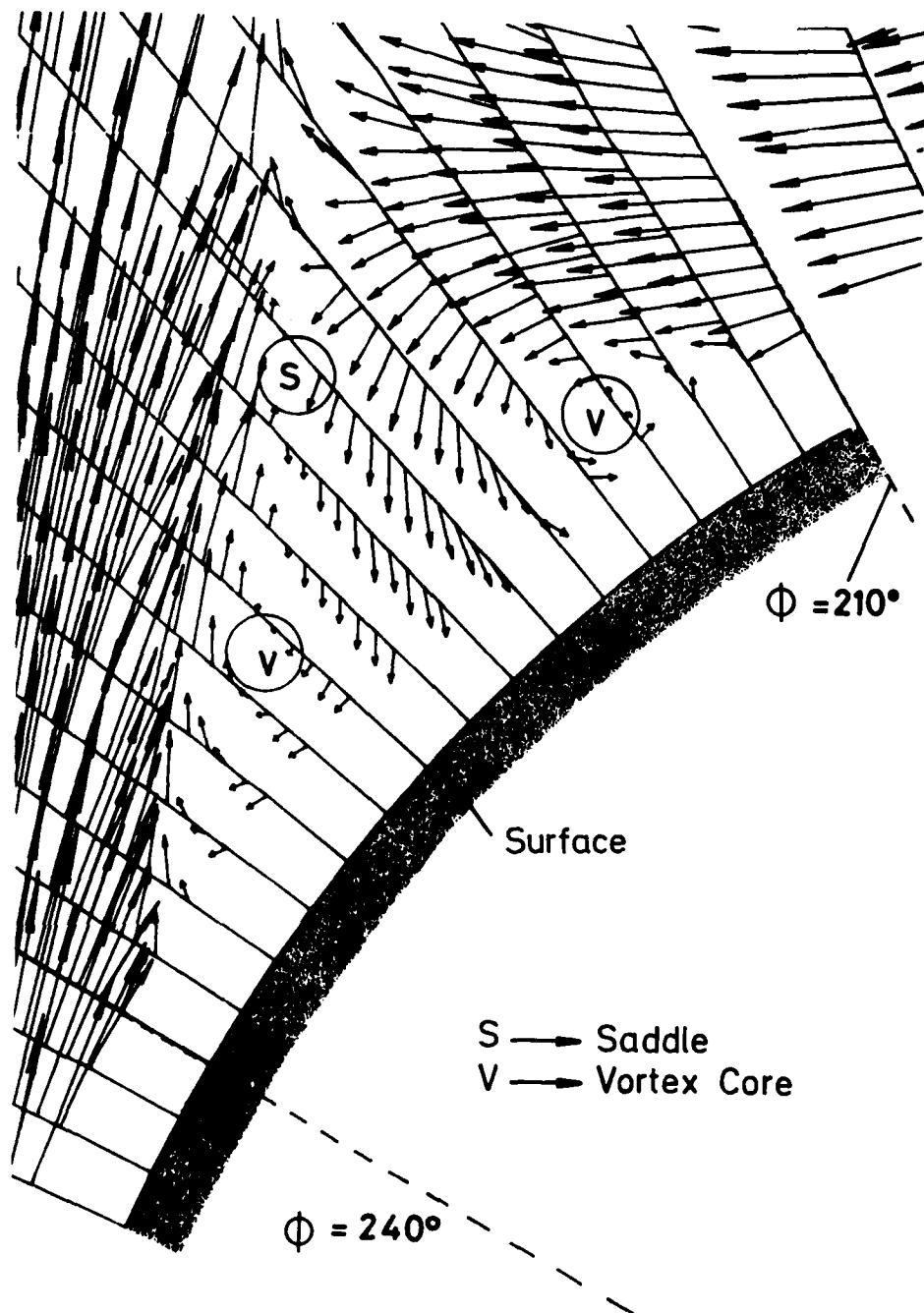


Fig. 8b: Detail (A) of Fig. 8a, indicating two vortices and a saddle point, a topological structure as described in Fig. 7.



Fig. 9: Oil flow pattern for turbulent boundary layer separation ( $\alpha = 30^\circ$ ,  $U_\infty = 37$  m/s,  $p_0 = 6,5$  bar, model length  $L = 48$  cm,  $Re = 8 \times 10^4$ , DFVLR Pressurized Low Speed Wind Tunnel).

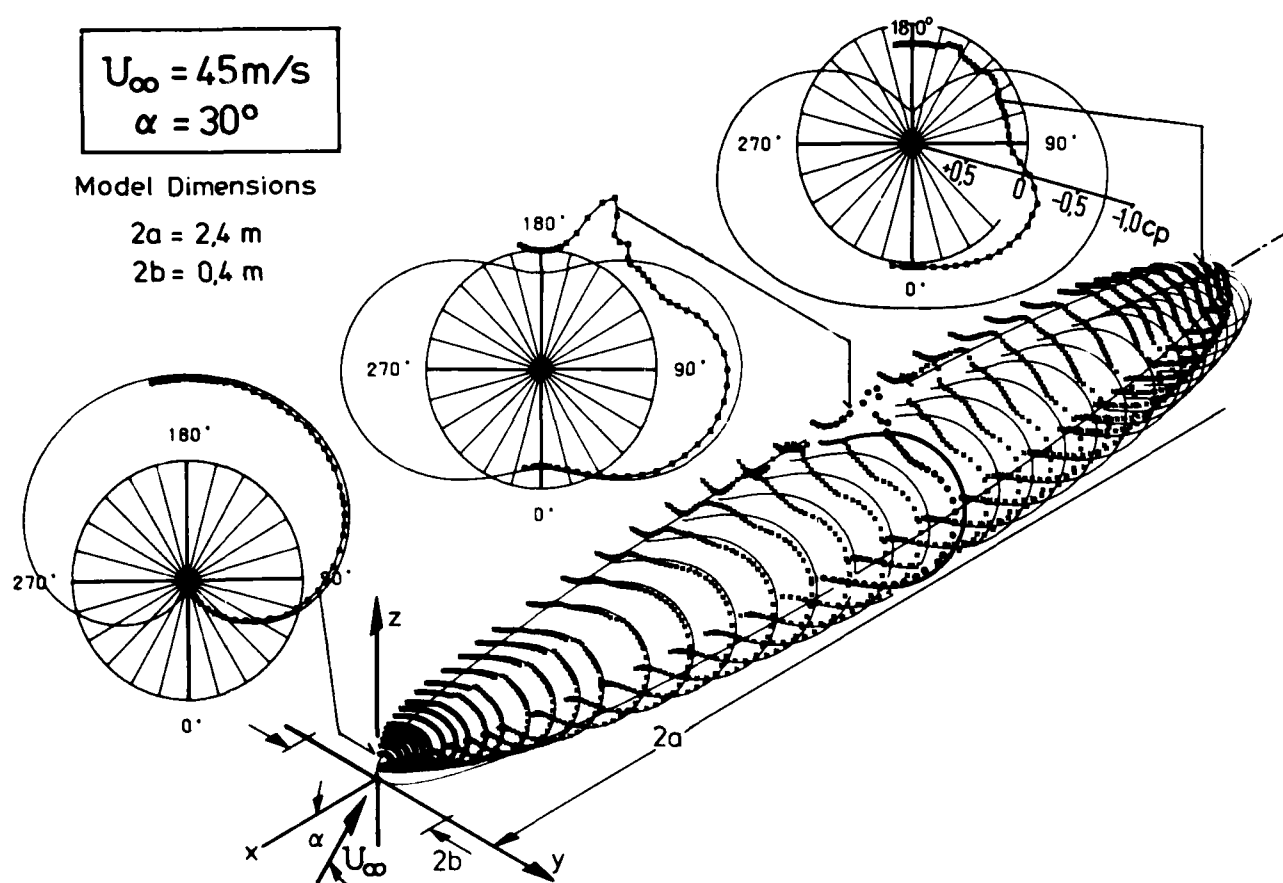


Fig. 10: Measured surface pressure distributions in comparison with calculated values based on potential flow theory (laminar, transitional and turbulent boundary layer flow,  $Re = 7 \times 10^4$ ).

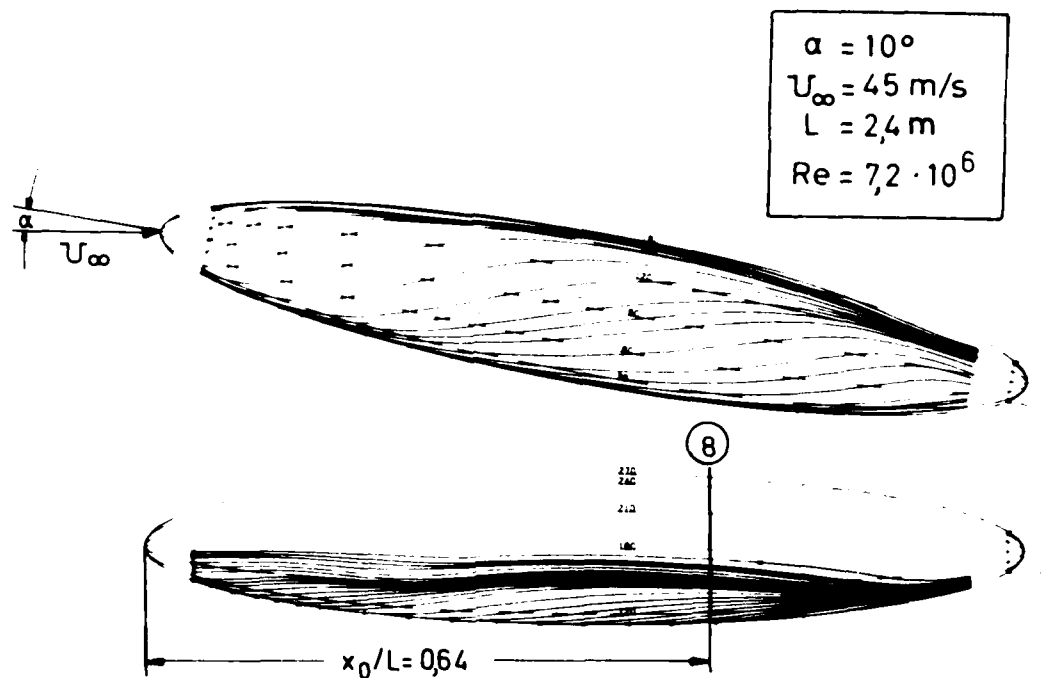


Fig. 11: Wall streamlines calculated from measured wall shear stress value distributions in 12 cross sections.



Fig. 12: Oil flow pattern for turbulent boundary layer separation ( $\alpha = 10^\circ$ ,  $U_\infty = 37$  m/s,  $p_0 = 5,9$  bar, model length  $L = 48$  cm,  $Re = 7.2 \times 10^6$ , DFVLR Pressurized Low Speed Wind Tunnel).

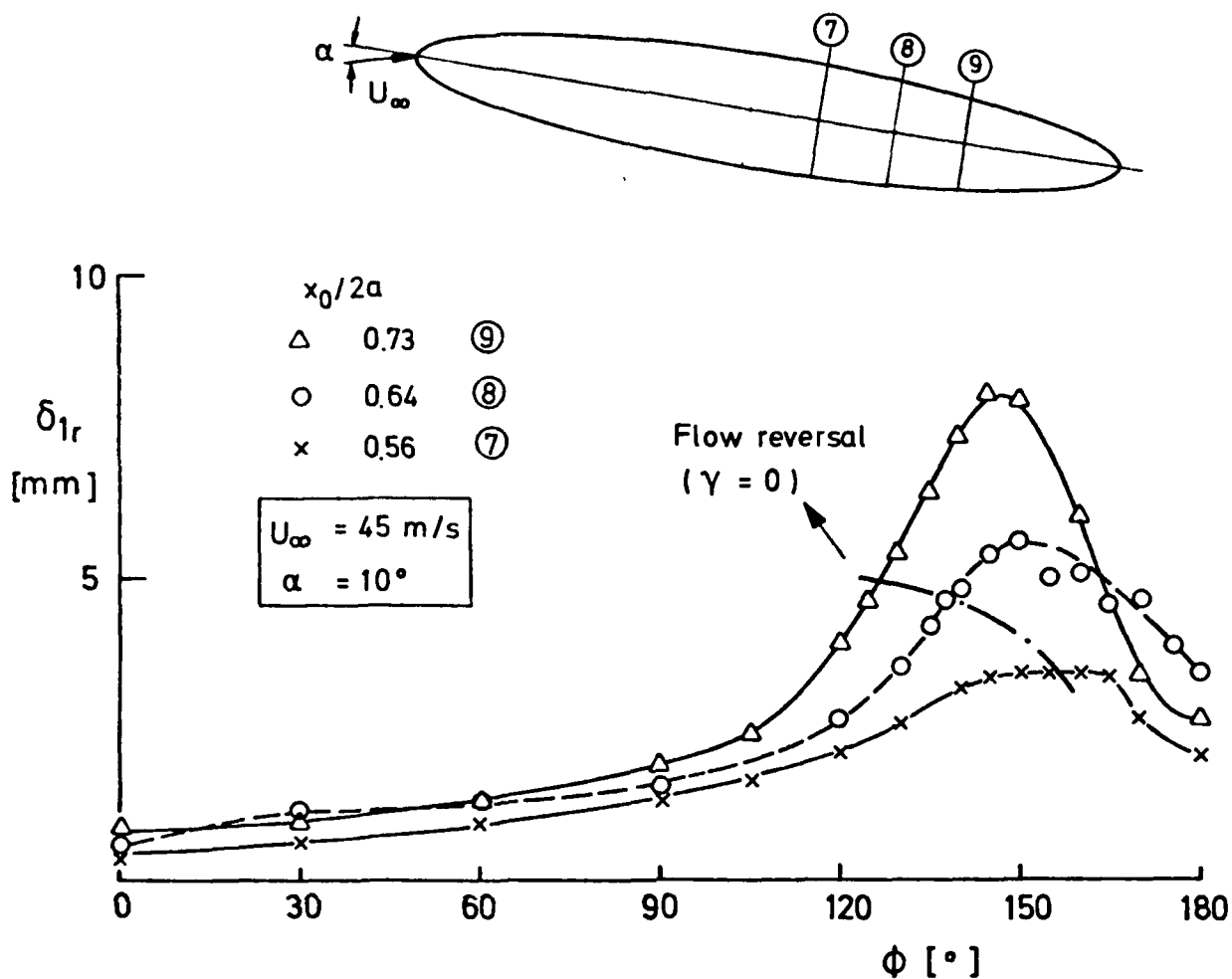


Fig. 13: The development of the three-dimensional boundary layer "displacement thickness"  $\delta_{1r}$  with natural transition,  $Re = 7 \times 10^6$ .

$$\delta_{1r} = \int_0^\delta \left(1 - \frac{u_r}{u_e}\right) dz$$

$u_r$  = resultant mean velocity in the three-dimensional boundary layer

$u_e = u_r$  at  $z = \delta$

$\gamma$  = cross flow angle

$\phi$  = circumferential angle (cf. Fig. 1)

# EXPERIMENTAL STUDY OF VORTICAL FEATURES IN THREE-DIMENSIONAL SEPARATED FLOWS

H. Bippes

## ABSTRACT

Possible topological structures of three-dimensional separated flows are studied on a hemisphere-cylinder at incidence. By means of a systematic variation of flow parameters a manifold of skin-friction patterns is produced. It is established that they develop from three basic structures simply by successive splitting of saddles in saddle-node-saddle combinations. The adjoining spatial flow field is visualized in low Reynolds number water tunnel flow, where similar kind of skin friction pattern develops as in fully turbulent flow. Velocity field measurements in the separated region on a rectangular wing indicate that on both models a similar topological structure, including unsteady effects, is possible.

## 1. INTRODUCTION

The prediction of three-dimensional separated flows is one of the most intricate problems in classical fluid mechanics. In many cases, complicated structures develop upon which unsteady effects may be superimposed. Theoretical treatment by Legendre [1], Lighthill [2] among others and recently by Hornung and Perry [3] and Dallmann [4] is based on local solutions on the surface or in planes of symmetry. The extension to the adjoining spatial flow field is inferred there from more by asymptotic arguments or even by intuition rather than by unequivocal analysis. Hence, there is a need for extensive experimental support.

Peake and Tobak [5] have revealed a series of typical features for a separated flows by reviewing available experimental evidence and by visualizing the skin-friction field on a hemisphere cylinder at incidence in supersonic flow, but their separation concept [6] does not include all the features found by Wang [7], Hornung [8] and Dallmann [4], [9]. As only the case of open separation (Wang [7]) seems to be sufficiently described, above all by the extensive experiments on a prolate spheroid of Meier et al. [10], [11],

further experiments are needed which, by a systematic variation of the related flow parameters reveal as much as possible of the whole band-width of possible structures.

With experiments on a hemisphere cylinder and on a rectangular wing an attempt has been made to supplement experimental data by varying systematically Reynolds number, Mach number and angle of incidence in laminar, transitional and turbulent flow. For providing qualitative data flow field and unsteady pressure measurements are performed on the rectangular wing at high incidence.

In the following a survey on some of the results is given. For details the reports of Bippes and Turk [12], [13] may be referred to.

## 2. DESCRIPTION OF THE EXPERIMENTS

For the systematic parametric study a hemisphere cylinder is used (Fig. 1). The skin-friction fields are visualized with the aid of the oil film technique in a low-speed and a high-speed wind tunnel. The adjoining spatial flow field is displayed by a special wet surface coating method applicable in stable laminar water tunnel flow.

In order to study the fully turbulent case in the wind tunnels, either the turbulence level of the oncoming flow is increased or the boundary layer is tripped.

Qualitative data are obtained by time averaging flow field measurements and unsteady pressure measurements on a rectangular wing with an aspect ratio of 3.1 in a low speed wind tunnel (Fig. 2).

### 3. SKIN FRICTION PATTERNS

#### 3.1 Incompressible Laminar Flow

A typical skin-friction pattern developing on the leeside of a hemisphere cylinder in stable laminar flow, where transition to turbulence takes place only sufficiently downstream of separation is shown in Fig. 3. Although the resolution of surface patterns visualized in water is rather poor it is established that the skin-friction lines exhibit structural features with saddle-node combinations as in fully turbulent flows, i.e. if transition takes place upstream of separation.

This result is also important for laboratory tests because it means that structures, developing in the turbulent case, may possibly be studied in small facilities and in water, favourable for visualization techniques.

#### 3.2 Incompressible Transitional Flow

In these experiments the transitional flow range is meant to be the range in which transition takes place immediately after separation. In this case a bubble type of separation occurs, which has essentially the features of two-dimensional bubbles with apparently undefinable three-dimensional quantitative features (Fig. 4). It may be similar to the three-dimensional "standing eddy" defined by Maskell [14].

As it is shown in Fig. 4a such bubbles originate on the nose and in a slightly modified form on the flanks as well. In the oil flow patterns this bubble type of separation manifests itself in the sense that the skin-friction lines retain their direction across the bubble. This is in contradiction to the general understanding of three-dimensional separation lines along which skin-friction lines run closely together.

If transition to turbulence takes place before separation this bubble type of separation disappears on the flanks (Fig. 4b) as well as on the nose (Fig. 5a), whereas the ordinary three-dimensional separation seems hardly affected.



### 3.3 Incompressible Turbulent Flow

As mentioned in Sect. 2 for studying turbulent separation the turbulence level in the oncoming flow must be increased by a screen or by tripping device has to be applied. In the first case only the open separation as defined by Wang [7] is observed (Fig. 5a) whereas in the second case "owl-face" type patterns originate (Fig. 5b). These patterns are structurally the same as those found on the rectangular wing (Fig. 6), although the two models are of quite different geometry.

### 3.4 Compressible Transitional Flow

In the high-speed wind tunnel used for our tests in compressible range Reynolds numbers are such that on the nose transitional separation occurs. Hence, separation bubbles arise in the high speed wind tunnel tests at Mach numbers of 0.6 (Fig. 7a). Single turbulent streaks shift the separation line downstream and produce typical three-dimensional patterns.

At higher Mach numbers separation is shock induced. In this case again separation patterns of the owl-face type develop as in incompressible turbulent flow (Fig. 7b), but with different topological structure (see also Sect. 4).

### 3.5 Compressible Turbulent Flow

If transition is forced by a tripping device upstream of the shock, separation originates further downstream. The separation pattern again is of an owl-face type. Fig. 8 reveals that there exist at least two topologically different forms. Within a certain range of the flow parameters both forms seem to be structurally stable in the sense of Dallmann [9].

#### 4. DISCUSSION OF THE TOPOLOGICAL STRUCTURES IDENTIFIED IN THE TESTS

Among the manifold of separation patterns visualized in our tests by systematically varying the flow parameters certain families can be distinguished. The different forms within such families develop from a basic structure by successive splitting of saddles and nodes into saddle-node-saddle and node-saddle-node combinations, respectively. This is illustrated by the example given in Fig. 9 and by the pertinent schematics in Fig. 10. It should be remarked, however, that in Fig. 9c in addition an open separation of Wang's type develops.

In our tests on the hemisphere cylinder three basic structures are established (Figs. 11 and 12). Wang's open type of separation (Fig. 5a) is seen as an isolated case with separation lines not originating in a saddle point.

It should be noted that the basic structures in Fig. 11 and 12 are defined here as the most simple structures of one of the families visualized in our tests on the hemisphere cylinder. A definition of general validity, however, must be derived from an analysis as given e.g. by Dallmann [4], [9]. Dallmann introduced the notation "elementary structures" and indeed it can be shown that all the skin-friction patterns visualized in our experiments are composed of Dallmann's elementary structures.

#### 5. THE SPATIAL SEPARATED FLOW FIELD

In order to obtain information about the spatial topological structure of the three-dimensional separated flow on the hemisphere cylinder we resorted to low Reynolds number water tunnel flows in which transition takes place only sufficiently downstream of separation. Fig. 13 displays the flow in a side view. The related skin-friction pattern is of an owl-face type. In this photograph stream surfaces close to the free sheets of dividing stream surface bifurcations (see Hornung and Perry [3]) become visible because the dye emanates from the surface only along the separation lines or from points of separation. It appears that the vorticity concentrates around different axes. Two of them originate in the spiral nodes, two others from some

location in the separated region from where they extend downstream (Fig. 14a). The free sheet of dividing stream surface bifurcation, a layer of high shear, becomes unstable with respect to a rolling-up process with axis essentially in the crosswise direction (Fig. 14b). Due to the interference with the outer flow an unsteady motion is caused. It is suggested that the resulting structure may look like that sketched in Fig. 14c. - While comparing Fig. 13 and Fig. 14c it must be taken into account that with our wet surface coating method a streak line pattern and not an instantaneous flow pattern is visualized.

## 6. QUANTITATIVE STUDY OF THE SEPARATED FLOW ON A RECTANGULAR WING

For the quantitative study of the spatial structure of a three-dimensional separated flow field a rectangular wing was chosen. Fig. 15 shows the sectional stream lines calculated from time averaged velocity field measurements. In a stream surface parallel to the suction side of the wing the structure of the sectional stream lines (Fig. 15a) is similar to the related surface pattern in Fig. 6. The cross-section, Fig. 15b, exhibits vortex structures with axes coming out of the plane. In the plane of symmetry, Fig. 15c, vortex structures with axes into the spanwise direction are formed. Comparison of Fig. 14 and 15 leads to the suggestion that the topological structure of the separated flow on the wing between the trailing edge vortices is similar to that visualized on the hemisphere cylinder in the low Reynolds number flow. The vortex structures in Fig. 14a and Fig. 15a and b as well as those in Fig. 14b and 15c, correspond to one another.

Unsteady pressure measurements in the plane of symmetry of the separated region indicate an unsteady motion which may be superimposed on the vortical flow as suggested in Sect. 5. It has a distinct periodicity (Fig. 16), with a Strouhal number, based on the thickness of the separated flow, of about 0.25.

## 7. SUMMARY

The qualitative study of the time averaged skin-friction patterns in the separated flow on a hemisphere cylinder reveals a complicated but regular structure. By systematic variation of related flow parameters such as Reynolds number, Mach number, angle of attack and flow state (stable laminar, transitional, and turbulent) a manifold of separation patterns is produced. Among those three basic types are to be distinguished from which even the most complicated structure found in the tests can be derived simply by splitting saddles and nodes in saddle-node-saddle and node-saddle-node combinations, respectively. The open separation as defined by Wang [7] is seen as a further basic structure, which in many cases may be superimposed on the others.

For one typical surface pattern the adjoining spatial flow field is also visualized. Comparison with the results of the flow field measurements on a rectangular wing at incidence indicates that similar vortical structures develop. In both cases unsteady periodic motions are superimposed. Thus the both experiments reveal the physical nature and the topological structure of a separated flow field in three dimensions which seems to be of general meaning.

## 8. LITERATURE

- [1] Legendre, R.: Séparation de l'écoulement laminaire tridimensionel, La Recherche Aéronautique, No. 54, 1956.
- [2] Hightmire, M.J.: Boundary Layer Theory, in: Laminar Boundary Layers, ed. L. Rosenhead, Chap. II, 2.6 and Chap. II, 2.7, pp. 72-82, Oxford University Press, 1963.
- [3] Hocking, G., Perry, A.E.: Streamsurface Bifurcation Vortex Skeletons and Separation, DFVLR, TB 221-82 A 25, 1982.
- [4] Dürst, G.: Topological Structures of Three-Dimensional Flow Separations, DFVLR, TB 221-82 A 07, 1982.

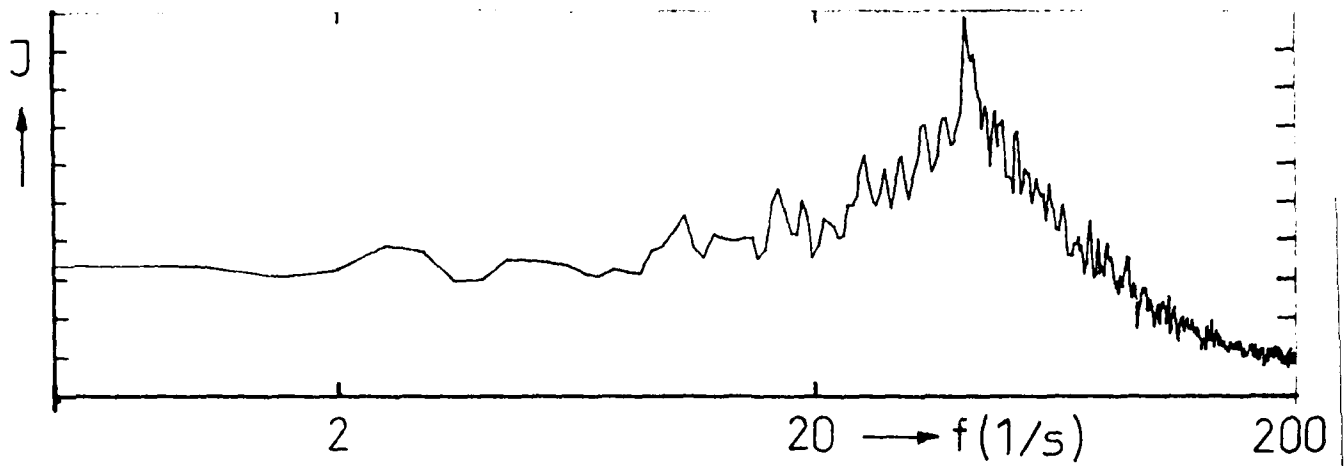


Fig. 16: Frequency spectrum from pressure measurements in the three-dimensional separated flow on a rectangular wing.  
 $\alpha = 21.5^\circ$ ,  $Re = 2.1 \times 10^6$

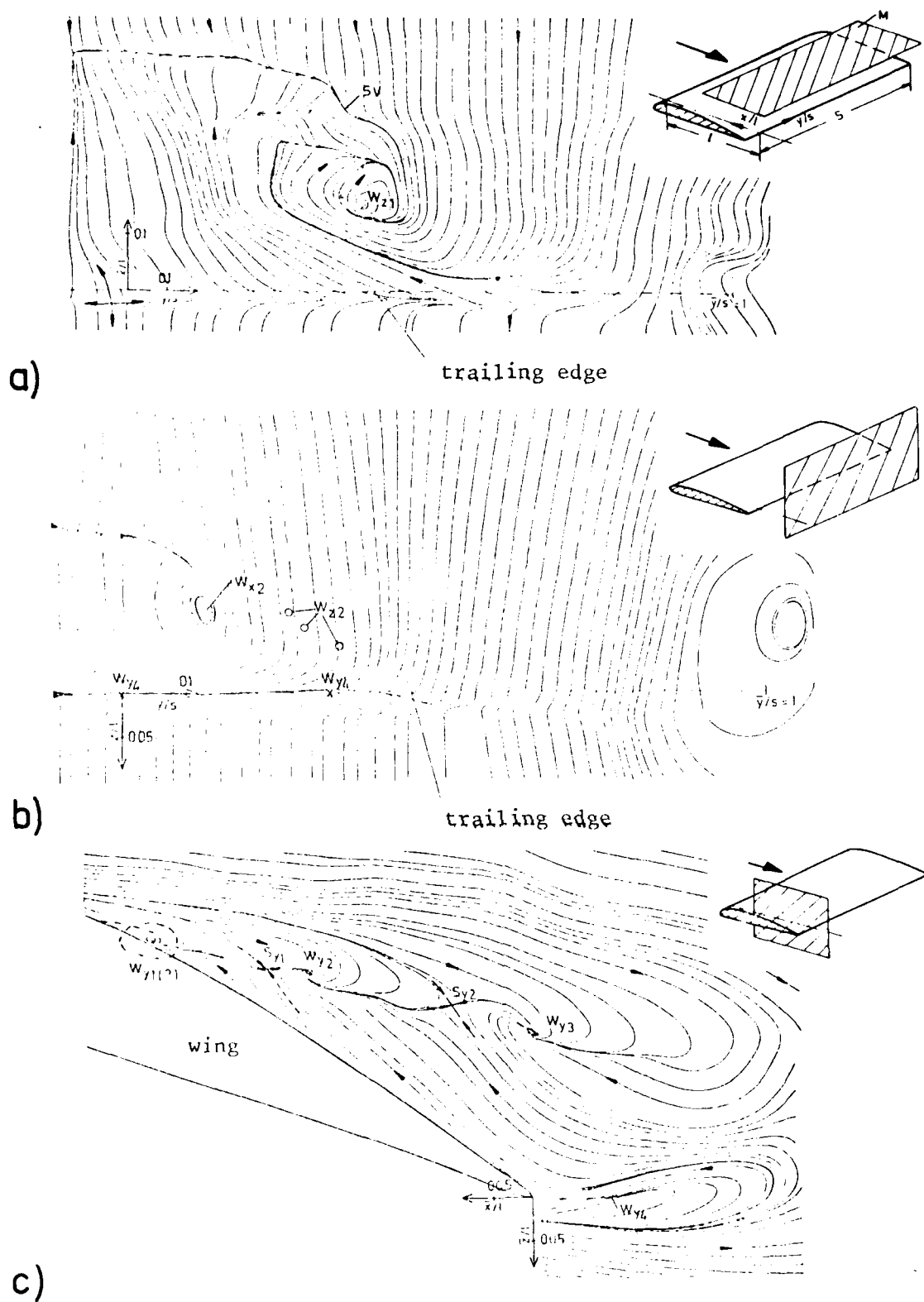


Fig. 15: Sectional streamlines calculated from the time averaged flow field measurements on a rectangular wing.  $s$  = half-span  
 $\alpha = 21.5^\circ$ ,  $Re = 2.1 \times 10^6$ ,  $M$  = measuring plane  
 (a) Plane parallel to the wing surface on the suction side  
 (b) Plane of symmetry  
 (c) Cross-section behind the trailing edge

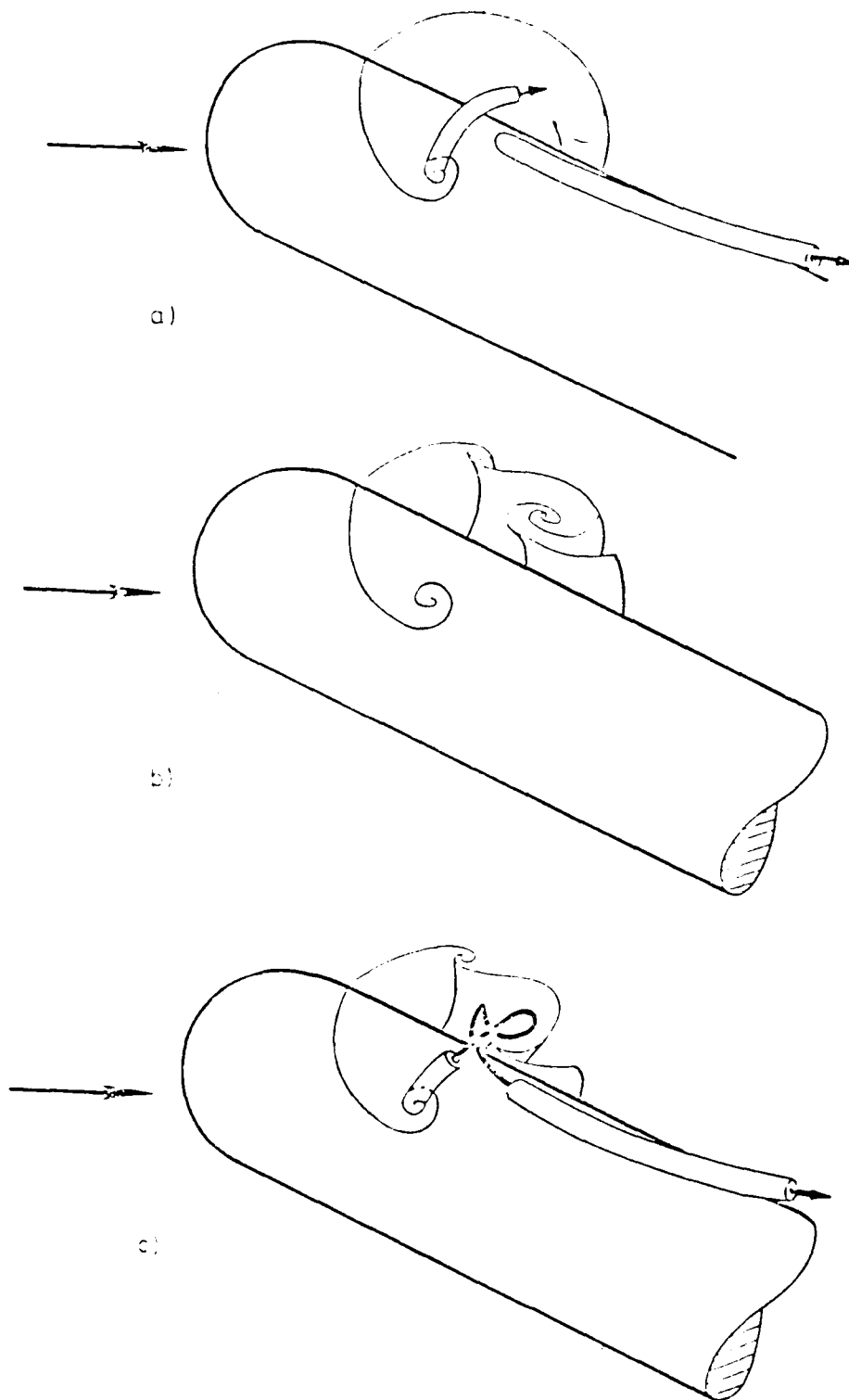


Fig. 14: Sketch of the spatial structure of the flow visualized in Fig. 13

- a) Vortex filaments of the steady motion
- b) Rolling-up of the free sheet of the dividing streamsurface bifurcation
- c) Structure of the resultant motion

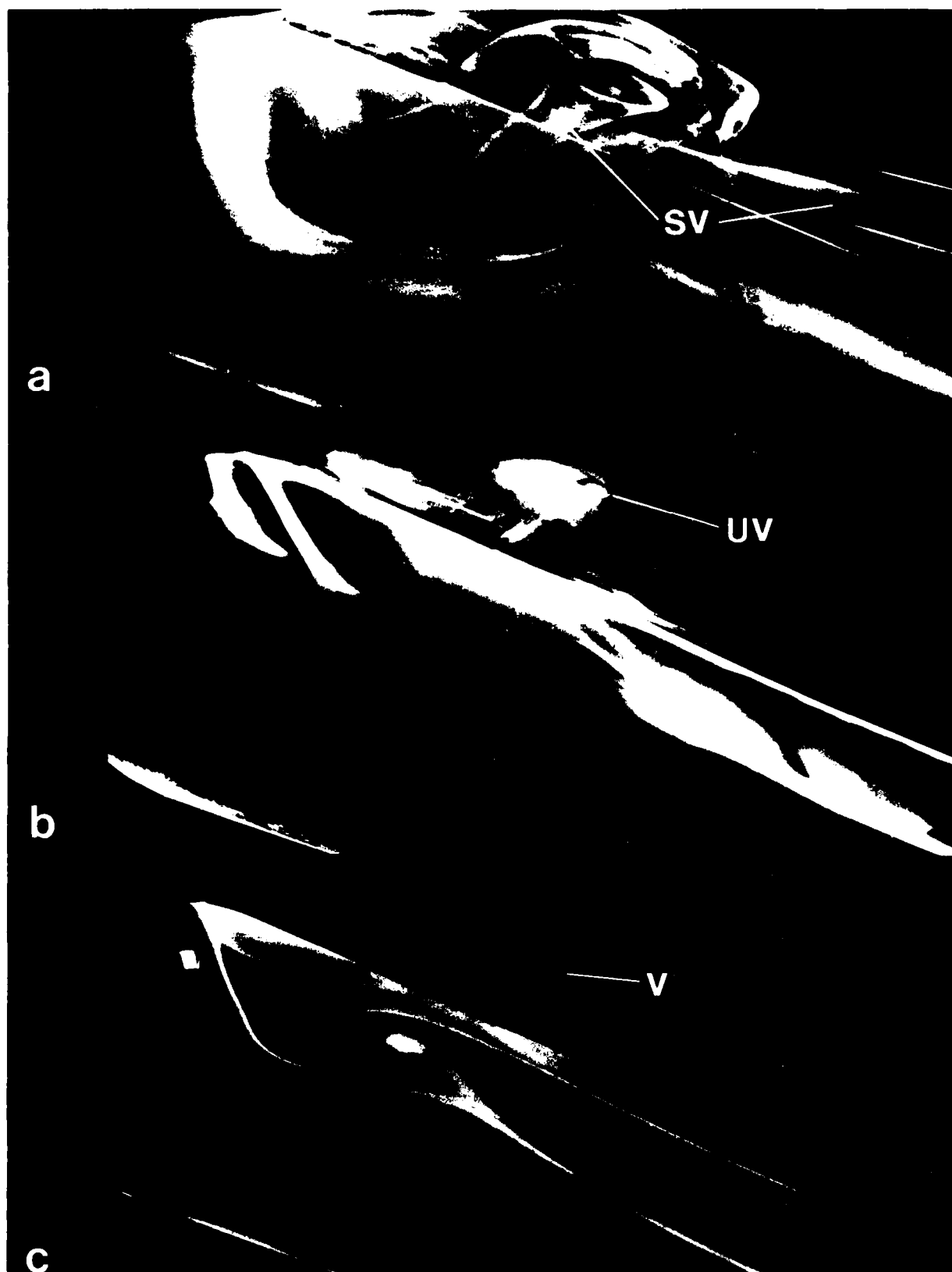


Fig. 13: Separated flow on the hemisphere cylinder in stable laminar flow (water tunnel test),  $\alpha = 28^\circ$ ,  $Re = 5 \times 10^3$

- a) At the beginning of the test, SV = steady vortex motion
- b) After part of the dye is carried away from the surface, UV = unsteady vortex motion
- c) Most of the dye is carried away, V = axis of the resultant vortex motion



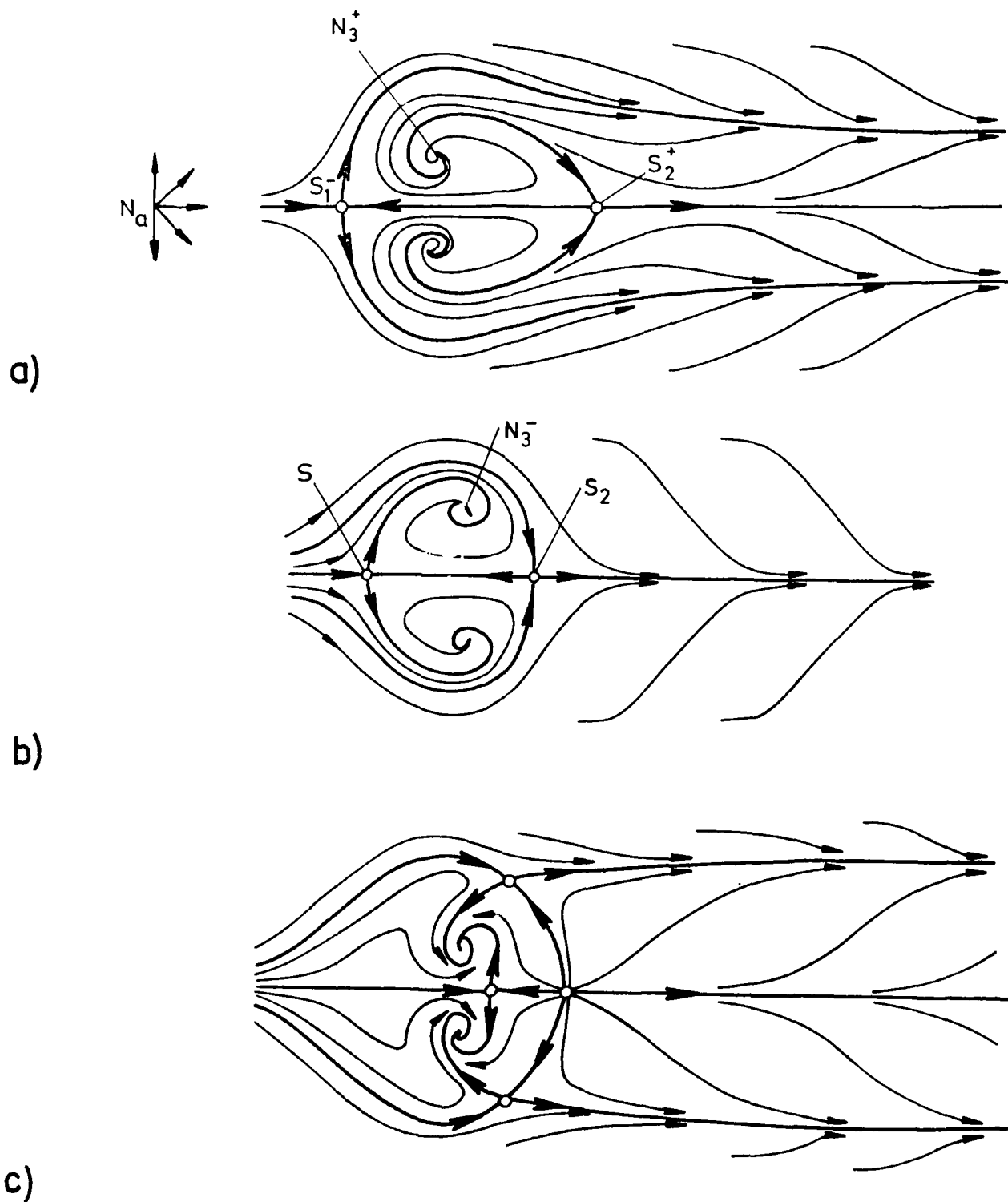


Fig. 12: Schematics of the basic structures in Fig. 11 (the open separation in Fig. 12b and c is not transferred to the schematics)

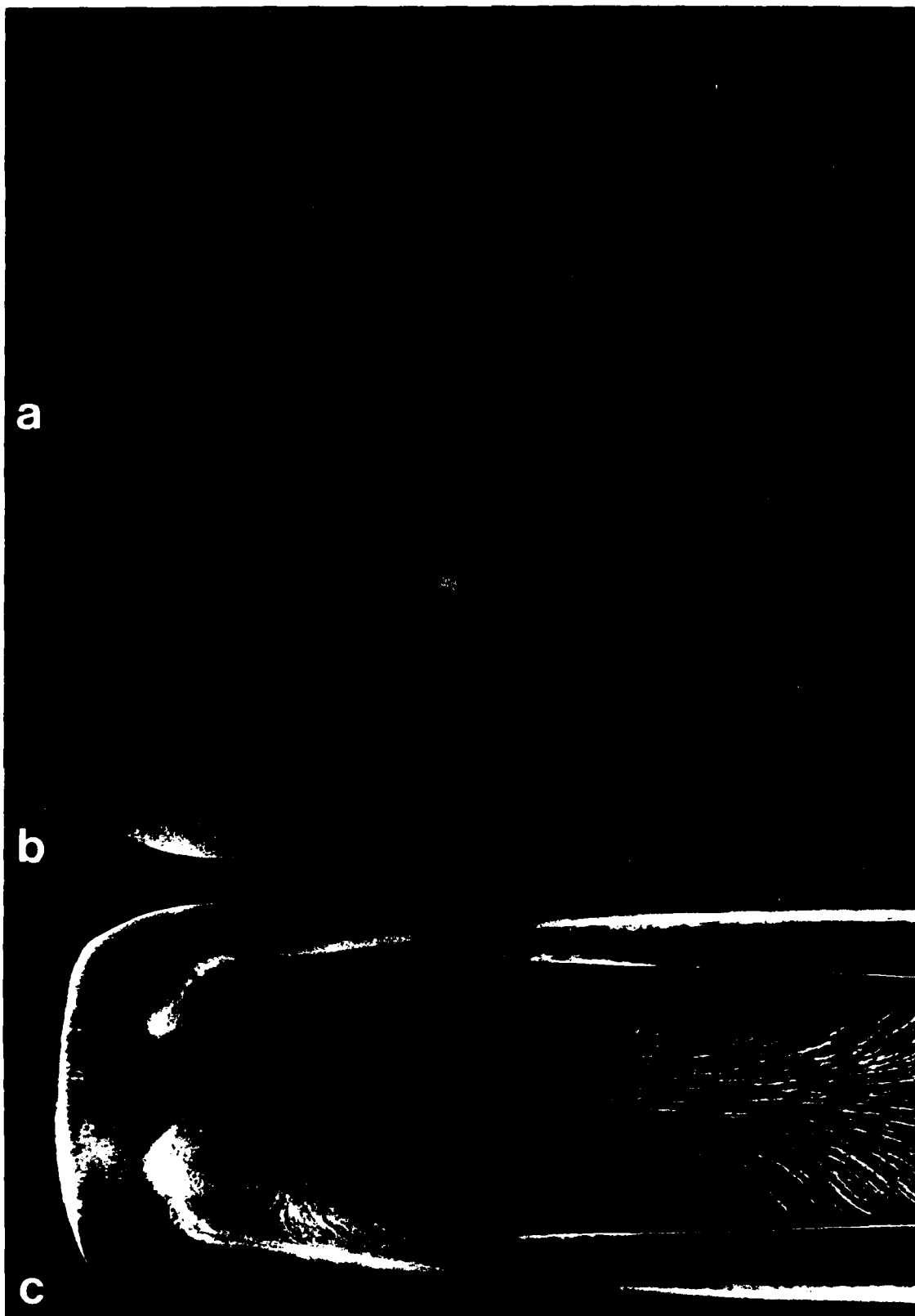


Fig. 11: Basic structures identified on the hemisphere cylinder

- a)  $\alpha = 10^\circ$ ,  $Ma = 0.8$ ,  $Re = 2.1 \times 10^6$  (transitional flow)
- b)  $\alpha = 15^\circ$ ,  $Ma = 0.7$ ,  $Re = 1.9 \times 10^6$  (with tripped boundary layer)
- c)  $\alpha = 33.5^\circ$ ,  $Ma = 0.6$ ,  $Re = 1.7 \times 10^6$  (with tripped boundary layer)

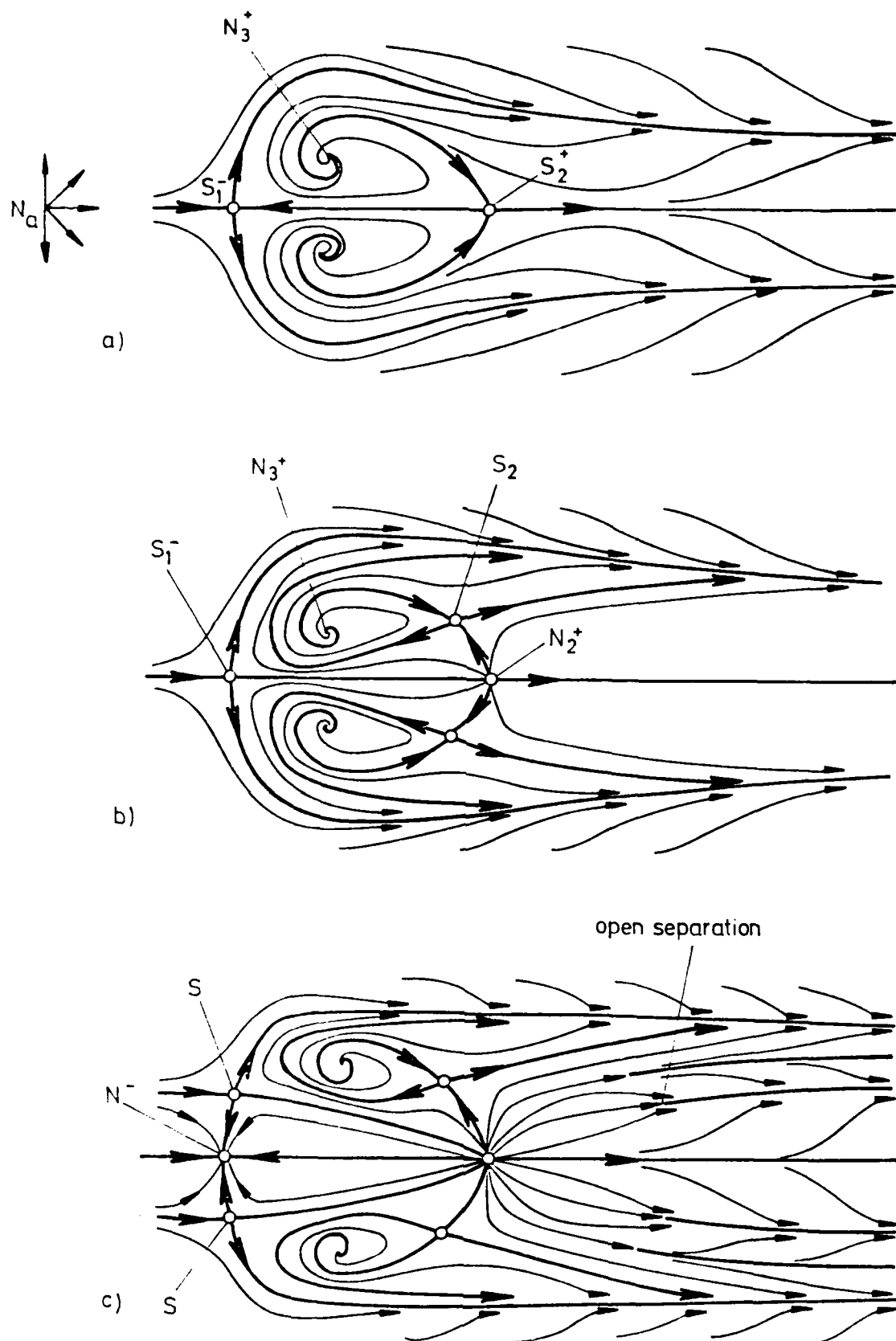


Fig. 10: Schematics of the surface patterns in Fig. 9



Fig. 9: Expansion from a basic structure by successive splitting of saddles in saddle-node-saddle combinations.

$Ma = 0.8$ ,  $Re = 2.1 \times 10^6$

a) Basic structure,  $\alpha = 10^\circ$

b) Splitting of the downstream saddle point,  $\alpha = 20^\circ$

c) splitting of the front saddle point,  $\alpha = 33.5^\circ$

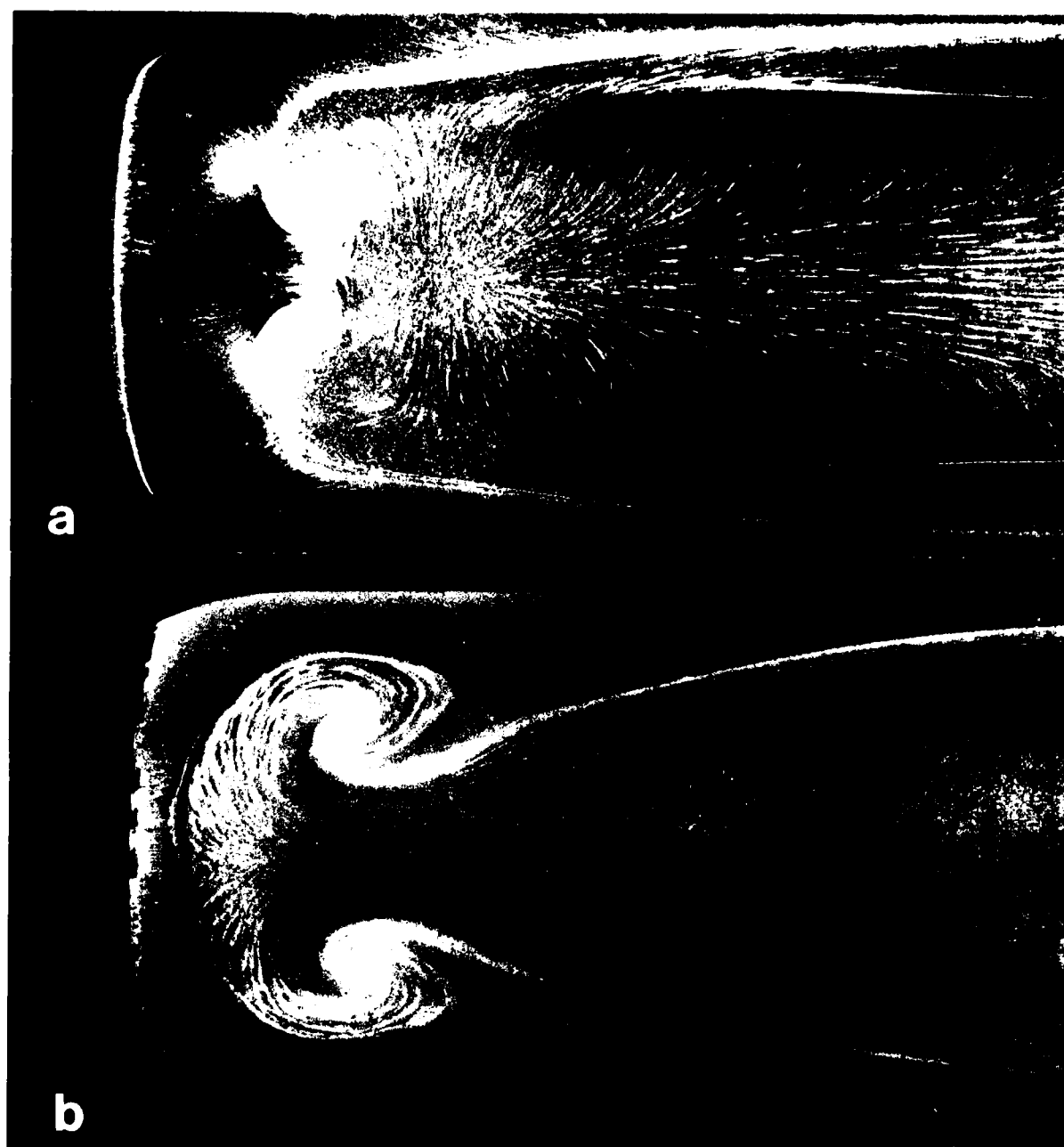


Fig. 8: Separation patterns in incompressible flow with forced  $\Gamma = 0$

a)  $\alpha = 24.5^\circ$ ,  $M_\infty = 0.2$ ,  $\rho_\infty = 1.7 \times 10^{-3}$

b)  $\alpha = 18.5^\circ$ ,  $M_\infty = 0.2$ ,  $\rho_\infty = 1.8 \times 10^{-3}$

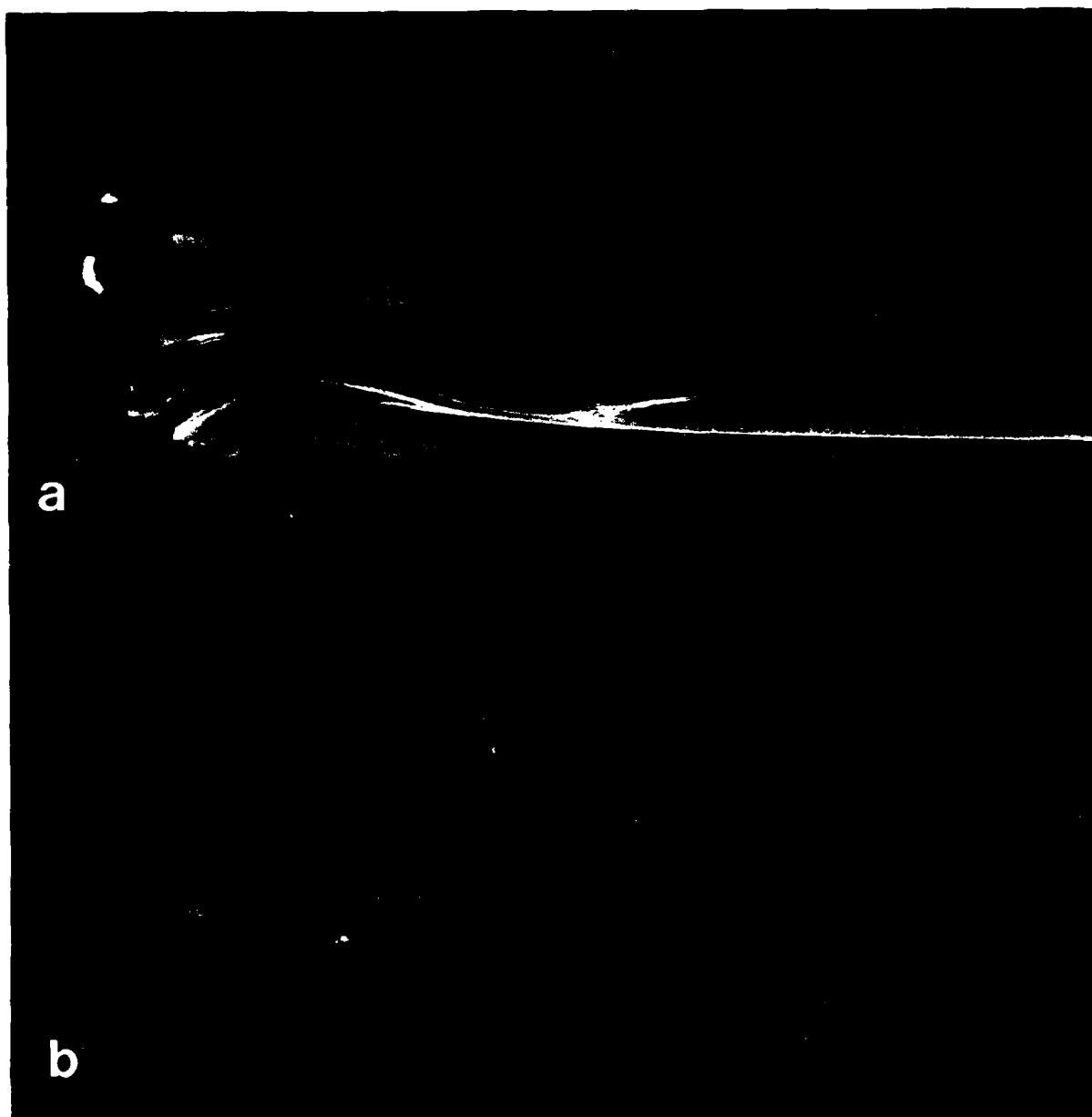


Fig. 7: Separation patterns in compressible transitional flow

- a) with bubble type of separation.  $\alpha = 33.5^\circ$ ,  $Ma = 0.7$ ,  
 $Re = 1.9 \times 10^6$
- b) with separation induced by shock.  
 $\alpha = 33.5^\circ$ ,  $Ma = 0.7$ ,  $Re = 1.9 \times 10^6$

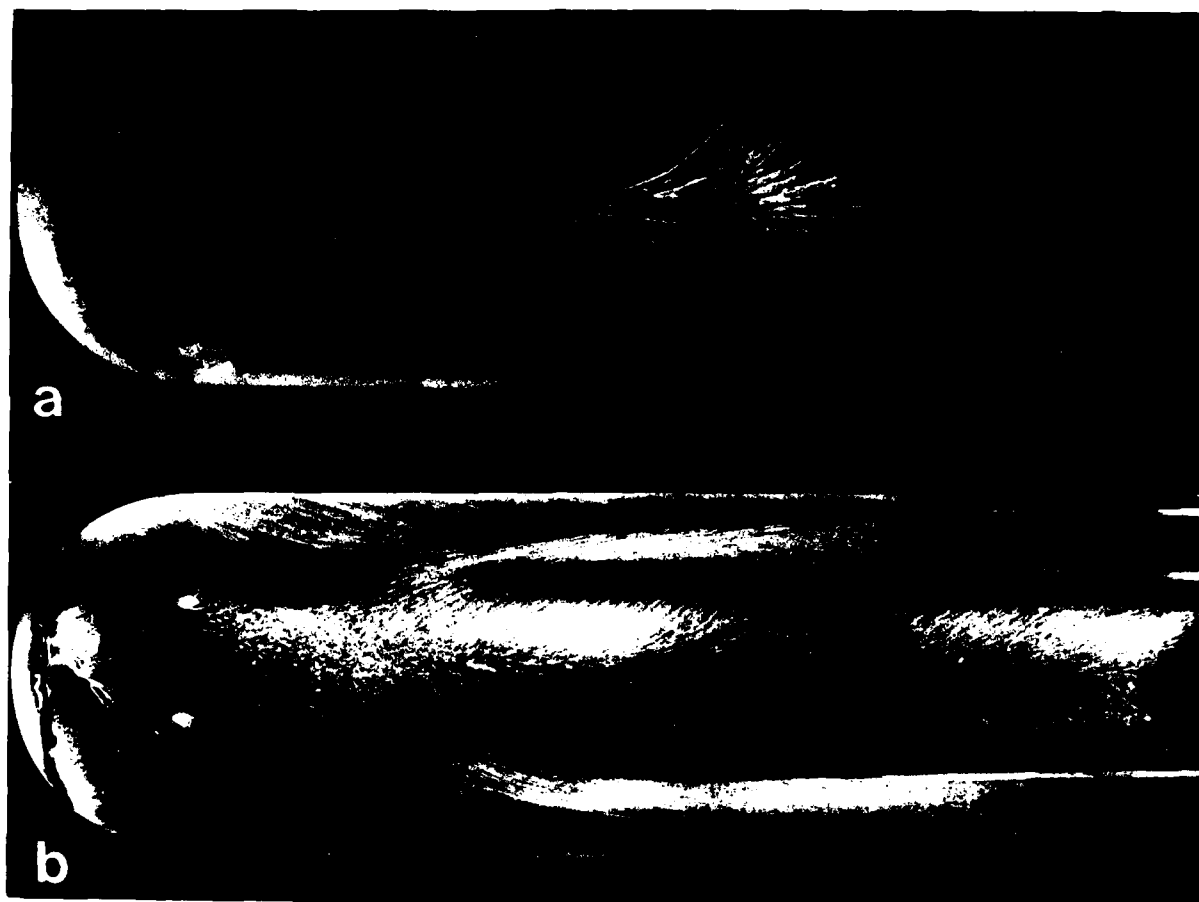


Fig. 5: Separation patterns in incompressible transitional flow if turbulence is forced

a) by increased turbulence level

b) by boundary layer tripping

$\alpha = 30^\circ$ ,  $Re = 6 \times 10^5$

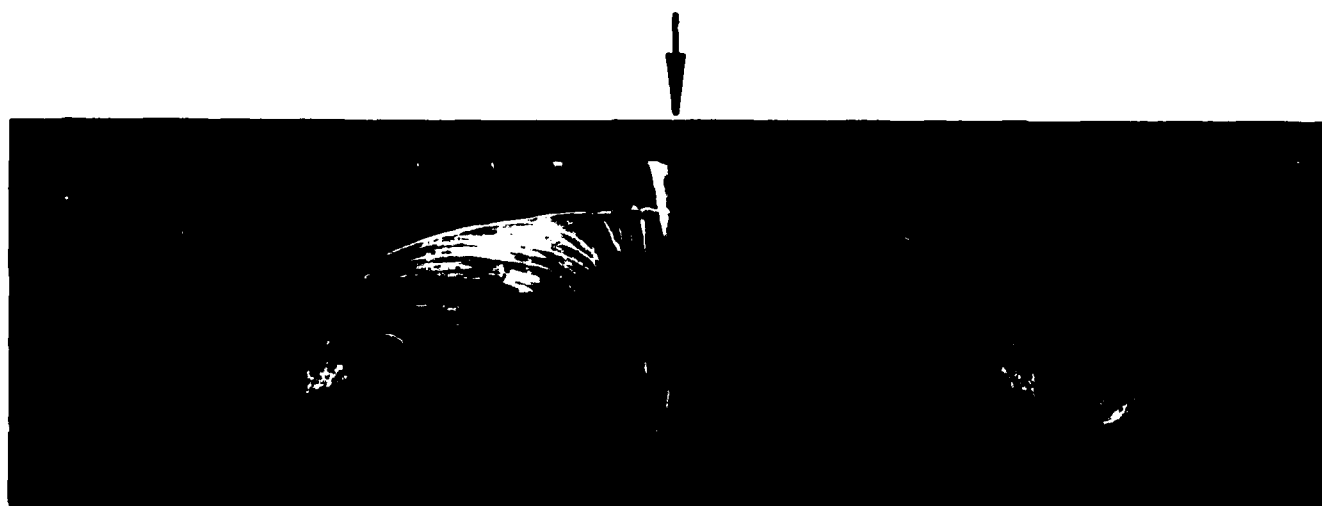


Fig. 6: Separation pattern on the suction side of a rectangular wing (top view).  $\alpha = 21.5^\circ$ ,  $Re = 2.1 \times 10^6$

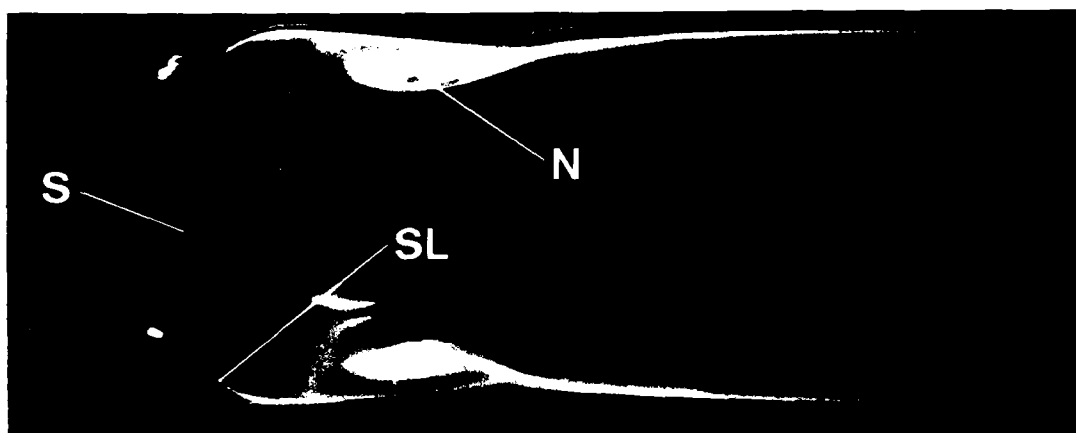


Fig. 3: Separation pattern on the leeside surface of the hemisphere cylinder (top view) in stable laminar water tunnel flow.

$\alpha = 28^\circ$ ,  $Re = 5 \times 10^3$ .

S = saddle point, N = spiral node, SL = separation line

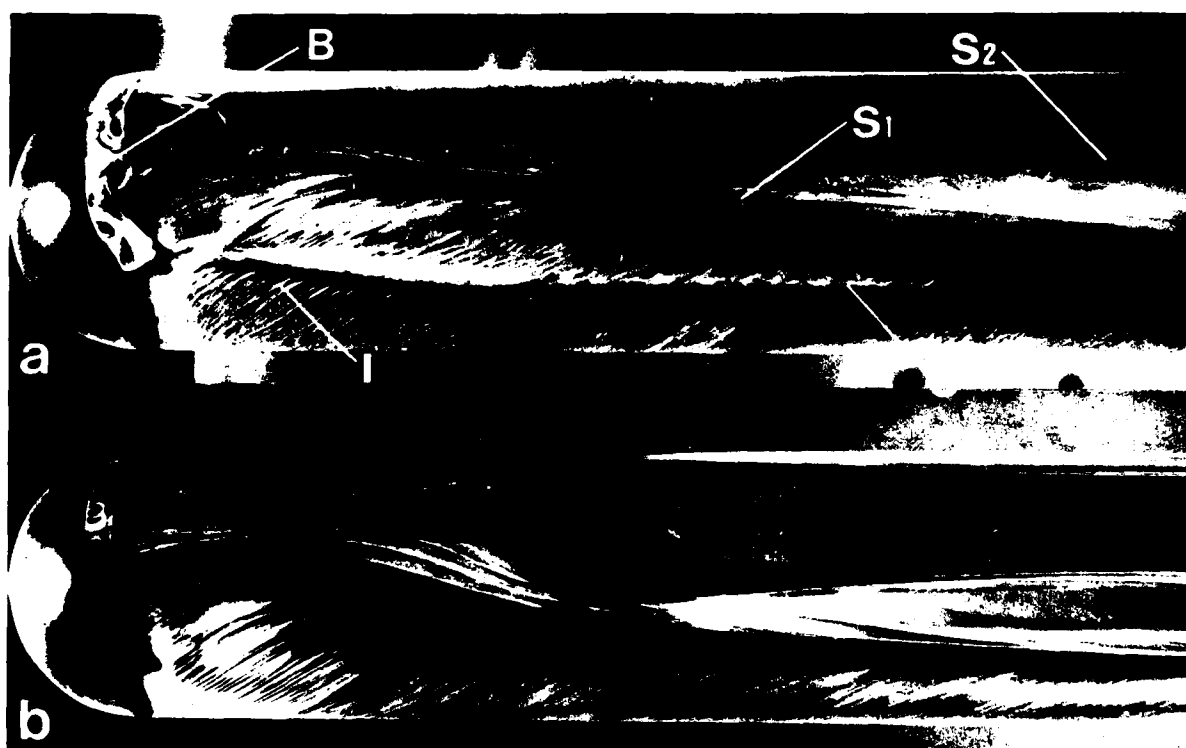
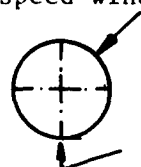


Fig. 4: Separation patterns in the case of natural transition in the low speed wind tunnel



oblique view

windward side

B = separation bubble

$S_{1/2}$  = 3-D separation lines

$\bar{S}$  = separation bubble

I = cross flow instabilities

a)  $\alpha = 25^\circ$ ,  $Re = 3 \times 10^5$ ,  $Ma = 0.09$

b)  $\alpha = 25^\circ$ ,  $Re = 6 \times 10^5$ ,  $Ma = 0.09$



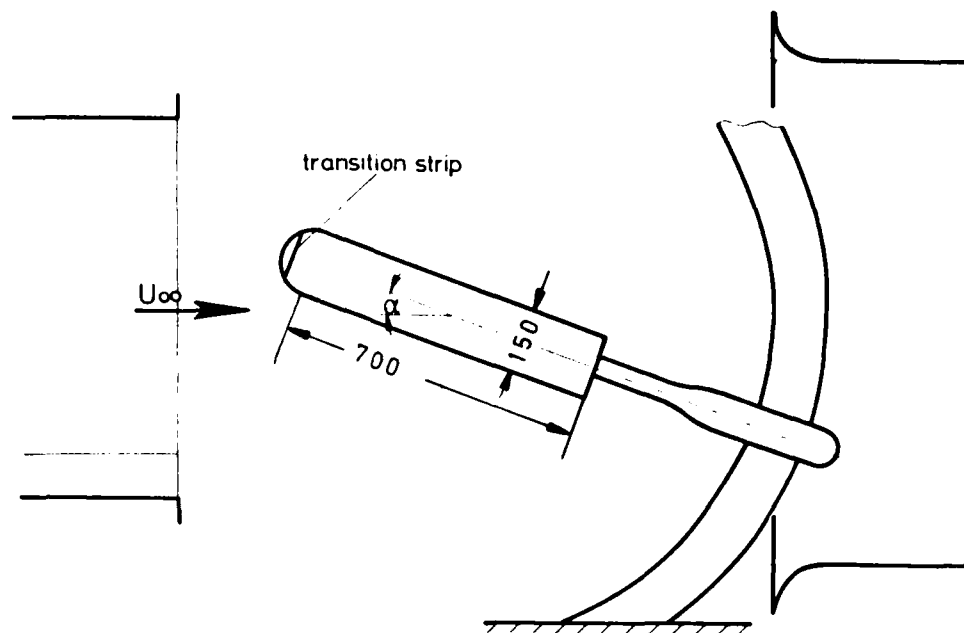


Fig. 1: Sketch of the hemisphere cylinder in the wind tunnel

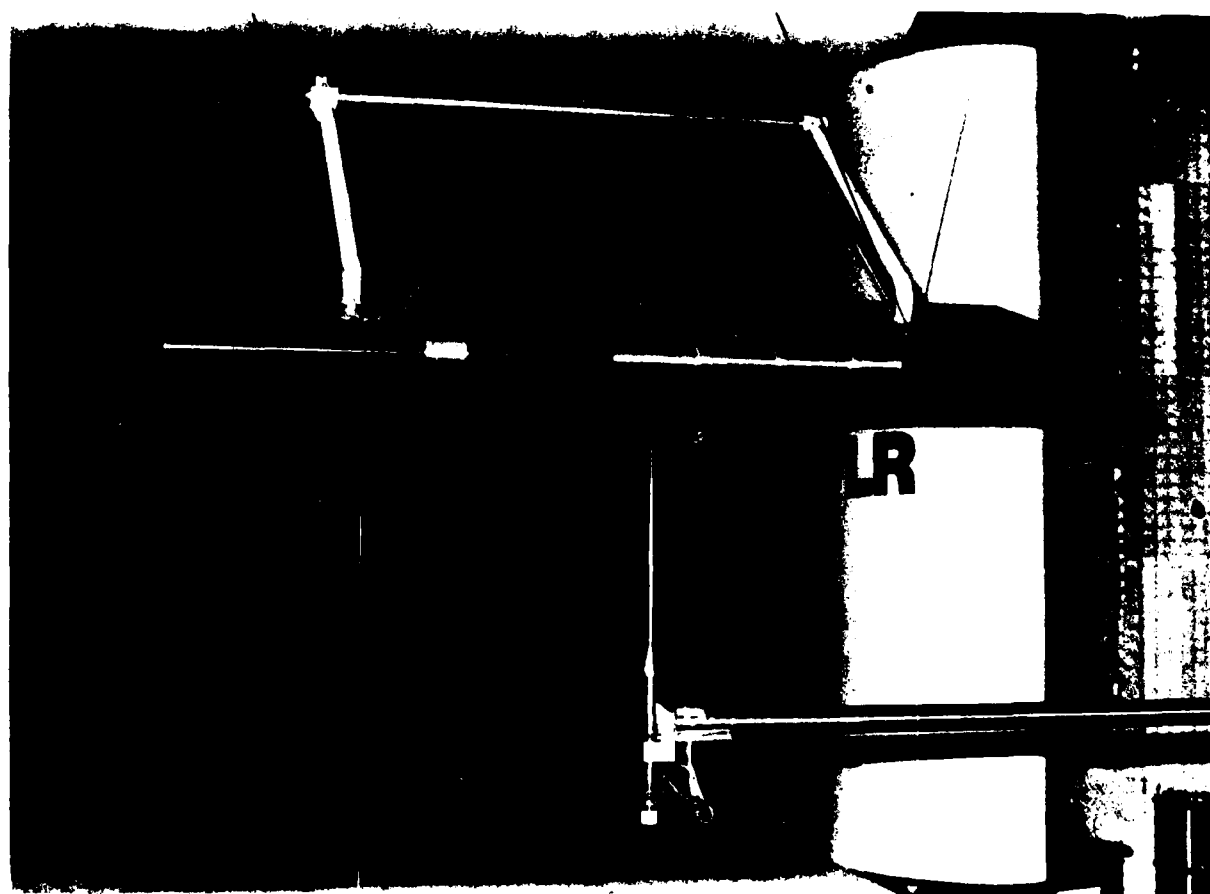


Fig. 2: Rectangular wing in the low-speed wind tunnel of the DFVLR in Göttingen

- [5] Peake, D.J.; Tobak, M.: Three-Dimensional Flows about Simple Components at Angle of Attack, AGARD-Lecture Series No. 121, Paper No. 2, 1982.
- [6] Tobak, M.; Peake, D.J.: Topological Structures of Three-Dimensional Separated Flows, Ann. Rev. Fluid Mech. 14, pp. 61-85, 1982.
- [7] Wang, K.C.: Boundary Layer Over a Blunt Body at High Incidence with an Open Type of Separation, Proc. R. Soc. London Ser. A 340, pp. 33-35, 1974.
- [8] Hornung, H.: The Vortex Skeleton Model for Three-Dimensional Flow Separations, AGARD-CP-342, July 1983.
- [9] Dallmann, U.: Topological Structure of Three-Dimensional Vortex Flow Separation, AIAA 16th Fluid and Plasma Dynamics Conf., Danvers, Mass., 1983.
- [10] Kreplin, H.-P.; Vollmers, H.; Meier, H.U.: Measurements of the Wall Shear Stress on an Inclined Prolate Spheroid, ZFW 6, pp. 248-252, 1982.
- [11] Vollmers, H.; Kreplin, H.-P.; Meier, H.U.: Separation and Vortical-Type Flow Around a Prolate Spheroid - Evaluation of Relevant Parameters -, AGARD-CP-342, July 1983.
- [12] Bippes, H.; Turk, M.: Oil Flow Patterns of Separated Flow on a Hemisphere Cylinder at Incidence, DFVLR, IB 222-83 A 07, 1983.
- [13] Bippes, H.; Turk, M.: Messungen im Ablösegebiet eines Rechteckflügels, DFVLR, IB 222-83 A 02, 1983.
- [14] Maskell, E.C.: Flow Separation in Three Dimensions, RAE Report No: AERO 2565, 1965.

AXISYMMETRIC BLUFF-BODY DRAG REDUCTION  
THROUGH GEOMETRICAL MODIFICATIONS

Floyd G. Howard and Wesley L. Goodman

NASA Langley Research Center  
Hampton, Virginia 23665

Presented at the 1984 U.S. Air Force-MWDDEA Data Exchange Meeting  
"Viscous and Interacting Flow Field Effects"

Silver Spring, Maryland  
May 9-10, 1984

# AXISYMMETRIC BLUFF-BODY DRAG REDUCTION THROUGH GEOMETRICAL MODIFICATIONS

F. G. Howard, and W. L. Goodman  
NASA Langley Research Center  
Hampton, Virginia 23665

## ABSTRACT

The effect of shoulder radiusing and grooving (longitudinally or circumferentially) the afterbodies of bluff bodies to reduce the base drag at low speeds is discussed. Shoulder radii as large as 2.75 body diameters are examined. Reynolds number ( $Re_D$ ) based on body diameter varied from 20,000 to 200,000. Results indicate that increasing the shoulder radius to 2.75 body diameters can reduce the drag levels to those of a streamline body having 67 percent greater fineness ratio. For the relatively sharp shoulder case, body drag reductions as large as 50% are obtained using circumferential or longitudinal grooves.

## INTRODUCTION

For performance and energy conservation, it is desirable to reduce the base drag of bluff bodies such as bombs, bullets, automobiles, trucks, buses, planetary-entry shapes and the upswept fuselage of some military cargo aircraft. In recent years, as a result of dwindling petroleum resources, increased emphasis has been focused upon drag reduction research for all forms of transportation. The drag on the aforementioned bodies is dominated by base or afterbody flow-separation effects (i.e., form or pressure drag). Estimates indicate that a 40 percent reduction in automobile aerodynamic drag would result in an increase in fuel economy the order of 16 percent. By definition, bluff bodies have low fineness ratio (order of 3 or less). It is possible, by moving the maximum body thickness far forward and using a gradual afterbody closure, to eliminate most flow separation and thereby obtain low drag coefficients even for such low fineness ratios. However, this approach typically does not provide sufficient volume for passengers, cargo, and motive power when the length is restricted. Therefore, ground transportation bodies are typically truncated rather sharply resulting in large form drag.

Two non-passive (powered) techniques that have been successful in reducing flow separation in axisymmetric or fully three-dimensional cases are blowing (mass addition) and suction (mass removal).<sup>2-4</sup> Recently, Howard et al investigated the effectiveness of afterbody modifications on base separation.<sup>5-7</sup> The modifications, reported herein, included (1) shoulder radiusing (2) circumferential rectangular grooves in the shoulder region, and (3) four longitudinal V-grooves cut through the shoulder.

## DISCUSSION

### Shoulder Radiusing

The minimum-drag configuration for a bluff body is a shape such that the boundary layer remains attached on the entire surface of the afterbody. Such a configuration is the "streamline" body shown in Figure 1(a). This body utilizes a gradual afterbody closure and a radius of  $R_s/D = 1.0$  at the shoulder to minimize the pressure gradient effects that would separate the boundary layer on smaller fineness-ratio bodies.

In some practical applications, gradual afterbody closure (such as that

for the streamline body of the present study) results in excessive vehicle length; therefore a more rapid closure of the body is required (Figure 1(b)). To first order the parameter which governs flow separation is the history and magnitude of the longitudinal adverse pressure gradient ( $dp/dx$ ) for a given set of flow conditions. If the shoulder radius ( $R_s/D$ ) of a highly truncated afterbody is zero, the pressure gradient would theoretically be nearly infinite. One obvious way to reduce the pressure gradient and thus to retard the separation is a well-known approach, shoulder radiusing.<sup>8-9</sup> As the shoulder radius is made larger, the pressure gradient becomes less severe and the flow remains attached further around the shoulder region. This, of course, reduces the base drag and thus the total drag (see Figure 2 where the bluff afterbody shoulder radius ( $R_s/D$ ) varied from 0.0 to 2.75). The figure also shows that for a given radius the flow remains attached over a greater distance as Reynolds number ( $Re_D$ ) increases. For comparison the drag on the streamline body (fineness ratio = 5.0) is also shown in Figure 2.

Flow visualization indicates that the boundary layer on the afterbody with  $R_s/D = 0.0$  separates immediately at the shoulder and does not reattach on the afterbody. For  $R_s/D > 2.5$ , the base drag appears to approach a limiting value and at the higher  $Re_D$  the afterbody with  $R_s/D = 2.75$  (and large closure angle of  $30^\circ$ ) has approximately the same  $C_D$  level as the streamline body. This favorable influence of afterbody shoulder radiusing was expected since previously-documented research had indicated that shoulder radiusing was an effective method for reducing base drag of axisymmetric bluff bodies.<sup>8-9</sup> The effects of shoulder radiusing shown in Figure 2 are directly related to the mitigation of body adverse pressure gradients. The pressure gradient at the shoulder is inversely proportional to shoulder radius; as the shoulder radius is increased, the pressure gradient that drives the boundary layer towards separation is reduced.

### Circumferential Grooves

The concept of using transverse surface grooves for delaying separation in diffusers evidently originated in the Soviet Union.<sup>10-11</sup> References 12-13 also indicate that grooves are effective in controlling separation.

In the present paper, the number of open grooves on the circumferentially grooved afterbodies (see for example Figure 1 (c)) were varied by filling selected grooves with dental plaster. The influence of circumferential grooves on the drag of a  $R_s/D = 0.0$  afterbody is shown in figure 3. The data indicated that grooves located at or downstream of the shoulder (i.e., grooves 5-12) had no drag-reduction effect on the afterbody base drag; however, as the grooves ahead of the shoulder are opened, a reduction in drag occurs at lower  $Re_D$ . The beneficial effect of the upstream grooves reaches an asymptotic level around the first or second groove. Figures 4 & 5 present the drag data for circumferentially-grooved afterbodies having a shoulder radius of  $R_s/D = 0.5$ . The downstream side of the first groove coincided with the upstream tangency point of the shoulder radius. Also groove 13 roughly corresponds to the second tangency point of the shoulder radius. Figure 4 shows the reductions in drag obtained by opening successive grooves downstream of the first tangency point. As the second tangency point is approached, the drag approaches an asymptotic limit for a given  $Re_D$ . It should be noted that the first three grooves actually increase the drag over certain  $Re_D$  ranges. The beneficial effect of the grooves on separation is not sufficient to overcome

the drag penalty of the grooves.

Figure 5 examines the influence of the grooves near the first tangency point when the downstream grooves are opened. The data for grooves 7-13 indicate that drag reductions can be obtained with the first open groove located downstream of the first tangency point. As the first open groove approaches the first tangency point, drag reduction is obtained at lower values of  $Re_D$ . As  $Re_D$  is increased the boundary layer becomes thinner and remains attached further around the shoulder before separating. It is near this separation point where the grooves should evidently be placed.

Flow-visualization photographs for the grooved and ungrooved afterbodies with  $R_s/D$  of 0.5 are shown in Figure 6 for  $Re_D = 50 \times 10^3$ . The ungrooved afterbody configuration in Figure 6(a) indicates no turning of the streamlines, boundary-layer separation just downstream of the first tangency point, and no flow reattachment on the afterbody. This large region of afterbody separation corresponds to the high drag levels shown in Figure 4 and 5 for the ungrooved afterbody with  $R_s/D = 0.5$ . Figure 6(b) shows that grooves placed between the tangency points of the shoulder radius turn the streamlines, move the separation point downstream, and greatly decrease the regions of afterbody base separation.

Although all flow visualization results are not shown here, indications are that the dominant effect of the circumferential grooves is to trade the large region of separated flow over the ungrooved afterbody for smaller regions of separated flow that occur in the individual grooves e.g. by replacing the usual "no slip" boundary condition by a series of stable (imbedded) shear layers. For each cavity the flow reattaches on the fin separating the two grooves. Before the boundary layer is able to thicken, separate, and form a large base separation region, the second groove or cavity is encountered.

#### Longitudinal V-Grooves

Examples of drag reduction which can be achieved by use of four longitudinal V grooves<sup>6-7</sup> cut through the bluff afterbody shoulder region (see Figure 1(d)) are shown for  $R_s/D = 0.0$  and  $R_s/D = 0.5$  in Figure 7, where a comparison is made with previously discussed transverse (circumferential) grooves.

The mechanism which is believed to cause this reduction is illustrated by comparing cross sectional smoke patterns for a longitudinal station near the apex of the conical base (see Figs. 8(a) and (b)). These flow visualization data indicated that the smoke lines continue to be bowed outward as they pass the apex of the smooth (ungrooved) afterbody. However, a very noticeable difference occurs when grooves are employed. Figure 8(b) shows that the smoke lines are drawn inward in the region of the grooves suggesting that the flow remains attached in the grooves. Furthermore, the residual separated flow regions on the grooved model (Fig. 8(b)) are of considerable smaller extent than the corresponding pie-shaped sections on the smooth model (Fig. 8(a)). These visualization results suggest the following drag reduction mechanism: the bottoms of the grooves (which begin upstream of the shoulder) have a much smaller afterbody closure angle ( $19.4^\circ$ ) than the balance of the afterbody ( $30^\circ$ ); the flow in the grooves therefore remains attached and probably provides an ejector-like pumping action for the remaining, fully three-dimensional, separated flow segments of the afterbody.

Up to this point all bluff afterbodies discussed had a closure angle ( $\alpha$ ) of  $30^\circ$ . However, during the study<sup>8</sup> of longitudinal V-grooves, additional

closure angles of 45, 60, and 90 degrees were investigated with  $R_s/D$  varying from 0.0 to 1.5. The V-grooves generally reduced drag for all combinations of closure angles and shoulder radius when the closure angle of the groove (3) was 19.4°. Also, drag was decreased slightly for  $R_s/D = 0.0$  as  $\alpha$  was increased from 30° to 90° for both the grooved and the ungrooved case. This effect diminished as  $R_s/D$  increased from 0.0 to 1.5. For the ungrooved case, this is in agreement with the well known Kamback principle (i.e. only a slight effect of  $\alpha$  on drag, once separation has occurred). The slight decrease in drag with increase in  $\alpha$  on the grooved afterbodies is probably partially due to the decrease in the remaining (ungrooved portion) axially projected base surface area.

#### CONCLUDING REMARKS

The effectiveness of shoulder radiusing and grooving (circumferentially or longitudinally) the bluff afterbody to reduce base drag was determined for a range of Reynolds numbers based on body diameter ( $Re_D$ ) between 20,000 and 200,000. For  $Re_D > 100,000$  shoulder radiusing ( $R_s$ ) relative to body diameter (3) or  $R_s/D = 2.75$  was found to reduce the body drag to levels equivalent to a streamline body having 67 percent greater fineness ratio. Circumferential grooves were found to provide up to 50 percent drag reduction. The data indicate that to be effective the grooves must be located in the region of large longitudinal pressure gradient. The mechanism of the circumferential grooves appear to be one of simply substituting several small regions of separation (which provide a wall slip boundary condition) for a larger separated flow region.

Drag reductions the order of 33 percent were measured for configurations having bluff afterbodies with four longitudinal V grooves. The mechanism apparently is associated with a) attached flow in the grooves, and b) the ejector (pumping) action of the attached groove flow on the residual (highly three-dimensional) separated flow regions.

A trip wire was placed on the nose of the forebody. Although not shown the results indicate that whether the flow is laminar or turbulent, grooves (circumferential or longitudinal) are beneficial if flow is detached over a sufficient area of the ungrooved afterbody. That is, the grooves can retard both laminar and turbulent separation.

#### REFERENCES

1. "Vehicle Aerodynamics: The Next Fuel Economy Frontier." Automotive Engineering, Vol. 36, No. 7, July 1978, pp. 19-24.
2. Quigley, Harvey C.; and Hom, Francis W. K.: A Flight Investigation of Area Suction and Blowing Boundary-Layer Control on the Trailing-Edge Flaps of a 35° Swept-Wing Carrier-Type Airplane. NACA RM-A57B14, April 1957.
3. Lachmann, G. V.: Boundary Layer and Flow Control. Vol. I, Pergamon Press, New York, 1961.
4. Chang, P. K.: Control of Flow Separation. Hemisphere Publishing Corporation, McGraw-Hill Book Co., 1976.
5. Howard, F. G.; Goodman, W. L.; and Walsh, M. J.: Axisymmetric Bluff-Body Drag Reduction Using Circumferential Grooves. AIAA Applied Aerodynamic Conference, Danvers, Massachusetts, July 13-15, 1983.
6. Howard, F. G.; Quass, B. F.; Weinstein, L. M.; and Bushnell, D. M.: Longitudinal Afterbody Grooves and Shoulder Radiusing for Low-Speed Bluff Body

Drag Reduction. ASME Winter Annual Meeting, November 15-20, 1981, Washington, DC, 81-WA/FE-5.

7. Quass, B. F.; Howard, F. G.; Weinstein, L. M.; and Bushnell, D. M.: Longitudinal Grooves for Bluff Body Drag Reduction. AIAA Journal, Vol. 19, No. 4, April 1981, pp. 535.

8. Silhan, Frank V.; and Cabbage, James M., Jr.: Drag of Conical and Circular-Arc Boattail Afterbodies at Mach Numbers From 0.6 to 1.3. NASA RM L56K22, 1957.

9. Aerodynamic Drag Mechanisms of Bluff Bodies and Road Vehicles. Edited by Sovran, Morel, Mason. Plenum Press, New York-London, 1978.

10. Migay, V. K.: The Efficiency of Cross Ribbed Curvilinear Diffuser. Energomashinostroyeniye, No. 1, 1962, pp. 45-46.

11. Migay, V. K.: A Study of Finned Diffusers. Teploenergetika, No. 10, 1962, pp. 55-59.

12. Stull, F. D.; and Velkoff, H. R.: Effects of Transverse Ribs on Pressure Recovery in Two-Dimensional Subsonic Diffusers. AFAPL, October 1974.

13. Stull, Frank D.; Curran, Edward T., and Velkoff, Henry R.: Investigation of Two-Dimensional Cavity Diffusers. Air Force Systems Command, Wright-Patterson Air Force Base, Ohio, AFAPL-TR-73-84, October 1973.

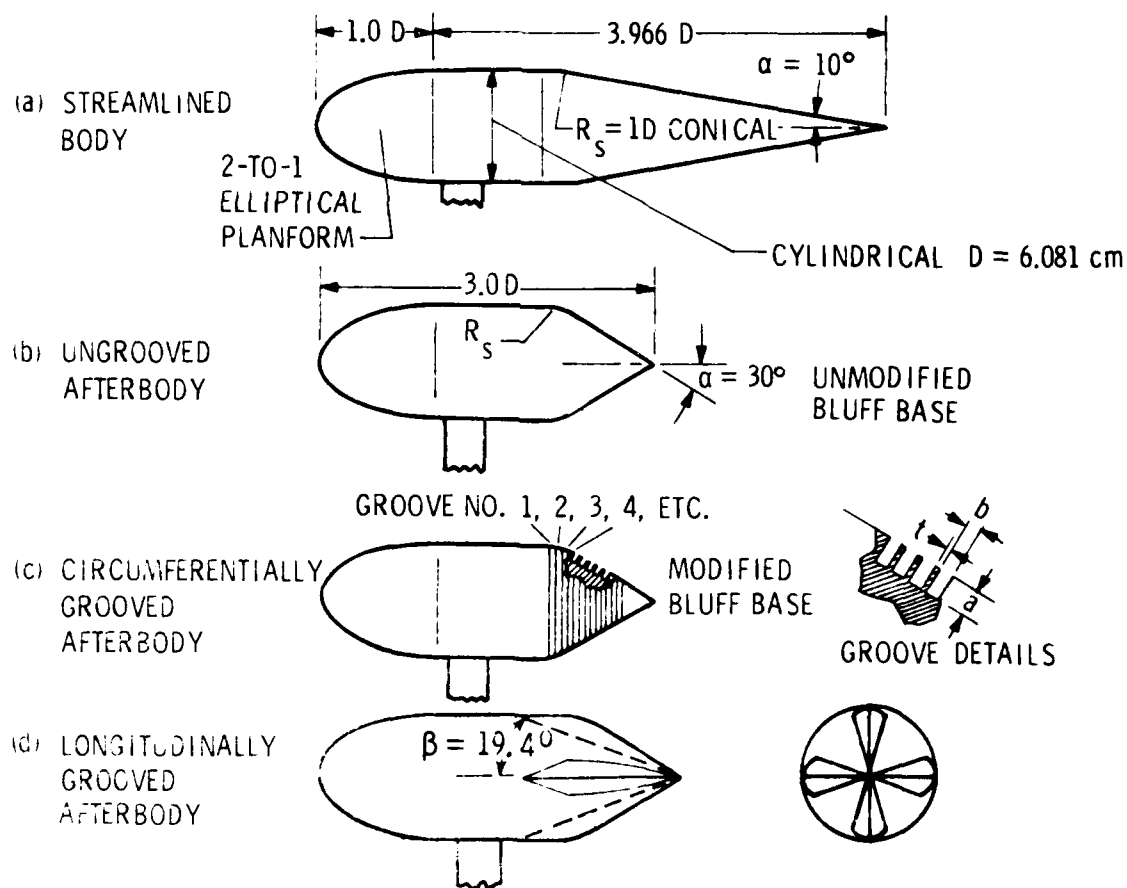


Figure 1.- Examples of Test Configurations.



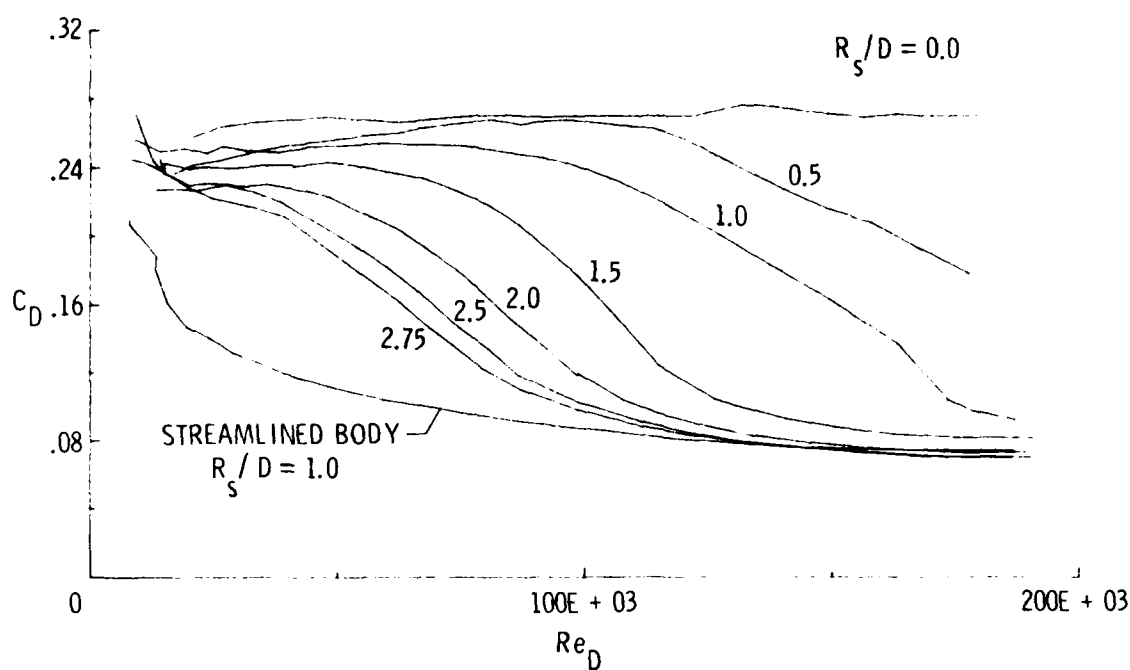


Figure 2.- Effect of afterbody shoulder radius on drag coefficient.

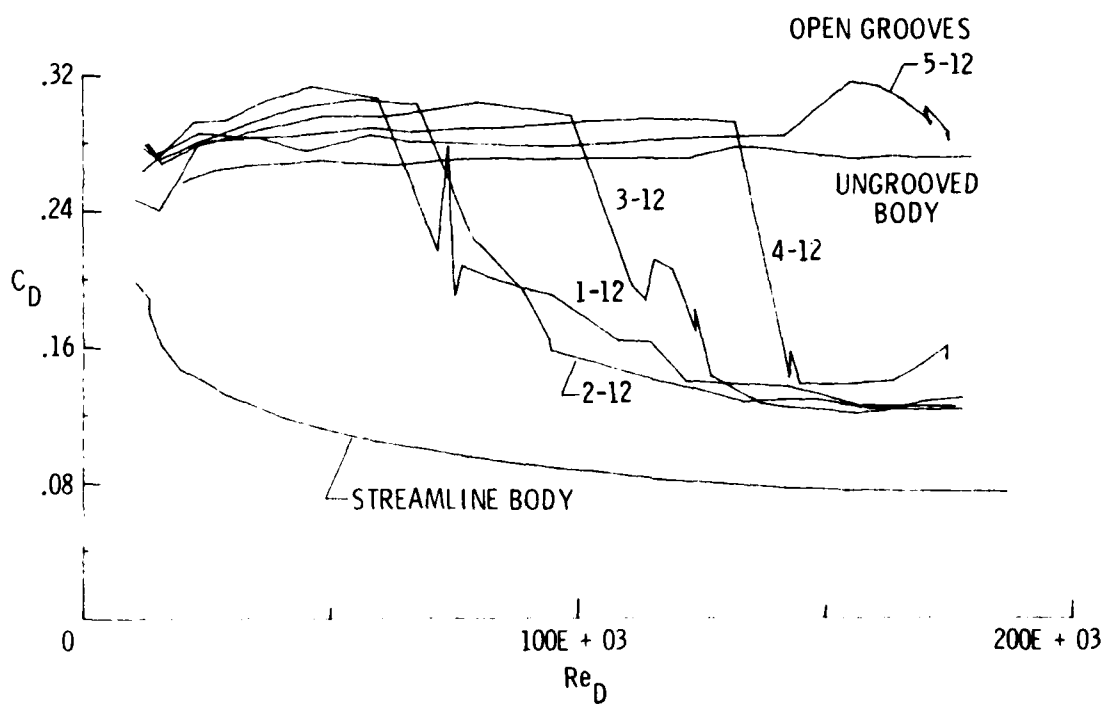


Figure 3.- Influence of initial circumferential groove location on drag coefficient for  $R_s/D = 0.0$ .

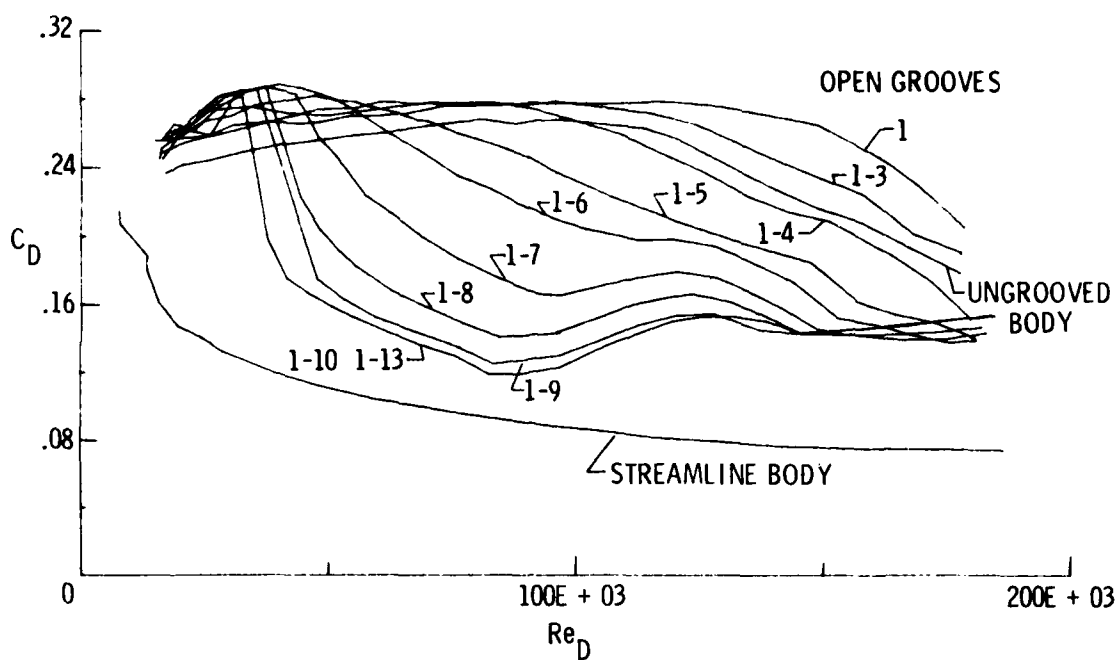


Figure 4.- Influence of number of circumferential groove on drag coefficient for  $R_s/D = 0.5$

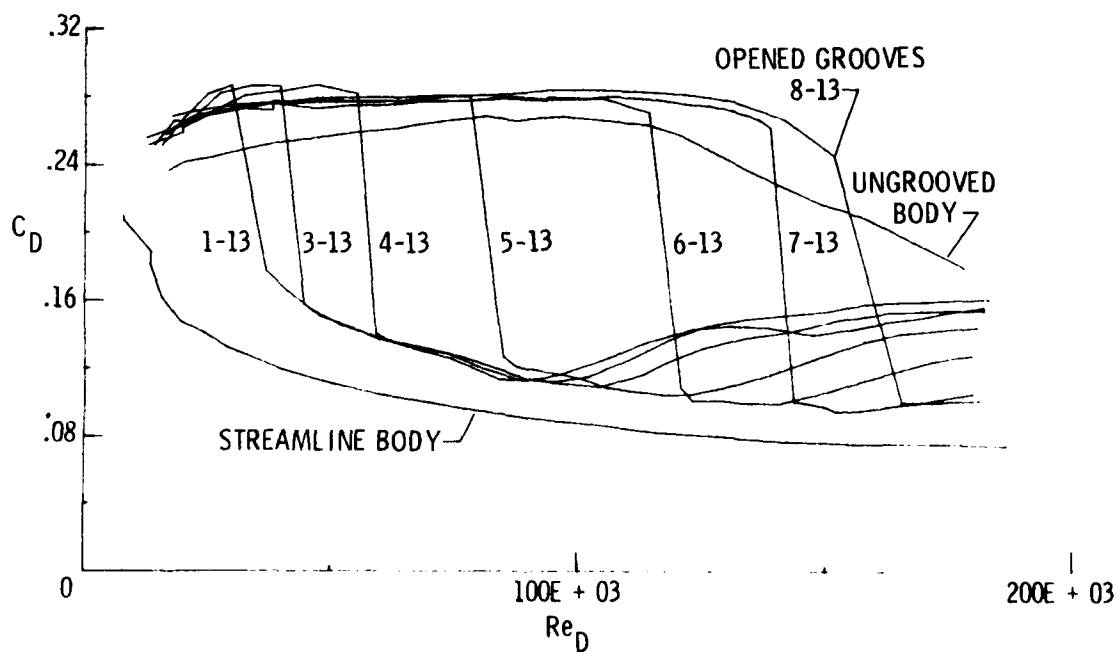
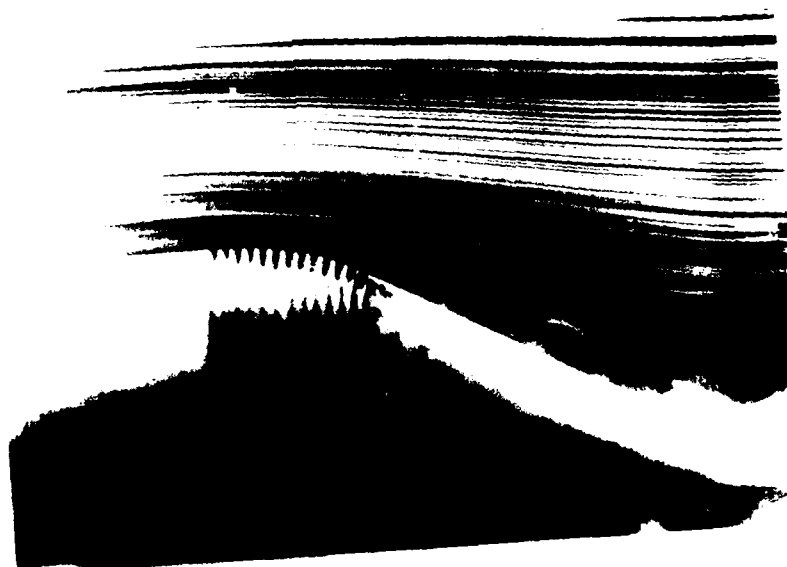


Figure 5.- Influence of initial circumferential groove location on drag coefficient for  $R_s/D = 0.5$ .

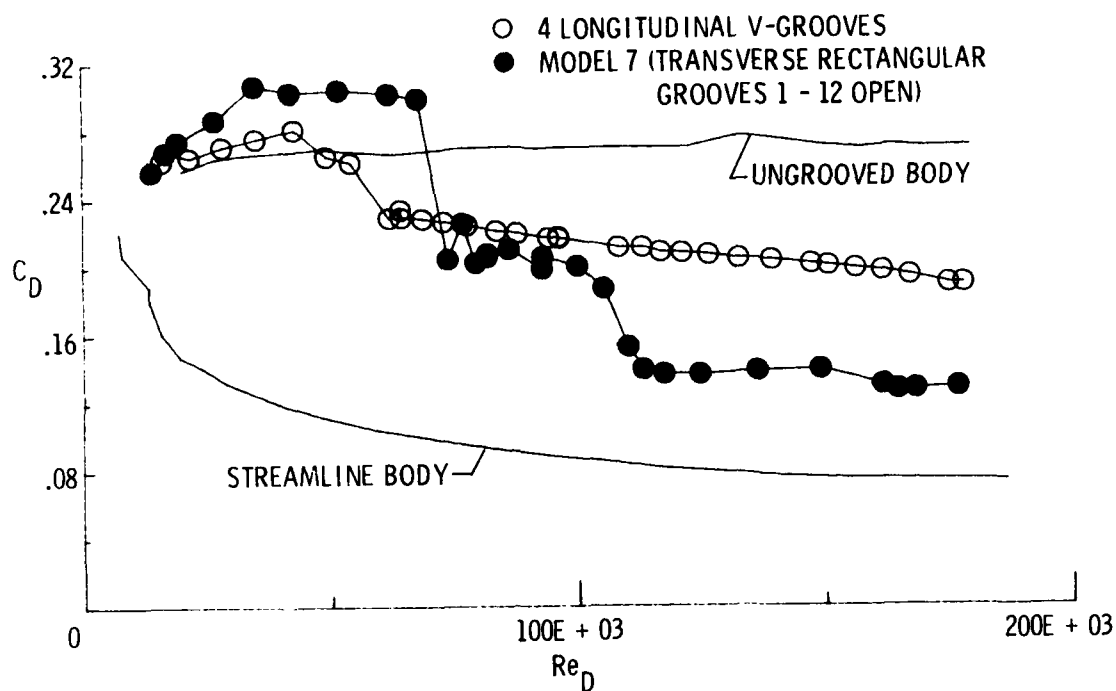


(a) Without grooves.

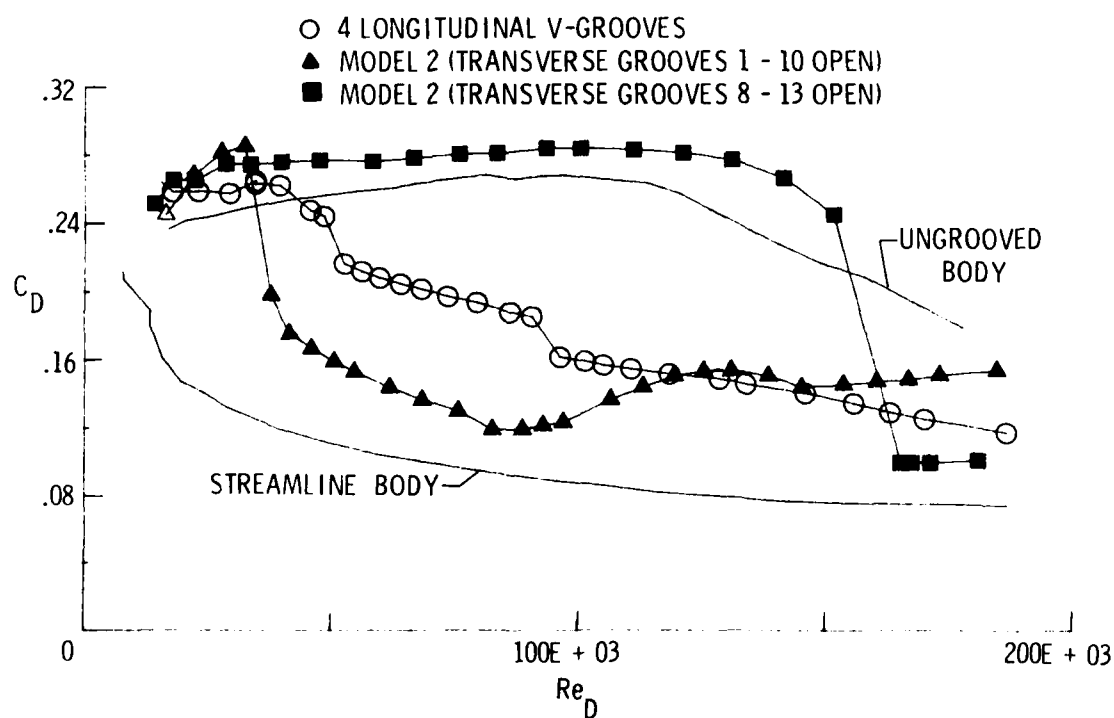


(b) With circumferential grooves.

Figure 6.- Flow Visualization.  $R_s/D = 0.5$ .



(a)  $R_s/D = 0.0$

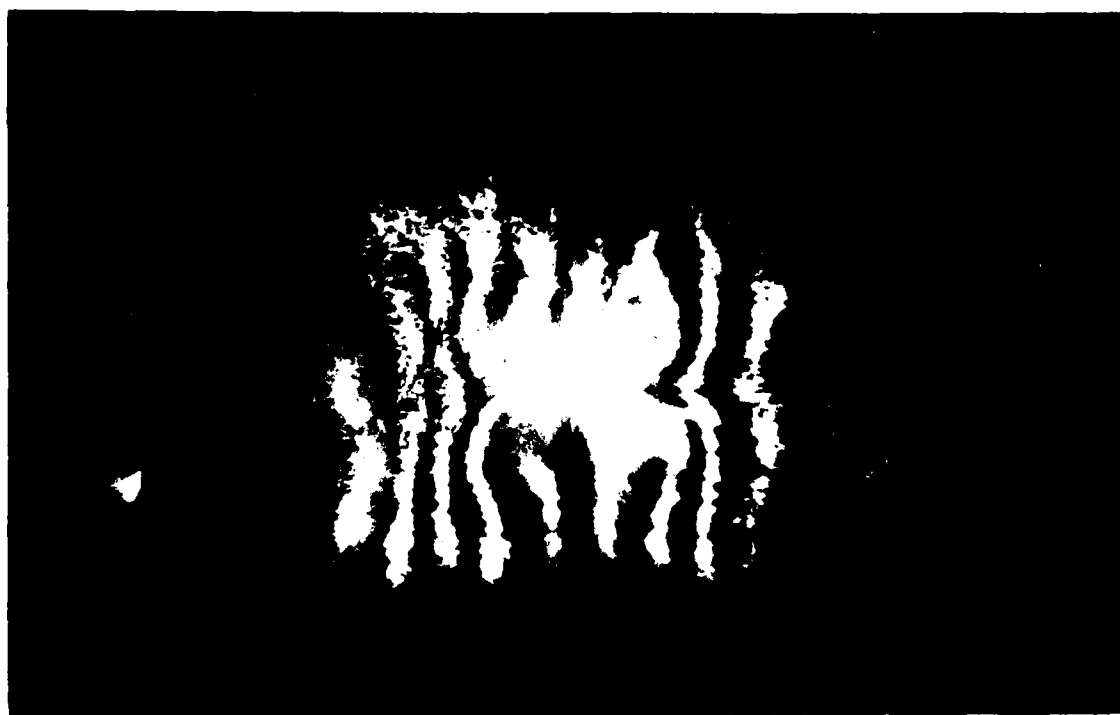


(b)  $R_s/D = 0.5$

Figure 7.- Longitudinal V-grooves compared to circumferential (transverse) rectangular grooves.



(a) Without grooves.



(b) With longitudinal V-grooves.

Figure 8.- Example of visualization data in a lateral plane near the base apex.

EXPERIMENTAL INVESTIGATIONS ON BODIES WITH  
NONCIRCULAR CROSS SECTIONS IN COMPRESSIBLE FLOW  
(Pressure Distributions)

W. Schneider  
DFVLR-AVA Göttingen

---

9th US-FRG DEA Meeting on "Viscous and Interacting Flow Field  
Effects", 9-10 May 1984,

Naval Surface Weapons Center White Oak, Silver Spring,  
Maryland, USA.

EXPERIMENTAL INVESTIGATIONS ON BODIES WITH  
NONCIRCULAR CROSS SECTIONS IN COMPRESSIBLE FLOW  
(Pressure Distributions)

W. Schneider

Deutsche Forschungs- und Versuchsanstalt  
für Luft- und Raumfahrt e. V. Köln  
(AVA-Göttingen)

The present results were obtained in a continuation of extensive investigations on bodies with noncircular cross sections which have already been discussed within these data exchange meetings. Such bodies became important for various payload transport missions of missiles rather than for their smaller radar signature. The objective of these studies is to get a better insight into the complex flow phenomena and to provide a useful data base for theoretical efforts in this area. The tests were conducted in the Mach number range  $M_\infty = 0.5$  to  $M_\infty = 2.0$ , the angle of attack was varied between  $\alpha = 0^\circ$  and  $\alpha = 30^\circ$  and the angle of roll between  $\varphi = 0^\circ$  and  $\varphi = 45^\circ$ . The mean Reynolds number (based on calibre D) was  $0.5 \times 10^6$ . The models, Fig. 1, and the test set-up were described in detail in Ref. 1. For the pressure measurements only the model series with the square section as basic shape was used. By corner rounding, it is possible to get a simple transition to the circular cylinder and hence a connection to the very detailed experimental results for this body. Because of its size, the model could only be equipped with pressure taps in two sections. The selection of these sections (5 and 9 calibres from the nose apex) was based on oil flow pictures (see Ref. 1), obtained for the sharp edged body. These oil flow patterns show, depending on model length and incidence, two significant areas along the body for which one has to expect different flow fields. A detailed interpretation of oil flow patterns on box-type bodies is given in Ref. 2 and 3.

The following results only represent a limited selection, which is expected to show the essential change in the flow fields at the bodies if, as already mentioned, the cross sections are modified from a square to a circle by rounding the corners and, furthermore, the development of vortex systems, due to flow separation, with increasing angle of incidence and roll at subsonic and supersonic speeds.

Before discussing the pressure distributions it seems necessary to provide an impression of the flow separation and the development of the vortex systems by simplified topological representations in the cross flow plane for the various bodies.

Fig. 2 shows the flow field and the pressure distribution for section 1 of the square body at a Mach number of 0.5 and an incidence of  $20^\circ$ . Primary separations occur at the bottom edges like on a sharp-edged flat plate. The flow reattaches at the sides of the body in half-saddle points. In the space between the points of separation and reattachment a first pair of strong vortices can develop. The flow component directed leeward from the point of reattachment separates at the top edges and rolls up to a suction side vortex pair. The intensity of vortices on the suction side is weaker because the main part of the vorticity is fed into the side vortices. The streamwise points of reattachment, or half saddles, lie on lines of reattachment originating from the windward edges and terminating at the leeward edges on the sides of the body. The inclination of these lines with respect to the body axis depends on the angle of attack. Where the reattachment line reaches the upper edges of the body, the vortex pair on the suction side will be strengthened by the feeding sheet, while the intensity of the vortex pair on the sides becomes smaller. Section 2 is representative for this part of the body. The flow field in this section is shown in Fig. 3. One should notice the difference in the pressure distribution in comparison to section 1. The essential feature of a box-type body in comparison with a circular body are the two pairs of vortices



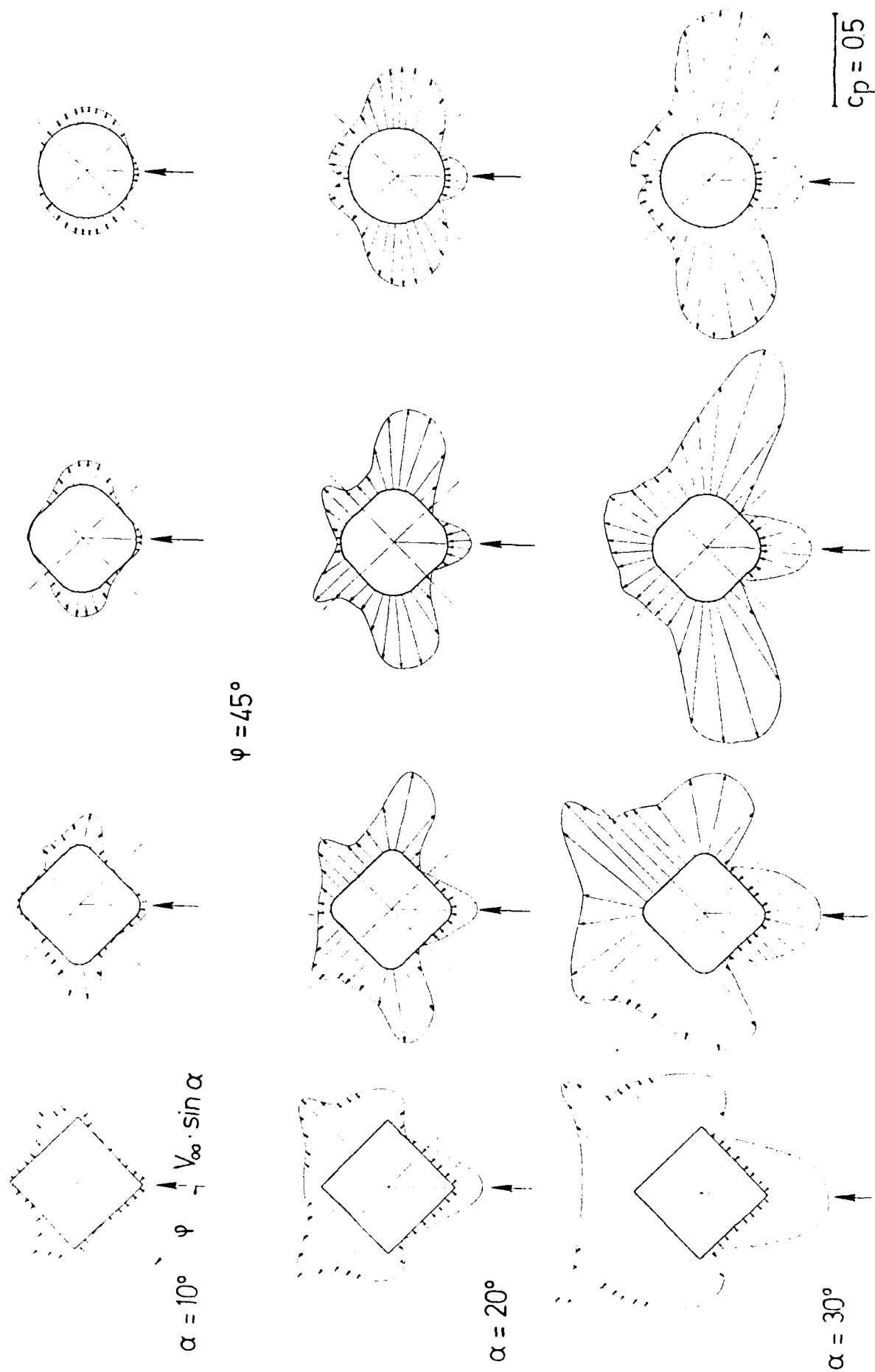


Fig. 14 Pressure Distribution in Section 1,  $M_\infty = 0.5$

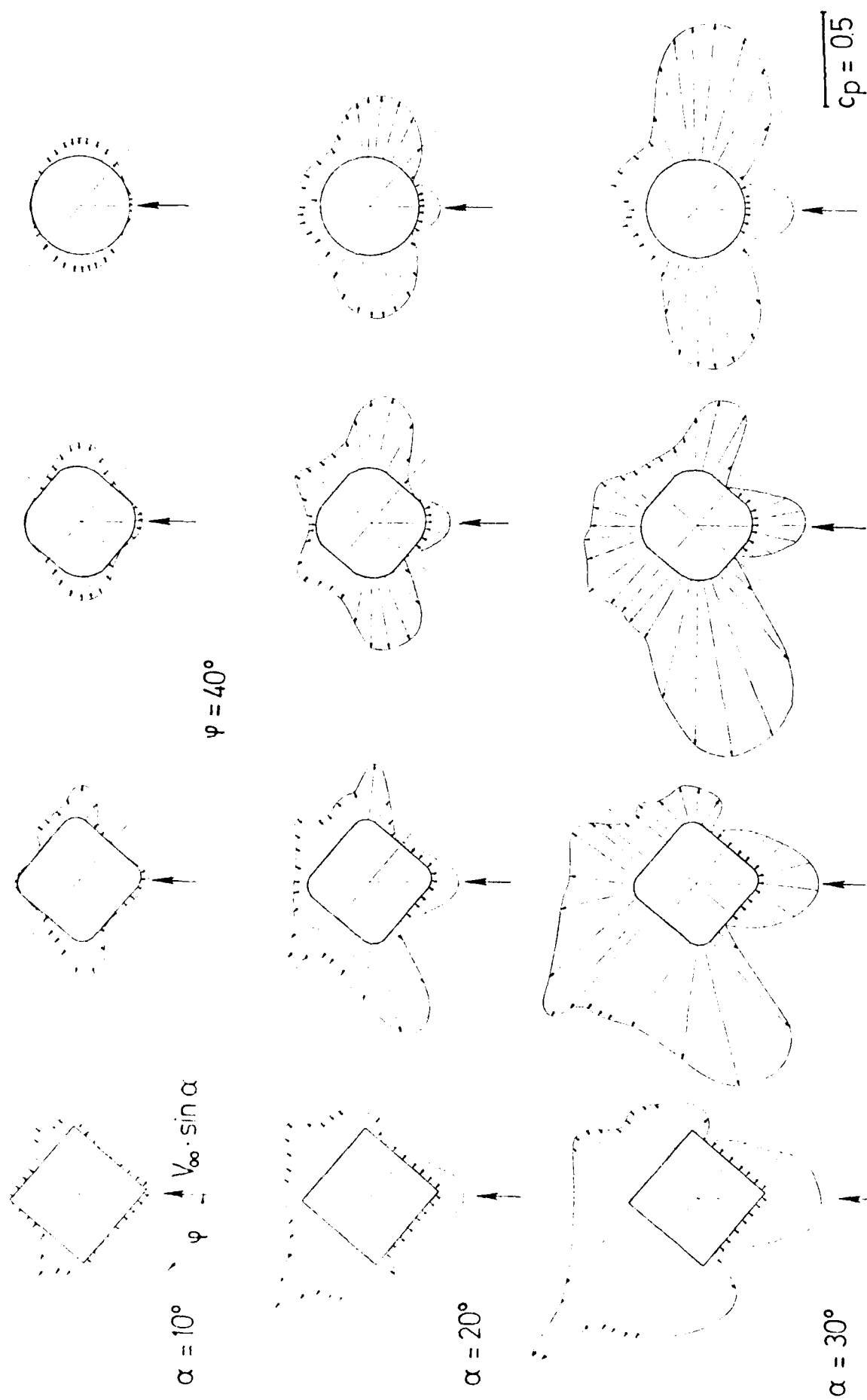


Fig. 13 Pressure Distribution in Section 1,  $M_\infty = 0.5$

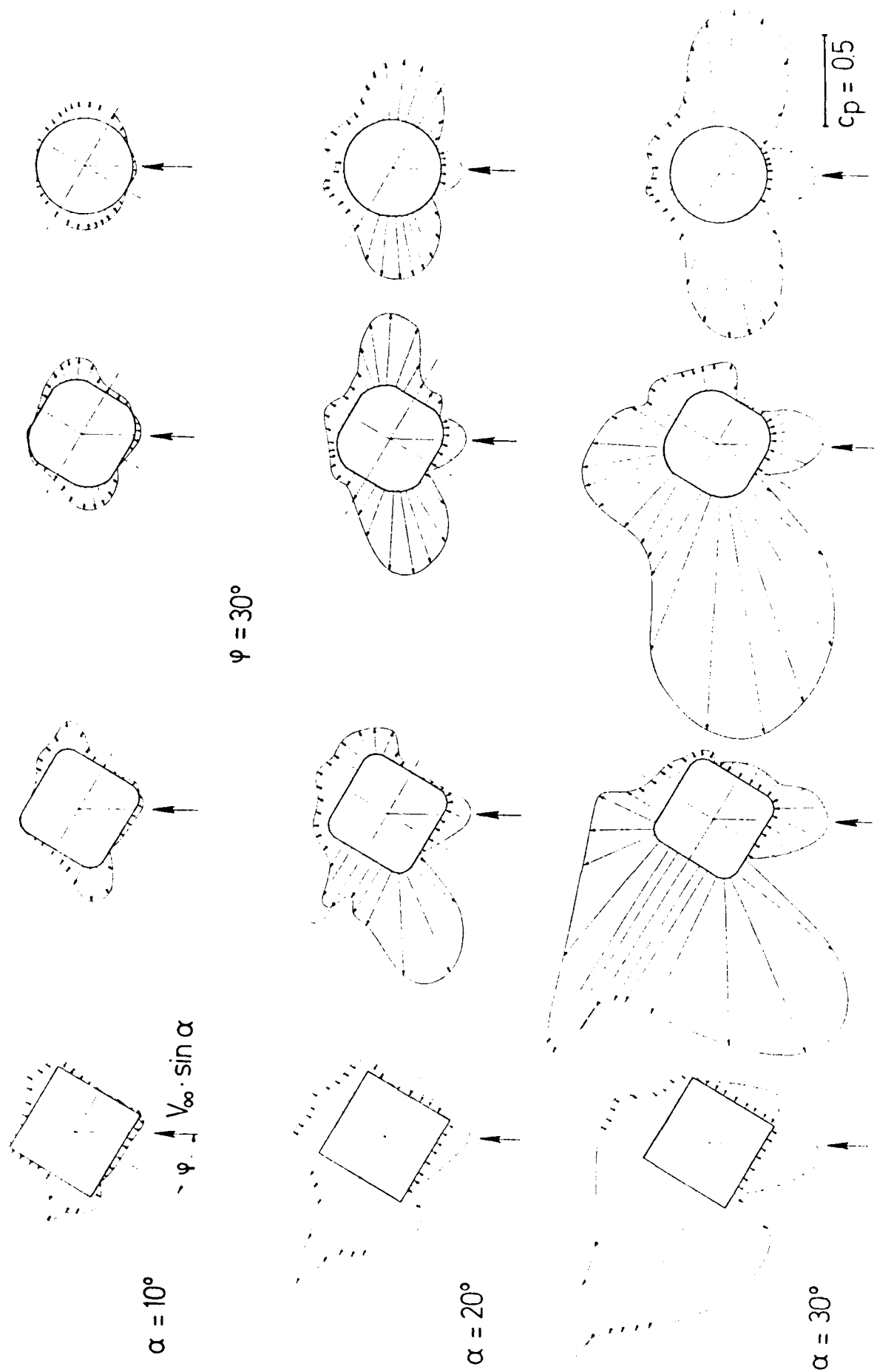


Fig. 12 Pressure Distribution in Section 1,  $M_\infty = 0.5$

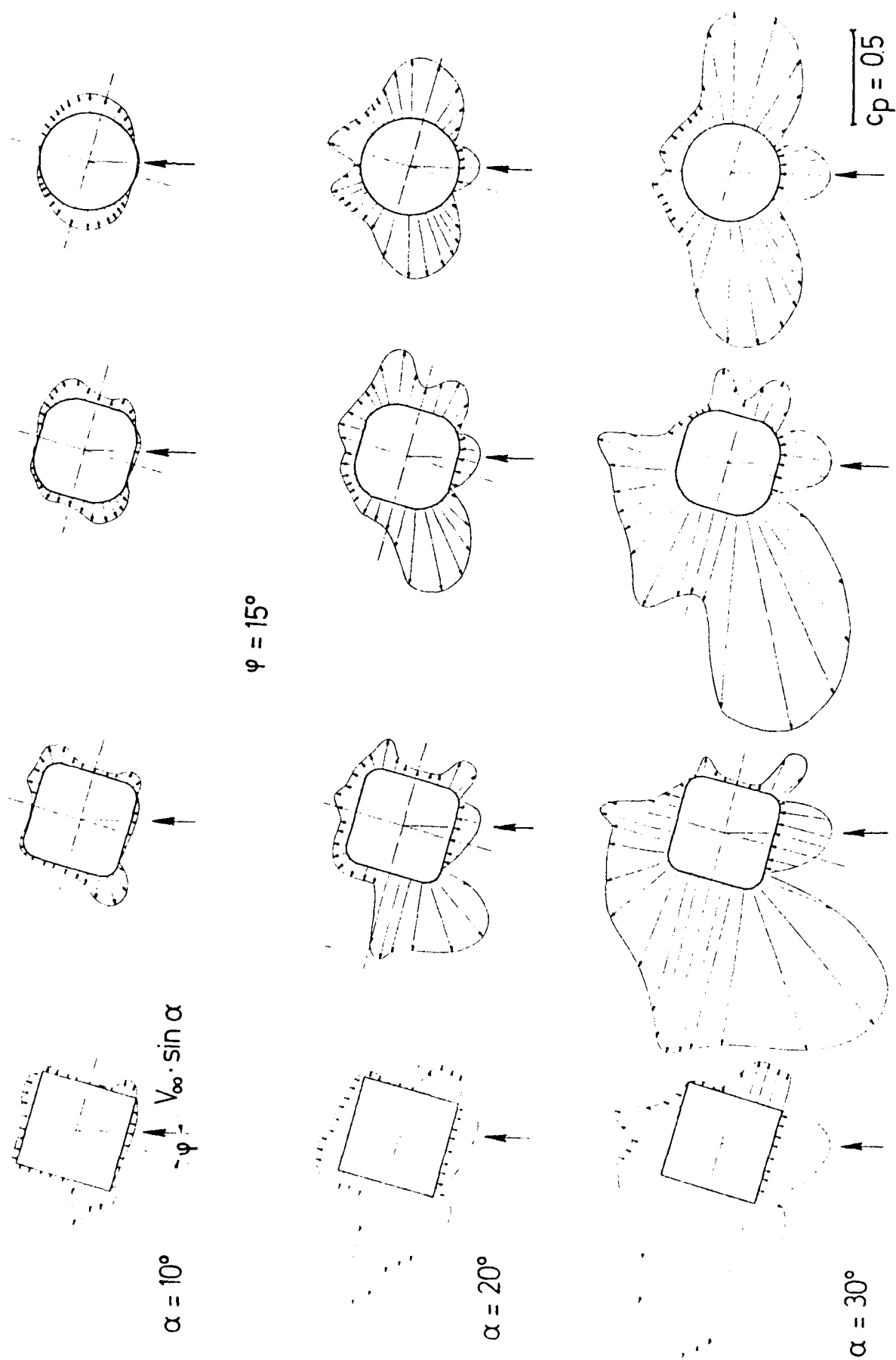


Fig. 11 Pressure Distribution in Section 1,  $M_\infty = 0.5$

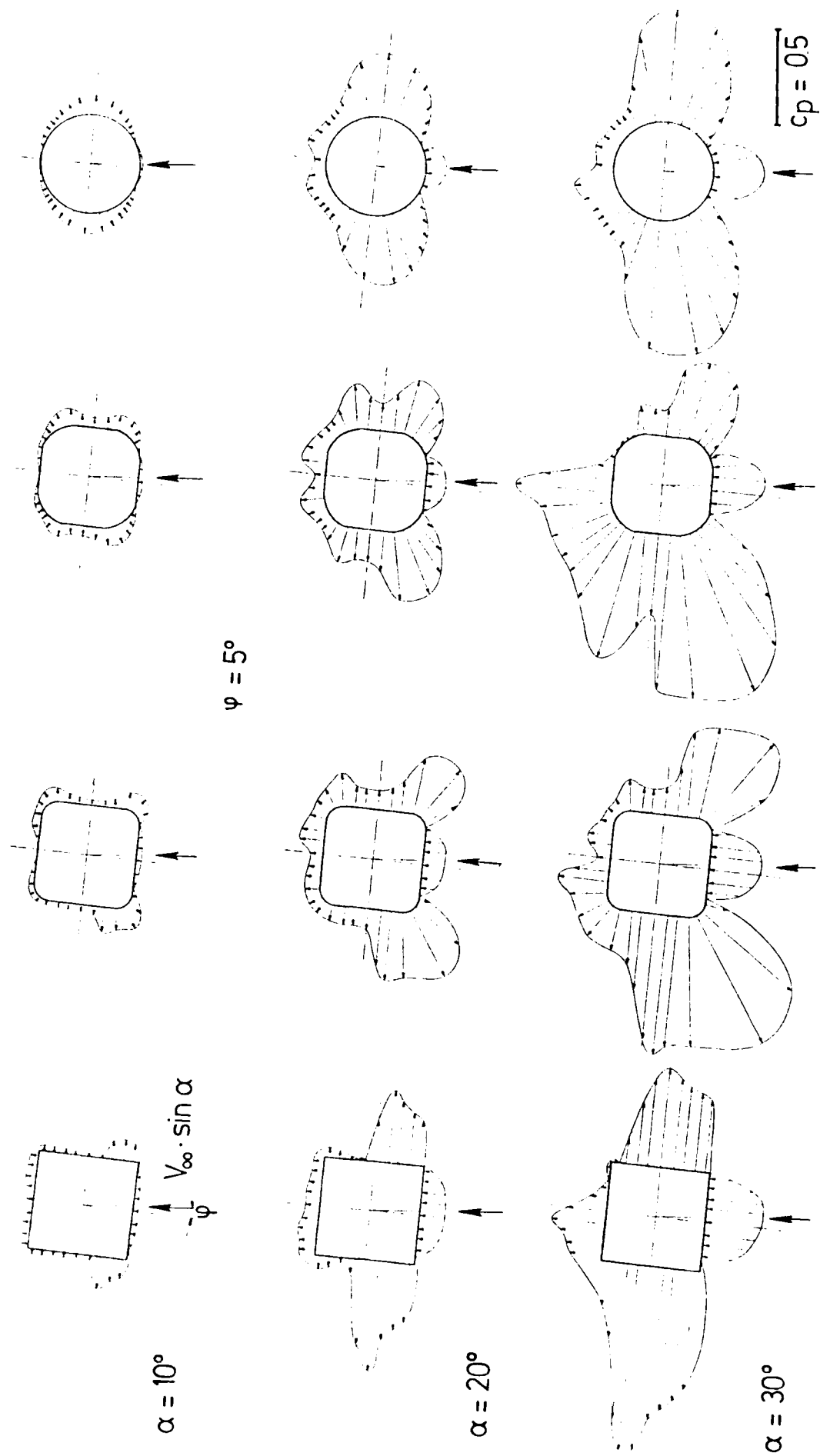


Fig. 10 Pressure Distribution in Section I,  $M_\infty = 0.5$

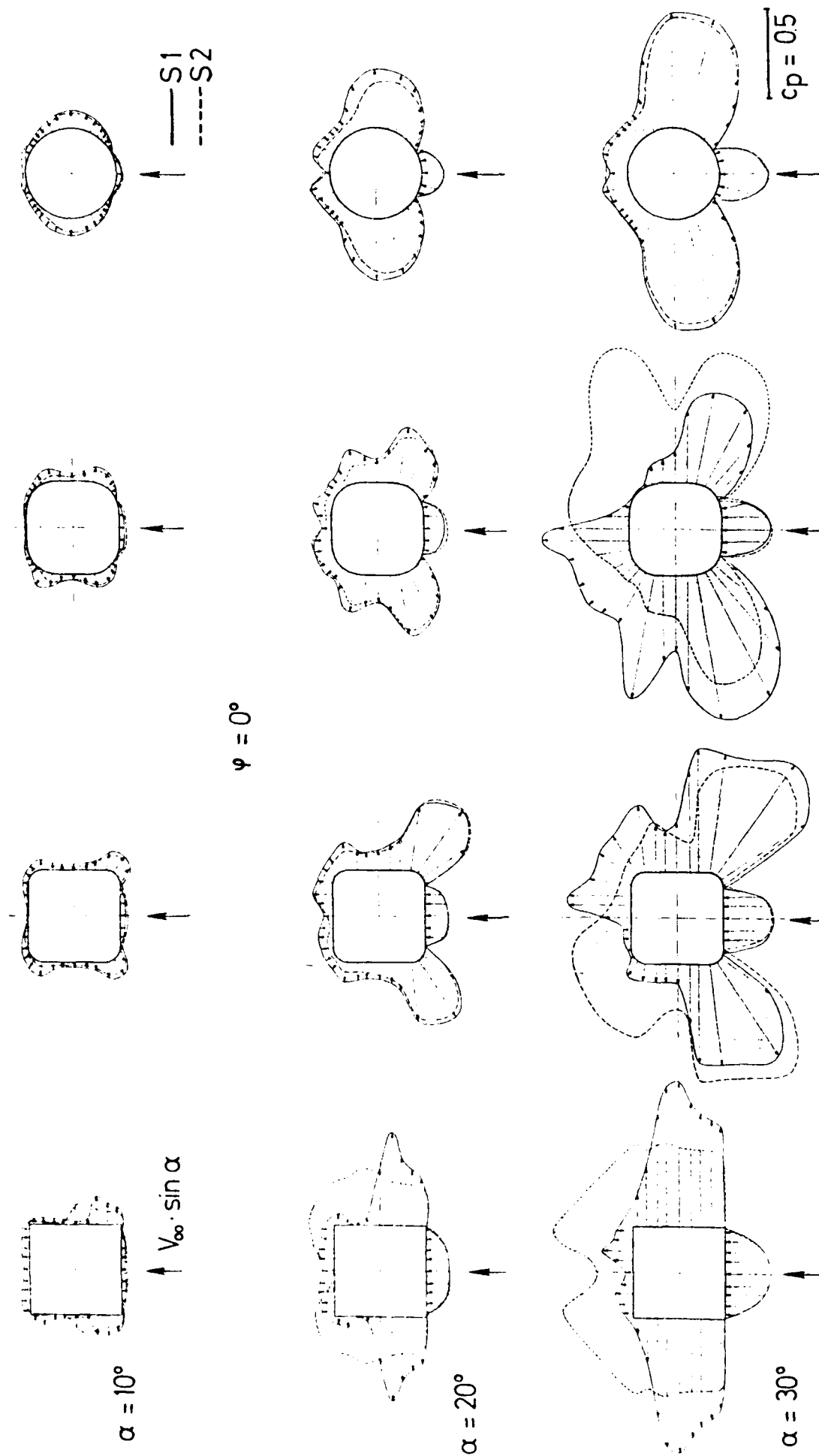


Fig. 9 Pressure Distribution in Section 1 and 2,  $M_\infty = 0.5$

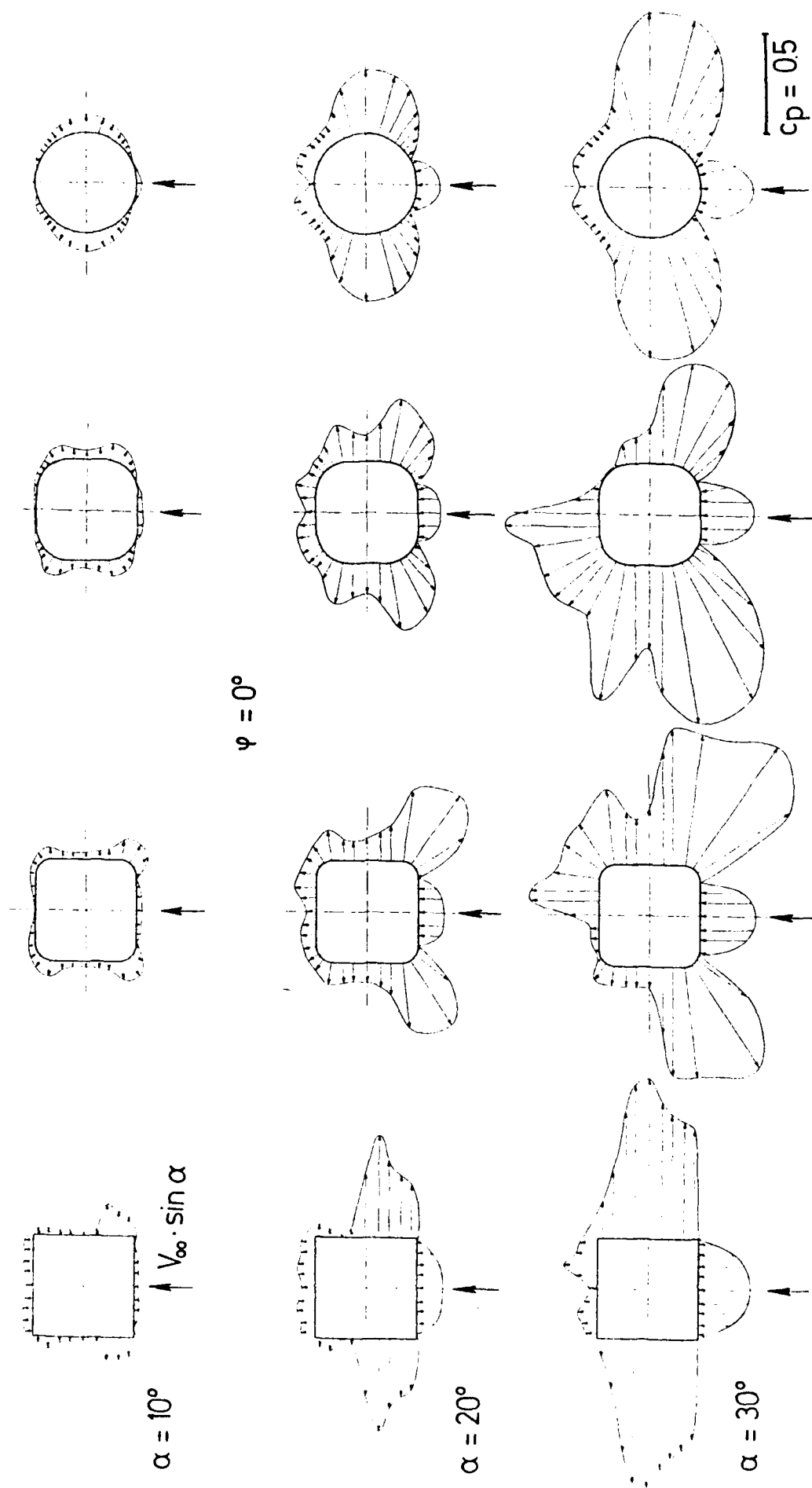


Fig. 8 Pressure Distribution in Section 1,  $M_\infty = 0.5$

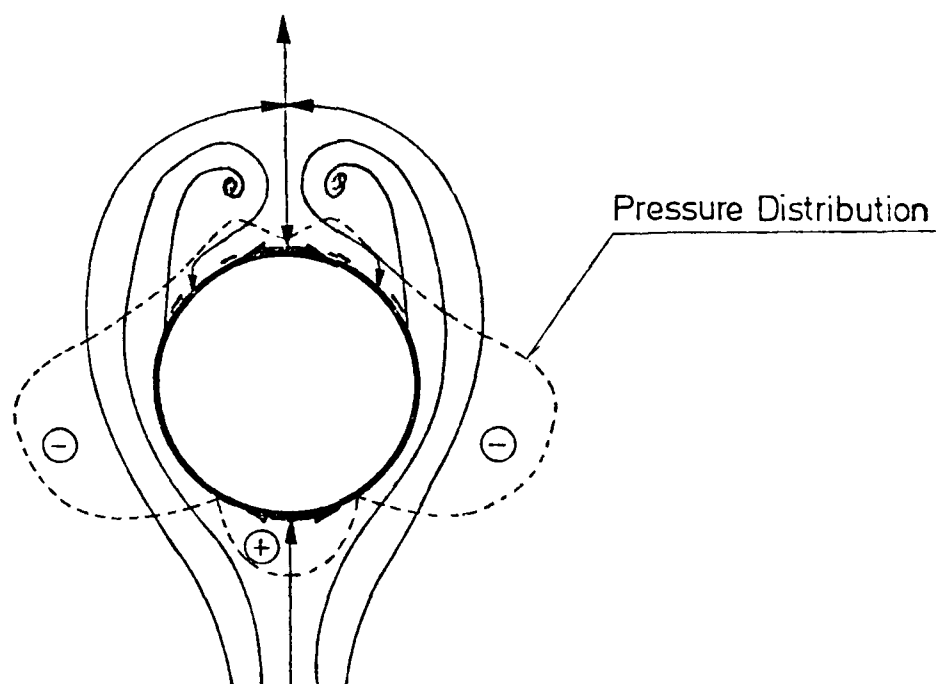


Fig. 6 Cross-Flow Topology for Section 1,  $M_{\infty} = 0.5$ ,  $\alpha = 20^\circ$

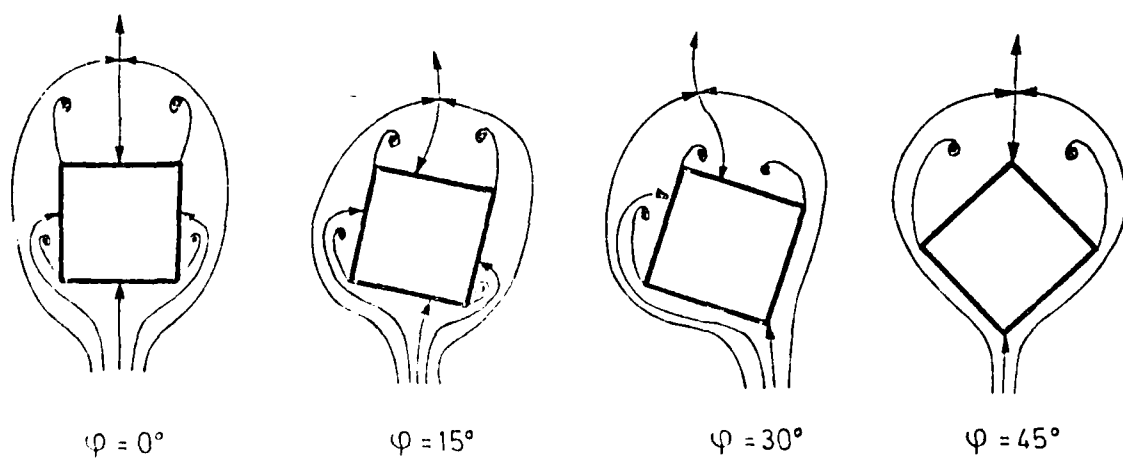


Fig. 7 Development of Cross-Flow Topology on a Body with a Square Section



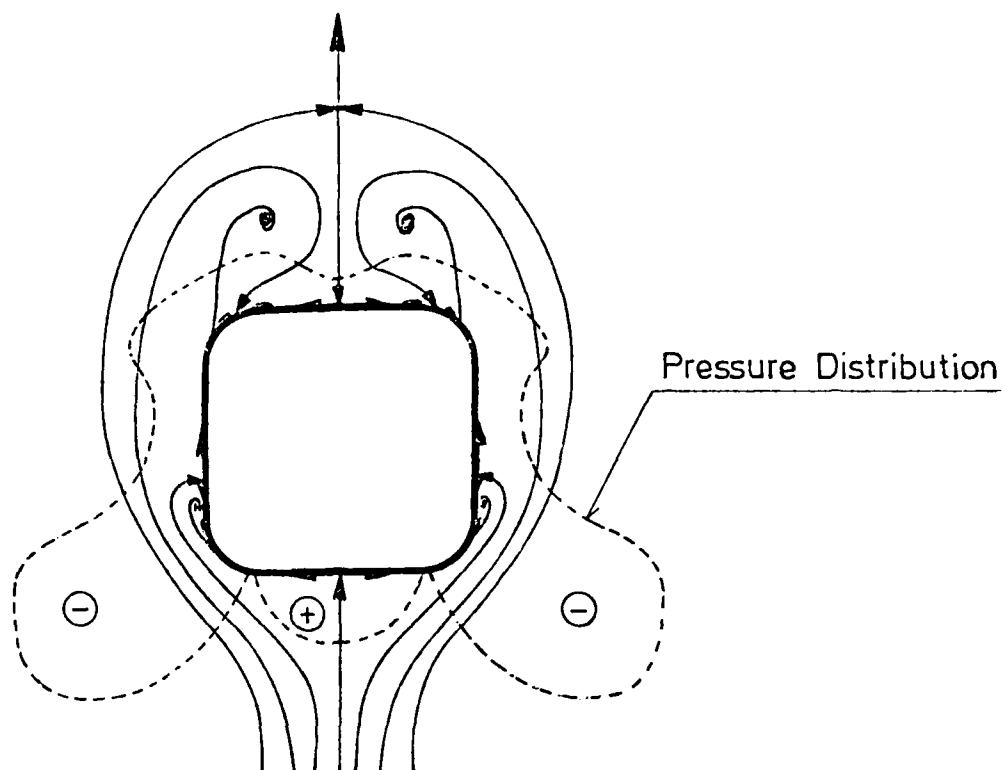


Fig. 4 Cross-Flow Topology for Section 1,  $M_{\infty} = 0.5$ ,  $\alpha = 20^{\circ}$

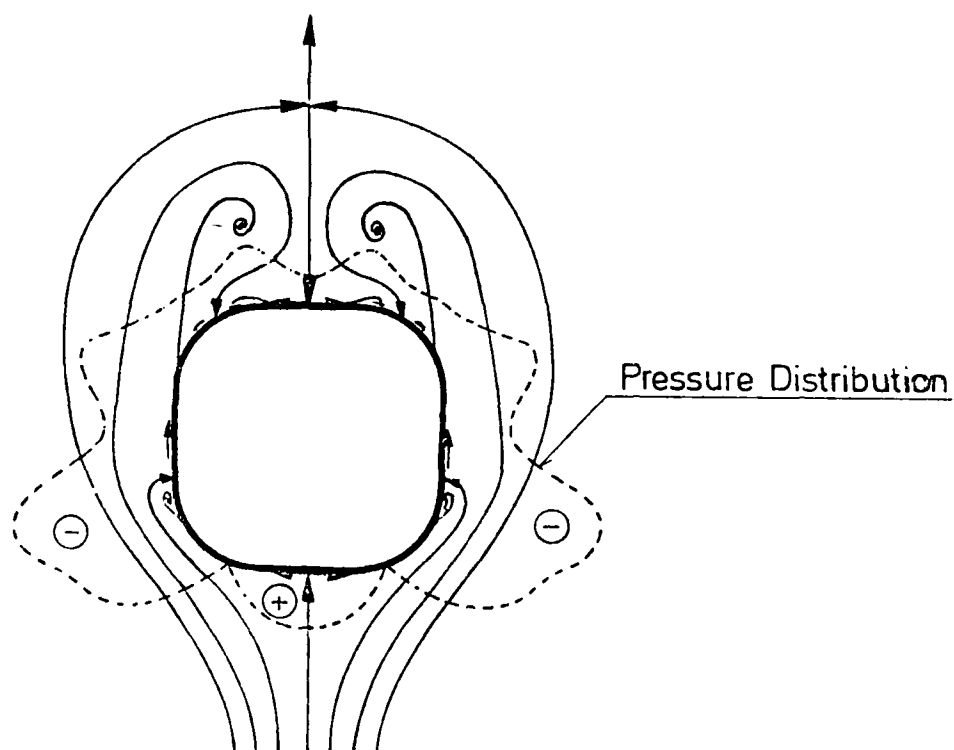


Fig. 5 Cross-Flow Topology for Section 1,  $M_{\infty} = 0.5$ ,  $\alpha = 20^{\circ}$

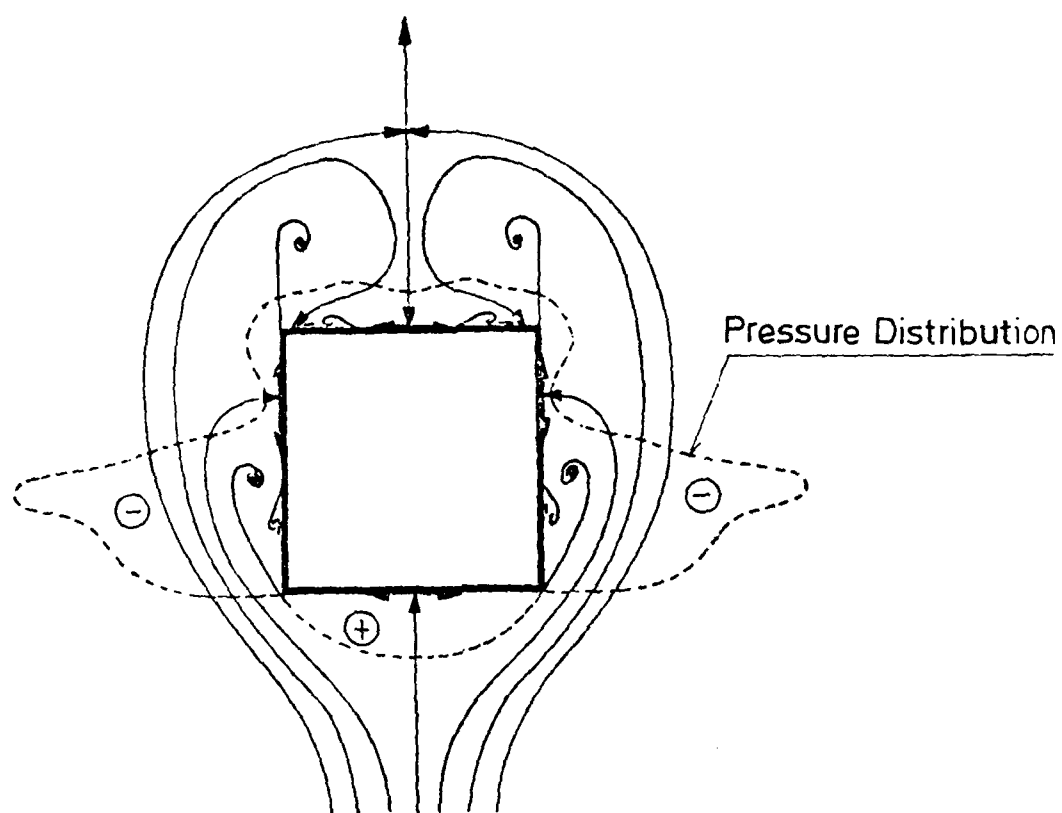


Fig. 2 Cross-Flow Topology for Section 1,  $M_{\infty} = 0.5$ ,  $\alpha = 20^\circ$

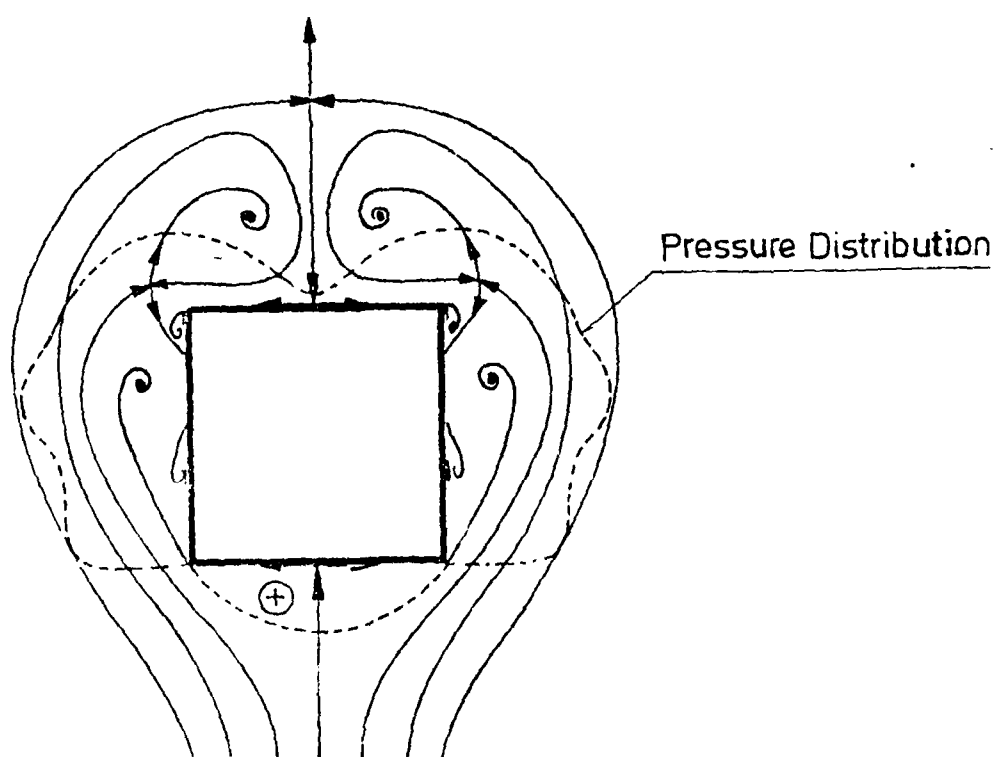


Fig. 3 Cross-Flow Topology for Section 2,  $M_{\infty} = 0.5$ ,  $\alpha = 20^\circ$

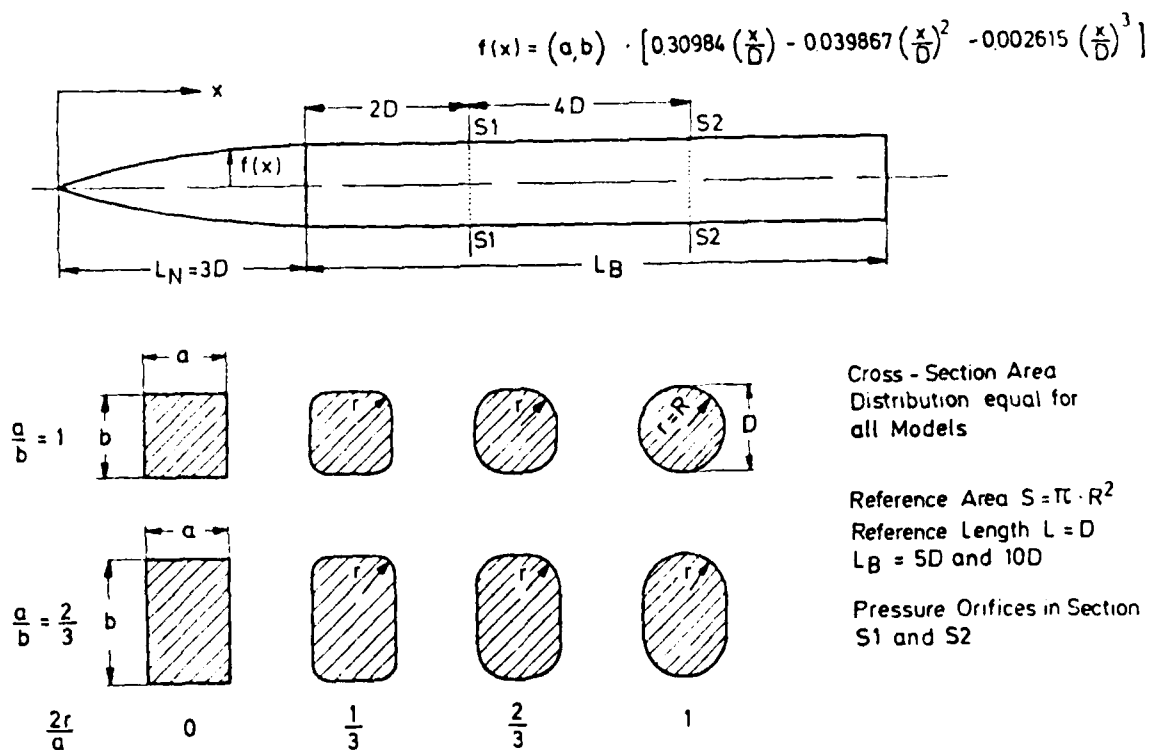


Fig. 1 Model Dimensions

standing of the complex flow phenomena on such bodies, enhance the data base, and incite theoretical activities.

#### REFERENCES

- [1] Schneider, W.                      Experimental Investigations on Bodies with Noncircular Cross Sections in Compressible Flow.  
Proc. 7th U.S.-FRG Meeting  
DEA AF-6-7400, Aberdeen 1982
- [2] Daniel, D.C.                      Experimental Aerodynamic Studies of Missiles with Square Cross Sections.  
Lejevski, L.E.                      AGARD CP 336, 1983
- [3] Chapman, G.T.                      Flow Visualization Studies of Bodies with Square Cross Sections.  
AIAA Paper -83-0563, 1983
- [4] Polhamus, E.C.                      Effects of Flow Incidence and Reynolds Number on Low-Speed Aerodynamic Characteristics of Several Noncircular Cylinders with Applications to Directional Stability and Spinning.  
NASA TR-29, 1959
- [5] Kordulla, W.                      Computation of Viscous-Supersonic Flows Past Pointed Non-Axisymmetric Bodies.  
Jettmar, R.U.                      Proc. 8th U.S.-FRG Meeting  
DEA AF-75-G-7440, Göttingen, 1983

distribution for the circular cylinder is still symmetrical, it becomes asymmetrical for the rounded box shapes. For section 2, Fig. 9, these asymmetrical distributions lie on the opposite sides, an effect, which is known from circular cylinders only at higher angles of attack. In addition, the Reynolds numbers of these tests already are in the range of critical values for the cylinder in cross flow. Flows with secondary separations have shown to be extremely sensitive in this range, see Ref. 4. In Fig. 10 to Fig. 14, the pressure distributions for different roll angles are shown. With the explanations already given the positions of the primary vortex systems may be found by the induced suction peaks. Force measurements have shown extreme side forces at a roll angle of nearly  $30^\circ$  which is reflected by the pressure distributions, see Fig. 12.

The results at supersonic speeds are compared with those at subsonic speeds for the same angles of attack and roll, see Fig. 16 to Fig. 20. As is known, the strength of vortices will diminish with increasing compressibility. High suction peaks on the bodies, like they occur at subsonic speeds will not appear at supersonic speeds. The large forces in the bodies are mainly due to opposite fields of compressions and expansions. For small angles of incidence ( $\alpha = 10^\circ$ ), when cross flow velocities do not reach critical values, the pressure distributions for sub- and supersonic speeds are largely similar. At higher angles of attack (at nearly  $30^\circ$ ) when the cross flow velocities become supersonic, the flow field is bounded by shocks and becomes more stable than at subsonic speeds and for symmetric flow conditions no asymmetrical pressure distributions appear. So it seems that numerical methods, see Ref. 5, in modelling the flow phenomena for noncircular bodies, will be more successful at supersonic than at subsonic velocities.

From an extensive study on bodies with noncircular cross sections, selected results in the form of pressure distributions were presented. It is hoped that they will contribute to the under-

which, depending on the angle of incidence and the length of the body, may reach equal strength. In practical aerodynamics considerable problems may occur when such bodies are equipped with wings or controls.

When the edges are rounded from the square section to the circle, the flow on the windward side will first try to follow the surface contour and the points of primary separation, depending on curvature, will move leeward on the vertical sides, while the points of reattachment will move downward (see Fig. 4). Flow separation and vortex development on the sides of the body will diminish with increasing radius of curvature as indicated in Fig. 5. The leeward vortices become dominant until one finally reaches the limiting case of the circular cylinder with its well known flow structure (see Fig. 6). It must be mentioned again that only the main flow features are being pointed out, while secondary effects have been omitted in the representations for the sake of clarity.

Force measurements have indicated that on sharp edged bodies in asymmetric flow the side forces may be of the order of the normal forces. The process of rolling is topologically represented in Fig. 7. (Secondary vortices have not been included.) Symmetric flow conditions for  $\Phi = 0^\circ$  are characterized by two pairs of primary vortices, while, when rolling the body into the other symmetric position,  $\Phi = 45^\circ$ , the flow must go to one pair of primary vortices. At the intermediate roll angles, one of the opposite vortices weakens, while the other strengthens. Normally, the process of rolling and the change in the primary vortex structure is a very complex one, as flow visualizations show, and the transition from one state into the other, which is considerably influenced by secondary effect, is not uniform along the body.

Fig. 8 shows the pressure distributions on the model series for section 1 at a Mach number of 0.5 and three angles of attack. It is noticeable that at an incidence of  $30^\circ$ , where the pressure

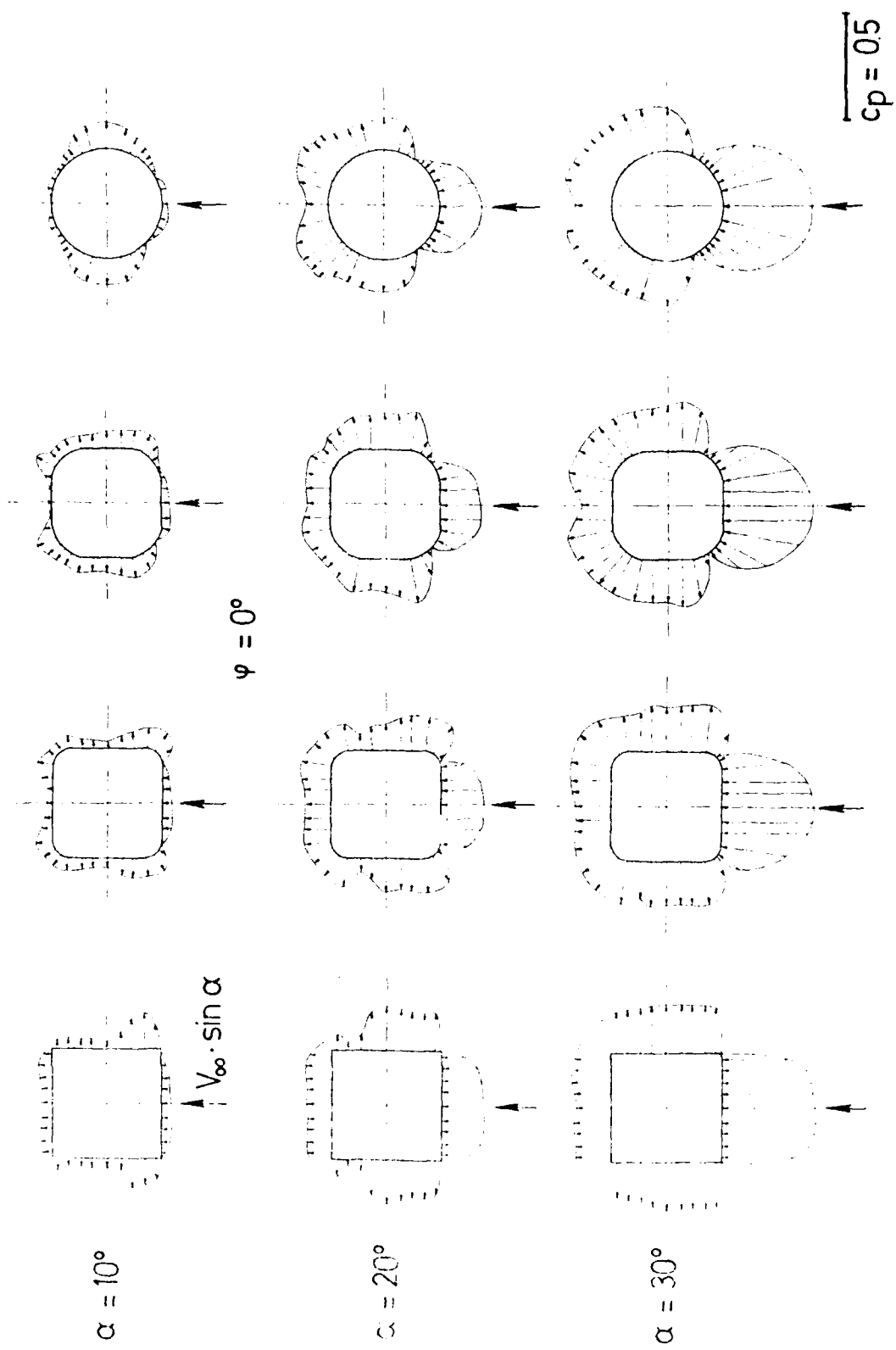


Fig. 15 Pressure Distribution in Section 1,  $M_\infty = 2.0$

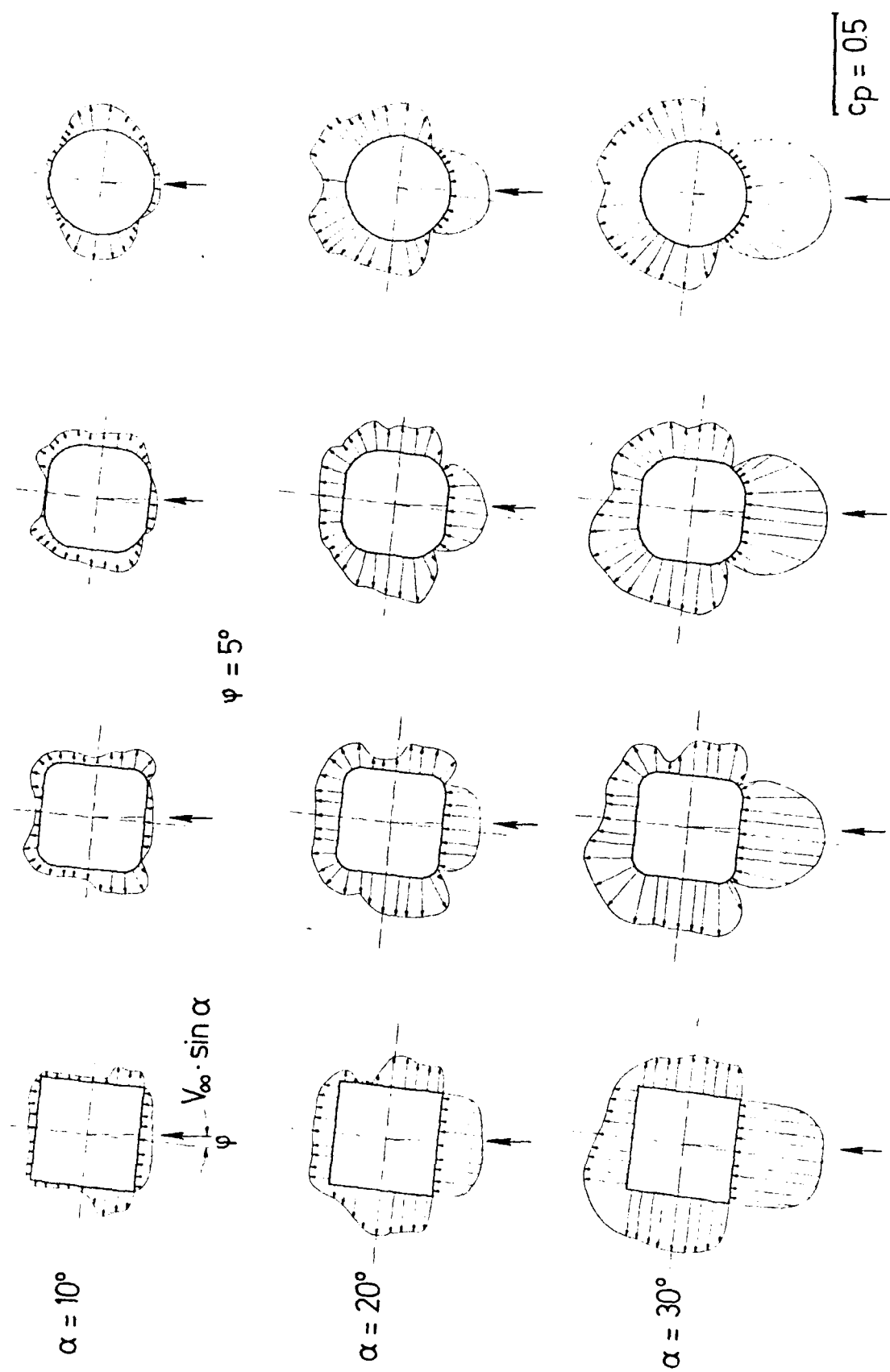


Fig. 16 Pressure Distribution in Section 1,  $M_\infty = 2.0$



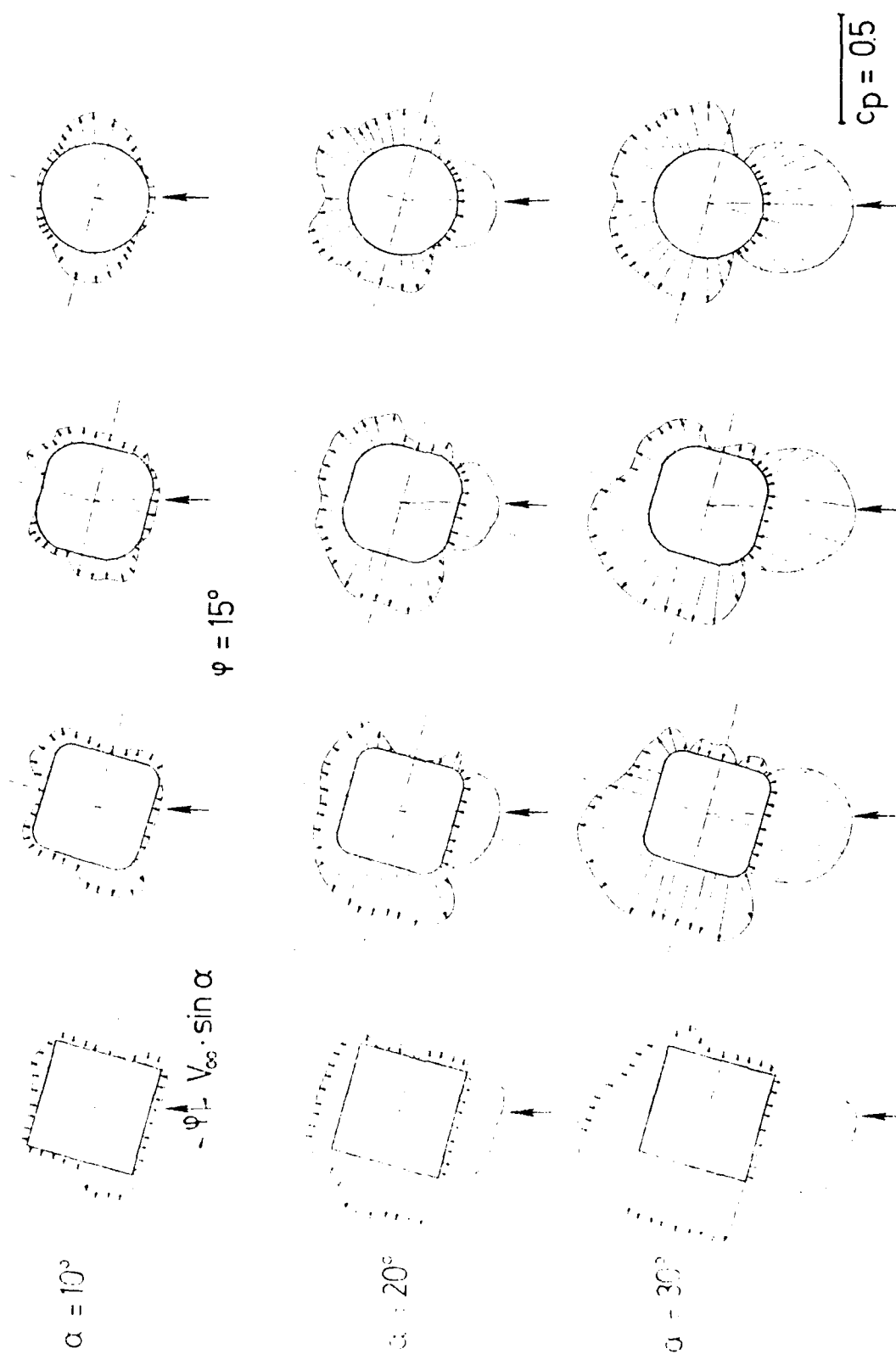


Fig. 17 Pressure Distribution in Section 1,  $M_\infty = 2.0$

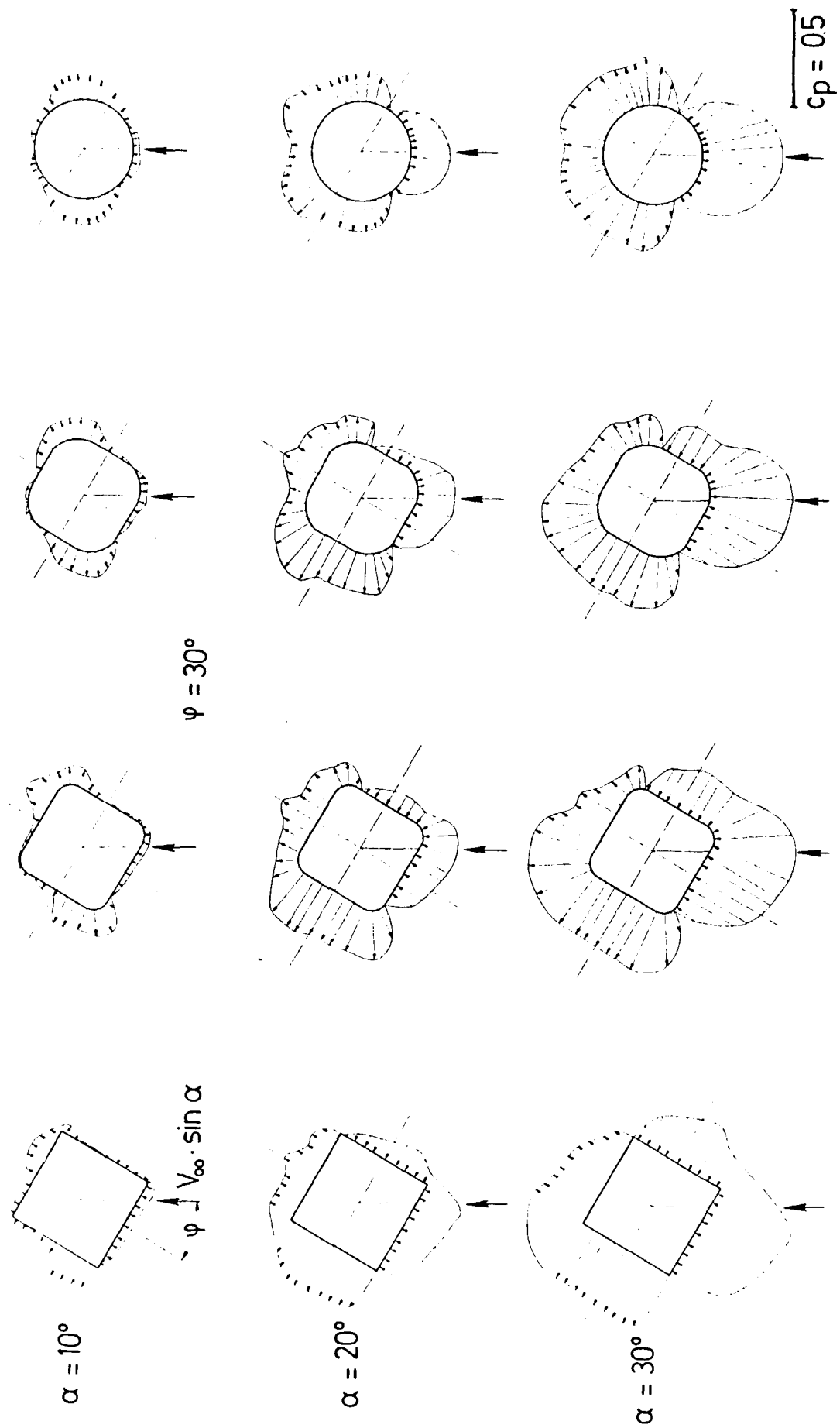


Fig. 18 Pressure Distribution in Section 1,  $M_\infty = 2.0$

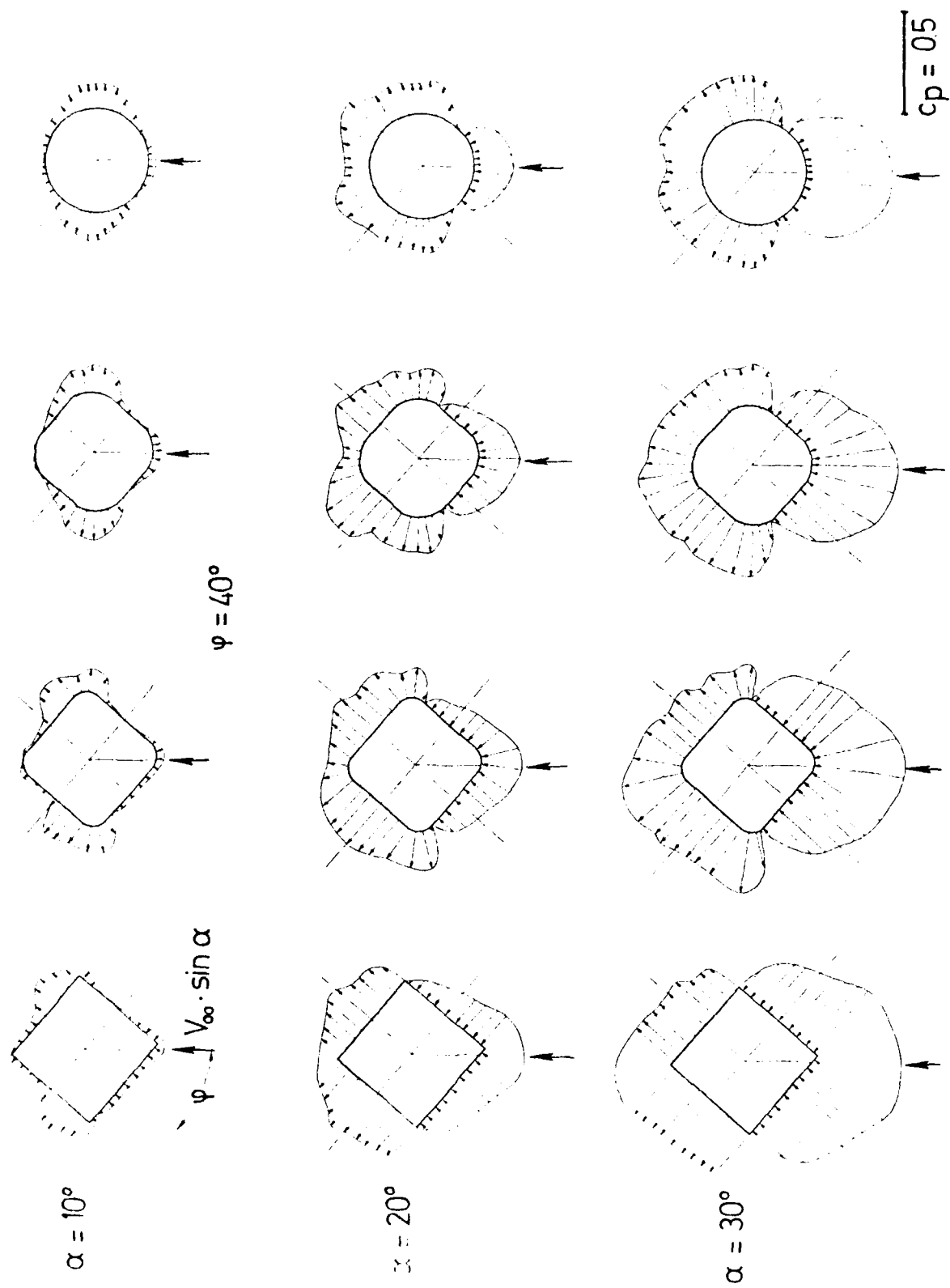


Fig. 19 Pressure Distribution in Section 1,  $M_\infty = 2.0$

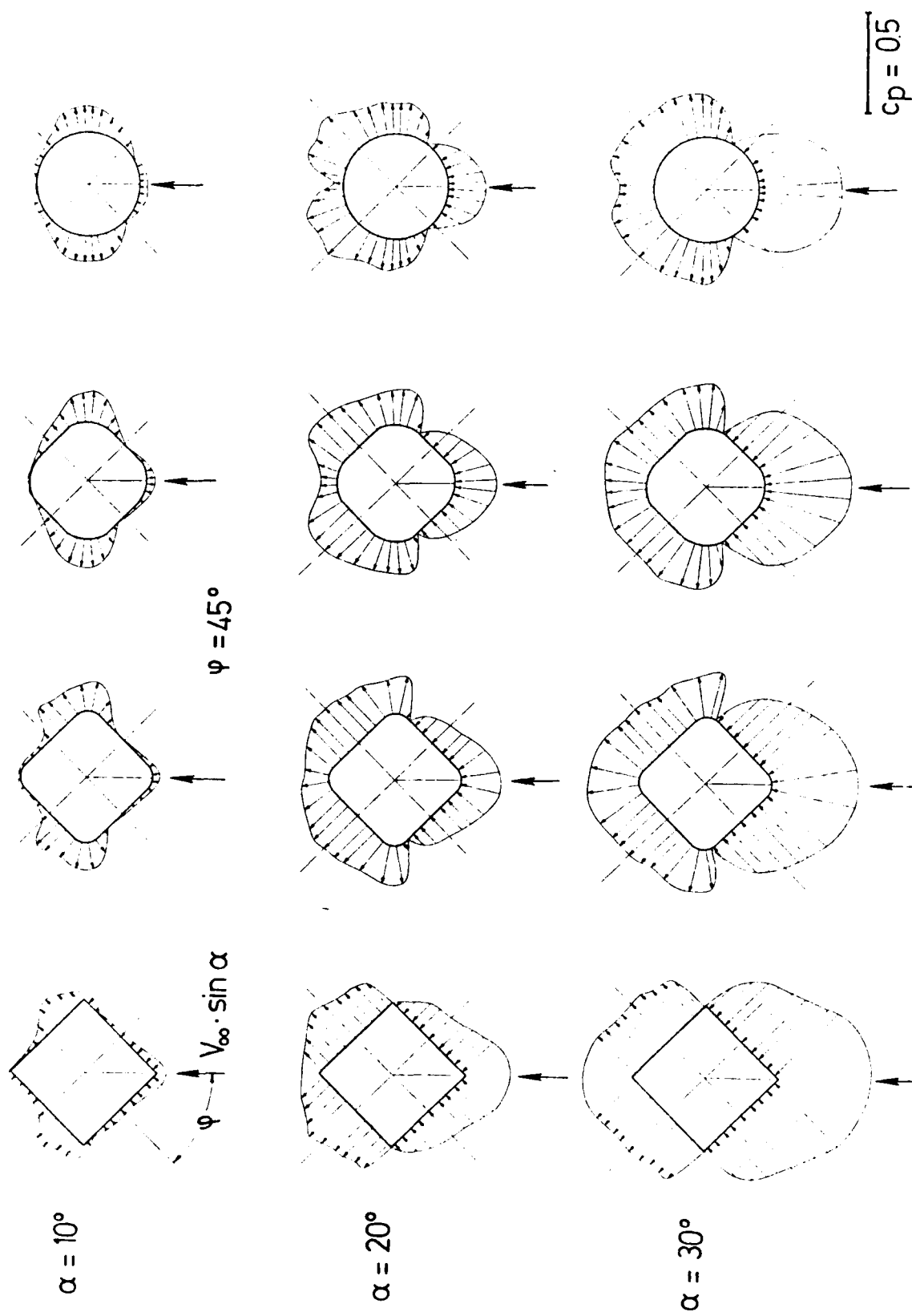


Fig. 20 Pressure Distribution in Section 1,  $M_\infty = 2.0$

MACH 3 THREE-DIMENSIONAL BOUNDARY LAYER TURBULENCE  
TRANSPORT PROPERTIES ON A SPHERICALLY BLUNT CONE

BY

DONALD W. AUSERMAN

WILLIAM J. YANTA

NAVAL SURFACE WEAPONS CENTER  
WHITE OAK, SILVER SPRING, MARYLAND, USA 20910

ABSTRACT

Three-dimensional boundary layer measurements were carried out on a 7-degree semi-vertex angle conical body configuration for angles-of-attack of  $0^\circ$ ,  $2^\circ$ , and  $4^\circ$  in the NSWC Supersonic Tunnel Number Two. Tests were conducted at a freestream Mach number of 3 for a nominal freestream Reynolds number of  $2.3 \times 10^6/\text{ft}$  ( $7.5 \times 10^6/\text{m}$ ) on a cone with a nominal 22% spherically blunt nose. Measurements of the three mean velocity components, turbulence intensities, and Reynolds stresses were obtained at various circumferential locations around the body for one axial station using a 3-D Laser Doppler Velocimeter (LDV) system. In addition, surface Preston probe and static pressure measurements were obtained at five axial stations along the body. The effects of angle-of-attack and model roll position on the three-dimensional mean velocities, boundary layer turbulence properties, and surface parameters are discussed herein.

# NOMENCLATURE

A	= speed of sound
CP, $C_p$	= pressure coefficient (Equation 1)
D	= model base diameter
d	= Preston Probe diameter
K	= Prandtl's constant=0.4
$\ell_u$	$= \left[ \frac{\overline{u'v'}}{\frac{\partial U}{\partial Y} \left  \frac{\partial U}{\partial Y} \right } \right]^{1/2}$ =mixing length
$\ell_w$	$= \left[ \frac{\overline{v'w'}}{\frac{\partial W}{\partial Y} \left  \frac{\partial W}{\partial Y} \right } \right]^{1/2}$ =mixing length
n	= exponent of power law relation
P	= Static pressure
$\bar{q}$	= magnitude of 3-D velocity vector
T	= temperature
$U_\tau$	= friction velocity= $(\tau_s/\rho_s)^{1/2}$
U, V, W	= mean velocity components (in X, Y, Z direction)
$u', v', w'$	= components of turbulent velocity fluctuations
X, Y, Z	= system of rectangular physical coordinates (X parallel to model surface, Y normal to surface, Z tangential to surface)
X'	= distance from model nose measured along model centerline
$\alpha$ , ALPHA	= model angle of attack
$\Delta P$	= differential pressure between Preston probe's Pitot and static
$\delta$	= boundary layer thickness
$\delta_i^*$	= incompressible boundary layer displacement thickness (Equation 2)
$\epsilon_u$	= eddy viscosity= $\ell_u^2 \left( \frac{\partial U}{\partial Y} \right)$
$\epsilon_w$	= eddy viscosity= $\ell_w^2 \left( \frac{\partial W}{\partial Y} \right)$

# NOMENCLATURE (CONT'D)

$\phi$	= model circumferential angle measured from windward ray
$\rho$	= gas density
$\tau_x$	= nondimensional Reynolds stress $-\overline{\rho u'v'}/\tau_s$
$\tau_y$	= nondimensional Reynolds stress $-\overline{\rho u'w'}/\tau_s$
$\tau_z$	= nondimensional Reynolds stress $-\overline{\rho v'w'}/\tau_s$
$\tau_s$	= wall shear stress measured with Preston probe

## Subscripts:

e	Boundary layer edge
s	wall value
$\infty$	freestream

## INTRODUCTION

In order to accurately predict the aero/thermodynamic performance of reentry vehicles or tactical missiles flying at an angle-of-attack, a thorough knowledge of the three-dimensional boundary layer development on such configurations must be obtained. Unfortunately, the exact computation of a 3-D compressible, turbulent boundary layer will probably not occur for some years because of limitations on computer speed, memory storage, and numerical techniques. An additional limitation is the accuracy of the turbulence models now available.

If the generalized Navier-Stokes equations are to be used to predict turbulent flowfields about various configurations, it becomes necessary to make simplifying assumptions about the stress tensor. One such simplification is to time average these equations so that the difficulty of describing every possible discrete turbulent motion can be avoided.<sup>1</sup> This time averaging results in more unknowns than governing equations. These extra unknowns are then represented by physically plausible quantities which are modeled as constants or empirical functions. These modeled quantities are precisely the required turbulence models.

The objective of this wind tunnel test series was to provide a data base for use in conjunction with computer codes which will predict the flowfield over a conical body configuration at small angles-of-attack. Data were obtained to gain an understanding of the effects of angle-of-attack and model roll position on the aerodynamics of the flowfield over a conical body configuration. The three-dimensional mean velocity, turbulence intensity, and Reynolds stress profiles and the surface skin friction and static pressure distribution data were obtained to provide a comparison with predictions from 3-D computer codes.

## EXPERIMENTAL APPROACH

These experiments were conducted in the Naval Surface Weapons Center (NSWC). Supersonic Tunnel Number Two at a freestream Mach number of 3 for a supply pressure of one atmosphere and a nominal supply temperature of 560°R (311°K). The model used for these tests, shown in Figure 1, was a 7° half-angle cone with a 22% spherically blunt nose. The model had a base diameter of 5.94 inches (15.08cm) and a sharp cone length of 24.2 inches (61.41cm).

In order to ensure a fully turbulent boundary layer at the model measurement stations, a trip ring was used on the model nosetip to artificially trip the boundary layer for all runs in this test series. The trip was a circular stainless steel band with a thickness of 0.035 inch (0.89cm) and a width of 0.225 inch (0.572cm). Two rows of 0.056 inch (0.142cm) diameter stainless steel spheres were spot-welded to the band. The spheres were circumferentially spaced at angles of 1.5° from each other, but the two rows were



staggered so that the effective circumferential spacing of the spheres was  $3.75^\circ$ . The leading edge of the trip ring was an axial distance of 3.5 inches (8.9cm) from the model nose and the trip was affixed to the model with epoxy.

The model was instrumented with Preston probes at five axial stations along the body. The most rearward station was approximately 1.375 inches (3.493cm), measured along the model surface, from the model base and each subsequent station was spaced an additional 2.50 inches (6.35cm) from the preceding station. The stations were numbered 1 through 5, starting with the most forward and ending with the most aft model location, respectively. Only one station was instrumented at a given time so that there would be no interference effects from upstream probes. A schematic of the Preston probe instrumentation is shown in Figure 2. Instrumentation consisted of the Preston probe itself (a surface impact probe), a surface static pressure tap, and a wall thermocouple. A Preston probe with a diameter of 0.049 inch (0.124cm) was used for these tests.

For the Preston probe testing, the model was initially mounted in the tunnel at  $0^\circ$  angle-of-attack with the probe instrumentation installed at a particular station on the model. The tunnel was then started and brought up to the desired supply pressure. Once the pressure was reached, the model was rolled about its axis of symmetry using the tunnel roll mechanism. The probe was initially set on the windward meridian, a model roll position of  $0^\circ$ , and was rolled through approximately  $270^\circ$  giving a continuous distribution of surface static and Pitot pressure, differential pressure between static and Pitot, and surface wall temperature versus model roll. The roll was limited to approximately  $270^\circ$  by the limits on the potentiometer used to provide model roll readout. After the procedure was completed at  $0^\circ$  angle-of-attack, the model was pitched to  $2^\circ$  and then  $4^\circ$  angle-of-attack and the procedure was repeated at each. The model attitude was then returned to  $0^\circ$  and the tunnel was shut down. The same procedure was carried out for all five instrumentation stations.

A schematic of the 3-D LDV system used for these tests is shown in Figure 3 and described in References 2 and 3. The system consists of three one-dimensional LDV components used in a non-orthogonal manner. From the known geometry of the system and the three measured velocity components, the velocity vector can be computed. For these particular tests, a new measurement concept described in Reference 4 was employed. This system was capable of measuring the cross-flow velocity component directly while still utilizing the three non-orthogonal LDV components. The Doppler frequency of the cross-flow velocity component was obtained directly through appropriate electronic mixing and filtering of the two other appropriate Doppler frequencies.

A typical LDV profile consisted of approximately 25 vertical survey positions ranging from approximately 0.025 inch (0.064cm) to 0.8

inch (2.03cm) vertically above the model with more points being taken closer to the model in order to give better definition to the boundary layer profile. The boundary layer thickness was typically on the order of 0.2 to 0.3 inch (0.51 to 0.76cm), but additional points were surveyed in the inviscid flowfield so that the velocity and turbulence property profile behavior could also be checked in that region.

The LDV system was traversed perpendicular to the centerline of the wind tunnel rather than normal to the model surface. This introduced an error in the measurement of the vertical distance from the model surface. However, for the worst case when the model was at  $4^\circ$  angle-of-attack, the error in measuring Y was still less than two percent. These measurement errors were considered to be negligible so that the corrections were not included in the data reduction process.

Approximately 2100 samples for each of the U, V, and W velocity components were taken at each survey location. Provisions were made so that the three velocity components were measured from the same particle or from different particles for which the period of time in which all three measurements were made was short enough so that the measurements could be considered to be instantaneous. The coincidence time used for these tests was 10 microseconds.

LDV surveys were obtained for angles-of-attack of  $0^\circ$ ,  $2^\circ$ , and  $4^\circ$  at model roll positions of  $0^\circ$ ,  $45^\circ$ ,  $90^\circ$  and  $135^\circ$  on the spherically blunt cone configuration. Note that no LDV surveys were taken on the leeward ( $180^\circ$ ) meridian. This was due to the fact that there were an insufficient number of particles in the leeward flowfield of the model at angle-of-attack to be able to make measurements in a timely manner. The particles used to seed the flow were olive oil particles with a mean diameter of approximately 1.5 microns. They were generated with an atomization type generator which utilized a Laskin nozzle.<sup>5</sup> The generator was run at a pressure approximately 5 psi (34.5 kPa) over the tunnel supply pressure.

The instantaneous velocity values have all been transformed into model coordinates so that the U, V, and W velocities are the velocity parallel to the model surface, velocity perpendicular to the model surface, and transverse velocity component, respectively. Using the multiple values obtained by the LDV for the instantaneous velocity components at each survey point, the mean velocities, the turbulence intensities, and the Reynolds stresses were statistically computed. These boundary layer properties will be discussed in this paper.

## RESULTS

The wall shear stress distributions were computed from the Preston probe measurements using the empirical relations described in Reference 6. As was mentioned previously, the wall static pressure was measured simultaneously with the Preston probe pressure by a static pressure orifice which was located approximately 0.25 inch

(0.64cm) ahead of the Preston probe tip. The local wall static pressures,  $P_s$ , have been used to calculate the pressure coefficient,  $C_p$ , distributions from the formula

$$C_p = \frac{P_s - P_\infty}{0.7 P_\infty M_\infty^2} \quad (1)$$

where  $P_\infty$  and  $M_\infty$  are the freestream pressure and Mach number ahead of the model. Wall shear stress and pressure coefficient distributions were obtained on the spherically blunt cone configuration for angles-of-attack of  $0^\circ$ ,  $2^\circ$  and  $4^\circ$ . The model roll angle was varied from  $0^\circ$  to  $270^\circ$ , where  $0^\circ$  is the windward meridian. Figures 4 and 5 show some of the shear stress and pressure coefficient distribution results. Figure 4 shows the variation of these parameters at measurement stations 2 through 5 for an angle-of-attack of  $4^\circ$ . Both the wall shear stress and the wall pressure coefficient distributions are nearly identical for all measurement stations. Shown in Figure 5 are the wall shear stress and pressure coefficient distributions at measurement station 4 for  $\alpha = 0^\circ$ ,  $2^\circ$ , and  $4^\circ$ . Station 4 corresponds to an  $X'/D$  of 2.622 and is the measurement station where LDV surveys were obtained. It can be seen that the shear stress and pressure are relatively constant at  $\alpha = 0^\circ$ . However at angle-of-attack, the wall shear stress and pressure coefficient are highly dependent on model roll angle. The maximum magnitudes occur on the windward side of the model and the minimums on the leeward side. The variations of the pressure coefficient distributions are more pronounced than the shear stresses.

LDV surveys were conducted at measurement Station 4 only. Runs were made for  $\alpha = 0^\circ$ ,  $2^\circ$ , and  $4^\circ$  at model roll angles of  $0^\circ$ ,  $45^\circ$ ,  $90^\circ$ , and  $135^\circ$ . Vertical surveys of the instantaneous velocity components were made and were then used to compute the mean velocities, the standard deviations of the velocities which are related to the turbulence intensities, and the double velocity correlations which are related to the Reynolds stresses. A discussion of the mean velocity results now follows. The velocity profiles have all been transformed into model coordinates so that the U, V, and W velocities are the velocity parallel to the model surface, velocity perpendicular to the model surface, and cross-flow velocity component, respectively. In addition, all velocities have been nondimensionalized by the freestream speed of sound.

Shown in Figures 6a through 6c are the U, V, and W velocity distributions at a roll position of  $0^\circ$  (windward meridian) and angles-of-attack of  $0^\circ$ ,  $2^\circ$ , and  $4^\circ$  for the spherically blunt cone. The U velocity profiles for the windward meridian are shown as a function of angle-of-attack in Figure 6a. It can be seen that in the boundary layer at the same vertical distance away from the model surface, the U velocity increases with increasing angle-of-attack. This is an

expected effect due to decreasing windward meridian boundary layer thickness with increasing angle-of-attack. Even though the magnitudes of the turbulence quantities indicate windward meridian boundary layer thicknesses in the range of 0.16 to 0.24 inch (0.41 to 0.61cm), the U velocity component continues to increase well into the inviscid region of the flowfield. However, at still larger distances from the model surface, the U velocity becomes nearly constant with increasing vertical distances from the model. The normal component, V velocity profiles for the windward meridian are shown in Figure 6b. Here we see the large influence of the inviscid portion of the flowfield on this component. It can also be seen that the value of the normal velocity does not approach zero near the model surface as is expected. It should be pointed out that experimentally, the V component is more difficult to measure accurately. The value of  $V/A_\infty$  at the wall is only 0.02 which corresponds to a velocity of approximately 15 ft/sec (4.57 m/sec), less than one percent of the freestream velocity. The cross-flow, W, velocity profiles are shown in Figure 6c. By symmetry, this velocity should be zero. It can be seen that the maximum error in W is about 25 ft/sec (7.63 m/sec) since  $A_\infty$  was approximately 700 ft/sec (213.4 m/sec) for these tests. It would appear that this small cross-flow velocity is probably due to a slight model misalignment. When these tests were carried out, the model was aligned with the flow by monitoring the model wall pressure as the model was rolled about its longitudinal axis. The model was adjusted in pitch and yaw until the trace was flat. It was then assumed that the model was at  $0^\circ$  angle-of-attack. It can be seen that the measured value of W is very low at  $\alpha = 0^\circ$ . However, the error in W is larger when the model is at an angle-of-attack indicating that model misalignment will be more evident at angle-of-attack.

The development of the flow around the circumference of the spherically blunt cone model at angles-of-attack of  $2^\circ$  and  $4^\circ$  is shown in Figures 7 and 8. As the model circumferential position is increased from  $0^\circ$  (windward meridian) toward  $180^\circ$  (leeward), the U velocity decreases for a survey position at the same vertical distance from the model surface. This is an expected effect due to thickening of the boundary layer from the windward to leeward meridian. Also, the U component undergoes a larger change on the leeward half of the model. The V component of velocity is highly dependent on the circumferential position on the model at least around to a circumferential angle of  $135^\circ$ . This is true at angles-of-attack of  $2^\circ$  and  $4^\circ$ . As expected, the W component reaches its maximum magnitude at a circumferential position of  $90^\circ$ . Here the maximum value for  $W/A_\infty$  is approximately 0.3 at  $\alpha = 4^\circ$ . It can be seen that the W profiles for roll angles of  $45^\circ$  and  $135^\circ$  differ slightly due to the effect of boundary layer thickening.

As was previously stated, the turbulence quantities were statistically computed from the multiple instantaneous velocity measurements. A discussion of these turbulence quantity measurements now follows. All turbulence properties have been nondimensionalized.

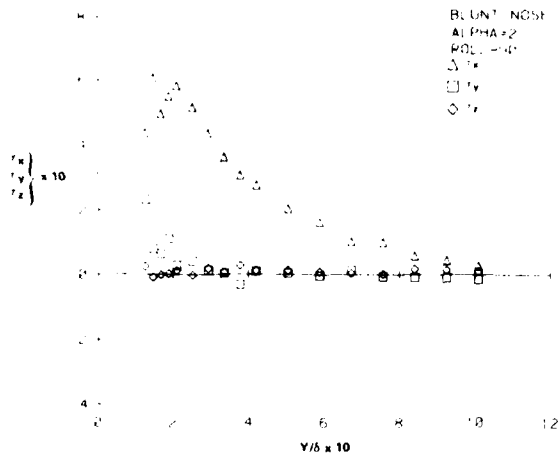


FIGURE 11d REYNOLDS STRESS DISTRIBUTIONS

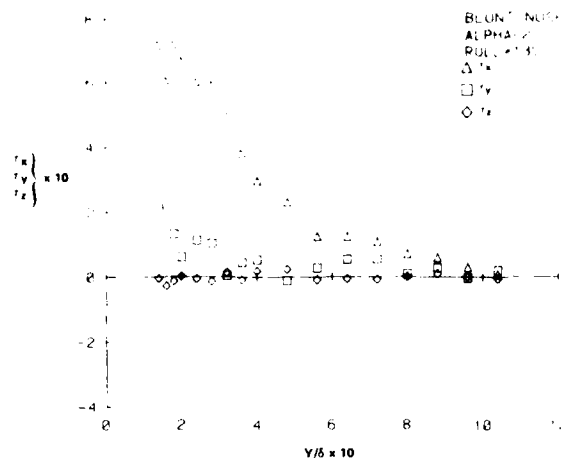


FIGURE 11e REYNOLDS STRESS DISTRIBUTIONS

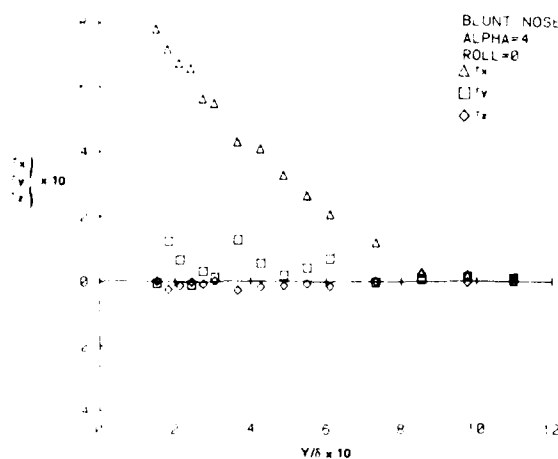


FIGURE 11f REYNOLDS STRESS DISTRIBUTIONS

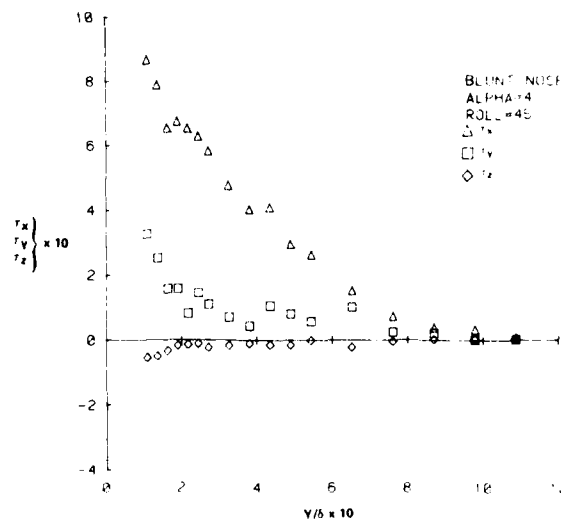


FIGURE 11g REYNOLDS STRESS DISTRIBUTIONS

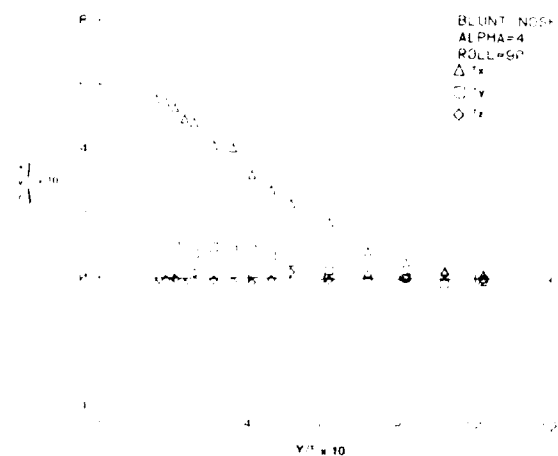


FIGURE 11h REYNOLDS STRESS DISTRIBUTIONS

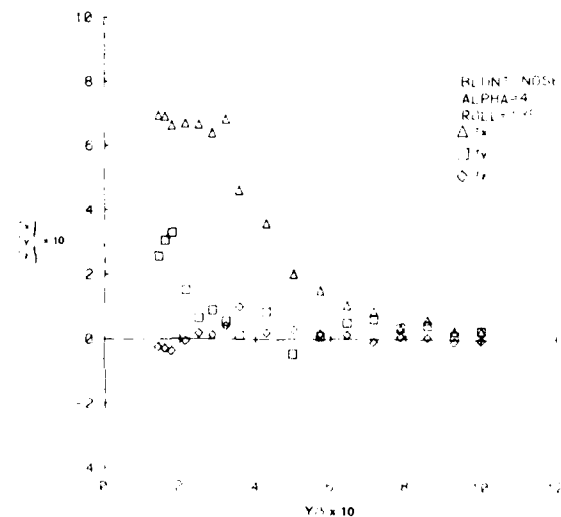


FIGURE 11i REYNOLDS STRESS DISTRIBUTIONS

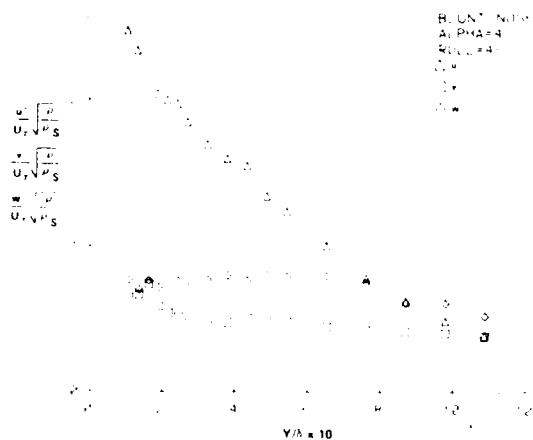


FIGURE 10a. TURBULENCE INTENSITIES DISTRIBUTIONS

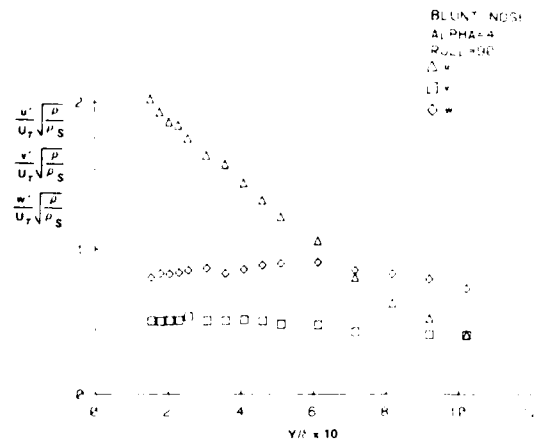


FIGURE 10b. TURBULENCE INTENSITIES DISTRIBUTIONS

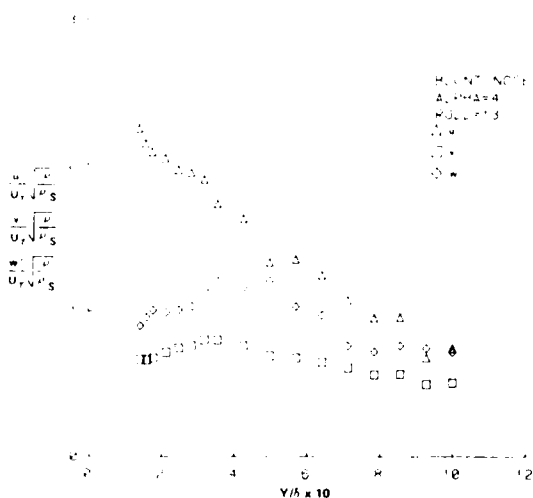


FIGURE 10c. TURBULENCE INTENSITIES DISTRIBUTIONS

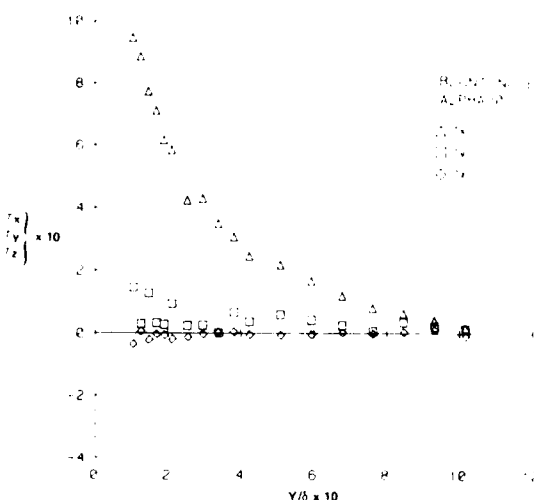


FIGURE 11a. REYNOLDS STRESS DISTRIBUTIONS

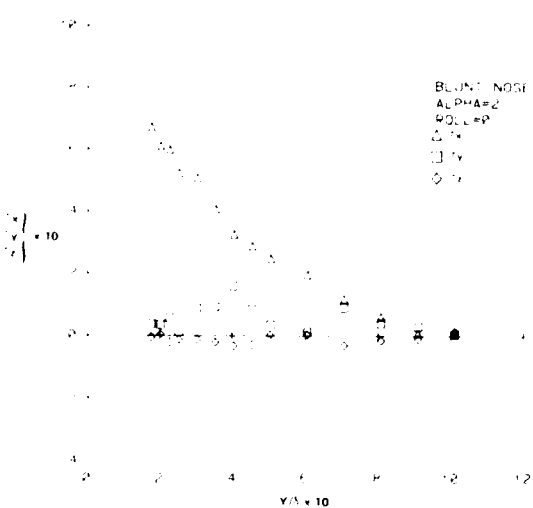


FIGURE 11b. REYNOLDS STRESS DISTRIBUTIONS

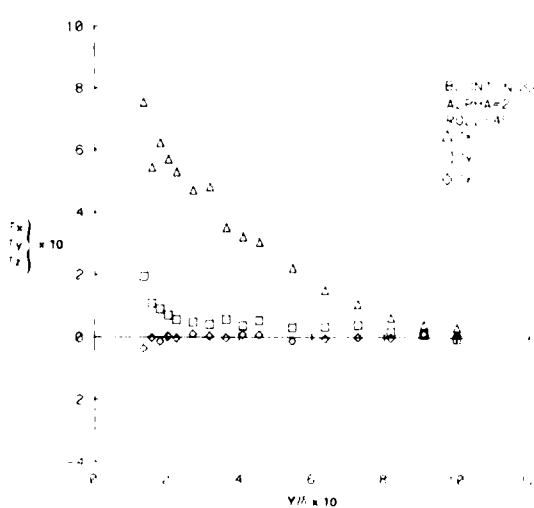


FIGURE 11c. REYNOLDS STRESS DISTRIBUTIONS

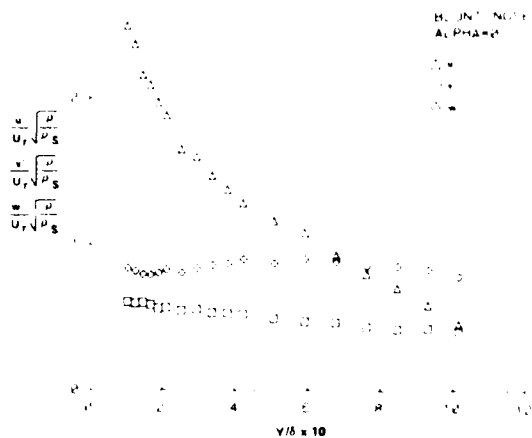


FIGURE 10a: TURBULENCE INTENSITIES DISTRIBUTIONS

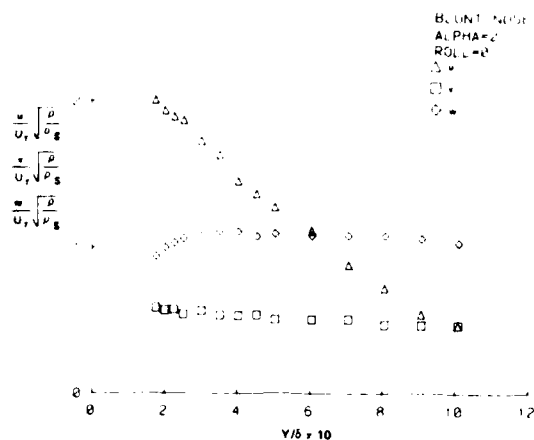


FIGURE 10b: TURBULENCE INTENSITIES DISTRIBUTIONS

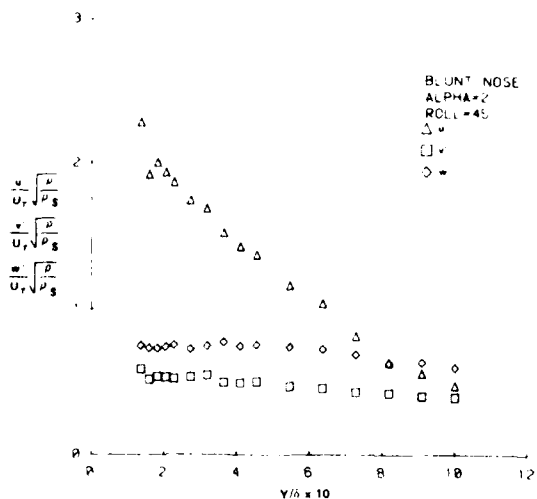


FIGURE 10c: TURBULENCE INTENSITIES DISTRIBUTIONS

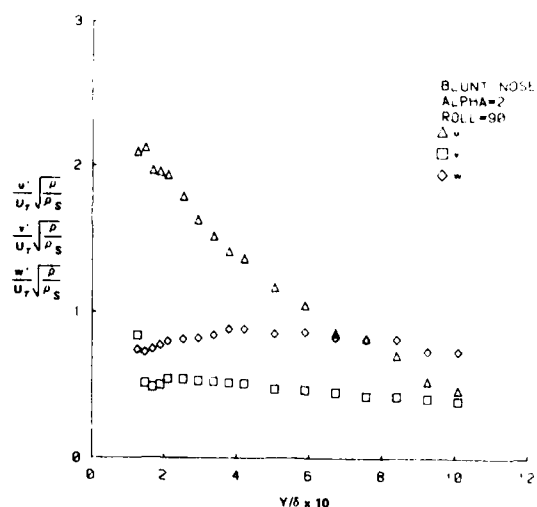


FIGURE 10d: TURBULENCE INTENSITIES DISTRIBUTIONS

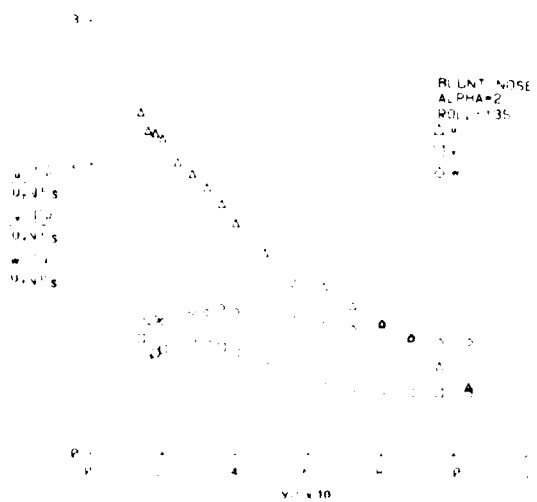


FIGURE 10e: TURBULENCE INTENSITIES DISTRIBUTIONS

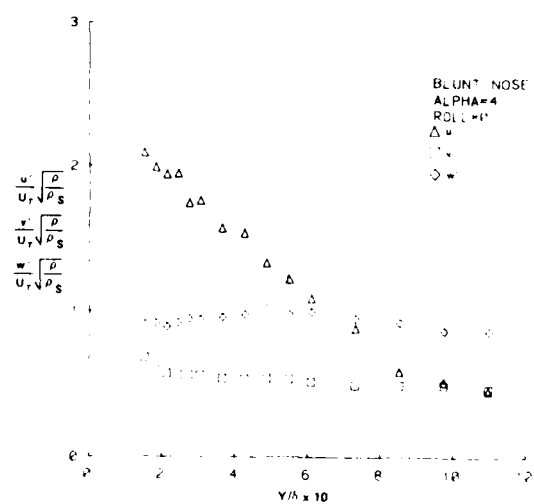


FIGURE 10f: TURBULENCE INTENSITIES DISTRIBUTIONS

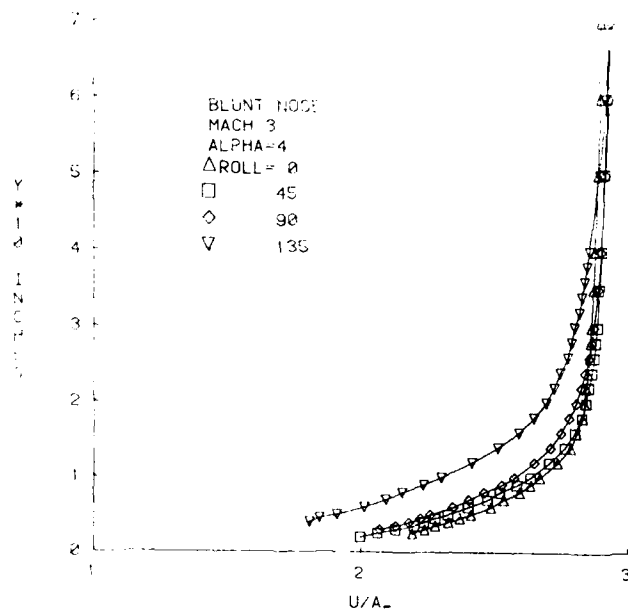


FIGURE 8a. U VELOCITY DISTRIBUTIONS

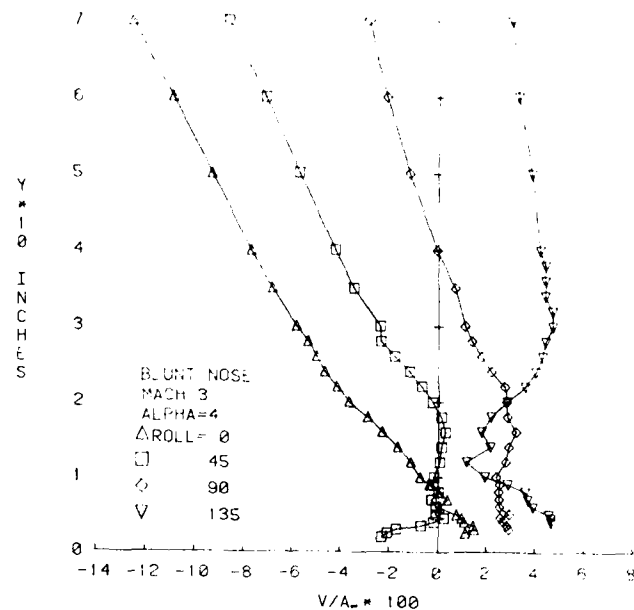


FIGURE 8b. V VELOCITY DISTRIBUTIONS

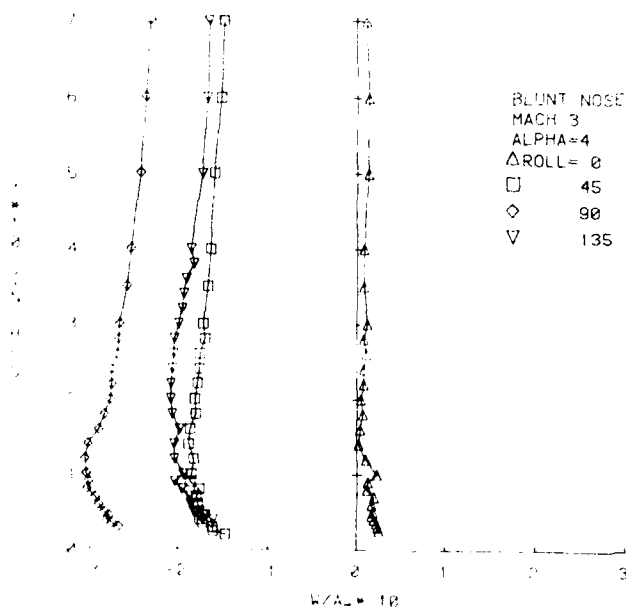


FIGURE 8c. W VELOCITY DISTRIBUTIONS

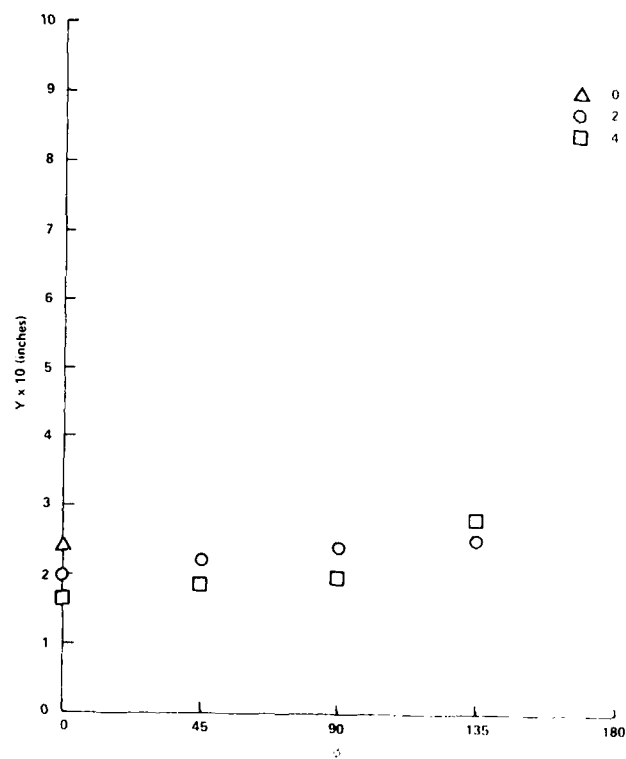


FIGURE 9. BOUNDARY LAYER THICKNESS DISTRIBUTIONS



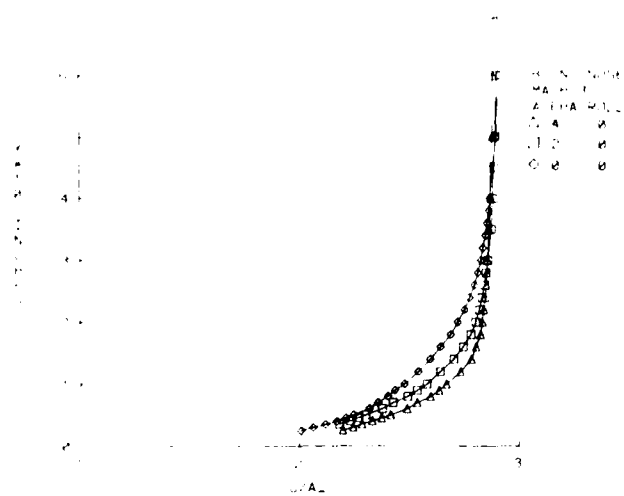


FIGURE 6a U VELOCITY DISTRIBUTIONS

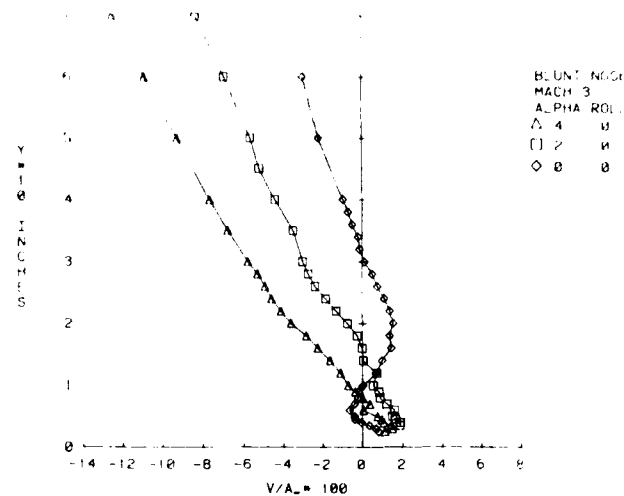


FIGURE 6b V VELOCITY DISTRIBUTIONS

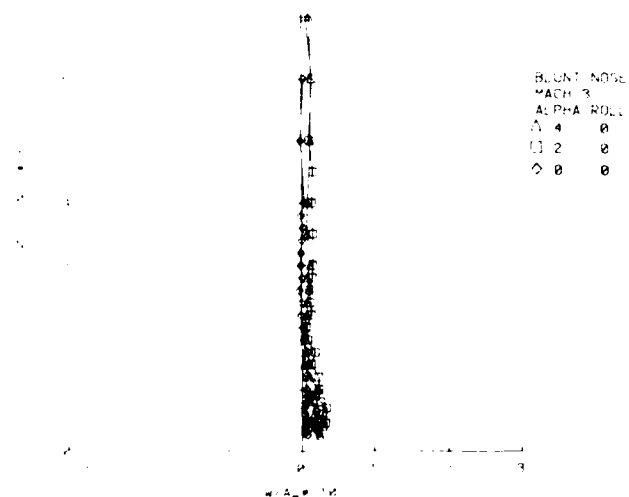


FIGURE 6c W VELOCITY DISTRIBUTIONS

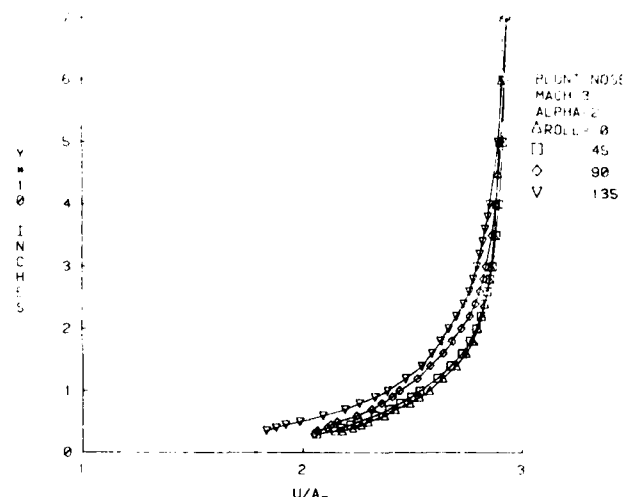


FIGURE 7a U VELOCITY DISTRIBUTIONS

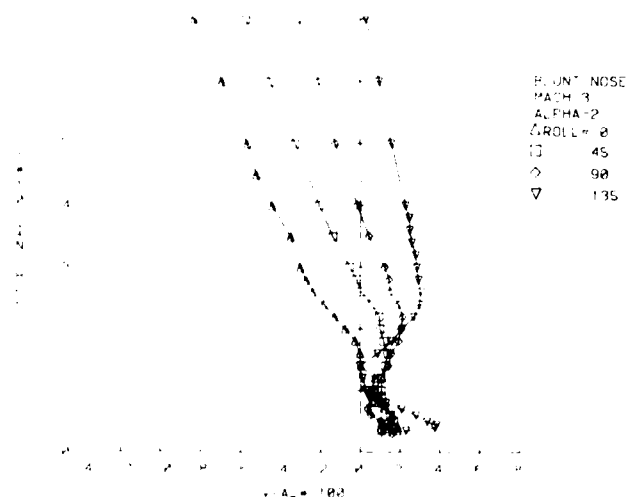


FIGURE 7b V VELOCITY DISTRIBUTIONS

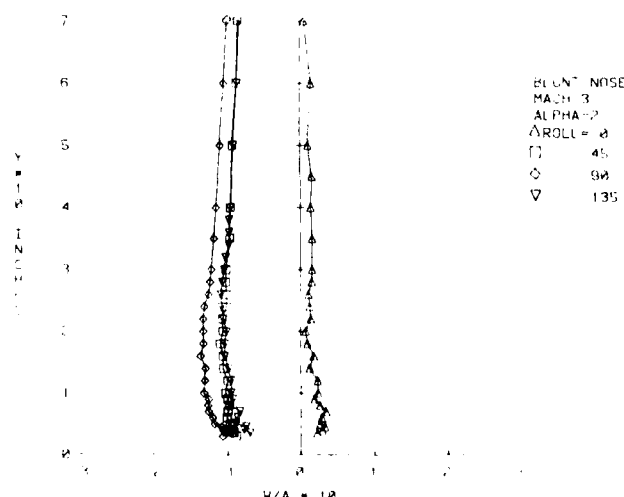


FIGURE 7c W VELOCITY DISTRIBUTIONS

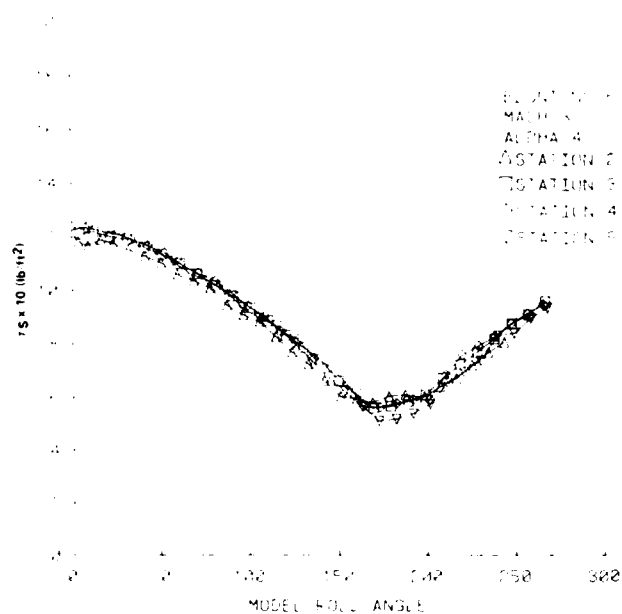


FIGURE 4a. WALL SHEAR STRESS DISTRIBUTIONS

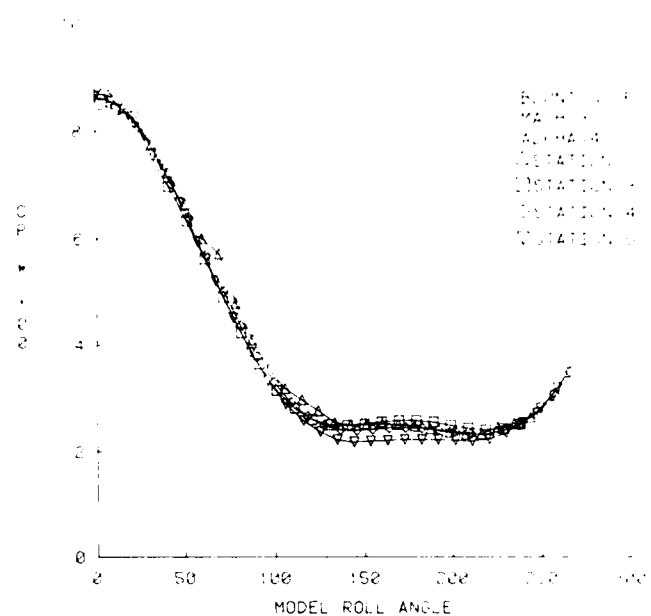


FIGURE 4b. WALL PRESSURE DISTRIBUTIONS

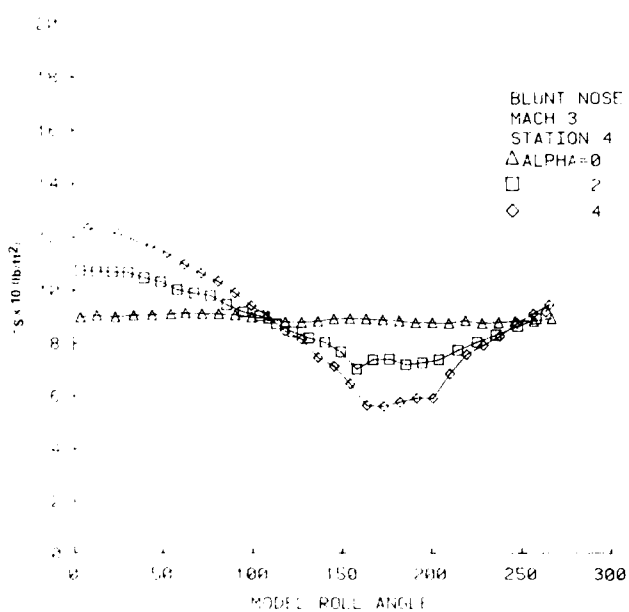


FIGURE 5a. WALL SHEAR STRESS DISTRIBUTIONS

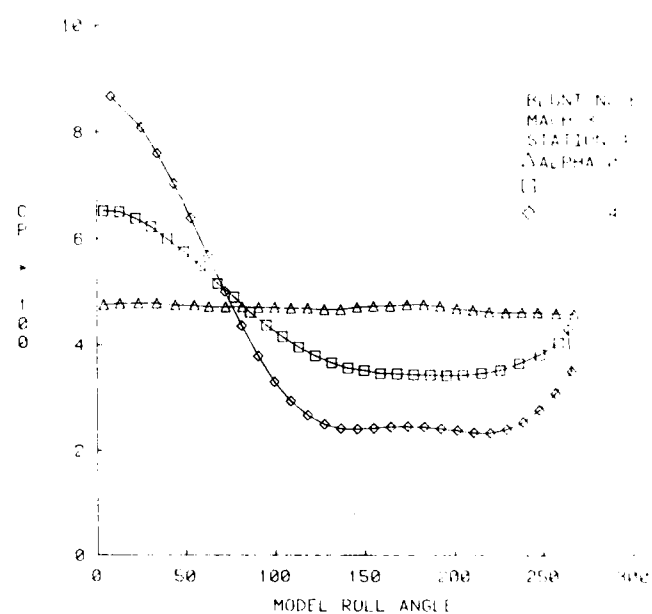


FIGURE 5b. WALL PRESSURE DISTRIBUTIONS

# MODEL CONFIGURATION

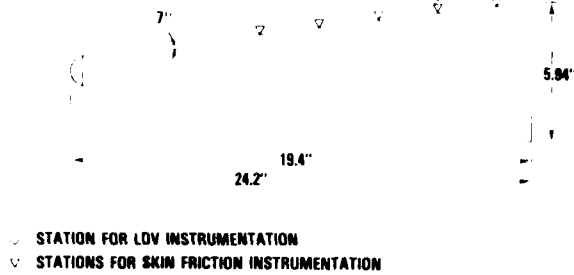


FIGURE 1 SCHEMATIC OF SPHERICALLY BLUNT CONE MODEL

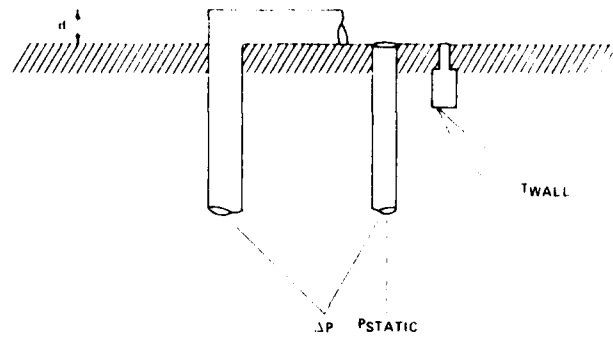


FIGURE 2 PRESTON PROBE INSTRUMENTATION

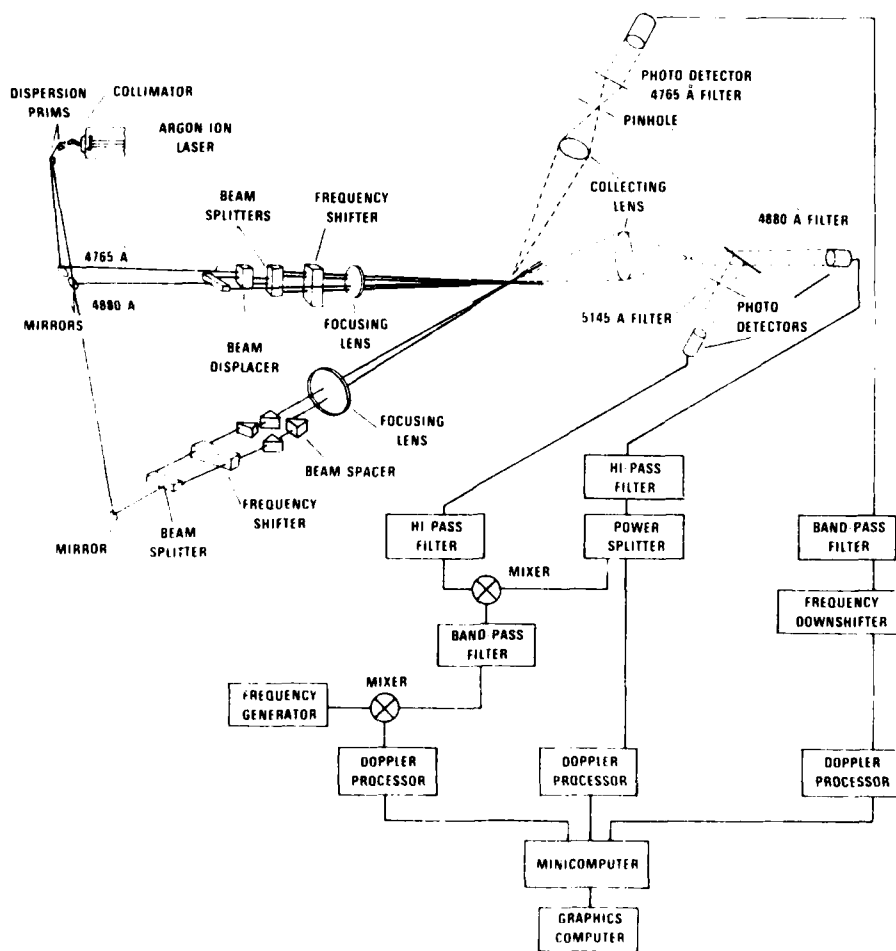


FIGURE 3 3-D LDV SCHEMATIC

7. Yanta, W. J. and Ausherman, D. W., "The Turbulence Transport Properties of a Supersonic Boundary Layer on a Sharp Cone at Angle-of-Attack," AIAA Paper No. 83-0456, January 1983.
8. Bushnell, D. M. and Morris, D. J., "Shear Stress, Eddy Viscosity and Mixing-Length Distributions in Hypersonic Turbulent Boundary Layers," NASA TM X-2310, Langley Research Center, Hampton, Virginia, August 1971.
9. Yanta, W. J. and Lee, R. E., "Measurements of Mach 3 Turbulence Transport Properties on a Nozzle Wall," AIAA Journal, Vol. 14, No. 6, June 1976, pp. 725-729.
10. Laderman, A. J., "Pressure Gradient Effects on Supersonic Boundary Layer Turbulence," Report No. U-6467, Ford Aerospace & Communications Corp., Newport Beach, California, October 1978.
11. Cebeci, T. and Smith, A. M. O., Analysis of Turbulent Boundary Layers, Academic Press, N.Y., 1974.
12. van den Berg, B. and Elsenaar, A., "Measurements in a Three Dimensional Incompressible Turbulent Boundary Layer in an Adverse Pressure Gradient Under Infinite Swept Wing Conditions," National Aerospace Laboratories, NLR-TR-72092U, The Netherlands.
13. Cebeci, T. and Meier, H. U., "Modeling Requirements for the Calculation of the Turbulent Flow Around Airfoils, Wings and Bodies of Revolution," Paper No. 16, AGARD-CP-271, 1980.
14. Yanta, W. J., Ausherman, D. W., and Hedlund, E. R., "Measurements of a Three-Dimensional Boundary Layer on a Sharp Cone at Mach 3," AIAA Paper No. 82-0289, January 1982.
15. Ausherman, D. W., Yanta, W. J., and Rutledge, W. H., "Measurement of the Three-Dimensional Boundary Layers on Conical Bodies at Mach 3 and Mach 5," AIAA Paper No. 83-1675, July 1983.
16. Ausherman, D. W. and Yanta, W. J., "The Three-Dimensional Turbulence Transport Properties in the Boundary Layers of Conical Body Configurations at Mach 3," AIAA Paper No. 84-1528, June 1984.

4. The Reynolds stresses exhibited a variety of trends. The  $\tau_x$  stress exhibited the usual trends of 2-D data. The magnitudes of the  $\tau_y$  stress were surprisingly large, approaching one-half of the values of the  $\tau_x$  stress for some cases. The  $\tau_z$  stress was relatively small as compared to the other stress components.
5. The streamwise eddy viscosity,  $\epsilon_u$ , was found to be highly dependent upon roll angle and angle-of-attack. This dependency upon  $\alpha$  and  $\phi$  will have to be modeled accurately when eddy viscosities are to be used in 3-D computations.
6. The slopes of the  $\ell_u$  mixing length distributions appear to approach Prandtl's value of  $K = 0.4$  in the near wall region. In the mid-portion of the boundary layer, the mixing lengths were found to be dependent on both  $\alpha$  and  $\phi$ .
7. The ratio of  $\epsilon_w/\epsilon_u$  appears to have values which are primarily less than 0.75 indicating that isotropy of the eddy viscosities is probably not a good computational assumption for this test case. Further tests would need to be run to determine a more exact value for  $\epsilon_w/\epsilon_u$ .

#### REFERENCES

1. Marvin, J. G., "Experiments Planned Specifically for Developing Turbulent Models in Computations of Flowfields Around Aerodynamic Shapes," Proceedings from the 5th U.S. Air Force/Federal Republic of Germany Data Exchange Meeting, AFFDL TR-77-61.
2. Yanta, W. J., "A Three-Dimensional Laser Doppler Velocimeter (LDV) for Use in Wind Tunnels," IEEE Publication 79 CH 1500-8 AES, September 1979.
3. Wardlaw, A. B. and Yanta, W. J., "The Flowfield About and Forces on Slender Bodies at High Angle-of-Attack," AIAA Paper No. 80-0184, January 1980.
4. Yanta, W. J. and Ausherman, D. W., "A 3-D Laser Doppler Velocimeter for Use in High-Speed Flows," Proceedings from the 7th Biennial Symposium on Turbulence, September 1981.
5. Yanta, W. J., "The Use of the Laser Doppler Velocimeter in Aerodynamic Facilities," AIAA Paper No. 80-0435-CP, March 1980.
6. Yanta, W. J., Brott, D. L., and Lee, R. E., "An Experimental Investigation of the Preston Probe Including Effects of Heat Transfer, Compressibility and Favorable Pressure Gradient," AIAA Paper No. 69-648, June 1969.

in two experimental programs which investigated the effects of nose shape, Mach number, angle-of-attack, and roll angle on conical body flowfields. Additional description of the model geometries, test procedures, and results can be found in Reference 7 and References 14 through 16.

## CONCLUSIONS

Three-dimensional boundary layer measurements were carried out on a  $7^\circ$  semi-vertex angle conical body with a 22% spherically blunt nose at Mach 3 for angles-of-attack of  $0^\circ$ ,  $2^\circ$ , and  $4^\circ$ . The 3-D mean velocities, turbulence intensities, and Reynolds stresses were measured at various body circumferential locations using an LDV system. Other measurements included wall shear stress and wall static pressure distributions. From examining the results, the following conclusions were reached:

1. At angle-of-attack, the wall shear stress and surface pressure are highly dependent on model roll angle. Maximum magnitudes occur on the windward meridian of the model and minimums on the leeward meridian.
2. Inviscid flowfield velocity gradients are superimposed on the boundary layer velocities. The U velocity component continues to increase in magnitude well into the inviscid region of the flowfield. Also, the V velocity profiles are greatly influenced in the inviscid flowfield by these gradients. These inviscid flowfield velocity gradients also made it difficult to evaluate the boundary layer thickness and incompressible displacement thickness by normal procedures.
3. Angle-of-attack and roll angle have various effects on the three turbulence intensity components. The  $u'$  streamwise intensities were similar to those of 2-D data and were unaffected by either model transverse position or angle-of-attack. On the windward side of the model, the  $v'$  vertical component was relatively constant across the boundary layer and was unaffected by transverse position or angle-of-attack. However, for  $\phi = 135^\circ$ ,  $v'$  increases and then decreases with increasing distance from the model surface. In general, the magnitudes of the  $w'$  component are largest on the windward meridian and reach a minimum for  $\phi = 45^\circ$ . The magnitudes then increase again towards  $\phi = 180^\circ$ . The  $w'$  intensities are relatively insensitive to changing angle-of-attack.

exhibit negative values. Although this is not physically plausible, the data are shown as computed. To avoid numerical problems of taking the square root of negative numbers, the various mixing lengths were computed by the following definitions:

$$\ell_u = \frac{\ell_u^2}{|\ell_u^2|} \sqrt{|\ell_u^2|} \quad \text{and} \quad \ell_w = \frac{\ell_w^2}{|\ell_w^2|} \sqrt{|\ell_w^2|} \quad (6)$$

Shown in Figures 13a, 13b, and 13c are the distributions of the mixing length  $\ell_u/\delta$ . Also plotted is a line with a slope which corresponds to Prandtl's value of  $K = 0.4$ . The slopes of all of the distributions appear to approach values close to 0.4 in the near wall region. The mixing length appears to have some dependence on angle-of-attack and roll angle at least in the middle portion of the boundary layer. However, it is difficult to ascertain what the effects of angle-of-attack or roll angle are on the slopes near the wall.

The cross-flow eddy viscosity,  $\epsilon_w$ , distributions as determined from  $\tau_z$  and  $\partial W/\partial Y$  are shown in Figures 14a and 14b. The scatter in this data is rather severe. However, it appears that the trend of the cross-flow eddy viscosity is to increase with increasing distance from the model wall to about the middle of the boundary layer and then to decrease with increasing  $Y/\delta$  beyond that point for both  $2^\circ$  and  $4^\circ$  angle-of-attack.

One of the most common simplifying assumptions which is made in the computation of 3-D viscous flows is isotropy of the eddy viscosities. That is that the cross-flow component of eddy viscosity,  $\epsilon_w$ , is equal to the streamwise component,  $\epsilon_u$ . A series of experiments at the NLR<sup>12</sup> showed that considerable changes could occur in the turbulence structure of three-dimensional boundary layers from the structure in 2-D flows. In Reference 13, Cebeci and Meier found that significant inaccuracies in the predicted flowfield parameters could occur when computational methods which assumed an isotropic eddy viscosity were used. Shown in Figures 15a and 15b are the distributions of the ratio of the cross-flow eddy viscosity component to streamwise eddy viscosity component,  $\epsilon_w/\epsilon_u$ , at  $\alpha = 2^\circ$  and  $4^\circ$ . From this data it can be seen that for both  $2^\circ$  and  $4^\circ$  angle-of-attack,  $\epsilon_w/\epsilon_u$  is probably less than 1. Instead, the values for  $\epsilon_w/\epsilon_u$  appear to primarily be less than 0.75. Thus isotropy of the eddy viscosity is probably not a good assumption to make when performing computations for this case.

As was mentioned in the Introduction, the objective of these experiments was to provide a data base which extends the current understanding of three-dimensional viscous and inviscid flows about conical bodies. It should be pointed out that the experimental data presented in this paper is a small portion of a data base obtained

of the  $\tau_y$  stress in the circumferential direction which is used in computations and the variation is small for this case. However, if the full Navier-Stokes equations were computed, it would be necessary to include a model of this stress term.

The  $\tau_z$  stress is of great interest to both the experimentalist and the computationalists. However, because of a lack of experimental data, it has been necessary to make various assumptions about the magnitude and the trends of this stress when employing numerical solvers such as the parabolized Navier-Stokes equations to compute 3-D compressible turbulent flows. The data presented in this paper show that the magnitude of the  $\tau_z$  stress is small for these experiments. However, this is not surprising since the maximum angle-of-attack for these tests was only  $4^\circ$  and the resulting cross-flow velocity had a maximum value of approximately 10% of the freestream velocity. This relatively small velocity resulted in the occurrence of a large amount of scatter in the  $\tau_z$  measurements. Interpretation of the behavior of  $\tau_z$  is difficult because of its dependence on model circumferential position when at angle-of-attack. A more meaningful interpretation of these stresses is obtained when they are used to compute the eddy viscosity and the mixing length which are important parameters used in current algebraic modeling of the turbulence shear term.

Two different techniques were used to compute the derivatives of  $U$  and  $W$  with respect to  $Y$ . These derivatives are necessary for calculating the eddy viscosity and mixing length values from the shear stresses. The  $U$  velocity profiles were curve fit with a series of overlapping curve fits of seven consecutive points using a least squares polynomial for each segment of the profile. The derivative at the desired point was computed from the polynomial. The  $W$  velocity profiles were fit with single curves rather than a series of overlapping curve fits. Entire  $W$  velocity profiles were curve fit with series of least squares polynomial fits of various degrees from two to eight. These polynomial fits were then plotted along with the corresponding  $W$  velocity profile. The polynomial which best fit the inner half of the  $W$  velocity profile was chosen and was differentiated and used to compute values for the derivatives at all profile points.

Shown in Figures 12a, 12b, and 12c are the nondimensionalized eddy viscosity  $\epsilon_u/U_\infty \delta_i^*$ , profiles for  $0^\circ$ ,  $2^\circ$ , and  $4^\circ$  angle-of-attack, respectively. These eddy viscosities were computed from the  $\tau_x$  shear stress and  $\partial U/\partial Y$ . At  $\alpha = 0^\circ$ , the maximum value of  $\epsilon_u/U_\infty \delta_i^*$  is nearly equal to the value of 0.0168 which is used in the algebraic model developed by Cebeci and Smith<sup>11</sup> for 2-D flows. However, it is obvious from Figures 12b and 12c that the eddy viscosity is highly dependent on model angle-of-attack and roll position as well as on vertical position in the boundary layer. Thus, modeling of the eddy viscosity requires a functional dependence on angle-of-attack, roll angle, and height in the boundary layer. It should be pointed out that because of experimental scatter and inflections in the velocity profiles and shear stresses, the eddy viscosities and mixing lengths do occasionally



measured, some assumptions were made to determine the local density distributions. Since the flow in the boundary layer is adiabatic, then the local energy equation can be written in the form

$$\frac{T}{T_e} = \left(1 - \frac{T_s}{T_e}\right) \frac{U}{U_e} + \frac{T_s}{T_e} \quad (4)$$

Assuming the static pressure to be constant across the boundary layer, the local density can be determined. It has also been assumed that the local velocity  $\bar{q}$  can be written as

$$\bar{q} = (U^2 + V^2 + W^2)^{1/2} \cong (U^2)^{1/2} = U \quad (5)$$

For the present experiments, the multiple records for each of the individual velocity components were used to generate individual histograms for each component. These histograms were inspected individually and upper and lower data limits were chosen to eliminate spurious data points. This was preferred to the usual method of rejecting data outside of a certain number of standard deviations from the mean. Neither the mean results or the turbulence results were corrected for velocity or sampling bias.

Shown in Figures 10a through 10i are the turbulence intensities  $u'$ ,  $v'$ , and  $w'$  for all measured combinations of angle-of-attack and model roll. The RMS values of  $u'$ ,  $v'$ , and  $w'$  have been nondimensionalized by the factor  $(\rho/\rho_s)^{1/2}/U_\infty$ . In general, it appears that angle-of-attack and model circumferential angle have little effect on the longitudinal component  $u'$ . This turbulence intensity component decreases with increasing distance from the model surface. On the windward side of the model, the  $v'$  component distribution appears to be relatively constant across the boundary layer and also appears to be insensitive to angle-of-attack and roll position. However at a circumferential position of  $135^\circ$ , the  $v'$  component increases and then decreases with increasing distance from the model surface. Also, the magnitude of  $v'$  is larger at  $\alpha = 4^\circ$  than at  $\alpha = 2^\circ$ . The  $w'$  component exhibits a slightly different behavior. In general, the magnitudes are largest at  $\phi = 0^\circ$  and reach a minimum for  $\phi = 45^\circ$ . The magnitudes then increase again with increasing roll angle. At a roll position of  $135^\circ$  the magnitude is approximately equal to the magnitude at  $\phi = 0^\circ$ . It is also interesting to note that for a given roll position, the  $w'$  component magnitudes are approximately equal for  $\alpha = 2^\circ$  and  $4^\circ$ .

Shown in Figures 11a through 11i are the three nondimensional Reynolds stresses  $\tau_x$ ,  $\tau_y$ , and  $\tau_z$ . The data are shown for all measured conditions. The general trend of  $\tau_x$  is quite similar to that for experimental data from 2-D flows.<sup>8-10</sup> The magnitudes of the  $\tau_y$  stress approach one-half of the values of the  $\tau_x$  stress for some angle-of-attack and roll combinations. In general, this stress term is neglected when computations are being made because it is the gradient

One of the important parameters needed to nondimensionalize many of the turbulence quantities is the boundary layer thickness,  $\delta$ . The normal procedure for determining  $\delta$  is to choose a value where  $U$  is equal to some specified percentage (99%, 99.5%, etc.) of the constant inviscid velocity at the edge of the boundary layer. However for these flowfields, there never is a constant inviscid flow velocity because the  $U$  velocities continue to increase, due to the gradient in the inviscid region of the flowfield. Instead, the behavior of the  $u'$  turbulence intensity profiles was examined to determine boundary layer thickness. The turbulence intensities do approach a constant value near the boundary layer edge and in general, a value for  $\delta$  was chosen where  $u'$  was 10 ft/sec (3.05 m/sec) greater than its constant inviscid flowfield value. The value of 10 ft/sec (3.05 m/sec) was chosen because it is approximately 0.005 of the edge velocity and it was felt that using this technique to choose  $\delta$  was comparable to choosing  $\delta$  where  $U$  is equal to 0.995 of the inviscid flowfield velocity for the case where the inviscid flowfield velocity is constant. The values for the boundary layer thickness that were determined for the blunt cone using this technique are shown in Figure 9 as a function of circumferential angle and angle-of-attack. There is a distinct increase in boundary layer thickness as one proceeds from the windward ( $\phi = 0^\circ$ ) towards the leeward ( $\phi = 180^\circ$ ) meridian. This change becomes more obvious with increasing angle-of-attack.

Another parameter of importance is the "incompressible" boundary layer displacement thickness,  $\delta_i^*$ , which is required to evaluate eddy viscosity models.  $\delta_i^*$  is defined by the equation

$$\delta_i^* = \int_0^\delta \left(1 - \frac{U}{U_e}\right) dy \quad (2)$$

The normal procedure for evaluating the incompressible boundary layer displacement thickness is to fit a power law profile to the  $U/U_e$  versus  $Y/\delta$  curve. By letting the velocity profile be represented by a power law profile,  $U/U_e = (Y/\delta)^n$ , it can be shown that

$$\frac{\delta_i^*}{\delta} = \frac{1}{n+1} \quad (3)$$

where  $n$  is the exponent of the power law fit. For this particular test series, the superimposition of the inviscid flowfield velocity gradient on the boundary layer velocity makes this approach for computing  $\delta_i^*$  questionable. Previous experiments on a sharp cone<sup>7</sup> have shown that the trends for the circumferential variation of  $\delta_i^*$  are quite similar to those of  $\delta$  and that the approximate ratio of  $\delta_i^*$  to  $\delta$  was 1/8. Thus,  $\delta_i^*/\delta$  has been specified to equal 0.125 in this analysis.

Another parameter which is necessary for turbulence modeling is the local gas density. Since neither temperature nor density were

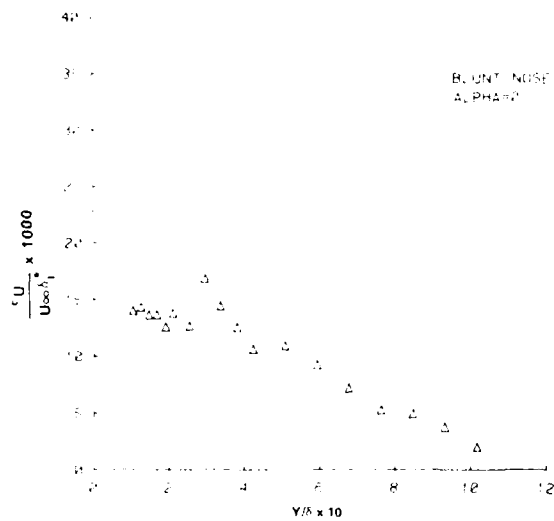


FIGURE 12a. EDDY VISCOSITY DISTRIBUTIONS

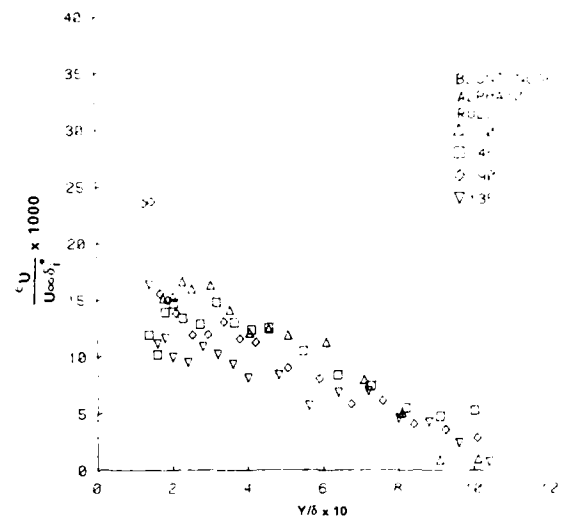


FIGURE 12b. EDDY VISCOSITY DISTRIBUTIONS

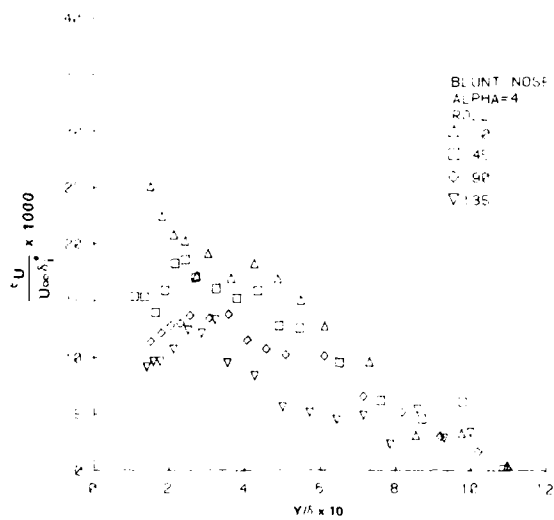


FIGURE 12c. EDDY VISCOSITY DISTRIBUTIONS

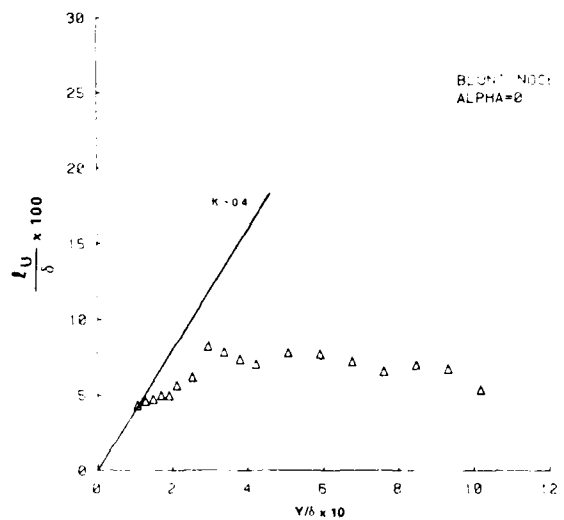


FIGURE 13a. MIXING LENGTH DISTRIBUTIONS

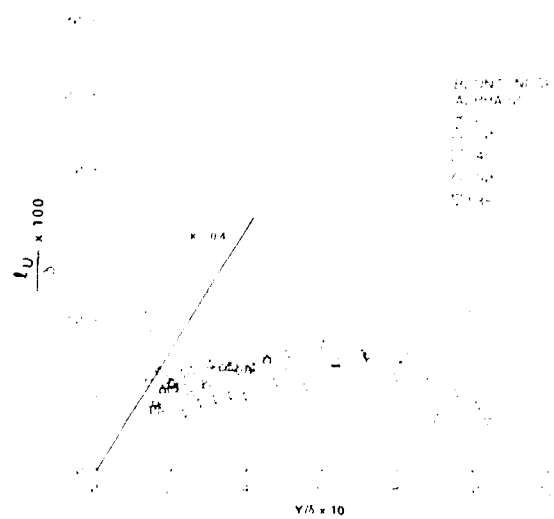


FIGURE 13b. MIXING LENGTH DISTRIBUTIONS

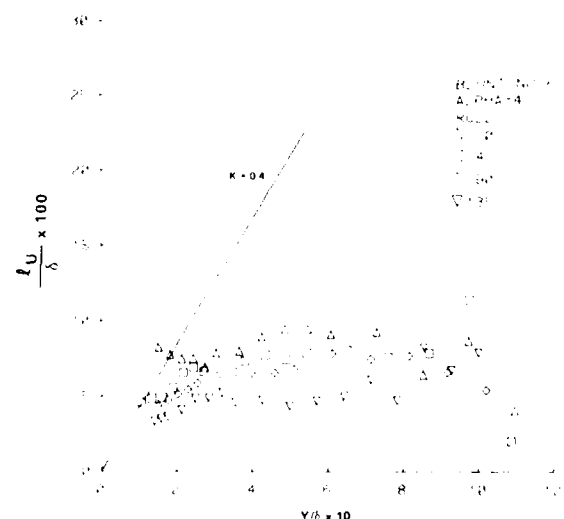


FIGURE 13c. MIXING LENGTH DISTRIBUTIONS

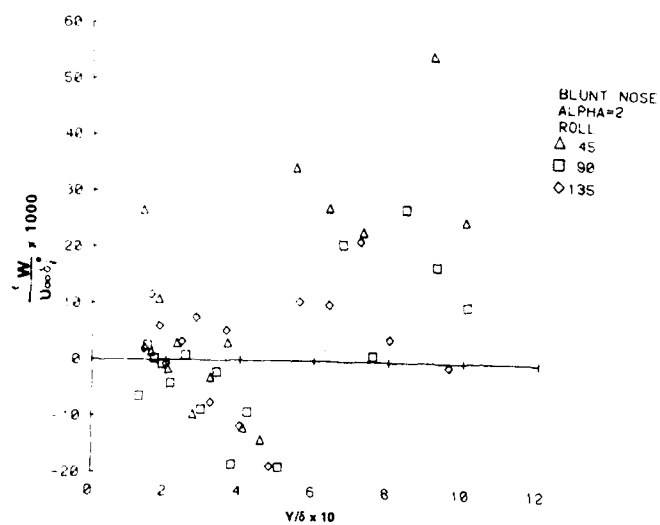


FIGURE 14a. EDDY VISCOSITY DISTRIBUTIONS

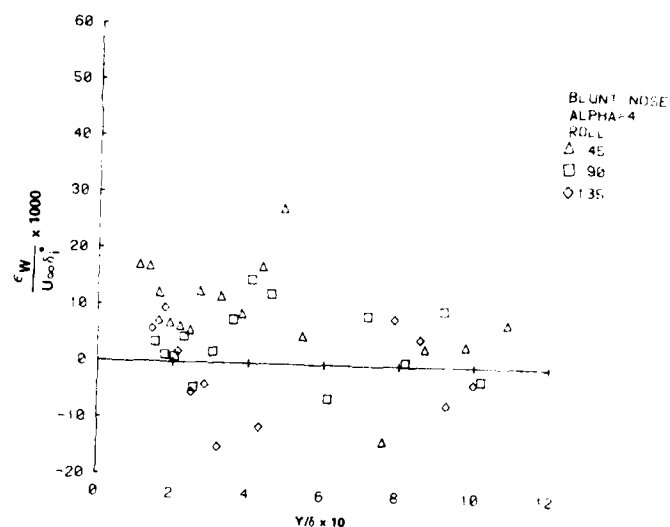


FIGURE 14b. EDDY VISCOSITY DISTRIBUTIONS

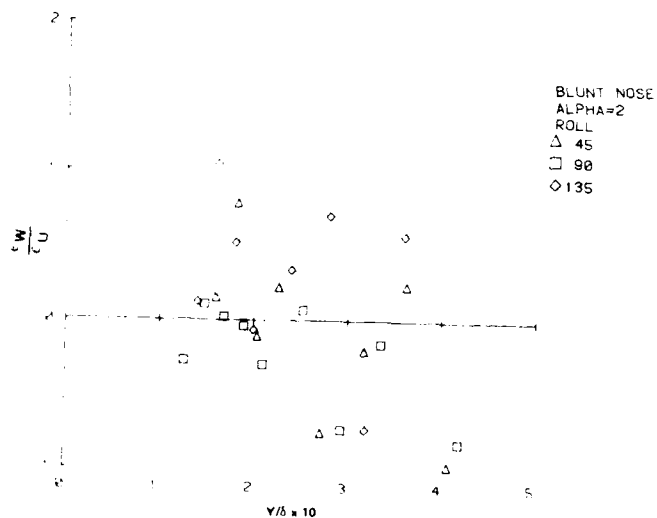


FIGURE 15a. RATIOS OF EDDY VISCOSITIES

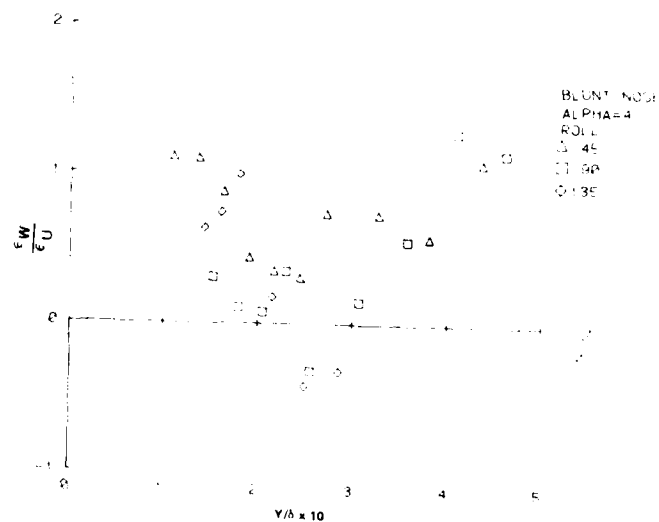


FIGURE 15b. RATIOS OF EDDY VISCOSITIES

AN EXPERIMENTAL INVESTIGATION OF THE STABILITY  
OF THE LAMINAR BOUNDARY LAYER ON A CONE  
AT  $M_\infty = 8$

KENNETH F. STETSON  
AF WRIGHT AERONAUTICAL LABORATORIES, WRIGHT-PATTERSON AFB, OHIO

ELTON R. THOMPSON  
ARNOLD ENGINEERING DEVELOPMENT CENTER, ARNOLD AFS, TENN

JOSEPH C. DONALDSON AND LEO G. SILER  
ARVIN/CALSPAN FIELD SERVICES, INC., ARNOLD AFS, TENN

ABSTRACT

The stability of the laminar boundary layer on a 7-degree half angle cone at  $M_\infty = 8$  was experimentally investigated using hot-wire anemometry techniques. The principle instability of the hypersonic boundary layer was associated with second mode disturbances. The frequency of the most amplified disturbances was directly related to the boundary layer thickness. Small nosetip bluntness was found to make significant changes, compared to a sharp cone, in the stability characteristics of the boundary layer. A nosetip bluntness of 3% of the base radius was found to damp disturbances of all frequencies to a local Reynolds number of  $5.1 \times 10^6$ . The region of the cone frustum where the entropy layer was being swallowed by the boundary layer was found to be stable and the location of the critical Reynolds number coincided approximately with the location where the entropy layer was swallowed. Once the critical Reynolds number was exceeded, the disturbance amplification rates steadily increased and soon became larger than the amplification rates obtained in the boundary layer of the sharp cone. For the cone with 3% nosetip bluntness, disturbances were amplified up to frequencies of approximately 600 kHz (higher than the sharp cone boundary layer) and there were no regions of stable frequencies, as found in the sharp cone boundary layer. Further increases in the size of the nosetip produced additional changes in the stability characteristics of the frustum boundary layer. It was discovered that large amplitude disturbances existed outside the boundary layer, in the entropy layer, indicating the existence of an inviscid instability. As the entropy layer was swallowed by the boundary layer these disturbances entered the boundary layer and proceeded to grow rapidly. It is speculated that the large amplitude disturbances feeding into the boundary layer may force the boundary layer disturbances to grow in an otherwise stable boundary layer.

Nomenclature

A	Disturbance rms amplitude (arbitrary units)
F	Dimensionless frequency ( $2\pi f/u_e Re_e/FT$ )
f	Frequency, Hz
M	Mach number
$Re_x$	( $Re_x$ ) <sup>1/2</sup>
Re	Reynolds number
$Re_x$	Reynolds number based upon conditions at the edge of the boundary layer and surface distance from the nosetip
$r_n$	Nosetip radius, in.
x	Surface length, in.

$y$	Distance normal to the model surface
$-\alpha_i$	Amplification rate $\frac{1}{2A} \frac{\partial A}{\partial R}$
$\delta$	Boundary-layer thickness, in.
$\lambda$	Wavelength of disturbance

#### Subscripts

$e$	Boundary layer edge conditions
$\infty$	Free Stream

#### Discussion

Fig. 1 shows the fluctuation spectra at the location of peak energy in the boundary layer in a pictorial format to illustrate the growth of disturbances in a laminar boundary layer. A unique feature of the hypersonic boundary layer is that it is very selective in the disturbance frequencies which are most amplified. Large disturbances were found to grow in the frequency range from about 70 to 150 kHz. These fluctuations have been identified (by comparison with Mack's theoretical results) as second mode disturbances. It can also be observed that higher frequency disturbances develop as the boundary layer grows. These disturbances are believed to be a first harmonic. Even though the boundary layer disturbances had grown to a relatively large amplitude by the end of the model, the boundary layer still had the mean flow characteristics of a laminar boundary layer.

Fig. 2 contains the same data as shown in Fig. 1, but to better illustrate the frequency of the disturbances spectral data from several stations have been overlaid. The first and second mode fluctuations are merged. The first mode corresponds to the lower frequency fluctuations which show an increase in amplitude, without any special selectivity in frequency of the disturbances which are amplified. These disturbances are similar to the Tollmien-Schlichting instability of incompressible flow. The second and higher modes are unique to compressible, high Mach number flows. The large increase in fluctuation amplitude in the frequency range of about 70 to 150 kHz are second mode waves. The stability theory of Mack predicted that the second mode would be the predominant instability at  $M_\infty = 8$  and these data confirm that prediction. The fluctuations which show a peak in the frequency range from about 175 to 200 kHz are believed to be a first harmonic of the second mode.

Fig. 3 is a pictorial view showing the spectral density variations through the boundary layer. These data were obtained at the last measuring station (37 inches) where the local Reynolds number was  $4.4 \times 10^6$ . Fig. 3a is a view from outside the boundary layer, looking in. The second mode disturbances were found to extend well beyond the defined boundary layer edge. Fig. 3b contains the same data as Fig. 3a, but now the view is from the surface, looking out. It can be seen that the disturbances did not grow in the inner half of the boundary layer and remained essentially at the noise level of the flow.

Fig. 4 is the resulting stability diagram for a sharp cone, with a boundary layer edge Mach number of 6.8 and an equilibrium wall temperature. The multiple unstable regions of a hypersonic boundary layer are designated by the shaded areas. These regions represent frequency and Reynolds number conditions where disturbances are amplified. The unshaded areas correspond to conditions where disturbances are damped. The boundaries of the shaded areas are neutral stability conditions where the amplification rate is zero. The

ashed neutral stability lines at the higher frequencies denote an approximate determination since the disturbances were small and the conditions had to be estimated.

Fig. 5 shows in pictorial format the fluctuation spectra at the location of peak energy in the boundary layer for the cone with a 0.15 inch nosetip radius. Initially, disturbances of all frequencies were damped. The sharp cone, at corresponding local Reynolds numbers, showed a steady growth of disturbances. The major peak in the fluctuation spectra developing near the rear portion of the model was believed to be second mode disturbances (based upon an estimation of disturbance wave length and utilizing the sharp cone results). Unlike the sharp cone results, disturbances of very high frequencies were amplified.

The high frequency disturbances in the sharp cone boundary layer were found to have wave lengths which were directly related to the boundary layer thickness, with the second mode fluctuations having a wave length approximately twice the boundary layer thickness. The wave length of the first major peak in the fluctuation spectra shown in Fig. 5 was estimated in the same manner as the sharp cone data, by assuming that the wave velocity was the same as the boundary layer edge velocity. The results are shown in Fig. 6, along with the sharp cone results. For both nosetip configurations the disturbance wave length was related to the boundary layer thickness in a consistent manner, along with a weak dependence upon local Reynolds number. These sharp cone disturbances had been identified as second mode disturbances, based upon a comparison with Mack's theoretical results. The similarity of these  $R_N = 0.15$  inch data led to the belief that these disturbances were also second mode disturbances.

Fig. 7 compares maximum amplification rates associated with second mode disturbances for the cone with sharp and  $R_N = 0.15$  inch nosetips. As mentioned previously, this 3% blunt nosetip completely stabilized the laminar boundary layer to local Reynolds numbers corresponding approximately to transition on a sharp cone. Once the disturbances started to amplify in the boundary layer of the cone with 3% nosetip bluntness, the amplification rates steadily increased and surpassed the maximum rates obtained for the sharp cone.

Fig. 8 is the resulting stability diagram for the cone with a nosetip radius of 0.15 inches. The shaded area represents the frequency and Reynolds number conditions where disturbances are amplified. The unshaded areas correspond to conditions where disturbances are damped. The boundary of the shaded area represents neutral stability conditions where the amplification rate is zero. The dashed neutral stability lines at the higher frequencies denote an approximate determination since the disturbances were small and the conditions had to be estimated.

#### REFERENCES

1. Stetson, K.F., Thompson, E.R., Donaldson, J.C. and Siler, L.G., "Laminar Boundary Layer Stability Experiments on a Cone at Mach 8, Part 1: Sharp Cone", AIAA Paper No. 83-1761, July 1983
2. Stetson, K.F., Thompson, E.R., Donaldson, J.C. and Siler, L.G., "Laminar Boundary Layer Stability Experiments on a Cone at Mach 8, Part 2: Blunt Cone", AIAA Paper No. 84-0006, Jan 1984

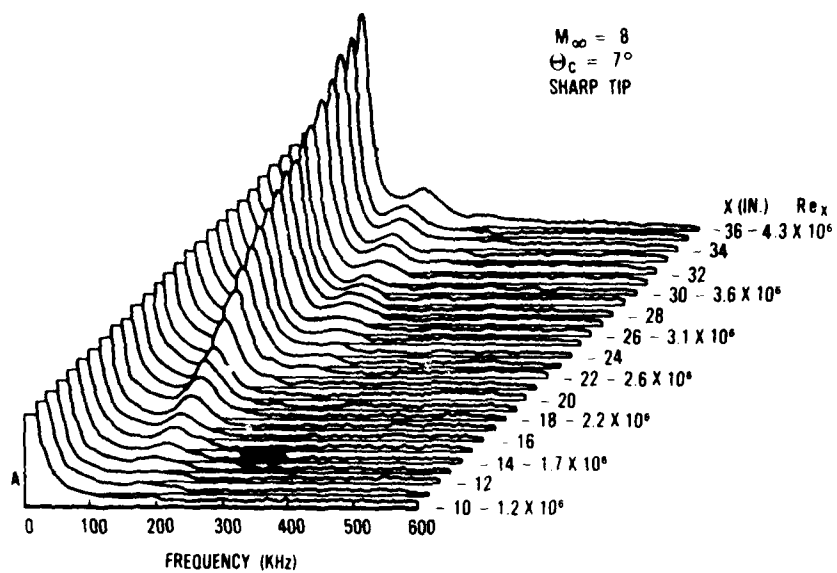


Fig. 1 Fluctuation spectra, sharp cone

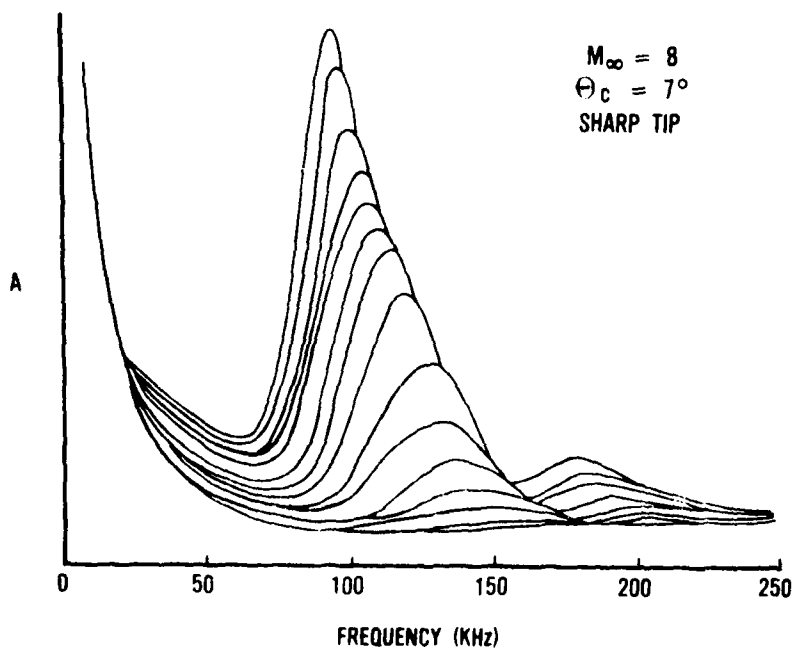


Fig. 2 Fluctuation spectra overlaid



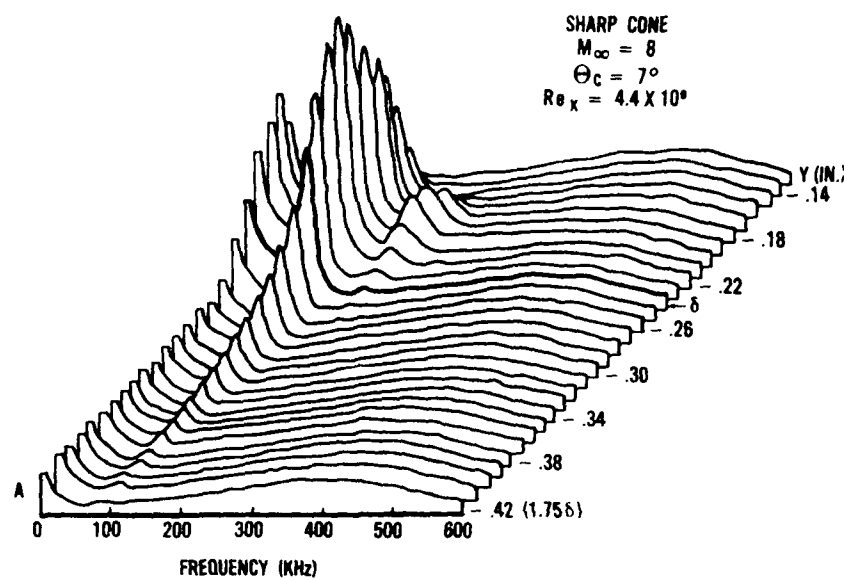


Fig. 3a Fluctuation spectra, normal to the surface.  
 Outside the boundary layer, looking in

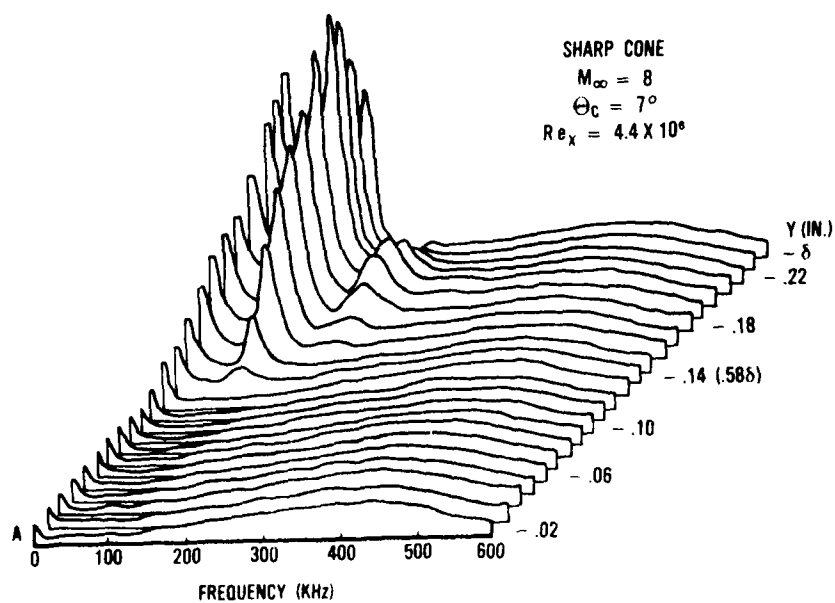


Fig. 3b Fluctuation spectra, normal to the surface.  
 From the surface, looking out

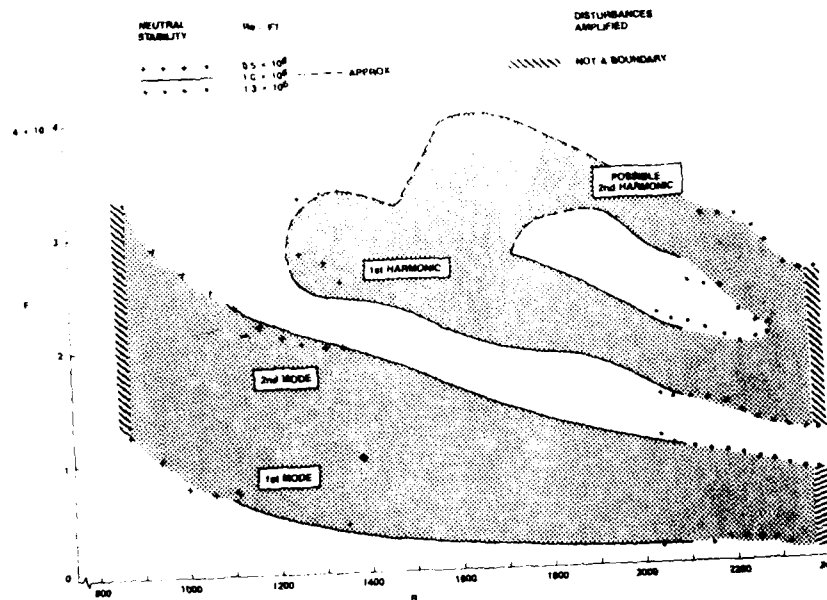


Fig. 4 Stability diagram, sharp cone

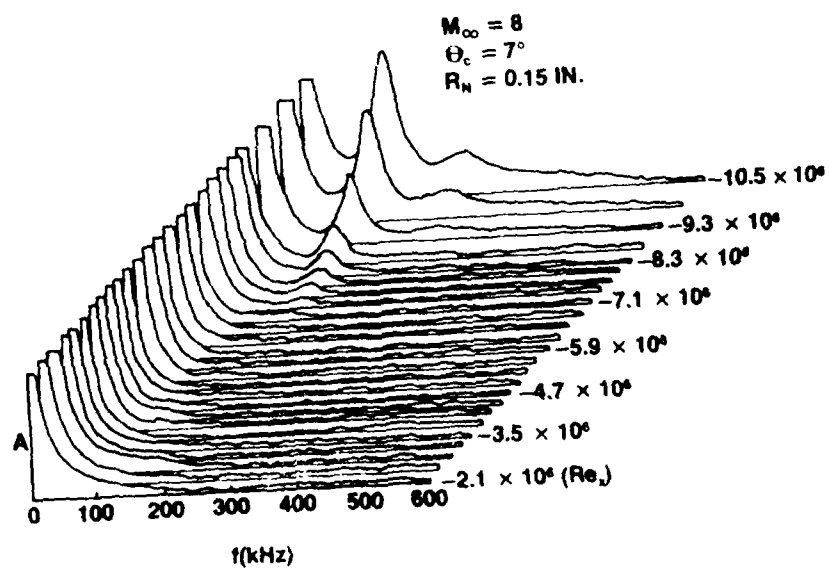


Fig. 5 Fluctuation spectra,  $R_N = 0.15$  in.

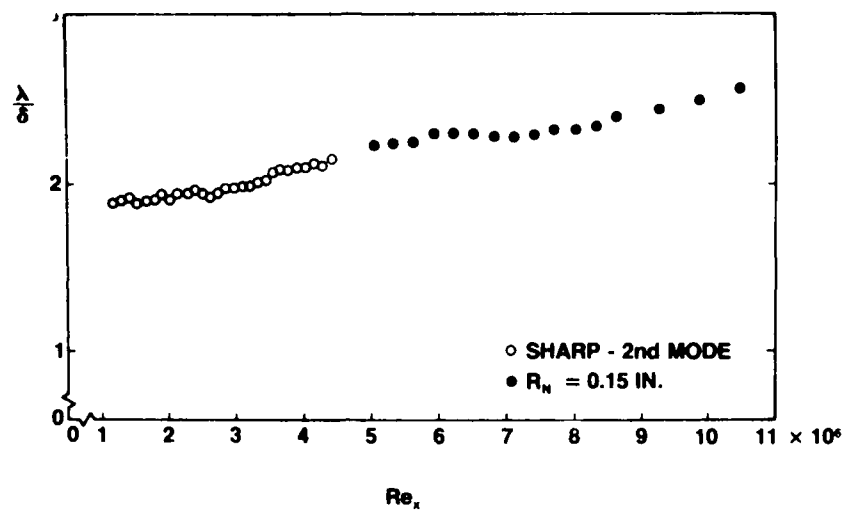


Fig. 6 Fluctuation wave length

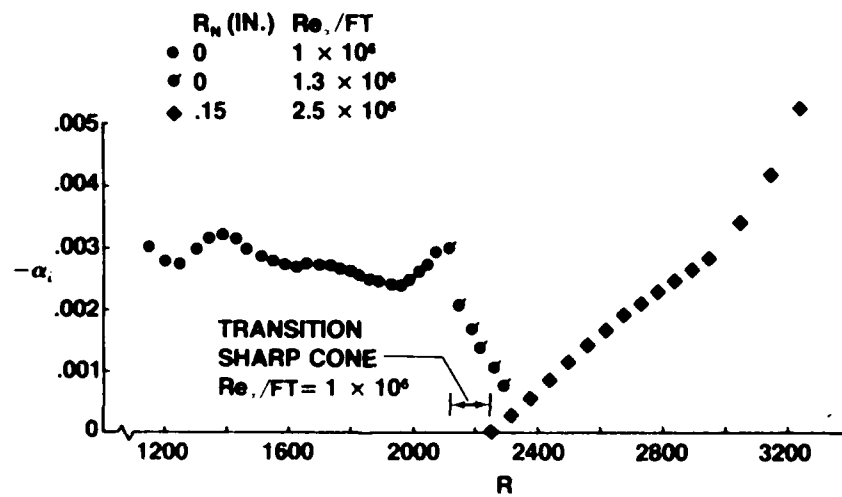


Fig. 7 Maximum amplification rates associated with the second mode

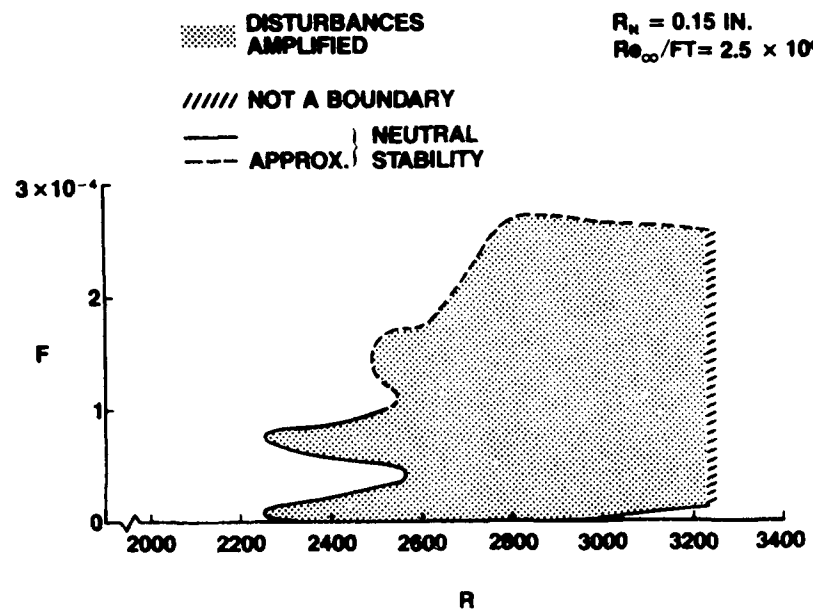


Fig. 8 Stability diagram,  $R_N = 0.15 \text{ in.}$

BOUNDARY-LAYER TRANSITION ON  
BLUNT SLENDER CONES AT MACH 10

Jacques A. F. Hill

Rita L. Bell

Naval Surface Weapons Center  
Silver Spring, Maryland 20910

(This is a preliminary report on work in progress.)

## BACKGROUND

Investigations of the effects of nose blunting on the location of boundary-layer transition on slender cones at supersonic or hypersonic speeds go back 25 years. For some time it was thought that the movement of the transition point was simply due to the reduction in local Reynolds number associated with the loss in total pressure through the bow shock. More recently, as in Reference 1, it has been shown that variations in the local transition Reynolds number also occur on a blunt cone and that both these effects must be taken into account in explaining the observed movement of transition along the cone frustum.

In Reference 1, Stetson has identified two flow regimes which he distinguishes on the basis of the nature of the rise in heat transfer through transition. With reference to Figure 1, he calls the behavior in (a) normal transition and the behavior in (b) transition dominated by nosetip instabilities. For "smooth" nosetips he suggests that the boundary between the two regimes occurs when the value of the momentum-thickness Reynolds number at the sonic point on the nose,  $Re_{\theta}^*$ , is about 100. He then chooses to look almost exclusively at data for  $Re_{\theta}^* < 100$ , citing problems with asymmetry and lack of repeatability for  $Re_{\theta}^* > 100$ .

Most of the previous investigations of boundary-layer transition on blunt cones do not distinguish between these regimes. Some years ago Hill (Reference 2) correlated a number of sets of data as shown in Figure 2, using the Reynolds number behind the shock as the scaling parameter. Within the admittedly large

scatter, all the data fell in a smooth band for values of  $Re_\theta^*$  extending to both sides of  $Re_\theta^* = 100$ . All of Stetson's recent data, restricted to  $Re_\theta^* < 100$ , agrees well with the earlier data. In terms of the parameter used, the data for  $Re_\theta^* > 100$  blends smoothly into the data for lower Reynolds numbers.

So far, the discussion has been about data for zero angle of attack. Many investigations of angle-of-attack effects have been published, from which we select Holden's data (Reference 3) for illustration. Figure 3 shows the transition patterns observed for  $\alpha \approx 3$  deg. on cones with two different bluntness ratios. In one case transition has moved forward on the leeward ray and in the other case it has moved aft. Both patterns of behavior have been observed elsewhere but the transition between them has not been associated with any value of any particular flow parameter.

#### PRESENT INVESTIGATION

The present investigation was carried out as a demonstration test for the development of a new capability in Hypervelocity Tunnel 9 at NSWC. The objective of this development effort was to raise the Reynolds number at Mach 10 from about  $5 \times 10^6$  per foot to  $20 \times 10^6$  per foot. This was done so that naturally turbulent boundary layers (i.e. without tripping) could be obtained on R/V models. Thus an investigation of boundary layer transition was an appropriate choice for the demonstration test.

Figure 4 shows the layout of the model and instrumentation. There were three noses, with nose radii as shown. Heat-transfer measurements were used to locate transition and the coaxial thermocouples were used to measure the heat-transfer rates. Transient data were taken during pitch sweeps from -5 deg. to

+5 deg., yielding Stanton number variations with angle of attack as shown in Figure 5 for two stations opposite each other on the top and bottom of the model.

### PRELIMINARY RESULTS

Preliminary results illustrating two transition regimes as identified by Stetson are shown in Figure 6. The heat transfer rise is steep at the low Reynolds number and gradual at the high Reynolds number. When the data from the present tests (for zero angle of attack) are plotted as in Figure 2 they fall into two groups, as shown in Figure 7. The data for the lower Reynolds numbers, exhibiting a sharp rise in heat transfer, falls on the curve labeled 1 and the data for high Reynolds numbers, exhibiting a gradual rise in heat transfer, falls on the curve labeled 2.

For one run at a value of  $Re_{N,S} \approx 3.4 \times 10^5$  two points are shown; one on each curve. They have been derived from Stanton number plots like the one shown in Figure 8, where the rise from laminar to turbulent values occurs in two steps. The first step produces the point shown on curve 2 and the second step the one shown on curve 1, corresponding to "normal" transition as labeled by Stetson. At this Reynolds number the other transition mechanism (postulated by Stetson to be associated with instabilities in the flow over the nosetip) is just beginning to affect the flow. It produces the small early rise in heat transfer but is not strong enough to produce transition to fully turbulent flow. At higher Reynolds numbers it dominates the transition process as shown in the lower half of Figure 6.

The transition pattern at  $\alpha = 2^\circ$  is shown for low and high Reynolds numbers in Figure 9. We see the two patterns previously observed by Holden but now we can associate them with a change in the character of the transition process. (Data for other angles of attack have not been analyzed in detail but appear to



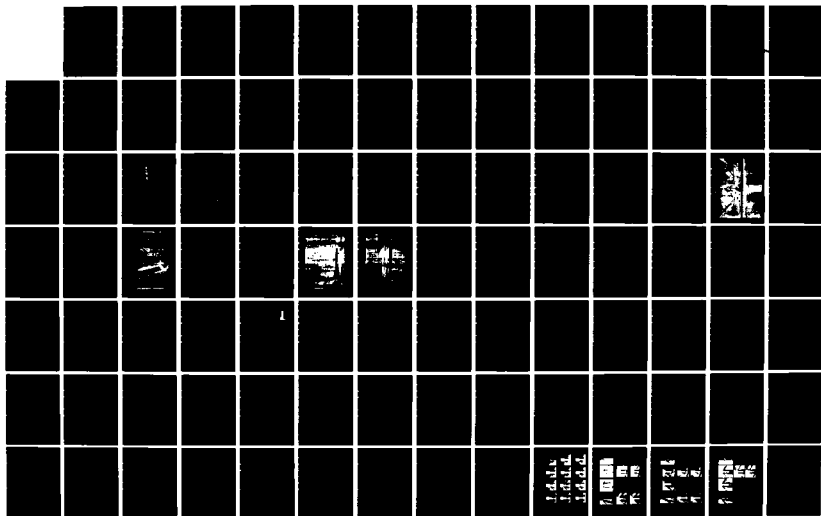
AD-A153 020

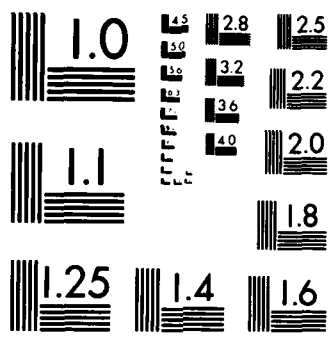
PROCEEDINGS OF THE US AIR FORCE AND THE FEDERAL  
REPUBLIC OF GERMANY DATA. (U) AIR FORCE WRIGHT  
AERONAUTICAL LABS WRIGHT-PATTERSON AFB OH A W FIDRE  
AUG 84 F/G 20/4

3/4

UNCLASSIFIED

NL





MICROCOPY RESOLUTION TEST CHART  
NATIONAL BUREAU OF STANDARDS-1963-A

exhibit similar behavior.) Stetson's observation that the high-Reynolds number data is asymmetrical is not borne out by the data shown here.

#### PRELIMINARY DISCUSSION

It seems that two different kinds of phenomena can play a role in boundary-layer transition on sphere-cones. In Figure 7 the crossover from one to the other occurs at a value of nose Reynolds number

$$Re_{N,S} = \rho_S V_m R_N / \mu_S \approx 3.4 \times 10^5$$

where

$\rho_S$  = density at the stagnation point

$V_m$  = limiting velocity

$R_N$  = nose radius

$\mu_S$  = viscosity at the stagnation point

This value of  $Re_{N,S}$  corresponds to a unique value of momentum-thickness Reynolds number at the sonic point on the nose, in this case  $Re_\theta^* \approx 70$ , somewhat lower than Stetson's value of  $Re_\theta^* \approx 100$ .

The crossover point between the two transition regimes may also be related to a particular stage in the entropy-layer swallowing process on the cone. Figure 10 illustrates the entropy-layer swallowing process for this model at  $\alpha = 0$ , based on calculations performed with the GE Three Dimensional Viscous Code (reference 4). The similarity parameter used for the abscissa collapses the calculations over the full range of nose radii and Reynolds numbers onto a single curve. This curve describes the decay of boundary-layer-edge entropy from the initial normal-shock value towards the free-stream value. At the point where the transition data switches between the two curves in Figure 7, we have

$$Re_{N,S} \approx 3.4 \times 10^5$$

$$S/R_N \approx 35 \text{ (mean value)}$$

so that

$$(S/R_N) (Re_{N,S})^{-\frac{1}{3}} \approx 0.5$$

This value is indicated in Figure 10 and is located roughly at the beginning of the steep portion of the decay curve. It may be that transition is triggered differently where the entropy layer is being rapidly swallowed than where swallowing has hardly begun.

Note that the distinction between the two kinds of behavior may also be made on the basis of bluntness. For cones with  $S_{\max}/R_N < 25$ , only the high-Reynolds number regime should be expected, and the transition front at incidence will look like the lower graph in Figure 9.

#### COMPARISON WITH FLIGHT DATA

Reference 5 presents a large number of measurements of boundary-layer transition on R/V's during reentry. For comparison with wind tunnel data we have selected a subset of these measurements so as to minimize the effects of blowing due to ablation. These are the vehicles with graphite noses and beryllium frusta.

The characteristic Reynolds number used in Reference 5 was

$$Re_S = \rho_e u_e S / \mu_e$$

evaluated at  $X = 2R_N$  back of the stagnation point. At the wind tunnel test conditions,

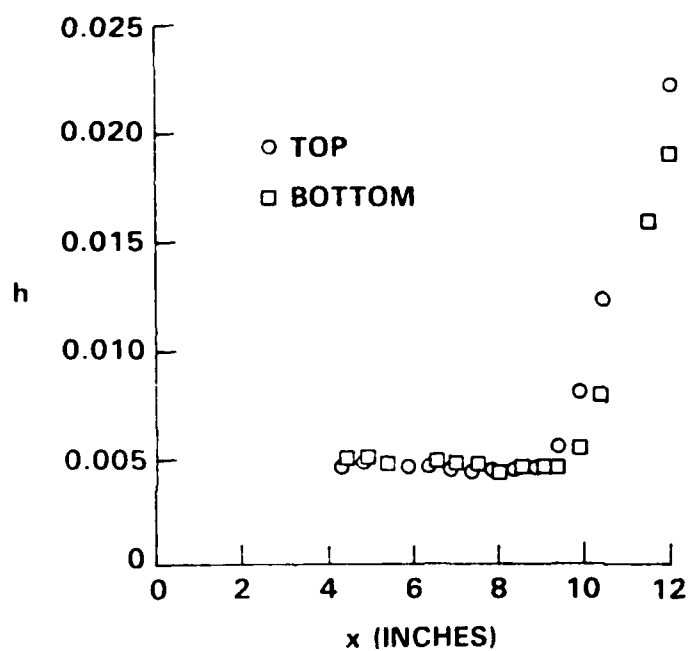
$$Re_S \approx 0.32 Re_{N,S}$$

and the wind tunnel data may simply be expressed in terms of the flight test parameter. This has been done in Figure 11, where, except for two flight points

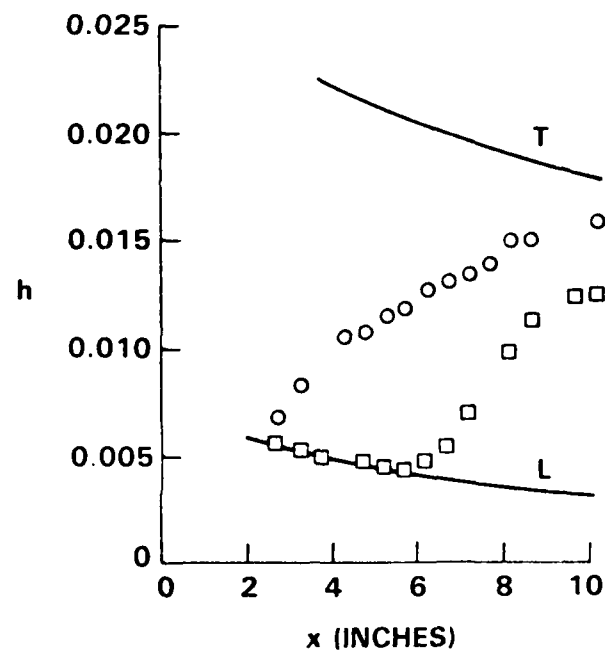
at the highest Reynolds number, the agreement between flight and ground tests is remarkably good. To speculate again, one possible interpretation of these data is that only "normal" transition (curve 1 in Figure 7 and 11) is seen in flight and that early transition (curve 2 in Figure 7 and 11) occurs only in wind tunnels.

## REFERENCES

1. Stetson, K. F. Nosetip Bluntness Effects on Cone Frustum Boundary Layer Transition in Hypersonic Flow. AIAA Paper 83-1763, July 1983.
2. Hill, J. A. F., Wardlaw, A. B., Jr., Pronchick, S. W., and Holmes, J. E. Verification Tests in the Mach 14 Nozzle of the Hypervelocity Tunnel at NSWC White Oak Laboratory. AIAA Paper 77-150, January 1977.
3. Holden, M. S. Studies of the Effects of Transitional and Turbulent Boundary Layers on the Aerodynamic Performance of Hypersonic Reentry Vehicles in High-Reynolds Number Flows. Report AB 5834-A-2 CALSPAN ATC, December 1978.
4. Hecht, A. M. and Nestler, D. E. A Three-Dimensional Boundary-Layer Computer Program for Sphere-Cone Type Reentry Vehicles. AFFDL-TR-78-67, June 1978.
5. Berkowitz, A. M., Kyriss, C. L., and Martellucci, A. Boundary Layer Transition-Flight Test Observations. AIAA Paper 77-125, January 1977.



(A) NORMAL TRANSITION  
UNAFECTED BY NOSETIP  
INSTABILITIES



(B) "ERRATIC" TRANSITION  
CAUSED BY NOSETIP  
INSTABILITIES

FIGURE 1. STETSON'S (REF. 1) TWO FLOW REGIMES FOR TRANSITION

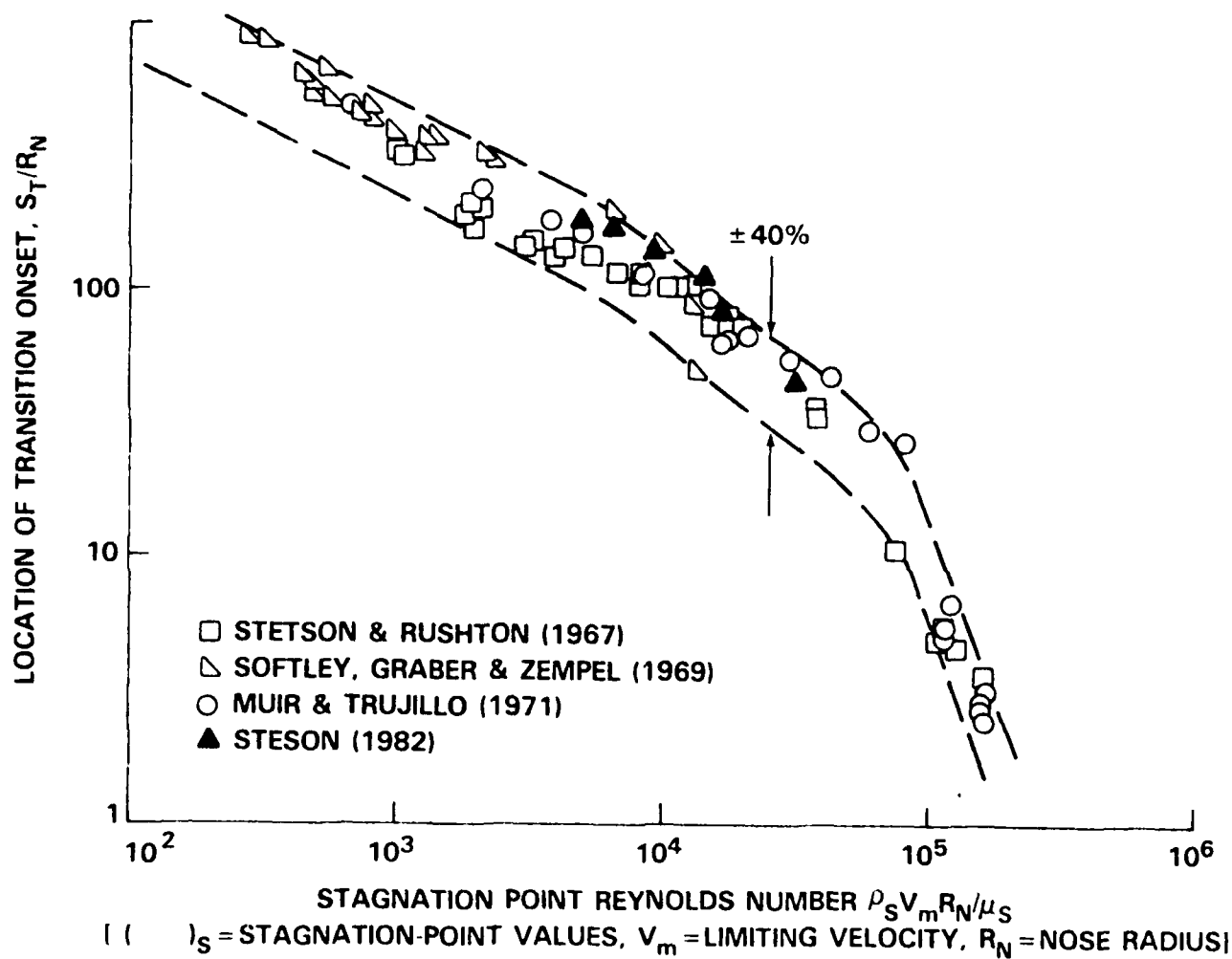


FIGURE 2. BLUNTED-CONE TRANSITION CORRELATION (HILL, 1973)



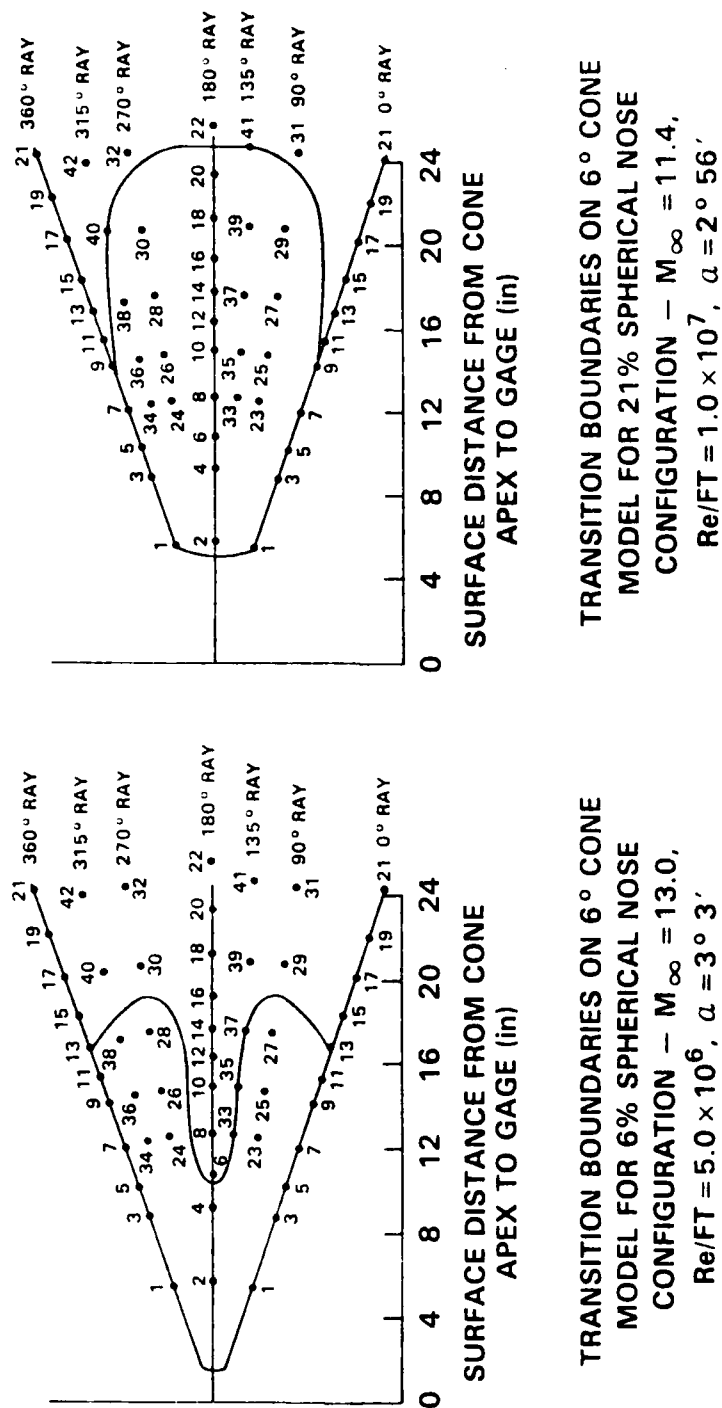


FIGURE 3. TRANSITION FRONT SHAPES OBSERVED BY HOLDEN (REF. 3)

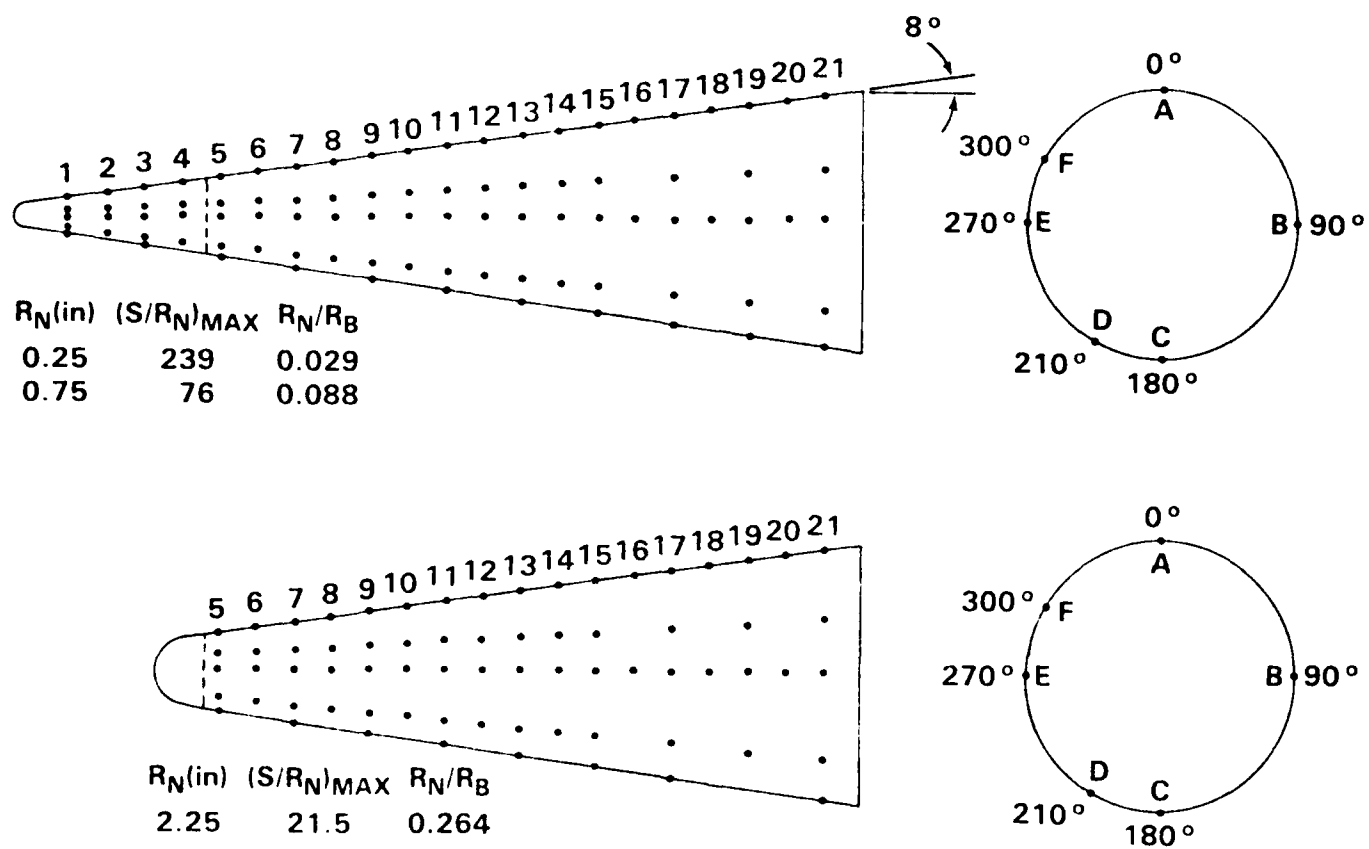


FIGURE 4. LAYOUT OF COAXIAL THERMOCOUPLES ON MODEL

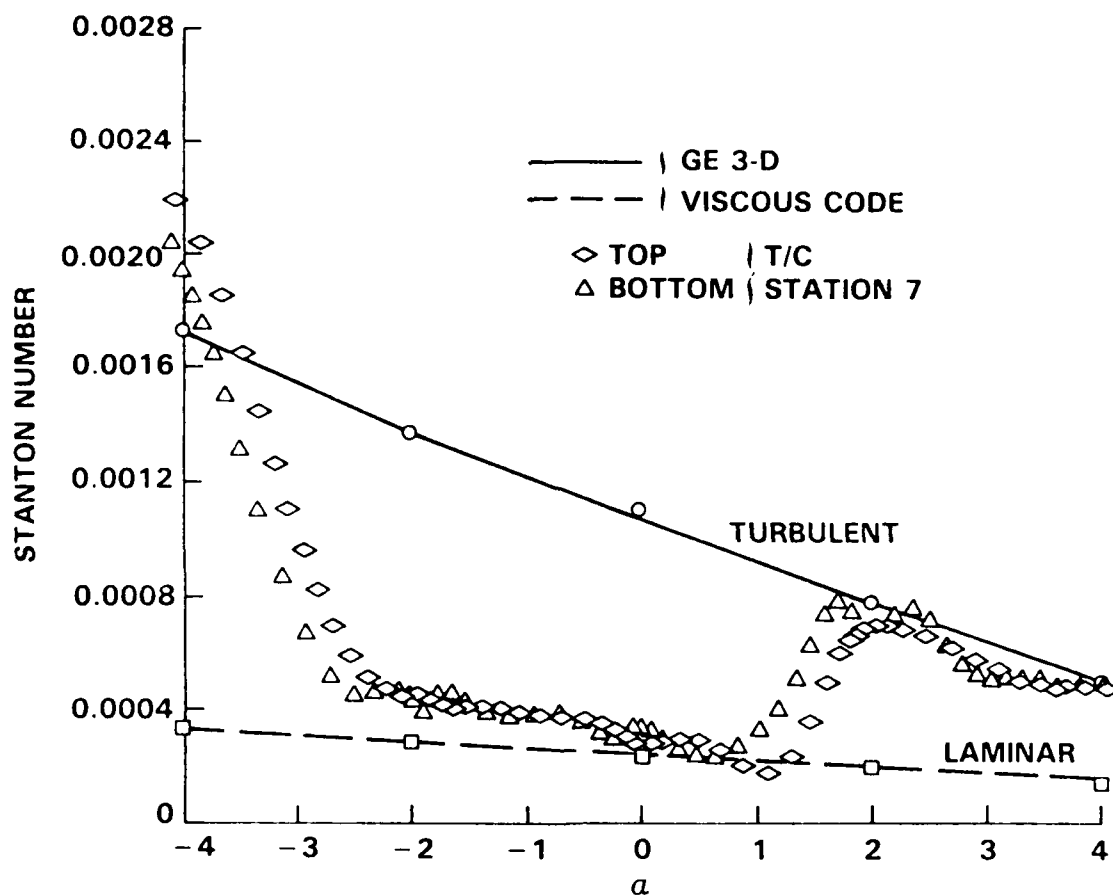


FIGURE 5. VARIATION WITH  $\alpha$  OF STANTON NUMBER ON TOP & BOTTOM OF MODEL

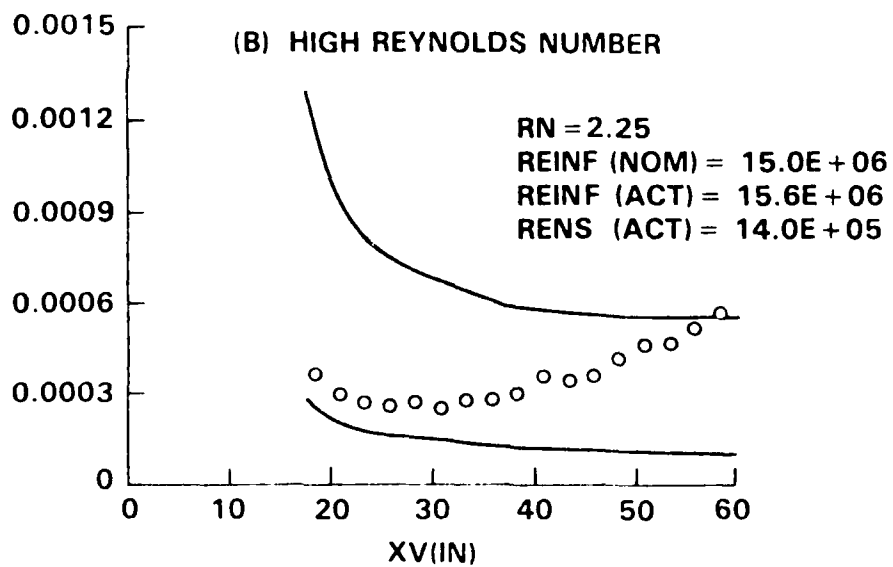
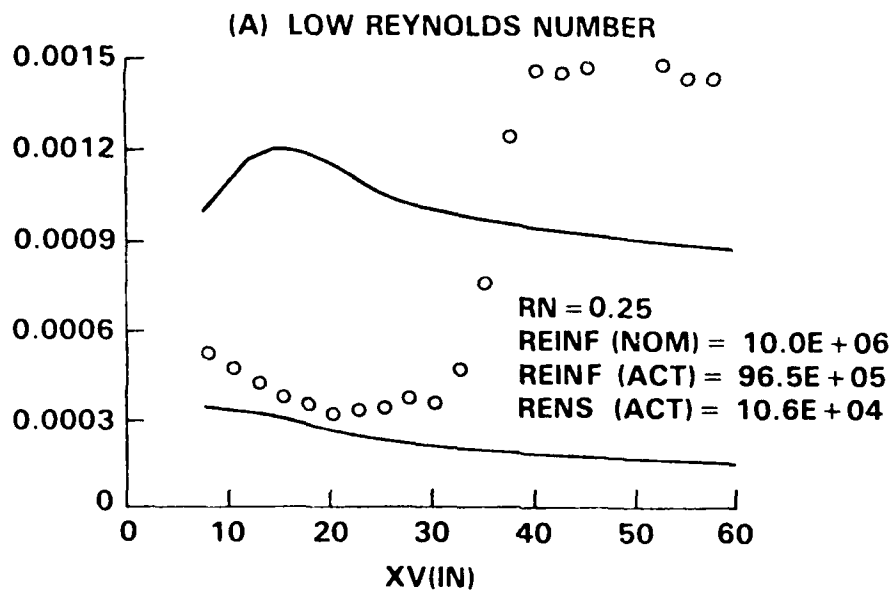


FIGURE 6. HEAT TRANSFER RISE AT TRANSITION ( $\alpha = 0, 270^\circ$  RAY)

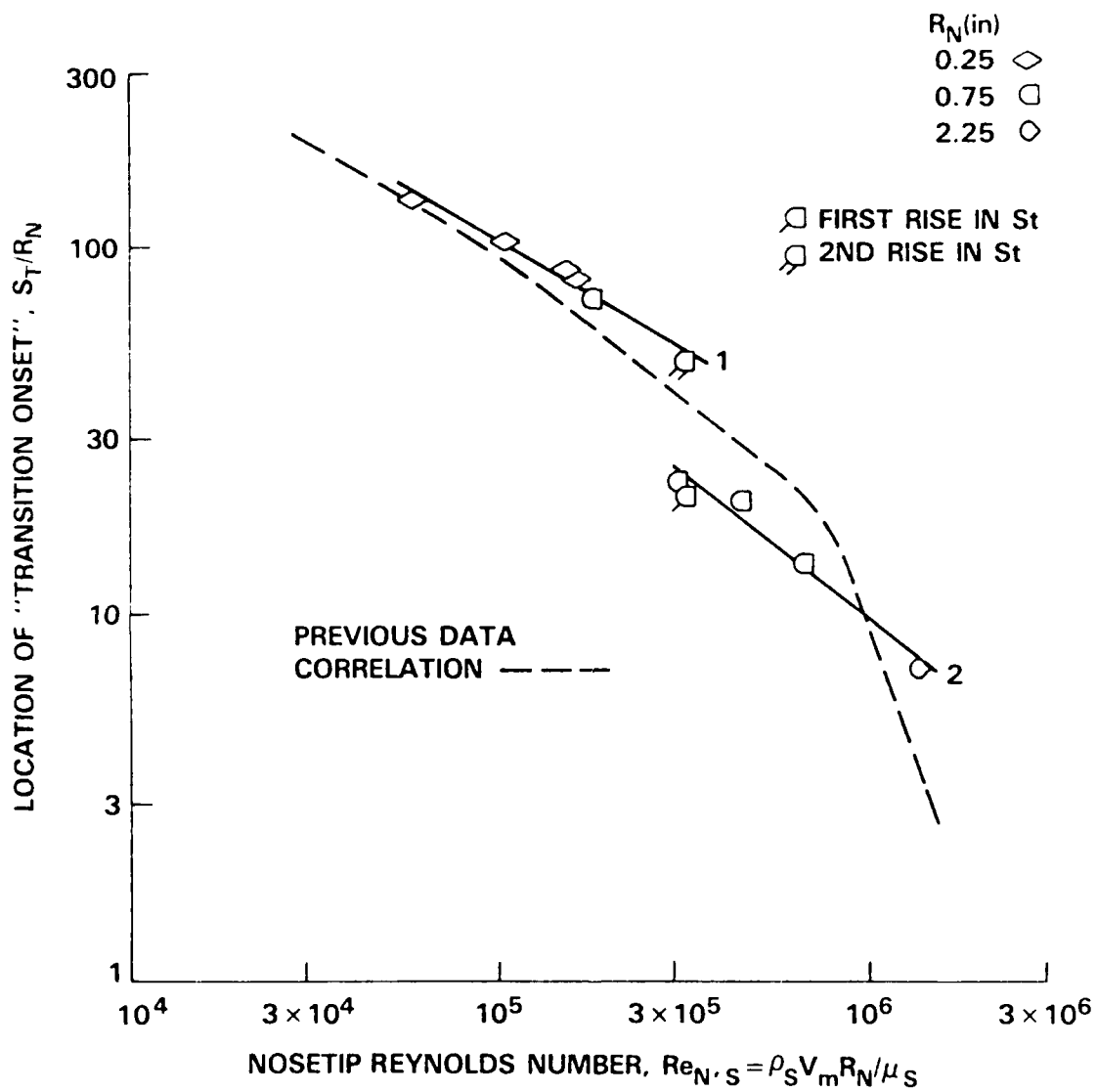


FIGURE 7. "TRANSITION ONSET" DATA

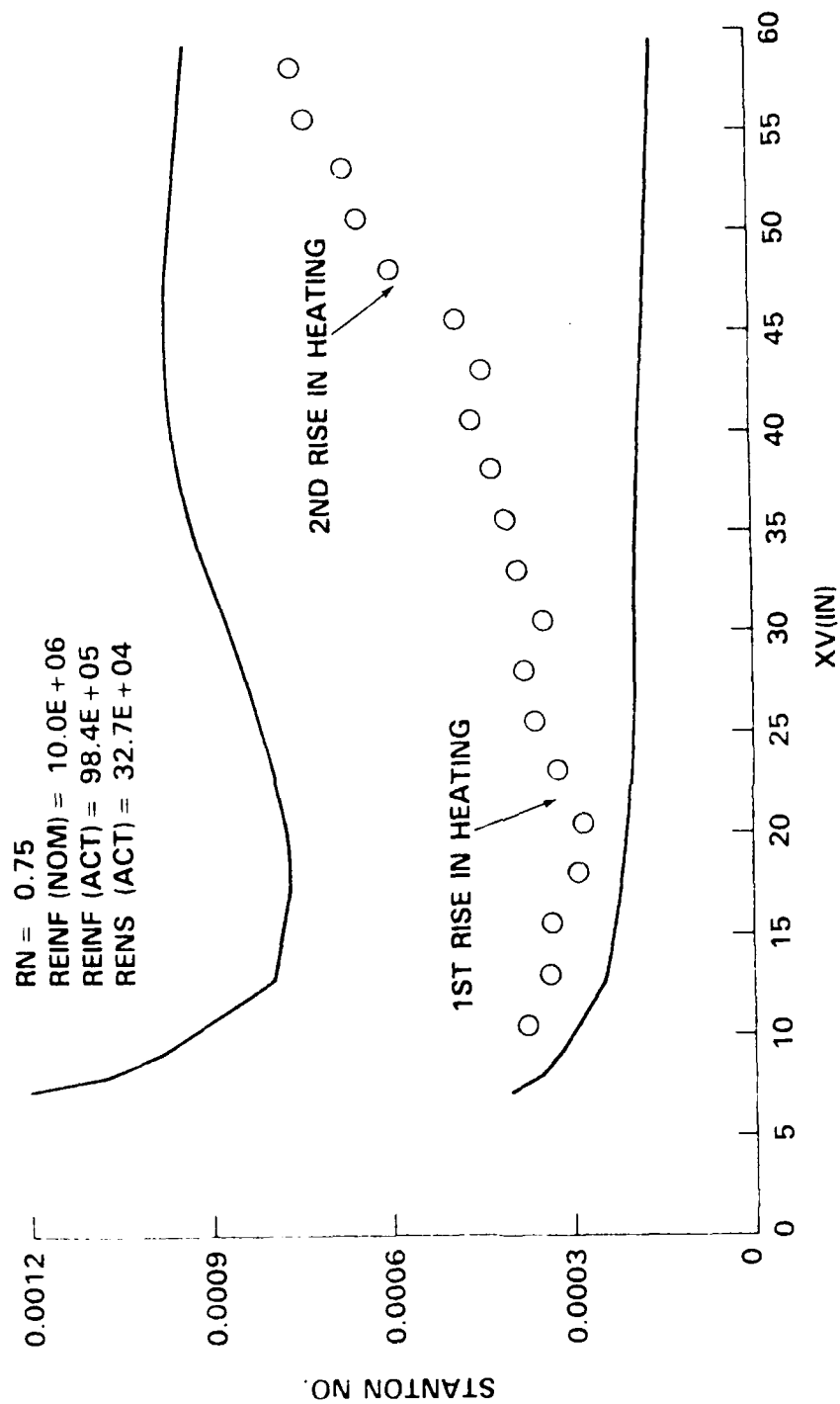


FIGURE 8. INTERMEDIATE REYNOLDS NUMBER ( $\alpha = 0^\circ$ ,  $270^\circ$  RAY)

Figure 16 illustrates the possible heating scenarios that could occur during a wind tunnel run. Figure 17 shows a schematic of the internal model hardware. The model shell was fabricated of aluminum with a steel nosetip. To prevent the flow of heat from the stagnation point into the balance, a ceramic insulator was placed between the junction of the model shell and the balance. A beryllium-copper shield surrounded the balance and absorbed heat from gas flowing into the model base cavity as well as heat which would radiate from the model's inner surface. Another ceramic insulator was seated between the sting and the beryllium-copper shell. To prevent heat flow up the sting originating from the "hot spot" produced by bow shock impingement, the sting was manufactured with an outer protective sleeve. A .005 inch air gap between the sleeve and the sting insulated the sting from any heat flow. Base plates were also added to the model to further reduce sting-base effects as well as increase thermal protection for the balance. Figure 18 is a photograph of all the model hardware.

Wind tunnel tests were conducted to insure that no balance heating would occur during testing. A dummy balance shown in figure 19 was manufactured with similar dimensions as the actual balance, and thermocouples were placed at the gage sections. The model hardware, dummy balance, and the dogleg sting were mounted in the tunnel and pitched from 45 - 90 degrees at supply pressure of 380 and 100 psia. There was no change in the balance temperature during either run indicating that the balance had adequate thermal protection.

#### STATIC STABILITY VERIFICATION TESTS

Following the tunnel calibrations at the new extended operating conditions, a series of verification tests were conducted on a six-inch sphere-cone model.

## MODEL AND STING DESIGN

Traditionally, Tunnel 9 tests are conducted with full-scale models with the intent of simulating the highest Reynolds number possible. For high altitude testing, it is highly desirable to use subscale models in order to decrease the simulated flight Reynolds number. Decreasing model size, however, makes accurate force and moment measurements more difficult. Very small subscale models (less than 1 foot length) had never been tested in Tunnel 9 before so special attention had to be paid in the design of the model and sting hardware. Furthermore, angles-of-attack greater than 50 degrees had not been tested which equally complicated the design.

Because the Tunnel 9 pitch mechanism allows for a maximum sweep of 50 degrees, two separate pitch sweeps were required to obtain data for the full 0 - 90 degree angle of attack range. Figure 14 shows a picture of the straight sting which allowed a pitch sweep from 0 - 45 degrees, and figure 15 illustrates the dogleg sting that allowed a sweep from 45 - 90 degrees. The sting to model base diameter ratio for both stings was .3 and the distance to the nearest sting diameter increase was five base diameters. These dimensions were based on suggestions found in reference 8 to minimize sting interference effects.

A miniature semiconductor strain gage balance was used to measure static forces and moments. From balance calibrations the accuracy was determined to be +.001 lbs. in pitch and yaw. Because the model was to be pitched to 90 degrees angle-of-attack, and run times would be approximately 20 seconds, significant heat transfer to the model sting assembly would occur during testing. Therefore, special model hardware had to be designed.



## TUNNEL CALIBRATION

With the new Tunnel 9 operating conditions, flowfield surveys were taken to determine flow quality. Figure 11 illustrates the test section calibration hardware. A pitot tube and a fine-wire thermocouple were mounted on the Tunnel-9 traversing probe (see ref. 5). The probe took data spanning the vertical direction from the nozzle centerline to seven inches from the nozzle wall. Also mounted in the test section were two fixed pitot tubes, PTS and PTN, and a nine tube pitot rake that spanned the horizontal direction (PT1 - PT9).

Figure 12 is a plot of normalized pitot pressure vs. radial distance in the test section for a supply pressure of 380 psi. There is very good agreement between the fixed pitot and the traversing pitot. These measurements repeat data documented in reference 1. Similar data were obtained at supply pressures of 100 psi and 60 psia at two axial locations in the test cell. Uniformity between axial locations was found to be excellent. Values for test core diameter decreased as supply pressure decreased due to thickening of the nozzle wall boundary layer. Figure 13 is a plot of test core diameter vs. freestream Reynolds number. At a supply pressure of 60 psi the freestream Reynolds number is about 50,000/ft. The fine-wire thermocouple data were reduced using methods in references 6 and 7. Preliminary results indicate agreement to within 10% of the temperature measured at the nozzle throat. Further analysis of that data is ongoing.

the time required would cause an undesirable heat soak into the heater insulation. Modification of hardware would be costly and complex. Another alternative considered was to operate the heater in a compression heating cycle.

Figure 7 is a pictorial description of compression heating. During normal heater operation cold driver vessel gas enters the base of the heater at the same pressure as the hot gas. During compression heating the cold gas enters at a significantly higher pressure so as to compress the hot gas. The compression process is accomplished in 1 to 2 seconds, is nearly isentropic, and raises the temperature of the hot gas by several hundred degrees, depending on the compression ratio. Figure 8 shows a plot of heater temperature vs. time during a compression heating run. An advantage of compression heating is that gas in the horizontal elbow, which is not affected by the initial heating with the carbon element, also increases in temperature during the compression cycle, thereby, increasing the wall temperature of the elbow as well. Heat transfer to the wall from the subsequent heater gas is reduced because the thermal gradient is reduced. One problem, however, is that the elbow temperature increases and decreases rapidly during the compression cycle causing undesirable thermal stresses in the elbow materials. As a result, cooling of the elbow was required during the compression. Figure 9 graphically illustrates the elbow temperature for normal heater operation and compression heating with and without cooling.

The result of compression heating was a significant increase in nozzle supply temperature. Different compression ratios were tried and the optimum was found to be 1.8. Higher compression ratios (3 and 4) were tried but because of the large reduction in hot gas volume and the mixing of the cold and hot gases, very short run times were observed with varying tunnel conditions. Figure 10 illustrates the increase in supply temperature with compression heating vs. supply pressure.

from the top of the heater, through the horizontal elbow, and into the throat area. The flow restrictor serves two purposes. It reduces the strength of the rarefaction wave travelling into the heater caused by the abrupt diaphragm rupture, and it reduces the pressure from that in the heater to the desired tunnel supply pressure. A particle separator is located downstream of the flow restrictor to remove any particles or diaphragm fragments that may be in the flow. As the hot gas exits the top of the heater, cold gas enters the base of the heater and acts as a fluid piston to drive the hot gas. Normally, the cold gas which is stored in the driver vessels enters the heater at the same pressure as the hot gas leaving the heater.

High Reynolds number operation of Tunnel 9 at Mach 14 begins with the heater at 20,000 psi and 3300<sup>0</sup>F. The heater vessel and diaphragm area are fortified with large amounts of metal to structurally withstand the severe operating conditions. At a supply pressure of 20,000 psi, the final temperature at the nozzle throat is slightly less (3200<sup>0</sup>F) because of small heat losses into the surrounding metal. However, as the supply pressure decreases, the mass flow also decreases, and the heat losses have a greater effects on the gas temperature. Figure 6 shows a plot of nozzle supply temperature vs. supply pressure. At a supply pressure of 100 psia, the supply temperature decreases from 3300<sup>0</sup>F in the heater to 1250<sup>0</sup>F at the nozzle throat. Most of the heat is lost into the large amounts of metal surrounding the elbow and diaphragm sections.

With the additional ejector stage, operation of Tunnel 9 below supply pressures of 100 psia was now possible. However, lower pressures would result in a loss of supply temperature and condensation-free flow would not be achieved. Therefore, tunnel supply temperature would have to be increased. The carbon heater element could heat the gas initially to a higher temperature, however,

Figure 4 shows a plot of sphere pressure vs. tunnel supply pressure indicating the minimum sphere pressure for tunnel start-up. The chart shows that for supply pressures below 100 psia the sphere pressure would have to be less than 1 torr (.02 psia).

The vacuum sphere is evacuated by a series of four centrifugal compressors and a supersonic ejector. The compressor plant alone can pump the sphere to approximately 3 torr before surging begins in the fourth compressor. The ejector operates by allowing external atmospheric air to flow through supersonic nozzles into a constant area mixing duct. The high-energy supersonic air entrains the flow from the sphere at low pressure and delivers a higher total mass flow at a higher pressure to the plant. The plant along with a single ejector can evacuate the sphere to approximately 1 torr.

In order to get lower initial test cell pressure, a second ejector was designed and installed between the sphere and the existing ejector (see ref. 3). Modifications were also made to the first ejector to achieve maximum efficiency from the two-stage system. Pump-down sequences of the two-stage ejector produced sphere pressures of approximately .25 torr (.005 psia). With this lower sphere pressure the tunnel could now be operated at a lower supply pressure. Figure 4 indicates the tunnel could start with a supply pressure as low as 30 psia.

#### COMPRESSION HEATING

Figure 5 shows a diagram of the heater, diaphragm and nozzle throat sections of Tunnel 9. Prior to a wind tunnel run, the hot pressurized gas in the heater is separated from the low pressure test section by a series of metal diaphragms upstream of the nozzle throat. The diaphragms are ruptured and hot gas flows

4.0E + 05 to 2.0E + 07). Nozzle supply pressures ranged from 1000 psia to 20,000 psia corresponding to altitudes ranging from 70,000 ft to 120,000 ft at Mach 14 and from 40,000 ft to 120,000 ft at Mach 10 (fullscale). In 1982, test objectives required a higher altitude simulation at Mach 14. Tunnel 9 had to be operated at lower supply pressure thereby producing lower Reynolds numbers. However, the existing compressor plant could not maintain a low enough sphere pressure for tunnel start-up. A supersonic ejector was added in series with the compressor plant which enabled the tunnel to operate at a supply pressure of 100 psia ( $Re/ft = 90,000$ ).

Average run time in Tunnel 9 at Mach 14 is a function of supply pressure. For a typical high Reynolds number ( $4.0E + 06/ft$ ) run, the time from diaphragm rupture to flow breakdown is about 1.3 seconds with nearly 0.8 seconds of steady condensation-free flow. Figure 3 graphically illustrates the timing sequence for a Tunnel 9 run. For this operation the run time is dictated by the initial volume of hot gas in the heater. At the lower Reynolds number ( $1.0E + 05$ ), steady condensation-free flow can last as long as 20 seconds because the mass flow is small and the heater volume is large. In this case the run time is limited by the sphere pressure increasing to a level where the hypersonic nozzle expansion cannot be maintained.

#### TWO-STAGE EJECTOR

To decrease the Reynolds number in the test cell, the tunnel would have to operate at a lower supply pressure. The minimum supply pressure for tunnel start-up is governed by the diffuser efficiency,  $\eta$ , which is equal to the ratio of the vacuum sphere pressure,  $P_{sph}$  to the test cell pitot pressure,  $P_{o_2}$ .

Tests on a subscale sphere-cone model pitched from 0 to 90 degrees angle-of-attack were used to test the new tunnel capabilities. The subscale model effectively decreased the Reynolds number simulation further through model length scaling. Figure 1 illustrates the Reynolds number simulation for Tunnel 9. Details of the new tunnel capability and the verification tests are described below.

#### HYPERVELOCITY WIND TUNNEL 9 OPERATION

The Hypervelocity Wind Tunnel 9 is a blowdown facility that can be operated at either Mach 10 or 14. The tunnel has a five-foot diameter test cell and uses nitrogen as the working fluid. Generally, the operation of Tunnel 9 is as follows. Prior to each wind tunnel run, a fixed volume of nitrogen is simultaneously heated and pressurized in the heater vessel. The test section and vacuum sphere are evacuated to a low pressure and are separated from the heater vessel by a series of metal diaphragms. When the nitrogen in the heater reaches the proper temperature and pressure, the diaphragms are ruptured and the gas flows out of the top of the heater and expands through the nozzle. As the hot nitrogen exits the heater, cold gas from pressurized driver vessels is allowed to enter the bottom of the heater. The cold gas drives the hot gas at a constant pressure in a piston-like fashion and allows constant supply conditions to be maintained for a relatively long period of time compared to impulse facilities. Models can be swept through angles of attack from 0 to 50 degrees during the steady flow period.

Traditionally, Tunnel 9 has been operated as a high mass flow, high Reynolds number facility (Mach 14,  $Re/ft = 4.0E + 05$  to  $4.0E + 06$ , Mach 10,  $Re/ft =$

## INTRODUCTION

In the last two decades the high altitude, high angle-of-attack aerodynamics of reentry vehicles travelling at hypersonic speeds have been of considerable interest to the strategic community. Accurate simulation of the high altitude environment in a ground test facility has been difficult. At a given Mach number, altitude simulation increases as Reynolds number decreases. In 1982, the operation of the Mach 14 leg of the Naval Surface Weapons Center Hypervelocity Wind Tunnel 9 was modified so that a Reynolds number as low as 90,000/ft could be attained in the test cell (see ref. 1). The new high altitude capability supported tests in which porous blowing models simulated asymmetric heatshield outgassing (see refs. 1 and 2). At this low Reynolds number the tunnel supply pressure was 100 psia and the Mach number was 13.1.

In March, 1984 two facility modifications allowed Tunnel 9 to operate at a lower freestream Reynolds number of 50,000/ft. First, a second supersonic ejector was incorporated in the vacuum system to maintain a lower test section pressure so that Tunnel 9 could be operated at a lower supply pressure of 60 psia. Secondly, the tunnel heater was operated in a "compression heating" mode which provided for an increased tunnel supply temperature. Pressure and temperature surveys of the flowfield were obtained and the test core was found to maintain its uniformity at the new operating conditions.

### NOMENCLATURE

$\alpha$	=	Angle-of-attack
$\eta$	=	Diffuser efficiency, $P_{sph}/P_{o_2}$
$P_o$	=	Tunnel supply pressure
$P_{o_2}$	=	Test section pitot pressure
$P_{sph}$	=	Sphere pressure
$P_T$	=	Pitot pressure
$Re/ft$	=	Freestream Reynolds number
$Re L$	=	Reynolds number based on model length
$T_o$	=	Tunnel supply temperature
$X_{CP}/L$	=	Center-of-pressure location normalized by model length



LOW REYNOLDS NUMBER HYPERSONIC

TESTING IN THE NSWC

HYPERVELOCITY WIND TUNNEL 9

by

Eric R. Hedlund

William C. Ragsdale

Robert L. P. Voisinet

Naval Surface Weapons Center  
Silver Spring, Maryland 20910

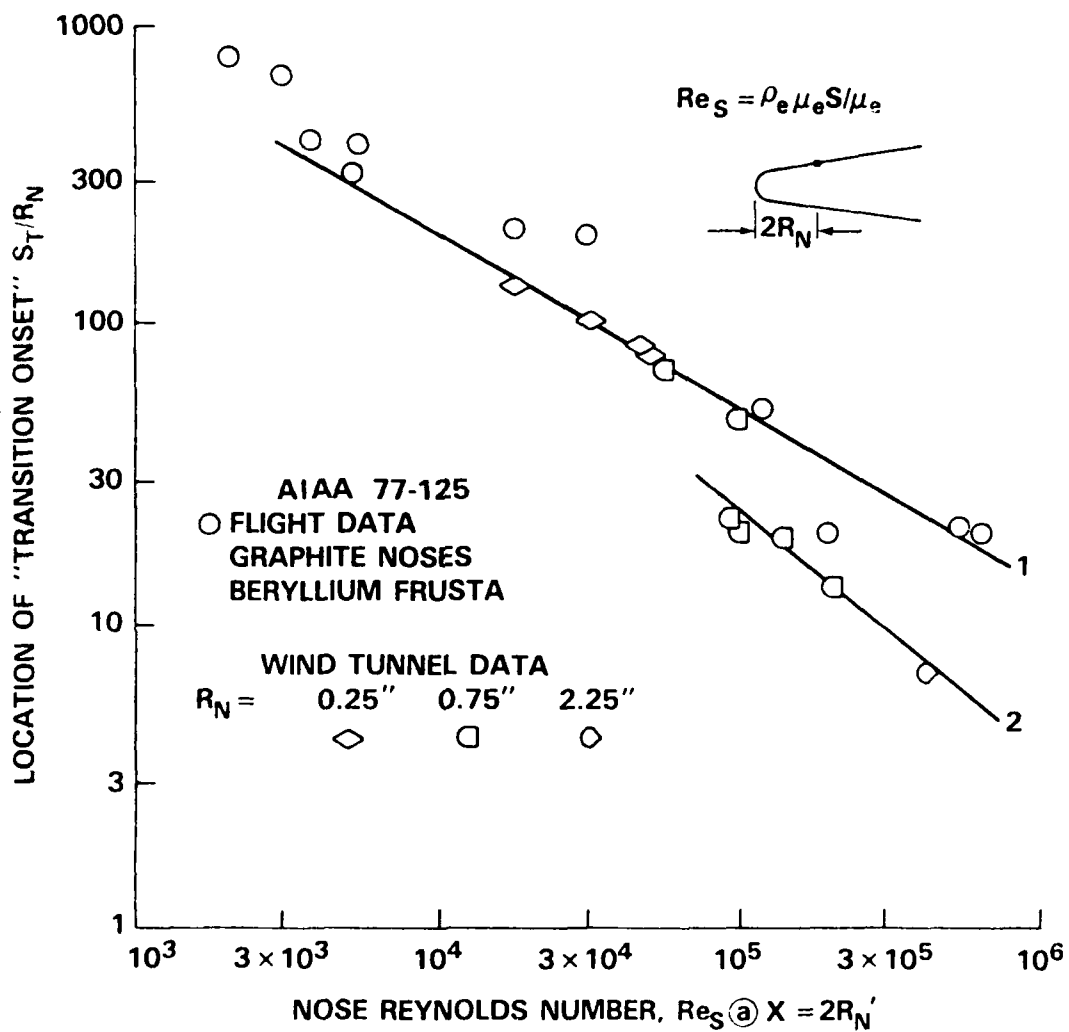


FIGURE 11. COMPARISON OF FLIGHT & WIND-TUNNEL DATA

(REFERENCE ENTROPY IS FREE-STREAM VALUE)

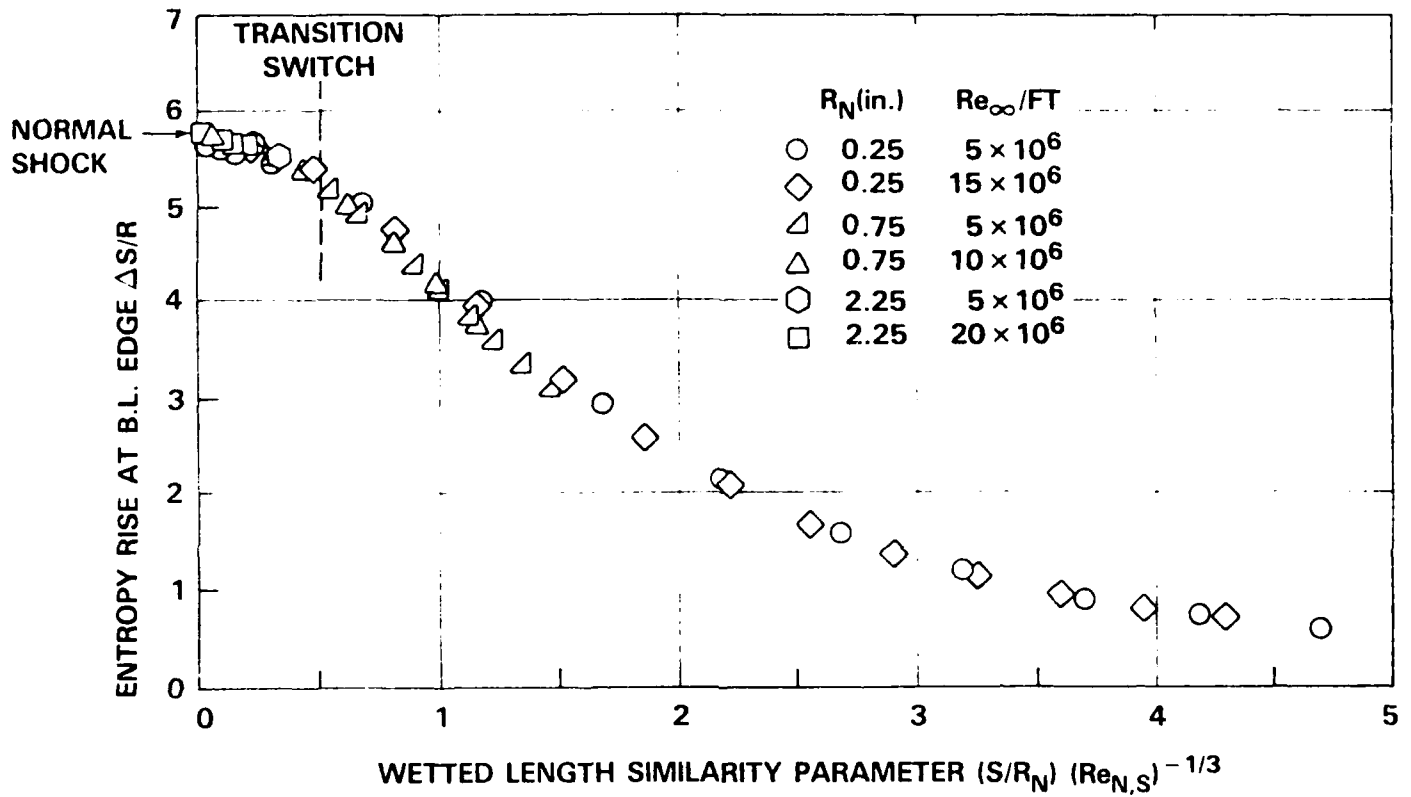


FIGURE 10. ENTROPY LAYER SWALLOWING (GE 3-D VISCOUS CODE)

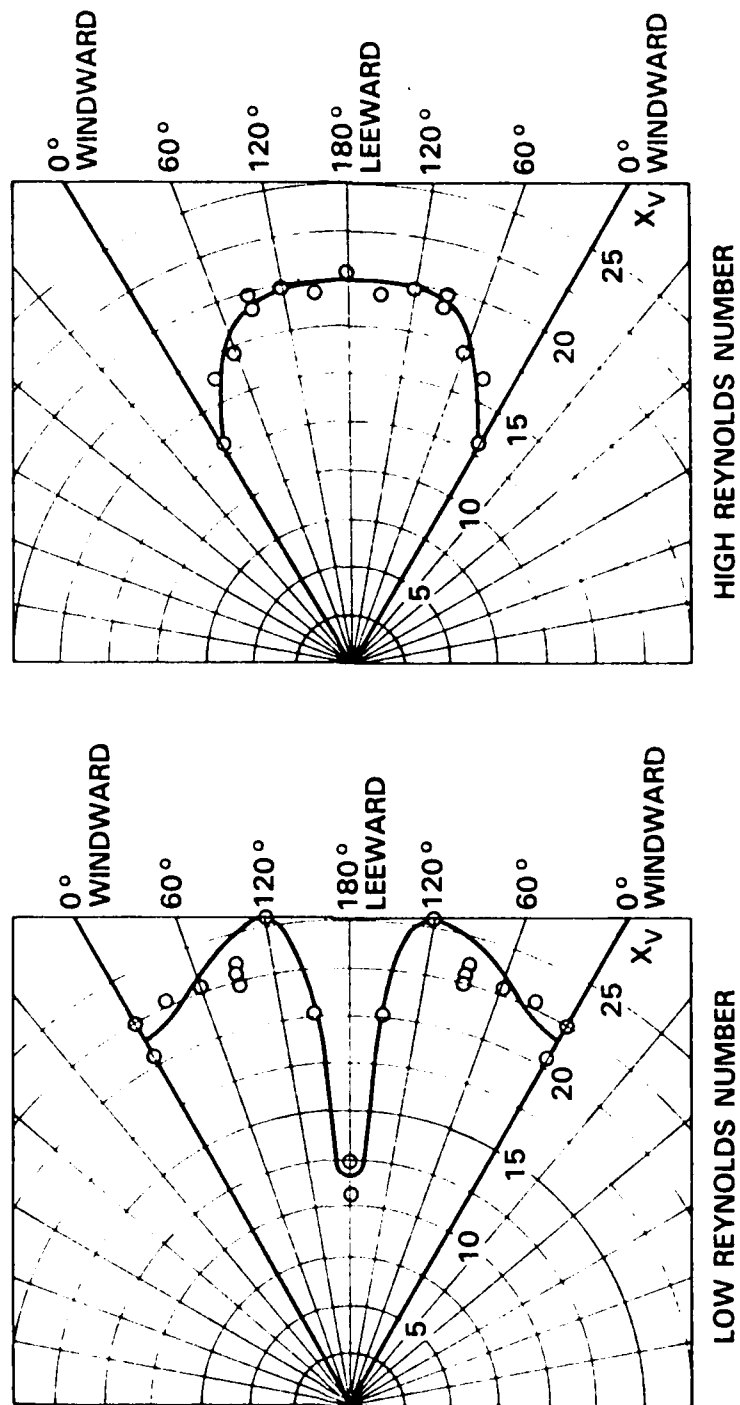


FIGURE 9. TRANSITION FRONT SHAPE AT ANGLE OF ATTACK =  $2^\circ$

Three Reynolds numbers were tested and static forces and moments were measured. The angle-of-attack ranged from 0 - 90 degrees. The following is a matrix of test conditions:

<u>RUN</u>	<u>P<sub>0</sub> (psi)</u>	<u>Re/ft</u>	<u>Mach</u>	<u><math>\alpha</math></u>	<u>Re<sub>L</sub> (model length)</u>
1	380	180,000	13.2	0 - 45	90,000
2	380	180,000	13.2	45 - 90	90,000
3	100	80,000	13.0	0 - 45	40,000
4	100	80,000	13.0	45 - 90	40,000
5	60	50,000	12.9	0 - 45	25,000
6	60	50,000	12.9	45 - 90	25,000

Figure 20 shows normal force coefficient vs. angle-of-attack at a supply pressure of 60 psia (Re<sub>L</sub> = 25,000). Data obtained for the other two conditions agreed with the 60 psia data within the experimental accuracy. Results (see ref. 2) for the same configuration at Re<sub>L</sub> = 360,000 are plotted for comparison. Data obtained at the lower Reynolds number seems to be consistent with other data at the higher Reynolds number. Figure 21 shows normalized center-of-pressure vs. angle-of-attack at Re<sub>L</sub> = 25,000. Again, results from reference 2 are plotted and appear consistent. Further data analysis is also ongoing.

#### SUMMARY

The capabilities of the NSWC Hypervelocity Wind Tunnel 9 have been extended to simulate higher altitudes. A second ejector has been installed to allow operation at a supply pressure of 60 psia. Compression heating has been used to increase the supply temperature. High quality flow is obtained in a large core diameter. Static forces and moments on a subscale model have been successfully measured in a series of verification tests.

## REFERENCES

1. Roberts, M. M., Voisinet, R. L. P., Hedlund, E. R., and Fiscina, C. "Extended Capabilities for High-Altitude Reentry Simulation in the NSWC Hypervelocity Wind Tunnel." AIAA-84-0412, Jan 1984.
2. Fiscina, C. Voisinet, R. L. P., Hedlund, E. R., and Roberts, M. M. "High Altitude Aerodynamic Tests with Simulated Heatshield Outgassing." NSWC-MP-82-572, Dec 1982.
3. Engineering Incorporated, "Tunnel 9 Vacuum System Ejector Analysis," EI-212-R-463, Hampton, Va., Jan 1984.
4. Kavetsky, Robert A. "Mach 10/14 Operations in the NSWC Hypervelocity Wind Tunnel No. 9 (Vertical Heater Vessel Leg)." NSWC-TR-80-487, Jul 1982.
5. Voisinet, Robert L. P. "Flowfield Surveying Techniques Used in the NSWC Hypervelocity Wind Tunnel No. 9." Proceedings of the ICIASF, Sep 1981.
6. Yanta, William J. "A Fine-Wire Stagnation Temperature Probe." NOL-TR-70-81, Jun 1970.
7. Vas, Irwin E. "Flowfield Measurements using a Total Temperature Probe at Hypersonic Speeds." AIAA Journal, Vol. 10, No. 3, Mar 1972.
8. Uselton, Bob. L. and Cyran, Fred B. "Critical Sting Length as Determined by the Measurement of Pitch-Damping Derivatives for Laminar, Transitional, and Turbulent Boundary Layers at Mach Number 3 for Reduced Frequencies of 0.0033 and 0.0056." AEDC-TR-77-66, Jul 1977.

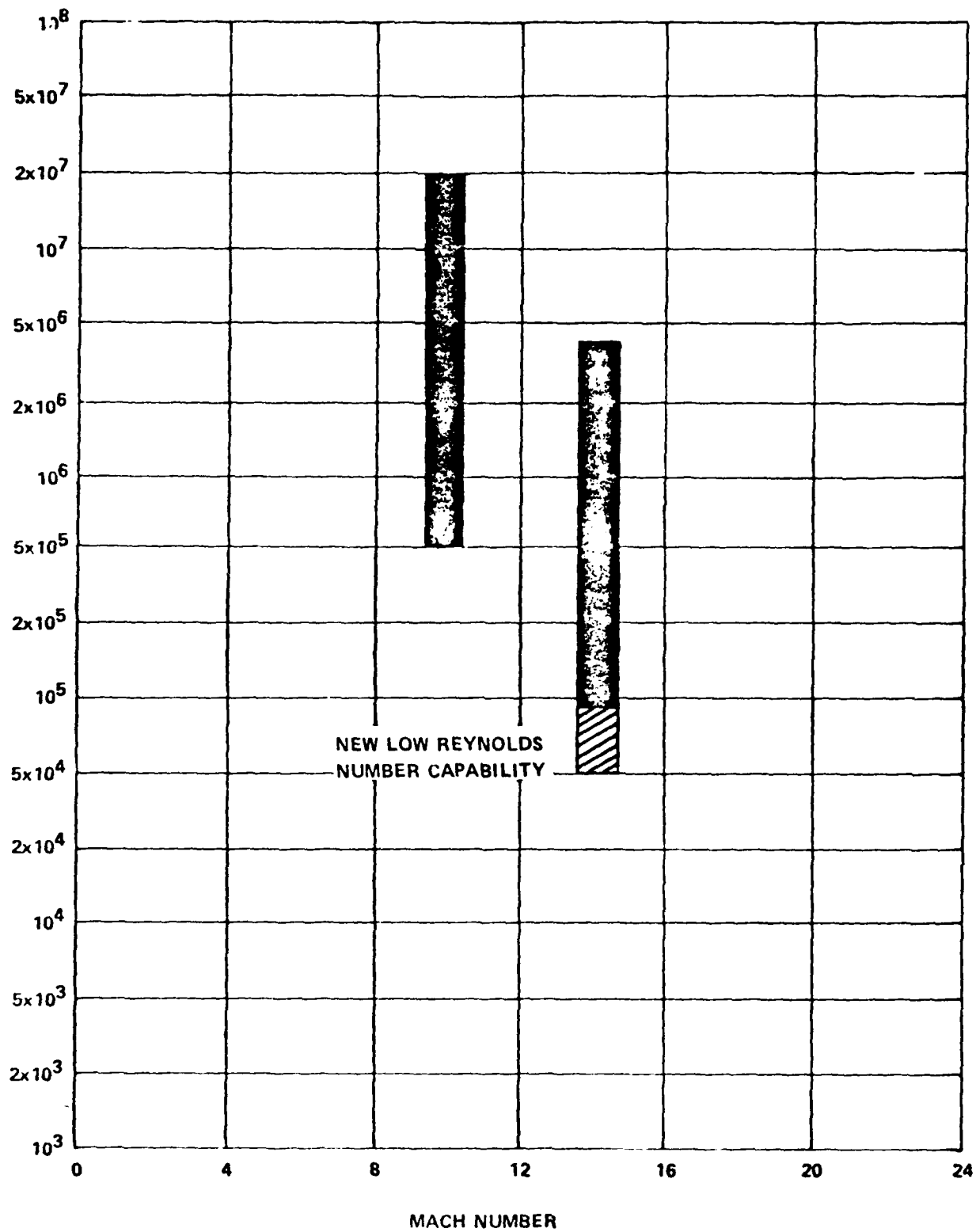


FIGURE 1 REYNOLDS NUMBER CAPABILITY FOR TUNNEL 9

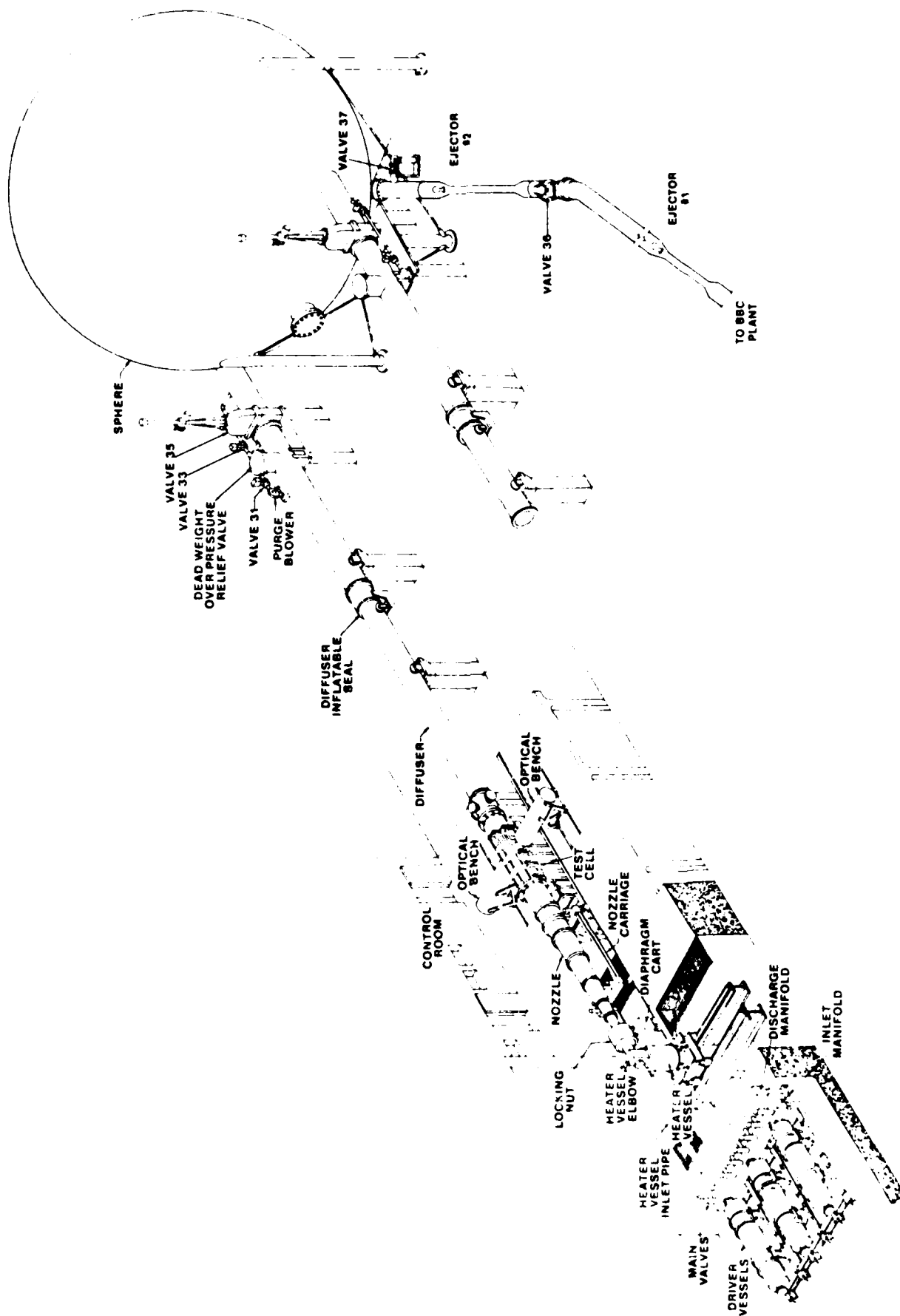


FIGURE 2. HYPERVELOCITY TUNNEL NO. 9



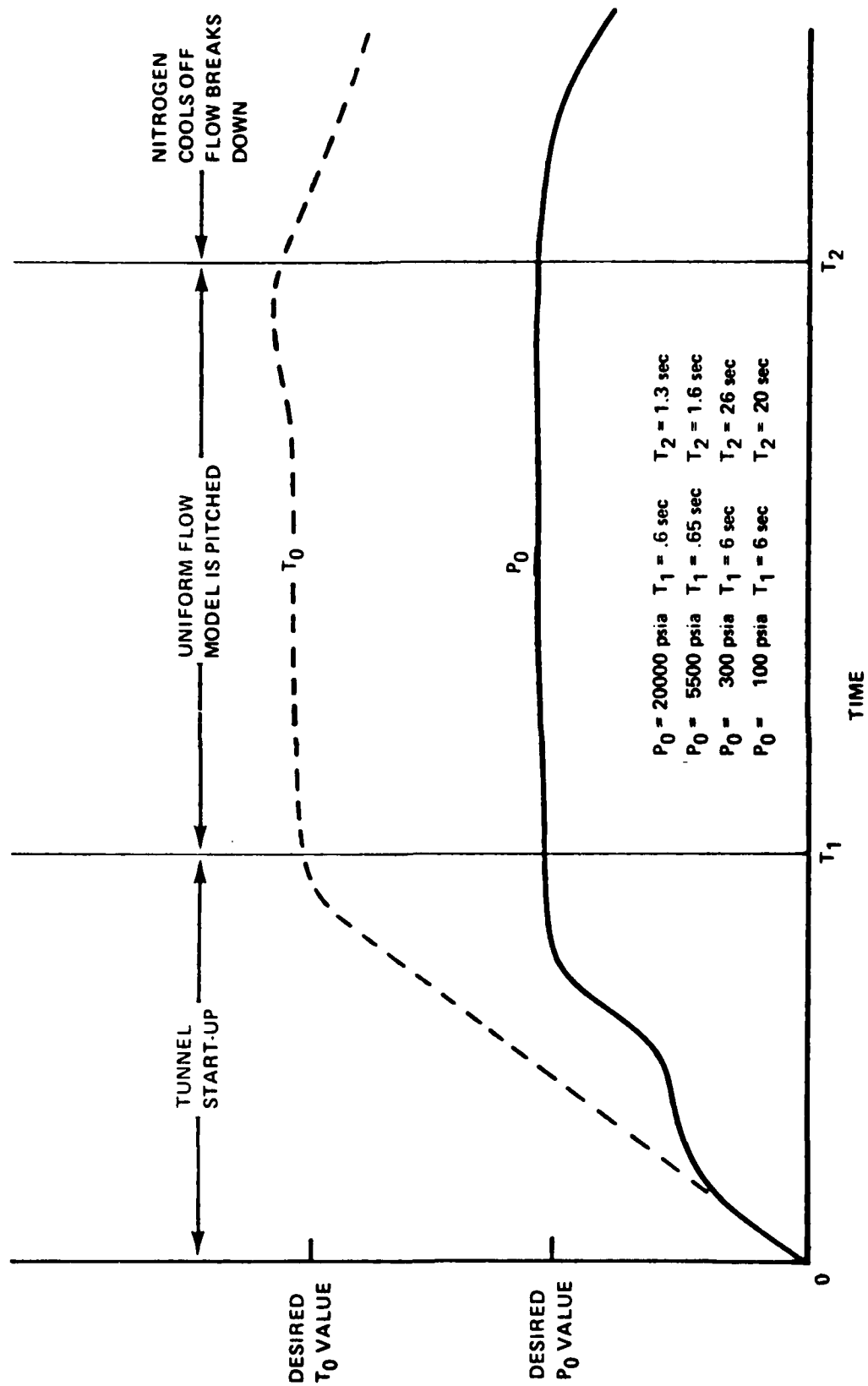


FIGURE 3. TIME SEQUENCE OF EVENTS FOR TUNNEL 9

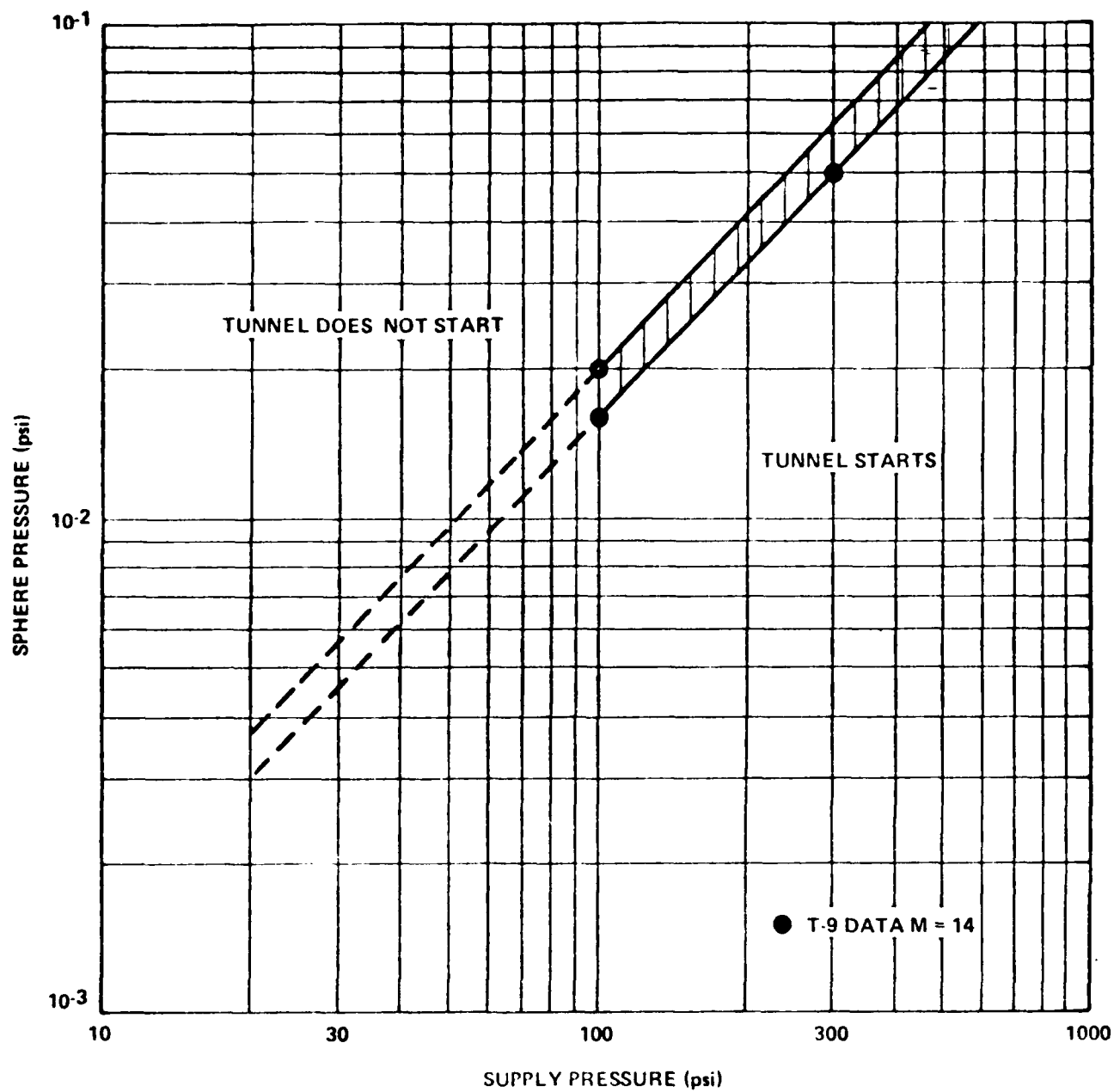


FIGURE 4. SPHERE PRESSURE vs. SUPPLY PRESSURE

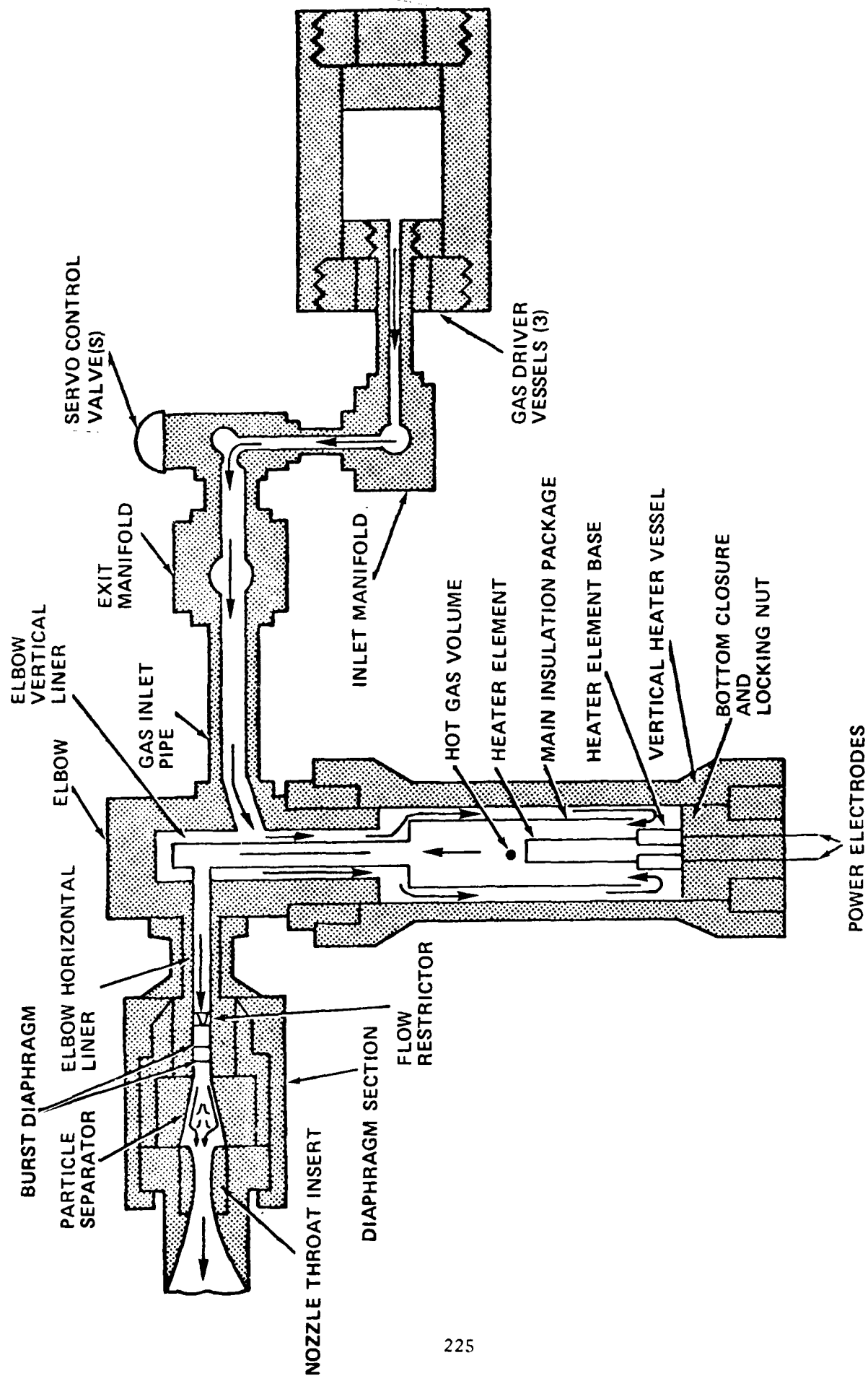


FIGURE 5. TUNNEL 9 VERTICAL HEATER AND FLOW PASSAGE ARRANGEMENT

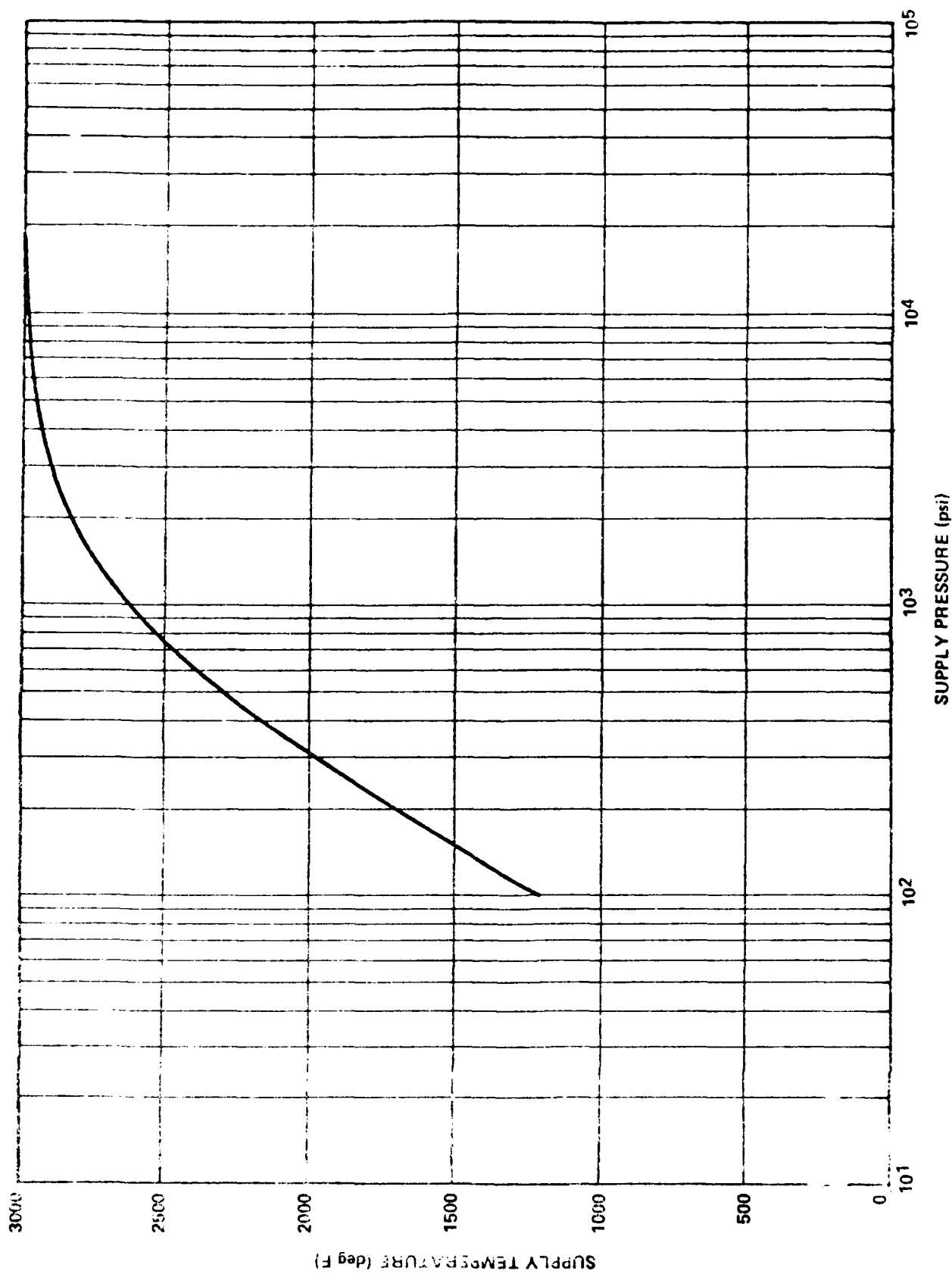


FIGURE 6. SUPPLY TEMPERATURE vs. SUPPLY PRESSURE

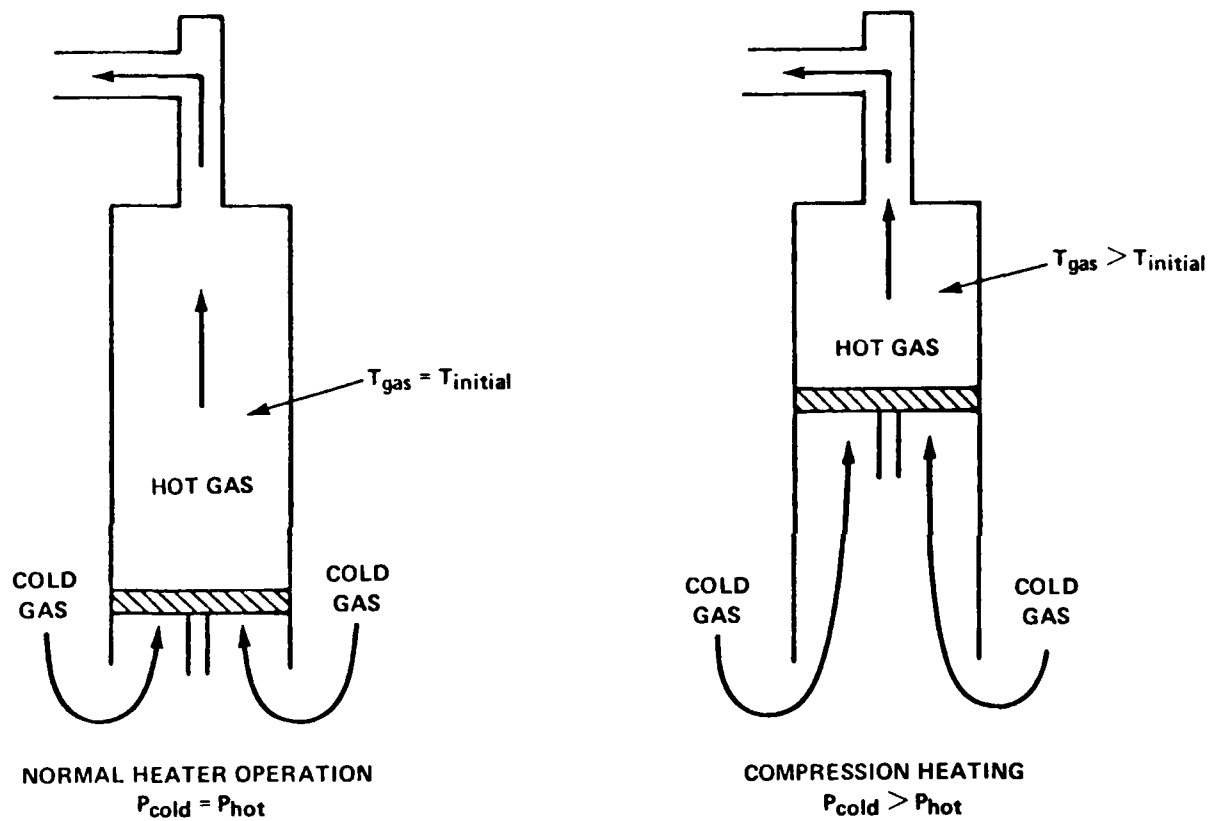


FIGURE 7. NORMAL AND "COMPRESSION HEATING" MODE OF OPERATION

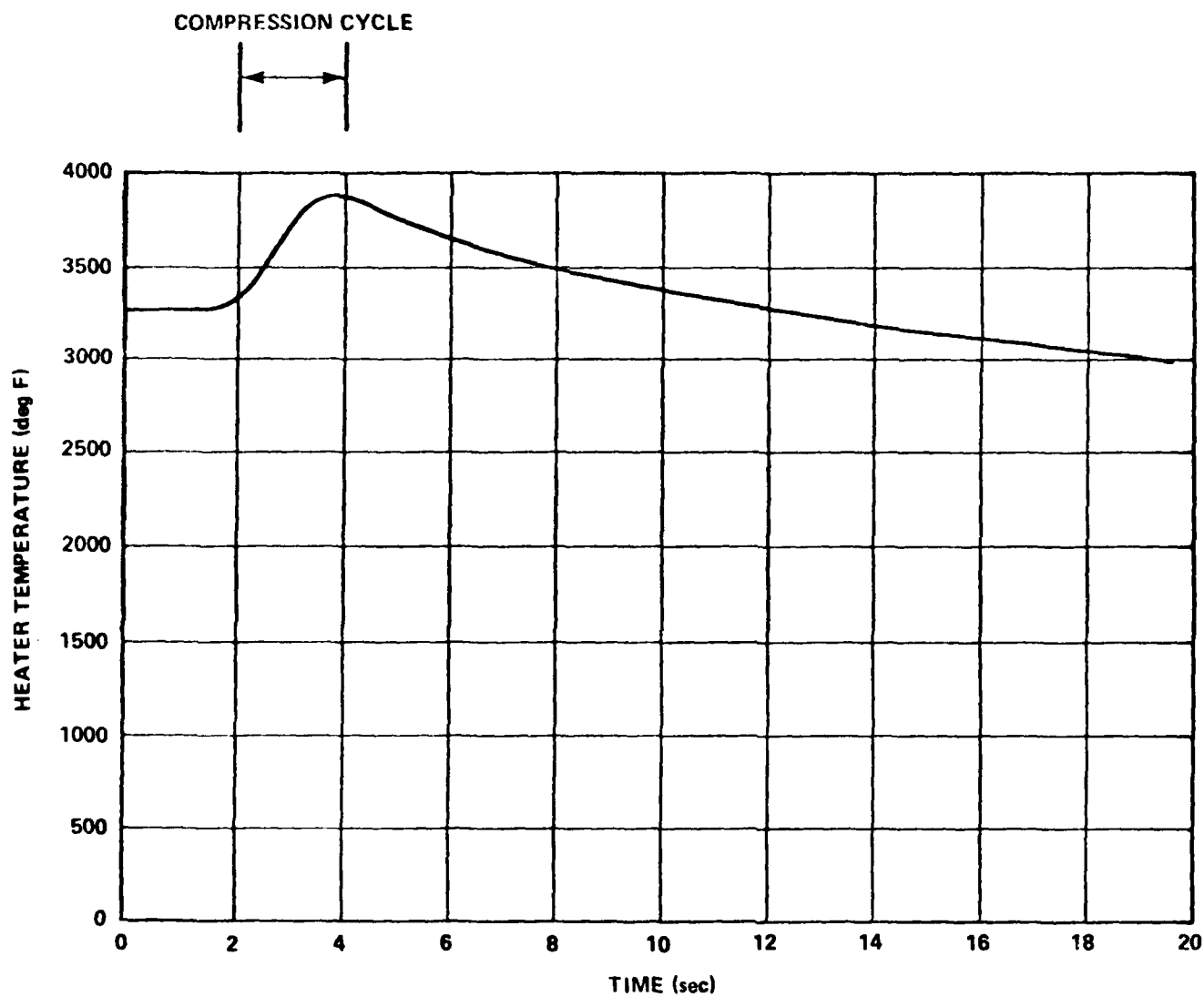


FIGURE 8. HEATER TEMPERATURE WITH COMPRESSION HEATING

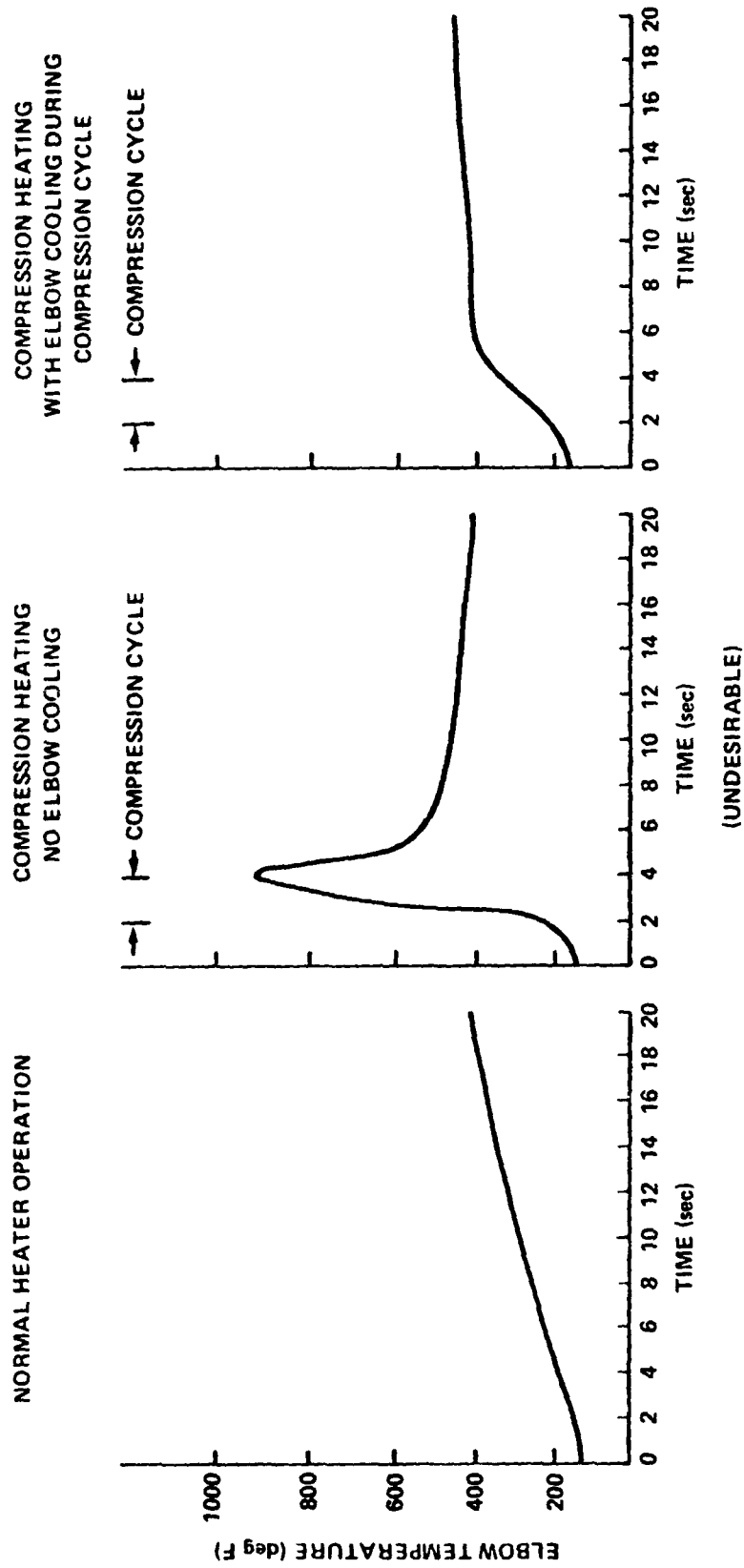


FIGURE 9. ELBOW TEMPERATURE FOR DIFFERENT MODES OF HEATER OPERATION

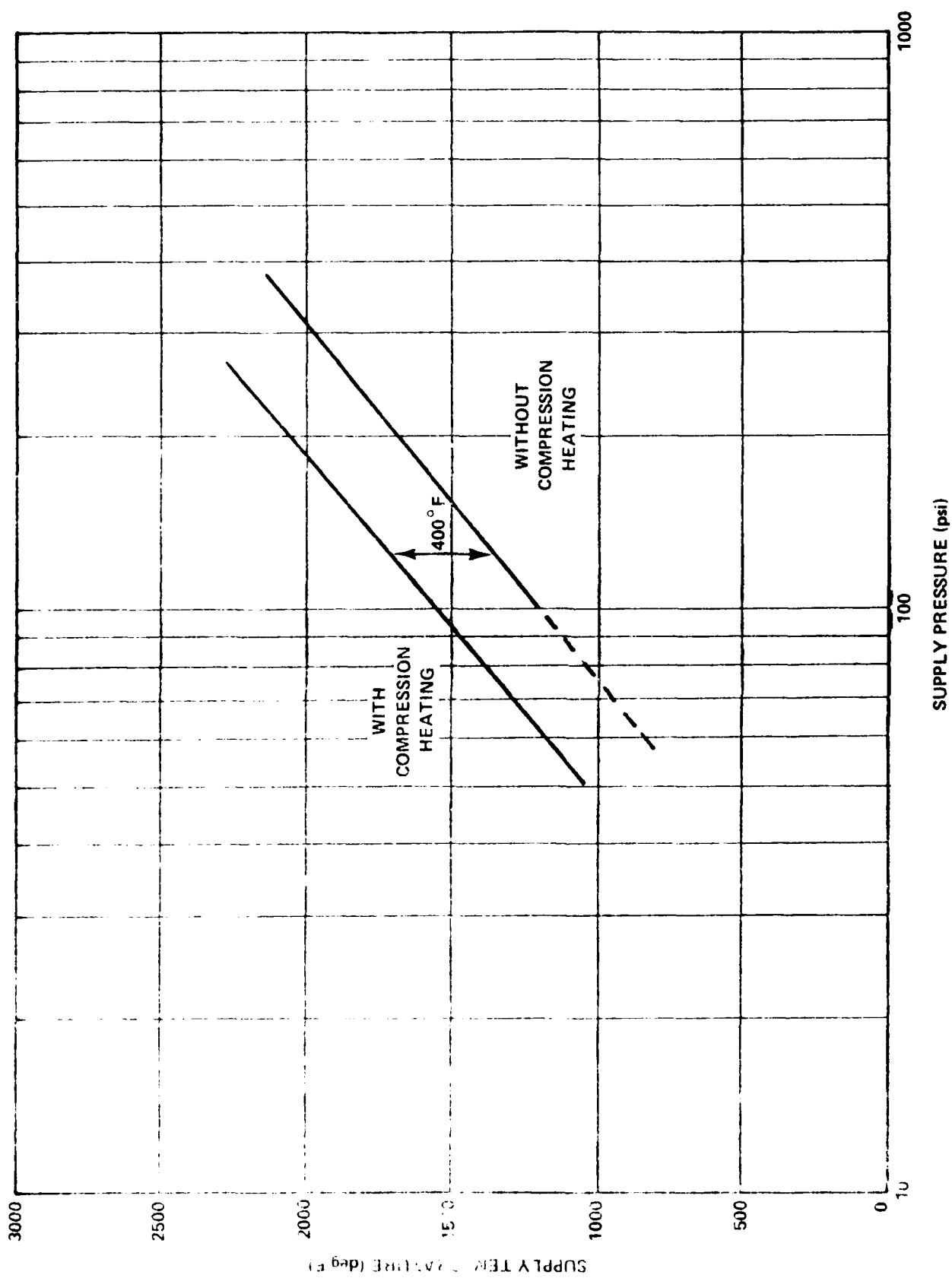


FIGURE 10. SUPPLY TEMPERATURE vs. SUPPLY PRESSURE



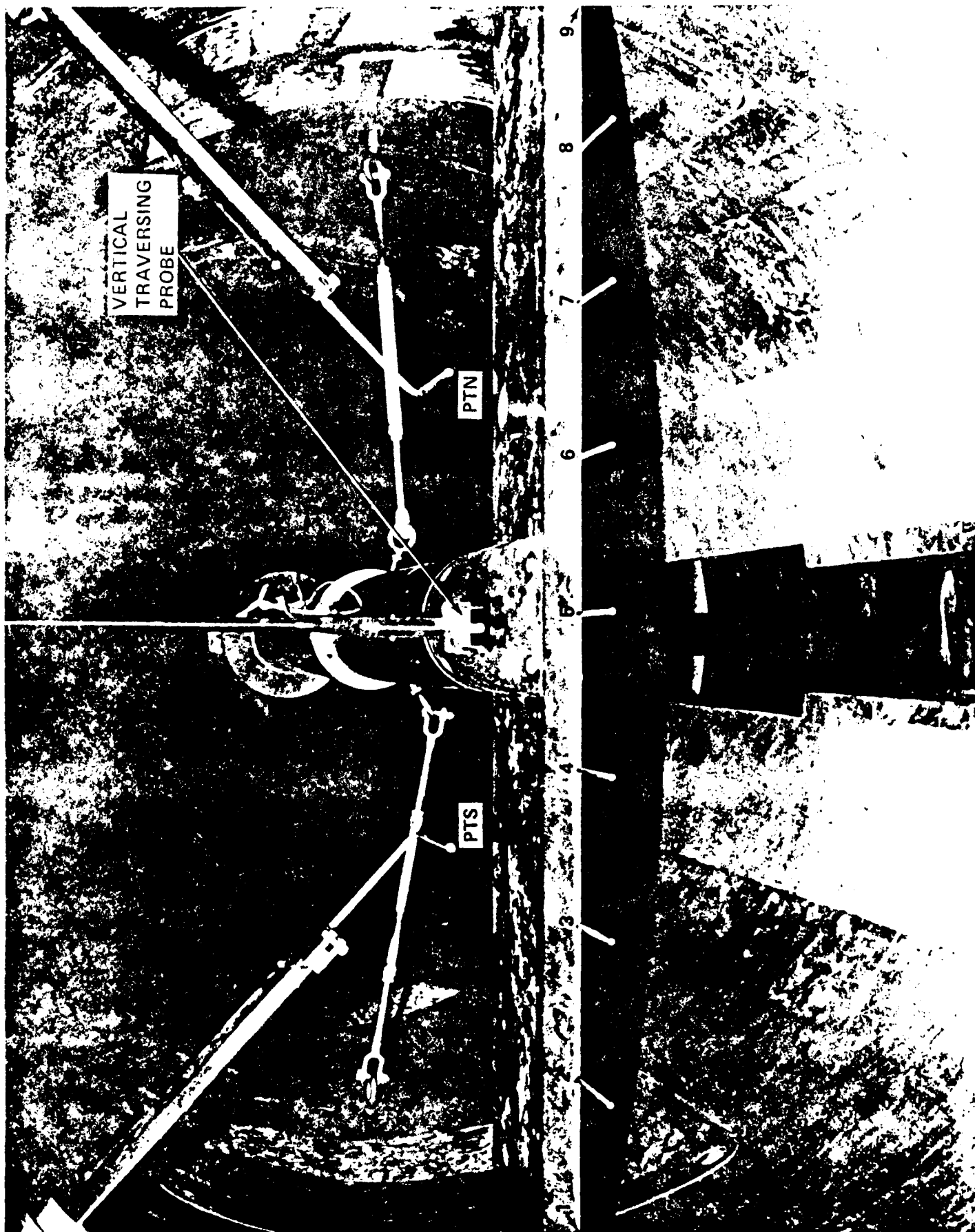


FIGURE 11. PITOT ARRANGEMENT

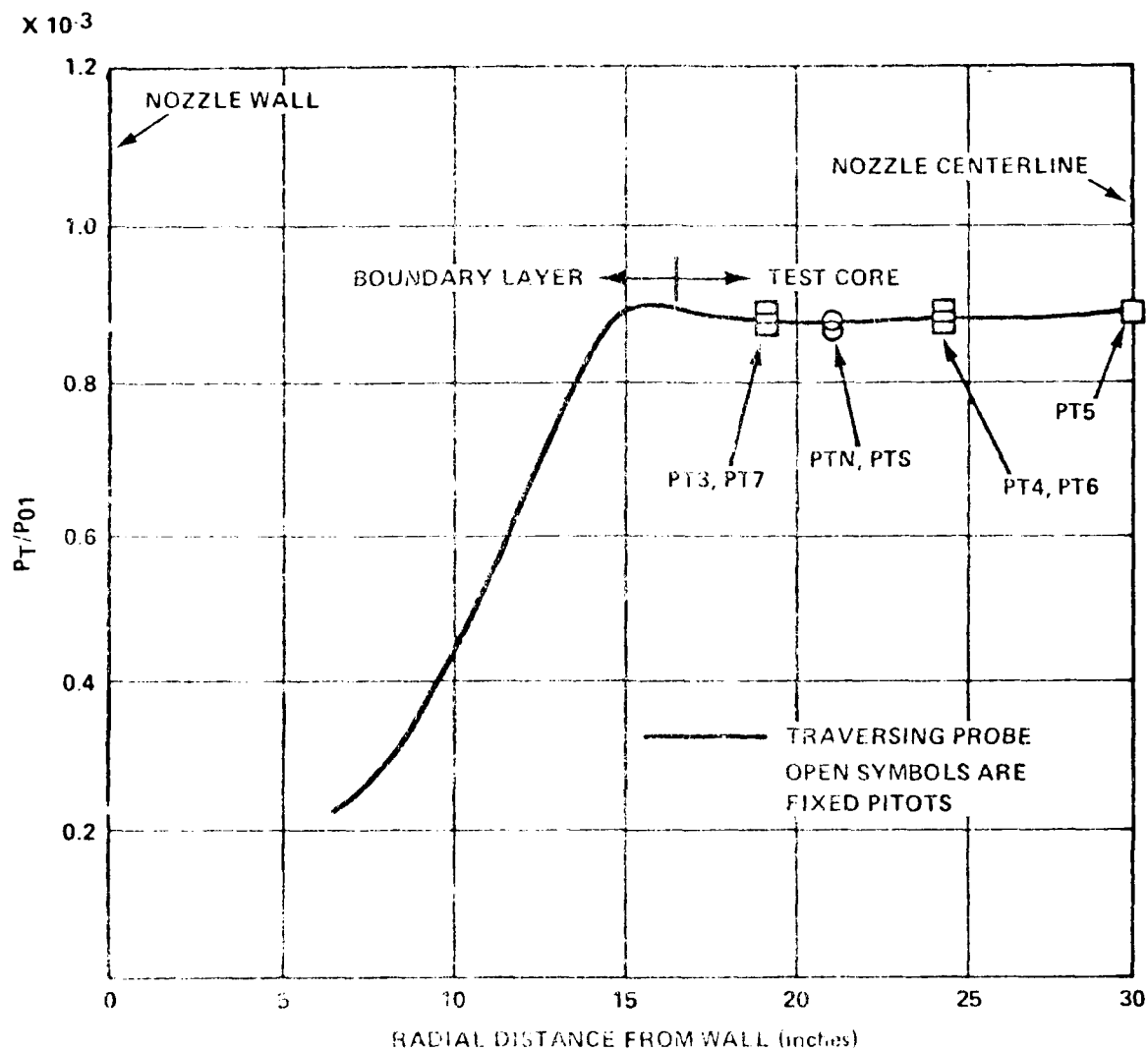


FIGURE 12 TYPICAL PITOT SURVEY

Equation (1) is solved first for the mean flow quantities. Next the turbulence field equations (2) are solved for  $k$  and  $\epsilon$  using the just computed mean flow quantities. The turbulent viscosity  $\mu_t$  is related to the turbulent kinetic energy,  $k$  and the turbulent dissipation rate,  $\epsilon$  and is computed then as follows:

$$\mu_t = C_\mu \rho \frac{k^2}{\epsilon} \quad (3)$$

This becomes the input in equation (1) which is solved for the mean flow variables. This process is continued at each time step until steady state results are achieved. The solution procedure of the turbulence field equations lag that of the mean flow equations by one time step. Calculations are extended up to the wall and  $k = \epsilon = 0$  are used at the wall. In the outer far field boundary, zero derivatives of  $k$  and  $\epsilon$  i.e.,  $\frac{\partial k}{\partial \zeta} = \frac{\partial \epsilon}{\partial \zeta} = 0$  are used. First order extrapolation is usually used at the other boundaries.

#### IV. Results

Numerical computations have been made for transonic turbulent flow over an axisymmetric projectile. Both the algebraic and the two-equation  $k$ - $\epsilon$  eddy viscosity turbulence models were used. Computed results are presented in the form of surface pressure plots, velocity, turbulent kinetic energy, turbulent dissipation rate and turbulent eddy viscosity profiles. Comparison with experimental data has been made to assess the performance of both turbulence models.

All the computed results shown are for  $\alpha = 0^\circ$ ,  $Re = 13 \times 10^6/m$  and  $M = 0.94$  and  $0.97$ . Numerical results are compared with experimental measurements<sup>11,12</sup> performed for the same shape in the NASA Langley Research Center 8 foot Transonic Pressure Tunnel.

The model geometry is shown in Figure 1. It is an artillery projectile consisting of a secant-ogive nose, a cylindrical mid-section and a  $7^\circ$  conical afterbody or boattail of half a caliber (one caliber  $\equiv$  one diameter).

The computational grid used for the numerical computations was obtained from a versatile grid generation program developed by Steger et al<sup>13</sup>. This program allows arbitrary grid point clustering thus enabling grid points to be clustered near the body surface. The full grid is shown in Figure 2. The computational domain extended to four model lengths in front, four model lengths in the normal direction and four model lengths behind the projectile. Such an extended domain is used to eliminate the possibility of any wave reflection back on to the model. The grid consists of 78 points in the longitudinal direction and 40 points in the normal direction. An expanded view of the grid near the model is shown in Figure 3. The dark region near the model surface results from clustering of grid points which are needed to resolve the viscous boundary layer region. The grid points in the normal direction were exponentially stretched away from the surface with a minimum spacing at the wall of .00002 D. This spacing locates at least two to three points within the laminar sublayer. Clustering in the longitudinal direction was used at

sity of finding the outer edge of the boundary layer. The details of the model can be found in Reference 8.

## B. Two-Equation Model

The two-equation model used here is Chien's<sup>9</sup> k-ε model which is similar to that of Jones and Launder<sup>10</sup>. To be consistent with the mean flow equations, the turbulent kinetic energy and dissipation rate equations have been transformed to a body-fitted coordinate system. These equations are also marched in time to obtain a steady state solution. These equations can be written in a form similar to Equation (1),

$$\frac{\partial \hat{q}_t}{\partial \tau} + \frac{\partial \hat{E}_t}{\partial \xi} + \frac{\partial \hat{G}_t}{\partial \zeta} = \frac{1}{Re} \left( \frac{\partial \hat{H}_t}{\partial \zeta} + \hat{S}_t \right) \quad (2)$$

where

$$\hat{q}_t = \frac{1}{J} \begin{bmatrix} \rho k \\ \rho \epsilon \end{bmatrix}$$

$$\hat{E}_t = \frac{1}{J} \begin{bmatrix} \rho k U \\ \rho \epsilon U \end{bmatrix}, \quad \hat{G}_t = \frac{1}{J} \begin{bmatrix} \rho k W \\ \rho \epsilon W \end{bmatrix}$$

$$\hat{H}_t = \frac{1}{J} \begin{bmatrix} (\zeta_x^2 + \zeta_y^2 + \zeta_z^2) \left( \frac{\mu_t}{\sigma_k} + \mu \right) \frac{\partial k}{\partial \zeta} \\ (\zeta_x^2 + \zeta_y^2 + \zeta_z^2) \left( \frac{\mu_t}{\sigma_\epsilon} + \mu \right) \frac{\partial \epsilon}{\partial \zeta} \end{bmatrix}$$

$$\hat{S}_t = \frac{1}{J} \begin{bmatrix} \rho - \rho \epsilon Re - 2\mu \frac{k}{y_n^2} \\ \left( 1 - \frac{\epsilon}{k} \right) \rho - C_2 \mu \frac{\epsilon^2}{k} Re - 2\mu \frac{\epsilon}{y_n^2} e^{-\frac{y}{2}} \end{bmatrix}$$

$$\mu_t = \frac{\rho}{\sigma_k} \left( \zeta_x^2 + \zeta_y^2 + \zeta_z^2 \right) \left( u^2 + v^2 + w^2 \right) + \mu_t \left( \zeta_x u_\zeta + \zeta_y v_\zeta + \zeta_z w_\zeta \right)^2$$

$$\hat{H} = J^{-1} \begin{bmatrix} 0 \\ 0 \\ \rho V [R_{\xi}(U - \xi_t) + R_{\zeta}(W - \zeta_t)] \\ -\rho VR (V - \eta_t) - p/R \\ 0 \end{bmatrix}$$

$$\hat{S} = \begin{bmatrix} 0 \\ \mu(\zeta_x^2 + \zeta_y^2 + \zeta_z^2)u_{\zeta} + (\mu/3)(\zeta_x u_{\zeta} + \zeta_y v_{\zeta} + \zeta_z w_{\zeta})\zeta_x \\ \mu(\zeta_x^2 + \zeta_y^2 + \zeta_z^2)v_{\zeta} + (\mu/3)(\zeta_x u_{\zeta} + \zeta_y v_{\zeta} + \zeta_z w_{\zeta})\zeta_y \\ \mu(\zeta_x^2 + \zeta_y^2 + \zeta_z^2)w_{\zeta} + (\mu/3)(\zeta_x u_{\zeta} + \zeta_y v_{\zeta} + \zeta_z w_{\zeta})\zeta_z \\ \{(\zeta_x^2 + \zeta_y^2 + \zeta_z^2)[(\mu/2)(u^2 + v^2 + w^2)_{\zeta} + \kappa Pr^{-1}(\gamma - 1)^{-1}(a^2)_{\zeta}] \\ + (\mu/3)(\zeta_x u + \zeta_y v + \zeta_z w)(\zeta_x u_{\zeta} + \zeta_y v_{\zeta} + \zeta_z w_{\zeta})\} \end{bmatrix}$$

The velocities

$$U = \xi_t + \xi_x u + \xi_y v + \xi_z w$$

$$V = \eta_t + \eta_x u + \eta_y v + \eta_z w$$

$$W = \zeta_t + \zeta_x u + \zeta_y v + \zeta_z w$$

represent the contravariant velocity components. Equation (1) is solved in a time asymptotic fashion with interest only in the steady-state solution. The numerical algorithm used is a fully implicit, approximately factored finite difference scheme. The algorithm is first order accurate in time and fourth order in space. Details of the assumptions and the algorithm are included in References 5-7. For turbulent flows,  $\mu$  and  $\kappa$  consist of their molecular and the turbulent counterparts ( $\mu_t$  and  $\kappa_t$ ).

### III. Turbulence Models

#### A. Algebraic Model

The algebraic eddy viscosity model used is that developed by Baldwin and Lomax<sup>8</sup>. It is a two-layer model in which an eddy viscosity is calculated for an inner and an outer region. The inner region follows the Prandtl-Van Driest formulation. In both the inner and outer formulations, the distribution of vorticity is used to determine the length scales thereby avoiding the neces-

## I. Introduction

The critical aerodynamic behavior of projectiles occurs in the transonic speed regime. This can be attributed to the complex shock structure which exists on the projectiles at transonic speeds. The flow field for such cases is complex due to strong viscous/inviscid and shock/boundary layer interactions. It is advantageous to use the Navier-Stokes computational technique since it considers these interactions in a fully-coupled manner. This technique has been used<sup>1-4</sup> to predict the flow about slender bodies of revolution at transonic speeds.

An important element of calculating such flows described above is the turbulence modeling. The simplest model is the algebraic eddy viscosity model. However, it contains a large amount of empiricism that may not, in general, be valid for complex flows. Another class includes the two-equation model which has been popular for its less empiricism and wider applicability to a class of complex fluid flow problems. A need exists for a general turbulence model to compute the transonic turbulent flows especially in the presence of large separated region and using such a model in a thin-layer Navier-Stokes code would thus be an important advance. Implicit algorithms that simultaneously solve the mean flow equations can be extended to solve the turbulence field equations using block tridiagonal matrix inversions. The objective of this proposed paper is to incorporate into a thin-layer, time dependent Navier-Stokes code, a two-equation turbulence model which uses the same implicit algorithm and generalized geometry.

## II. Computational Technique

The Azimuthal Invariant (or Generalized Axisymmetric) thin-layer Navier-Stokes equations for general spatial coordinates  $\xi, \eta, \zeta$  can be written as<sup>1</sup>

$$\frac{\partial}{\partial \xi} \hat{G} + \frac{\partial}{\partial \zeta} \hat{E} + \frac{\partial}{\partial \zeta} \hat{G} + \hat{H} = Re^{-1} \frac{\partial}{\partial \zeta} \hat{S} \quad (1)$$

where  $\xi = \xi(x, y, z, t)$  is the longitudinal coordinate

$\eta = \eta(x, y, z, t)$  is the near normal coordinate

$t$  is the time

and

$$\hat{G} = \begin{bmatrix} \rho u \\ \rho u^2 + \xi_x p \\ \rho v u + \xi_y p \\ \rho w u + \xi_z p \\ (\rho e + p)(1 - \xi_x) \end{bmatrix}, \quad \hat{E} = \begin{bmatrix} \rho w \\ \rho u w + \xi_x p \\ \rho v w + \xi_y p \\ \rho w w + \xi_z p \\ (e + p)w - \xi_t p \end{bmatrix}, \quad \hat{H} = \hat{H}^{-1}$$

NAVIER-STOKES COMPUTATIONS OF TRANSONIC FLOW OVER A PROJECTILE  
WITH A TWO-EQUATION MODEL OF TURBULENCE

Jubaraj Sahu  
U.S. Army Ballistic Research Laboratory, AMCCOM  
Aberdeen Proving Ground, Maryland 21005

and

James E. Danberg  
Department of Mechanical and Aerospace Engineering  
University of Delaware  
Newark, Delaware 19711

Abstract

A thin-layer Navier-Stokes code has been used to compute the axisymmetric turbulent flow over a projectile at transonic speeds. The thin layer form of the compressible Navier-Stokes equations is solved using a time dependent, implicit numerical algorithm. Numerical computations have been made using zero-equation (algebraic) and two-equation (kinetic energy and length scale) turbulence eddy viscosity models. The algorithm, and how the turbulence models are incorporated into it, are described. Computed results have been obtained for a secant-ogive-cylinder-boattail shape at  $M_\infty = .94$  and  $.97$  using both models and are compared with experiment.

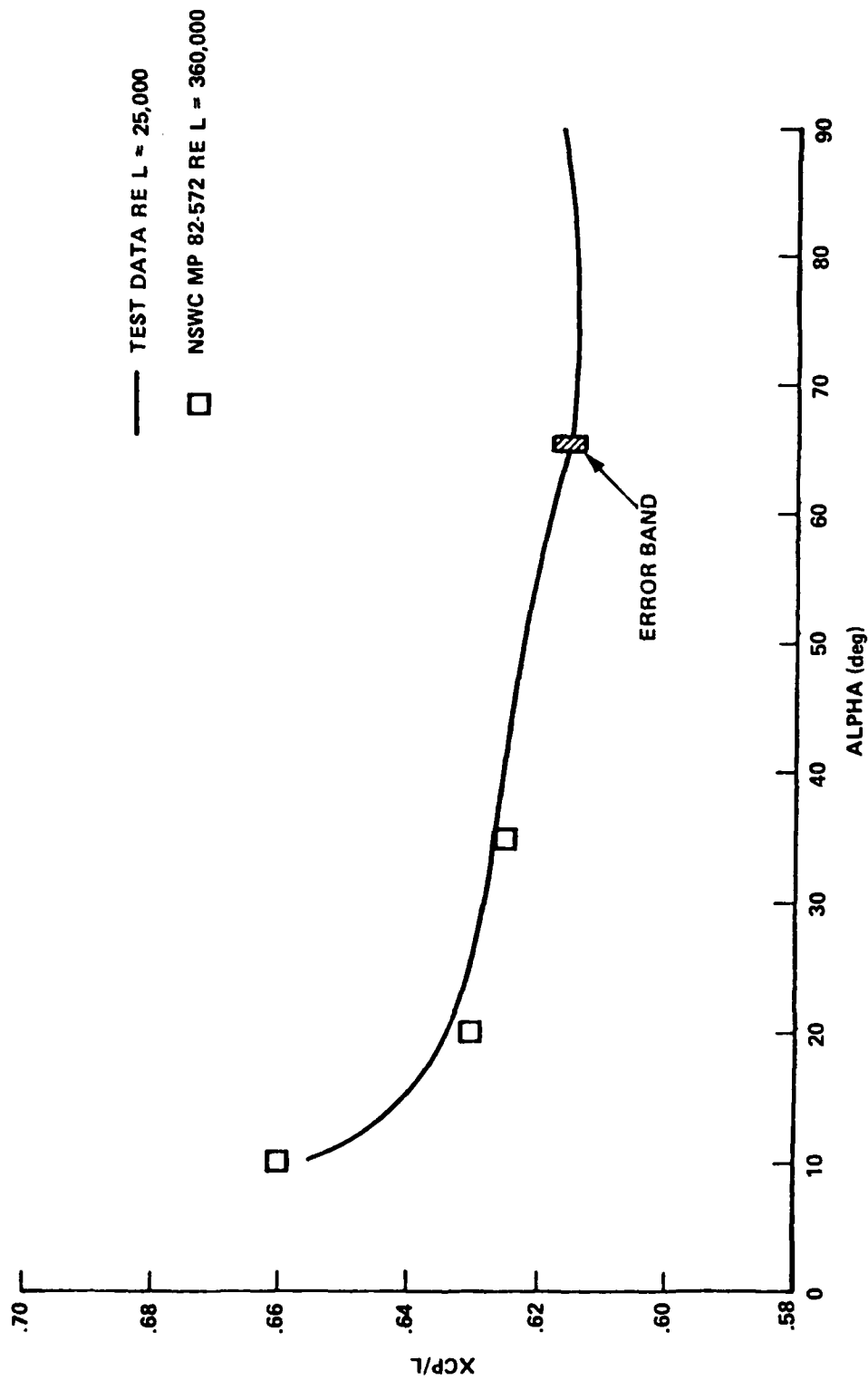


FIGURE 21.  $XCP/L$  vs.  $\alpha$



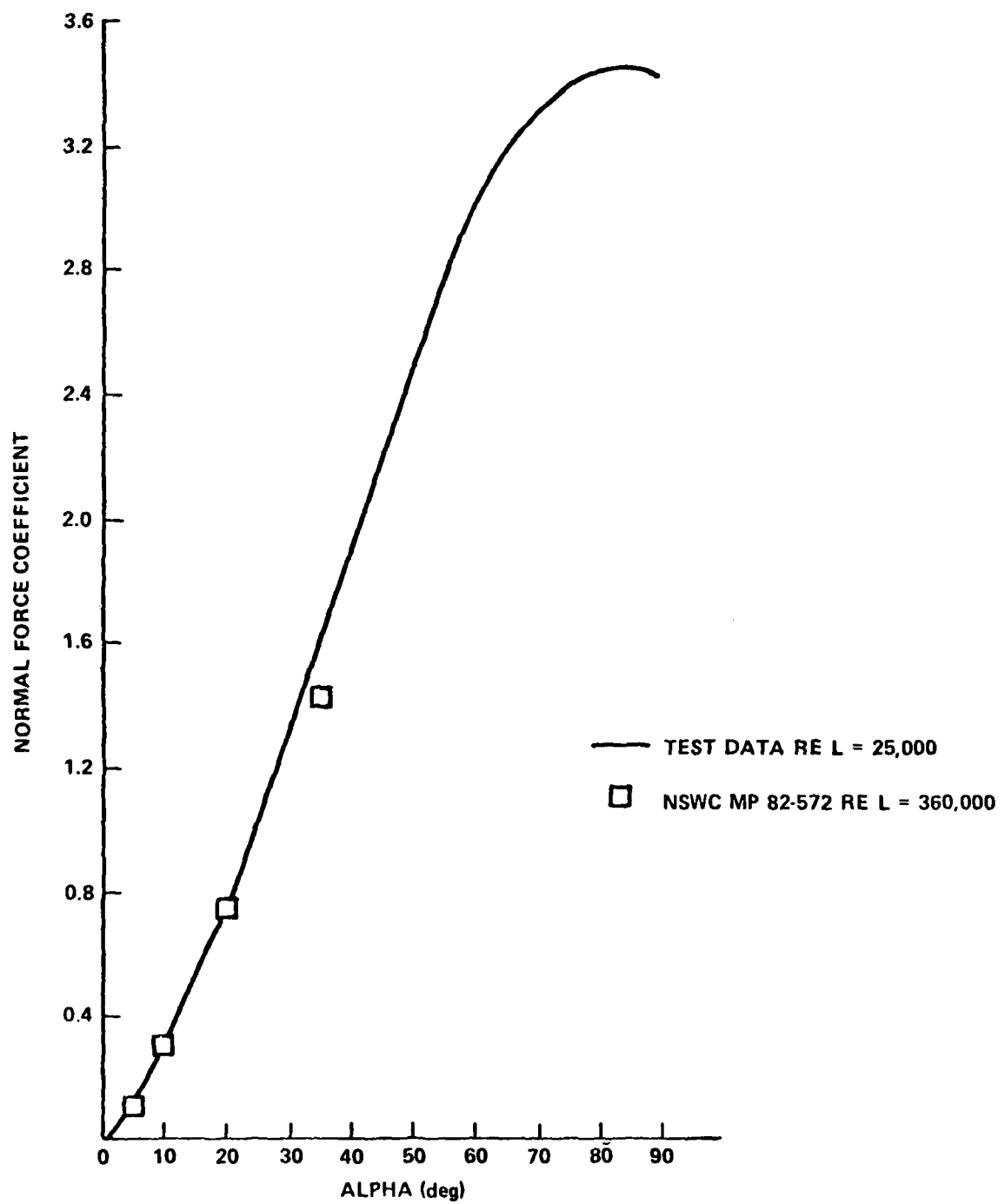


FIGURE 20. NORMAL FORCE vs.  $\alpha$

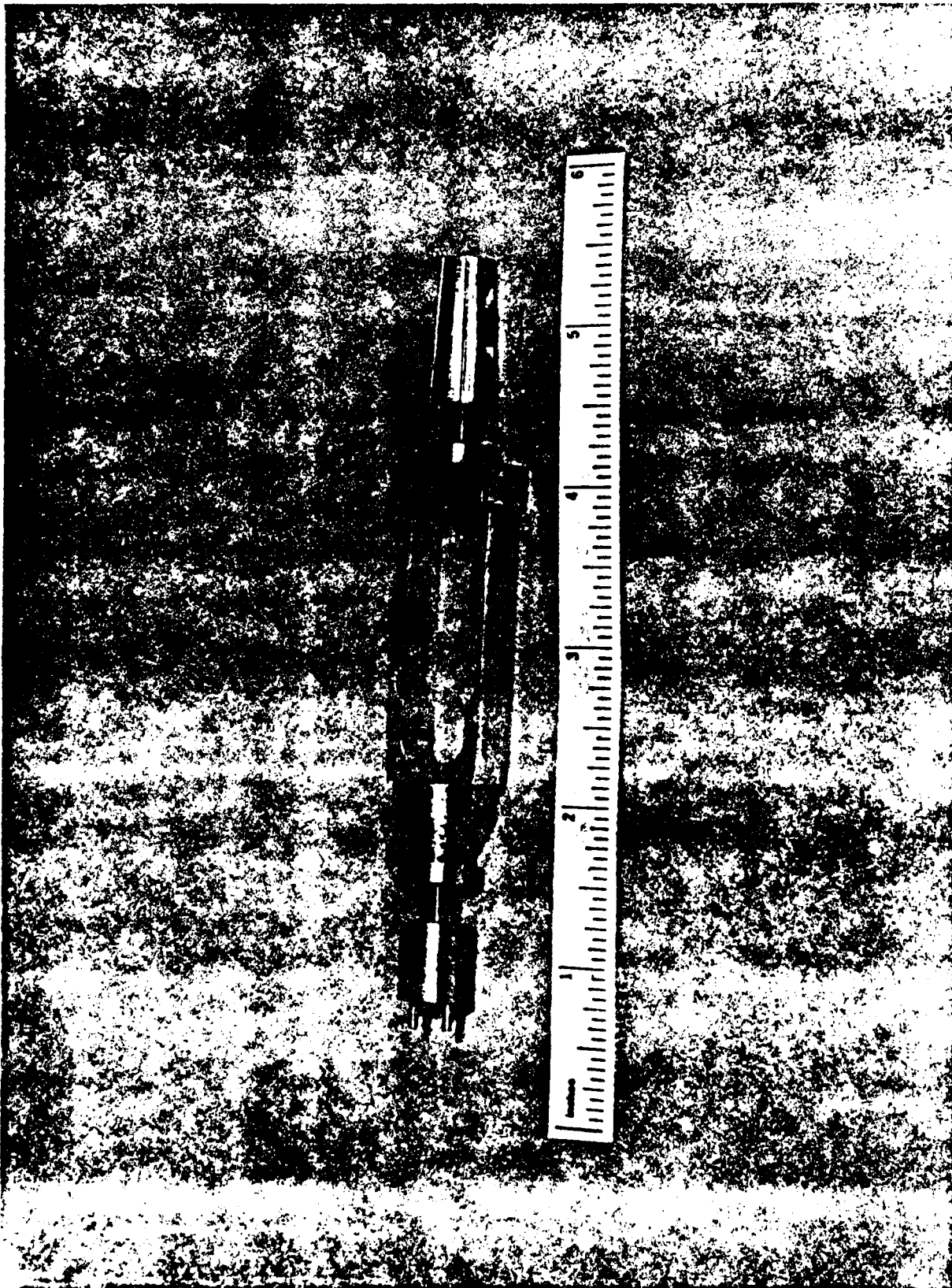


FIGURE 19. DUMMY BALANCE

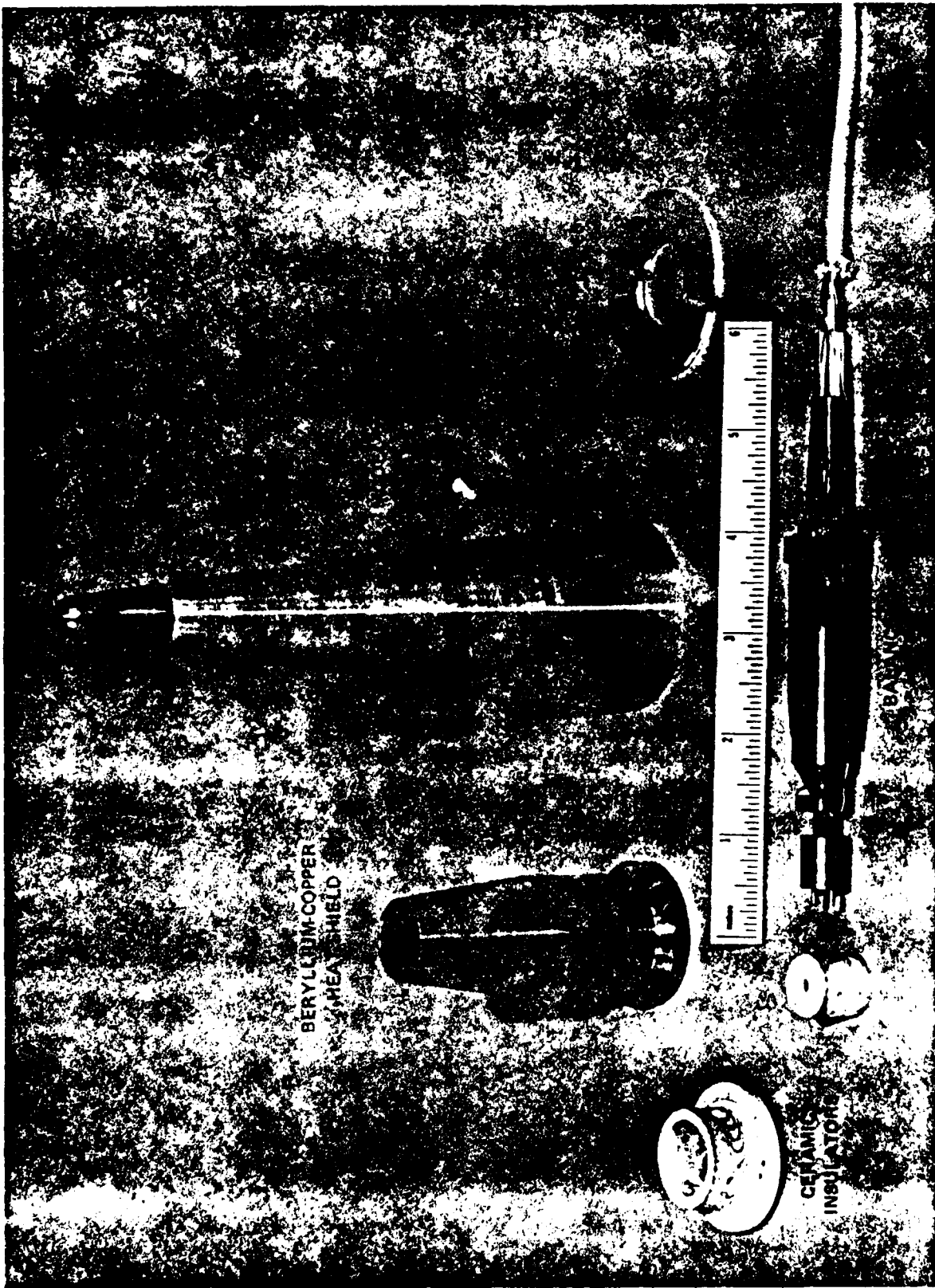


FIGURE 18. MODEL HARDWARE

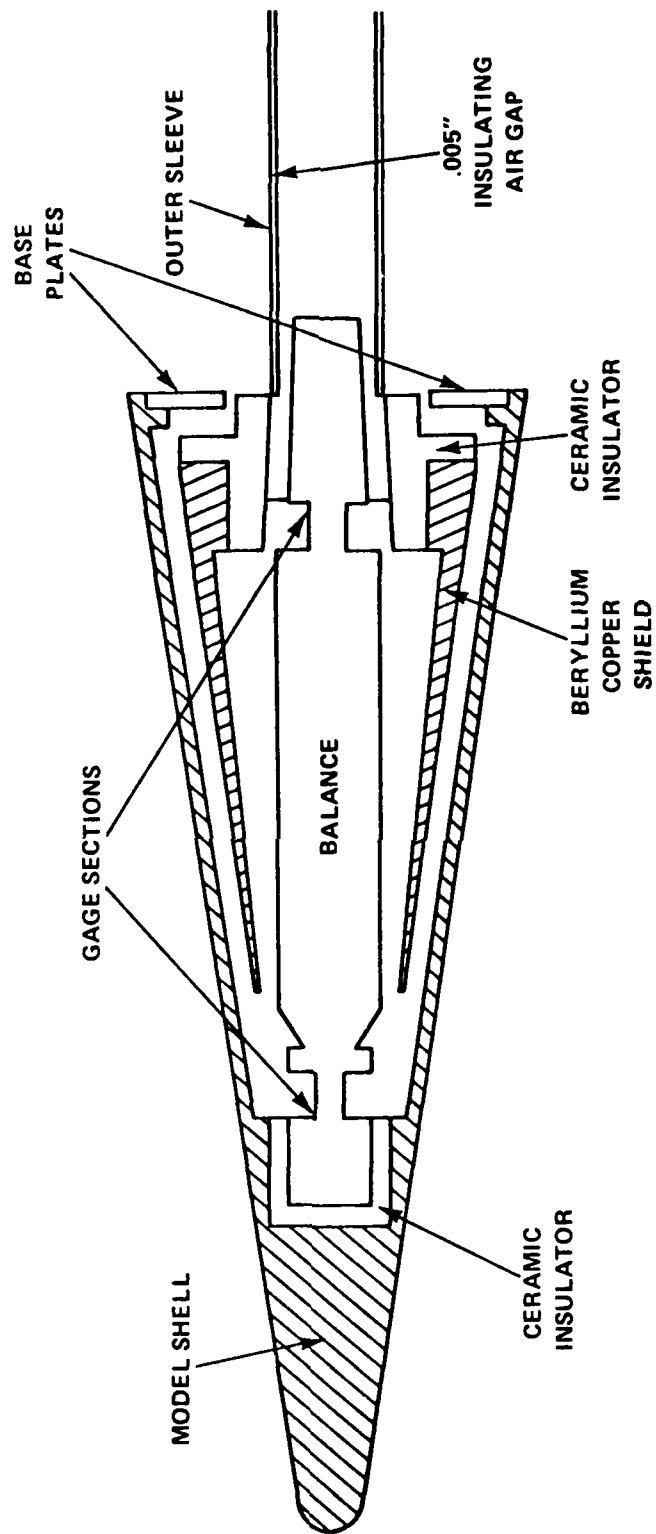


FIGURE 17. BALANCE HEATING PROTECTION

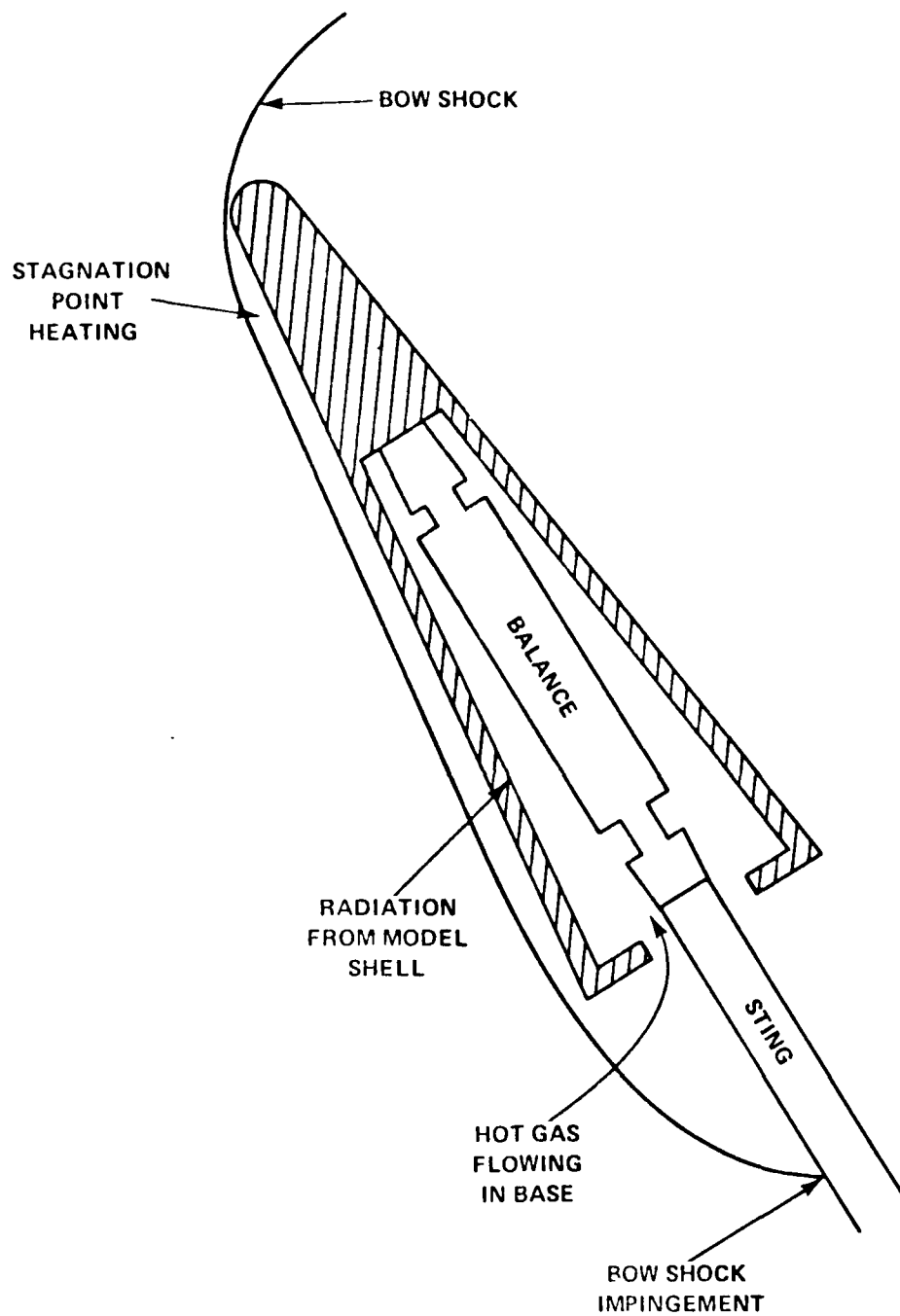


FIGURE 16. SOURCES OF BALANCE HEATING AT HIGH ANGLES OF ATTACK

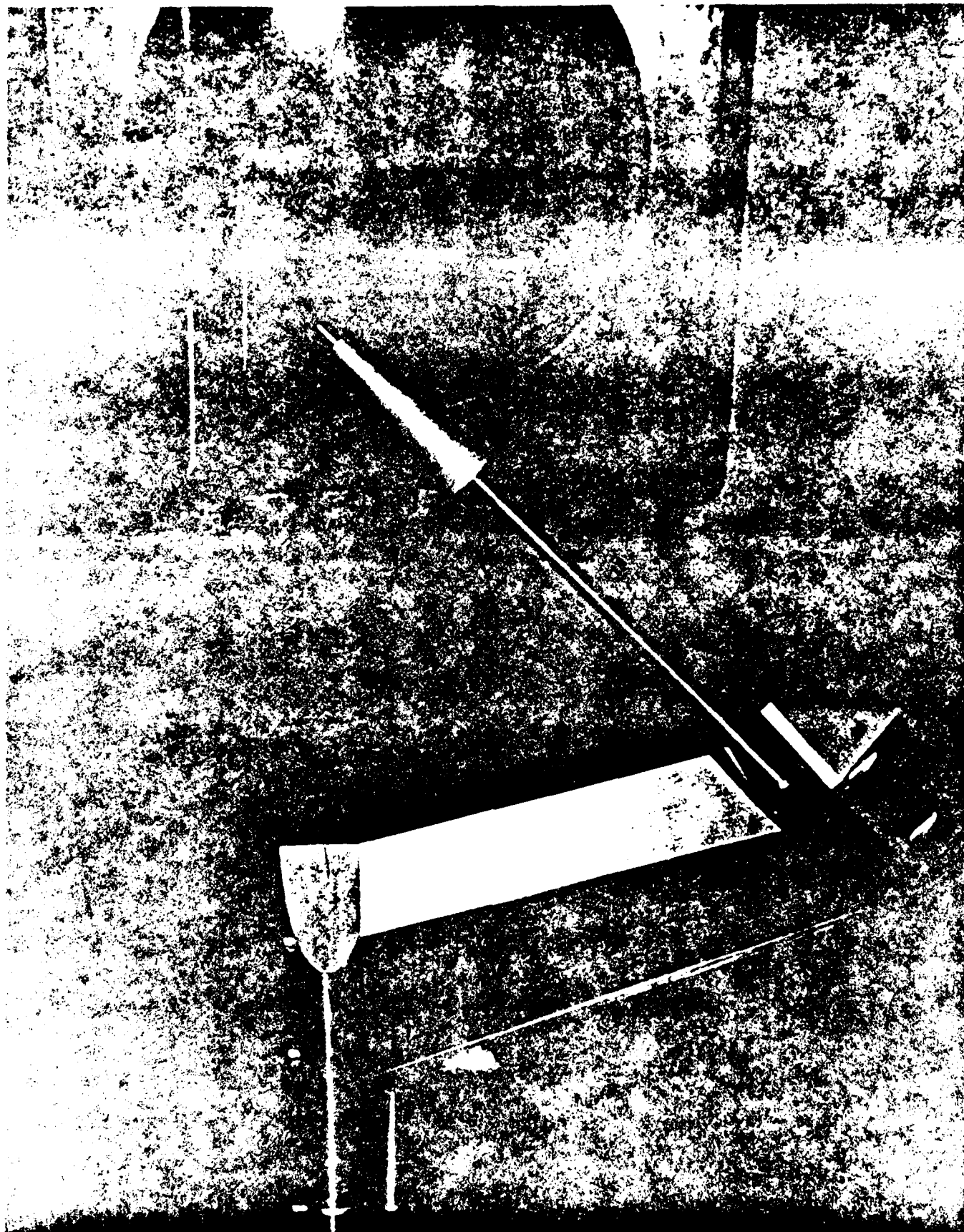


FIGURE 15. DOGLEG STING ( $\alpha = 45^\circ - 90^\circ$ )

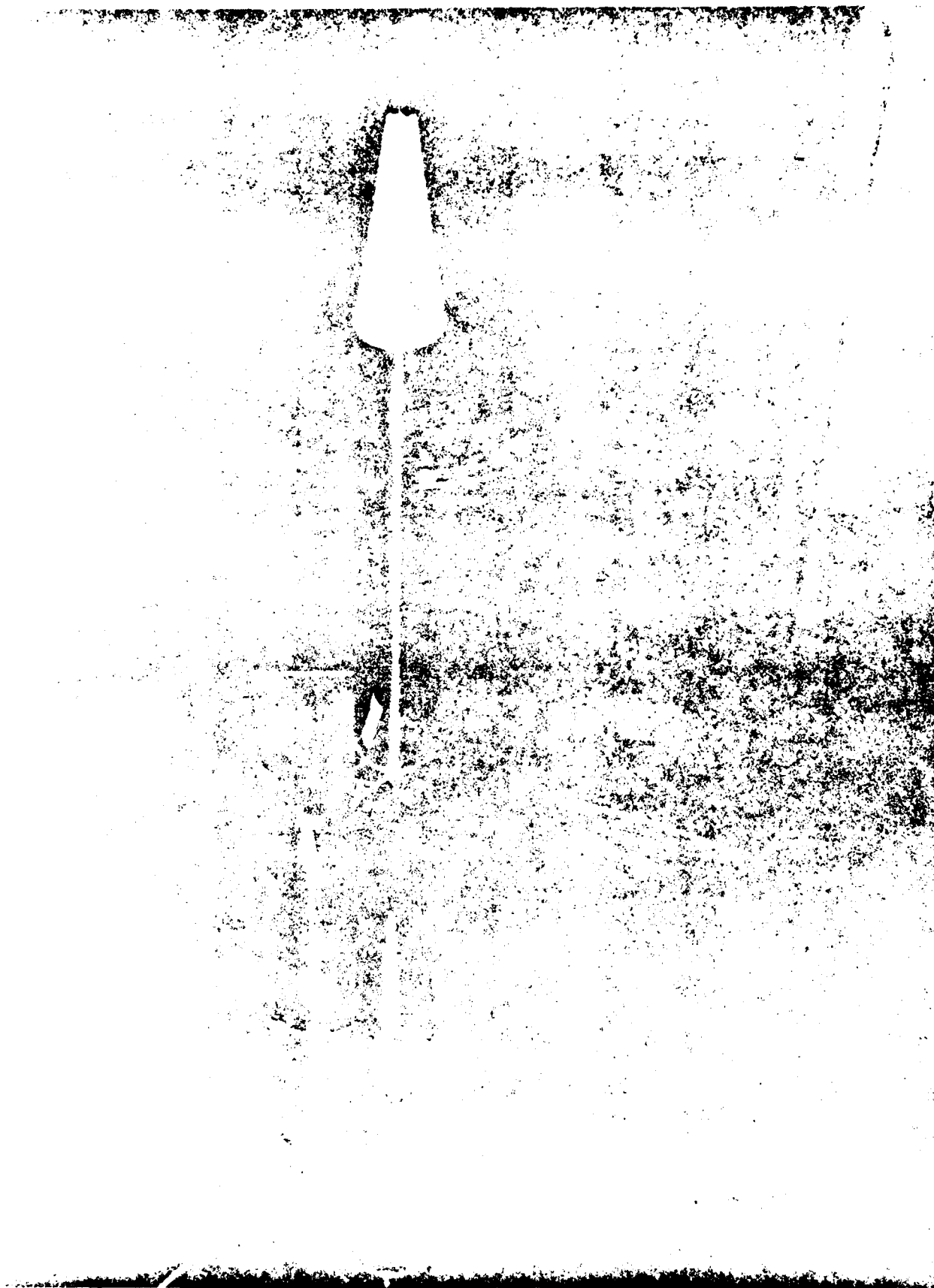


FIGURE 14. STRAIGHT STING ( $\theta = 0$ ).

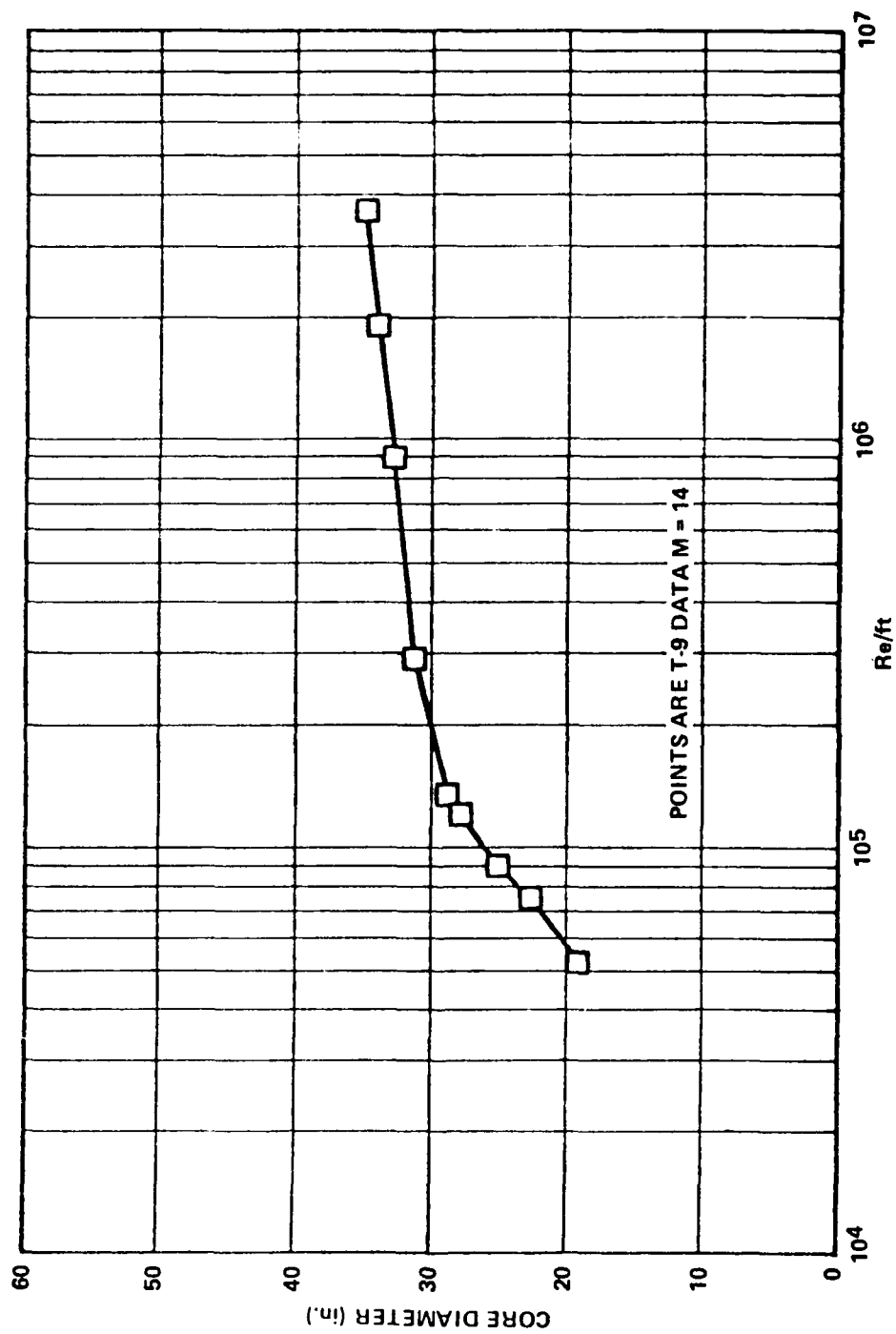


FIGURE 13. CORE DIAMETER vs. REYNOLDS NUMBER



$X/D = 3.2$  and  $5.3$ , the ogive and boattail junction respectively where appreciable changes in the flow variables are expected. The projectile base was modeled as an extension of the  $7.0^\circ$  boattail for a distance of two calibers. The surface line was then turned parallel to the model axis for the remainder of the wake region. The base flow is thus modeled as an extended sting.

Results are first presented for  $M_\infty = .94$  and  $\alpha = 0$ . The turbulence quantities  $k$  and  $\epsilon$  obtained with the two-equation turbulence model are shown in Figures 4 and 5 respectively for selected longitudinal stations. One of the longitudinal stations selected is near the ogive-cylinder junction and the others are located either near the boattail junction or on the boattail itself. Note that the station  $X/D = 6.19$  is off the physical model. It is on the extension of the boattail and  $k$ - $\epsilon$  model prediction is compared with that of the algebraic model at this station. Figure 4 shows the turbulence kinetic energy profiles in the law of the wall coordinate. The station  $X/D = 5.05$  is in front of the boattail corner and  $X/D = 5.36$  is just after the boattail corner. Because of the severe expansion at the boattail junction, the turbulence kinetic energy is increased by a factor of two between these stations. It then drops off on the boattail as shown by the profiles at stations  $X/D = 5.61$  and  $6.19$ . The humps in these profiles are believed to be the result of the interaction of the shock and expansion waves with the turbulent boundary layer and occur outside the edge of the boundary layer. The peaks in the  $k$  profiles occur at  $y^+ \approx 20$  although the peak is moved slightly further away from the wall near the boattail corner i.e., between  $X/D = 5.05$  and  $5.36$ . As shown in Figure 5 the turbulence dissipation rate profiles show identical behavior for the same stations with the exception that there are no humps present in the region outside the edge of the boundary layer. Additionally, the peaks now occur closer to the wall at  $y^+ \approx 10$ . This agrees with the observed behavior of the peaks by other researchers.

Turbulent eddy viscosities are found from  $k$  and  $\epsilon$  with the two-equation model and algebraically using Baldwin and Lomax model. These are referenced to the molecular viscosity  $\mu_\infty$  and plotted in Figures 6 and 7 for the same longitudinal positions discussed above. Figure 6 shows the  $\mu_t$  profiles obtained with the algebraic model. The profiles have rather flat peaks and go to zero outside the boundary layer. It drops off sharply in magnitude near the boattail corner i.e.,  $X/D = 5.05$  to  $5.36$  and then rises sharply on the boattail as seen by the profiles between  $X/D = 5.61$  and  $6.19$ . The algebraic model is based on local information and such sharp increase or decrease in  $\mu_t$  results. The  $\mu_t$  profiles obtained with the  $k$ - $\epsilon$  model on the other hand shows gradual change in  $\mu_t$  on the boattail as seen in Figure 7. The profiles have sharper peaks and then fall off to values other than zero outside the edge of the boundary layer. Although  $k$  and  $\epsilon$  profiles drop off to practically zero,  $\mu_t/\epsilon$  does not drop off from its peak value monotonically with increasing distance from the surface and results in non-zero  $\mu_t$ 's. The mean flow gradients outside the boundary layer are however exceedingly small and the  $\mu_t$ 's in no way adversely affect the solution of the mean flow quantities.

Figure 8 shows the mean velocity profiles at the same selected stations. Velocity profiles obtained with both turbulence models compare well at  $X/D =$

3.42 and 6.19. Experimental data is available at the other three stations and are used for comparison with the calculations. Both models predict almost the same profile at  $X/D = 5.05$  and comparison with experiment is good. Just downstream of the boattail corner i.e., at  $X/D = 5.36$  and  $5.61$ , comparison of the  $k-\epsilon$  calculations with experiment are in better agreement than the algebraic model predictions. Figure 9 is a plot of the surface pressure distribution as a function of the longitudinal position over the projectile. The rapid expansion at the ogive and boattail junctions is apparent. Computed results obtained with both models are compared with experiment and the results are in good agreement. A small improvement of the results with  $k-\epsilon$  model can be seen on the boattail.

Results are now presented for another Mach number,  $M = .97$  where strong shock/boundary layer interactions occur. Figure 10 shows the turbulent kinetic energy profiles at various longitudinal positions. These look similar to those discussed previously for  $M = .94$ . The peak values occur at  $y^+ \approx 25$ .  $k$  increases over the boattail corner ( $X/D = 5.05$  to  $5.36$ ) and then decreases over the boattail. The turbulent dissipation rate profiles are shown in Figure 11. These profiles behave better than  $k$  profiles in the region outside the edge of the boundary layer and drop off to small values without the presence of any humps in the profiles in that region. As expected, the peaks in  $\epsilon$  profiles occur closer to the wall ( $y^+ \approx 10$ ) than those of the  $k$  profiles ( $y^+ \approx 25$ ).

Figures 12 and 13 show the turbulent eddy viscosity profiles obtained with the algebraic model and the  $k-\epsilon$  model respectively and are plotted in physical  $y$  coordinate.  $\mu_t$  rises to its peak and then drops off sharply over a very small distance from the surface. The magnitudes of  $\mu_t$  at each of these longitudinal stations differ in both the model predictions and are clearly shown in the next Figure 14. Figure 14 is plotted in the law of the wall coordinate and shows the variation of  $\mu_t$  near the wall more clearly. The profiles with  $k-\epsilon$  model have sharper peaks compared to those obtained with the algebraic model. Algebraic model predicts sharp increase ( $X/D = 5.61$  to  $6.19$ ) and decreases ( $X/D = 5.05$  to  $5.36$ ) in  $\mu_t$  whereas  $k-\epsilon$  model predicts rather gradual change since it takes into account the upstream effects. Comparison of  $\mu_t$  profiles at  $X/D = 5.36$  and  $5.61$  is not satisfactory and comparison at the other three stations is in good agreement. This kind of a disagreement is local and may or may not have a large overall influence on the results.

Figure 15 shows the mean velocity profiles at the same longitudinal stations. There is very slight difference between the computed results obtained with both turbulence models. Comparison of the calculated profiles have been made with experimental data at  $X/D = 5.05$ ,  $5.36$  and  $5.61$  and the comparison in general is in good agreement. The slight difference in the computed results and experimental measurements is for the  $X/D = 5.36$  case. This profile is only .06 calibers downstream of the boattail corner and is in the vicinity of severe expansion. The experimental data was reduced using static pressure measurements. The greater the distance from the wall, the more the velocity data may be in error. This is particularly true just downstream of the expansion corner where the profile may extend through the

expansion fan with significantly varying static pressures. A small error in experimental measurements thus could account for the slight difference. The computed and experimental surface pressure coefficient are again shown in Figure 16 and compare favorably.

#### V. Summary

A paper has been described in which a thin-layer Navier-Stokes computational technique has been used to compute the axisymmetric, turbulent flow over a projectile at transonic speeds. Numerical computations have been made at  $M_\infty = .94$  and  $.97$  using zero-equation and two-equation turbulence eddy viscosity models. Implicit algorithm used to solve the Navier-Stokes equations has been extended to solve the turbulence field equations for  $k-\epsilon$  model.

Computed results show the turbulent kinetic energy, dissipation rate and turbulent eddy viscosity profiles. The velocity profiles and surface pressure distribution have been obtained using both turbulence models and are compared with experiment. A small improvement with the  $k-\epsilon$  model prediction is found at  $M_\infty = .94$ . The comparison of predictions by both models shows generally good agreement with the experimental data.

#### References

1. Nietubicz, C.J., Pulliam, T.H., and Steger, J.L., "Numerical Solution of the Azimuthal-Invariant Thin-Layer Navier-Stokes Equations", ARBRL-TR-02227, U.S. Army Ballistic Research Laboratory, Aberdeen Proving Ground, Maryland 21005, March 1980. (AD A085716) (Also see AIAA Paper No. 79-0010, January 1979).
2. Nietubicz, C.J., "Navier-Stokes Computations for Conventional and Hollow Projectile Shapes at Transonic Velocities", ARBRL-MR-03184, U.S. Army Ballistic Research Laboratory, Aberdeen Proving Ground, Maryland 21005, July 1982. (AD A116866) (Also see AIAA Paper No. 81-1262, June 1981).
3. Sahu, J., Nietubicz, C.J., and Steger, J.L., "Numerical Computation of Base Flow for a Projectile at Transonic Speeds", ARBRL-TR-02495, U.S. Army Ballistic Research Laboratory, Aberdeen Proving Ground, Maryland 21005, June 1983. (AD A130293) (Also see AIAA Paper No. 82-1358, August 1982).
4. Sahu, J., Nietubicz, C.J., and Steger, J.L., "Navier-Stokes Computations of Projectile Base Flow with and without Base Injection", AIAA Paper No. 83-0224, January 1983.
5. Beam, P., and Warming, R.F., "An Implicit Factored Scheme for the Compressible Navier-Stokes Equations", AIAA Paper No. 77-645, June 1977.
6. Steger, J.L., "Implicit Finite Difference Simulation of Flow About Arbitrary Geometries with Application to Airfoils", AIAA Journal, Vol. 16, No. 7, July 1978, pp. 679-686.

7. Pulliam, T.H., and Steger, J.L., "On Implicit Finite-Difference Simulations of Three-Dimensional Flow", AIAA Journal, Vol. 18, No. 2, February 1980, pp. 159-167.
8. Baldwin, B.S., and Lomax, H., "Thin-Layer Approximation and Algebraic Model for Separated Turbulent Flows", AIAA Paper No. 78-257, 1978.
9. Chien, K.-Y., "Predictions of Channel and Boundary-Layer Flows with a Low-Reynolds-Number Turbulence Model", AIAA Journal, Vol. 20, No. 1, January 1982, pp. 33-38.
10. Jones, W.P., and Launder, B.E., "The Prediction of Laminarization with a Two-Equation Model of Turbulence", International Journal of Heat and Mass Transfer, Vol. 15, 1972, pp. 303-314.
11. R. P. Reklis, J. E. Danberg, and G. R. Inger, "Boundary Layer Flows on Transonic Projectiles", AIAA Paper 79-1551, 1979.
12. C. J. Nietubicz, G. R. Inger, and J. E. Danberg, "A Theoretical and Experimental Investigation of a Transonic Projectile Flow Field", AIAA Paper 82-0101, January 1982.
13. Steger, J.L., Nietubicz, C.J., and Heavey, K.R., "A General Curvilinear Grid Generation Program for Projectile Configurations", ARBRL-MR-03142, U.S. Army Ballistic Research Laboratory, Aberdeen Proving Ground, Maryland 21005, October 1981. (AD A107334)

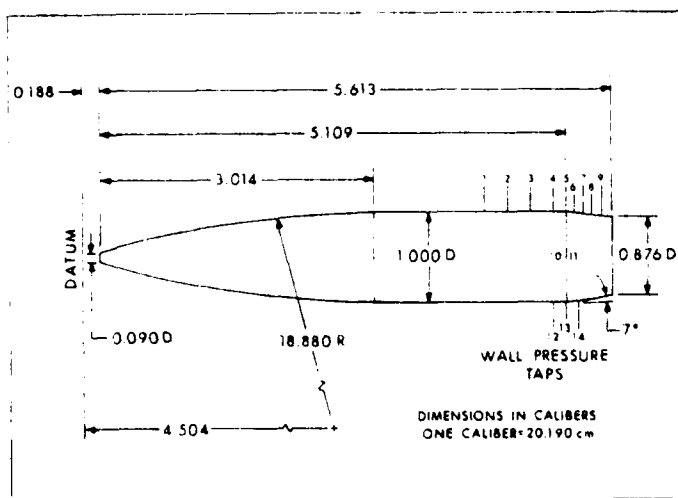


Figure 1. Model Geometry

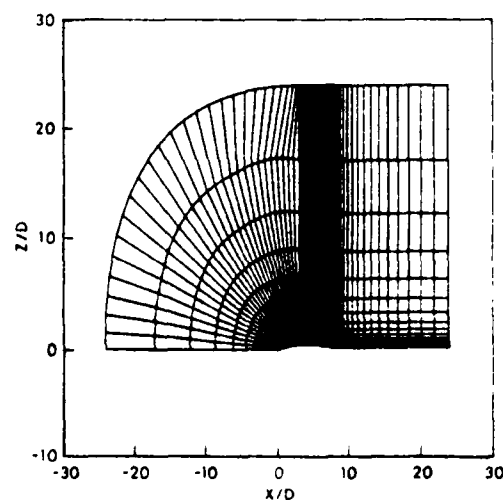


Figure 2. Computational Grid

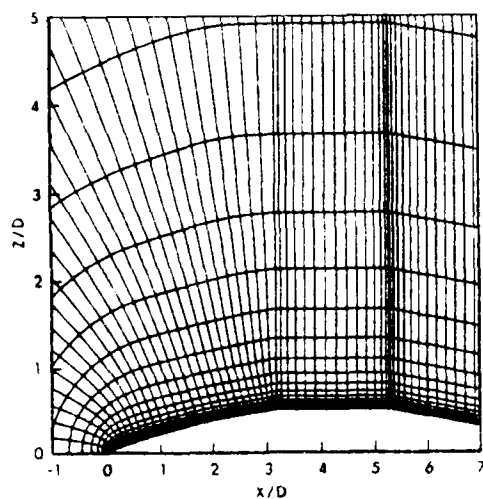


Figure 3. Expanded View of the Grid Near the Model

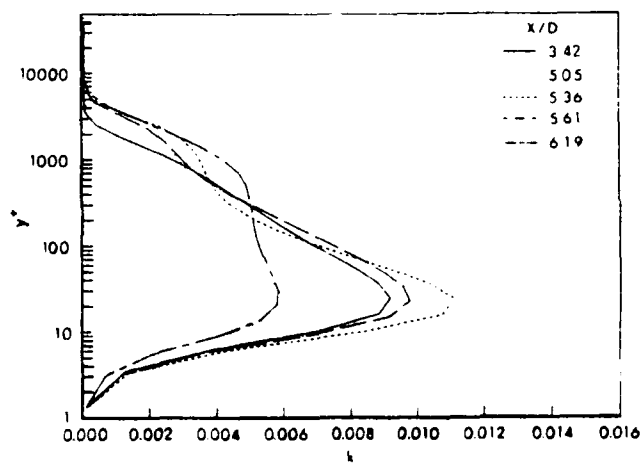


Figure 4. Turbulent Kinetic Energy Profiles,  $M_\infty = .94$ ,  $\alpha = 0$

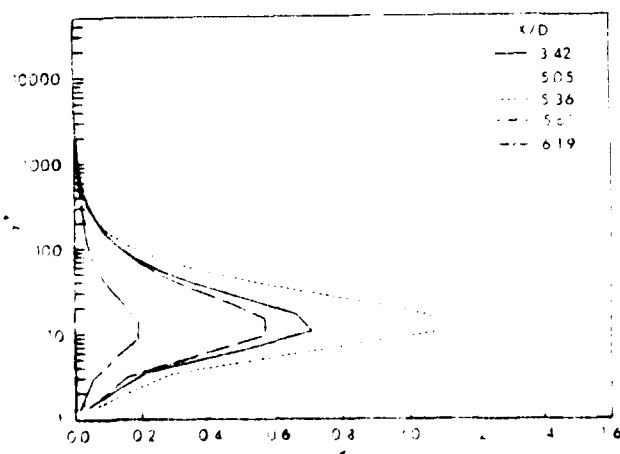


Figure 5. Turbulent Dissipation Rate Profiles,  $M_\infty = .94$ ,  $\alpha = 0$

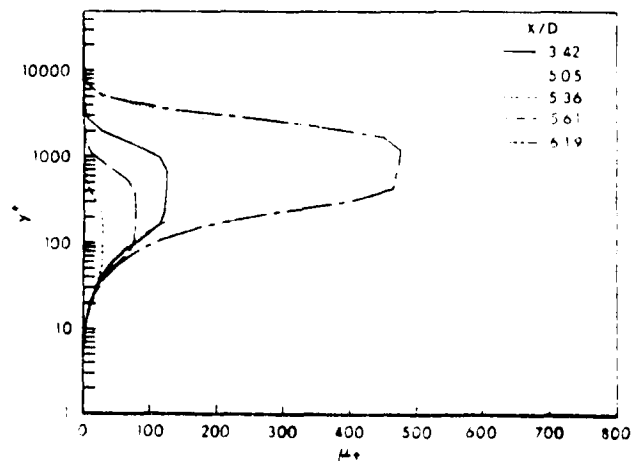


Figure 6. Turbulent Viscosity Profiles,  $M_\infty = .94$ ,  $\alpha = 0$  (Algebraic Model)

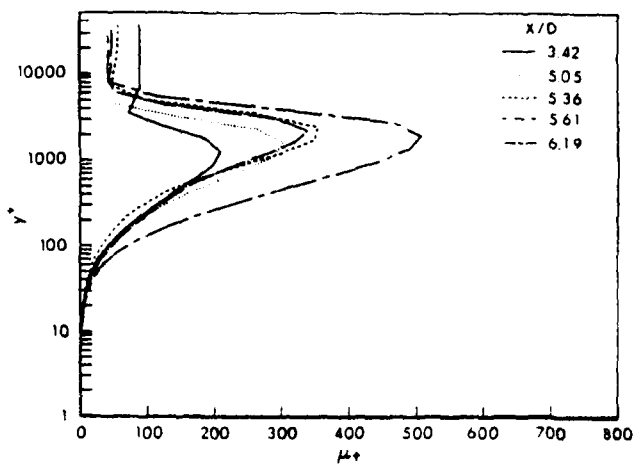


Figure 7. Turbulent Viscosity Profiles,  
 $M_\infty = .94$ ,  $\alpha = 0$  (k- $\epsilon$  Model)

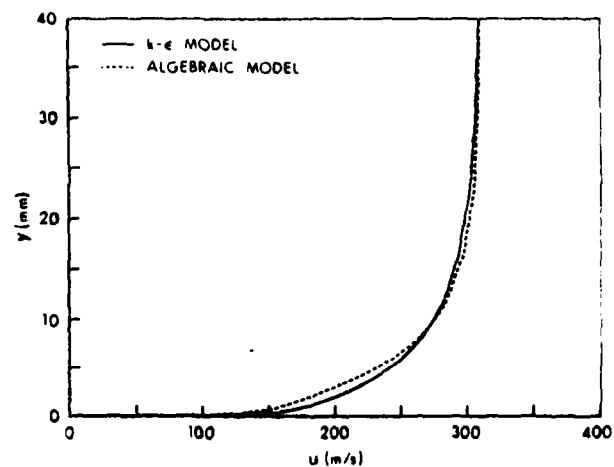


Figure 8a. Velocity Profiles,  
 $M_\infty = .94$ ,  $\alpha = 0$ ,  
 $X/D = 3.42$

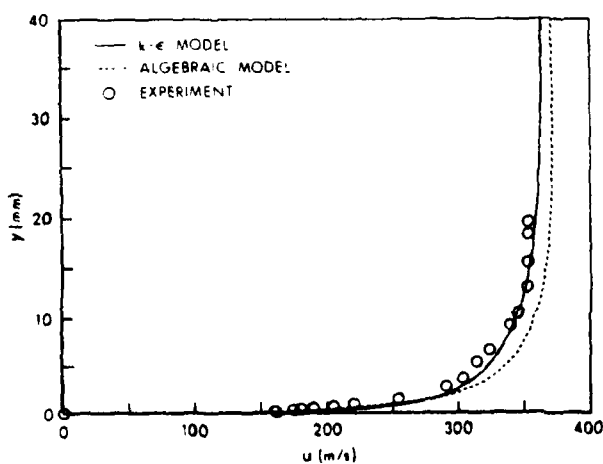


Figure 8b. Velocity Profiles,  
 $M_\infty = .94$ ,  $\alpha = 0$ ,  
 $X/D = 5.05$

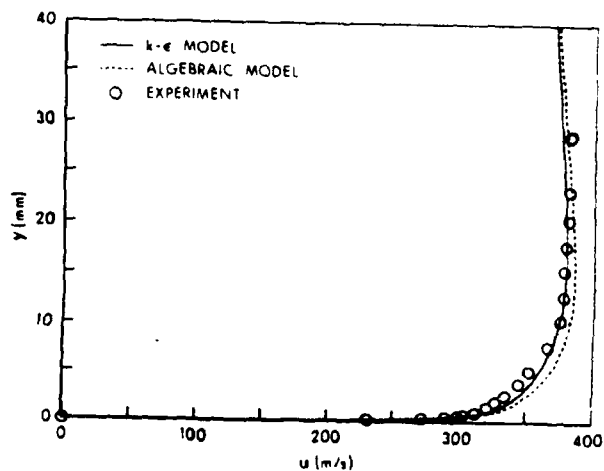


Figure 8c. Velocity Profiles,  
 $M_\infty = .94$ ,  $\alpha = 0$ ,  
 $X/D = 5.36$

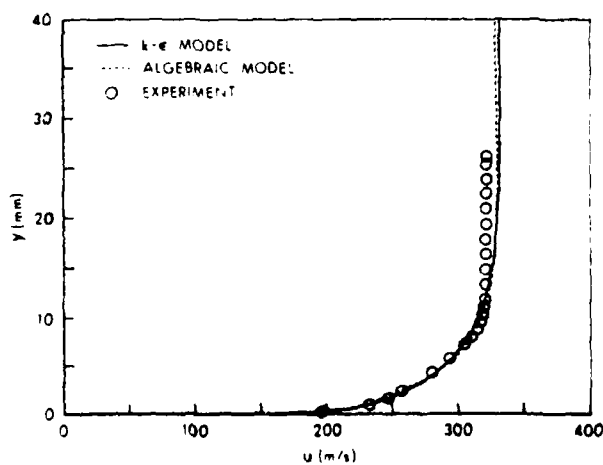


Figure 8d. Velocity Profiles,  
 $M_\infty = .94$ ,  $\alpha = 0$ ,  
 $X/D = 5.61$

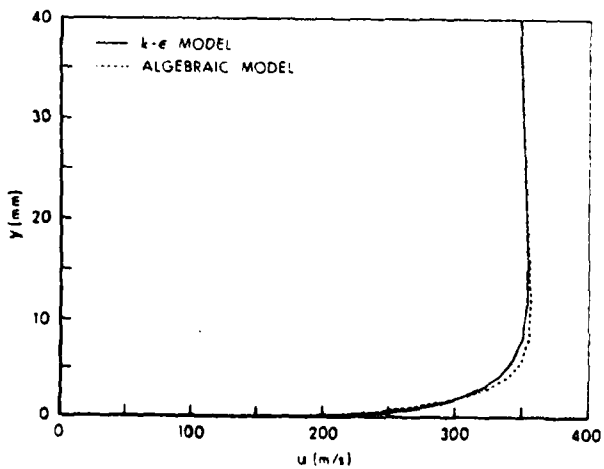


Figure 8e. Velocity Profiles,  
 $M_\infty = .94$ ,  $\alpha = 0$ ,  
 $X/D = 6.19$

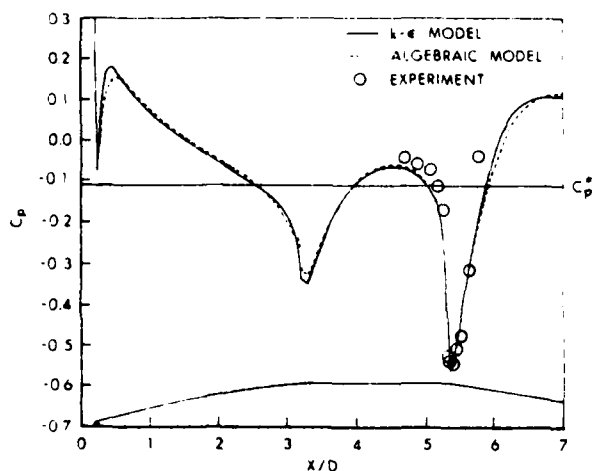


Figure 9. Surface Pressure Distribution,  
 $M_\infty = .94$ ,  $\alpha = 0$

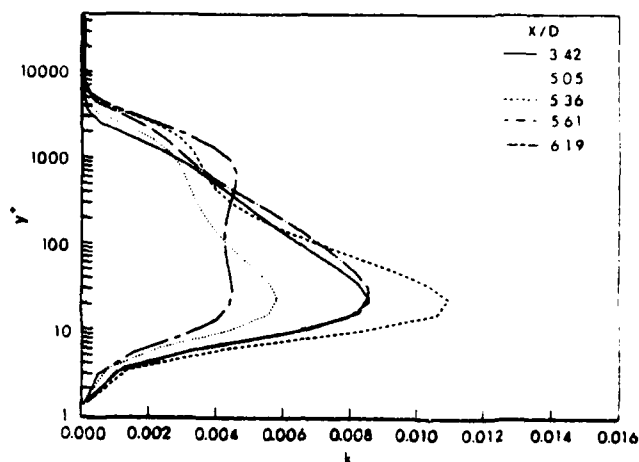


Figure 10. Turbulent Kinetic Energy  
Profiles,  $M_\infty = .97$ ,  $\alpha = 0$

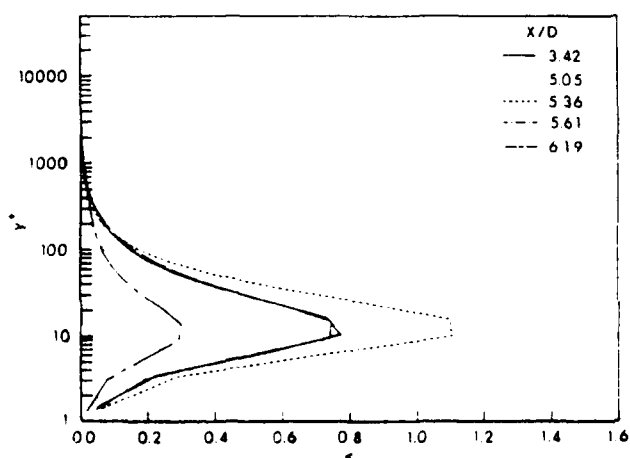


Figure 11. Turbulent Dissipation Rate  
Profiles,  $M_\infty = .97$ ,  $\alpha = 0$

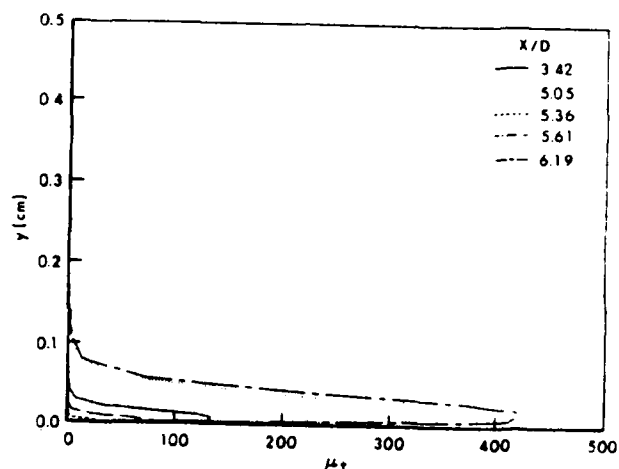


Figure 12. Turbulent Viscosity Profiles,  
 $M_\infty = .97$ ,  $\alpha = 0$  (Algebraic Model)

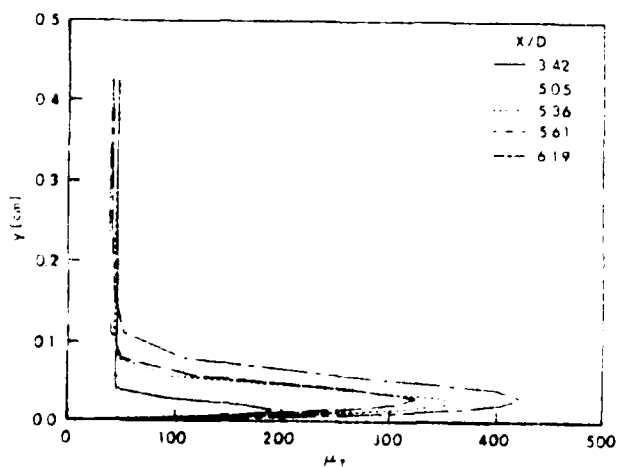


Figure 13. Turbulent Viscosity Profiles,  
 $M_\infty = .97$ ,  $\alpha = 0$  (k-epsilon Model)

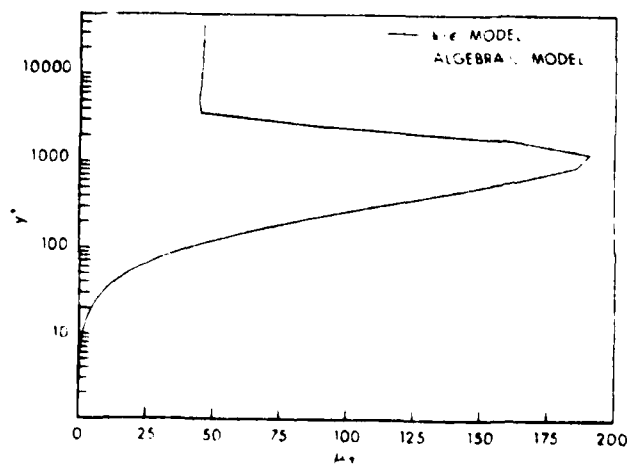


Figure 14a. Turbulent Viscosity Profiles,  
 $M_\infty = .97$ ,  $\alpha = 0$ ,  $X/D = 3.42$

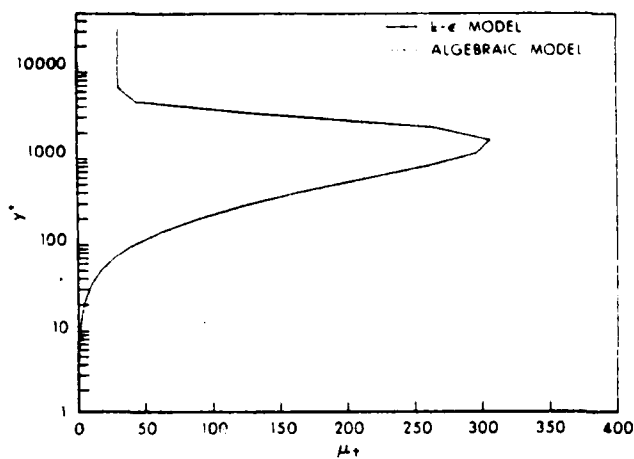


Figure 14b. Turbulent Viscosity Profiles,  
 $M_\infty = .97$ ,  $\alpha = 0$ ,  $X/D = 5.05$

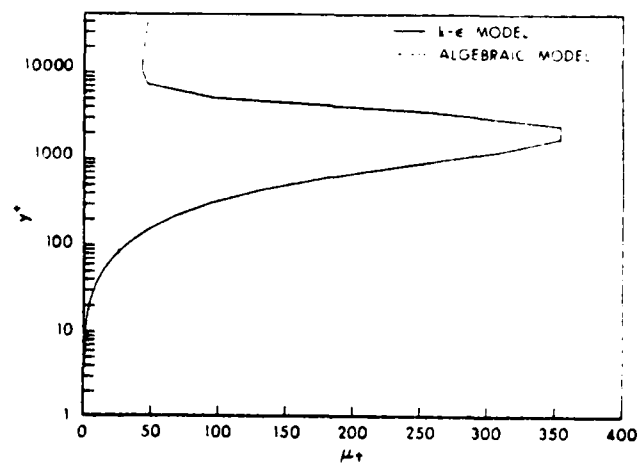


Figure 14c. Turbulent Viscosity Profiles,  
 $M_\infty = .97$ ,  $\alpha = 0$ ,  $X/D = 5.36$

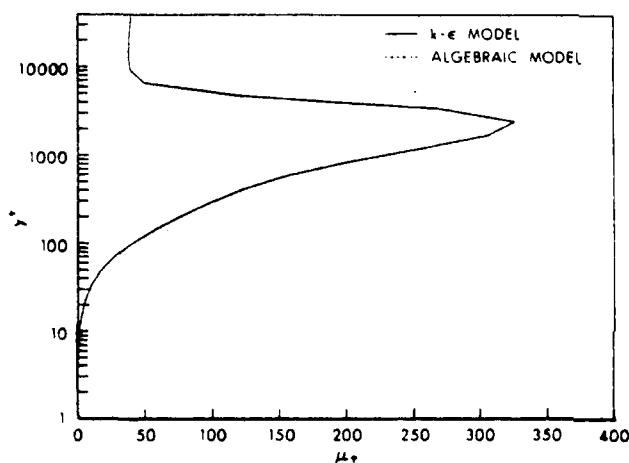


Figure 14d. Turbulent Viscosity Profiles,  
 $M_\infty = .97$ ,  $\alpha = 0$ ,  $X/D = 5.61$

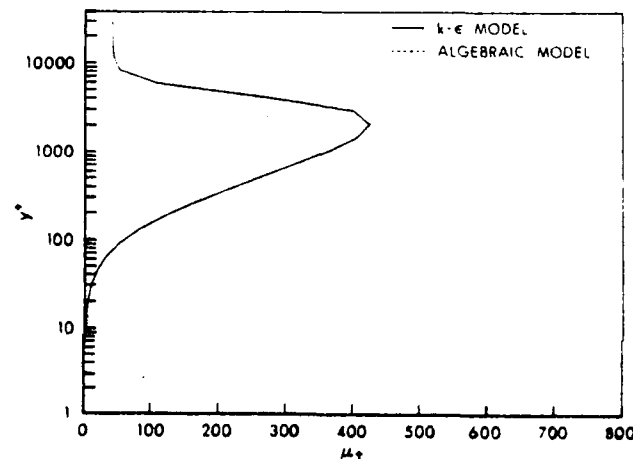


Figure 14e. Turbulent Viscosity Profiles,  
 $M_\infty = .97$ ,  $\alpha = 0$ ,  $X/D = 6.19$

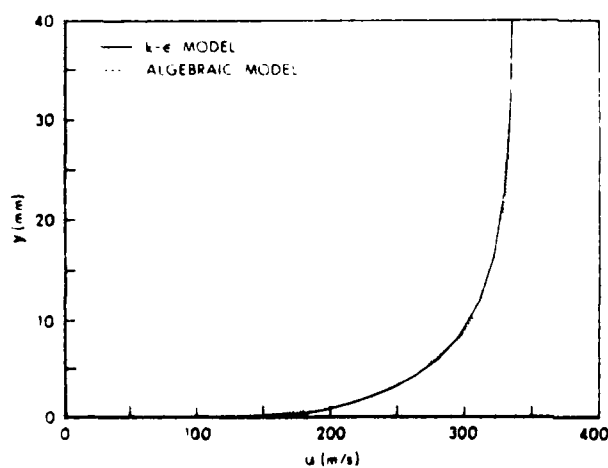


Figure 15a. Velocity Profiles,  
 $M_\infty = .97$ ,  $\alpha = 0$ ,  
 $X/D = 3.42$

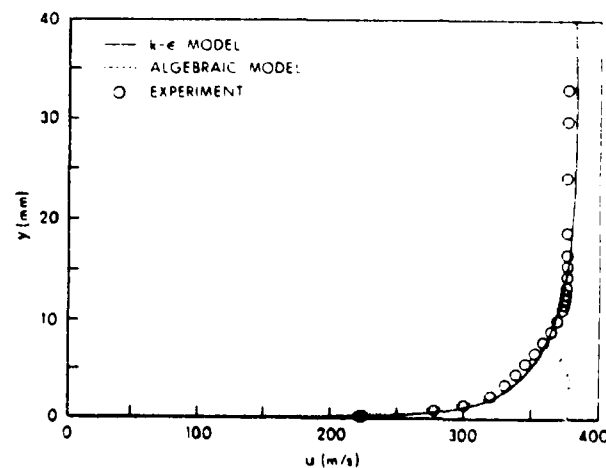


Figure 15b. Velocity Profiles,  
 $M_\infty = .97$ ,  $\alpha = 0$ ,  
 $X/D = 5.05$



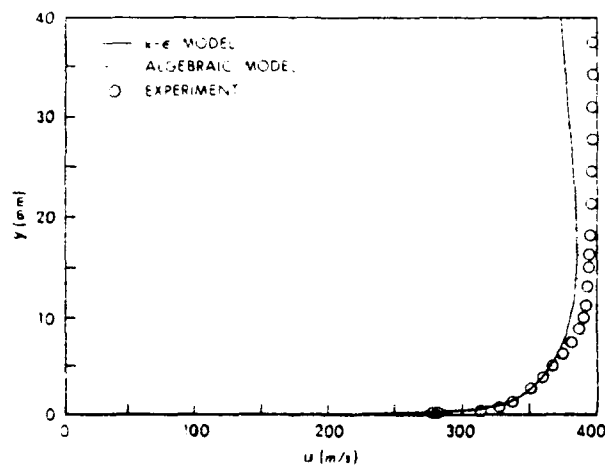


Figure 15c. Velocity Profiles,  
 $M_\infty = .97$ ,  $\alpha = 0$ ,  
 $X/D = 5.36$

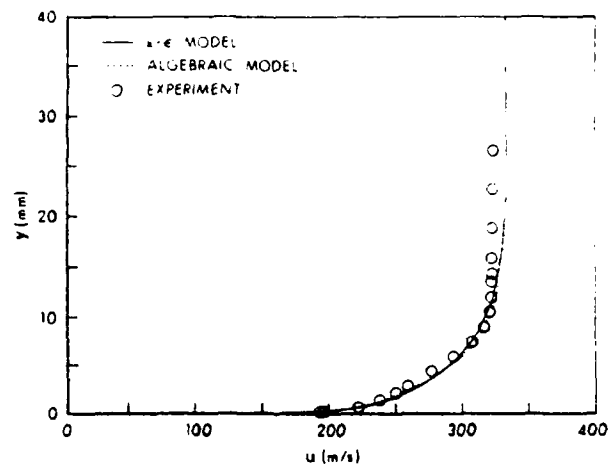


Figure 15d. Velocity Profiles,  
 $M_\infty = .97$ ,  $\alpha = 0$ ,  
 $X/D = 5.61$

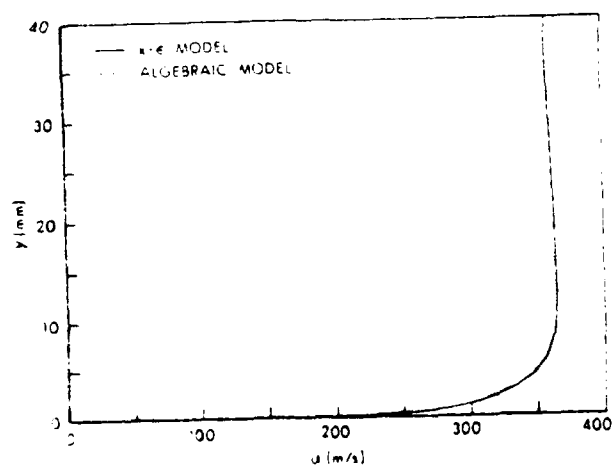


Figure 15e. Velocity Profiles,  
 $M_\infty = .97$ ,  $\alpha = 0$ ,  
 $X/D = 6.19$

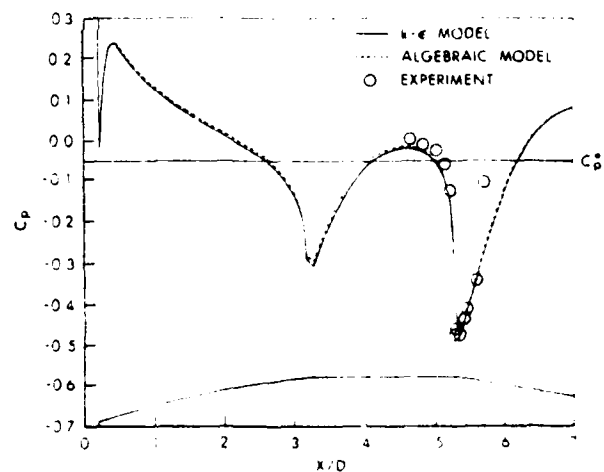


Figure 16. Surface Pressure Distribution,  
 $M_\infty = .97$ ,  $\alpha = 0$

PNS Computations for Non-Circular and Finned Body  
Configurations at Supersonic Velocities

R. H. Jettmar, NSWC, Silver Spring, Md.

and

W. Kordulla, DFVLR-AVA, Goettingen

Abstract

The Parabolized Navier-Stokes (PNS) equations are used to predict the viscous supersonic flow field over tangent-ogive-cylinder bodies with non-circular cross-section and finned body configurations. Current design interests make it desirable to gain some advanced knowledge of the aerodynamic characteristics of such bodies. Since the solution of the full, unsteady, Reynolds-averaged Navier-Stokes equations has its limitation due to computational resources, considerable interest exist in applying the PNS model to obtain a viscous supersonic flow field over realistic, complex configurations.

## Introduction

The prediction of a three-dimensional viscous supersonic flow field over complex real configurations has been the topic of numerous research efforts [1-7]. A practical means of predicting the nonlinear viscous supersonic shock layer on such configurations is to solve the Parabolized Navier-Stokes (PNS) equations. These equations are of evolutionary type and are obtained from the full, time dependent Navier-Stokes equations by (1) neglecting the unsteady terms and the streamwise viscous diffusion terms and (2) modifying the streamwise convection flux vector to obtain a well-posed problem that can be marched in the downstream direction from an initial set of data. This initial data plane is considered time accurate and the problem has a preferred direction. The finite difference scheme used in this study was developed by Schiff and Steger [8]. Using the Beam and Warming algorithm [9] the non-iterative implicit marching algorithm in delta form requires that the velocity in marching direction remains positive, ruling out flow separation in marching direction. The algorithm is approximately-factored and uses central differences to compute the crossflow components, therefore allowing for cross flow separation.

In this study the PNS methodology is applied to two body configurations of great interest to the aerodynamic designer, (1) bodies with non-circular cross-section and (2) finned missiles. The results for the bodies with non-circular cross-section are an enhancement of results presented in [7]. The approach to the finned missile configuration is a departure from the basic computations strategy used in [6] where a "wraparound" grid is used considering fins and body as one entity. Here the computational grid is generated using the body only and the fin surfaces are allowed to extend into the computational region, a "thin-fin" approximation as proposed in [10]. A no-slip boundary condition is imposed on the fin surface.

### Overview of Numerical Scheme

The steady thin-layer Parabolized Navier-Stokes equations used to solve the viscous, supersonic flow field can be written in general non-orthogonal coordinates  $\xi, \eta, \zeta$  as

$$\frac{\partial \hat{E}_S}{\partial \xi} + \frac{\partial \hat{F}}{\partial \eta} + \frac{\partial \hat{G}}{\partial \zeta} = \frac{1}{Re} \frac{\partial \hat{S}}{\partial \zeta} \quad (2)$$

where

$\xi = \xi(x)$  is the marching coordinate (main flow)

$\eta = \eta(x, y, z)$  is the circumferential coordinate

$\zeta = \zeta(x, y, z)$  is the normal coordinate.

The inviscid flux vectors in Eq. 1 are

$$\hat{E}_S = J^{-1} \begin{bmatrix} \rho U \\ \rho U U + \xi_x p \\ \rho V U \\ \rho W U \\ (e + p_s) U \end{bmatrix}, \quad \hat{F} = J^{-1} \begin{bmatrix} \rho V \\ \rho U V + \eta_x p \\ \rho V V + \eta_y p \\ \rho W V + \eta_z p \\ (e + p) V \end{bmatrix}$$

$$\hat{G} = J^{-1} \begin{bmatrix} \rho W \\ \rho U W + \zeta_x p \\ \rho V W + \zeta_y p \\ \rho W W + \zeta_z p \\ (e + p) W \end{bmatrix}, \quad \hat{q} = J^{-1} \begin{bmatrix} \rho \\ \rho u \\ \rho v \\ \rho w \\ e \end{bmatrix}$$

with the contravariant velocity components

$$U = \xi_x u, \quad V = \eta_x u + \eta_y v + \eta_z w, \quad W = \zeta_x u + \zeta_y v + \zeta_z w$$

The convection terms of the "Thin-Layer" approximation are contained in  $\hat{E}_S$  term of equation 1. The right-hand term of equation 1 containing the viscous terms of the "Thin-Layer" approximations is given as

$$\hat{\zeta} = \zeta^{-1} \left[ \begin{aligned} &u(\zeta_x^2 + \zeta_y^2 + \zeta_z^2)u_{\zeta} + (u/3)(\zeta_x u_{\zeta} + \zeta_y v_{\zeta} + \zeta_z w_{\zeta})\zeta_x \\ &u(\zeta_x^2 + \zeta_y^2 + \zeta_z^2)v_{\zeta} + (u/3)(\zeta_x u_{\zeta} - \zeta_y v_{\zeta} + \zeta_z w_{\zeta})\zeta_y \\ &u(\zeta_x^2 + \zeta_y^2 + \zeta_z^2)w_{\zeta} + (u/3)(\zeta_x u_{\zeta} + \zeta_y v_{\zeta} + \zeta_z w_{\zeta})\zeta_z \\ &[(\zeta_x^2 + \zeta_y^2 + \zeta_z^2)\{(\mu/2)(u^2 + v^2 + w^2)_{\zeta} \\ &\quad + \rho r^{-1}(\gamma-1)^{-1}(a^2)_{\zeta}\} + (u/3)(\zeta_x u \\ &\quad + \zeta_y v + \zeta_z w)(\zeta_x u_{\zeta} + \zeta_y v_{\zeta} + \zeta_z w_{\zeta})] \end{aligned} \right]$$

The numerical algorithm to advance equation 1 along  $\xi = \text{constant}$ , including implicit and explicit smoothing terms for stabilizing the solution is given in detail in reference [11]. Equation 1 is parabolic with respect to  $\xi$  and can be marched in the  $\xi$  direction which represents the main flow direction. In the crossflow plane  $(\eta, \zeta)$  defined to be normal to the body axis Equation 1 is elliptic in the subsonic crossflow region and hyperbolic in the supersonic crossflow region. The conservative formulation of Equation 1 allows for the capturing of any possible crossflow shocks.

The computation is started from a converged conical solution near the tip of the body. The full solution is obtained by marching along the body axis downstream. A two-layer algebraic eddy viscosity model [12] is incorporated for the computation of fully turbulent flows. The grid generator employed is of the elliptic type [13] and generates gridlines every  $2.5^\circ$  in circumferential direction in the case of circular cross-section. For the non-circular cross-section the body contour is represented by 73 equal spaced points. The outer boundary of the computational regime is the shock surface. The grid points between body and shock are clustered toward the body to adequately represent the boundary layers on the body.

## Results

The present paper compares results of normal force, axial forces and pitching moment for  $\alpha = 5.1^\circ$  angle of attack at  $M_\infty = 2$  with experimental measurements performed at the DFVLR-AVA, Goettingen [14]. The objective of these experiments were to determine the aerodynamic characteristics on rectangular slender bodies and the influence of rounding the corners on these bodies on normal, axial and side forces, as well as pitching and yawing moments. The body consists of a 3-caliber ogival nose with a 5- or 10-caliber cylindrical aftbody (Tangent-Ogive-Cylinder, TOC). The corner rounding radii of the edges of the bodies investigated were 1/6 and 2/6 of the width of the body. These non-circular cross sections are uniform from the tip of the body to the base (Fig. 1).

Integrating the computed pressure distribution, one obtains a value for the local normal forces. Figure 2 shows the computed normal forces on the circular TOC-configuration for the PNS computation and an inviscid computation [10] and compares the results to measurements [14] obtained at various angles of attack. As seen, good agreement for the viscous computation at  $x/D=13$  is obtained up to  $\alpha=7.6^\circ$ . At  $\alpha=10.2^\circ$ , the error in predicting the normal force increases dramatically with the length of the body. Viscous and inviscid computation agree very closely in the region of favorable down-stream pressure gradient and start to deviate from each other along the cylinder portion of the body.

Using the marching solution for  $\alpha=5.1^\circ$  obtained with the smallest values for smoothing and reasonable step size in marching direction circumferential pressure distribution for the four cross-section ( $2r/a=0, 1/3, 2/3, 1$ ) at various stations  $x/D$  are shown in Figures 3-5. No quantitative or qualitative comparison can be given at this time, because no pressure distributions are available to the authors, a purely intuitive judgement has to be passed on the performance of the PNS model for the present results. Figure 3 shows the computed circumferential pressure distribution at the starting plane  $x/D = .275$  for the marching solution. The results exhibits the expected behavior. At station  $x/D = 2.52$ , a station on the ogive-portion of the SOC body the rounded cross-section exhibited again the expected pressure distribution, while the sharp corner of the square cross-section generates a "ringing" typically exhibited by computational methods in the presence of

## 2.4 Test program and procedure

All investigations were carried out at free-stream Mach numbers of  $Ma_\infty = 1.5$  and  $1.98$  with corresponding Reynolds numbers of  $Re_{l_\infty} = 7.8 \cdot 10^6$  and  $6.5 \cdot 10^6$ . The jet exit Mach number was for all tests  $Ma_E = 2.5$ , but the ratio of jet static exit pressure to the free-stream static pressure  $p_{JE}/p_\infty$  was varied substantially from about 2 to 30. Base pressures, afterbody pressure distributions and Schlieren flow-field photos were obtained in order to study the jet influence on the tail flow field. Angles of incidence were varied between  $\alpha = -4^\circ$  and  $\alpha = +8^\circ$ .

All tests were performed in the following way. After flow establishment in the wind tunnel, the pressure recording system was set in operation and then the jet flow was actuated for 0.15 s. This procedure allowed to get for every pressure tap a pressure recording covering jet-off and jet-on conditions, as shown in Fig. 6 for the base pressure.

## 3. Results and discussion

First results have been reported in [9], the following is a continuation of this earlier work.

### 3.1 Jet influence on pressure distributions along afterbodies

#### 3.1.1 Cylindrical afterbody, $Ma_\infty = 2.0$

Schlieren pictures in Fig. 7a give some insight into the flow field in the tail region of the missile with a cylindrical afterbody and the smallest nozzle (N3), in the presence of a jet of various exit pressure ratios,  $p_{JE}/p_\infty$ , at free-stream Mach number,  $Ma_\infty = 2$ , incidences being  $\alpha = 0^\circ$ ,  $4^\circ$ , and  $8^\circ$ .

diameter of  $d = 2.5$  cm is installed outside the tunnel. The connection to the missile model is made by two flexible high pressure hoses and by two tubes running through the strut support. The model itself is equipped with fast opening valves, jet running time is about 0.15 s. In detailed calibration tests of the jet nozzle and the jet flow it was found that splitting of the Ludwig tube into two separate tubes and bending of the tubes inside the strut did not impair the flow quality.

### 2.3 Model and instrumentation

A sketch of the missile model, including the most important internal equipment parts, namely gas supply tubes, valve system, secondary stagnation chamber, jet nozzle, and pressure transducer installation are shown in Fig. 3. In order to get fast response pressure measurements 12 Kulite pressure transducers were installed in the forward part and connected by tubes to the pressure taps. The Ludwig tube pressure and the secondary stagnation chamber pressure were measured by additional pressure transducers. For fast speed data recording, jet actuation, triggering of the Schlieren photography a Digital Equipment MINC was used, allowing a measurement and recording rate of 20 kHz.

An ogive/cylinder body with a diameter of  $d = 40$  mm and a length of  $l = 560$  mm served as basic model. The main body data are summarized in Fig. 4. The tail of this model could be equipped with three different afterbodies (cylindrical, 5°-, 10°-conical tails) and three different jet nozzles for exit Mach numbers of  $Ma_E = 2.5$ . Geometrical data of the afterbodies, the nozzles and the combinations tested are summarized in Fig. 5.



## 1. Introduction

The flow field in the tail region of a missile moving at supersonic speeds will be strongly influenced by the presence of a propulsive jet (Fig. 1). It causes changes in the pressure distribution, influencing drag and stability of the missile. Therefore, it is necessary to have adequate theoretical and experimental methods to treat these problems in the missile design phase. General understanding and modelling of this flow interference seems adequate, but nevertheless detailed knowledge of various effects involved seems still somewhat insufficient for design predictions, without using empirical parameters [1,2,3]. Therefore, experiments and new simulation techniques are still needed in order to improve prediction techniques.

## 2. Experimental set-up

### 2.1 Wind tunnel

The external flow past the missile was simulated in the test-section of the High-Speed Wind Tunnel of DFVLR-AVA Göttingen [4]. Air is sucked in from the atmosphere, dried and discharged through the supersonic nozzle and test section into a large vacuum vessel. Free-stream Mach numbers range from  $Ma_\infty = 0.4$  to  $0.95$  and  $Ma_\infty = 1.22$  to  $2.25$ ; the supersonic test section cross-sectional area is  $0.71 \text{ m} \times 0.725 \text{ m}$ ; typical tunnel running times are 10 - 20 seconds.

### 2.2 Jet flow simulation

In order to avoid large high-pressure gas supply installations the Ludwieg tube principle was adopted to produce the supersonic jet flow [5,6]. Fig. 2 shows the application of this jet simulation method in the wind tunnel. The Ludwieg tube with a length of  $L = 25 \text{ m}$  and an internal

### List of symbols

$c_p$	pressure coefficient, $c_p = \frac{p-p_\infty}{q_\infty}$
$\Delta c_{pJ}$	change in local pressure coefficient due to jet interference, $\Delta c_{pJ} = \frac{p_J - p}{q_\infty}$
$d$	diameter, model diameter
$l$	model length
$L$	length of Ludwieg tube
$Ma$	Mach number
$p$	pressure
$q$	dynamic pressure
$Re_{l_\infty}$	Reynolds number, $Re_{l_\infty} = \frac{U_\infty \cdot l}{\nu_\infty}$
$t$	time
$U_\infty$	free-stream velocity
$\alpha$	angle of attack
$\theta_A$	afterbody boat-tail angle (Fig. 5)
$\theta_N$	nozzle-wall angle (Fig. 5)
$\nu$	kinematic viscosity

### Indices

A	afterbody
B	base of afterbody
E	nozzle exit
J	conditions with jet influence
JE	jet exit condition
max	maximum
n	nose
N	nozzle
$x'$	lengthwise coordinate for afterbody
o	stagnation condition
l	approach condition
$\infty$	free-stream condition
*	nozzle throat

EFFECTS OF PROPULSIVE JET ON THE FLOW FIELD IN THE  
TAIL REGION OF A MISSILE IN A SUPERSONIC STREAM

G. Koppenwallner, D. Rammenzweig, W. Stahl  
DFVLR Institute for Experimental Fluid Mechanics  
D-3400 Göttingen, Bunsenstrasse 10, W-Germany

Abstract

The present work concentrated on the effects of an under-expanded supersonic jet on the external supersonic flow past a typical missile configuration. Jet simulation in the wind tunnel was achieved by means of a small Ludwieg tube, which allowed jet operation times of about 0.1 s. The circular cylindrical missile model with ogival nose had three different afterbody configurations: Cylindrical and conical boat tailing of  $5^\circ$  and  $10^\circ$  respectively. The experiments were carried out in the DFVLR High-Speed Wind Tunnel at free-stream Mach numbers of  $Ma_\infty = 1.5$  and  $Ma_\infty = 1.98$ ; angles of attack were varied between  $\alpha = -4^\circ$  and  $\alpha = 8^\circ$ . Base pressures and pressure distributions on the afterbodies were measured without jet and with jets of various exit-pressure ratios. Schlieren pictures were taken in order to get some insight into the flow field in the tail region of the missile, especially with respect to flow separation.

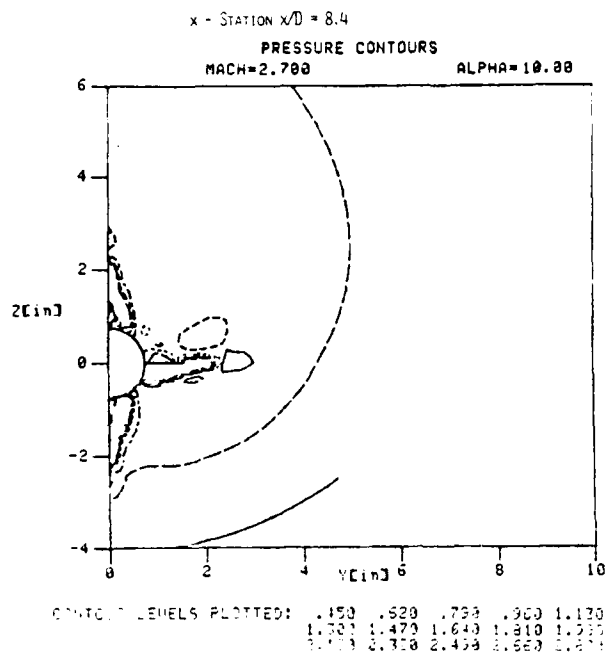


Fig. 12 Pressure contour map for wing-body configuration in "+" roll position,  $M_\infty = 2.7$ ,  $\alpha = 10^\circ$ .

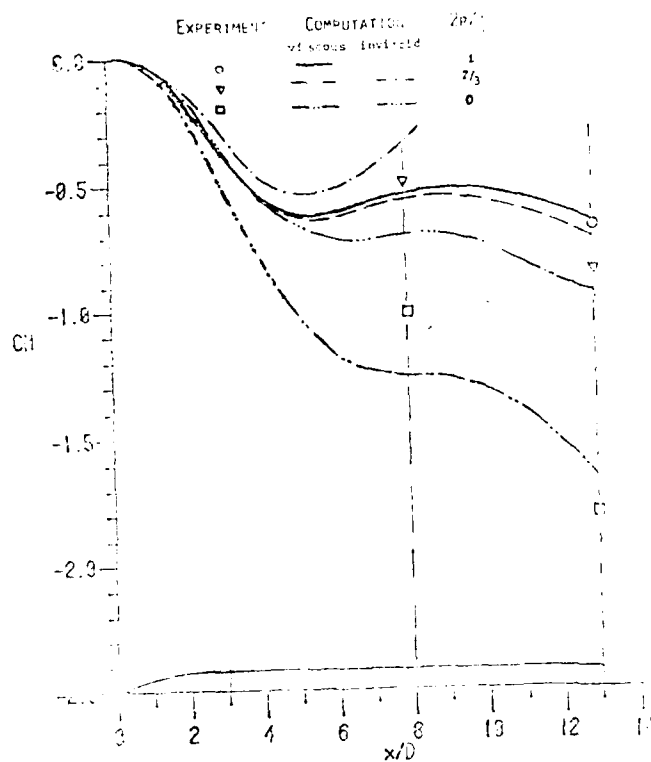


Fig. 8 Pitching moment coefficient,  $M_\infty = 2$ ,  $\alpha = 5.1^\circ$ ,  $Re_\infty = 0.7 \times 10^6$ .

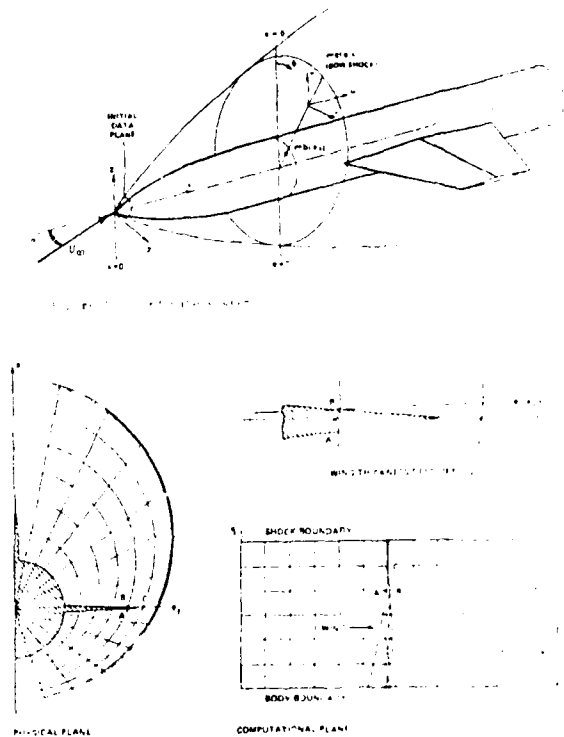


Fig. 9 Thin fin approximation in physical and computational space.

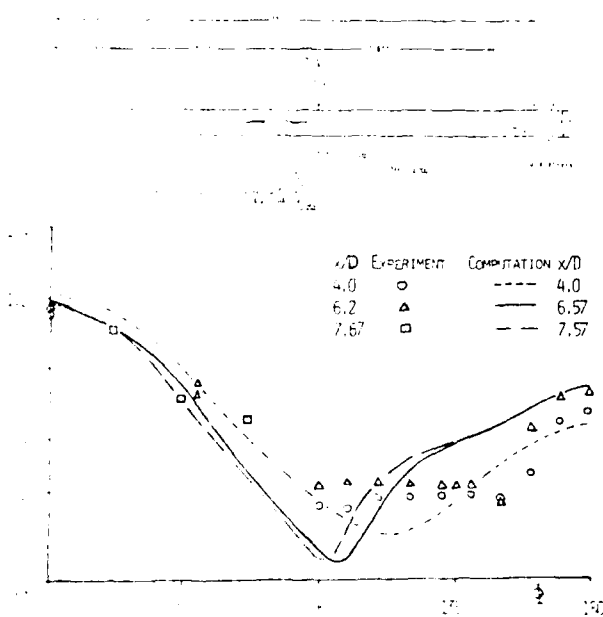


Fig. 10 Predicted and experimental circumferential pressure distribution,  $M_\infty = 2.7$ ,  $\alpha = 10^\circ$ ,  $Re_\infty = 2.5 \times 10^5$ .

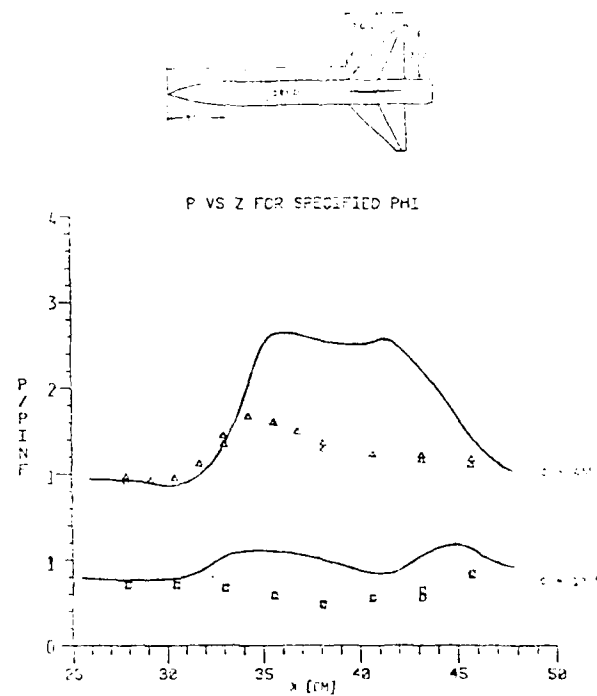


Fig. 11 Predicted and measured longitudinal pressure distribution in "4" roll position,  $M_\infty = 2.7$ ,  $\alpha = 10^\circ$ .

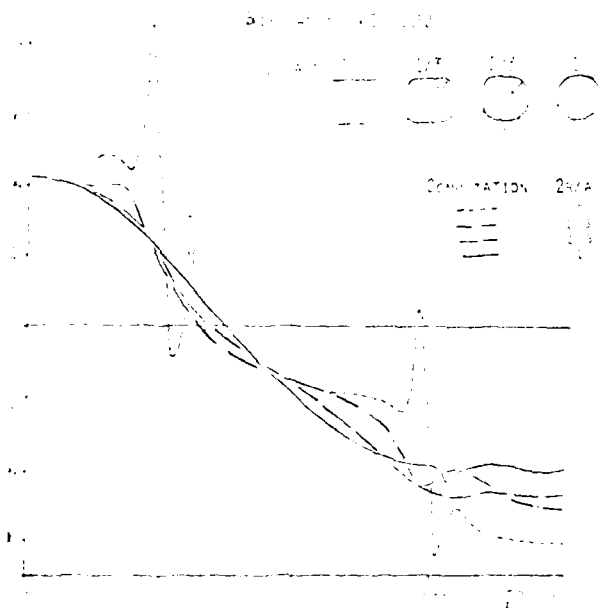


Fig. 4 Predicted circumferential pressure distribution,  $M_\infty = 2$ ,  $\alpha = 5.1^\circ$ ,  $Re_\infty = 0.7 \cdot 10^6$ .

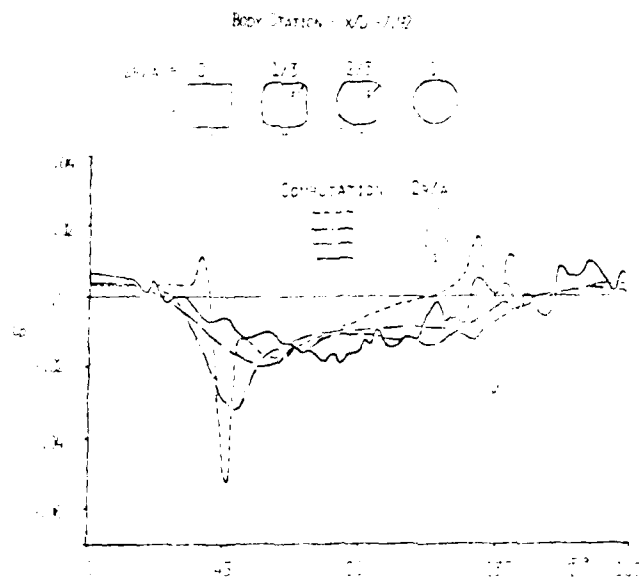


Fig. 5 Predicted circumferential pressure distribution,  $M_\infty = 2$ ,  $\alpha = 5.1^\circ$ ,  $Re_\infty = 0.7 \cdot 10^6$ .

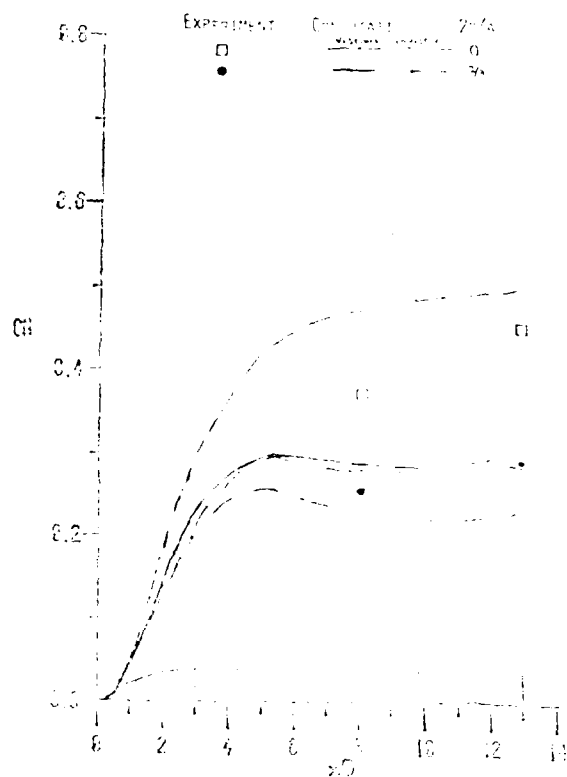


Fig. 6 Normal force coefficient,  $M_\infty = 2$ ,  $\alpha = 5.1^\circ$ ,  $Re_\infty = 0.7 \cdot 10^6$ .

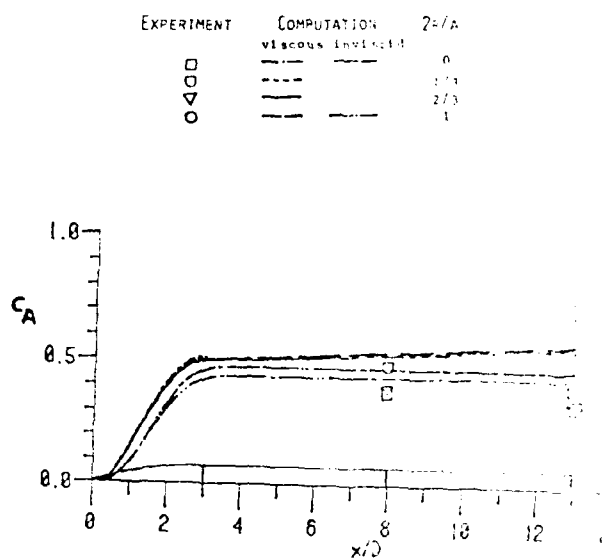


Fig. 7 Axial force coefficient,  $M_\infty = 2$ ,  $\alpha = 5.1^\circ$ ,  $Re_\infty = 0.7 \cdot 10^6$ .

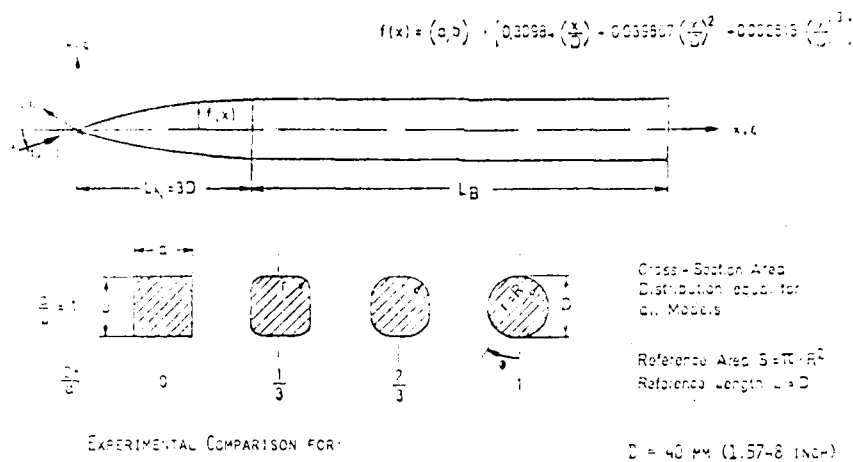


Fig. 1 Model configuration, coordinate systems and experimental cases.

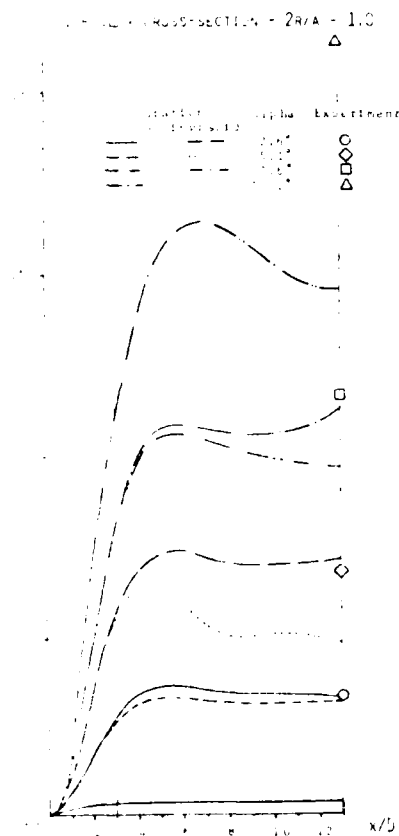


Fig. 2 Normal force coefficient,  $M_\alpha = 2$ ,  $Re_{\alpha, D} = 0.7 \cdot 10^6$ .

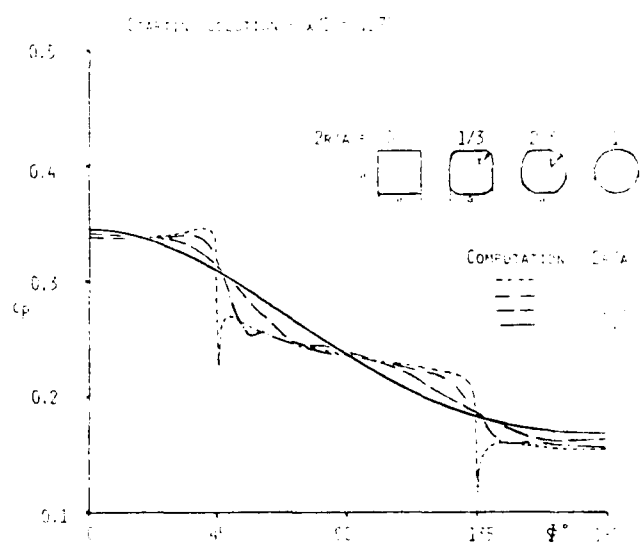


Fig. 3 Predicted circumferential pressure distribution,  $M_\alpha = 2$ ,  $i = 5.1^\circ$ ,  $Re_{\alpha, D} = 0.7 \cdot 10^6$ .

14. Schneider, W., "Experimental Investigations on Bodies with Noncircular Cross Section in Compressible Flow," AGARD-CCP-336, AGARD Fluid Dynamic Panel Symposium on "Missile Aerodynamics", Trondheim, Norway, Sep 1, 1982.
15. Stallings, Jr., R. L., Lamb, M. and Watson, C. B., "Effect of Reynolds Number of Stability Characteristics of a Cruciform Wing-Body at Supersonic Speeds," NASA TP-1638, July 1980.

Table A. Values for Stability, Implicit and Explicit Smoothing Factors and Marching Stepsize

$\alpha$	$2r/a$	1	2/3	1/3	0
5.1	$\Delta x$	.1	.1	.1	.1
	$\epsilon_A$	.2*	2.0*	4.0*	4.0*
	$\epsilon_I$	.1	.1	.1	1.0
	$\epsilon_E$	.2	.2	.2	2.0

\* Values for SOC,  $\epsilon_A$  = fin starting value

$\Delta x$  - Marching Stepsize

$\epsilon_A$  - Stability Coefficient

$\epsilon_I$  - Implicit Smoothing Coefficient

$\epsilon_E$  - Explicit Smoothing Coefficient



## References

1. Kutler, P., Pulliam, T. H., and Vigneron, Y. C., "Computation of the Viscous Supersonic Flow over External Axial Corners," AIAA J. Vol. 17, No. 6, Jun 1979, pp. 571-578.
2. Schiff, L. B., and Sturek, W. B. - Numerical Simulation of Steady Supersonic Flow over an Ogive-Cylinder-Boattail Body. AIAA Paper 80-0066, Jan 1980.
3. Chaussee, D. S., Patterson, J. L., Kutler, P., Pulliam, T. H., and Steger, J. L. - A Numerical Simulation of Hypersonic Viscous Flows Over Arbitrary Geometries at High Angle of Attack. AIAA Paper 81-0050, St. Louis, Mo., 1981.
4. Rizk, Y. M., Chaussee, D. S., and McRae, D. S. - Computation of Hypersonic Flow around Three-Dimensional Bodies at High Angles of Attack. AIAA Paper 81-1261, Palo Alto, Calif., 1981.
5. Chaussee, D. S. and Rizk, Y. M. - Computation of Viscous Hypersonic Flow Over Control Surfaces. AIAA Paper 82-0291, Jan 1982.
6. Rai, M. M., Chaussee, D. S., and Rizk, Y. M. - Calculation of Viscous Supersonic Flows over Finned Bodies. AIAA Paper 83-1667, 1983.
7. Jettmar, R. H. and Kordulla, W. - Computation of Aerodynamic Forces on Bodies with Non-Circular Cross-Section in Supersonic Viscous Flow. AIAA Paper 83-2077, August 1983.
8. Schiff, L. B., and Steger, J. L. - Numerical Simulation of Steady Supersonic Viscous Flow. AIAA Paper 79-130, New Orleans, La., 1979.
9. Beam, R. and Warming, R. F. - An Implicit Factored Scheme for the Compressible Navier-Stokes Equations. AIAA J., Vol. 16, Apr 1978.
10. Wardlaw, A. R., Solomon, J. M., and Baltakis, F. P., "Supersonic Inviscid Flow Fields Computations of Missile Type Bodies," AIAA J., Vol. 19, No. 7, Jul 1981, pp. 899-906.
11. Chaussee, D. S., "NASA Ames Parabolized Navier-Stokes Code (PANS)," Computational Fluid Dynamics Workshop, March 1984, University of Tennessee Space Institute, Tullahoma, Tenn.
12. Degani, D. and Schiff, L. B., "Computation of Supersonic Viscous Flows Around Pointed Bodies at Large Incidence," AIAA 83-0034, AIAA 21st Aerospace Sciences Meeting, Jan 1983.
13. Steger, J. L., and Sorenson, R. L., "Automatic Mesh-Point Clustering Near a Boundary in Grid Generation with Elliptic Partial Differential Equations," J. Comp. Physics, Vol. 33, No. 3, Dec 1979, pp. 405-410.

### Concluding Remarks

Using the PNS methodology to compute viscous, supersonic flow over secant-ogive-cylinder bodies with arbitrary cross-section is a possible alternative to the full Navier-Stokes equation if one restricts oneself to moderate angle of attack to avoid flow reversal in the marching direction. To accomplish the flow field prediction for complex, realistic configuration the concept of "wrap-around" grid has to be extended. The computational space of "wrap-around" grid has only one impesmeable boundary, the mapping of the body onto the plane,  $\zeta=0$ . An extension to this concept is to introduce impermeable surfaces normal to the plane,  $\zeta=0$  at various positions,  $\eta=\text{const}$ . The above results indicate that this concept is feasible but careful attention has to be given to the newly introduced boundaries with a no-slip condition and the corner points. Further work is currently conducted at NSWC to extend the PNS methodology to a multi-zone concept which allows complicated shapes to be mapped to multiple connected regions of computation.

### Acknowledgement

This work is performed under the sponsorship of NAVAIR and NAVSEA. Special thanks are extended to Dr. W. B. Stureck, Launch and Flight Division of the Ballistic Research Laboratory, Aberdeen Proving Grounds, Md. under whose auspices the computer support for this project was provided.

surfaces which would float within the basic grid, with the application of a no-slip boundary condition on the fin surfaces. The analysis is restricted to relatively thin fins with sharp edges which lie approximately along constant  $\phi$  planes. A thin fin approximation is employed which neglects the fin thickness but retains the actual fin surface slopes. For an important class of body-fin configurations, the thin fin approximation allows the direct use of the basic grid generated for the body alone shape with only one additional computational point in the circumferential coordinate per fin (i.e., the original grid point represents the upper fin surfaces and the additional point the lower surface), Figure 8. Using experimental data given in [15] a wing-body configuration of  $M=2.7$  and  $\alpha=10^\circ$  is used to test this concept of introducing thin fins. The configuration is shown in Figure 9. Calculated circumferential pressure distributions are compared with experimental data at different positions along the cylindrical body. On the windward side the computation gives reasonable agreement with the data. The leeward data indicates separated flow which is not predicted by the PNS computation. Through the necessary use of smoothing in the computation certain effects of separation can be masked and the marching procedure does not encounter reversed flow condition. In the present calculation, an infinitely thin flat plate is used to simulate the fins. Following the pressure distribution along the body between the "cruciform" fin position at  $\psi=45^\circ$  (windward) and  $\psi=135^\circ$  (leeward) the computation agrees well with the data at the onset of the fins Figure 10. This situation changes as the influence of introducing the fins is felt further downstream at the midpoint between the fins and the predicted pressure distribution disagrees sharply with the measurements as seen in Figure 11. Further improvement on treating the no-slip condition at the fin-body corners are necessary at this point. A contour plot for the pressure of  $x/D=8.4$  is shown in Figure 12. The plot indicates qualitatively the correct wrapping around of the pressure contour lines from the lower to the upper wing surface.

large pressure jumps. Only additional experiments will be able to guide the research efforts for this situation by establishing the correct physics for the flow around sharp corners. As the solution is marched further down the body the effects of smoothing for the marching solution can be observed. The circular cross-section needs the least amount of smoothing to be successfully marched (See Table A). Accordingly at  $x/D=7.92$  the calculated circumferential pressure distributions exhibits large "wiggles", (Figure 5) while the computed results for the other cross-section, needing larger amounts of smoothing to be successfully marched show the expected outcome.

Integrating the pressure field obtained by the PNS computation, Figure 6 shows the local normal force for the two different cross-sections ( $2r/a=0$  and  $2r/a=2/3$ ) for  $M=2.0$  and  $\alpha=5.1^\circ$ . They are compared to measured data at  $x/D=8$  and  $x/D=13$  and an inviscid computation for the exact same flow condition. In the case of  $2r/a=2/3$ , the viscous result agrees reasonably close with the data only at  $x/D=13$ . For all non-circular cross-sections, the viscous computation overestimates the normal forces but exhibits the right trend of the data. The inviscid computations underestimate the experimental results.

Figure 7 compares viscous and inviscid results for the axial force coefficient with the data at  $\alpha=5.1^\circ$ . The computed local axial force coefficient does change very little for the different cross-sections, an expected result because all cross-sectional areas are of the same size. The inviscid computation does not predict an increase in axial force when the cylindrical portion is reached as the inviscid theory demands. The slight increase along the body for the viscous result represents the contribution of the wall shear-stress. The experimental data does not agree with the computational results and shows a decrease in axial force with the increase in body length.

In the case of the circular cross-section, the experimental overall lift/drag moment coefficient agrees with the computed results (Figure 8) while for the other cross-section the experimental data is over or under predicted, depending on body-length and shape of the cross-section. Inviscid results exhibit the same trend, but deviate from the data more than the viscous results as the angle of attack increases.

Within this framework a "thin fin" approximation is incorporated. The program is instructed to extend the far-field points to represent the fin

The main features of the flow field are indicated in the upper, left-hand picture.

The characteristic pattern of the external flow with a shock wave downstream of the base due to interference of the jet remains basically unchanged for all pressure ratios and incidences investigated. With increasing incidence the jet boundary and the barrel shock on the pressure side are slightly blown in crossflow direction at all pressure ratios. This is also observed for the interference shock.

It is evident that with increasing jet exit pressure ratio,  $p_{JE}/p_{\infty}$ , the jet width increases for all incidences,  $\alpha$ , furthermore the barrel shock widens, and there is a steepening of the interference shock.

The corresponding results of pressure measurements are shown in Fig. 9 in the bottom diagram. There is no influence of the jet on the afterbody pressure distribution for all incidences and jet exit pressure ratios considered, as far as this afterbody-nozzle combination (with the smallest nozzle) is concerned.

The influence of the nozzle-exit diameter, i.e. the jet exit diameter, on the afterbody pressure distribution can be seen in Fig. 8 and 9 for various incidences and exit pressure ratios. While there is no influence of the jet forward of the base with the smallest nozzle (N3), independent of incidence and jet exit pressure ratio; the jet makes itself felt increasingly with the larger nozzles.

One can conclude, that decreasing the nozzle exit diameter, effectively reduces the influence of the propulsive jet on the pressure distribution along the afterbody.

The effect of increasing jet exit pressure ratio has been seen in the Schlieren pictures of Fig. 7a for the smallest

nozzle, consisting in an increase of the jet width for all incidences. A similar effect is expected for the other two nozzles with larger exit diameters (N2, N1). There is no influence due to the jet on the afterbody pressure distribution in the case of the smallest nozzle (N3), and only for the largest pressure ratio in the case of the intermediate nozzle (N2). However, for the largest nozzle (N1) it can be deduced from Fig. 8 that increasing pressure ratios lead to increasing disturbances due to jet interference, and the disturbance is felt farther and farther upstream.

### 3.1.2 Conical afterbodies, $Ma_\infty = 2.0$

Next is considered the effect of boat-tailing on the external flow/jet interference phenomena. In the Schlieren pictures in Figs. 7b and 7c the influence can be seen for the  $5^\circ$  and  $10^\circ$  conical afterbodies, again with the smallest nozzle (N3), at free-stream Mach number  $Ma_\infty = 2$ .

Again, the jet width increases with increasing jet exit pressure ratio for all incidences, the jet influence on the external flow is felt increasingly further upstream, reaching forward on the afterbody. The upstream influence becomes more severe as the boat-tail angle is increased. This is confirmed by the pressure distributions, depicted in Fig. 10 and Fig. 11, which show that the pressure disturbances move upstream on the afterbody with increasing boat-tail angle. In contrast, on the cylindrical afterbody, only limited forward influence is observed.

For the  $10^\circ$  conical afterbody, with the highest pressure ratio,  $p_{JE}/p_\infty = 24.5$ , large separated regions, starting near the shoulder, are assumed to be present, with distinct plateau type pressure distributions, as seen in the bottom graph of Fig. 11. (On this, one has to add the fairly

linear, pressure,  $p$ , without jet influence, in order to get the actual pressure with jet influence.) In this graph, there is also indicated the position of the separation shock; it can be noticed, that the pressure rise in the shock is communicated upstream in the subsonic portion of the boundary layer.

The effect of the jet on the flow field around the conical afterbodies with increasing incidence seems to be more expressed on the lee side. The separation shock on the pressure side is moving downstream with incidence, leaving more and more of the afterbody flow undisturbed, as is seen in the Schlieren pictures Fig. 7b and 7c and also in the changes of local pressure coefficient,  $\Delta c_{pJ}$ , in Fig. 10 and Fig. 11. It is evident from the pressure measurements, that the interference due to the jet is communicated farther upstream on the suction side (measured at  $\alpha = -4^\circ$ ) than on the pressure side ( $\alpha = +4^\circ$ ).

In Fig. 7e the shock positions on the conical afterbodies (with the smallest nozzle, N3) are given as function of the jet exit pressure ratio for zero incidence at  $Ma_\infty = 2.0$  and  $Ma_\infty = 1.5$ , as obtained from the Schlieren pictures. The figure demonstrates how the shock moves upstream with increasing jet exit pressure ratio in all cases.

In Fig. 7f the position of the separation shock on the same conical afterbody/nozzle configurations are shown in dependance of incidence for a small and a large jet exit pressure ratio at free-stream Mach number  $Ma_\infty = 2.0$ . In all cases, the shock (on the windward side) is moving downstream with increasing incidence.

### 3.1.3 Cylindrical afterbody, $Ma_\infty = 1.5$

The test carried out with the cylindrical afterbody at the lower free-stream Mach number,  $Ma_\infty = 1.5$ , gave basically

the same results as were obtained at  $Ma_\infty = 2.0$ . Fig. 12 shows again for the three different nozzles, that the effect of the exhaust jet on the afterbody flow field is reduced and even vanishes with decreasing jet width. The jet influence is felt farther upstream on the suction side ( $\alpha = -4^\circ$ ) than on the pressure side ( $\alpha = +4^\circ$ ).

The influence of decreasing free-stream Mach number is expressed in a stronger interference of the jet on the afterbody pressure distribution, as is seen by comparing Fig. 8 and 9 with Fig. 12 at  $p_{JE}/p_\infty \approx 6$  for the various cylindrical afterbody/nozzle combinations.

#### 3.1.4 Conical afterbody, $Ma_\infty = 1.5$

The tests carried out on the  $5^\circ$ -boat-tailed afterbody at the lower free-stream Mach number,  $Ma_\infty = 1.5$ , show also that the influence of the jet on the pressure distribution is felt further upstream than on the cylindrical afterbody (with same nozzle, N3); as can be seen by comparison of Fig. 13 and Fig. 12. Again, the influence of the jet on the flow field about the afterbody at incidence is communicated further forward on the suction side ( $\alpha = -4^\circ$ ) than on the pressure side ( $\alpha = +4^\circ$ ). The corresponding flow visualization pictures are given in Fig. 7d.

Decreasing the free-stream Mach number, results again in a stronger interference of the jet on the afterbody pressure distribution, as is seen when comparing Fig. 10 and Fig. 13, for jet exit pressure ratios  $p_{JE}/p_\infty \approx 6$ . Corresponding Schlieren pictures of Fig. 7b and 7d bear out the same result.

#### 3.2 Influence of jet on base pressure

The propulsive jet will influence the base pressure,  $p_B$ . For small jet exit pressure ratios,  $p_{JE}/p_\infty$ , an entrainment



effect of the jet dominates, which may lead to an unwanted decrease of base pressure. At high jet exit pressure ratios a displacement effect of the jet dominates, which usually causes an increase of base pressure [7, 8].

On the cylindrical afterbody, equipped with the nozzles of various exit diameters at free-stream Mach number  $Ma_\infty = 2$ , it is found that the influence on the base pressure due to the jet becomes stronger with increasing jet exit pressure ratio, as is seen in Fig. 8 and 9. There is no conclusive trend to be found as to the effect of incidence.

The influence is reduced as the jet diameter decreases and the base area increases correspondingly (Fig. 8 and 9).

Boat-tailing causes an increased pressure rise due to jet interference, as is seen in Fig. 9, 10, and 11 for jet exit pressure ratio  $p_{JE}/p_\infty \approx 6$ .

#### 4. Conclusions

It is shown, that a small Ludwig-tube installation is a practicable means for producing short-duration propulsive-jet flows for a missile model in a wind tunnel. It was used to study the interference of underexpanded jets and the supersonic flow past cylindrical and conical afterbodies, without and with incidence.

It is concluded, that decreasing nozzle exit diameter effectively reduces the influence of the propulsive jet on the pressure distribution along the afterbody. The upstream influence of the jet gets stronger as the boat-tail angle is increased. The shock on the conical afterbodies, at zero incidence, moves upstream with increasing jet exit pressure ratio; the shock moves downstream on the windward side with

increasing incidence. At incidence, the interference due to the jet is communicated farther upstream on the suction side than on the pressure side. Decreasing the free-stream Mach number results in a stronger interference of the jet.

These results are considered as a base for investigating the influence of jet temperature; the hot gas flow to be provided by a heated Ludwig tube, presently under construction.

## 5. References

- [1] A.L. Addy, H.H. Korst, R.A. White, B.J. walker:  
A Study of Flow Separation in the Base Region and its  
Effects During Powered Flight. AGARD CP-124; 1973.
- [2] R.A. White, J. Agrell: Boattail and Base Pressure Pre-  
diction Including Flow Separation of Afterbodies with  
a Centered Propulsive Jet and Supersonic External Flow  
at Small Angles of Attack. AIAA Paper 77-958, AIAA/SAE  
13th Propulsion Conference, Orlando, Florida, July 1977.
- [3] B. Wagner, R.A. White: Supersonic Base Flow Problem in  
Presence of an Exhaust Jet. AIAA Journal, Vol. 18, 1980,  
pp. 876-882.
- [4] H. Ludwieg, Th. Hottner: Die Überschall-Meßstrecke  
(710 mm  $\times$  725 mm) des Hochgeschwindigkeitskanals der  
AVA. ZFW, Vol. 11, 1963, pp. 137-142.
- [5] H. Ludwieg: Der Rohrwindkanal. ZFW, Vol. 3, 1955,  
pp. 206-216.
- [6] G. Hefer, G. Koppenwallner: Kurzzeitversuchsstand zur  
Treibstrahlsimulation bei hohen Druckverhältnissen.  
DFVLR-IB 252-76 H 12, 1976.
- [7] W.L. Peters: A comparison of Jet Temperature Effects  
on Afterbody Drag with Those From Jet Molecular Weight  
and Nozzle Area Ratio Variations. AIAA Paper 80-1161,  
AIAA/SAE Conference, Hartford, Connecticut/USA, June  
1980.
- [8] J. Agrell, R.A. White: An Experimental Investigation  
of Supersonic Axisymmetric Flow over Boattails Con-  
taining Centered Propulsive Jets. FFA Technical Note  
AU913, Stockholm/Sweden, 1974.
- [9] G. Koppenwallner, D. Rammenzweig, V. Strunck:  
Rocket Exhaust Jet Flow and Upstream Flow Field Inter-  
ference - Experiments and Flow Field Analysis -.  
AGARD-CPP-336, 1982, pp. 28-1 to 28-12.

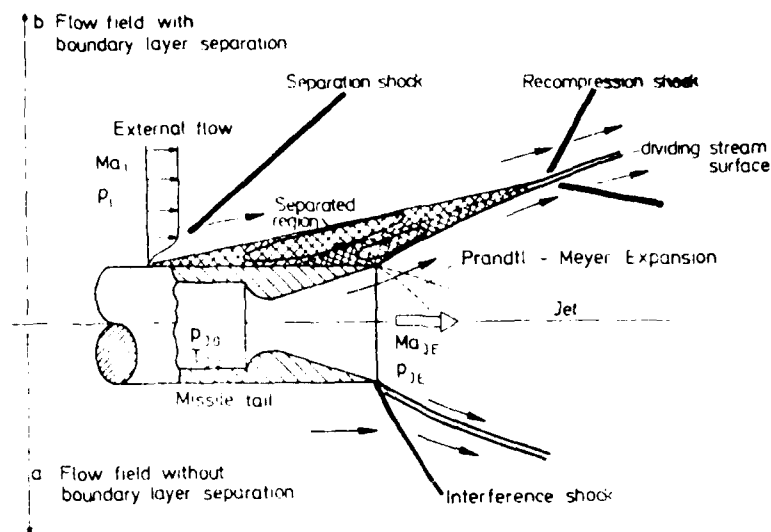


Fig. 1: Interaction of supersonic external flow and jet in tail region of missile.

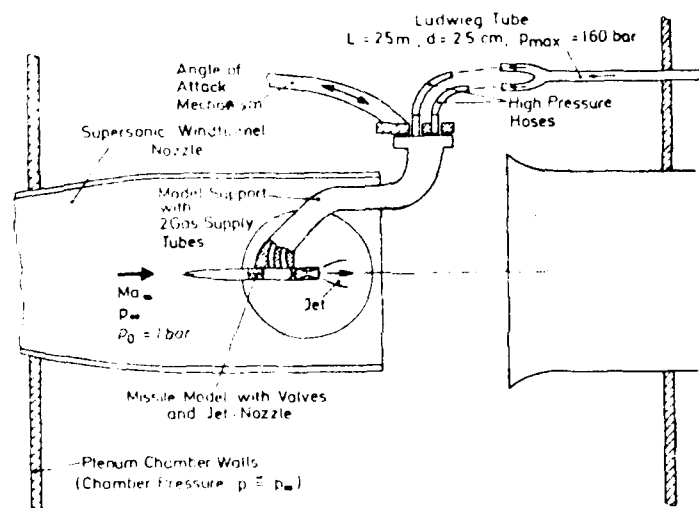


Fig. 2: Jet simulation with Ludwig-tube gas supply in DFVLR-AVA High-Speed Wind Tunnel (schematically).

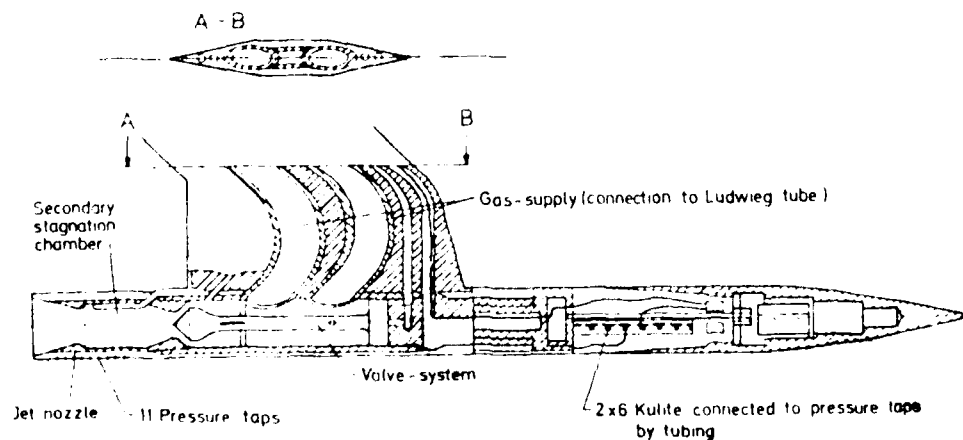
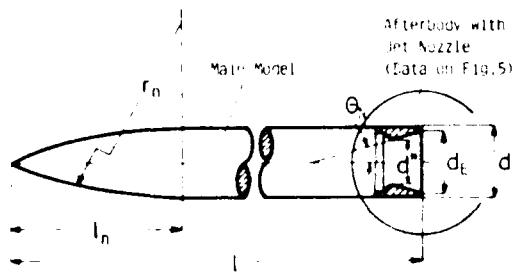
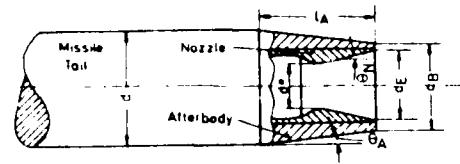


Fig. 3: Sketch of missile model.



Model part	Dimension	Normalized Dimension
Body		
Diameter $d$	40 mm	$l_b/d = 14$
Length $l_b$	560 mm	
AGILE-NOSE		
Length $l_n$	10 mm	$l_n/d = 4$
Radius $r_n$	650 mm	$r_n/d = 16.25$

Fig. 4: Summary of model data.



External - Afterbody Data				
No.		$\theta_A$ [°]	$l_A/d$	$d_e/d$
A1	Cylindrical	0	1	1
A2	Cylindrical	5	1	0.825
A3	Cylindrical	10	1	0.6473

Internal - Nozzle Data					
No.		$\theta_N$ [°]	$Ma_E$	$d^*$ [mm]	$d_E$ [mm]
N1		15	2.5	22.13	36
N2		15	2.5	19.71	32
N3		15	2.5	14.78	24

Afterbody - Nozzle Combinations				
No.		$d_t/d$	$d_e/d$	$d_e/d_B$
1	A1 - N1	0.9	1	0.9
2	A1 - N2	0.8	1	0.8
3	A1 - N3	0.6	1	0.6
4	A3 - N3	0.6	0.647	0.927
5	A2 - N3	0.6	0.825	0.727

Fig. 5: Summary of afterbody and nozzle data.

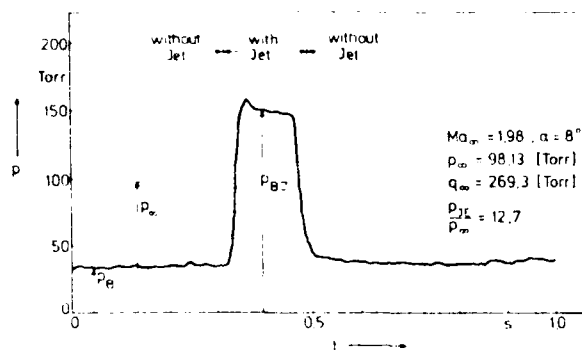


Fig. 6: Typical base pressure trace without and with jet.

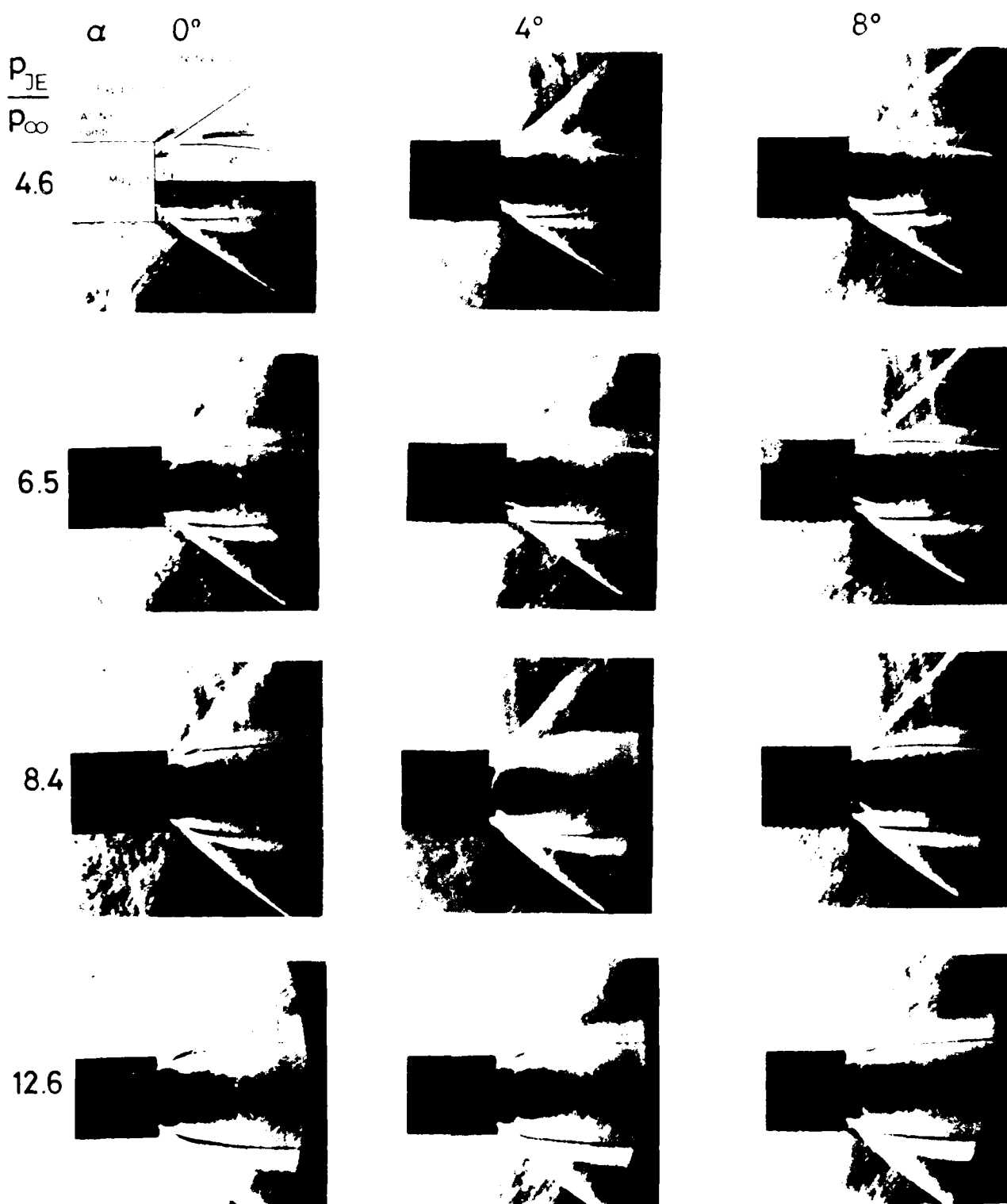


Fig. 7a: Flow field without and with incidence with jet  
at various exit pressure ratios.

$Ma_\infty = 2.0$ , cylindrical afterbody

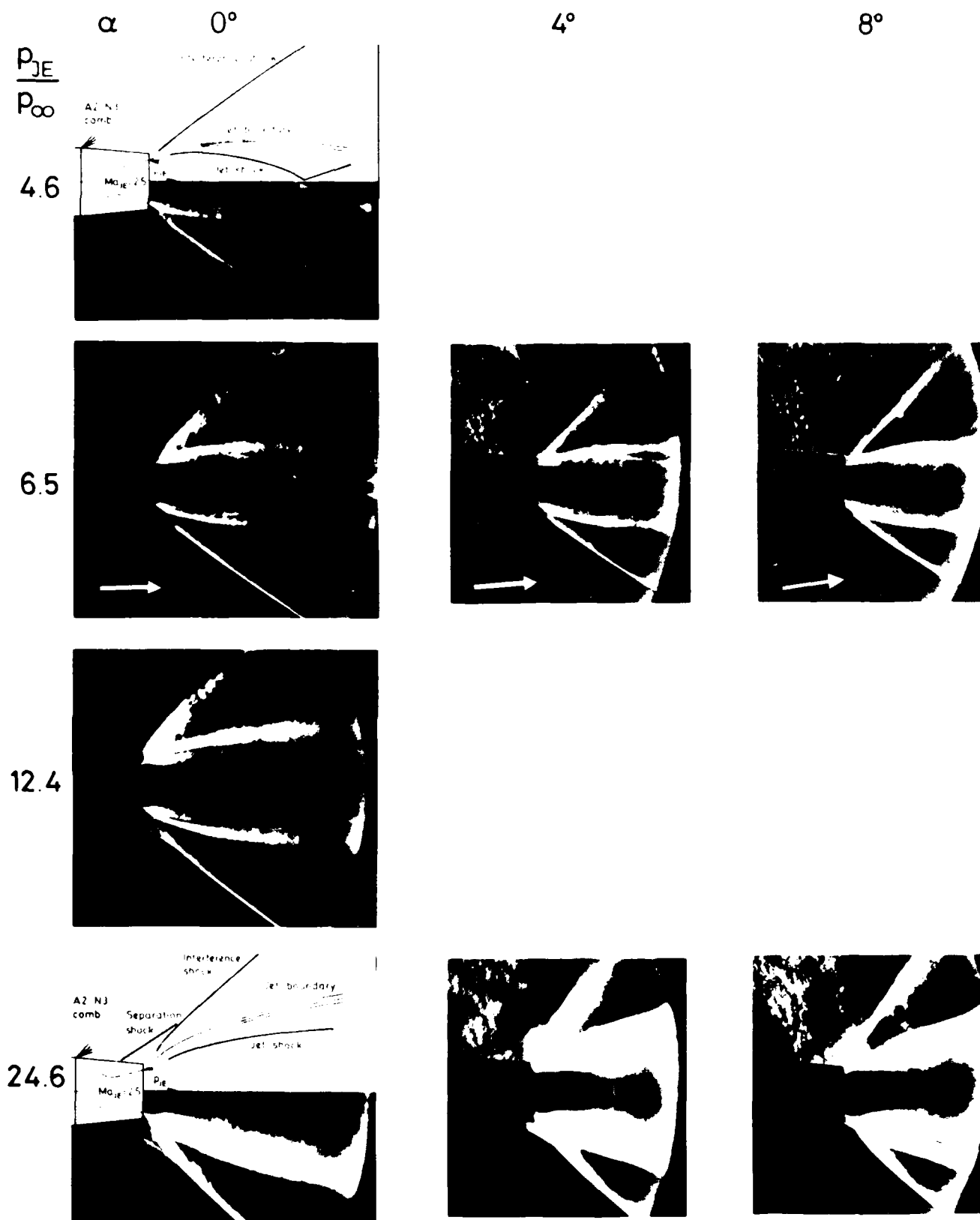


Fig. 7b: Flow field without and with incidence with jet at various exit pressure ratios.

$Ma_\infty = 2.0$ , 5° conical afterbody

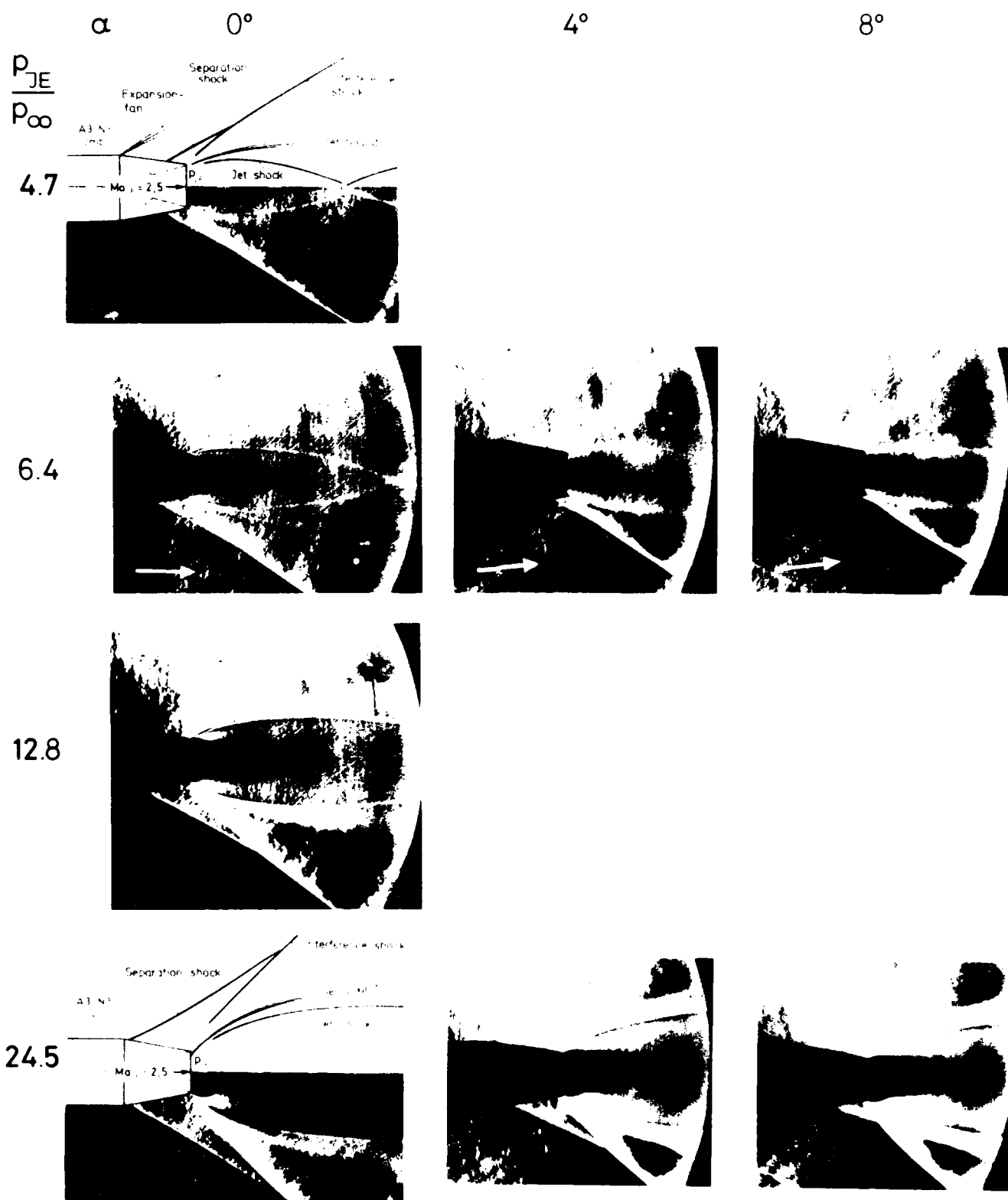


Fig. 7c: Flow field without and with incidence with jet at various exit pressure ratios.

$Ma_{\infty} = 2.0$ ,  $10^\circ$  conical afterbody



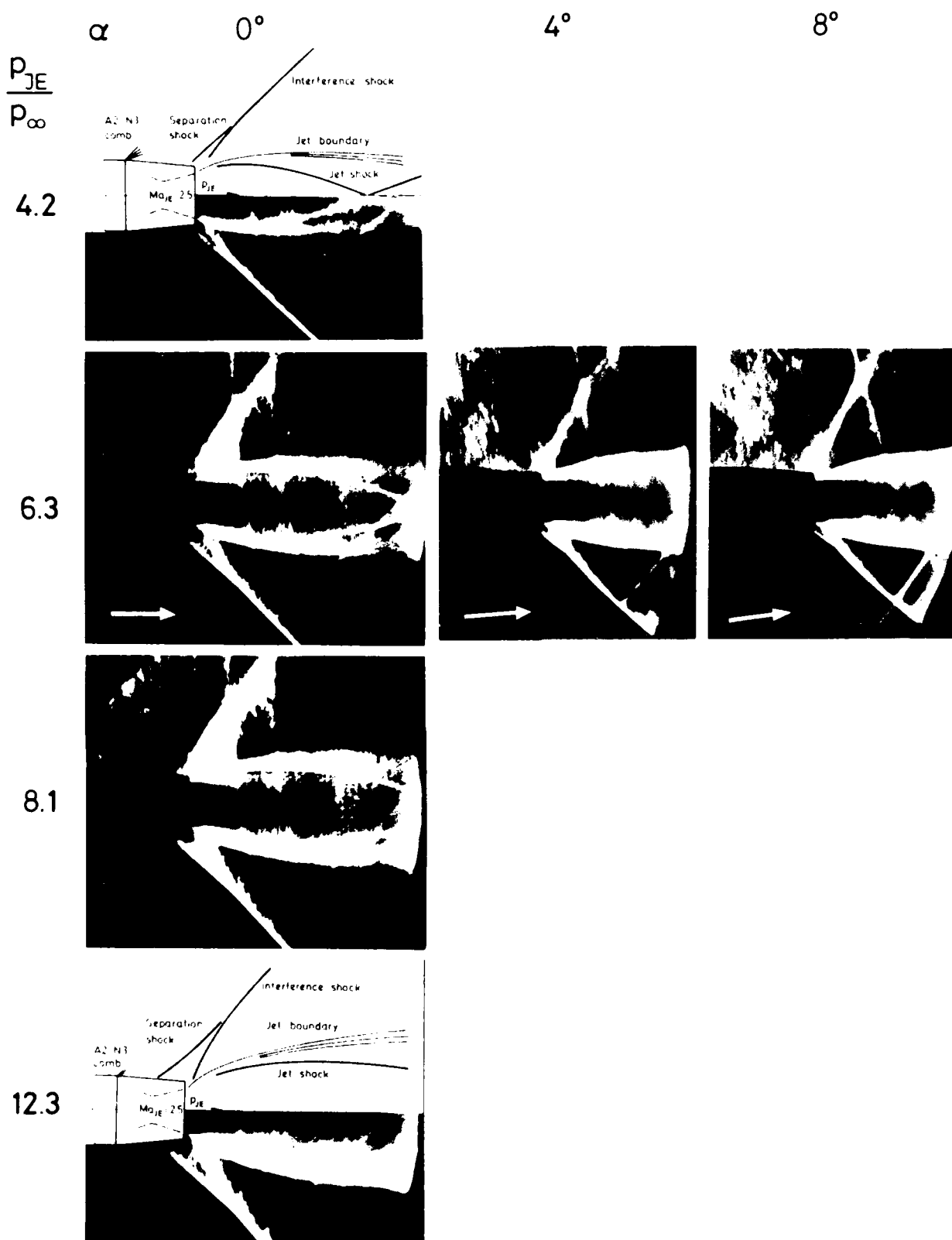


Fig. 7d: Flow field without and with incidence with jet  
at various exit pressure ratios  
 $Ma_\infty = 15$ ,  $5^\circ$  conical afterbody

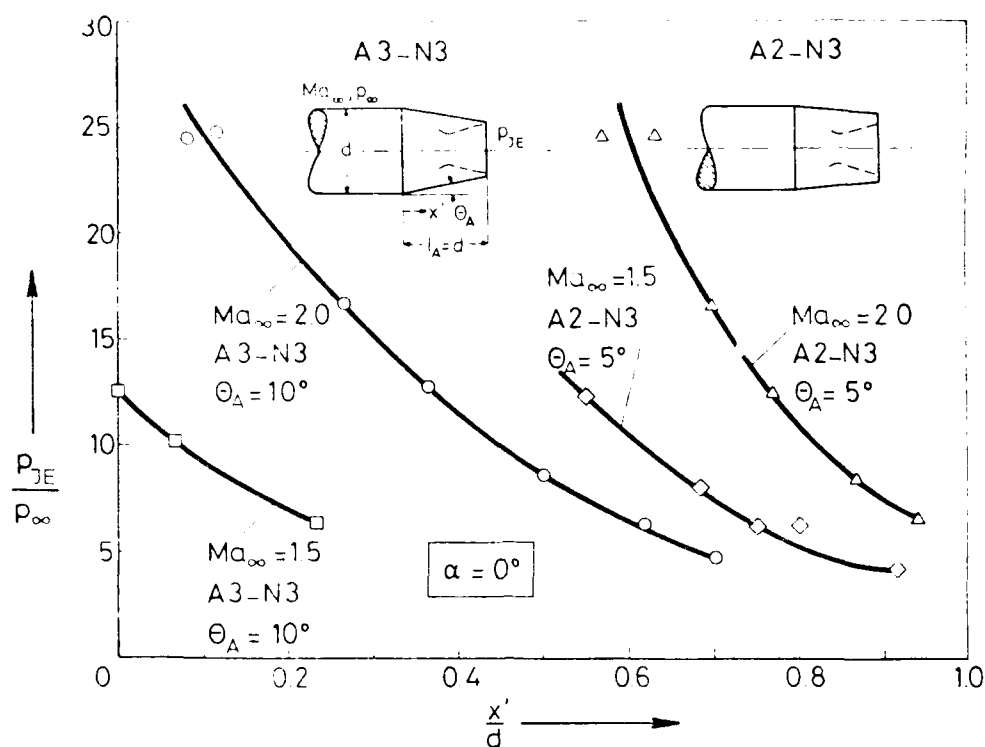


Fig. 7e: Shock position,  $x'/d$ , on conical afterbodies versus jet exit pressure ratio,  $p_{JE}/p_\infty$ , from Schlieren pictures;  $\alpha = 0^\circ$ .

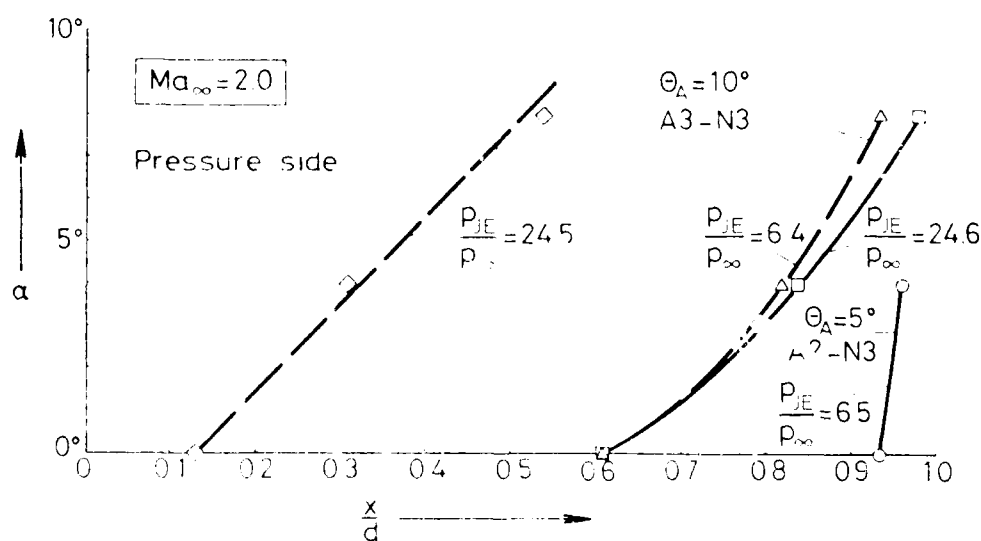


Fig. 7f: Shock position,  $x'/d$ , on conical afterbodies versus incidence,  $\alpha$ , from Schlieren pictures,  $Ma_\infty = 2.0$ .

AD-A153 020

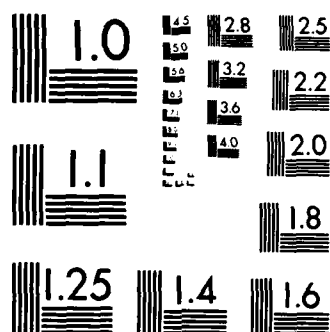
PROCEEDINGS OF THE US AIR FORCE AND THE FEDERAL  
REPUBLIC OF GERMANY DATA. (U) AIR FORCE WRIGHT  
AERONAUTICAL LABS WRIGHT-PATTERSON AFB OH A W FIORE  
AUG 84 F/G 20/4

4/4

UNCLASSIFIED

NL





MICROCOPY RESOLUTION TEST CHART  
NATIONAL BUREAU OF STANDARDS-1963-A

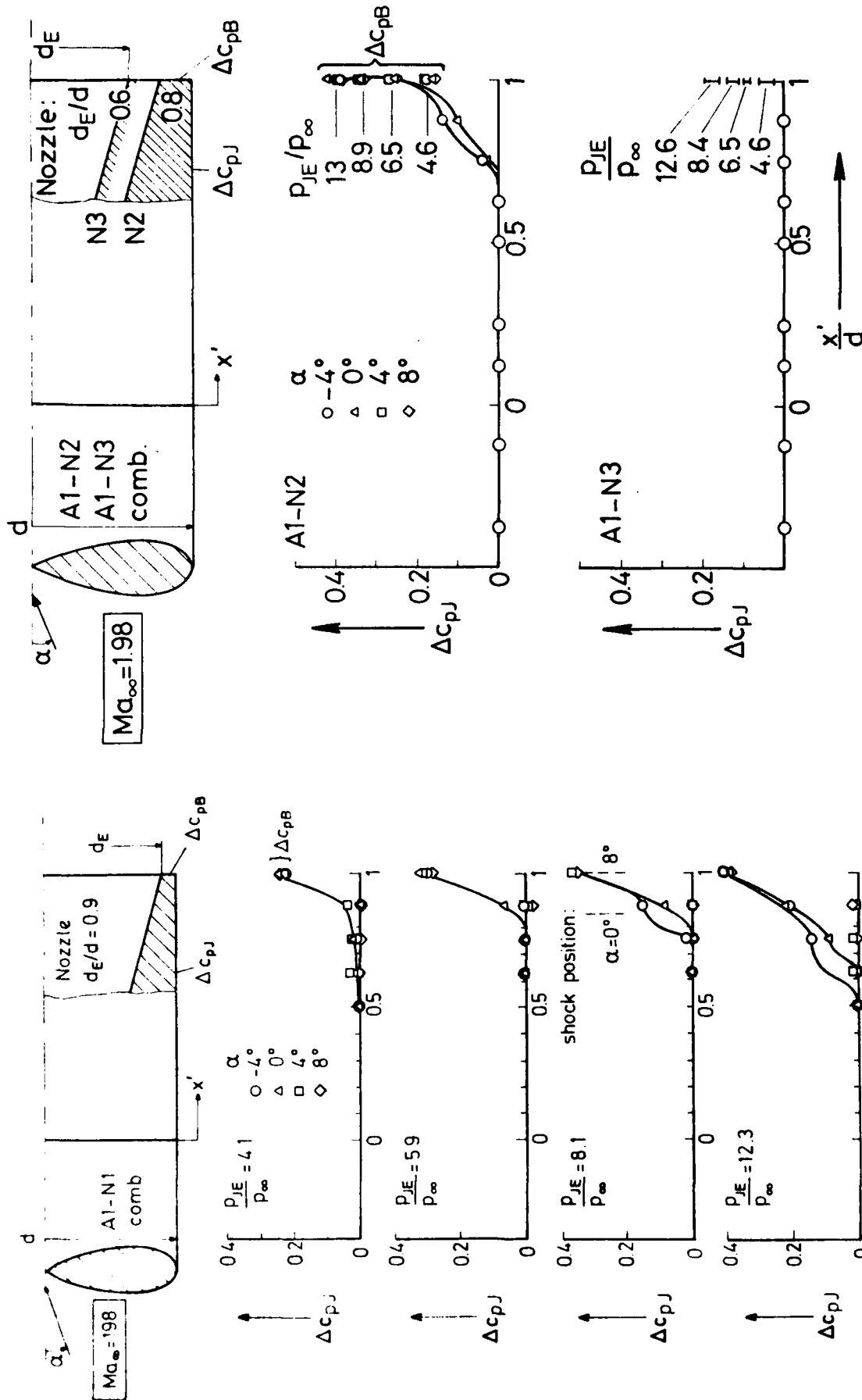


Fig. 8: Change in local pressure coefficient,  $\Delta c_{PJ}$ , due to jet interference on cylindrical afterbody, with nozzle N1;  $Ma_\infty = 1.98$ .

Fig. 9: Change in local pressure coefficient,  $\Delta c_{PJ}$ , due to jet interference on cylindrical afterbody, with nozzles N2 and N3;  $Ma_\infty = 1.98$ .

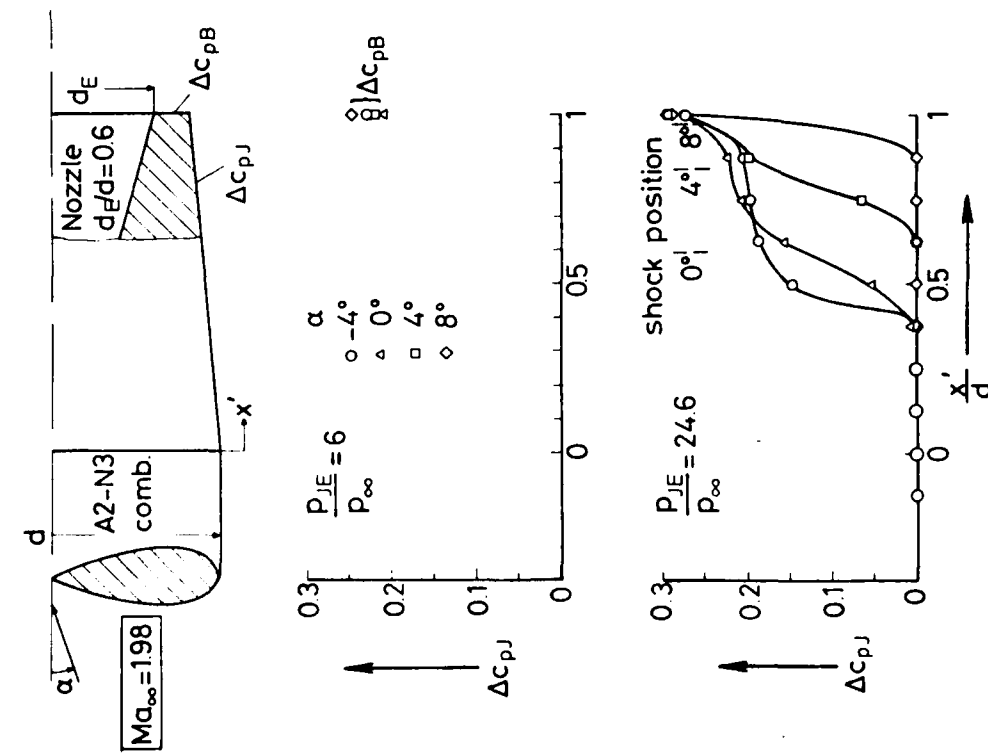


Fig. 10: Change in local pressure coefficient,  $\Delta c_{pJ}$ , due to jet interference on 5° conical afterbody;  $Ma_\infty = 1.98$ .

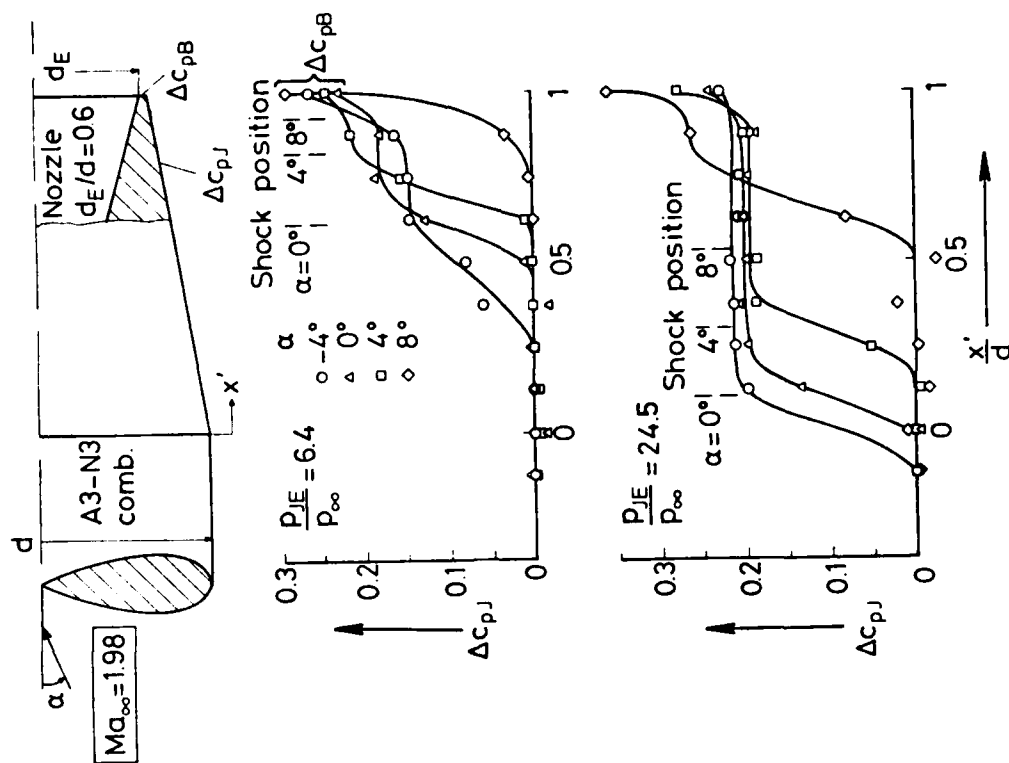


Fig. 11: Change in local pressure coefficient,  $\Delta c_{pJ}$ , due to jet interference on 10° conical afterbody;  $Ma_\infty = 1.98$ .

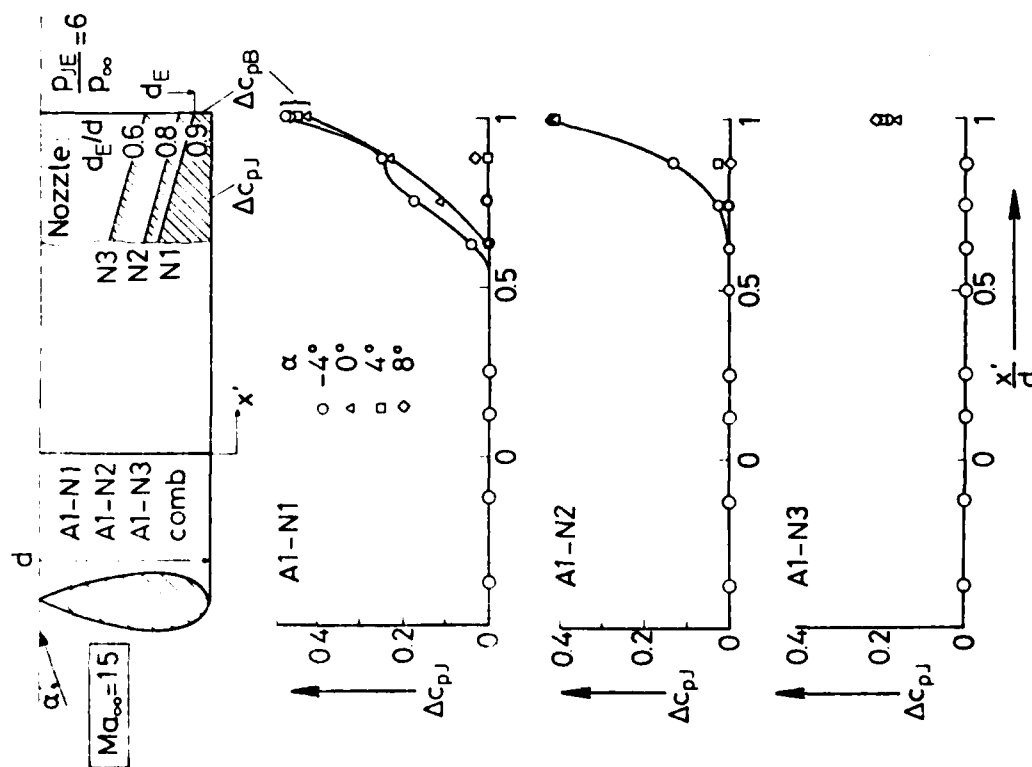


Fig. 12: Change in local pressure coefficient,  $\Delta C_{pJ}$ , due to jet interference on cylindrical afterbody;  $Ma_\infty = 1.5$ .

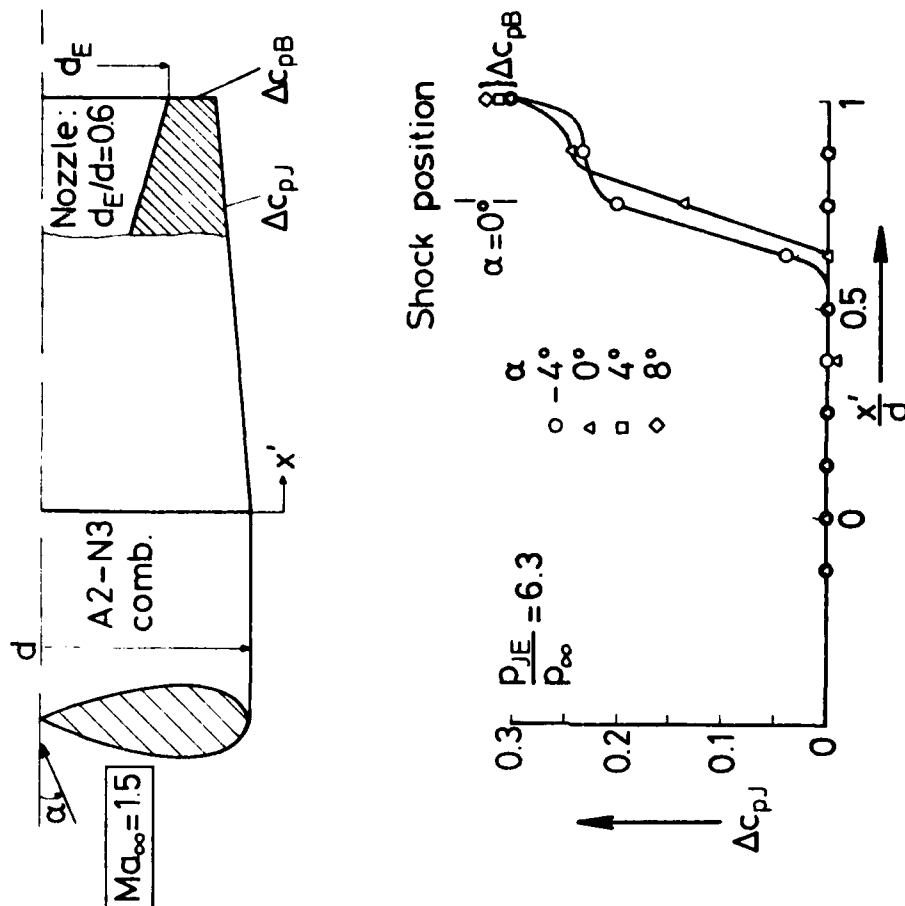


Fig. 13: Change in local pressure coefficient,  $\Delta C_{pJ}$ , due to jet interference on conical afterbody;  $Ma_\infty = 1.5$ .

# NAVIER-STOKES CALCULATIONS OF BASE REGION FLOW FIELDS FOR BODIES OF REVOLUTION

Juharaj Sahu  
Charles J. Nietubicz  
U.S. Army Ballistic Research Laboratory, AMCCOM  
Aberdeen Proving Ground, Maryland 21005

Joseph L. Steger  
NASA Ames Research Center  
Moffett Field, California 94035

## ABSTRACT

A computational capability has been developed for predicting the entire flow field about bodies of revolution including the base region. The additional complexity of base bleed and base jet effects have also been incorporated into this new capability. The thin-layer form of the compressible Navier-Stokes equations is solved using a time dependent, implicit algorithm. Numerical solutions have been obtained for a secant-ogive-cylinder projectile for  $.9 < M < 1.2$  both with and without base bleed. Base drag has been computed and compared with experimental and semi-empirical data. The reduction in base drag with base bleed has been clearly shown for various mass injection rates. Additionally, the effect of a centered propulsive jet on base flow has been computed where the free stream Mach number is 1.343 and the jet exit Mach number is 2.7. Computed results show both qualitative and quantitative features of the base region flow fields.

## INTRODUCTION

A major area of concern in shell design is the accurate prediction of the total aerodynamic drag. Both range and terminal velocity of a projectile, two critical factors in shell design, are directly related to the total aerodynamic drag. The total drag for projectiles can be divided into three components: (1) pressure drag (excluding the base region), (2) viscous (skin friction) drag, and (3) base drag. At transonic speeds, base drag constitutes a major portion of the total drag. For a typical shell at  $M = .90$  the relative magnitudes of the aerodynamic drag components are: (1) pressure drag, 20%, (2) viscous drag, 30%, and (3) base drag, 50%.

The pressure and viscous components of drag generally cannot be reduced significantly without adversely affecting the stability of shell. Recent attempts to reduce the total drag have therefore been directed at reducing the base drag. A number of studies have been made to examine the total drag reduction due to the addition of a boattail [1]. Although this is very effective in reducing the total drag, it has a negative impact on the aerodynamic stability, especially at transonic velocities. An excellent review of the effect of boattailing on total drag and base pressure is presented in Reference [1].



Another effective means of reducing the base drag is that of 'base bleed' or 'base injection'. In this method a small amount of mass is injected into the base region to increase the base pressure and thus reduce the base drag. Recent range and precision tests [2] of a 155mm projectile with and without base bleed have been conducted and an 85% reduction in base drag was obtained. Presently the XM364 is an active projectile design that uses the base bleed concept for increased range. This concept of mass injection at the projectile base has been widely studied for supersonic flows [3,4], while less data is available the transonic flow regime [5]. Only until very recently, with the advent of LDV instrumentation, is extensive base flow data becoming available.

Recently, Navier-Stokes solvers [6,7] have been used to compute the aft end flow field of axisymmetric bodies at supersonic velocities. Limited computational work has also been reported recently by Sullins, et al [8] on the numerical computations of the base region flow of a supersonic combustion ramjet engine using two-dimensional Navier-Stokes equations. At transonic speeds, a limited study of the flow past a boattailed afterbody has been performed by Chow, et al [9] using the potential equation and integral formulations. Recent papers [10,11] have described the development and application of a thin-layer Navier-Stokes computational code to predict the transonic flow about slender bodies of revolution. In References [10] and [11], the technique was shown to be a viable computational tool for predicting both external and internal flows for spinning and nonspinning projectiles of various geometric shapes. These calculations, however, modeled the base flow as an extended sting and thus the base pressure and recirculatory base flow were not computed.

This article describes a unique flow field segmentation procedure [12,13] which has greatly simplified the development of the computer code for the simulation of the complete projectile with base. The code is used here to predict the base pressure of shell at transonic speeds including the effects of base bleed and a centered propulsive jet. Computed results show the quantitative and qualitative details of the base flow structure.

#### COMPUTATIONAL TECHNIQUE

The Azimuthal Invariant (or Generalized Axisymmetric) thin-layer Navier-Stokes equations for general spatial coordinates  $\xi, \eta, \zeta$  can be written as [10]

$$\partial_{\tau} \hat{q} + \partial_{\xi} \hat{E} + \partial_{\zeta} \hat{G} + \hat{H} = \text{Re}^{-1} \partial_{\zeta} \hat{S} \quad (1)$$

In Equation (1) the thin-layer approximation is used and restrictions for axisymmetric flow (with or without spin) are imposed. The vector  $\hat{q}$  contains all the dependent variables i.e.,  $\hat{q} = (\rho, \rho u, \rho v, \rho w, e)^T$ . The transformed flux vectors  $\hat{E}$  and  $\hat{G}$  are linear combinations of the Cartesian flux vectors, e.g.,  $\hat{E} = (\xi_x F + \xi_z G)/J$  where  $J$  is the Jacobian of transformation. The source term  $\hat{H}$  results from assuming invariance in the azimuthal direction while viscous terms are contained in the vector  $\hat{S}$ .

The numerical algorithm used is the Beam-Warming fully implicit, approximately factored finite difference scheme. The algorithm can be first or second order accurate in time and second or fourth order accurate in space. Since the interest is only in the steady-state solution, Equation (1) is solved in a time asymptotic fashion and first order accurate time differencing is used. The spatial accuracy is fourth order. Details of the algorithm are included in References [14-16]. For the computation of turbulent flows a turbulence model must be supplied. In the present calculations a two layer algebraic eddy viscosity model by Baldwin and Lomax [17] is used. In their two layer model the inner region follows the Prandtl-Van Driest formulation. Their outer formulation can be used in wakes as well as in attached and separated boundary layers.

## METHOD OF SOLUTION

The procedure used to compute the base flow for projectile configuration has been described in Reference [12]; however, limited details will be repeated here for clarity. The code computes the full flow field (including the base region) of a projectile. Figure 1 shows a schematic illustration of the flow field segmentation used in this study for computational purposes. It shows the transformation of the physical domain into the computational domain and the details of the flow field segmentation procedure in both domains. This flow field segmentation procedure is equivalent to using multiple adjoining grids. An important advantage of this procedure lies in the preservation of the sharp corner at the base and allows easy blending of the computational meshes between the regions ABCD and AEFG. No approximation of the actual sharp corner at the base is made. Thus, realistic representation of the base is inherent in the current procedure.

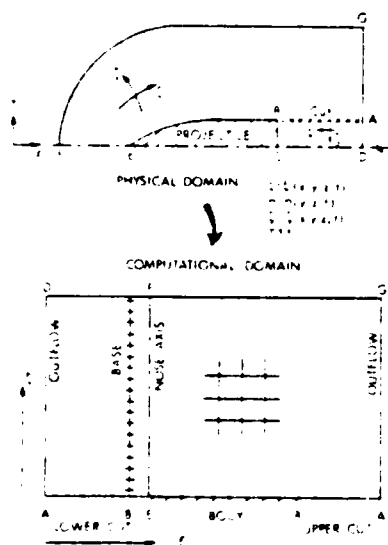


Figure 1. Schematic Illustration of Flow Field Segmentation

The cross hatched region represents the model. The line BC is the base and the region ABCD is the base region or the wake. The line AB is a computational cut through the physical wake region which acts as a repetitive boundary in the computational domain. Implicit integration is carried out in both  $\xi$  and  $\zeta$  directions (see Figure 1). Note the presence of the lines BC (base) and EF (nose axis) in the computational domain. They both act as boundaries in the computational domain and special care must be taken in inverting the block tridiagonal matrix in the  $\xi$  direction. The details of these can be found in References [12] and [13] and are not included here.

The no slip boundary condition for viscous flow is enforced by setting

$$U = V = W = 0 \quad (1)$$

on the body surface. At the base boundary, inviscid boundary condition has been used. Along the computational cut (AB), the flow variables above and below the cut are simply averaged to determine the boundary conditions on the cut. On the centerline of the wake region, a symmetry condition is imposed and free stream conditions are used on the outer boundary. The detailed boundary conditions for base flow with base bleed and jet exhaust can be found in References [13] and [18] respectively.

### COMPUTATIONAL GRID

Figure 2 shows an expanded view of the computational grid near the model. This grid was obtained in two segments consistent with the flow field segmentation procedure described earlier. The first segment of the computational mesh is for region AEFG (see Figure 1) and was obtained from a grid generation program developed by Steger, et al [19]. The grid for the second segment, region ABCD, was obtained by another procedure to be described later in this section. The grid generation program by Steger, et al [19] allows arbitrary grid point clustering, thus enabling grid points for the projectiles to be clustered in the vicinity of the body surface. The grid consists of 108 points in the longitudinal direction with 25 points in the base region and 40 points in the radial direction. The grid points in the normal direction were exponentially stretched away from the surface with a minimum spacing at the wall of .000020. This spacing locates at least two points within the laminar sublayer.

As stated earlier, the grid shown in Figure 2 was generated in two segments. First, the grid in the outer region AEFG is obtained using an elliptic solver [19] for the ogive portion and straight-line rays for the remaining portion which runs all the way to the downstream boundary. Second, the grid in the base region ABCD is obtained simply by extending the straight lines perpendicular to line AB down to the center line of symmetry (line CD). In other words, same grid stretching is used in the longitudinal direction in both the regions above and below the line AB. It remains then to generate the grid spacings in the normal direction in the base region ABCD. For base flow computations with and without base bleed, grid in the normal direction in base region was exponentially stretched. For base flow computations with a centered propulsive jet, it is desirable to cluster grid points near the cut to resolve the flow gradients in the shear layer as well as near the center line of symmetry where jet is present. Therefore, a 1-D elliptic equation solver was used to generate the grid spacings in the normal direction in the base region ABCD which maintains the minimum spacing desired at both these ends (see Figure 3). It should be noted that the same minimum spacing .000020 is specified on both sides of the cut thus maintaining a smooth variation of grid across the cut. This spacing could, of course, be increased downstream of the base. The number of grid points above and below line AB is the same (40 points). As can be seen in Figure 2, the grid points are clustered near the nose-cylinder junction and the projectile base where appreciable changes in flow variables are expected.

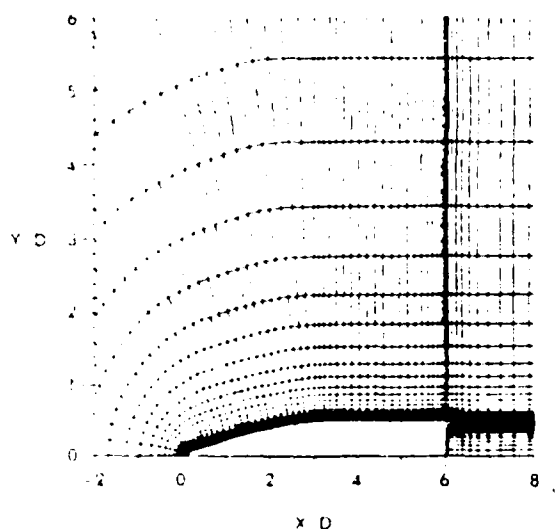


Figure 2. Expanded Grid in the Vicinity of the Projectile

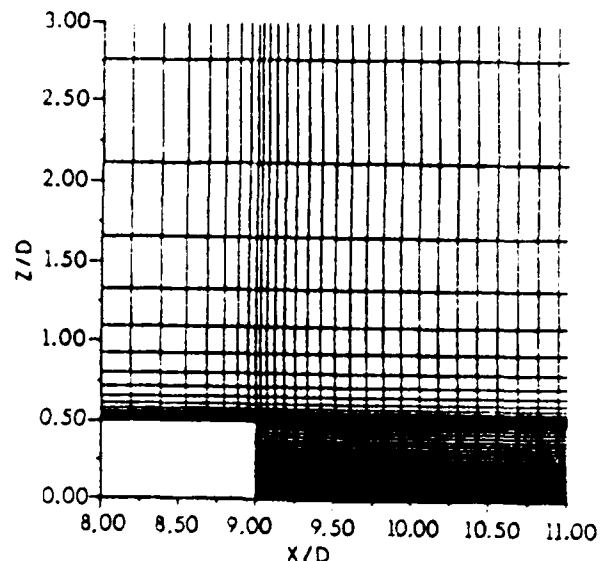


Figure 3. Expanded Grid for the Isolated Base Region Flow Field Computations

## RESULTS

The model geometry used for base flow computations with and without base bleed is shown in Figure 4. It consists of a 3 caliber secant-ogive nose and a 3 caliber cylinder. Figure 5 is a schematic illustration of the base region flow field and shows the important features of the flow field in the near wake. Results are presented in two sections, first for base flow without and with base bleed and second, for base flow in the presence of a centered propulsive jet.

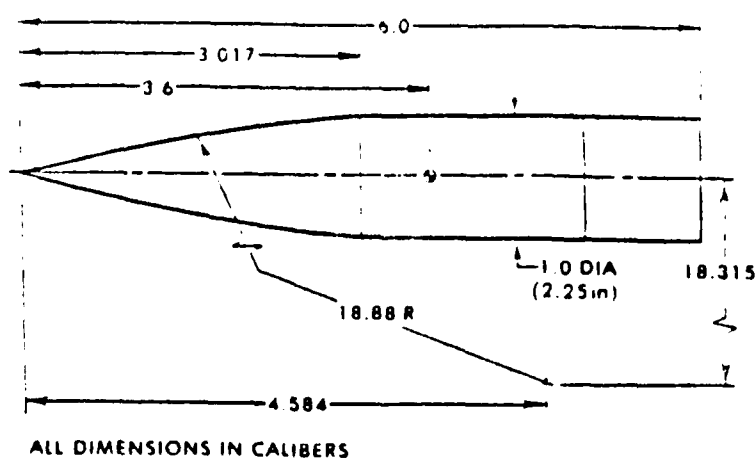


Figure 4. Model Geometry

### Base Flow without and with Base Bleed:

Figure 6 shows the velocity vector field in the base region for  $M = 0.9$ ,  $\alpha = 0$  and  $I = 0$ . Each vector shows the magnitude and the direction of the velocity at that point. The figure shows the velocity field when there is no base bleed and the recirculatory flow in the base region is clearly evident. The velocity vector plot in Figure 7 shows the effect of base bleed on the near wake flow field. It shows the effect of base bleed for a

mass injection parameter of .13. The flow field in the base region has now been dramatically altered. The recirculation pattern has been totally swept downstream.

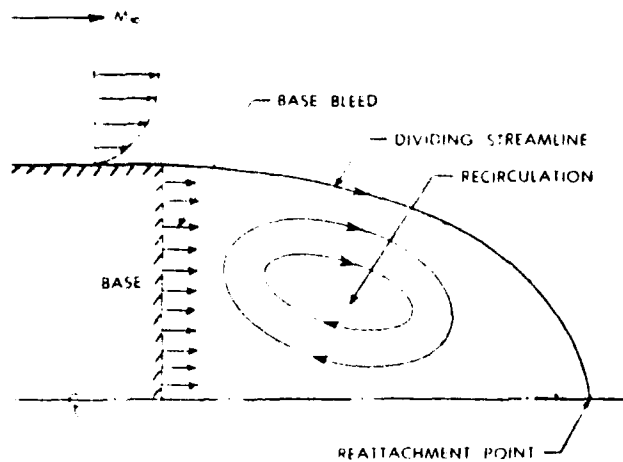


Figure 5. Schematic Illustration of Base Region Flow Field

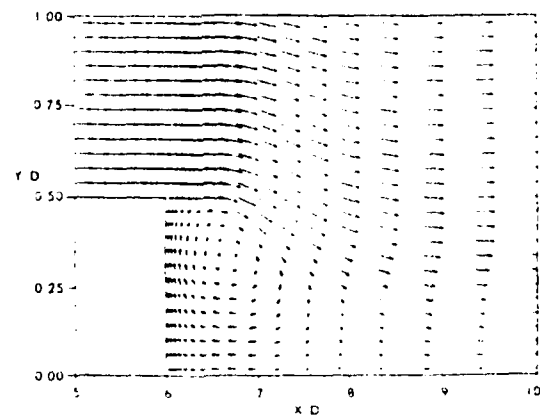


Figure 6. Velocity Vector Field,  $M = 0.9$ ,  $\alpha = 0$ ,  $I = 0$

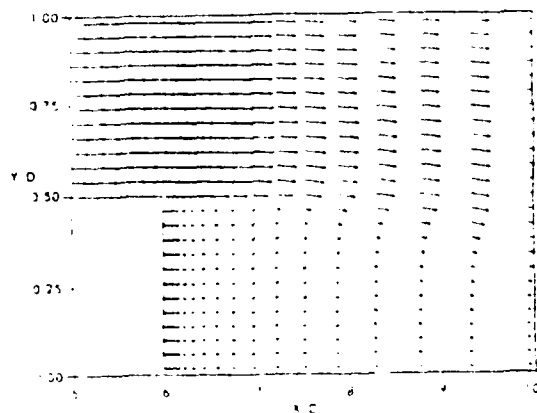


Figure 7. Velocity Vector Field,  $M = 0.9$ ,  $\alpha = 0$ ,  $I = .13$

The next two Figures 8 and 9 are stream function contour plots in the wake region, again for  $M = 0.9$  and  $\alpha = 0$ . These figures are deliberately stretched in  $y$  direction (not drawn to the same scale in  $x$  and  $y$ ) to show the flow pattern in the base region as clearly as possible. Figure 8 is for the case of base flow with no mass injection at the base. It clearly shows the recirculation region and the position of the dividing streamline which separates the recirculatory base flow from the main flow. The reattachment point is about 2 calibers down from the base. Note the strong shear layer in the base region.

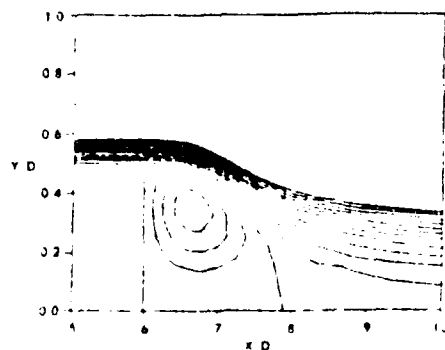


Figure 8. Stream Function Contours,  $M = 0.9$ ,  $\alpha = 0$ ,  $I = 0$

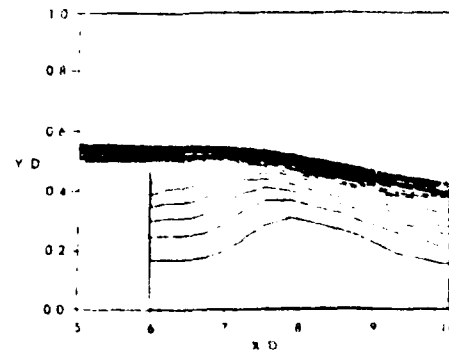


Figure 9. Stream Function Contours,  $M = 0.9$ ,  $\alpha = 0$ ,  $I = .13$

Figure 9 shows the effect of base bleed when the mass injection parameter is .13. The flow pattern in the near wake flow field has changed considerably. The recirculation region has been eliminated and the shear layer has been displaced markedly.

A more critical check of the computational results is presented in Figure 10 where base drag is plotted as a function of Mach number. Computational results are indicated by circles, experimental results [20] by triangles, the results obtained using a semi-empirical technique developed in McCoy [21] by squares and data base results [22] by diamonds. The results from data base are based on correlation of base pressures obtained from a number of experiments and other analytical techniques. Base drag, as expected, increased as the Mach number increases from 0.9 to 1.2. The semi-empirical technique shows generally higher base drag when compared with computational and experimental results. The computational results predict the expected drag rise that occurs from  $0.9 < M < 1.2$ . The computational results, however, indicate a greater increase in drag than predicted by either the semi-empirical code or the experimental measurements. The agreement between the computational and data base results is very satisfactory.

Since the entire projectile flow field, including the base flow, has been computed, all three drag components have been computed and thus the total drag determined. Figure 11 shows the variation of the total aerodynamic drag with Mach number. The total drag, as expected, increases as Mach number increases from 0.9 to 1.2. The computational results are compared with the results obtained by semi-empirical technique and are in satisfactory agreement.

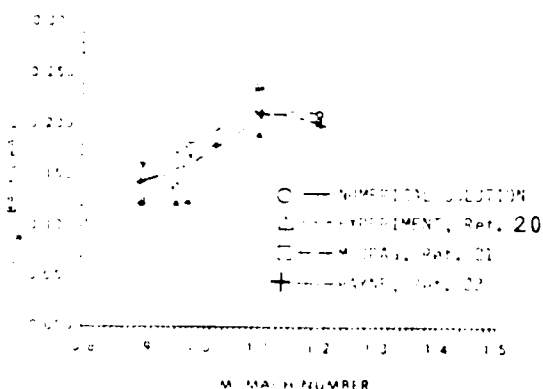


Figure 10. Variation of Base Drag Coefficient with Mach Number,  $\alpha = 0$

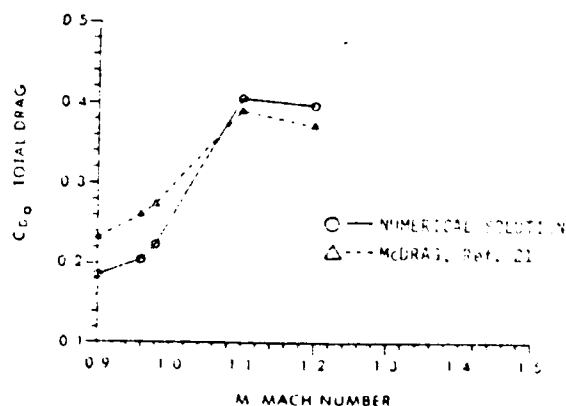


Figure 11. Variation of Total Drag Coefficient with Mach Number,  $\alpha = 0$

Another critical look at the computational results is presented in Figures 12 and 13. These figures show the quantitative details of base region flow field with base bleed. Figure 12 shows the variation of base drag with mass injection rates for  $M = 0.9$  and  $\alpha = 0$ . The reduction in base drag with base injection can be seen clearly. The percent reduction in base drag increases with the increase in the injection rate. Figure 13 shows the variation of base drag with Mach number both with and without base injection. In this

Figure the computational results without injection at the base are shown by the solid line whereas the dotted line represent the computational results obtained with injection at the base. The reduction in base drag with base injection can be clearly seen. Figure 13 indicates that the percent reduction in base drag has increased with an increase in Mach number from .9 to .98. The expected drag rise in the transonic speed regime is well predicted for  $.9 < M < 1.2$  and the reduction in base drag and the total drag, due to base bleed has been clearly demonstrated.

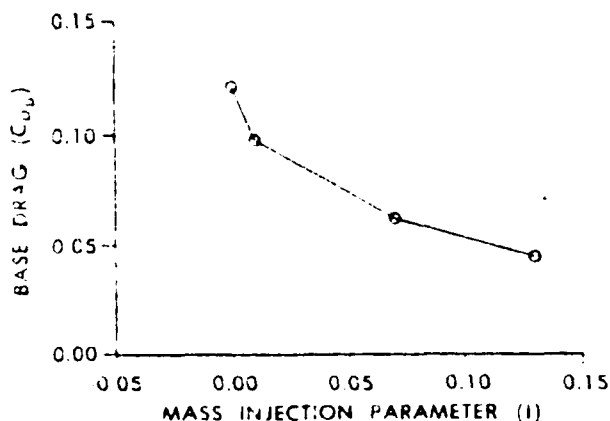


Figure 12. Variation of Base Drag Coefficient with Base bleed,  $M = 0.9$ ,  $\alpha = 0$

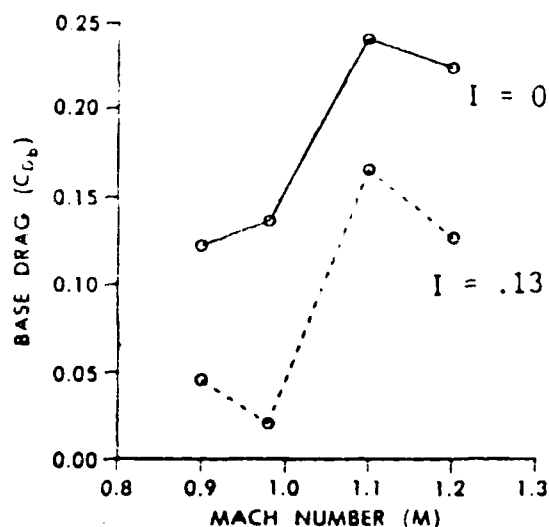


Figure 13. Variation of Base Drag Coefficient with Mach Number,  $\alpha = 0$  (with and without Base Bleed)

#### Base Flow with a Centered Propulsive Jet:

Computations for a missile configuration have also been made in the presence of a centered propulsive jet at  $M = 1.343$ . The model geometry for this case is shown in Figure 14. It consists of a 4 caliber tangent-ogive nose and a 5 caliber cylindrical afterbody. The base diameter is 1 caliber and the nozzle exit diameter is 0.2 caliber. The experimental model was side-wall mounted in AEDC Wind Tunnel [23] as shown in the Figure. The detailed computational results for this model can be found in Reference [18].

Results are now presented for both jet-off and jet-on cases. Figure 15 shows the velocity vectors in the base region when there is no jet present. The recirculatory flow in the base region is clearly evident. Figure 16 shows the effect of the centered jet on the near wake flow field. The near wake flow field has changed considerably. The recirculation region has been reduced.

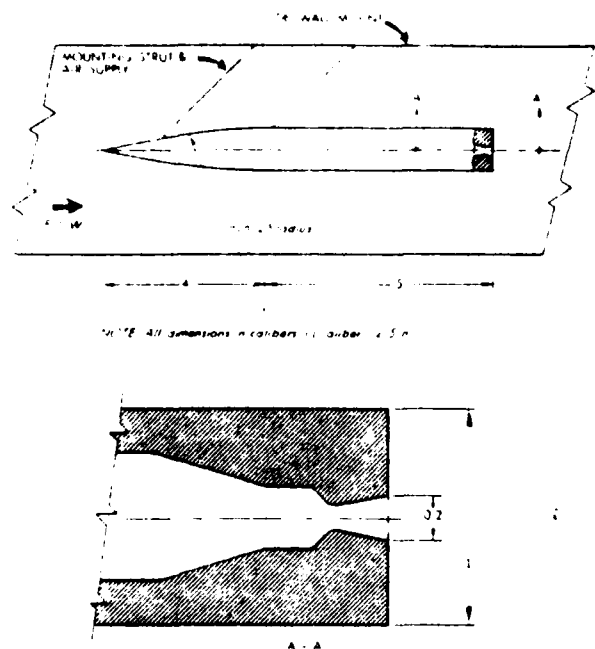


Figure 14. MICOM Base-Flow Model Mounted in the Wind Tunnel

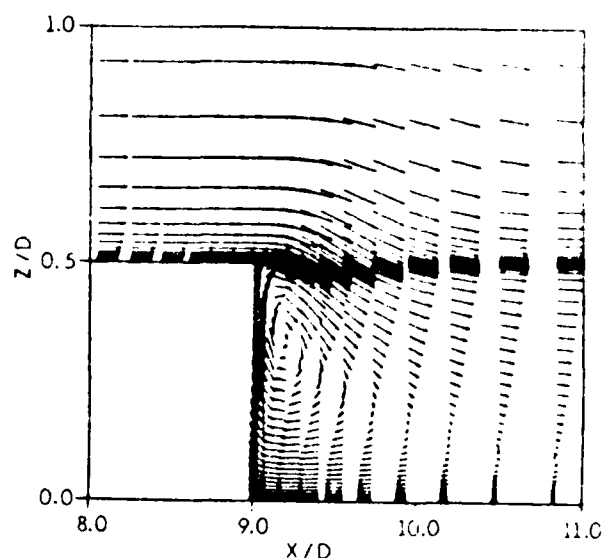


Figure 15. Velocity Vectors,  $M_{\infty} = 1.343$ ,  $\alpha = 0$ , Jet-Off

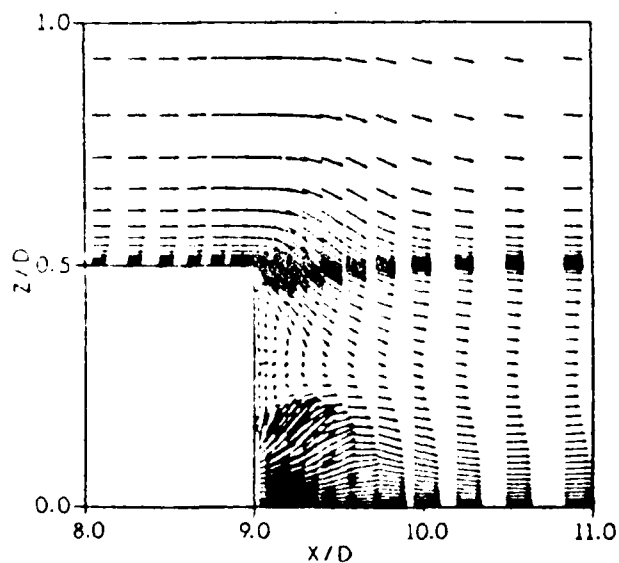


Figure 16. Velocity Vectors  $M_{\infty} = 1.343$ ,  $\alpha = 0$ , Jet-on

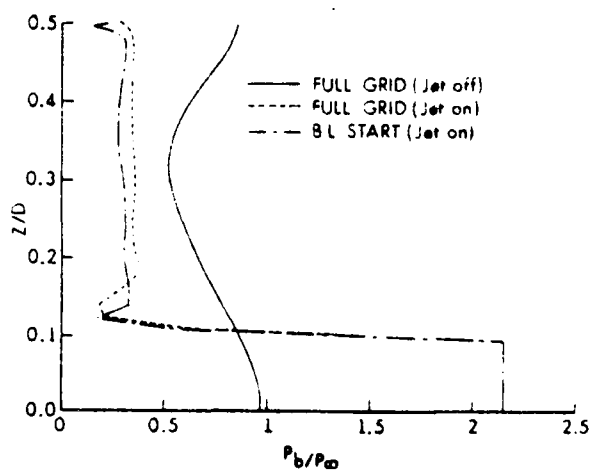


Figure 17. Variation of Base Pressure along the Base,  $M_{\infty} = 1.343$ ,  $\alpha = 0$ , Jet-off and Jet-on

Quantitatively, one is interested in how the complex flow field in the base region affects the base pressure. Figure 17 shows the variation of base pressure along the base for both jet-off and jet-on conditions. When there is no jet present, base pressure is high near the corner of the base. It decreases



gradually and then recovers to almost the free-stream static pressure near the center line of symmetry. The same grid used for jet-off computations was used for jet-on calculations. Additionally, to determine grid dependency on the solution, a large number of grid points were used in the base region and solutions were obtained for another grid. Both of these jet-on calculations give practically the same base pressure variation along the base. At the nozzle exit plane, the base pressure shown is the specified jet pressure. For the remaining portion of the base, the effect of the jet has been to reduce the base pressure. The small oscillations in the base pressure distribution along the base are located near the two corners, one at the base, and the other formed by the base boundary and the nozzle. These oscillations are not physical and are believed to be due to the numerical difficulties associated with the boundary conditions at these corners. The base pressure distribution in general however, is a realistic representation associated with the base region flow field.

### SUMMARY

A computational capability has been developed which computes full flow field over bodies of revolution including the base region. Additionally, the code allows computations of base flow with jet-on or base bleed.

Numerical computations have been made to predict the base drag both with and without base bleed for Mach numbers  $.9 < M < 1.2$ . The effect of mass injection in reducing the base drag has been clearly demonstrated. Solutions have also been obtained to show the effect of a centered propulsive jet on base flow at  $M = 1.343$ . Computed results in all cases show the qualitative details of the flow field in the base region.

### NOMENCLATURE

A	cross sectional area
$A_j$	injection area for base bleed
D	body diameter (57.15mm)
e	total energy per unit volume/ $\rho_\infty a_\infty^2$
I	mass injection parameter, $\dot{m}_j / \rho_\infty u_\infty A$
$\dot{m}_j$	mass flow rate for air injection at the base, $\rho_j u_j A_j$
M	Mach number
R	body radius
Re	Reynolds number, $\rho_\infty a_\infty D / \mu_\infty$
u, v, w	Cartesian velocity components/ $a_\infty$
U, V, W	Contravariant velocity components/ $a_\infty$
x, y, z	physical Cartesian coordinates
$\alpha$	angle of attack
$\xi, \eta, \zeta$	transformed coordinates in axial, circumferential and radial directions
$\rho$	density/ $\rho_\infty$
$\tau$	transformed time

Subscript:

- b base
- c jet conditions
- ∞ free stream conditions

REFERENCES

1. Sednev, R., "Review of Base Drag," U.S. Army Ballistic Research Laboratory, Aberdeen Proving Ground, Maryland, Report No. 1337, October 1966. (AD 808767)
2. "155mm ERFB Base Bleed Range and Precision Test," Conducted at Proff and Experimental Test Establishment, Nicolet, Quebec for Space Research Corporation, 11 January 1978.
3. Murthy, S. N. B. (Ed.), "Progress in Astronautics and Aeronautics: Aerodynamics of Base Combustion," Vol. 40, AIAA, New York, 1976.
4. Dickinson, E. R., "The Effectiveness of Base-Bleed in Reducing Drag of Boattailed Bodies at Supersonic Velocities," U.S. Army Ballistic Research Laboratory, Aberdeen Proving Ground, Maryland, ARBRL-MR-1244, 1960. (AD 234315)
5. Sykes, D. M., "Cylindrical and Boattailed Afterbodies in Transonic Flow with Gas Ejection," AIAA Journal, Vol. 8, No. 3, March 1970, pp. 588-589.
6. Diewert, G. S., "A Computational Investigation of Supersonic Axisymmetric Flow Over Boattails Containing a Centered Propulsive Jet," AIAA Paper No. 83-0462, January 10-13, 1983.
7. Weinberg, B. C., McDonald, H., and Shamroth, S. J., "Navier-Stokes Computations of Aft End Flow Fields," Final Report, Army Research Office Contract No. DAAG29-79-C-0003, May 1982.
8. Sullins, G. A., Anderson, J. D., and Drummond, J. P., "Numerical Investigation of Supersonic Base Flow with Parallel Injection," AIAA Paper No. 82-1001, June 1982.
9. Chow, W. L., Bober, L. J., and Angerson, B. H., "Strong Interaction Associated with Transonic Flow Past Boattails," AIAA Journal, Vol. 13, No. 1, 1975, pp. 112-113.
10. Nietubicz, C. J., Pulliam, T. H., and Steger, J. L., "Numerical Solution of the Azimuthal-Invariant Thin-Layer Navier-Stokes Equations," U.S. Army Ballistic Research Laboratory, Aberdeen Proving Ground, Maryland, ARBRL-TR-02227, March 1980. (AD A085716) (Also see AIAA Journal, Vol. 18, No. 12, December 1980).
11. Nietubicz, C. J., "Navier-Stokes Computations for Conventional and Hollow Projectile Shapes at Transonic Velocities," U.S. Army Ballistic Research Laboratory, Aberdeen Proving Ground, Maryland, ARBRL-MR-03184, July 1982. (AD A116866) (Also see AIAA Paper No. 81-1262, June 1981).

# REFERENCES (cont'd)

12. Sahu, J., Nietubicz, C. J., and Steger, J. L., "Numerical Computation of Base Flow for a Projectile at Transonic Speeds," U.S. Army Ballistic Research Laboratory, Aberdeen Proving Ground, Maryland, ARBRL-TR-02495, June 1983. (AD A130293) (Also see AIAA Paper No. 82-1358, August 1982).
13. Sahu, J., Nietubicz, C. J., and Steger, J. L., "Navier-Stokes Computations of Projectile Base Flow with and without Base Injection," U.S. Army Ballistic Research Laboratory, Aberdeen Proving Ground, Maryland, ARBRL-TR-02532, November 1983. (Also see AIAA Paper No. 83-0224, January 1983).
14. Beam, R., and Warming, R. F., "An Implicit Factored Scheme for the Compressible Navier-Stokes Equations," AIAA Journal, Vol. 16, No. 4, April 1978, pp. 393-402.
15. Steger, J. L., "Implicit Finite Difference Simulation of Flow About Arbitrary Geometries with Application to Airfoils," AIAA Journal, Vol. 16, No. 4, July 1978, pp. 679-686.
16. Pulliam, T. H., and Steger, J. L., "On Implicit Finite-Difference Simulations of Three-Dimensional Flow," AIAA Journal, Vol. 18, No. 2, February 1980, pp. 159-167.
17. Baldwin, B. S., and Lomax, H., "Thin-Layer Approximation and Algebraic Model for Separated Turbulent Flows," AIAA Paper No. 78-257, 1978.
18. Sahu, J. and Nietubicz, C. J., "Numerical Computation of Base Flow for a Missile in the Presence of a Centered Jet," AIAA Paper No. 84-0527, January 1984.
19. Steger, J. L., Nietubicz, C. J., and Heavey, K. R., "A General Curvilinear Grid Generation Program for Projectile Configurations," U.S. Army Ballistic Research Laboratory, Aberdeen Proving Ground, Maryland, ARBRL-MR-03142 October 1981. (AD A107334)
20. Kayser, L. D., "private communications", Ballistic Research Laboratory, Aberdeen Proving Ground, Maryland 21005. (being published as a BRL report).
21. McCoy, R. L., "McDrag - A Computer Program for Estimating the Drag Coefficients of Projectiles," U.S. Army Ballistic Research Laboratory, Aberdeen Proving Ground, Maryland, ARBRL-TR-02293, February 1981. (AD A098110)
22. Payne, P. R., and Hartley, R. M., "Afterbody Drag, Volume 1 - Drag of Conical and Circular Arc Afterbodies without Jet Flow," Final Report, DTNSRDC/ASED-80/10, Bethesda, Maryland, May 1980.
23. Walker, B. J., "Tactical Missile Base Flow," Paper presented at Symposium on Rocket/Plume Fluid Dynamic Interactions, Huntsville, Alabama, April 1983.

## LIST OF PARTICIPATES

Dr. G. Gregoriou  
Messerschmitt-Bolkow-Bloha  
Ottobrunn/Muchen  
Federal Republic of Germany

Dr. H.U. Meier  
DFVLR SM-ES  
Bunsenstr. 10  
3400 Gottingen  
Federal Republic of Germany

Dr. W. Stahl  
DFVLR Gottingen  
Bunsenstr. 10  
3400 Gottingen  
Federal Republic of Germany

Dr. Hans W. Stock  
Dornier GmbH  
Theoretical Aerodynamics  
799 Friedriethshafen Post Box 1420  
Federal Republic of Germany

Dr. Anthony Agnone  
N.Y. University  
Antonio Ferri Laboratories  
425 Merrick Ave.  
Westbury, NY 11590

Dr. John E. Allen  
US Naval Academy  
Aerospace Engineering Dept.  
Annapolis, MD 21402

Dr. Hugh W. Coleman  
Mechanical Engineering Department  
Mississippi State University  
Mississippi State, Mississippi 39762

Dr. Anthony W. Fiore  
Flight Dynamics Laboratory  
AFWAL/FIMG  
Wright-Patterson AFB, OH 45433

Dr. J. Gillerlain  
Mechanical Engineering Dept.  
U.S. Navy Academy  
Annapolis, Maryland 21402

Dr. G.R. Inger  
University of West Virginia  
Dept. Of Mech. & Aerospace Engr.  
Morgantown, West Virginia 26506

Dr. Hans Lugt  
David W. Taylor Naval Ship R&D Center  
Bethesda, Maryland 20084

J. Douglas McLean  
The Boeing Company  
P.O. Box 3707, MS 3N-19  
Seattle, Washington 98124

C.J. Nietwbicz  
U.S. Army Ballistic Research Laboratory  
ARRADCOM  
Aberdeen Proving Ground, MD 21005

Lionel Pasiuk  
Code SEA, 62R41  
Naval Sea Systems Command  
Washington, DC 20363

J. Sahu  
U.S. Army Ballistic Research Laboratory  
ARRADCOM  
Aberdeen Proving Ground, MD 21005

Dr. Joseph A. Schetz  
Virginia Polytechnic Institute  
and State University  
Blacksburg, Virginia 24061

Dr. Joanna Schot  
David Taylor Naval Ship R&D Center  
Numerical Mechanics Division  
Code 184  
Bethesda, Maryland 20084

Dr. Kenneth Stetson  
Flight Dynamics Laboratory  
Wright-Patterson AFB, OH 45433

Dr. W. B. Sturek  
U.S. Army Ballistic Research Laboratory  
ARRADCOM  
Aberdeen Proving Ground, MD 21005

LIST OF PARTICIPANTS (CONT'D)

Dr. P.S. Granville  
David Taylor Naval Ship R&D Center  
Code 1540  
Bethesda, Maryland 20084

Dr. B.K. Hodge  
Mechanical Engineering Dept.  
Mississippi State University  
Mississippi State, Mississippi 39762

Dale Hutchines  
Code AIR, 311-C  
Naval Air Systems Command  
Washington, DC 20362

Donald W. Ausherman  
Aerodynamics Branch (K24)  
NSWC/WD

Dr. W.J. Glowacki  
Applied Mathematics Branch (R44)  
NSWC/WD

J.A. F. Hill  
Aerodynamics Branch (K24)  
NSWC/WD

Dr. R.U. Jettmar  
Applied Mathematics Branch (R44)  
NSWC/WD

Dr. F. Moore  
Aeromechanics Branch (K21)  
NSWC/DL

Dr. William Ragsdale  
Aerodynamics Branch (K24)  
NSWC/WD

Dr. A.H. Van Tuyl  
Applied Mathematics Branch (R44)  
NSWC/WD

Dr. Drew Wardlow  
Applied Mathematics Branch (R44)  
NSWC/WD

Dr. T. F. Zien  
Applied Mathematics Branch (R44)  
NSWC/WD

Dr. T.C. Tai  
David W. Taylor Naval Ship R&D Center  
Bethesda, Maryland 20084

Dr. Robert P. Taylor, Jr  
Mechanical Engineering Dept.  
Mississippi State University  
Mississippi State, Mississippi 39762

Dr. Floyd G. Howard  
Fluid Mechanics Branch  
MS 163  
NASA Langley Research Center  
Hampton, Virginia 23300

Dr. K.-Y. Chien  
Applied Mathematics Branch (R44)  
NSWC/WD

E. Hedlund  
Aerodynamics Branch (K24)  
NSWC/WD

Dr. T. Hsieh  
Applied Mathematics Branch (R44)  
NSWC/WD

Dr. M. Kruains  
Aerodynamics Branch (K24)  
NSWC/WD

F. Priolo  
Applied Mathematics Branch (R44)  
NSWC/WD

Dr. J.M. Solomon  
Applied Mathematics Branch (R44)  
NSWC/WD

Robert L.P. Voisinot  
Aerodynamics Branch (K24)  
NSWC/WD

Dr. William J. Yanta  
Aerodynamics Branch (K24)  
NSWC/WD

**END**

**FILMED**

**5-85**

**DTIC**